THE UNIVERSITY *of* EDINBURGH

This thesis has been submitted in fulfilment of the requirements for a postgraduate degree (e. g. PhD, MPhil, DClinPsychol) at the University of Edinburgh. Please note the following terms and conditions of use:

- This work is protected by copyright and other intellectual property rights, which are retained by the thesis author, unless otherwise stated.
- A copy can be downloaded for personal non-commercial research or study, without prior permission or charge.
- This thesis cannot be reproduced or quoted extensively from without first obtaining permission in writing from the author.
- The content must not be changed in any way or sold commercially in any format or medium without the formal permission of the author.
- When referring to this work, full bibliographic details including the author, title, awarding institution and date of the thesis must be given.

Classification and Quantification of Uncertainties for a Tidal Turbine Power Performance Assessment

Luke Evans

Doctor of Engineering

THE UNIVERSITY OF EDINBURGH

2023

An IDCORE - EMEC Project

Author: Luke Evans

Supervisors: Dr B. G. Sellar, Dr I. G. C. Ashton, Dr L. Jia.

University of Edinburgh, Exeter University, Strathclyde University.

A thesis submitted in partial fulfilment of the requirements for the award of an Engineering Doctorate

August 31st, 2023

Quote

"*So what do we do? Anything. Something. So long as we just don't sit there. If we screw it up, start over. Try something else. If we wait until we've satisfied all the uncertainties, it may be too late*." – Lee Iacocca.

"Information is the resolution of uncertainty." Claude Shannon.

IDCORE

This thesis is submitted in partial fulfilment of the requirements for the award of an Engineering Doctorate, jointly awarded by the University of Edinburgh, the University of Exeter, and the University of Strathclyde. The work presented has been conducted as a part of the research component of the Industrial Doctoral Centre for Offshore Renewable Energy (IDCORE) programme and was sponsored by the European Marine Energy Centre (EMEC).

University of Exeter

University of Strathclyde Glasgow

Abstract

As part of the worldwide initiative to lower carbon emissions, renewable energy sources are playing a crucial role in decarbonising our energy systems. Tidal energy, known for its reliability and predictability, is emerging as a contributor to the expanding array of renewable energy sources. As the tidal industry advances towards commercialisation and larger arrays reducing uncertainties is increasingly important.

Uncertainties around power production increase commercial risk. This thesis classifies and quantifies uncertainties in Power Performance Assessments (PPAs) and offers guidance for future deployments. It examines uncertainties arising from data processing and flow variations, using in-situ measurements obtained from Acoustic Doppler Current Profilers (ADCPs) situated in close proximity to an operational Tidal Energy Converter (TEC) . At present developers often follow guidance from International Electrotechnical commission (IEC) Technical Specification 62600-200, that provides recommended positioning of instruments relative to the turbine of two types: *in-line* and *adjacent*, where *in-line* involves deploying separate instruments upstream and downstream of the turbine, and adjacent involves placing an instrument to either side of the turbine, across the rotor plane.

The performance of two closely-located *in-line* ADCPs (spaced 45 m apart) was assessed, demonstrating their ability to gather usable data in this layout. However, this work identified for the first time interference between the ADCPs throughout the campaign and quantified subsequent impact on Annual Energy Prediction (AEP) estimates. A method to remove data anomalies caused by interference between closely positioned ADCPs has been developed and demonstrated, resulting in a 7% variation in estimated AEP.

It was found that instrument placement is critical. Whilst small differences in velocity were found for *in-line* ADCPs, for *adjacent* ADCPs an uncertainty in AEP of 2.6% and 7.3% was measured for flood and ebb tides respectively. Where the difference stems from flow structures causing measurement bias during the ebb tide. Results show that for regions of high vertical shear, AEP estimates can be misrepresented by up to 2.3% and 5.5% under an imposed vertical misalignment of 1 and 2 metres respectively.

TEC developers require knowledge of flow direction to design and operate turbines. A study on methods to estimate characteristic flow directions found variation in direction of 1.2° when averages across the rotor plane were considered and, 4° when only operational velocities were considered. The flow direction naturally evolves over a tidal cycle resulting in non-yawing (nacelle rotation mechanism) TEC concepts being susceptible to off-axis currents. A sensitivity study to misalignment was conducted and under 5°, 10° and 15° misalignment, the AEP differed by 2%, 6% and 13% respectively.

The work highlights that the impact of TEC misalignment on AEP estimates is influenced by the rated velocity of the TEC and the maximum velocity at the site, particularly affecting TECs rated close to or over the maximum flow velocity. However, the work highlights that non-yawing TECs rated at least 10% below the maximum flow velocity can still operate at full capacity even with a 25° misalignment. During periods of slow speeds (tidal velocities at the Fall of Warness were found to exhibit a difference of approximately 30% between neap and spring tides) misalignment is shown to become more important.

The methodology of uncertainty analysis demonstrated in this thesis gives comprehensive instructions for PPA of tidal devices, including instrument setup, data processing and accurate uncertainty estimates. Recognising and dealing with uncertainties in measurements remains vital for tidal energy projects. By adopting the methods outlined in this work, data integrity, accuracy, and dependability can be enhanced, resulting in better decision-making, improved evaluations of performance, and heightened investor trust within the tidal energy sector.

Lay Summary

As people all around the world strive to reduce the amount of pollution caused by carbon emissions, renewable energy sources are stepping up to help clean up our energy systems. Tidal energy, known for its reliability and predictability, is emerging as a contributor to the expanding array of renewable energy sources. As the tidal industry advances towards commercialisation and larger arrays reducing uncertainties is increasingly important.

Uncertainties in power production pose commercial risks. This thesis focuses on measuring uncertainties - by comparing differences among simultaneous sets of data - in power performance assessments for tidal energy deployments. It analyses uncertainties arising from data processing and flow variations using real measurements obtained from specialised instruments - known as acoustic Doppler current profilers - placed near operational tidal energy converters.

Current industry guidelines recommend two types of instrument placements for the purpose of power performance assessments: *in-line*, involving instruments upstream and downstream of the turbine, and *adjacent*, placing instruments on either side of the turbine. I examined two closely-located acoustic instruments and discovered for the first time from this data set a bias in the current flow data commonly related to acoustic interference. I developed an algorithm to identify and remove features of acoustic interference, thus providing an accurate estimate of energy production.

This work has demonstrated how turbine performance metrics are sensitive to the flow reference (placement of an ADCP relative to a tidal turbine) used. Specifically examining seabed acoustic instruments, a noticeable difference in the flow reference was evident among five instruments positioned in close proximity to an operational tidal turbine - with the most substantial variation observed among adjacent instruments. This occurrence isn't attributed to a flaw in the instrument itself but rather stems from the spatial and temporal influences within the tidal site.

Subsequently, I found that misrepresenting the alignment of the acoustic instrument and tidal turbine during data post-processing led to a notable difference in energy estimates, with the most notable variation seen in areas of pronounced vertical shear.

I have investigated techniques to assess flow directions, highlighting their variability and consequent impact on estimates of power and energy. For tidal turbines incapable of adapting to flow direction changes, natural tidal flow fluctuations hold substantial relevance. Particularly, instances such as slow water movement coupled with a misalignment between the rotor extraction plane and the principle flow direction.

The methods developed in this thesis have introduced a detailed way to analyse uncertainties in tidal energy projects. It provided clear steps for handling uncertainties in areas like instrument placement, data post-processing, and including relevant uncertainties that are understood to exist but are not fully characterised or quantified. Recognising and addressing uncertainties is still crucial in tidal energy projects. By following the methods described in the study, the quality of data can be improved, leading to better decisions, more accurate performance evaluations, and increased trust from investors in the tidal energy field.

Acknowledgements

I would like to thank the following people for their input through this EngD experience:

At the start of the EngD, I was fortunate to get sponsored by EMEC, which truly stood out as an innovative company. Naturally, given the project's unformed nature at the start of the EngD, it was fitting that the project scope centred around uncertainty. I had the privilege of engaging in enlightening conversations with David Darbinyan, Brian Sellar, and Ian Ashton upon starting the EngD. It was during these discussions that the project took shape, as we explored novel ideas and aimed to address industry-related challenges.

Dr. Brian Sellar and Dr. Ian Ashton played pivotal roles as dependable and unwavering sources of guidance and support throughout the course of the research. Their expertise and commitment were complemented by the IDCORE academic supervisory team, who collectively provided invaluable insights and mentorship that significantly enriched my research journey.

The camaraderie and encouragement extended by the members of the 2019 IDCORE cohort were truly indispensable throughout my academic journey. Shared experiences and mutual motivation created a positive and uplifting atmosphere that enhanced both my personal and academic growth. Through collaborative learning, open discussions, and shared challenges, we formed strong bonds that transcended the academic setting. I am immensely grateful for the friendships forged and the encouragement received from the 2019 IDCORE cohort.

Throughout the research journey, the persistent support of my family and friends was a constant source of strength. I would like to extend special gratitude to my brother, Daniel, and my father, Thomas, for their consistent words of encouragement and motivation during the crucial final year of my research.

I extend heartfelt gratitude to Alyona Naberezhnykh for her unwavering support, from the very beginning to the completion of this journey, serving as a true source of inspiration. The memories forged, from enduring a coronavirus lockdown, embarking on new adventures, and living on a windswept rock are truly unforgettable.

EMEC's guidance and resources have played an integral role in my comprehensive exploration of tidal energy and its potential applications since the inception of my research. As I conclude my EngD journey, I proudly recognise EMEC's pivotal contribution to my academic and personal growth. Their constant commitment to advancing marine renewable energies has ignited a passion within me for a career dedicated to sustainability and environmental preservation.

Completing this journey would not have been possible without the collective efforts, knowledge, and support of all these individuals and entities. I am truly fortunate to have had such remarkable people by my side, and I extend my heartfelt thanks to each and every one of you.

Funding is gratefully acknowledged: Engineering & Physical Sciences Research Council (EPSRC) and Natural Environment Research Council (NERC) for the Industrial CDT in Offshore Renewable Energy (EP/S023933/1) and sponsored by EMEC.

Declaration

I declare that this thesis was composed by myself, that the work contained herein is my own except where explicitly stated otherwise in the text, and that this work has not been submitted for any other degree or professional qualification except as specified.

Luke Evans

Contents

Abstract v

Lay Summary vii

Acknowledgements viii

Declaration ix

Figures and Tables xiv

Nomenclature xxiv

List of Acronyms 1

1 Introduction 2
- 1.1 Global Context for Renewable Energy . . . 2
- 1.2 Renewable Energy from the Marine Environment . . . 4
  - 1.2.1 Tidal Stream Energy . . . 5
- 1.3 Uncertainty in the Tidal Stream Energy Sector . . . 6
  - 1.3.1 Tidal Energy Converter Power Performance . . . 6
- 1.4 Research Motivation . . . 7
- 1.5 Knowledge Gaps . . . 8
- 1.6 Research Aims and Objectives . . . 9
- 1.7 Thesis Structure . . . 9

2 Theory 11
- 2.1 Chapter Overview . . . 11
- 2.2 Theory of Tides . . . 11
  - 2.2.1 Astronomical and Non-Harmonic Tidal Forces . . . 11
  - 2.2.2 Type of Tidal Stream Site . . . 13
- 2.3 Measurement of Tidal Stream Resource . . . 15
  - 2.3.1 Site Characterisation: Field Instrumentation . . . 18
  - 2.3.2 Acoustic Doppler Technology . . . 20
  - 2.3.3 Cross-talk Between Acoustic Instruments In Close Proximity . . . 29
  - 2.3.4 Tidal Stream Environment . . . 31
- 2.4 Exploitation of Tidal Stream Energy . . . 33
  - 2.4.1 Introduction to Tidal Stream Turbine Devices . . . 33
  - 2.4.2 Horizontal Axis Turbine Physics . . . 35
- 2.5 Uncertainty Theory . . . 37
  - 2.5.1 Term Definition . . . 39
  - 2.5.2 Common Sources of Uncertainty . . . 46

2.5.3 Propagation of Uncertainty . . . 47
2.6 Uncertainty Analysis Methods . . . 50
2.6.1 Sensitivity Studies . . . 50
2.6.2 Analysis of Residuals . . . 51
2.6.3 Jack-Knife Method . . . 52
2.6.4 Monte Carlo Analysis . . . 53
2.6.5 Guide to the Expression of Uncertainty in Measurement: ISO-GUM . . . 54
2.7 Power Performance Assessment for Tidal Energy Converters . . . 56
2.8 Summary of Theory in the Context of the Thesis . . . 60

3 State of the Art Review - In-situ measurements and Tidal Devices 61
3.1 Chapter Overview . . . 61
3.2 Tidal Energy Site Measurement Campaigns . . . 61
3.2.1 ADCP: Design Considerations . . . 62
3.2.2 ADCP: Mounting Solutions . . . 65
3.2.3 ADCP: Hardware, Software and Configuration . . . 73
3.2.4 Quality Assurance of Real-Time Oceanographic Data: QARTOD . . . 74
3.3 Tidal Energy Site Exploitation Devices . . . 75
3.3.1 Seabed fixed: Surface Piercing TEC Concepts . . . 75
3.3.2 Seabed fixed: Gravity Based TEC Concepts . . . 76
3.3.3 Sea Surface: Floating TEC Concepts . . . 77

4 Uncertainties in the power Performance Assessment 82
4.1 Chapter Overview . . . 82
4.2 Power Performance Assessment as per IEC . . . 82
4.2.1 Relevant Guidance and Standards for Tidal Energy . . . 83
4.3 Comparison of Wind and Tidal Energy Performance Methodology . . . 90
4.3.1 Wind Energy Measurement Campaign Procedure . . . 92
4.3.2 Tidal Energy Measurement Campaign Procedure . . . 94
4.3.3 Resource and Power Performance Procedure Analogies . . . 98
4.3.4 Uncertainty Categorisation: Knowledge Exchange from the Wind Sector . . . 99
4.3.5 ADCP specific guidance: Measured Power Curve . . . 102
4.4 Sources of Uncertainty . . . 104
4.4.1 Sensor Characteristics and Performance . . . 107
4.4.2 Data Quality Control . . . 110
4.4.3 Spatial and temporal scales of heterogeneity in tidal stream sites . . . 110
4.5 Summary and elements carried forward in this Thesis . . . 116

5 Full-Scale Turbine Data and Proximal Flow Data (ReDAPT data set) 119
5.1 Chapter Overview . . . 119
5.2 Instrument Specification: Measurement campaign . . . 119
5.3 Instrument Specification: Location . . . 123
5.4 Data Post-Processing: Quality Control . . . 128
5.4.1 Seabed Placed Profilers . . . 128

5.4.2 Turbine Mounted Single Beam Profilers . . . 133
5.5 Instrument Uncertainty . . . 135
5.5.1 Electrical Test Equipment . . . 136
5.5.2 Uncertainty of Ancillary sensors . . . 138
5.5.3 Propagation of Uncertainty . . . 142
5.6 Turbine Specification: Operational Characteristics . . . 142
5.7 Turbine Specification: Power Curve . . . 144

6 Cross-talk Between Multiple Acoustic Instruments Measuring Concurrently 150
6.1 Chapter Overview . . . 150
6.2 Flood and Ebb Conditions . . . 151
6.3 Cross-talk - Data Featuring Interference Characteristics . . . 151
6.3.1 Data restrictions and quality control . . . 159
6.4 ADCP: Identification of Interference Features . . . 159
6.5 Interference Impact on the Measured Power Curve . . . 163
6.6 Post-processing data sets: Interference Detection Algorithm . . . 167
6.6.1 Data Treatment Post Interference Removal . . . 171
6.7 Discussion . . . 172
6.8 Conclusions . . . 175

7 Uncertainty in Power Estimates due to Spatial Variability in Flow Velocity 176
7.1 Chapter Overview . . . 176
7.2 Instrumentation Configuration and Deployment . . . 177
7.2.1 Horizontal Variation in the Measured Flow Velocity . . . 180
7.2.2 Vertical Variation in the Measured Flow Velocity . . . 186
7.2.3 Calculating Combined Uncertainties for Spatial variance in Velocity . . . 190
7.3 Discussion . . . 192
7.4 Conclusions . . . 194

8 Uncertainty in Power Estimates due to the Spatial Variability in Flow Direction 195
8.1 Chapter Overview . . . 195
8.2 Instrumentation Configuration and Deployment . . . 196
8.3 Horizontal Variation in the Measured Flow Direction . . . 196
8.3.1 Estimates of the established flow direction . . . 199
8.4 Impact of Misalignment on the Power Performance . . . 200
8.4.1 Axial Rotation Impact . . . 200
8.4.2 Power Performance Impact . . . 201
8.5 Consequence to Annual Energy Estimates . . . 202
8.6 Vertical Variation in the Measured Flow Direction . . . 204
8.7 Flow direction variation across tidal phases . . . 205
8.8 Discussion . . . 209
8.9 Conclusions . . . 211

9 Industry Recommendations, Research Contributions and Final Work Conclusions 212

9.1 Recommendations for Tidal PPAs . . . 212
9.1.1 Acoustic Doppler Measurement Uncertainty . . . 212
9.1.2 Estimation of Power Performance for a Tidal Device . . . 213
9.2 Research Contributions . . . 215
9.2.1 Key Findings . . . 215
9.2.2 Commercial Impact . . . 217
9.2.3 Future Work Recommendations . . . 217
9.3 Final Conclusions . . . 218

Bibliography **219**

10 Appendix for Chapter 5 **243**
10.1 DEEP-Gen IV Pre-defined Power Curve . . . 243

11 Appendix for Chapter 6 **245**
11.1 On the utility of partially corrupted flow measurement data arising from adjacent acoustic Doppler current profilers for energy yield assessment. . . . 245

12 Appendix for Chapter 7 **259**
12.1 Tidal turbine power performance assessments following IEC TS 62600-200 using measured and modelled power outputs . . . 259

13 Appendix for Chapter 8 **273**
13.1 Impact on Energy Yield of Varying Turbine Designs under Conditions of Misalignment to the Current Flow . . . 273

Figures and Tables

Figures

1.1 Annual total global CO2 emissions – from fossil and land-use change – between 1959 and 2022 for 2020, 2021 and 2022 versions of the Global Carbon Project's Global Carbon Budget, in billions of tonnes of CO2 per year (GtCO2). The shaded area shows the estimated one-sigma uncertainty for the 2022 budget. Data from the Global Carbon Project. . . . 3

2.1 Illustration of the effects of the gravitational forces of the Moon and Sun causing Spring and Neap tides. 12
2.2 Global variability in tidal patterns. . . . 13
2.3 Daily tide patterns. . . . 13
2.4 Illustrations of principal direction plots for both asymmetrical (left) and nearly symmetrical (right) sites. 14
2.5 Tidal flow velocities for the Pentland Firth and Fall of Warness generated through the utilisation of the MIKE 21 Flow model by the University of Edinburgh (UoE). . . . 15
2.6 Illustration of a tidal basin at Digby Gut in Nova Scotia, featuring estimated flow velocities (left) and corresponding Yellow maps (right). . . . 15
2.7 Iroise Sea model progression: a) Regional assessment, b) Site assessment pre-feasibility covering the Fromveur Strait and neighboring islands, c) Site assessment full-feasibility of the Fromveur Strait. 16
2.8 Orkney Islands model progression: a) Regional Assessment of the Orkney Islands, b) Site Assessment Pre-Feasibility encompassing the Fall of Warness and nearby islands, c) Site Assessment Full-Feasibility for the Fall of Warness. . . . 16
2.9 Example of a tide gauge from Valeport. . . . 18
2.10 Impeller mounted to a directional vane. . . . 18
2.11 Coordinate system and hot-Wire probe configuration. . . . 19
2.12 Operating principle of a magnetic flow meter. . . . 19
2.13 Doppler Current Profiler Acoustic Beams: a) Mounted on a vessel, and b) Deployed on the seabed. . 21
2.14 Comparison of beam orientations for typical (a) Diverging ADCP and (b) Acoustic Doppler Velocimeter (ADV) devices. The grey arrow pointing towards the sample volume illustrates the direction of the emitted acoustic signal, while the dashed black arrow pointing towards the receiver signifies the direction of the reflected signal. . . . 22
2.15 Acoustic Velocimetry. a) Measurement of the velocity component aligned with the acoustic beam, representing radial velocity. b) Configuration of the acoustic beam in a standard diverging ADCP. c) Visualisation of blanking distance, cell size, and centre-weighted averages applied per cell. . . . 23
2.16 Range gating for a sensor featuring a bin size and blanking distance of 0.4 meters. Image adapted from Gordon 1996. . . . 24
2.17 The relationship of beam and earth velocity components. . . . 25
2.18 Example of different acoustic pulse types. These are: narrowband (a), broadband (b), and pulse-to-pulse (c). . . . 25
2.19 Example of the clearance zone width. . . . 26

2.20 Divergent acoustic Doppler profiler beam coordinates relative to xyz, ENU and uvw. 27
2.21 Rotation: Heading, Pitch and Roll. 28
2.22 Illustration of cross-talk, presenting a segment of the transmit/receive cycle for two acoustic instruments aligned in parallel. The black pulse originates from the active sensor, while the red pulse represents the -100 dB signal from the adjacent instrument in the same location. Pulse timing is indicated at the upper right corner of each panel, with the sequence initiating from the bottom left and progressing counterclockwise. 30
2.23 Amplitude and correlation for a single beam showing indications of interference for three separation distances. 31
2.24 Illustrating the significance of placing a rotor at a higher position within the water column. The set of vectors on the left demonstrates the usual reduction in velocity as submergence depth increases. . . 33
2.25 Vertical axis tidal turbine full-scale device (a), general VATT concepts (b). 34
2.26 Transverse horizontal axis tidal turbine full-scale device (a), general THATT concept (b). 34
2.27 CoRMaT tidal turbine concept at full-scale (a) tidal kite by Minesto (b). 35
2.28 Forces on an aerofoil/hydrofoil. 37
2.29 Distinguishing Mean, Median, and Mode. 39
2.30 Normal distribution where each band has a width of 1 standard deviation (σ). 41
2.31 Illustration comparing random and systematic errors using the analogy of multiple shots at a target. . 42
2.32 Normal distribution curve to show the differences between uncertainty and bias. 43
2.33 Probability distribution curves illustrating different distributions: a) Gaussian (normal) distribution, b) Rectangular (uniform) distribution, c) U-shaped distribution, d) Log-Normal distribution, e) Triangle Distribution, and f) Quadratic distribution. 44
2.34 Visual representation of the standard analysis process. 52
2.35 Visual representation of the jack-knife method for uncertainty determination. 52
2.36 Vertical variation of tidal currents across the projected capture area. Image revised from IEC. 58

3.1 Gravity-based ADCP frames: a) Prior to ADCP deployment, and b) Seabed-mounted ADCPs during deployment/retrieval. 67
3.2 AUV equipped with a ADCP for surface tracking and flow velocity measurements. 68
3.3 Vessel mounted ADCPs. 69
3.4 Buoy mounted ADCPs. 71
3.5 TEC mounted ADCPs. 72
3.6 Types of tidal stream devices utilising seabed-fixed monopile foundation: a) 300 kW SeaFlow, b) 1.2 MW SeaGen, and c) 250 kW OpenHydro. 76
3.7 Variants of seabed gravity-based tidal stream devices: a) 187.5 kW Gen5, b) 300 kW HS300, c) 1 MW HS1000, d) 1 MW DEEP-Gen IV, and e) 1 MW D10. 77
3.8 Variations of floating tidal stream devices: a) PLAT-I 6.40, b) 1.5 MW Magallanes, and c) 2 MW O2 Device. 78
3.9 Pentland Firth location in Scotland, UK. 79
3.10 Bluemull Sound location in Shetland, Scotland, UK. 80
3.11 PTEC tidal test site located south from the Isle of Wight. 81

4.1 IEC/TC 114: Marine Energy - Wave, tidal and other water current converters. List of standards and best practices published since 2007 to support the progression of marine technology [1]. 84

4.2 Overview of the methodology for assessing the power performance of tidal turbines. 86
4.3 Summary of TEC developers and PPAs carried out. Light grey, blue and dark blue represent tidal turbines fixed to pile foundations, the seabed (gravity-based) and floating concepts. 89
4.4 Wind measurement techniques - Met mast configuration. 93
4.5 Wind measurement techniques - LIDAR & SODAR applicability for onshore and offshore wind farms. . 94
4.6 The distribution of measurements. (a) single-ping data. (b) Measurements averaged over 200-pings. . 95
4.7 Schematic depicting the vertical current velocity profile observed at a standard tidal energy site. . . . 97
4.8 ADCP positioning adheres to Orientation A (in-line), wherein: a) the ADCPs plan view shows its placement between 2_{D_E} and 5_{D_E} from the TEC, and b) the section view of the ADCPs measuring volume indicates the distance involved. Figure adapted from IEC 62600-200. 103
4.9 ADCP positioning adheres to Orientation B (adjacent), wherein: a) the ADCPs plan view shows its placement between 1_{D_E} and 2_{D_E} from the TEC, and b) the section view of the ADCPs measuring volume indicates the distance involved. Figure adapted from IEC 62600-200. 104
4.10 ADCP positioning with respect to a floating TEC from a plan view perspective. Figure adapted from IEC 62600-200. 105
4.11 Vertical variation in streamwise current velocity was measured at two locations, 6a and 6b, within the Falls of Warness region in Orkney as part of the ReDAPT project. (a) illustrates the deployment positions of selected instruments, including ADCPs situated at 6a and 6b. (b) Depth profiles of streamwise velocities from the instruments at locations 6a and 6b is depicted, showcasing 5-minute ensemble averages juxtaposed with a reference velocity averaged over the rotor plane. Each line on the graph corresponds to a velocity bin width of 0.4 m·s^{-1}, encompassing velocities ranging from 0.6 m·s^{-1} to 3.8 m·s^{-1}. 111
4.12 Satellite imagery depicting expansive flow patterns within and around a tidal channel. 112
4.13 Fishbone of uncertainties associated with a tidal stream PPA. 118

5.1 Geographical position of EMEC tidal and wave test sites: The Alstom DEEP-Gen IV 1 MW turbine was positioned at the Eday grid-connected tidal test site. 120
5.2 Test site layout at Fall of Warness. The DEEP-Gen IV and all relevant instrumentation over the measurement campaigns were deployed at Berth 2 (green circle). 121
5.3 Instrument placement for Deployments 1, 5 and 7 showing distance (D_E) from the DEEP-Gen IV TEC, relative to North. Instrument locations from Deployment 5 are identified as A_1, A_2 and A_3 (green beam) targeting ambient conditions on the flood and ebb tides respectively. Deployment 6 featured B_1, B_2 data-sets (orange beam) targeting ambient flows on both the flood and ebb tide. Deployment 1 featured A_4 and A_5 (yellow beam) targeting ambient flow conditions on the flood and ebb tide. The rotor-attached and rearhub SB-ADP C_1, C_2, measured both flood and ebb tide (hence yawing with the TEC). 124
5.4 Instantaneous current velocities were measured at various locations at berth 2 within the Fall of Warness site. (a) Current velocities captured by ADCPs positioned at A_{1-5}, B_{1-2}, and upstream and downstream from the TEC-mounted SBD (C_1 and C_2), along with the actual TEC yaw angle (/100) and power between June 2013 and Jan 2015. (b) A two-week focused view of deployment B (B_1 and B_2) with corresponding TEC yaw and power data. (c) A one-day detailed view of deployment B. . . . 126

5.5 Bathymetry in the vicinity of the turbine, with a) showing the 10 D_E x 20 D_E area of interest (solid black rectangle within highlighted grey squared) at the Fall of Warness, and b) a closer view at the depth around the DEEP-Gen IV and IEC TS target locations with ADCP layouts. 127
5.6 Power Curves plotted by time averaging ensemble of 5, 10 and 15 minutes. (a) Full power curve. (b) Higher resolution. 130
5.7 Instrument stability measured by ADCP$_{A1}$ (a and b) and ADCP$_{A2}$ (c and d). Roll (a and c) and pitch (b and d) for two instruments, where one instrument is stable (A_1) and the other is unstable (A_2). . . . 131
5.8 Amplitude vs distance along the water column from the ADCP (upward from the seafloor to surface). The distribution is shown in terms of standard deviations from the mean, σ. 132
5.9 Amplitude (a) and correlation (b) vs distance upstream from the SB-ADP mounted on the TEC. The distribution is shown in terms of standard deviations from the mean, σ. The sea surface is depicted as a grey line. 133
5.10 Mean number of samples passing signal strength filter vs distance upstream of the rotor-attached SB-ADP C_1. 134
5.11 Flood and ebb areas used in the method of bins, where ADCPs A_1 (Northwest) and A_2 (Southeast) are used as an example. Turbine tilt included. Not to scale. 135
5.12 Comparison of the ADCP (A1 used for example) and the TEC rotor-mounted SB-ADP speed of sound during Deployment 5. 136
5.13 Variation in flood and ebb direction at seven individual locations in close proximity to the DEEP-Gen IV. DEEP-Gen IV aligned to $\approx 133^\circ$ and 312° for the flood and ebb tide respectively. ADCP locations are depicted in Figure 5.3. 136
5.14 Histogram of the typical angle between flow direction and TEC yaw angle (red dashed line) for the (a) flood tides and (b) ebb tides. 137
5.15 Plan view of the angle between flow direction and the DEEP-Gen IV yaw angle. 137
5.16 Contributors to uncertainty associated with the deployed instrument used to inform the power performance assessment. 138
5.17 Keller piezo resistive pressure sensor. (a) 10L series design (b) Sensor dimensions. (c) electrical diagram measuring bridge with compensation. 140
5.18 Input characteristics for the calculation of the combined uncertainty per ADCP deployment. 143
5.19 Average and maximum expected uncertainty per velocity bin - from the in house ancillary sensors. Note this does not account for all uncertainties external to the ADCP. 144
5.20 Alstoms DEEP-Gen IV 1 MW tidal turbine, deployed for seven separate measurement campaigns over 4 years (Jan 2011 to Jan 2015). 145
5.21 Vertical position of TEC$_{T1}$, TEC$_{T2}$ and TEC$_{T3}$ in the water column. 146
5.22 Therotical power curve for the three TEC concepts used in the project where the DEEP-Gen IV 1 MW TEC is based on real-world power and TEC$_{T1}$ and TEC$_{T3}$ are based on modelled data. 148
5.23 Power weighted rotor average velocity example. 148

6.1 Contributors to uncertainty associated with the placement of multiple ADCPs and potential interference features in the measurements used to inform the uncertainty in a power performance assessment. 152

6.2 Data obtained from two ADCPs positioned upstream from the DEEP-Gen IV turbine at a distance of 61 m (A_1) and 106 m (A_2). (a) Instantaneous streamwise flow speed. (b) Averaged (5 minute) velocity magnitude. (c) Flood tide measurements with periods of a large difference between the two close-proximity ADCPs (black spikes), the grey box outlines a section of data that is zoomed into. (d) Zoom in to the flood tide measurements from ADCP$_{A1}$ and ADCP$_{A2}$ that feature interference characteristics. 153

6.3 Illustration of the theory of two angled sensors measuring a component of the free stream velocity along the angle intersecting the two beams. NOTE the rhombus volumes represent the ADCP weighting as per user manuals where the depth cell is most sensitive to velocities at the centre of the cell. . 154

6.4 Example of seabed mounted ADCP echo amplitude measurements featuring interference characteristics, where A and B markers are strong vertical lines associated with the desent and as cent of a deployed remote-operated vehicle respectively. Markers C and D are diagonal and horizontal lines associated with interference from other acoustic instruments. 155

6.5 The four beam transducers located at A_2 measuring echo amplitude along the water column, with features of interference illustrated at the diagonal lines. Beams 3 and 2 (top and bottom right) show a significant increase in the echo amplitude, implying the interference is toward this location. 155

6.6 RDI WH 600 kHz ADCPs, A1 and A2 which are 61 m and 106 m northeast of the TEC location (upstream on a flood tide), respectively. (a) Side profile showing the vertical displacement between A1 and A2. (b) Showcases the top-down view of A1 and A2 beam paths and the clearance zones. (c) Illustration of the main lobes (solid), clearance zones (shaded), and the orientation of the two bottom-mounted ADCPs. 156

6.7 Averaged (5-min) in-situ measurements of instrument stability by the two ADCPs located at A_1 and A_2. (a) Time series of pitch measurements by ADCP$_{A1}$ and ADCP$_{A2}$. (b) Time series of roll measurements ADCP$_{A1}$ and ADCP$_{A2}$. 157

6.8 Representative amplitude (a) and flow velocity (b) for ADCP measurements without interference features. 157

6.9 Velocity for ADCP located at A_1 and A_2 showing indications of interference for four consecutive flood cycles. (a) Flow velocity time-series for ADCPs located at A_1 and A_2 and the difference between them (black line). Contour plot of the 5-minute averaged measurements across the water column measured by ADCPs located at (b) A_1, and (c) A_2. Ebb tidal cycles are removed. 158

6.10 Echo amplitude and velocity depth profile from ADCP$_{A1}$ (solid lines) and ADCP$_{A2}$ (dashed lines) averaged at intervals of 45 minutes to illustrate the movement of the interference feature one flood cycle apart. (a) Amplitude showing indications of interference at different heights from the seabed as the flood tide develops. (b) Effect on velocity measurement. 160

6.11 (a) Simultaneous velocity time series for measurements at A_1 and A_2, segmented to 1.5 hours with slack water removed (velocities < 1 m·s^{-1}). The upper, hub height and lower bound represent the swept area of the DEEP-Gen IV (TEC$_{T1}$) at a height of 9, 18 and 27 m respectively. Velocity depth profile for ADCP$_{A1}$ (b) and ADCP$_{A2}$ (c). 161

6.12 Correlation between flow velocities measured across the swept area of TEC$_{T2}$, TEC$_{T1}$ and TEC$_{T3}$ displayed in (a), (b) and (c) respectively, for data with (blue) and without (orange) features of interference. Correlation between the calculated PWRA velocities - weighted average of measurements taken across the rotors of TEC$_{T2}$, TEC$_{T1}$ and TEC$_{T3}$ - from ADCPs at locations A_1 and A_2 illustrated in (d), (e) and (f) for data with (blue) and without (orange) features of interference. Perfect correlation is illustrated as a the black line of 1-1 (x = y). 162

6.13 Tidal ellipse for the flood tide PWRA flow velocities $\bar{U}_{A1}$ (orange dot) and $\bar{U}_{A2}$ (blue dot), with the beam orientation of both instruments (solid line representing main beam heading - angle of beam 3 for RDI WH ADCPs) and the principle flood flow direction is shown as the black line. Ebb data (grey dot) is not used in this analysis. 164
6.14 Distance between neighbouring beam trajectories from ADCP$_{A1}$ and ADCP$_{A2}$. Beam distance at the upper rotor bound (circle) and close to the sea surface (square) and the mean water level for the flood (blue triangle) and ebb (grey triangle). IEC TS 62600-200 instrument target box is included as the lined box. 164
6.15 Six consecutive flood tide depth profiles measured from location ADCP$_{A1}$ featuring interference effects (dashed lines) and *clean* profiles (solid lines). The position of three variants of TECs are overlaid (T1,T2, and T3) with symbols showing corresponding interfered (unfilled) and *clean* (filled) PWRA velocities. 165
6.16 The effect of ADCP interference on the measured power curve for the averaged 5-minute PWRA velocities in increments of 0.1 m·s^{-1}. (a) Blue dots represent the flood tide measurements for ADCP A_1 ($\hat{U}_{A1}$) with features of interference from interacting with ADCP A_2, the orange dots represents data with interference features removed. (b) The mean PWRA velocity from ADCP A_1 ($\bar{U}_{A1}$) with (blue triangle) and without (orange triangle) features of interference in the 5-minute averaged measurements. 166
6.17 The mean PWRA velocity from ADCP A_1 ($\bar{U}_{A1}$) with (blue square) and without (orange square) features of interference in the 5-minute averaged measurements across the rotor span of TEC$_{T3}$ (z_{T3}). 167
6.18 Echo-Amplitude Depth Profile: (a) A data sample displaying a prominent peak in echo amplitude within the upper portion of the water column. (b) The amplitude profile detrended by subtracting the line of best fit. (c) The profile is then smoothed to remove multiple mini-peaks and then multiplied by negative one to identify the primary peak (d) The algorithm effectively identifies the peak (indicated by a triangle) within the data sample, while also eliminating measurements between the designated square markers that represent bias from cross-talk features. 168
6.19 An area of interference is identified and highlighted in the grey box, and the good measurements (U_{A1}) and flagged contaminated measurements ($U_{A1,int}$) are given for one flood cycle. (a) Mean echo amplitude measurements in dB. (b) Mean flow velocity profile in m·s^{-1}. 169
6.20 Interference features identified throughout the averaged flow velocity profiles (by time on a flood cycle in intervals of 45 minutes). (a) Acceleration of the flood tide with interference features high up in the water column. (b) Interference features removed from the acceleration section of the data set, with a leftover sample close to the boundary layer. (c) Deceleration of the flood tide with interference features high up in the water column. (d) Interference features removed from the deceleration section of the data set, with a leftover sample close to the removed section. 170
6.21 (a) Time series comparison of power-weighted rotor average velocities from ADCPs A_1 and A_2, focusing on the TEC$_{T2}$ rotor. The yellow line represents the difference between the two measurements. (b) Power-weighted rotor average velocity time series from ADCP A_1, highlighting flagged data influenced by interference (black line). The difference between ADCP A_1 and A_2 measurements is also depicted. 171
6.22 Utilising the power law calculation for data gap restoration. (a, d) Display of two velocity profiles indicating gaps (grey area) at distinct depths. (b, e) Frequently used 1/7$^{\text{th}}$ velocity profile, anchored on the final velocity bin with reliable data (9 m and 13 m for b and e, respectively). (c, f) Visualisation of power law fits, showcasing different coefficients of α. 173

6.23 Velocity profile variability due to the power law exponent α chosen to represent the corrupted data removed for assumed conditions present at the Falls of Warness. 173

7.1 Velocity time-series of data sets: (a) flood tide measurements from ADCPs deployed at A_1 (NW01), A_2 (NW02), TEC rotor-attached SB-ADP C_1 (SB$_r$) matched with the power produced by the DEEP-Gen IV T_2. (b) Ebb tide measurements from an ADCP placed at A_3 (SE01), rotor-attached SB-ADP C_1 (SBr) matched with the TEC power generated. (c) Flood tide measurements from ADCPs placed at B_1 (SW$_{fm}$), B_2 (NE$_{fm}$) and the rotor-attached SB-ADP C_1 (SBr) matched with the TEC power generated. (d) Ebb tide measurements from ADCPs placed at B_1 (SW$_{em}$), B_2 (NE$_{em}$) and the rotor-attached SB-ADP C_1 (SBr) matched with the TEC power generated. 5-minute averaged data from the campaigns are highlighted as grey lines. 178
7.2 Directionality and strength of the flood and ebb tidal characteristics at Fall of Warness at each instrument location used in the analysis. 179
7.3 Velocity magnitude - long-term average (coloured) and individual 5 minute averaged measurement (grey) - along the rotor of the DEEP-Gen IV turbine from various nearby locations (a) Flood tide measurements from A_1 (NW01), A_2 (NW02), B_1 (NE$_F$) and B_2 (SW$_F$). (b) Ebb tide measurements from A_3 (SE01), B_1 (NE$_E$) and B_2 (SW$_E$). Averages are calculated using the entire dataset collected at each location around the TEC. 181
7.4 a) Inter-instrument correlation for the flood measurements, PWRA velocities $\bar{U}_{A1}$ vs $\bar{U}_{A2}$ (green) and $\bar{U}_{B1}$ vs $\bar{U}_{B2}$ (orange). b) Ebb tide correlation, for $\bar{U}_{A3}$ and $\bar{u}_{C1}$ (blue), and $\bar{U}_{B1}$ vs $\bar{U}_{B2}$ (orange). 182
7.5 Velocity depth profile for flood tide measurements for a) in-line ADCP pair A_1 and A_2, compared against the rotor-attached instrument C_1 (filled circle marker at hub-height, 18 m). b) Velocity measurements from the adjacent locations to the TEC B_1 and B_2, the rotor-attached SB-ADP C_1 is depicted as a filled circle at hub-height. 183
7.6 Velocity depth profile for ebb tide velocity measurements for a) in-line ADCP A_3, and SB-ADP C_1 (filled circle marker at hub-height of 18 m). b) Velocity measurements from the adjacent locations to the TEC, B_1 and B_2, and the rotor-attached SB-ADP C_1. 183
7.7 The effect of ADCP placement - per IEC TS 62600-200 - on measured power curve for the averaged 5-minute velocities in increments of 0.1 m·s^{-1}. a) The flood tide measurements from the in-line ADCP pair $\bar{U}_{A1}$ and $\bar{U}_{A2}$, the adjacent pair are included $\bar{U}_{B1}$ and $\bar{U}_{B2}$. b) The ebb tide measurements from the rotor-attached SB-ADP, $\bar{u}_{C1}$ and $\bar{U}_{A3}$, and the adjacent pair $\bar{U}_{B1}$ and $\bar{U}_{B2}$. The black line represents the published power curve of the DEEP-Gen IV. 184
7.8 In-line placed ADCPs (black dashed line) A_1, A_2, A_3 and adjacent placed ADCPs B_1, B_2 (black solid line) and their calculated PWRA velocity in increments of 0.1 m·s^{-1}. a) Flood tide PWRA velocity difference between pair: $\bar{U}_{A1}$ and $\bar{U}_{A2}$, and pair $\bar{U}_{B1}$ and $\bar{U}_{B2}$. b) Average velocity difference between $\bar{u}_{C1}$, $\bar{U}_{A3}$, and the PWRA velocity difference between $\bar{U}_{B1}$ $\bar{U}_{B2}$. 185
7.9 Three TEC concepts are placed accordingly to their hub-height reference. U$_{B1}$ and U$_{B2}$ represent the peak rated velocity for the flood and ebb tide. The mean water level for the flood (MFL) and ebb (MEL) tide is represented by the blue solid and dashed line respectively. NOTE rotor diameter to scale, TEC dimensions are not to scale. 186
7.10 Presentation of the power curve for flood tide measurements at location B_1, showing the variation in mean velocity $\bar{U}_{B1}$ when the incorrect depth bin is paired with the TEC hub height. 187

7.11 Adjacent placed ADCP (B_1) PWRA velocity in increments of 0.1 m·s^{-1}. Difference between PWRA velocity taken at hub height reference ($\bar{U}_{z,HH}$ where HH is 18 m and rotor diameter is 18 m) and an imposed misalignment of up to 2 m ($\bar{U}_{z,HH\pm2}$). 188
7.12 Presentation of the overall efficiency of the TEC for flood tides using measurements taken at B_1, showing the variation in TEC efficiency η when the incorrect depth bin is paired with the TEC hub height. 188

8.1 (a) Channel bathymetry and ADCP locations relative to the DEEP-Gen IV at the FoW tidal test site. (b) Tidal ellipse for three bin depths, where z_1, z_2 and z_3 represent 15, 25, and 33 m above the seabed. The generic established flow direction for both flood and ebb is presented. TEC yaw heading rotations used throughout the analysis is illustrated, where both clockwise and anticlockwise rotations are considered ($\pm\alpha$). NOTE measurements shown indicate flow travelling toward that direction. . . . 197
8.2 Data obtained from two ADCPs positioned upstream (A_4) and downstream (A_5) from the DEEP-Gen IV turbine at a distance of 63 m and 53 m respectively. (a) 5-minute averaged flow velocity data sets for the flood (A_4) and ebb (A_5) tide measurements. (b) 5-minute averaged flow direction data sets. The purple box shows the velocity and direction data in detail. 197
8.3 Flow direction variation over a flood tide at the FoW, where a) the flow direction mean (square markers) of 30-minute periods throughout the flood cycle, the TEC yaw heading (solid black line), and the min and max (crosses) variation in direction. b) The tidal ellipse for the flood measurements at a chosen hub height (18 m), the black dashed line represents the TEC yaw heading. 198
8.4 Probability density distribution for varying flow speeds and flow directions (in Cartesian coordinates) for flood and ebb tides. The data has been generated from hub-height measurements sampled by an ADCP deployed $\approx$ 40m southwest of the DEEP-Gen IV TEC (in a region of flow undisturbed by the presence of the turbine). 201
8.5 Peak flow velocity recorded at the FoW (instrument location A_4) for the flood and ebb (solid and dashed line respectively) cycle during a neap (blue) and spring tide (black). The percent difference in velocity from misalignment from the principle flow by α is given by the relationship (green line). 201
8.6 Comparison of theoretical maximum power generated using U_{inflow} (red line) and the realistic power generated using velocity component $U_{\theta-\alpha}$, where the TEC is misaligned to the established flood direction. The DEEP-Gen IV power curve is presented (a) by the unfilled symbols, where the circle, square and triangle represent a misalignment from the established flow of 5° (b), 10° (c) and 15° (d), respectively. Filled symbols represent the percentage lost in power when flow data used features misalignment for TEC$_{T2}$ (filled grey) and TEC$_{T3}$ (filled black). 202
8.7 AEP loss based on flow velocity using U$_\alpha$, where α changed in increments of 1° up to 15° (α_1, α_2 and α_3 represent 5°, 10° and 15° respectively). The flood (right) and ebb (left) tide AEP estimates with a clockwise and anti-clockwise shift from the established flow. 203
8.8 Energy lost when TEC$_{T1}$ is misaligned to the flow, where the grey bar is the energy captured per tidal cycle. The blue, green, yellow and red bars represent the energy lost by the TEC facing the established flow θ, misaligned by α_1 (5°), α_2 (10°) and α_3 (°), respectively. 204
8.9 Flow direction variation along the measured water column (z) during the acceleration and deceleration phase of the tide for a) the ebb tide measurements and b) the flood tide measurements. The established flow direction estimate using θ_{HH} (solid red line) and θ_{PWRA} (red cross) methods are shown for TEC$_{T1}$. The position of all three TECs in the water column is shown in (b). 205

8.10 Flood time-series data set for (a) PWRA flow velocity and (b) direction measured by seabed mounted ADCP A_4 (refer to Fig 5.3). The neap (purple), intermediate (blue) and spring currents are shown over a fortnight at the Fall of Warness. . . . 206
8.11 Sea level comparison between pressure measurements obtained from the seabed mounted ADCP located at A_4. (a) Neap tide elevation variation. (b) intermediate tide elevation variation. (c) Spring tide elevation variation. . . . 206
8.12 Typical directionality and strength of neap, intermediate and spring tidal currents on the flood tide at the Fall of Warness. (a) A tidal ellipse indicates the direction from which the flood tide flows. (b) Estimated mean flow direction based on tidal phase (dashed lines), showing $\frac{2}{3}$ of the tidal phases that don't reach the TEC-rated velocity. . . . 207
8.13 The flow direction mean (square markers) of 30-minute periods throughout the flood cycle, the TEC yaw heading (solid black line), and the min and max (crosses) variation in direction. . . . 208
8.14 Flow direction variation along the measured water column (z) during the flood tide. The mean direction for the neap, intermediate and spring tide at a time (t) period of 1 hour 30 minutes, 3 hours and 4 hours 30 minutes into a flood tide. TEC swept area and yaw angle are defined by the grey box and blue dashed line respectively. . . . 208
8.15 Comparison of theoretical maximum power generated assuming the DEEP-Gen IV is positioned to the flow direction (black line) at each time-stamp, and the realistic power generated using velocity components equal to the misalignment of the turbine from the established flow direction during the neap, intermediate and spring tides. The percentage difference in velocity is given by the natural misalignment between the flow direction and the turbine extraction plane during each tidal cycle. . . . 209

10.1 Alstom DEEP-Gen IV 1 MW TEC Power Curve Data. . . . 244

Tables

2.1 Teledyne RDI acoustic instrument beam widths. . . . 26
2.2 Beam to Instrument Transformation Matrix. . . . 27
2.3 Taxonomy of yield loss categories proposed by OREC (2015a). . . . 48

3.1 Summary of measurement campaigns from the Fall of Warness, Orkney, Scotland. . . . 63
3.2 Summary of literature conducting a PPA as per the IEC/TS 62600-200 64

4.1 Overview of industrial standards and best guidance containing flow measurement requirements applicable to tidal stream energy, relevant to this thesis. . . . 84
4.2 Summary of industrial Technical specifications and best guidance for Flow measurement requirements applicable to tidal stream energy. Refer back to section 2.5.1 for category explanation. . . . 87
4.3 Typical ringing times, denoted as distances ahead of the transducer. . . . 96
4.4 Uncertainty categories for wind and tidal (with indicative values for wind and predicted change for tidal). Taken from Clayton et al [2]. . . . 100
4.5 Categorisation of yield loss domains as suggested by ORE. . . . 106

5.1 Instrumentation Summary. . . . 122
5.2 Key operating parameters of acoustic profilers used in the flow characterisation. . . . 122
5.3 Key parameters of acoustic profilers used in the flow characterisation. The visual representation is shown in Figure 5.3. . . . 123
5.4 Flags from in-situ data from ADCPs. . . . 128
5.5 QC checks that have been used to filter the in-situ data from the fixed current profilers. . . . 129
5.6 Spatial averaging regions in the vertical direction for three TEC installation types and a narrow mid-depth sampling regime. Distance are relative to the seabed. . . . 132
5.7 Pressure sensor datasheet accuracy. . . . 140
5.8 Key parameters of the DEEP-Gen IV TEC. . . . 145
5.9 Generic types of tidal energy converter parameters. . . . 146
5.10 Overview of sampled data used for power curve creation, shown as a percentage of the total amount of the data-sets. . . . 147
5.11 Flow current parameter list. . . . 149

6.1 Correlation parameters between concurrently measuring ADCPs located at A_1 and A_2. Velocities representative of the depth bins across the swept area of TEC_{T2}, TEC_{T1} and TEC_{T3} given by (a), (b) and (c) respectively. Correlation between PWRA velocities - calculated using depth bins across TEC_{T2}, TEC_{T1} and TEC_{T3} - with and without features of interference provided in (d), (e) and (f). . . . 163
6.2 Overview of total samples available, flagged, and removed during flood tides over a 26-day (days of overlap between the co-located ADCPs) measurement period. Note that only samples with matching timestamps were included in the analysis for comparison. The table summarises the total number of samples. . . . 170

7.1 Inter-instrument comparison table showing the available 5-minute ensembles, where colours correspond directly to instruments depicted in Figure 5.3. The light grey shaded region corresponds to flood conditions with data relating to ebb shown diagonally opposite. . . . 180
7.2 Sensitivity to the vertical misalignment of profiler depth bin to the proposed TEC hub-height, where each bin's mean velocity (U) is used. Values refer to the averaged velocity profile produced for each seabed instrument, where the profile for $B1$ is depicted in Figure 7.9. Diff refers to the percent difference between the hub-height AEP estimate and the estimate from an depth offset. . . . 189
7.3 The combined uncertainty of the two variables during the flood tide: instrument placement relative to the operational TEC and vertical misalignment of the hub height and ADCP bins. . . . 191
7.4 The combined uncertainty of the two variables during the ebb tide. . . . 191

8.1 Effect of pre-processing on the estimate of established flow direction. . . . 200
8.2 AEP percentage loss from misalignment (α), where both flood and ebb tidal cycles were analysed for a clockwise and anti-clockwise shift for the three TEC concepts. NOTE θ is equal to the established flow direction. . . . 203

Nomenclature

α	Empirically calculated power law coefficient
$\bar{P}_i$	Mean calculated turbine power in velocity bin i
$\bar{U}$	Mean power weighted rotor average velocity, m·s^{-1}
$\bar{u}$	Mean steamwise flow velocity, m·s^{-1}
η	TEC overall efficiency
$\hat{U}$	Instantaneous power weighted rotor average velocity, m·s^{-1}
λ	Sound wavelength
ρ	Density of water
σ	Standard deviation
A	Type-A configuration, instrument location, A_1, A_2 and A_3
A_k	Depth bin over the swept area of the turbine, m^2
B	Type-B configuration, instrument location, B_1, B_2
C	Speed of Sound
C_1	Rotor-Attached instrument
C_2	Rear-Attached instrument
C_P	Power coefficient
d	Distance between Earth's center and the Moon
D_E	Rotor equivalent diameter
F	Gravitational force exerted
f_d	Difference in frequency between the transmitted and received pulses
f_i	Time of each mean current velocity occupying a value within velocity bin i
f_{pulse}	Transmitted pulse frequency
G	Gravitational constant
h	Total water depth
i	Index related to velocity bin
j	Index related to time stamp
k	Von Karman's constant
L	Number of samples in the defined averaging period
m_e	Mass of Earth
m_m	Mass of Moon
n	Index related to data point
N_B	Total number of velocity bins in the power curve
P	Power produced from the tidal turbine
S	Number of depth bins across projected area of turbine
TEC_{AEP}	Expected annual power production from a tidal turbine
TEC_A	Predicted availability of the tidal turbine
$u*$	Estimate of friction velocity
U	Mean velocity, m·s^{-1}

u	Velocity magnitude, m·s^{-1}
u_{beam}	Fluid velocity along the beam axis
z	Height above seabed, m
z_0	Bed roughness length scale

List of Acronyms

This list defines the main abbreviations used in the main body of the thesis. Any abbreviations used in the thesis that are not defined here are clearly defined in the text.

ADCP	Acoustic Doppler Current Profiler
ADV	Acoustic Doppler velocimetry
AEP	Annual Energy Production
AUV	Autonomous Underwater Vehicle
EMEC	European Marine Energy Centre
ETI	Energy Technology Institute
FORCE	Fundy Ocean Research Centre for Energy
FoW	Fall of Warness
HATT	Horizontal Axis Tidal Turbine
IEA	International Energy Agency
IEC	International Electrotechnical Commission
IREA	International Renewable Energy Agency
IHO	International Hydrographic Organisation
TI	Turbulence Intensity
LIDAR	Light Detection and Ranging
MAE	Mean Absolute Error
MCT	Marine Current Turbines
MCA	Monte Carlo Analysis
MRE	Marine Renewable Energy
NaN	Not a Number
PWRA	Power Weighted Rotor Average
PPA	Power Performance Assessment
PTEC	Perpetuus Tidal Energy Centre
QC	Quality Control
QARTOD	Real-Time Quality Control of Stream Flow Observations
ReDAPT	Reliable Data Acquisition Platform for Tidal
RMS	Root-Mean-Square
RMSE	Root Mean Squared Error
SB-ADP	Single Beam - Acoustic Doppler Profiler
SODAR	Sonic Detection and Ranging
SNR	Signal-to-Noise Ratio
TEC	Tidal Energy Converter
TS	Technical Specification
VATT	Vertical Axis Tidal Turbine
SoS	Speed of Sound

Chapter 1

Introduction

1.1 Global Context for Renewable Energy

Renewable energy sources play a pivotal role in addressing the pressing global challenges of climate change and environmental degradation. The combustion of fossil fuels for energy generation is a major contributor to greenhouse gas emissions, leading to global warming, sea-level rise, and other adverse climatic impacts [3]. Transitioning to renewable sources like solar, wind, hydropower, and geothermal energy offers a sustainable alternative that significantly reduces carbon emissions and environmental pollution [4]. Renewable sources harness naturally occurring processes, thereby minimising the release of harmful pollutants and greenhouse gases into the atmosphere. According to the International Energy Agency (IEA), by diversifying the energy mix and expanding the use of renewables, the world can curtail global warming and mitigate the disastrous consequences of climate change on ecosystems, human health, and economies [5]. Moreover, renewables offer greater energy security by decreasing dependence on finite fossil fuel reserves and enhancing energy independence for countries.

Renewable energy not only addresses environmental concerns but also fosters economic growth and social development. The rapid advancements in renewable technology drive innovation, create jobs, and stimulate local economies. A report by the International Renewable Energy Agency (IREA) states that the renewable energy sector employed over 11 million people globally in 2018, with the potential to provide millions more jobs in the future [6]. Moreover, the decentralised nature of renewable energy infrastructure empowers communities by enabling energy self-sufficiency and promoting access to electricity in remote and underserved areas. By investing in renewables, countries can diversify their energy sources, enhance energy security, promote economic resilience, and contribute to a more sustainable and equitable future for all.

The motivation behind pursuing alternatives to fossil fuels stems from three fundamental considerations:

1. Finite Reserves: Traditional energy sources like coal, oil, gas, and nuclear fuels possess limited reserves. As these resources are finite, there is a growing awareness that their depletion is inevitable. This scarcity drives the exploration of sustainable energy options that can provide continuous power without the concerns of resource exhaustion.
2. Enhanced Energy Security: Incorporating renewable energy sources into the energy mix offers a means of strengthening energy security. By diversifying the range of sources contributing to electricity generation, a more resilient and dependable energy portfolio can be established. This diversity reduces susceptibility to disruptions caused by supply fluctuations or geopolitical factors affecting traditional fossil fuels.

3. Mitigating Greenhouse Gas Emissions: One of the most critical imperatives for transitioning to renewable energy is the reduction of greenhouse gas emissions. The shift from fossil fuels to renewable sources such as solar, wind, hydro, and geothermal power holds the potential to significantly curtail carbon dioxide and other harmful emissions. This transition aligns with global efforts to combat climate change and mitigate its far-reaching impacts on the environment, ecosystems, and human well-being.

Investing in clean energy and embracing energy-efficient practices holds the potential to pave the way for a more sustainable future [3, 7]. As the imperative for sustainable energy solutions grows stronger, the demand for electricity has also surged significantly. This surge extends beyond electricity supply to encompass transportation and heating systems, which are progressively shifting toward electrification to curtail their carbon footprint [8, 9]. Illustrated in Figure 1.1, the chart depicts global CO2 emissions estimates for 2022 (solid blue line), 2021 (dashed blue line), and 2020 (dashed red line) from the Global Carbon Project (representing three distinct emission models rather than separate years), accompanied by the uncertainty range (shaded area) of the latest 2022 budget [10]. This visualisation highlights the evolving landscape of carbon emissions on a global scale. Chart by Carbon Brief using high charts [10].

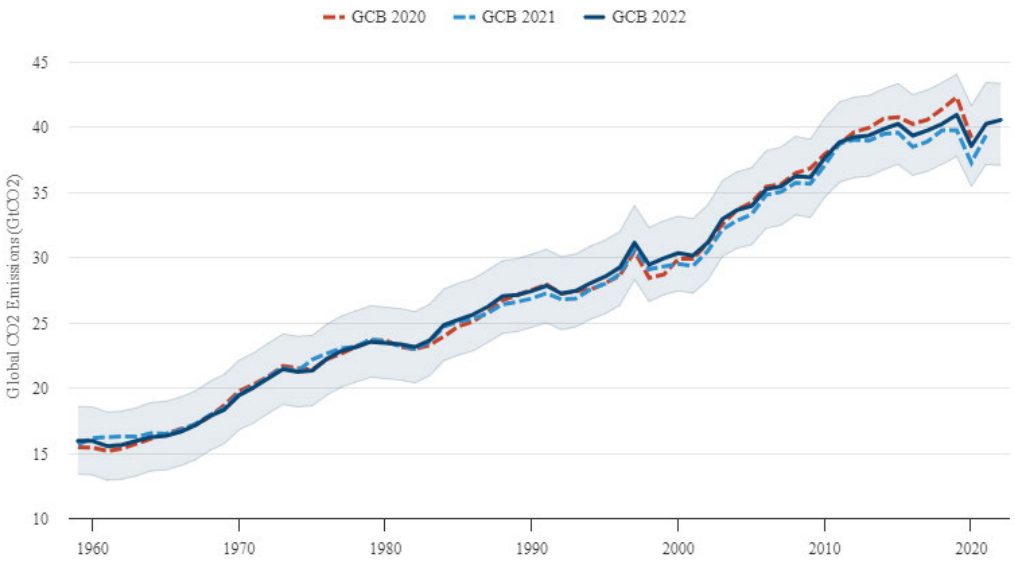

Figure 1.1: Annual total global CO2 emissions – from fossil and land-use change – between 1959 and 2022 for 2020, 2021 and 2022 versions of the Global Carbon Project's Global Carbon Budget, in billions of tonnes of CO2 per year (GtCO2). The shaded area shows the estimated one-sigma uncertainty for the 2022 budget. Data from the Global Carbon Project.

In the year 2015, a collective of 197 governments pledged their dedication to capping the escalation of global temperatures, aiming to keep the rise well under 2℃ and, ideally, even lower at 1.5℃. This commitment was enshrined in the Paris Agreement [11].

The apparent stabilisation of emissions in the 2022 budget provides a positive perspective in a world dealing with escalating emissions. However, this positive development needs careful consideration, as recent findings emphasise [10]. One crucial aspect to consider is that merely keeping emissions stable is not enough to achieve the global climate goals of limiting temperature rise to well below 2℃. Instead, there is an urgent need for emissions to decrease rapidly, ultimately reaching net-zero emissions in the latter part of the 21st century. If emissions persist significantly above zero, the trajectory of global warming will continue [10]. Another significant

point involves the uncertainties surrounding emissions linked to land use. This uncertainty makes it challenging to rule out the possibility that these emissions have continued to rise over the past decade. To address this uncertainty, further research and thorough data collection are essential to provide a more accurate representation of recent trends in global land-use emissions [10].

Renewable energy technologies such as wind turbines and solar panels have witnessed substantial growth in their installed capacity, reliability, availability, and overall performance. Nonetheless, the early stages of the wind industry were marked by technological setbacks and slow expansion [12]. Initial financial support primarily stemmed from government bodies through incentives and grants. Both wind and solar technologies have reaped benefits from insights gained during small-scale testing and continuous technological enhancements. In contemporary times, the wind energy sector is flourishing, with numerous turbines deployed and an increasing focus on offshore locations (including floating technologies) to capitalise on consistent wind speeds and expansive open areas.

1.2 Renewable Energy from the Marine Environment

Marine energy, also referred to as marine renewable energy (MRE), pertains to harnessing diverse forms of renewable energy derived from natural processes in the ocean. It encompasses an array of technologies aimed at capturing the energy inherent in oceanic phenomena such as tides, waves, currents, temperature gradients, and salinity variations. The overarching objective of marine energy is to convert these innate occurrences into practical sources of power, specifically electricity, in order to fulfil human energy requirements while minimizing ecological impacts.

Marine energy technologies can be categorized as follows:

1. Tidal Energy: Tidal energy results from the gravitational influence of the moon and the sun, culminating in tidal rises and falls. Tidal range energy capitalizes on the potential energy discrepancy between high and low tides, whereas tidal stream energy captures the kinetic energy found in the movement of water during tidal currents.
2. Wave Energy: Technologies centered on wave energy capture the kinetic and potential energy embodied in the motion of oceanic waves. These devices transform one or more modes of wave motion into mechanical energy, which is subsequently converted into electrical power.
3. Ocean Current Energy (as opposed to tidal steam energy): Utilising factors like temperature variations and Earth's rotation, ocean currents can be tapped as sources of energy. Devices positioned within ocean currents capture the kinetic energy of moving water, converting it into usable power.
4. Ocean Thermal Energy Conversion (OTEC): OTEC systems exploit the temperature contrast between warm surface water and cold deep water to generate electricity. This method relies on the heat-absorbing and heat-releasing qualities of substances like ammonia to drive turbines and produce power.
5. Salinity Gradient Energy: Also known as blue energy, salinity gradient energy harnesses the dissimilarity in salt concentration between freshwater and seawater to create electricity. This phenomenon arises when freshwater and saltwater blend, inducing a chemical potential that can be transformed into electrical energy.

It's worth mentioning that offshore wind energy is occasionally categorised as a marine renewable energy source. However, it's excluded from the aforementioned definition because it utilises sea space rather than tapping into the energy inherent in the seawater itself.

Marine energy possesses the potential to offer a dependable and unwavering source of renewable energy. This stems from the fact that oceanic processes, governed by elements like tides and waves, are inherently foreseeable. Consequently, it provides a sustainable alternative to conventional fossil fuel-based energy sources, contributing significantly to endeavours aimed at addressing climate change and minimising emissions of greenhouse gases. Nevertheless, marine energy technologies are currently at different stages of development and encounter technical, economic, and environmental hurdles that necessitate resolution for their comprehensive adoption.

1.2.1 Tidal Stream Energy

Among the marine sources, tidal energy has gained substantial recognition for its reliability and potential to provide a consistent and clean power supply. Tidal energy, which is generated through the gravitational interactions of the moon and sun, presents an appealing substitute for conventional fossil fuels. This appeal stems from its predictability and limited environmental footprint. This predictability is a result of the rhythmic nature of tidal patterns, rendering tidal energy an inherently reliable and sustainable source [13].

In the realm of renewable energy, tidal generation stands out as a notably dependable choice. In contrast to other energy sources, tidal generation boasts the remarkable advantage of near-perfect predictability over extended durations. This attribute implies that we can precisely anticipate the amount of energy that can be harnessed from tidal sources in the forthcoming years. This predictability offers substantial advantages for strategic planning and investment endeavours [14]. Furthermore, in comparison to wind farms, there is a relatively strong public receptiveness towards adopting this energy form, rendering it an appealing choice for sustainable energy solutions [15].

Although tidal energy is an evolving technology, there remains a degree of uncertainty surrounding its projected installed capacity both within the UK and on a global scale. Projections by the International Energy Agency suggest a potential of 101 GW of tidal stream energy capacity installed worldwide by 2050 [6]. However, past predictions have demonstrated discrepancies. The European Ocean Energy Association (2013) , for instance, forecasted 300 MW of tidal stream installed capacity by 2020 [16], yet the actual achieved was 10 MW.

In the UK, the National Grid's most recent iteration of the Future Energy Scenario (FES) document, released in July 2020, exhibited a substantial target for tidal energy generation. The projected installed capacity for tidal energy within the UK was ambitiously set at 10 GW by 2050 [17]. These variations in projections underscore the complexity and evolving nature of the tidal energy sector, with real-world outcomes sometimes deviating from initial expectations. Similar to the initial years of the wind industry, a comparable path holds promise for the emerging tidal stream sector. By drawing upon the lessons and experiences gained from the wind industry development, the nascent tidal stream industry has the potential to navigate a more efficient route towards achieving commercial feasibility [18, 19].

The UK is targeting net zero carbon emissions by 2050 [20]. Tidal energy has the potential to support this target as a clean and reliable energy source. The UK is surrounded by 50% of Europe's tidal energy potential, 25% of which is in Scotland [21]. It is pioneering the deployment of tidal current technologies, with leading research and innovation in an industry that is forecast to be worth £76 billion by 2050 [21]. To exploit this clean energy and economic opportunity, it is critical to accelerate the roll-out of commercial-scale tidal technologies. Currently, this acceleration is hindered by an insufficient understanding of the complex interactions that underlie physical ocean processes.

Notably, the European Marine Energy Centre (EMEC) serves as a host for device developers, both those from the past and present, encompassing their existing and projected deployments [22].

1.3 Uncertainty in the Tidal Stream Energy Sector

The uncertainty associated with the tidal energy industry stems from both technical intricacies and external factors. As tidal turbines are still emerging technologies, validating and demonstrating their power performance in real-world conditions is crucial for their successful integration and commercialisation within the tidal energy sector [23]. The sector's current state, which often falls short of initial expectations, can be largely attributed to these uncertainties, which deter potential investors from committing to projects. Over the past decades, ambitious projections like Garrad Hassan's estimate of 7.5 GW of capacity to be installed in the UK by 2010 have failed to materialise, creating a climate of unmet expectations. A history of over-promising and under-delivering has eroded investor confidence and contributed to the withdrawal of major players like Siemens, Alstom, and Scottish Power from the sector [24, 25, 26].

Long-term investments are imperative for the development of tidal energy projects, necessitating a stable and supportive policy environment. The UK government, for example, has played a role in fostering the sector's growth by offering attractive market conditions through high subsidies and grants [27]. However, this support has its limitations, and the industry continues to face challenges tied to the complexities of scaling up and reducing costs. A cycle of challenges emerges, as achieving cost reductions requires scaling to benefit from learning effects and economies of scale. Yet, scaling is hindered by the need for substantial investments, which are themselves contingent on lowering costs and comprehending associated risks [28].

Striking a balance between experience, investment, and risk management poses a formidable challenge for developers, who must surmount these hurdles to usher in the promised potential of tidal energy as a reliable and sustainable source of power.

1.3.1 Tidal Energy Converter Power Performance

Power performance assessment (PPA) details how efficiently tidal energy converters (TECs) convert kinetic energy into electrical energy. Uncertainties arise from model assumptions, inexact specifications of physical and numerical model parameters, and real-world measurements. As the tidal industry advances towards commercialisation and larger arrays, there are more opportunities to measure the behaviours of TECs whilst they produce power. This advancement will provide more field data, offering deeper insights into uncertainties, particularly in the context of PPAs which tidal developers must obtain to derisk and prove their devices. Uncertainties are an essential component of analysis for investment and certification in which risks cost money. The purpose of the assessment of power is the production of the measured power curve, this requires a true representation of the current flow to be paired with the corresponding electrical power of the device.

A demonstrable improvement in the accuracy of uncertainty estimates would allow investment decisions to be made with higher confidence. An increase in investor confidence can unlock funding for more early tidal stream arrays, the lessons from which can provide a further reduction in perceived risk, leading to further investment. Whilst it is by no means the only route to risk reduction, it is relatively unexplored to date and has the potential to improve the investment case for tidal energy.

Currently, guidance on assessing the uncertainties in PPAs is available from the wind industry and is considered to be applicable by ORE Catapult [29]. There are two main uncertainties:

1. Ambiguity in the outcomes of full-scale performance assessments (conducted at EMEC or similar facilities) that establish a rated power performance curve for the device.
2. Unpredictability arises when the device is positioned at the project site. This uncertainty stems from site-specific factors like variations in current shear, wave conditions, and turbulence.

The process for carrying out full-scale testing is described in the PPA IEC standards [30]. These standards also establish a core set of uncertainty parameters that should be incorporated into the evaluation, including elements like electrical power, current speed, and data acquisition. However, the standard doesn't specify a particular technique for quantifying the overall uncertainty associated with the measured power curve, although a similar methodology is detailed in the corresponding wind standard (IEC 61400-12 [31]). This approach is equally relevant and can be adapted for use in the domain of tidal energy.

To initiate the procedure of evaluating uncertainty, it is essential to grasp the context in which the device underwent testing. This comprehension plays a pivotal role in enabling a comparison between the testing conditions and the anticipated conditions at the designated project site.

1.4 Research Motivation

The motivation behind investigating uncertainties associated with PPAs for tidal turbines lies in the critical necessity to ensure accurate and reliable evaluation of these emerging renewable energy technologies. As the world strives to transition towards sustainable energy sources, tidal energy has gained prominence for its potential to contribute to decarbonising our energy systems. Tidal turbines offer a reliable and predictable source of energy, harnessed from the rhythmic motion of ocean tides. However, before tidal energy can be fully integrated into the energy landscape, it is crucial to address and quantify the uncertainties inherent in assessing the performance of these devices.

PPAs play a pivotal role in verifying the energy output of tidal turbines under various operating conditions. However, uncertainties surrounding data collection, processing, and the unique challenges posed by the marine environment can significantly impact the accuracy of these assessments. Investment decisions, project financing, and policy considerations are all contingent on reliable performance data. Therefore, understanding and quantifying uncertainties in PPAs is essential to provide a comprehensive and transparent evaluation of tidal turbine performance.

By undertaking research to dissect and quantify uncertainties, this study seeks to provide the tidal energy industry with a robust framework for conducting accurate and dependable PPAs. Addressing these uncertainties will not only enhance investor confidence but also facilitate the optimisation of turbine design, operation, and maintenance strategies. Ultimately, mitigating uncertainties in PPAs will contribute to advancing the adoption of tidal energy and its integration into the broader renewable energy mix, thus helping achieve sustainable energy goals and combat climate change.

The fundamental aim of this research is to offer a thorough methodology for assessing uncertainty, with the potential to enhance data integrity, accuracy, and dependability. This, in turn, can result in better decision-making, improved performance evaluations, and heightened investor trust within the tidal energy sector.

1.5 Knowledge Gaps

The tidal industry is heading towards commercialisation. The IEC TS 62600-200:2013 Technical Specification (TS) for assessing tidal energy power performance is presently undergoing revision [30]. This offers an opportunity to incorporate insights from prior tidal projects, thereby contributing to future standardisation efforts. While progress has been made in understanding and quantifying uncertainties associated with PPAs for tidal turbines, several knowledge gaps still exist that warrant further research and exploration [29]. These gaps include:

- Data Quality and Processing: Accurate data collection and processing are crucial for reliable PPAs. However, uncertainties can arise from sensor calibration, data synchronisation, and data post-processing techniques. Further research is needed to develop standardised protocols for data collection, processing, and quality assurance, reducing uncertainties associated with data integrity.
- Spatial Variability: Tidal conditions can vary significantly across different geographic locations, leading to spatial variability in the estimation of turbine performance. This spatial variability introduces uncertainties in measuring the performance of turbines using data from multiple locations. Research is needed to develop methods that account for these spatial variations and provide accurate assessments across diverse tidal environments.
- Environmental Conditions: Tidal turbines operate in harsh marine environments where factors like biofouling and corrosion can affect their performance. Understanding how these environmental factors introduce uncertainties in PPAs and developing methods to mitigate their impact is an important research area.
- Interaction Effects: Tidal turbines are to be deployed in arrays or clusters, which could lead to complex interactions between devices and alter local flow conditions. These interactions can impact the performance of individual turbines and introduce uncertainties in PPAs. Exploring the extent and nature of these interaction effects, along with their influence on uncertainty, is crucial for reliable array-wide performance assessments.
- Long-Term Performance: While short-term PPAs provide valuable insights, the long-term performance and degradation of tidal turbines are equally important. Understanding how uncertainties evolve over the operational lifespan of turbines is critical for accurate energy yield predictions and for informing maintenance strategies.
- Standardisation: Creating standardised approaches to quantify uncertainties in PPAs of tidal turbines is crucial to ensure uniformity and facilitate meaningful comparisons among projects. It is imperative to channel research endeavours towards formulating industry-wide protocols for uncertainty assessment, similar to the established methods in the wind sector.

Addressing these knowledge gaps will enhance the accuracy and reliability of PPAs for tidal turbines. It will contribute to informed decision-making, drive technological advancements, attract investments, and ultimately promote the integration of tidal energy into the broader renewable energy landscape.

1.6 Research Aims and Objectives

Aim

The aim of this thesis is to enhance the comprehension of uncertainty associated with the assessment of power performance for TECs. Additionally, this work aims to develop methodologies for quantifying and mitigating specific sources of uncertainty.

Objectives

In pursuit of the thesis objectives, the following goals are outlined:

1. Categorise the various sources of uncertainty that arise during the assessment of power performance for tidal stream energy through the utilisation of a fishbone diagram. This visual representation allows for a comprehensive exploration of the factors contributing to uncertainty and their interrelated connections. By employing this methodological approach, a structured analysis can be conducted to identify and classify diverse aspects that introduce uncertainty within the PPA for tidal stream energy systems.
2. Conduct a comprehensive assessment to thoroughly investigate the repercussions stemming from interference produced by co-located acoustic instruments on both the recorded power curve and the estimations of annual energy output.
3. Investigate and quantify uncertainties stemming from the estimation of power and energy production using various flow references (placement of an ADCP relative to a tidal turbine). The analysis of spatial flow variations is essential in determining the optimal placement of acoustic instruments for accurate PPAs.
4. Assess the uncertainties in power and energy estimations arising from the variations in both spatial and temporal flow directions. This evaluation utilises data collected from multiple acoustic instruments to comprehensively understand the impact of these fluctuations on the accuracy of PPAs.
5. Create and establish methods aimed at improving the incorporation of uncertainty quantification into the process of PPA for tidal energy, specifically at EMEC. These tools will offer practical means to systematically address uncertainties and variations that may arise during the assessment process.

1.7 Thesis Structure

This thesis is structured into the following chapters:

Chapter 2 provides a cohesive framework for understanding tidal currents by first establishing the foundational knowledge of their formation in Section 2.2. Techniques for both measuring the tidal resource and its exploitation are discussed in Sections 2.3 and 2.4, respectively. The chapter then shifts to addressing uncertainty by defining its scope in Section 2.5 and elaborating on the sources and analytical methods in Section 2.6. Concluding the chapter, Section 2.7 gives an overview of the power performance assessment for tidal energy converters, and Section 2.8 summarises key takeaways in the context of the thesis.

Chapter 3 systematically addresses two core elements of tidal energy technology: instrumentation and turbine installation methods. The section on instrumentation (Section 3.2) delves into the design, mounting, and hardware configurations of acoustic instruments, as covered in Sections 3.2.1, 3.2.2, and 3.2.3. Additionally, the chapter explores installation methods for tidal turbines, categorising them into surface-piercing (Section 3.3.1), gravity-based (Section 3.3.2), and floating (Section 3.3.3) concepts. This organisational framework enhances clarity and facilitates a deeper understanding of state-of-the-art tidal energy technologies.

Chapter 4 offers a comprehensive review of best practices and uncertainties in tidal energy, following the guidelines of IEC TS 62600-200. It begins with an introduction to the standard in Section 4.2 and proceeds to offer tailored guidance for tidal energy developers in Section 4.2.1. Comparative methodologies for wind and tidal energy performance are discussed in Section 4.3, which is further dissected into specific measurement campaign procedures for wind in Section 4.3.1 and for tidal energy in Section 4.3.2. Uncertainties within the IEC standard are covered in Section 4.3.4, followed by acoustic instrument guidance for power curve measurement in Section 4.3.5. The chapter concludes by identifying sources of uncertainties related to instrumentation, data processing, and spatial-temporal variations in Sections 4.4.1, 4.4.2, and 4.4.3, respectively.

Chapter 5 serves as the foundation for the analyses conducted in Chapters 6, 7, and 8. It initiates with the specifics of the measurement campaigns, including instrumentation features in Section 5.2 and spatial configurations relative to the deployed tidal turbine in Section 5.3. Quality assurance protocols for data filtration are detailed in Section 5.4. Subsequently, the chapter delineates instrumentation and post-processing uncertainties in Section 5.5, and rounds off with operational particulars of the tidal turbine in Section 5.6 and its corresponding theoretical maximum power curve in Section 5.7. This arrangement ensures a coherent and detailed introduction to the data sets and methodologies used in subsequent chapters.

Chapter 6 initiates with an introduction to instrument cross-talk in co-located acoustic instruments in Section 6.3. Utilising tidal flow data from two such instruments, it elaborates on the identification methods of interference features in Section 6.4, assesses their impact on measured power curves in Section 6.5, and evaluates their effects on annual energy production estimates. Remedial strategies for interference removal are then evaluated in Section 6.6, culminating in a discussion and conclusion in Sections 6.7 and 6.8, respectively.

Chapter 7 addresses the second topic, focusing on the overall uncertainty in tidal turbine power performance assessments. Data from five seabed-placed acoustic instruments are used to analyse spatial variations in flow velocity, both in the horizontal plane (Section 7.2.1) and vertical plane (Section 7.2.2). These variations are then correlated with power outputs from a full-scale tidal turbine to assess their influence on measured power curves and AEP estimates. The chapter concludes with discussions and summaries in Sections 7.3 and 7.4, respectively.

Chapter 8 explores the final topic, focusing on the uncertainty introduced by flow direction variations. It examines differences in flow direction as measured at various instrument locations (Section 8.3) and assesses their impact on the measured power curve (Section 8.4) as well as annual energy estimates. The analysis culminates in discussions and conclusions presented in Sections 8.8 and 8.9, respectively.

Chapter 9 serves as the thesis conclusion, outlining key contributions to existing knowledge. It offers actionable recommendations to the industry in Section 9.1 and evaluates the commercial implications of the key findings in Section 9.2. Future research directions are proposed in Section 9.2.3, with the chapter's final conclusions summarised in Section 9.3.

Chapter 2

Theory

2.1 Chapter Overview

This section serves as a comprehensive overview of the formation of energetic tidal sites and exploitation of energetic tidal sites for renewable electricity generation. It is organised into key subsections: Section 2.2 explains the fundamental forces and global variations shaping tides; Section 2.3 characterises the tidal resource and the instrumentation employed for in-situ measurements; Section 2.4 focuses in on tidal energy harnessing techniques, particularly horizontal axis turbines, the focus of this thesis; Sections 2.5 and 2.6 lay the groundwork on uncertainty sources and their quantification methods, respectively; and Section 2.7 outlines best practices in tidal energy converter power performance assessments. Concluding remarks tailored to this thesis are encapsulated in Section 2.8.

2.2 Theory of Tides

Tides are primarily driven by gravitational interactions among Earth, Moon, and Sun, causing cyclic rises and falls in seawater levels. The complexities of tidal behavior encompass various factors, allowing measurement, modeling, prediction, and energy extraction. This section introduces fundamental theories that underlie our comprehension of Earth's tides. Additional insight can be found in D. Pugh's comprehensive work on tidal theory [32].

2.2.1 Astronomical and Non-Harmonic Tidal Forces

The ocean tides on Earth are influenced by both the Moon and the Sun, with the former having a more dominant effect. The lunar tide results from the Moon's gravitational attraction to Earth's surface, described by Newton's inverse square law in Equation 2.1:

$$F = \frac{G m_{\mathrm{e}} m_{\mathrm{m}}}{d^2} \tag{2.1}$$

where (F) represents the gravitational force exerted, (G) gravitational constant, (m_{e}) mass of Earth, (m_{m}) mass of the Moon, and distance between Earth's center and the Moon (d).

The Earth's orbital rotation results in centrifugal forces, causing bulges on both the side facing and opposite to the Moon. These bulges form due to the balance between gravitational attraction and centrifugal force, which maintains their orbits. The centrifugal force is greater on the side of the Earth away from facing the Moon, leading to the formation of the centrifugal bulge. Additionally, there is a bulge towards the Moon on the side of the Earth facing it, resulting in two tidal bulges. According to the equilibrium theory of tides, which assumes the Earth is a sphere completely covered by an ocean of constant depth, an observer at any location on the Earth's surface will experience two high tides and two low tides per day as the Earth rotates under these bulges [32, 33].

Spring tides exhibit larger tidal ranges compared to the average monthly range, while neap tides show reduced tidal ranges. Spring tides occur after full and new Moons when the Sun, Moon, and Earth align, resulting in a high positive superimposition. This combines lunar and solar tides to create a larger total tide. Conversely, during the Moon's first or third quarter, forming a right angle with the Sun and Earth, neap tides occur. Here, the weaker solar tide partly offsets the lunar tide, resulting in a smaller total tide, as depicted in Figure 2.1.

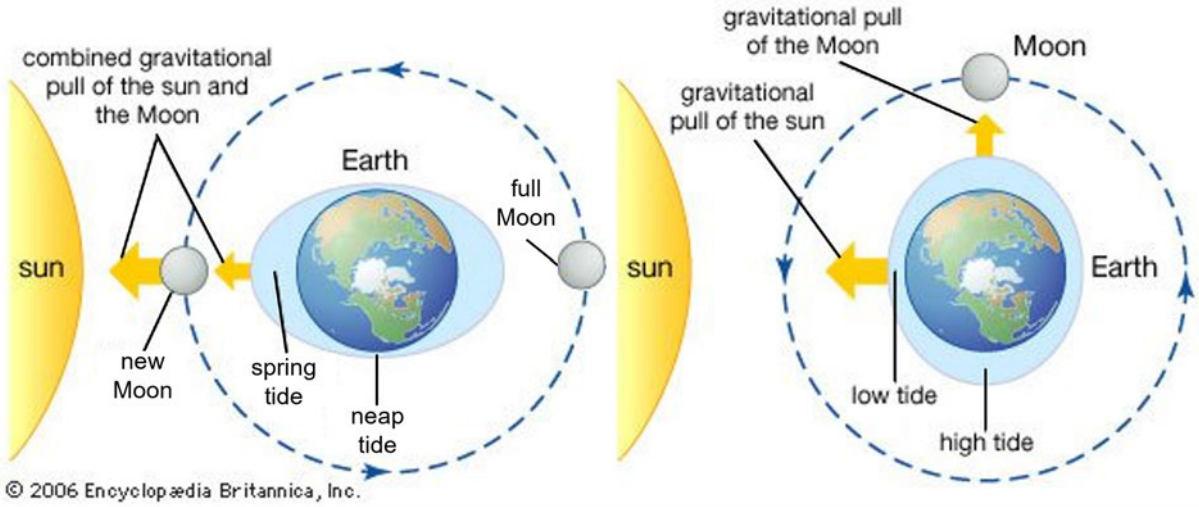

Figure 2.1: Illustration of the effects of the gravitational forces of the Moon and Sun causing Spring and Neap tides.

Moreover, additional astronomical variables associated with the Earth-Sun-Moon system influence tides. Their orbits are elliptical , causing variations in the distance between them over time, while the inclination of their orbits also impacts tidal generation. The significance of each factor varies depending on the location on the Earth's surface, as illustrated in Figure 2.2. Consequently, the combined influence of these factors, alongside the presence of landmasses and varying bathymetry, contributes to the diverse tidal patterns observed worldwide. Additionally, the relative importance of these factors changes over time for specific locations [32].

The global variations in tidal profiles, as illustrated in Figure 2.3, stemming from the factors mentioned, can be categorised into three primary groups:

1. **Diurnal tides** exhibit a pattern of one high tide and one low tide within a single tidal day. These tides are commonly found in regions such as Australia, Antarctica, and the Gulf of Mexico [32].
2. **Semi-diurnal tides** involve two high tides and two low tides of roughly equal magnitudes occurring in a lunar day.

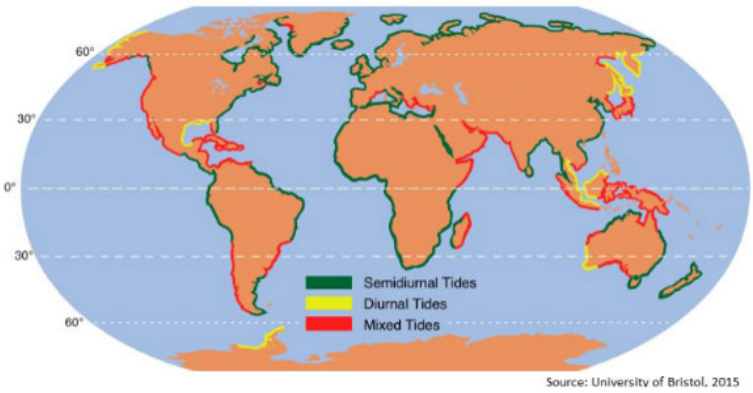

Figure 2.2: Global variability in tidal patterns.

3. **Mixed tides** are characterised by a sequence of a higher high tide followed by a lower high tide, and similarly, a higher low tide followed by a lower low tide. This tidal pattern is often observed in the Pacific region.

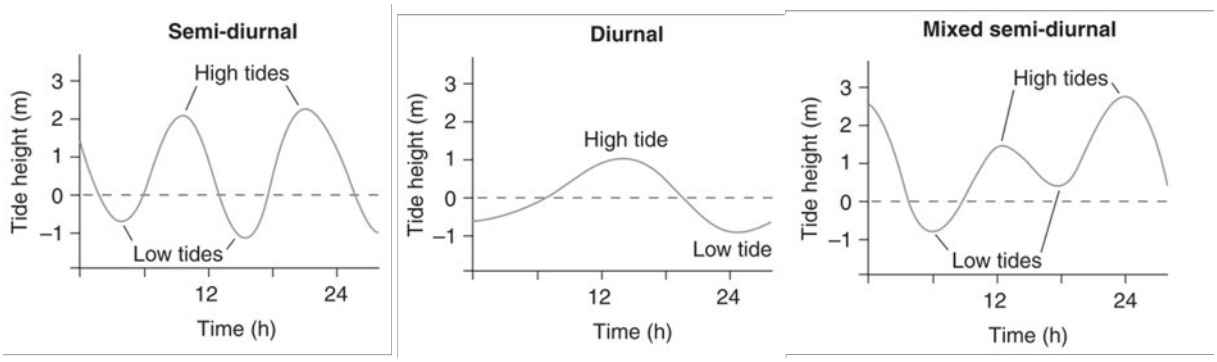

Figure 2.3: Daily tide patterns.

This thesis is primarily centered on the study of semi-diurnal tides occurring around the UK, with a specific focus on the coastal region of the Orkney Islands, Scotland.

2.2.2 Type of Tidal Stream Site

Met-ocean data encompasses water movement (including water level and current), offshore wind, and sea conditions like waves. Tidal basin shape and depth can induce resonance, altering tidal characteristics. Despite minor geographical differences, some regions exhibit distinct tidal profiles due to resonance, countering equilibrium tidal theory's predictions. For instance, Florida's East coast experiences semi-diurnal tides, while the West coast experiences mixed tides due to resonant basins [34]. Resonance can amplify tidal height, as seen in the Bristol Channel.

According to Polagye and Thomson's model [35], measured currents stem from deterministic, meteorological, and turbulent components, varying site-wise. Deterministic components comprise harmonic constituents and currents due to local features.

Three fundamental site types are:

1. Tidal basins,
2. Symmetrical (rectilinear) bi-directional channels,
3. Asymmetrical bi-directional channels.

Distinguishing between the latter two involves introducing the concept of the principle direction tidal ellipse. Tidal ellipse plots use polar coordinates to display velocity magnitudes (as radius) and directions (as radial coordinates derived from compass headings). These plots facilitate assessing flow variation in magnitude and direction at the site and identifying the established flow direction for turbine developers. If ebb and flood tidal cycle flow directions are $\approx 180^\circ$ apart, the site is considered symmetrical or rectilinear. Typically, velocity data points are 5 to 10 minutes temporally-averaged and spatially averaged over the channel depth (relative to a tidal turbine's predicted swept area). Grouping these tidal ellipses aids in understanding flow direction variation at the site.

Figure 2.4 contrasts symmetrical and asymmetrical tidal features. Symmetry is observed when the fastest flow directions for Flood and Ebb tides are nearly 180° apart. Flow is considered asymmetrical when this angle deviates significantly (greater than 10°) from this value.

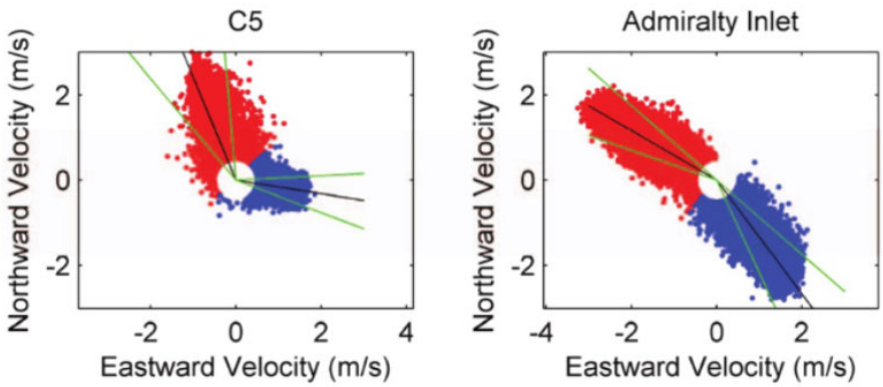

Figure 2.4: Illustrations of principal direction plots for both asymmetrical (left) and nearly symmetrical (right) sites.

Examples of rectilinear flow can be found in locations such as Admiralty Inlet in Puget Sound, as shown in Figure 2.4b, as well as the Pentland Firth and the Fall of Warness (FoW), depicted in Figure 2.5a,b [36]. It is important to note that this study primarily centers on the Fall of Warness (FoW) site in Orkney. The appeal of rectilinear sites lies in the ability to install turbines in a stationary position, aligning the blades to effectively capture tidal currents from both directions. In contrast, sites with a discernible offset between Flood and Ebb tides, such as the C5 site example in Figure 2.4a, would necessitate turbines equipped with yaw capabilities to optimally harness energy from both tidal directions. Another key aspect of this classification involves assessing the difference between the magnitudes of flood and ebb tides at specific sites.

Tidal basins manifest when a reservoir experiences the inflow and outflow of tides via a solitary narrow passage. Strangford Loch, the deployment site of SeaGen [37], and Digby Gut, featured in Figure 2.6, exemplify such basins. These locations offer optimal conditions due to their confined channels, which limit flow angle variations and yield highly symmetrical tidal ellipses. However, in specific areas like Ramsey Sound off the Welsh coast, one tide's velocity significantly surpasses the other's. This scenario is unfavorable as it often results in one tide maintaining an extractable flow velocity for a shorter duration, subsequently diminishing the turbine's resource utilisation potential.

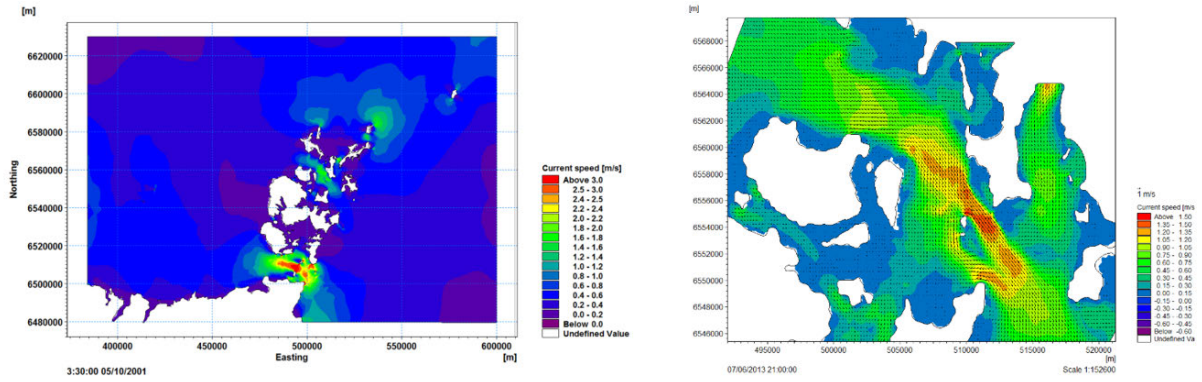

(a) Pentland Firth and Orkney waters (b) Fall of Warness, Orkney

Figure 2.5: Tidal flow velocities for the Pentland Firth and Fall of Warness generated through the utilisation of the MIKE 21 Flow model by the University of Edinburgh (UoE).

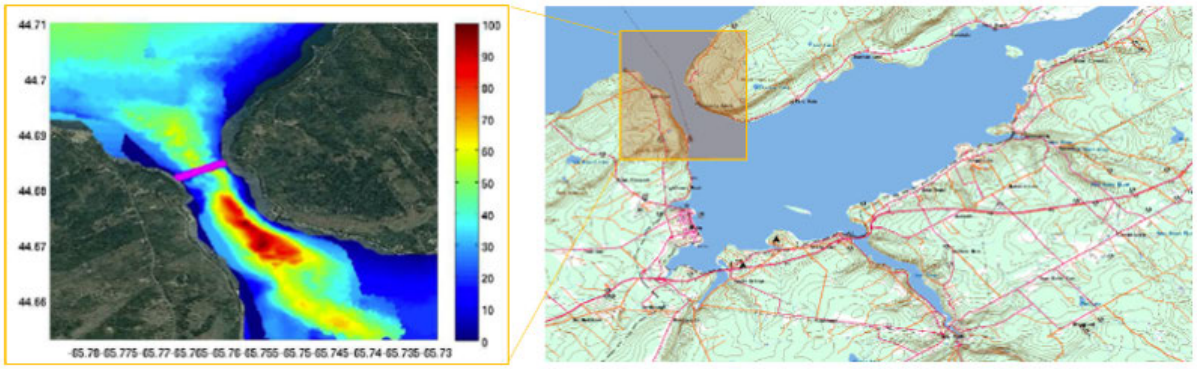

Figure 2.6: Illustration of a tidal basin at Digby Gut in Nova Scotia, featuring estimated flow velocities (left) and corresponding Yellow maps (right).

2.3 Measurement of Tidal Stream Resource

For tidal stream technology to attain commercial viability, it necessitates substantial current velocities, which are prevalent only in specific geographical zones. A comprehensive assessment of the natural resource is imperative before deploying any tidal device, ensuring the project's economic feasibility [38]. Understanding the tidal stream resource involves current measurements and numerical modeling of targeted areas. Numerical modeling serves various purposes, such as initial evaluation [39], extraction optimisation [40], and impact assessment [41, 42]. The primary approach for current measurement entails using an Acoustic Doppler Current Profiler (ADCP) - covered in Section 2.3.2 - either positioned on the seabed or mounted on a vessel for cross-channel transects. Alternative techniques, like radar systems [43], have been proposed but are yet to gain widespread adoption.

Initial feasibility studies and high-energy site characterization often prioritise velocities exceeding 2.5 $m{\cdot}s^{-1}$ and a specific range of water depths (25 - 50 m) [44, 45, 46]. These velocities result from the influence of landmasses that induce flow acceleration. Tidal site resource characterisation initiates during the regional assessment phase. Once a potential development zone is identified and the focus shifts to a specific area, it enters the 'site assessment' phase. This phase classifies the site into one of three types. The phases are as follows:

1. **Phase 1: Regional assessment** In this phase, the model's resolution should be coarse due to the extensive study area. If a suitable model for the area exists, it can be used; otherwise, a model with a grid resolution finer than 5 km should be developed. The limitations of using a coarse model, both for accuracy and location, should be acknowledged.
2. **Phase 2: Site assessment pre-feasibility** The maximum cell length scale in the area of interest should be finer than 500 m, and even finer (200 m) for areas with highly irregular bathymetry.
3. **phase 3: Site assessment full-feasibility** The grid resolution should be as fine as practical (finer than 50 m). The determination of the appropriate resolution depends on factors like area size, bathymetry availability, computational time, and cost, compared to alternative data collection methods like field surveys.

Experience has demonstrated that dedicating effort to constructing a well-designed domain mesh yields more stable and accurate models, thus minimising the occurrence of model run failures [47]. The mesh resolution should ensure the adequate representation of essential bathymetric features and islands while upholding mesh quality. Unstructured meshes are utilised for all models. For regional modeling sites, coastline delineation can be done manually in Quantum GIS (QGIS), utilising a combination of Open Street Maps base layers and Sentinel 2 satellite imagery. Figure 2.7 and Figure 2.8 illustrate the three previously discussed site characterisation phases, ranging from a broad regional context to a potential tidal test site [47].

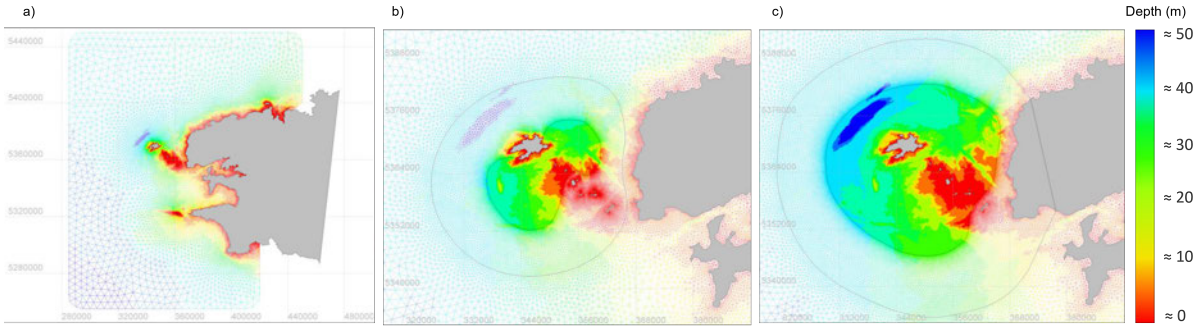

Figure 2.7: Iroise Sea model progression: a) Regional assessment, b) Site assessment pre-feasibility covering the Fromveur Strait and neighboring islands, c) Site assessment full-feasibility of the Fromveur Strait.

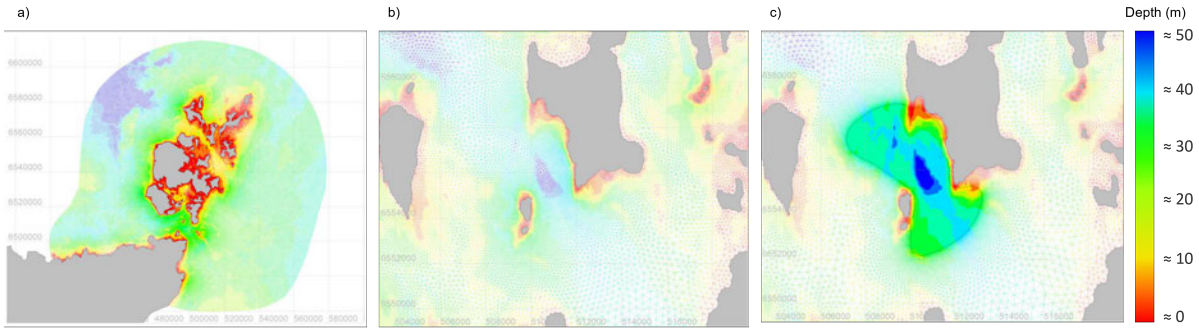

Figure 2.8: Orkney Islands model progression: a) Regional Assessment of the Orkney Islands, b) Site Assessment Pre-Feasibility encompassing the Fall of Warness and nearby islands, c) Site Assessment Full-Feasibility for the Fall of Warness.

Current descriptors typically encompass the three-dimensional velocity field (*u*, *v*, and *w*, corresponding to the streamwise, transverse, and vertical components of flow). These metrics involve the velocity profile throughout the water column (U_z), and water surface elevation referenced to a datum such as mean sea level, highest, or lowest astronomical tide [48]. To estimate long-term resource potential, Legrand [49] suggests collecting mean flow velocities and performing harmonic analysis, which involves separating observed tides or tidal currents into basic harmonic constituents. Flow measurements should align with the predicted hub height of a proposed Tidal Energy Converter (TEC) or be averaged over the expected rotor diameter. The positioning of TECs are strategically placed in energetic tidal flows to ensure economic viability. Consequently, these devices and their support structures are situated in the flow region that experiences seabed friction, often referred to as the boundary layer [50].

Tidal current flows experience significant velocity variations throughout the water column due to shear from the seabed. Various models have been employed to simplify this velocity profile [49], with the widely used $1/7^{th}$ power law [51] being a prominent example, the general statement of a velocity power law profile is provided in Equation 2.2:

$$U_z = \left(\frac{z}{\beta\, h}\right)^{\frac{1}{\alpha}} \cdot \bar{U} \tag{2.2}$$

where: the following variables are defined, U_z, velocity at a height z above the seabed, z, a point along the vertical axis indicating height above the seabed, β, bed roughness coefficient, h: total water depth, α, empirically calculated coefficient usually falling within the range of 7 to 10, and $\bar{U}$ is the depth-averaged velocity.

This is a general guideline, but field measurements are advised for accuracy. Osalusi et al. [52] conducted a measurement campaign at the EMEC full-scale tidal test site, producing flow velocity depth profiles that closely matched the pattern of Equation 2.2. It's important to acknowledge that Equation 2.2 does not account for wind and wave-induced surface influences, which could substantially impact the depth profile in the upper portion of the water column.

While Equation 2.2 originates from shelf-sea oceanographic studies, it's commonly employed in tidal energy research to describe velocity profiles [53, 54, 55]. Additionally, the log-law expressed in Equation 2.3 [56] can also serve this purpose by utilizing friction velocity ($u*$) and bed roughness length-scale (z_0), along with von Karman's constant ($k = 0.4$) [57].

$$U_z = \frac{u^*}{k} \ln\left(\frac{z}{z_0}\right) \tag{2.3}$$

where $u*$ represents estimates of friction velocity, k is von Karmans constant, and z_0 is the bed roughness length scale.

The characterisation of tidal stream sites remains an ongoing endeavour [58], though strides towards standardisation have been taken [59] with the introduction of the IEC's 62600. This standard was established to provide a consistent method for understanding site flow characteristics, predicting resources, and guiding design considerations for tidal developers. The standard mandates reporting of tidal ellipses and principal flood and ebb flow directions. Characterising the range of flow velocities and directions at potential tidal energy sites is crucial, as it establishes parameters for selecting appropriate tidal devices based on site-specific conditions.

2.3.1 Site Characterisation: Field Instrumentation

Numerous well-established techniques exist for measuring fluid velocities. This section provides an introduction to these methods, delving into their underlying theories, primary advantages, and corresponding limitations. Notably, acoustic sensors, extensively employed in this study, receive further elaboration in Section 2.3.2.

Tide Gauge

A tide gauge, also known as a water level meter, functions as a sensor that measures surface elevation while smoothing out wave-induced fluctuations. These sensors employ various technologies, such as pressure-based systems mounted on the seabed and radar-based systems installed on the shore. An advantage of tide gauges lies in their ability to provide a continuous record of water level variations. When coupled with knowledge of the channel's cross-sectional area, these measurements can inform the average volume flow rate. However, it's important to note that tide gauges lack the capability to capture depth-dependent flow variations or finer-scale motions, a tide gauge is illustrated in Figure 2.9 [60].

Figure 2.9: Example of a tide gauge from Valeport.

Velocimeters

Three types of velocimeters exist, namely:

1. **Rotational anemometer/impeller:** In the context of velocity measurement devices, an analogous tool to consider is the rotational cup anemometer, widely used in the wind industry. This device employs multiple cups rotating around a fixed axis, which responds to the fluid flow by generating a rotational motion. This cost-effective system effectively translates the rotational speed into wind speed measurements. It's noteworthy that this anemometer can capture wind from all directions, often accompanied by a vane to provide directional information. A similar adaptation, relevant to oceanography, replaces the rotating cups with an impeller attached to a directional vane. This apparatus is depicted in Figure 2.10 [61]. However, for tidal applications, a significant challenge emerges in deploying such a device at the appropriate depth within the water column.

Figure 2.10: Impeller mounted to a directional vane.

2. **Hot wire anemometer:** Another significant device to consider is the hot wire anemometer, which operates using a small heated wire positioned within the air or gas stream of interest for velocity measurement. As the stream flows past the wire, it causes cooling, the rate of which is influenced by the flow velocity. This principle has found application in tidal turbulence analysis, as demonstrated by Grant H. [62]. It's worth noting that while hot wire probes can estimate flow velocities in multiple directions, the filaments within them cannot be entirely isolated from convection effects due to off-angle flows. An illustration of a single-axis hot wire anemometer is presented in Figure 2.11 [63].

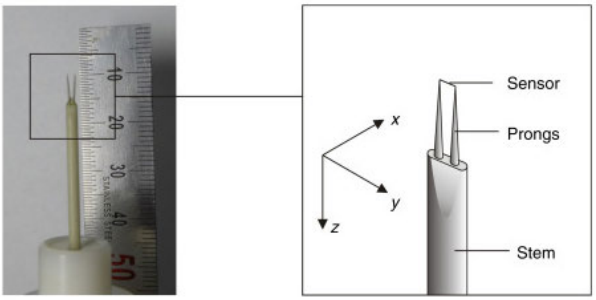

Figure 2.11: Coordinate system and hot-Wire probe configuration.

3. **Electromagnetic flow meter:** Another valuable tool for velocity measurement is the electromagnetic flow meter, suitable for fluids with electrical conductivity, such as water or molten metal. It operates based on the principles of electromagnetic induction. This type of sensor creates a magnetic field and, as the fluid flows through it, induces a potential difference proportional to the flow velocity perpendicular to the flux lines. By employing multiple electromagnetic fields, fluid flows across various axes can be resolved, as depicted in Figure 2.12 [64]. These devices often alternate the direction of the generated electromagnetic fields, inducing a voltage that changes in polarity, effectively mitigating interfering voltage effects. This approach has been adapted for tidal velocity measurements as well, although its limitation lies in providing a single-point measurement at the sensor's location.

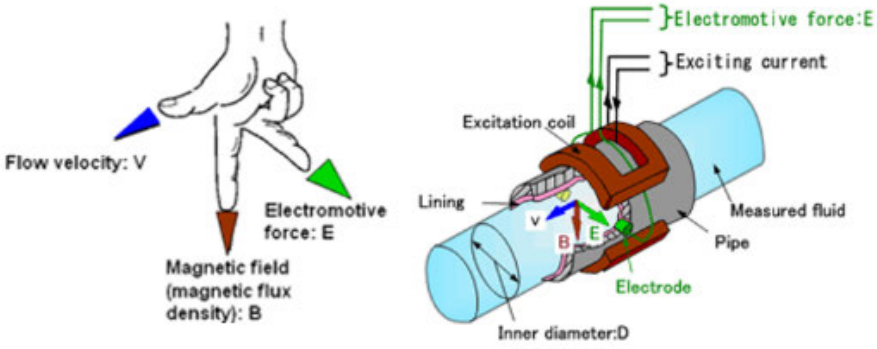

Figure 2.12: Operating principle of a magnetic flow meter.

Differential pressure sensors

Pressure-driven flow meters encompass a variety of sensor technologies, some of which are relevant to the tidal industry. These sensors operate based on Bernoulli's principle, which states that a moving fluid generates a pressure difference that increases in proportion to the square root of the velocity, assuming no changes to the ambient pressure. This pressure difference is typically measured as the dynamic pressure resulting from fluid flow minus the static pressure of stagnant flow. Such devices are often referred to as differential pressure gauges, an example being the Pitot tube commonly used in the aerospace industry.

Piezo-electic probes

A piezoelectric sensor comprises a solid surface, often made of ceramic, that generates an electrical charge in response to mechanical strain. When the dynamic pressure increases, causing strain on the probe surface, a voltage is generated. Multiple probes positioned at various angles can be utilised to measure velocity fluctuations along different axes. A notable advantage of these devices is their ability to accommodate a very small probe face, enabling measurements of finer scales of turbulent flow. Additionally, they can operate at high sample rates, up to 200 Hz. However, a limitation is that they don't measure mean velocity, necessitating a secondary sensor to provide a reference flow velocity for these fluctuations. Similar devices can use piezoresistive strain gauges, where a deformable diaphragm experiences strain due to dynamic pressure. When incorporated into a Wheatstone bridge, they can be calibrated to correlate a change in output voltage with a corresponding change in velocity.

2.3.2 Acoustic Doppler Technology

Acoustic Doppler Current Profilers (ADCPs) hold a pivotal role in the comprehensive characterisation of tidal resources. These devices utilise the Doppler effect to measure water velocities across different depths, enabling the collection of detailed velocity profiles within tidal flows. ADCPs are particularly significant in tidal resource assessment due to their ability to provide flow measurements remotely, even in challenging underwater environments. By offering accurate and high-resolution data on water velocities and currents, ADCPs contribute crucial insights for understanding the dynamic behavior of tidal flows and optimising the positioning and performance of tidal energy devices. These devices are versatile and adaptable, capable of being deployed on the seabed, fixed frames, buoys, and boats as shown in Figure 2.13.

The precursor to ADCPs was the Doppler speed log, an instrument originally designed to measure ship speed through water or over the sea bottom. In the mid-1970s, the first commercial ADCP emerged as a modification of the speed log, aimed at more accurately measuring water velocity and enabling measurements in range cells across a depth profile. This innovation gave rise to the first vessel-mounted ADCP. Then, in 1982, Teledyne RDI introduced its inaugural self-contained ADCP, designed for long-term, battery-powered deployments. This marked an important advancement in the field [65, 66].

Design Variations

Acoustic Doppler profilers exhibit diverse configurations catering to a wide array of applications, featuring variations in the number of range bins, ranging from single to as many as one hundred. Design choices entail a trade-off between range and resolution, with the potential for escalated random errors. While lower-frequency pulses traverse longer distances, they necessitate larger cell sizes to process signals without increasing noise. Conversely, higher frequency instruments excel at resolving fine spatial scales with reduced random errors, albeit potentially constrained to a few centimetres in range.

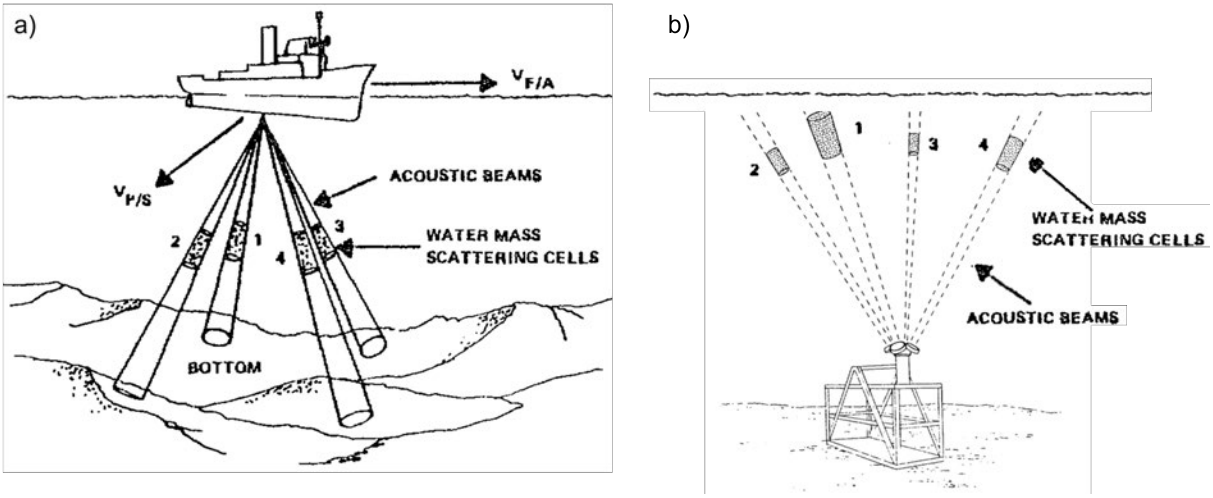

Figure 2.13: Doppler Current Profiler Acoustic Beams: a) Mounted on a vessel, and b) Deployed on the seabed.

In addition to taking range into account, the number of transducers used is another crucial aspect of design. A single beam can only determine one velocity component, whereas configurations with three beams allow for the determination of three velocity vectors. Often, designs include a fourth beam to provide an extra estimation of vertical velocity. Having two measurements of the same velocity vector allows for the calculation of error velocity, which indicates the quality of the measurement. For evaluating waves, an additional vertical beam is often employed to track changes in surface elevation.

Subsea Doppler sensors primarily fall into two distinct categories: Diverging Acoustic Doppler Profilers (D-ADPs) and Acoustic Doppler Velocimeters (ADVs). D-ADPs encompass a range of field sensors, extending from short to long-range capabilities. These sensors are designed with three to five transducers, each of which functions as both a transmitter and a receiver. One notable advantage of D-ADPs is their ability to conduct remote and comprehensive measurements throughout the water column. This characteristic makes them particularly valuable for stable seabed deployments, as it mitigates uncertainties associated with the constant movement of sensors.

In contrast, ADVs are composed of a single transmitting transducer and three to four receiving transducers. These transducers are strategically positioned at angles that converge on a specific measurement volume, often represented as a single cell. When deploying ADVs at mid-depth in tidal channels, it becomes imperative to implement mounting solutions that are customized to the specific depth requirements.

Apart from the aforementioned sensor types, there are also newly introduced single-beam (SB-ADP) versions of the D-ADP. These variants are specifically designed for straightforward installation at the midpoint of the water column, which is commonly seen on structures like tidal turbines. In the study at hand, these particular sensors were put to use.

Utilising a single pulse in these sensors eliminates the possibility of interference between pulses, and the solitary measurement volume lessens the extent to which the sensor needs a consistent flow condition. This design attribute helps to ensure accurate measurements even in situations where flow homogeneity varies.

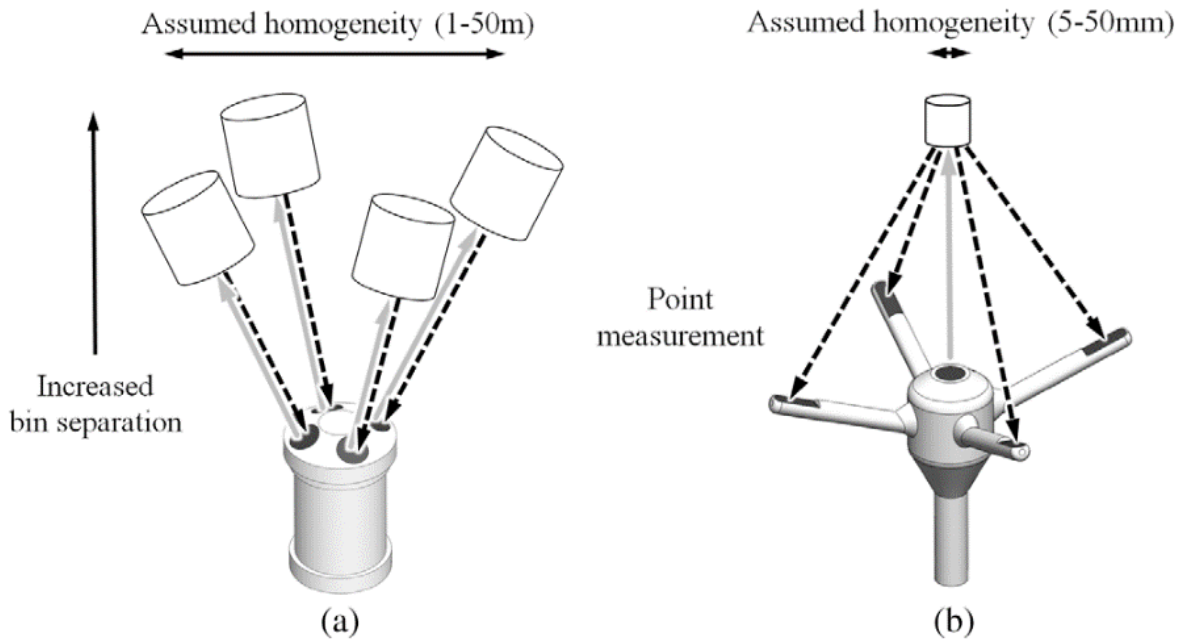

Figure 2.14: Comparison of beam orientations for typical (a) Diverging ADCP and (b) Acoustic Doppler Velocimeter (ADV) devices. The grey arrow pointing towards the sample volume illustrates the direction of the emitted acoustic signal, while the dashed black arrow pointing towards the receiver signifies the direction of the reflected signal.

Doppler Theory

A Doppler sensor employs a transducer to emit an ultrasonic pulse, often referred to as a 'ping,' into the water. The trajectory of this pulse within the water is designated as the 'beam.' During its passage, the pulse interacts with suspended particulate matter (typically ranging from 1 to 30 mm in size) present in the water, resulting in reflections known as back-scatters. Importantly, these back-scatterers are assumed to move at the same velocity as the surrounding water, even though the water itself does not contribute significantly to the reflected pulse's signal [67]. After the pulse transmission, the transducer switches its function to that of a receiver, detecting the echoes of the reflections sent back along the beam axis. The reflections undergo a phenomenon known as the Doppler shift.

Flow measurement employs the Doppler shift of backscattered acoustic signals originating from suspended particulate material that moves at the same speed as the water particles. This motion of the particles serves as an indicator of the local fluid flow's speed [68]. The alteration in frequency ratio (f_d) corresponds to the flow speed (u_{beam}) relative to the Speed of Sound (C) within the medium. Due to its dual role as a sound transmitter and receiver, the Doppler shift effectively undergoes duplication. This shift occurs when there is a relative change in distance between the sound source and the particles, resulting in radial motion. Conversely, when the direction between the source and particles changes without any alteration in distance (referred to as angular motion), no Doppler shift transpires—this is encapsulated by the term cos(A) in Equation 2.3.2, where A is defined in Figure **??**RDI2011fig:scattervelocity [67] $f_d = 2f_{\text{pulse}} \cdot \left(\frac{u_{\text{beam}}}{C}\right) cosA$ where f_d represents the difference in frequency between the transmitted and received pulses, f_{pulse} is the transmitted pulse frequency, u_{beam} is the fluid velocity along the beam axis, and C is the SoS in the appropriate medium, in this case seawater.

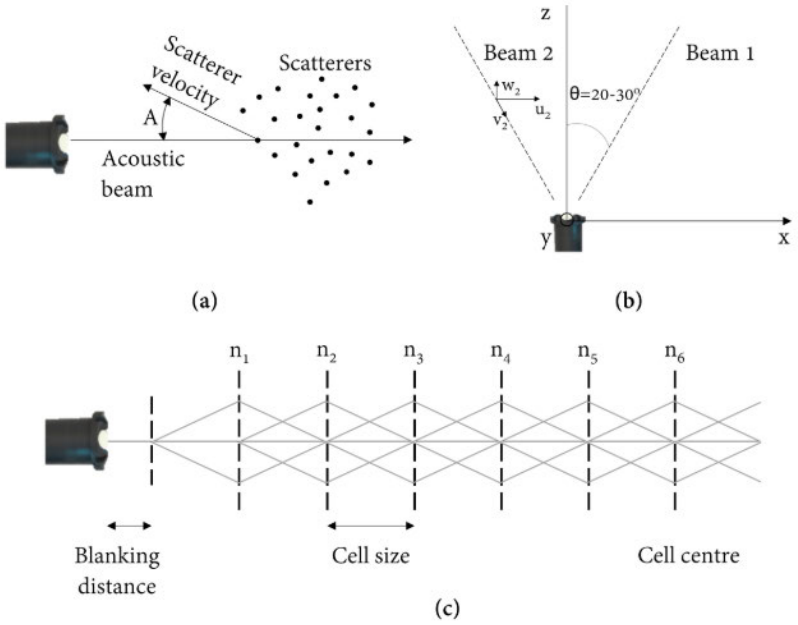

Figure 2.15: Acoustic Velocimetry. a) Measurement of the velocity component aligned with the acoustic beam, representing radial velocity. b) Configuration of the acoustic beam in a standard diverging ADCP. c) Visualisation of blanking distance, cell size, and centre-weighted averages applied per cell.

Speed of Sound

Sound refers to the propagation of pressure waves through mediums such as air, water, or solids. These sound waves share similarities with shallow-water ocean waves. The velocity at which sound waves travel, termed the Speed of Sound (SoS), can be calculated using the following Equation (2.4):

$$\mathrm{C} = f\lambda \tag{2.4}$$

where C represents the Speed of Sound, f is the frequency and λ is the sound wavelength.

Both the range and velocity measurements are influenced by the SoS. In seawater, the SoS relies on factors like temperature (T), depth (d), and salinity (S), and it can be computed using the Equation 2.5:

$$C = 1449.2 + 4.6T - 0.055T^2 + 0.00029T^3 + (1.34 - 0.01T)(S - 35) + 0.016d \tag{2.5}$$

Range gating

Range gating is a crucial technique used in ADCPs to process the continuous returned signal from the water column and obtain accurate measurements of water currents at different depths. The acoustic pulse will continue to travel through the water and gradually lose amplitude due to spreading and absorption. To accurately measure water currents at different depths, it's important to isolate and analyse discrete sections of the returned signal that correspond to specific ranges or depths within the water column. The resulting velocity profile provides valuable insights into the movement of water within the water column and is essential for understanding ocean currents, river flows, and other hydrodynamic processes. Each volume measured is referred to as a depth bin. This process is illustrated in Figure 2.16 [67].

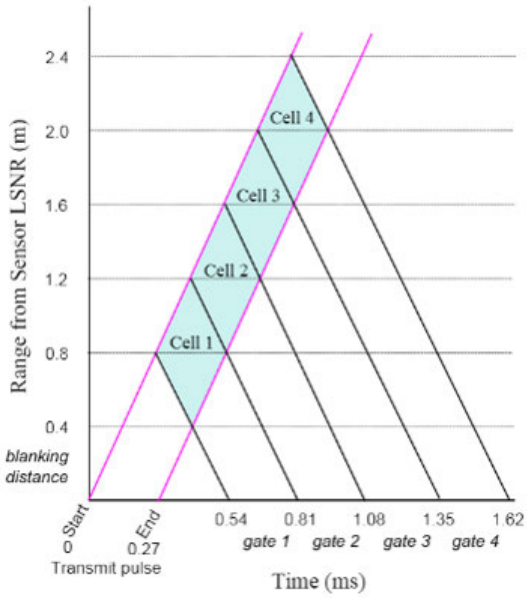

Figure 2.16: Range gating for a sensor featuring a bin size and blanking distance of 0.4 meters. Image adapted from Gordon 1996.

The interval between concluding the transmission of the pulse and commencing the initial listening phase is termed the 'blanking distance.' As depicted in Figure 2.16, the measurements are weighted towards the centreline of the measurement volume for each cell. In reality, the beam will disperse as it moves away from the sensor, resulting in a slight enlargement of the measurement columns as the distance extends.

Calculation of Velocity with Four ADCP Beams

Figure 2.17 showcases the computation of three velocity components utilising an ADCP with a conventional four-beam configuration, often referred to as the Janus configuration [67]. Each beam pair yields one horizontal and one vertical velocity component. This results in two estimates of the horizontal velocity components and two estimates of the vertical component. While Figure 2.17 depicts east/west and north/south beam orientations, it's important to note that the orientation is arbitrary [67].

Signal processing method

Three pulse types are commonly employed in Doppler devices, each presenting its own set of advantages and limitations:

1. **Narrowband:** Narrowband pulses consist of a single frequency pulse and excel in extended range coverage (refer to Fig 2.18a).
2. **Broadband:** Broadband pulses are composed of a sequence of changing frequencies. They strike a balance between narrowband and pulse-to-pulse configurations. By employing a pattern of varying frequencies, broadband pulses offer a more precise assessment of Doppler shift compared to single-frequency narrowband pulses. This enhancement significantly enhances velocity resolution. RDI, a prominent device developer, asserts that this technology reduces measurement variance by a factor of 100 (see Fig 2.18b) [67].

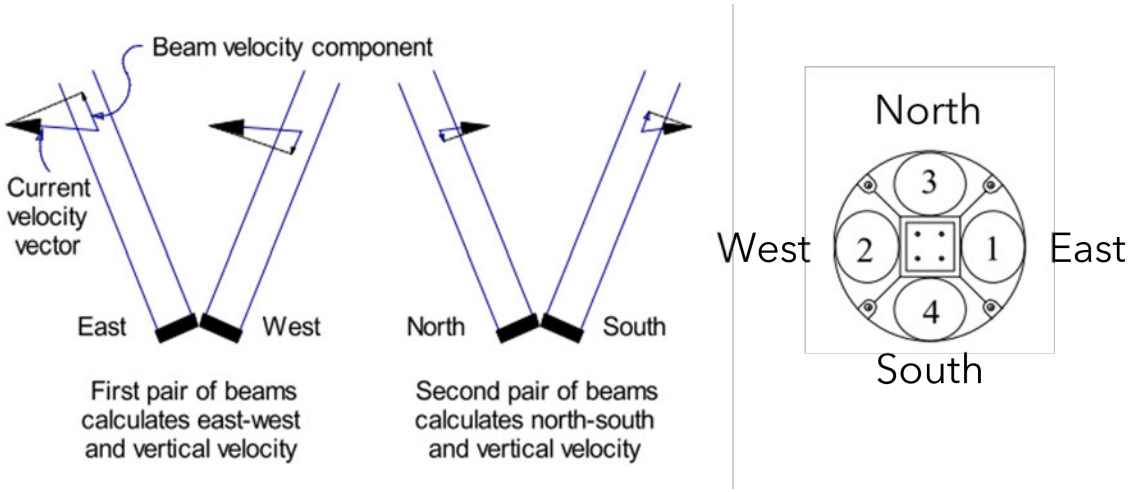

Figure 2.17: The relationship of beam and earth velocity components.

3. **Pulse-to-pulse:** Pulse-to-pulse configuration involves the transmission of one short pulse followed by a sufficient gap to dissipate any 'ringing' effects before transmitting a second pulse. This pulse type is effective only over short distances and offers the advantage of minimal noise levels (refer to Fig 2.18c) [68].

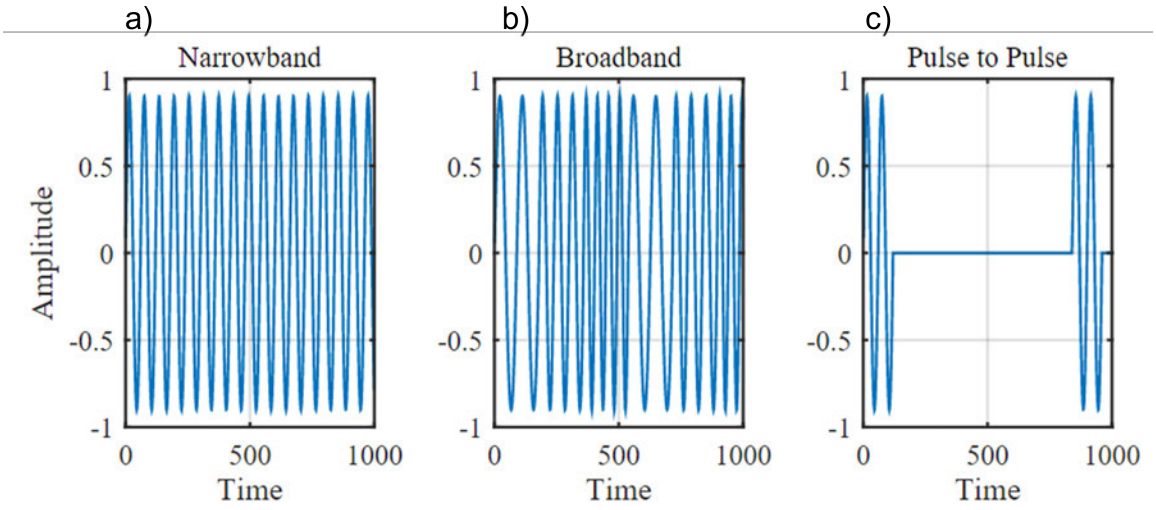

Figure 2.18: Example of different acoustic pulse types. These are: narrowband (a), broadband (b), and pulse-to-pulse (c).

Acoustic beam and side lobes

A single acoustic beam measures only one velocity component, specifically the velocity parallel to the beam, known as the along-beam radial velocity. Each acoustic beam comprises a main lobe and a side lobe, which represents acoustic energy that extends beyond the main lobe's coverage. To accurately determine all three velocity components, data is required from a minimum of three non-co-planar beams directed at varying angles relative to the profiler's principal non-co-planar axis. Additional beams offer error estimation capabilities. Notably, the measurement of velocity perpendicular to the beam direction is not physically possible.

Interference arises when side lobes are reflected more strongly by a boundary than the main lobe is by particles, leading to contamination of the returned signal [69, 70]. Figure 2.19 displays the main beam alongside the clearance zone (an area to be kept free of obstructions) surrounding the main beam. The edge of this clearance zone extends a maximum of 15 degrees from the main beam (which can range between 1.5 and 4 degrees), with an additional 11 degree spread beyond the main beam for a estimated one-way beam width of 4 degree.

It's worth noting that the instruments utilised in this thesis are manufactured by Teledyne RDI. For specific details about system types and their corresponding one-way beam widths, refer to Table 2.1 [69].

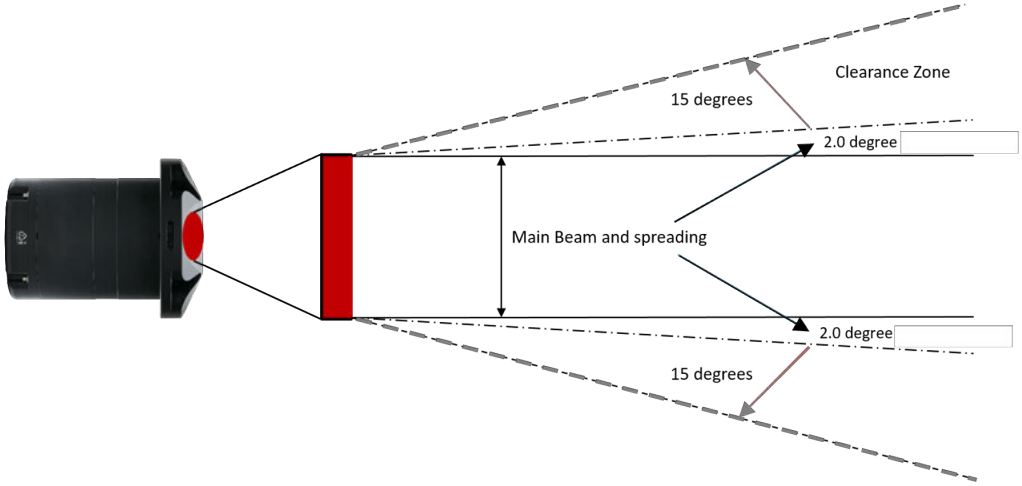

Figure 2.19: Example of the clearance zone width.

Table 2.1: Teledyne RDI acoustic instrument beam widths.

System type and frequency (kHz)	Estimated one-way beam width (degrees)
NB/BB 75, 150	4.0
NB/BB 300	2.0
NB/BB 600	1.5
NB/BB/WH 1200	1.5
WH Long Range 75	5.9
WH 300	4.0
WH 600	2.0
OS 150, 75, 38	4.0

Co-ordinate transform

Flow current along the beam is directly measured by utilising trigonometric relationships, velocities typically represent the components of flow velocity in the local coordinate system of the instrument (u, v, w). These are used to convert the flow velocity into the Cartesian coordinate system (x, y, z), which is fixed t the Earth's frame of reference. Then further converted into Earth coordinates (East, North, Up), representing the components of flow velocity in Earth centered coordinate system. This transformation involves a matrix that converts from beam to Cartesian coordinates, assuming a uniform horizontal flow between beams as illustrated in Figure 2.20) [71]. This transformation matrix is a fixed component of industry-standard instruments.

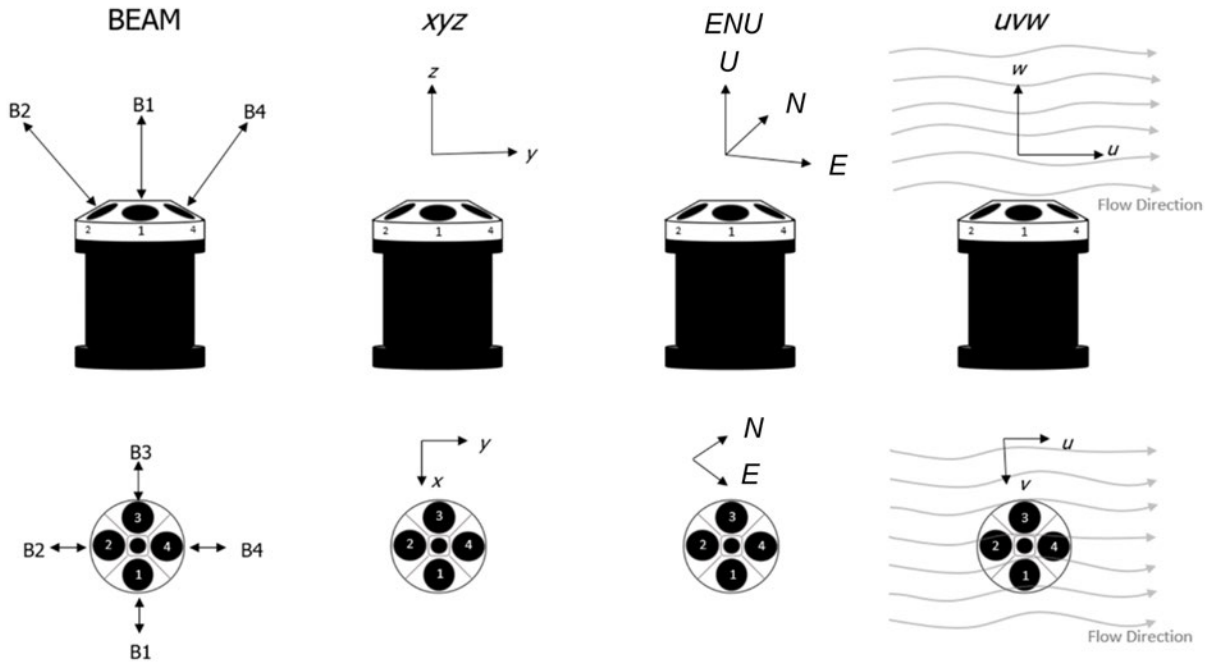

Figure 2.20: Divergent acoustic Doppler profiler beam coordinates relative to xyz, ENU and uvw.

The beam velocity is converted into a vector of velocity components within the instrument's fixed coordinate system using the instrument's transformation matrix. Unless the ADCP has been specifically calibrated to account for minor beam misalignment, the default value of the instrument transformation matrix is as shown in Table 2.2 [67].

Table 2.2: Beam to Instrument Transformation Matrix.

Component	Beam 1	Beam 2	Beam 3	Beam 4
x	c*a	-c*a	0	0
y	0	a	-c*a	c*a
z	b	b	b	b
e	d	d	-d	-d

where:

- $c = +1$ for a convex transducer head, -1 for concave,
- $a = \frac{1}{[2*sin(\theta)]}$,
- $b = \frac{1}{[4*cos(\theta)]}$,
- $d = \frac{a}{\sqrt{2}}$.
- θ is the transducer angle (20, 25, 30 degrees).

The initial three rows correspond to the generalised inverse of the beam directional matrix, symbolising the individual beam components within the instrument's coordinate framework. The last row, denoting the error velocity, is perpendicular to the other three rows and is standardised to align its magnitude (root-mean-square) with the mean of the magnitudes of the first two rows. This standardisation is selected such that, in horizontally consistent flows, the error velocity's variance indicates the proportion of variance in each nominally-horizontal component (x and y) attributed to instrument noise (short-term error) [67].

The above Table 2.2 is equivalent to the matrix presented below in Equation 2.6:

$$\begin{bmatrix} x \\ y \\ z \\ e \end{bmatrix} = \begin{bmatrix} ca(b_1 - b_2) \\ ca(b_4 - b_3) \\ b(b_1 + b_2 + b_3 + b_4) \\ d(b_1 + b_2 - b_3 - b_4) \end{bmatrix} \tag{2.6}$$

Typically, an extra rotation is required, which is accomplished by multiplying the instrument transformation matrix on the left by the rotational matrix M, this is responsible for aligning velocity components with ship or Earth coordinates. To account for alterations in the instrument's heading, roll, and pitch, the rotation matrix M is applied to the three velocity components (x, y, z) derived from along-beam velocities as shown in Equation 2.7:

$$\begin{bmatrix} \mathrm{E} \\ \mathrm{N} \\ \mathrm{U} \end{bmatrix} = \mathrm{M} \begin{bmatrix} x \\ y \\ z \end{bmatrix} \tag{2.7}$$

The rotation matrix M considers pitch (P), roll (R) and heading (H), where pitch is rotation around the y axis, roll is the rotation about the x axis and heading is the rotation about the z axis, see Figure 2.21 for representation, the rotational matrix is also shown in Equation 2.8 where C and S represent the trigonometric function cos and sin respectively:

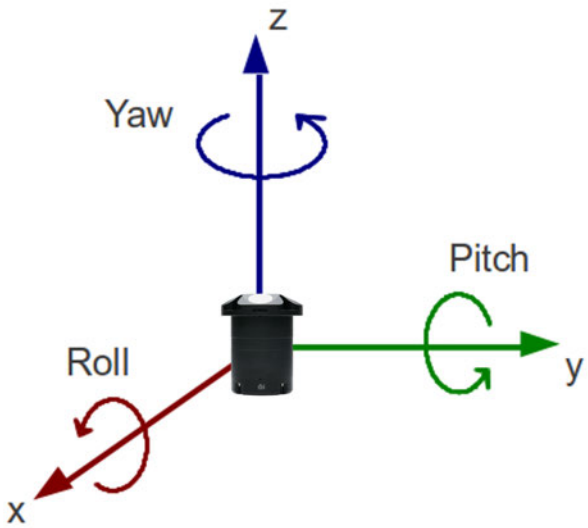

Figure 2.21: Rotation: Heading, Pitch and Roll.

$$M = \begin{bmatrix} CH & SH & 0 \\ -SH & CH & 0 \\ 0 & 0 & 1 \end{bmatrix} \begin{bmatrix} 1 & 0 & 0 \\ 0 & CP & -SP \\ 0 & SP & CP \end{bmatrix} \begin{bmatrix} CR & 0 & SR \\ 0 & 1 & 0 \\ -SR & 0 & CR \end{bmatrix} \tag{2.8}$$

$$= \begin{bmatrix} (CH*CR+SH*SP*SR) & (SH*CP) & (CH*SR-SH*SP*CR) \\ (-SH*CR+CH*SP*SR) & (CH*CP) & (-SH*SR-CH*SP*CR) \\ (-CP*SR) & (SP) & (CP*CR) \end{bmatrix} \tag{2.9}$$

To ascertain both the magnitude and direction of the current velocity, the longitudinal and lateral velocity components are utilised. The magnitude is computed as the hypotenuse of these two components, often denoted as $\bar{U}$. The direction is determined using the four-quadrant inverse tangent of the two components, yielding values in the closed interval of [-π, π]. This is in contrast to the ATAN($\frac{N}{E}$) function, which returns results confined within the interval of [-$\frac{\pi}{2}$, $\frac{\pi}{2}$]. Refer to Equation 2.10 for further clarity:

$$\text{Magnitude}(\bar{U}) = \sqrt{\text{E}^2 + \text{N}^2} \tag{2.10}$$

$$\text{Direction} = \text{ATAN2}(\text{E},\text{N}) \tag{2.11}$$

2.3.3 Cross-talk Between Acoustic Instruments In Close Proximity

Cross-talk is a well-known phenomenon whereby a signal emitted on one channel of a transmission system creates an undesired effect when received by a separate channel from another acoustic instrument. Acoustic pulses from sub-sea Doppler sensors are known to interact, but these interactions will vary with pulse frequency, sensor angle and separation. Cross-talk by co-located acoustic instruments is known to adversely affect measurements [72]. In ADCPs, noise in measurements is most often due to side-lobe interference between the beams, where energy not concentrated in the main acoustic beam interacts with the signal of a second beam [73]. As sampling volumes from multiple ADCPs approach closer proximity, the likelihood of the interactions between the returned signals are expected to intensify, potentially leading to interference. In order to give some context to the results of this investigation into the effects of cross-talk, it is worth detailing the underlying processes.

For instance, refer to Figure 2.22, which depicts two instruments aligned in parallel, image from [74]. The instrument emitting the beam that results in interference is labelled as the 'source', while the one being impacted is referred to as the 'affected' or 'receiving' instrument, irrespective of their type, configuration, or orientation.

The first panel (bottom left) displays the instrument configuration. The succeeding panel (top left) exhibits the full transmit phase of the cycle, wherein a 0.27 ms pulse covers the blanking distance, with the pulse's leading edge nearly reaching the centre of the initial sample volume. In the subsequent panel (top right), the leading edge of the 0 dB pulse, having a reflection intensity of 0 dB, has rebounded off the scatterers within the measurement volume of the first cell. This reflection has scattered in various directions. The leading edge of the reflection along the beam has reached the transducer of the 0 dB SB-ADP as the initial gating of its receive cycle commences. Meanwhile, the trailing edge of this reflection will have just arrived at the midpoint of the measurement volume, and the first gating of the receive cycle will persist from 0.54 ms to 0.81 ms. Conversely, the -100 dB sensor does not encounter the leading edge of the reflected pulse until 0.70 ms. As a result, the pulse coincides with both the initial and second gating of the receiving phase within its cycle.

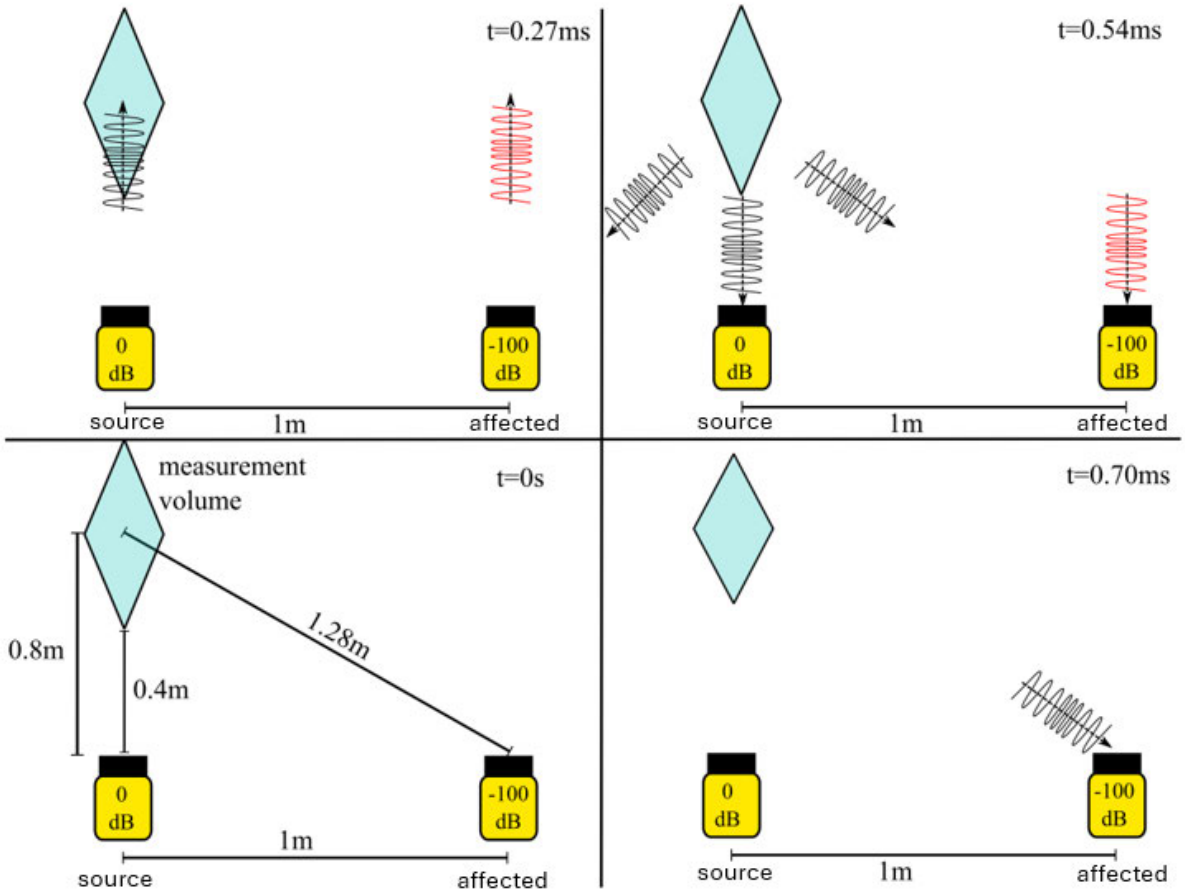

Figure 2.22: Illustration of cross-talk, presenting a segment of the transmit/receive cycle for two acoustic instruments aligned in parallel. The black pulse originates from the active sensor, while the red pulse represents the -100 dB signal from the adjacent instrument in the same location. Pulse timing is indicated at the upper right corner of each panel, with the sequence initiating from the bottom left and progressing counterclockwise.

The central objective of delving into cross-talk revolves around its impact on velocity measurements. Depicted in Figure 2.23 displays data from an experiment involving two ADCPs, assessing how their placement affects signal interference. The experiment shows that as ADCPs are moved further apart (from 1m to 3.2m apart), both the amplitude and correlation of the signals tend to become less pronounced but more stable, indicating a reduction in interference. This data is critical for optimising ADCP setup in field deployments to ensure accurate water flow measurements without interference from nearby instruments [74].

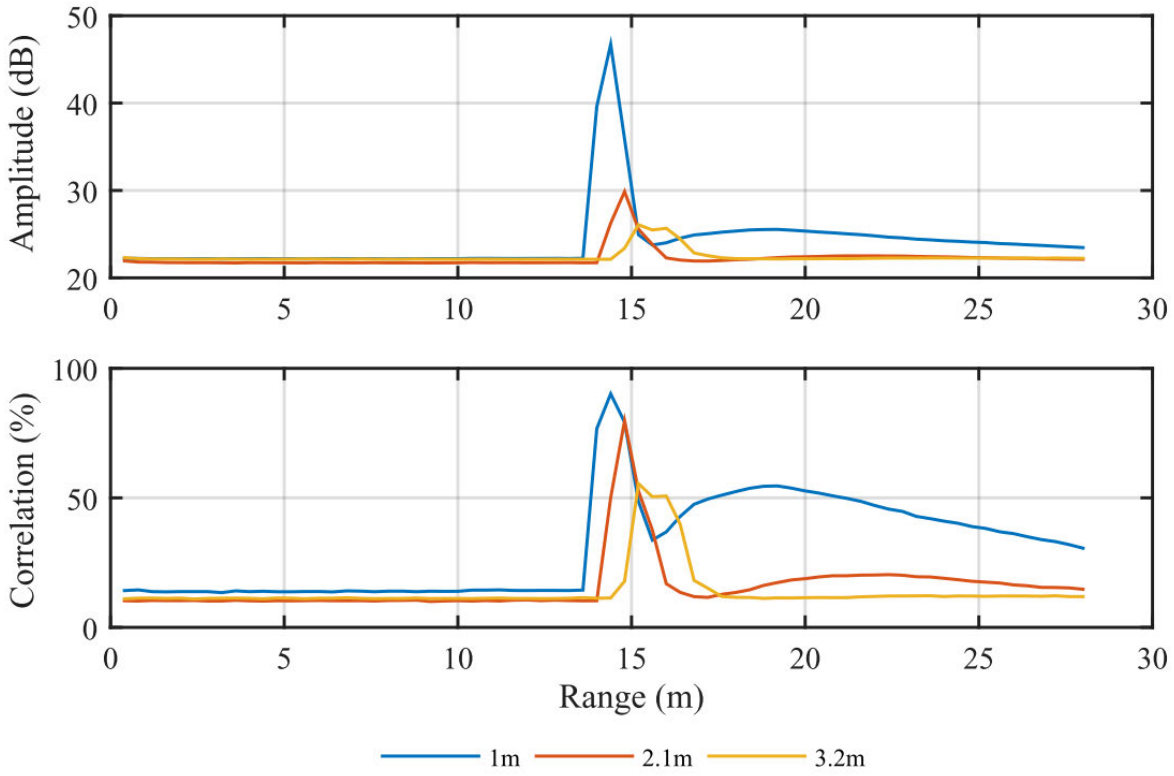

Figure 2.23: Amplitude and correlation for a single beam showing indications of interference for three separation distances.

2.3.4 Tidal Stream Environment

The tidal environment introduces intricate fluid dynamics that significantly influence the design and operation of tidal devices. Flow velocity undergoes temporal variations spanning broad tidal cycles and shorter periods linked to turbulence and surface effects. Spatial variation arises from bathymetry and seabed-induced shear. This section offers a succinct overview of these elements and their potential impact on a device's power output.

To enhance tidal machine design, an optimal rated power is chosen based on the typical flow velocities at the site, corresponding to the generator's maximum rotational speed. A rated velocity denotes the minimal flow speed required for maximum power generation. Similar to wind turbine setups, blade angles are adjusted to maintain constant rotational speed when flow velocities surpass the rated speed. The relationship between power extracted and inflow velocity is known as the "Power curve". This curve is specific to each site, underscoring the importance of precise, long-term resource predictions to enable tailored device design for specific locations [74]. Further details on power curves are outlined in Section 2.7.

Free Stream Energy

The kinetic energy flux available in a freestream tidal flow is a function of the fluid density, the volumetric flow rate and the fluid velocity as seen in Equation 2.12:

$$P = \frac{1}{2} \cdot \rho \cdot A_R \cdot U^3 \tag{2.12}$$

where:P represents the power available, measured in watts (W), ρ stands for the density of water, expressed in kilograms per cubic meter (kg/m^3), A_R denotes the cross-sectional area of the proposed tidal machine, and U represents the free stream flow velocity, measured in meters per second (m·s^{-1}).

As observed in Equation 2.12, identifying regions with elevated flow velocities becomes advantageous, given that the available power scales with the cube of the velocity.

Tidal Stream Currents

The power accessible within the tidal stream originates from the movement of substantial water masses across distinct elevation zones, influenced by the lunar and solar positions relative to the Earth [75] (see Section 2.2). While tides exert an influence on all oceans and seas, their capacity to facilitate tidal energy extraction significantly hinges on the specific tidal patterns prevailing at each site [76]. The nature of these patterns is dictated by the bathymetry of the area, its surroundings, and the constraints imposed by nearby coastal formations [77]. Temporal and spatial fluctuations in flow velocity's magnitude and direction occur due to the intricate interplay between tides and the complex dynamics of nearshore and bathymetric conditions [49, 51, 78]. These variations inherently impact the potential power generation of a tidal stream device.

Vertical Velocity Profile

Due to the velocity profile (refer to Section 2.5.1), the placement of the turbine's rotor within the water column holds substantial influence over its performance, as depicted in Figure 2.24. To optimise output, it's advisable to position the turbine away from the seabed. Similarly, keeping it clear of free surface conditions helps mitigate wave-related effects and potential interference with navigation routes, as suggested by Bryden [79] [80].

Environmental Turbulence

Tidal stream devices function within an environment characterised by significant turbulence, often featuring turbulence intensities of about 10% at hub height [58, 81]. This turbulence arises primarily due to intricate underwater topography near suitable sites for tidal energy generation.

Ongoing research aims to comprehend the turbulence's impact on tidal stream generator performance. Maganga et al. [82] conducted experiments using a horizontal axis turbine within a flume tank, at a blockage ratio of 3.5%. They evaluated their device's performance at turbulence intensities of 8% and 25%, covering a range of tip speed ratios. Results indicated that heightened turbulence intensity decreased peak power and thrust coefficients of the rotor by 14% and 13%, respectively.

Another investigation examined turbulence's influence on tidal turbine depth using high-frequency ADCP data collected in Banks Strait, an Australian potential tidal energy location. The gathered data represented a realistic amalgamation of waves, shear, and turbulence. Shifting the turbine hub from 12 m to 18 m above the seabed led to an increase in mean power (C_P) and thrust (C_T) coefficients from 9.10% to 16.29% [83].

This thesis does not focus on the effects of water turbulence on in-situ measurements and turbine power generation. While turbulence is briefly revisited as relevant in Chapters 3 and 4, it does not play a significant role in the novel research presented in Chapters 5 through 8.

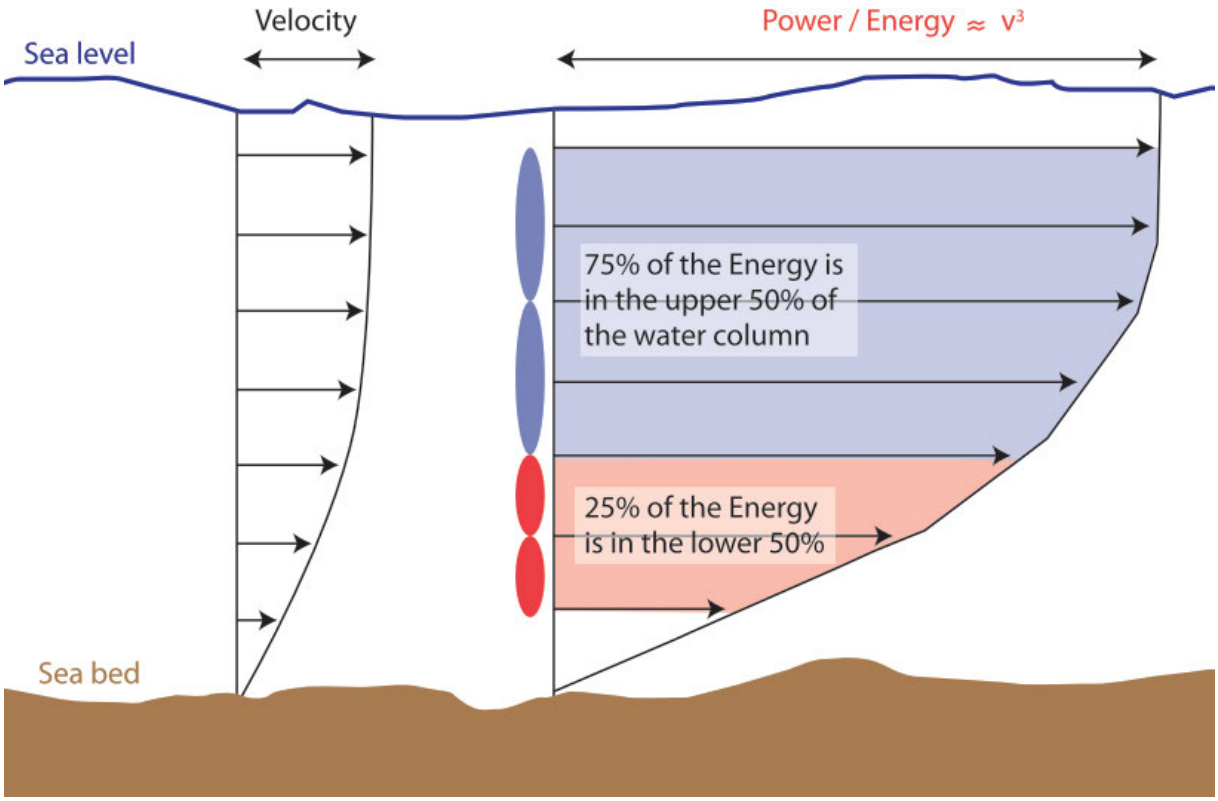

Figure 2.24: Illustrating the significance of placing a rotor at a higher position within the water column. The set of vectors on the left demonstrates the usual reduction in velocity as submergence depth increases.

2.4 Exploitation of Tidal Stream Energy

The common approach to harnessing tidal energy relies on sophisticated underwater turbine technology. These turbines are strategically positioned in areas with strong tidal currents, allowing the kinetic energy of the moving water to drive the turbine blades. As the blades rotate, they generate mechanical energy, which is then converted into electricity through generators. This innovative technology enables us to efficiently tap into the continuous and predictable power of tidal currents, contributing to the sustainable energy landscape. Numerous designs draw inspiration from established wind industry technology, adapting it for coastal and marine settings [45].

2.4.1 Introduction to Tidal Stream Turbine Devices

This section provides a concise overview of tidal turbine technology. For a more comprehensive understanding of the Horizontal Axis Tidal Turbine (HATT) concept, please refer to Section 2.4.2, as this concept serves as a cornerstone throughout the thesis.

Vertical Axis Tidal Turbines (VATT)

Vertical axis tidal turbines present an alternative approach to harnessing tidal energy. Unlike their horizontal axis counterparts, these turbines have their rotor axis aligned vertically, perpendicular to the water flow, see Figure 2.25 [84, 85]. One notable advantage of vertical axis turbines is their ability to operate efficiently regardless of the direction of tidal currents. This omnidirectional capability eliminates the need for turbines to be oriented towards the predominant flow direction, simplifying installation and positioning. Additionally, vertical axis turbines

often have a lower profile, making them suitable for shallow water depths and locations with challenging seabed conditions. However, vertical axis turbines may experience reduced efficiency at higher flow velocities due to their design characteristics. This trade-off between omnidirectional operation and potential efficiency limitations is a crucial consideration when choosing turbine technology for specific tidal energy projects.

(a)

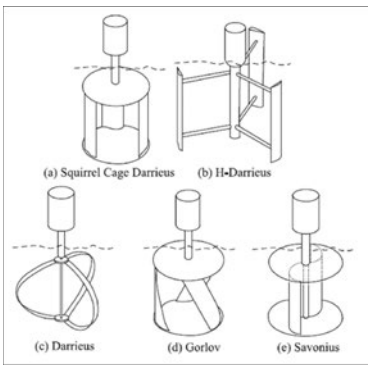

(b)

Figure 2.25: Vertical axis tidal turbine full-scale device (a), general VATT concepts (b).

The technology for VATTs has been demonstrated at full scale by commercial developers, namely, Blue Energy [86] (Canadian-based commercial company with a modular design rated at 0.62 MW that can be incorporated into a tidal fence or bridge arrangement) and New Energy Corporation [87] (another Canadian based company with a surface mounted design rated at 0.25 MW providing power to the local grid).

Transverse Horizontal Axis Tidal Turbines (THATT)

Transverse Horizontal Axis Tidal Turbines (THATT) present a distinct configuration that merits exploration, see Figure 2.26 [88, 89]. Unlike traditional horizontal axis turbines, THATT turbines are positioned transversely to the tidal flow, meaning their rotor axis aligns perpendicular to the direction of the current. This unique arrangement offers several advantages. Firstly, THATT turbines can capitalise on tidal flows from various directions, maximising energy capture without needing realignment, and their transverse orientation accommodates variations in flow direction, making them particularly suitable for regions with intricate or unpredictable tidal patterns, thereby enhancing operational efficiency and simplifying installation procedures.

(a)

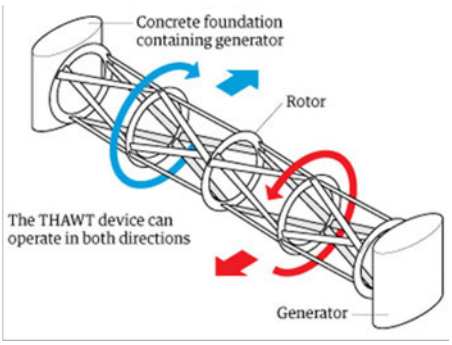

(b)

Figure 2.26: Transverse horizontal axis tidal turbine full-scale device (a), general THATT concept (b).

Nonetheless, this configuration introduces certain limitations. Due to their perpendicular rotor orientation, THATT turbines might experience slightly increased mechanical complexity and drag, potentially affecting overall efficiency. Design and engineering considerations need to balance these factors against the benefits of versatile energy capture.

The design can further enhance power extraction through the strategic optimisation of the blockage ratio [90]. Commercial application of this technology has been pursued by companies like Kepler Energy [91], a UK-based enterprise set to deploy a 30 MW tidal fence in the Bristol Channel by 2025. Additionally, Hydrovolts Inc [92], an American company utilising the Savonius style rotor, successfully deployed a 12.5 kW system in 2012. This setup functioned for over a year, providing power to charge a battery bank.

Miscellaneous Tidal Turbines

Strathclyde University has pioneered the development of the CoRMaT (Counter Rotating Marine Turbine) device, see Figure 2.27a [93, 94]. This innovative system incorporates co-axial rotors that are linked to both the stator and rotor of the generator. This configuration yields two notable advantages. Firstly, it enhances the differential rotation within the generator, thereby optimising performance even under lower flow velocities. Secondly, in conjunction with the device's inherent buoyancy, this design simplifies the supporting structure. The device's neutral torque around its rotational axis allows it to be tethered within the mid-water column without requiring a rigid frame.

A distinct approach is demonstrated by the kite design created by the Swedish company Minesto, aimed at maximising output in deeper waters with more subdued flow speeds, see Figure 2.27b [95]. This tidal kite generates an artificial velocity approximately 10 times greater than the surrounding flow as it glides through the water [96]. This approach showcases innovative strategies to harness tidal energy effectively.

(a) (b)

Figure 2.27: CoRMaT tidal turbine concept at full-scale (a) tidal kite by Minesto (b).

2.4.2 Horizontal Axis Turbine Physics

Horizontal Axis Tidal Turbines (HATT) - predominantly focused on in this thesis - represent a widely adopted approach to harnessing tidal energy. These turbines are configured with their rotor axis aligned horizontally, parallel to the direction of the tidal flow. One key advantage of HATT turbines is their compatibility with existing wind turbine technology, enabling the utilisation of established manufacturing and installation processes. This adaptability streamlines implementation and capitalises on the accumulated experience in the wind energy sector. Additionally, HATT turbines are renowned for their potential to efficiently convert tidal currents into electricity, delivering relatively high energy capture rates.

However, HATT turbines come with certain limitations. They require accurate alignment with the predominant tidal flow direction to maximise their performance, making proper siting critical. Additionally, the need for proper anchoring and foundations in often harsh marine environments can increase both installation complexity and maintenance demands (this applies to all tidal turbine configurations). In summary, while HATTs offer proven technology and efficient energy conversion, their success hinges on strategic deployment and management to overcome siting challenges and ensure optimal performance.

Theoretical Limits to Power Extraction

The power that a turbine can extract from the flow is inherently lower than what exists in the freestream flow. This is due to the relationship between the momentum change occurring across the plane of the rotor and the rate of mass flow. The available power is influenced by two factors: the mass flow rate across the rotor plane and the momentum change brought about by this flow. When the velocity at the turbine's exit reaches zero, the mass flow rate across the rotor plane also becomes zero, resulting in no power generation.

The Betz limit [97], or more accurately, the Lanchester-Betz-Joukowsky limit [98], establishes that the maximum energy capture for an infinitesimally thin rotor can only reach 59.3% of the available energy. This limit is derived by applying a momentum balance across the rotor, under specific assumptions. Nonetheless, the potential power that can be harnessed in a practical mechanical manner is restricted for a device operating within open water flow, as illustrated by Equation 2.13:

$$P_T = \frac{1}{2} \cdot \rho \cdot C_P \cdot A_R \cdot U^3 \tag{2.13}$$

where C_P is the power coefficient. The value of C_P for a turbine in a flow of incompressible fluid is limited to a maximum theoretical value of around 60%. The value of C_P for a real device is generally a function of the ratio between the speed of the turbine tip and the flow speed, commonly known as the tip speed ratio [79].

These assumptions encompass axial and incompressible flow conditions, a consistent upstream velocity, and the rotor being devoid of a central hub or mass. Furthermore, it can be demonstrated that the maximum power extraction occurs when the downstream wake flow velocity diminishes to one-third of the freestream velocity. This complex interplay of factors defines the theoretical upper boundary for energy capture in such turbine systems.

Blade Forces and Power Output

A horizontal axis turbine exploits the kinetic energy of a fluid by employing profiled blades, which induce the fluid to follow a curving path, thereby creating a lift force. This lift force operates perpendicular to the local relative flow velocity and propels the turbine. The generation of lift triggers the creation of an opposing force that acts on the fluid in the opposite direction to the lift. Alongside the lift force, there's a drag force produced as the blade traverses through the fluid. This drag force further generates a counteracting force within the fluid, contributing to the overall thrust of the turbine. The dynamics of these forces and their respective orientations in relation to the blade section are visually illustrated in Figure 2.28, where (α) is the angle of attack, (γ) is the geometric pitch angle and (ϕ) is the angle between the rotor plane and the resultant velocity vector [99].

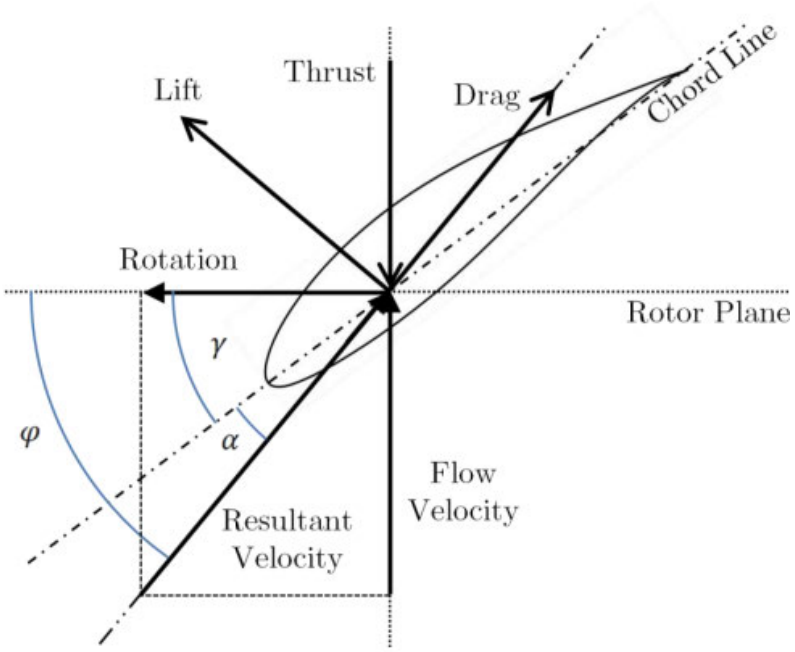

Figure 2.28: Forces on an aerofoil/hydrofoil.

Wake of a Horizontal Axis Turbine

The turbine blade forces exert two significant effects on the wake of a HATT, as highlighted by Lee [100]: a wake velocity deficit and a bulk swirling of the flow. The wake velocity deficit emerges due to the thrust force applied by the rotor onto the fluid. This force causes the expansion of incoming flow around the rotor. According to continuity, this leads to the slower movement of flow within the wake compared to the freestream flow. The wake swirling is an outcome of Newton's third law. The interaction between the fluid and the rotor prompts the rotation of the turbine, which reciprocally compels the flow to rotate.

Understanding the velocity deficit and turbulence characteristics of the far wake of a HATT is crucial, as they govern the interactions between devices within an array [101]. The structure of the near wake significantly influences the device's potential for power generation [82]. Advances have been made in modelling the far wake using uniform actuator disc models [102, 103, 104]. However, these models don't fully encompass the device's impact on the flow due to the omission of factors like swirl and turbulence generation. The repercussions of neglecting the interaction between the near and far wake remain uncertain [103].

2.5 Uncertainty Theory

In the realm of measurements for tidal projects, it's important to recognize that while some numerical values may be exact, nearly all measurements carry an inherent degree of uncertainty stemming from various sources. This understanding prompts the practice of evaluating measurements along with their associated uncertainties, commonly referred to as uncertainty analysis or error analysis [105].

Error analysis constitutes a comprehensive exploration of uncertainties, with a direct objective of quantifying the level of doubt surrounding a given measurement. This approach empowers us to gauge the extent of uncertainty, identify its major contributors, and strive to minimize them where feasible. When quantifying a measurement, it's advisable to express the measured value alongside an associated uncertainty value. This practice not only showcases the result's accuracy but also instils confidence in its validity. For instance, consider the simple act of measuring the distance with a ruler; uncertainties can arise from diverse factors, such as equipment specifics (resolution and calibration), to human factors, like the skill of the operator.

Recognising measurement uncertainty holds utmost significance, as genuine measurements can never achieve absolute accuracy. Uncertainties and errors can arise from a multitude of reasons [106, 107], including:

- The complexity of the measurement process, particularly for intricate measurements like determining the position or movement of an object.
- The nature of the measured parameter, especially when it's prone to instability and rapid fluctuations over short intervals.
- Operator skill and precision, encompassing the operator's experience and physical capabilities that influence measurement accuracy (e.g., eyesight, concentration).
- The condition of the measurement equipment, where instruments not regularly calibrated might exhibit biases due to wear, ageing, drift effects, poor readability, or electrical noise (in the case of electronic instruments).
- "Imported" uncertainty, considering that the calibration of any instrument inherently carries an uncertainty, which should be factored in when presenting final results.
- Environmental factors, as measurements requiring specific conditions, may introduce uncertainty if performed under different conditions. Variables like pressure, temperature, humidity, and other conditions differing from the instrument's calibration report can contribute to uncertainty.
- Sampling, emphasising that measurements should accurately represent the observed process. For instance, measuring room temperature should be done diligently, ensuring the thermometer is placed away from a radiator.

In the course of a measurement campaign, multiple errors are likely to be present. As the number of observations increases, the uncertainty value remains nonzero. As noted in [107], errors linked to a series of measurements or interconnected calculations tend to accumulate as they are combined.

When we gain a comprehensive understanding of the unique characteristics of individual uncertainties influencing the performance of a turbine or the estimated annual yield, it becomes imperative to amalgamate them to fully grasp their collective impact of the uncertainty. It's important to note that the combination of two uncertainties in a resource estimate, each quantified with a standard deviation of 2%, doesn't necessarily result in a straightforward 4% standard uncertainty in the resource. This divergence arises due to the potential independence and lack of correlation between these uncertainties. Simple addition of uncorrelated uncertainties is unsuitable, as the simultaneous occurrence of two extreme values is unlikely. Hence, there's a need for a method to consolidate uncertainties that duly acknowledges the interdependence of these sources. Further exploration of these methods to calculate uncertainty through propagation is explored in Section 2.5.3.

2.5.1 Term Definition

Mean

The mean is a prevalent statistical measure utilised to gauge the uncertainty of a measurement. It signifies the numerical average within a dataset. Calculating the mean involves summing up the dataset and then dividing the sum by the total number of samples. The distinction among the mode, median, and mean is depicted in Figure 2.29. The selection of which statistic to use – mode, median, or mean – hinges on the specific circumstances, type of measurement, and desired outcomes. The median is the middle value in a data set when it is arrange in ascending order, while the mode is the value that appears most frequently in a data set. Unlike the mean, which is the average of all values in a data set, the median and mode are not influence by extreme values (outliers in the data set). However, it's essential to acknowledge that outliers can wield substantial influence on the mean statistic, potentially rendering it an inaccurate representation of the data. To mitigate this, a common practice is to calculate and present the standard deviation alongside the mean value, as exemplified in Equation 2.14:

$$A = \frac{1}{n}[\Sigma_{i=1}^{n} a_i] \tag{2.14}$$

where: A is the arithmetic mean, n is the number of samples and a_i is the data set.

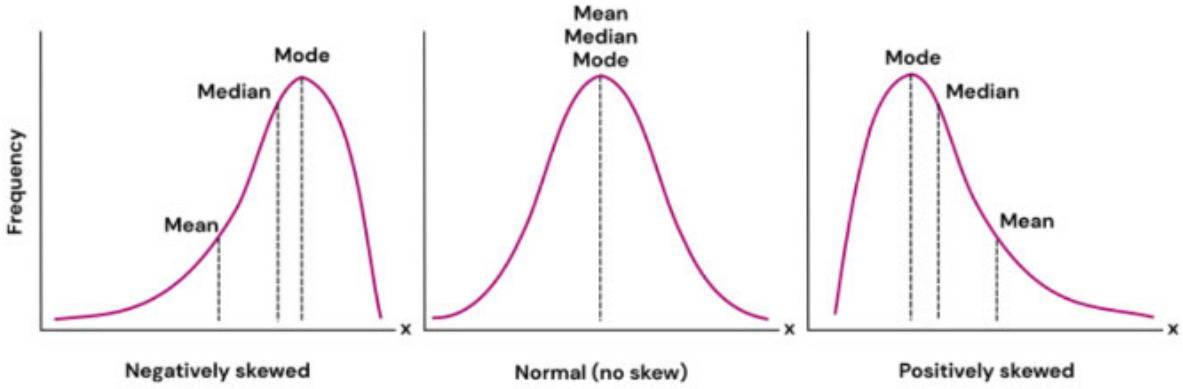

Figure 2.29: Distinguishing Mean, Median, and Mode.

Error

The term 'error' is often confused with 'uncertainty'. The distinction lies in the comparison between the 'true value' and the measured value, known as the error. This discrepancy can be presented as a numerical value or a percentage. In the realm of science, the term 'error' doesn't bear the typical meanings of 'mistake' or 'blunder'. Instead, it signifies the inherent uncertainty inherent in all measurements. Consequently, errors are not necessarily the result of mistakes; they are not eradicated through carefulness. However, it is possible to mitigate the extent of errors to ensure they remain reasonably minimised, thereby fostering a dependable estimate of the measurement obtained. Equation 2.15 presents the formula for calculating the percentage error:

$$\delta = |\frac{v_A - v_E}{v_E}| \times 100 \tag{2.15}$$

where: δ is the error percentage, v_A is the actual value observed and v_E is the true expected value.

Uncertainty

Uncertainty quantifies the extent of knowledge gaps surrounding a recorded measurement. When doubt arises from calibration certificates, it becomes crucial to rectify them. However, errors whose values remain elusive contribute to uncertainty [106]. Therefore, quantifying uncertainty necessitates two values: the first denotes the range or interval width, while the second signifies the confidence level that the 'true value' lies within the specified range.

Standard uncertainty finds expression through a standard deviation, often evaluated via either statistical analysis of observation series or alternative methodologies. These align with the two distinct categories of uncertainties: Category A and Category B, respectively.

- **Category A - Random Uncertainty**

  Category A uncertainties emerge from the repetition of measurements, yielding random variations in the results. These uncertainties can be aptly described through probabilistic modelling, where increasing the number of repetitions increases the certainty of the expected estimate. Repeatability, stability, and reproducibility testing hold significance for Category A uncertainties. This kind of uncertainty is anchored in the standard deviations of the scatter within each bin. To accurately account for this, statistical theory mandates the inclusion of the number of samples of each estimator. The equation for calculating standard uncertainty, denoted as S_i, takes the following form:

  $$S_i = \frac{\sigma_i}{\sqrt{N_i}} \tag{2.16}$$

  where: N_i is the number of samples, and σ refers to the standard deviation of measurements for the ith bin.

- **Category B - Systematic Uncertainty**

  Category B uncertainties cannot be evaluated through the same method employed for Category A uncertainties, rendering the repetition of measurements ineffective. Category B uncertainties stem directly from limited knowledge regarding the properties, conditions, and behaviours of the utilised systems. In certain instances, a consistent influence impacts results across repeated measurements, presenting a considerable challenge for identification. Employing alternative techniques becomes imperative for estimating uncertainty due to systematic effects. These methods could encompass referencing calibration certificates, utilising published information, relying on user experience, and considering manufacturer specifications.

  Estimations of uncertainty within Category B should arise from familiarity with the employed instrument. For instance, if the instrument sensor is rated with an accuracy of $\pm U$, it is reasonable to infer that the true value falls within this specified tolerance.

  It's noteworthy that, in both instances, the standard uncertainty is derived from a distribution encompassing plausible values of the input quantity. The probability distribution function (PDF) might either be frequency-based, as directly linked to repeated measurements (Category A), or manifest as the most reliable estimate or a theoretical distribution (derived from available information - Category B).

Calibration and Traceability

Calibration involves the verification of an instrument's performance against a predefined accuracy standard. This process is typically carried out in relation to a reference device, often a secondary or lower-level reference. Traceability, in this context, signifies the ability to trace the instrument's measurements back to the reference. This is achieved through documentation, such as the recorded specifications in calibration certificates provided by instrument manufacturers or obtained from instrument testing.

Drift

Drift refers to the gradual time-dependent changes that occur in any analogue system. In the case of sensors, drift can be categorised into two components: offset change and sensitivity change. If the read-out circuit allows, offset change can be nullified by applying a known stimulus and adjusting the sensor output to match the expected value. Sensitivity change necessitates the measurement of sensor responses at various stimulus levels, with intermediate readings interpolated to achieve accurate results.

Standard Deviation

The standard deviation statistic assesses how a dataset's values deviate from its mean, which is the average distance between data points and the mean value. A larger standard deviation indicates that the data points are more widely spread around the mean, whereas a smaller standard deviation signifies a narrower spread. To calculate the standard deviation, each data point's deviation from the mean is squared, and the variance is then summed and averaged. The square root of the variance gives the standard deviation, as shown in Equation 2.17:

$$\sigma = \sqrt{\Sigma_{i=1}^{n} \frac{(x_i - \bar{x}_i)^2}{n-1}} \tag{2.17}$$

The standard deviation is crucial for describing the range within which data is expected to fall. This is illustrated by the empirical rule [107], applicable when the data follows a normal distribution (as depicted in Figure 2.30):

- 68.2% of the data will fall within one standard deviation (σ) of the mean ($\bar{x}_i$),
- 95.4% of the data will fall within two standard deviations of the mean,
- 99.7% of the data will fall within three standard deviations of the mean.

In risk analysis, standard deviation serves as a vital metric commonly employed by analysts, advisors, and portfolio managers. The dispersion of results or predictions indicated by standard deviation can provide insights into a project's success or reliability.

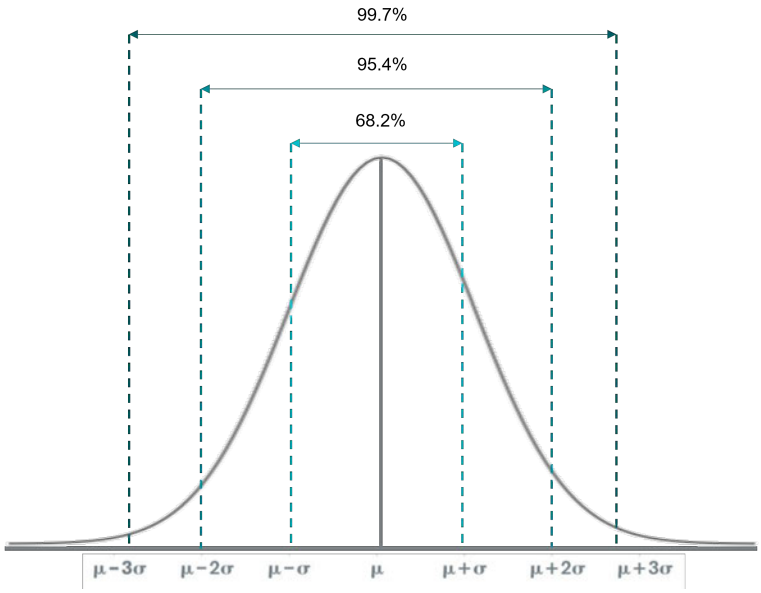

Figure 2.30: Normal distribution where each band has a width of 1 standard deviation (σ).

Bias

Bias is characterised by a predisposition to incline towards a specific direction—a form of consistent favouritism in the process of data collection [108]. It is synonymous with systematic error and can potentially be comprehended and rectified. Bias manifests in measurement procedures that result in the overestimation or underestimation of the measured parameter. Notably, bias stands apart from random error, as conducting repeated measurements will not inherently rectify the bias. For a visual distinction between random and systematic error, refer to Figure 2.31.

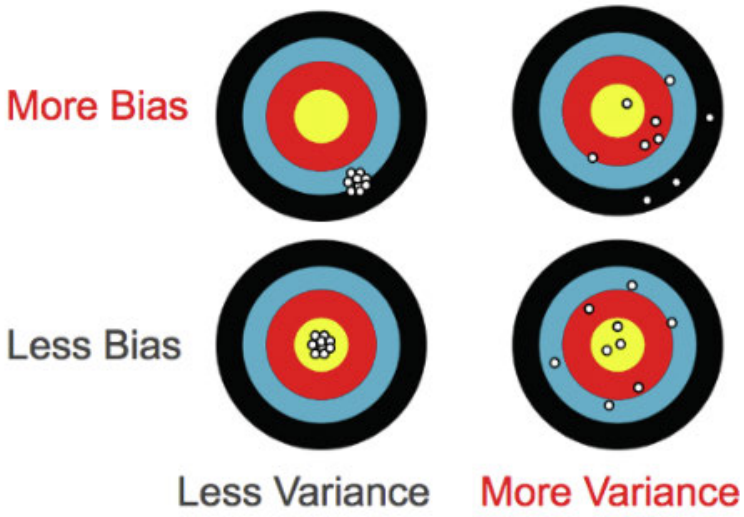

Figure 2.31: Illustration comparing random and systematic errors using the analogy of multiple shots at a target.

The bottom-right target exhibits a large random error, with widely scattered samples, yet only a small systematic error, as there is no consistent off-centre tendency. In contrast, the top-right target displays substantial systematic and random errors compared to the top-left target. In the top-left target, random errors are minimal, but systematic errors are pronounced. The bottom-left target reflects minimal levels of both random and systematic errors, with closely clustered samples distributed around the centre [108].

Bias can also be visualised using a probability distribution, depicted in Figure 2.32. The Gaussian or normal distribution is the most common probability distribution, with values concentrated around the mean. Every estimated value carries a degree of uncertainty. This uncertainty signifies the distribution's stretching or skewing away from the mean value. Bias emerges when the true value is known and introduces a shift in the mean value by a specific, known amount. If the true value is known, a correction factor can be applied.

Probability Distribution Curves

A Probability distribution links outcomes in an event with their corresponding probabilities of occurrence. These distributions can be discrete or continuous. Discrete distributions entail a fixed set of possible outcomes (e.g., coin toss results). Conversely, continuous distributions encompass outcomes that can take any value within a range (e.g., animal height). A Probability density function (PDF) is a mathematical function that defines the probability distribution. For Type A uncertainty estimation, we calculate a standard deviation using Equation 2.17. In the

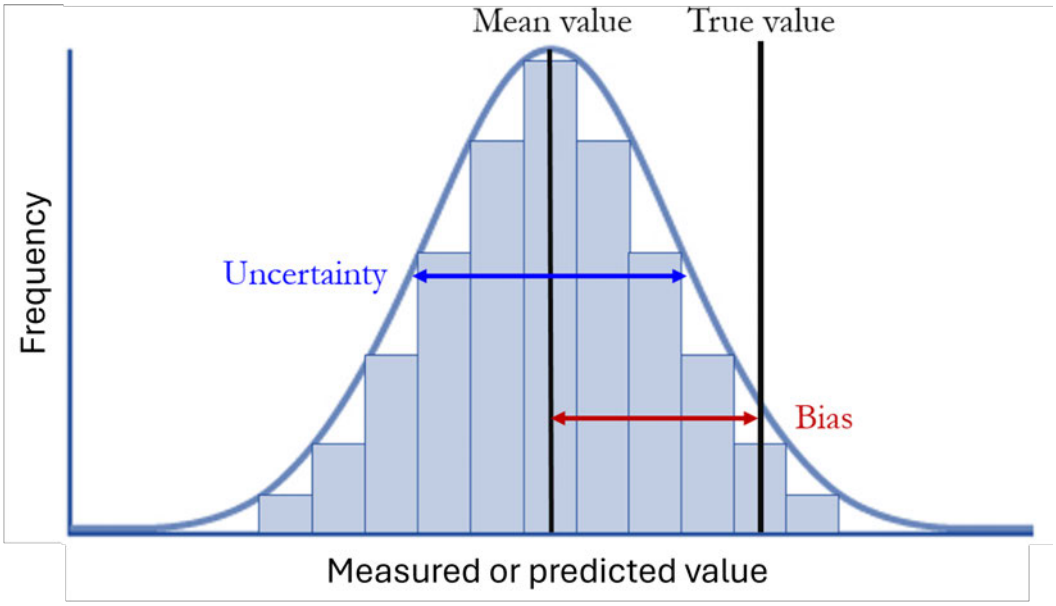

Figure 2.32: Normal distribution curve to show the differences between uncertainty and bias.

case of a Type B estimate, we work from a set of bounding limits known as error containment limits, along with a containment probability. This probability indicates the likelihood that errors or attribute values fall within these bounds. Various distributions can represent the underlying distribution of errors or deviations [109], as depicted in Figure 2.33.

The normal distribution is a mathematical function that depicts the distribution of numerous random variables in a symmetrical bell-shaped curve. The peak of the curve is centred around the mean and symmetrically spread based on the standard deviation, as depicted in Figure 2.33a [109]. The normal distribution is widely employed for evaluating Type A data uncertainties. This distribution curve has the characteristic bell-shaped appearance and is mathematically defined by Equation 2.18:

$$f(x) = \frac{1}{\sigma\sqrt{2\pi}} e^{-\frac{(x-x\text{mean})^2}{2\sigma^2}} \tag{2.18}$$

To convert normally distributed data into a standard deviation equivalent, the following Equation 2.19 is employed. In this equation, u_i is the uncertainty of variable i, a represents the value of the uncertainty identified (i), and k denotes the expansion factor. The value of k corresponds to the standard deviation of the mean discussed earlier ($k = 1$ corresponds to approximately 68% confidence level, $k = 2$ corresponds to approximately 95% confidence level, and $k = 3$ corresponds to approximately 99% confidence level). Typically, results are reported at a 95% confidence level.

$$u_i = \frac{a_i}{k} \tag{2.19}$$

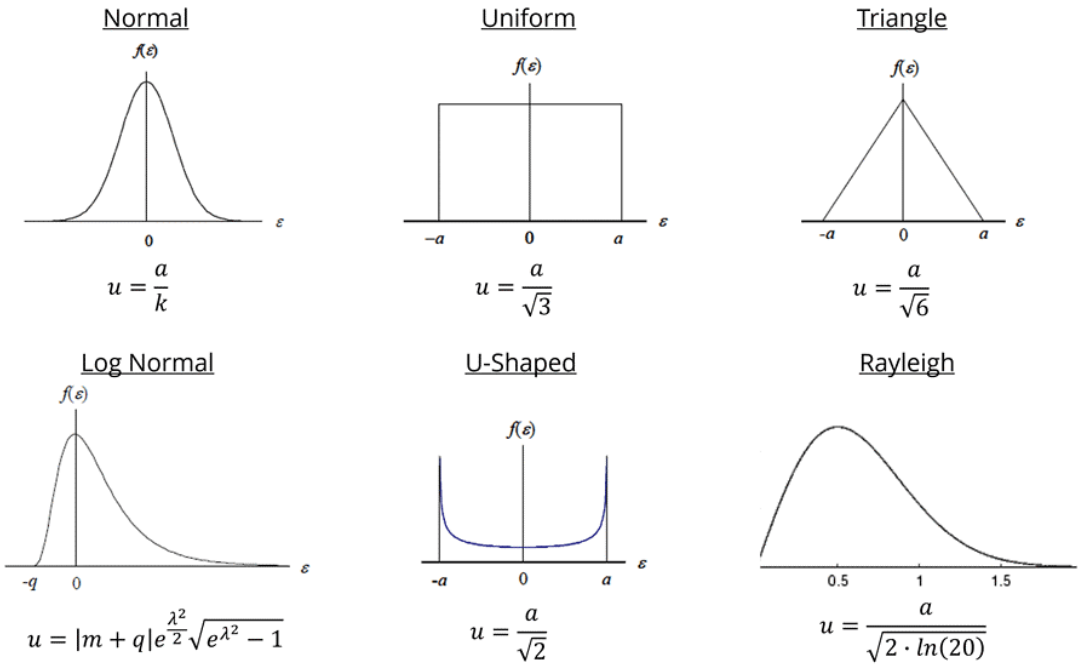

Figure 2.33: Probability distribution curves illustrating different distributions: a) Gaussian (normal) distribution, b) Rectangular (uniform) distribution, c) U-shaped distribution, d) Log-Normal distribution, e) Triangle Distribution, and f) Quadratic distribution.

The Rectangular Distribution is a function that models a continuous uniform distribution with a constant probability [110]. In this distribution, all possible outcomes are equally likely. The rectangular distribution is the most commonly employed probability distribution in uncertainty analysis, as illustrated in Figure 2.33b [109]. When facing uncertainty about the underlying data distribution, a conservative evaluation approach is advisable [109]. In such situations, the rectangular distribution serves as a suitable default option, which is why it's often recommended by ISO/IEC 17025 assessors [111]. The uniform distribution is defined by the probability density function (PDF) shown in Equation 2.20. The probability of a data point lying outside the range $\pm a$ is zero.

$$f(x) = \begin{cases} \frac{1}{2a}, & -a \leq x \leq a \\ 0, & \text{otherwise} \end{cases} \tag{2.20}$$

To reduce the uncertainty contributors to standard deviation equivalents, the following Equation 2.21, is used:

$$u_i = \frac{a_i}{\sqrt{3}} \tag{2.21}$$

The U-shaped distribution is a function that depicts outcomes with a higher likelihood of occurring at the extremes of the range, as depicted in Figure 2.33c [109]. This distribution takes the form of the letter 'U', but its symmetry is not a requirement. The U-shaped distribution is particularly valuable in scenarios where events frequently manifest at the range's extremes. A relevant example is a thermostat that regulates the temperature in a laboratory. Without the use of a proportional integral derivative (PID) controller, the thermostat activates only when temperatures reach extremes. The probability density function (PDF) for the U-shaped distribution is provided by Equation 2.22.

$$f(x) = \begin{cases} \frac{1}{\pi\sqrt{a^2-x^2}}, & -a \leq x \leq a \\ 0, & \text{otherwise} \end{cases} \tag{2.22}$$

To convert the uncertainty contributors into standard deviation equivalents, you can utilise the following Equation 2.23:

$$u_i = \frac{a_i}{\sqrt{2}} \tag{2.23}$$

The log-normal distribution arises from applying a natural logarithm to a normally distributed dataset, as depicted in Figure 2.33d [109]. This distribution is often employed to estimate uncertainty in equipment parameter bias when tolerance limits are asymmetric. It is also useful in scenarios where a physical limit near the nominal or mode value affects the parameter bias probability distribution in a way that deviates from the applicability of a normal distribution [109]. For instance, measurements involving finite quantities like length, height, or weight tend to exhibit a log-normal distribution. This distribution is particularly common in dimensional and mechanical metrology. The PDF for the log-normal distribution is defined by Equation 2.24:

$$f(x) = \frac{1}{\sqrt{2\pi\sigma|x-q|}} \cdot exp\left\{ - \left[\ln(\frac{x-q}{m-q}) \right]^2 / 2\sigma^2 \right\} \tag{2.24}$$

where: m represents the population median, q the physical limit for x, u the population mode, and σ referred to as the "shape parameter".

To convert the uncertainty contributors into standard deviation equivalents, you can utilise the following Equation 2.25:

$$u_i = (m-q)e^{\frac{\lambda^2}{2}} \sqrt{e^{\lambda^2} - 1} \tag{2.25}$$

The Triangle Distribution is a mathematical function that encapsulates a known minimum, maximum, and estimated central value, illustrated in Figure 2.33e [109]. It is often dubbed the "lack of knowledge" distribution since it finds utility in situations where a relationship between variables is understood, but data is limited [109]. Moreover, the triangle distribution is frequently employed in cases where data collection proves to be challenging or costly. The probability density function (PDF) for the triangular distribution is defined by Equation 2.26:

$$f(x) = \begin{cases} (x+a)/a^2, & -a \leq x \leq 0 \\ (a-x)/a^2, & 0 \leq x \leq a \\ 0, & \text{otherwise} \end{cases} \tag{2.26}$$

To convert the uncertainty contributors into standard deviation equivalents, you can utilise the following Equation 2.27:

$$u_i = \frac{a_i}{\sqrt{6}} \tag{2.27}$$

The quadratic distribution is a probability distribution that avoids sudden changes at the zero point, avoids unrealistic linear trends, and fulfils the requirement for a central tendency [109], as shown in Figure 2.33f [109]. Its probability density function (PDF) is defined by Equation 2.28:

$$f(x) = \begin{cases} \frac{3}{4a}[1-(x/a)^2], & -a \leq x \leq a \\ 0, & \text{otherwise} \end{cases} \tag{2.28}$$

The standard deviation for this distribution can be calculated (Equation 2.29) based on approximately 77% of the standard deviation estimate for the uniform distribution.

$$u_i = \frac{a_i}{\sqrt{5}} \tag{2.29}$$

2.5.2 Common Sources of Uncertainty

The origins of errors and uncertainties are distinct and can be rooted in various disciplines. When numerically simulating a physical system, the predictions often deviate from observations. This divergence stems from inherent limitations in a model's capacity to flawlessly capture all aspects of the system it represents. These limitations result in the emergence of errors and uncertainties, which can be categorised into three main types:

1. *Data Error*: To tailor predictions to specific sites, mathematical models require input data encompassing system geometry (e.g., bathymetric data and coastal features' geometry for oceanographic modelling), initial and boundary conditions (flow velocities, water depth), and other relevant physical parameters (bed roughness, gravitational acceleration, etc.). These data must be collected through field measurements, a challenging task in marine environments, especially for tidal stream energy conversion. The swift flow characteristic that qualifies a site for development introduces complexity, resulting in a rough, turbulent flow that hampers data characterisation. Moreover, inherent uncertainties within the system, such as nonlinear interactions between tidally driven flow and domain boundaries, can give rise to turbulent flow structures and chaotic behaviours.

2. *Numerical Error*: Solving mathematical models numerically involves discretising governing equations on a computational mesh. This discretisation introduces "discretisation" or "truncation" errors stemming from the approximation of continuous functions at discrete points. Reducing this error often necessitates mesh refinement, both spatially and temporally, although this comes at the cost of increased computational time. Additionally, due to the finite memory space of computers, exact mathematical values are rounded to a finite number of digits. Effective numerical methods aim to mitigate round-off errors through strategies such as ensuring model convergence.
3. *Model Error*: Expressing the physics of a system mathematically often involves applying simplifications to make a problem manageable. These assumptions lead to a loss of information, causing the model to deviate from real-world behaviour and consequently introduce errors and uncertainties in predictions. In tidal flow modelling, for instance, the derivation of shallow water equations involves reducing the system's dimensionality by integrating over flow depth. This projection onto a computationally less intensive two-dimensional coordinate system simplifies the problem but also entails potential inaccuracies.

The primary focus of this thesis centres around the initial category of uncertainties, which pertain to the data that describes the physical system. More specifically, the methods and analyses presented here are designed to elucidate the effects of variability within this data—essentially, the repercussions of imprecise information derived from instrumentation measurements.

An established and standardised classification for power production yield losses has been introduced by OREC [29], as detailed in Table 2.3. These losses can be quantified through diverse approaches, encompassing physical testing (e.g., tank testing for performance assessment), numerical modelling (e.g., reliability modelling for evaluating availability losses), leveraging existing datasets (e.g., manufacturer brochures for electrical loss calculations), and where necessary, drawing on expert opinion (OREC, 2015b) [110]. The factors of uncertainty highlighted in Table 2.3, which are consistently referenced throughout this thesis, pertain to availability and device performance. These specifically include aspects related to the marine energy converter, local resource characteristics, and power performance.

2.5.3 Propagation of Uncertainty

When a measurement encompasses a process consisting of multiple sequential steps, the assessment of uncertainties entails a similar multifaceted approach. It is crucial to comprehensively grasp the methodology for amalgamating uncertainties connected with distinct steps within the measurement process. Thus, the task involves gauging the uncertainty within the initial measurement and subsequently discerning how these uncertainties 'propagate' throughout subsequent calculations, culminating in an encompassing overall uncertainty [112]. The forthcoming subsections delineate a range of methods for amalgamating uncertainties, contingent on their interrelationships.

Uncertainty in summation and subtraction

In the scenario where multiple quantities a, b, and c are measured with associated uncertainties δa, δb, and δc, the obtained values are employed in the calculation of an equation like 2.30:

$$q = a + b - c \tag{2.30}$$

Subsequently, the uncertainty in the computed value of q is determined by the sum presented in Equation 2.30.

Table 2.3: Taxonomy of yield loss categories proposed by OREC (2015a).

Loss Category	Sub-Category
1) Availability	1a) Marine energy converter
	1b) Environmental
	1c) Balance of plant
	1d) Grid
	1e) Site access and other force majeure events
	1f) Other
2) Resource Array Interactions	2a) Internal resource array interactions
	2b) External resource array interactions
	2c) Future external resource array interactions
3) Device Performance	3a) Power performance
	3b) Local resource characteristics
	3c) Hysteresis
	3d) Performance degradation
	3e) Other
4) Electrical	4a) Electrical losses
	4b) Facility parasitic consumption
5) Curtailment	5a) Operational management
	5b) Grid curtailment/constraint
	5c) Offtaker curtailment
	5d) Environmental curtailment
6) Other	6a) Resource metric - energy relationship
	6b) Water density
	6c) Other

$$\delta q = \delta a + \delta b + \delta c \tag{2.31}$$

This illustrates that when calculating the uncertainty associated with the summation or subtraction of parameters, the approach is to combine the uncertainties of those quantities.

Uncertainty in products and quotients

When dealing with several measured quantities a, b, and c, each having uncertainties δa, δb, and δc respectively, and these values are utilised to calculate the uncertainty using equation 2.32:

$$q = \frac{a \cdot b}{c} \tag{2.32}$$

then the fractional uncertainty in the resulting value of q can be approximated by the summation given in equation 2.33:

$$\frac{\delta q}{|q|} \approx \frac{\delta a}{|a|} + \frac{\delta b}{|b|} + \frac{\delta c}{|c|} \tag{2.33}$$

This implies that when quantities are multiplied or divided, the fractional uncertainty accumulates, where the denominator is taken as the absolute value.

Uncertainty in unique cases

Two specific cases stand out as significant guidelines when dealing with uncertainty combinations. The first case involves measuring a quantity a and subsequently using this measured value to calculate a product as shown in Equation 2.34:

$$q = B \cdot a \tag{2.34}$$

where the value of B is certain and doesn't possess uncertainty. In such scenarios, the uncertainty in q simply becomes the absolute value, $|B|$, multiplied by the uncertainty in a, depicted in Equation 2.35:

$$\delta q = |B| \cdot \delta a \tag{2.35}$$

The second distinct scenario involves dealing with the computation of a power of a measured quantity. For instance, consider the measurement of the speed (v) of an object, which is then used to determine its kinetic energy using Equation 2.36:

$$\mathrm{KE} = \frac{1}{2} \cdot m \cdot v^2 \tag{2.36}$$

In this context, the square of v needs to be calculated. Expressing v^2 as $v \times v$, the fractional uncertainty in v^2 is twice that in v. In a more general sense, if a quantity a is measured with an uncertainty δa, and this measured value is employed to calculate the power $q = a^n$, then the fractional uncertainty in q is n times the fractional uncertainty in a, as demonstrated by Equation 2.37:

$$\frac{\delta q}{|q|} = n \cdot \frac{\delta a}{|a|} \tag{2.37}$$

By examining the propagation of uncertainty, not only can the total combined uncertainty be quantified, but also the most effective approaches to minimising uncertainty can be identified. This process involves assessing individual uncertainties that contribute to the overall uncertainty, enabling a focus on reducing the most significant contributors.

Dependent vs Independent Uncertainty

Two random variables are deemed statistically independent when their joint probability distribution is the product of their individual probability distributions. In the scenario where the original uncertainties are both independent and random, a more realistic and generally smaller estimation of the final uncertainty is obtained by adding the uncertainties (or fractional uncertainties) in quadrature.

To illustrate this concept, consider the computation of the sum, $q = a + b$, where a and b are two measured values with uncertainties δa and δb, respectively. The formula $\delta q \approx \delta a + \delta b$ that estimates the uncertainty of q is likely to overstate the actual value. This is due to the potential for q to reach its highest extreme when a is overestimated by δa and b is overestimated by δb. However, considering the independent and random nature of measurement errors, it's unlikely that both underestimations would occur simultaneously. In such cases, the probability of both a and b being underestimated by their full uncertainties δa and δb is relatively small. Therefore, the formula $\delta q \approx \delta a + \delta b$ tends to exaggerate the most probable error.

If measurements of a and b are independently made and both follow a normal distribution, the uncertainty in $q = a + b$ can be calculated using Equation 2.38, known as the root-mean-square (RMS) technique. To explain this approach, imagine each uncertainty contributor as a vector with independent magnitudes and directions. To compute the net magnitude and direction, these vectors are combined in quadrature. This method is commonly employed for combining independent uncertainties [107].

$$\delta q = \sqrt{(\delta a)^2 + (\delta b)^2} \tag{2.38}$$

The wind industry has comfortably adopted the RMS approach for combining independent uncertainties. However, the ORE Catapult [29] indicates that this assumption might not be applicable to tidal energy yield assessments. If one or two dominant contributors in the overall uncertainty are not normally distributed, the end results will also deviate from a normal distribution. In such cases, Monte-Carlo simulation, as discussed in Section 2.6.4, could potentially address these issues. However, this approach is more intricate and time-consuming than the RMS method, and its results are less intuitively interpretable. When uncertainties are interdependent, meaning the calculation of one value directly impacts another, a different approach is employed for combining uncertainties. The standard RMS method cannot be used when values are not independent.

2.6 Uncertainty Analysis Methods

Various methods are available for analysing uncertainty. The most straightforward approach is to assess the standard deviation, a term that was covered in Section 2.5.1. Nonetheless, situations may arise where obtaining the standard deviation is not feasible, prompting the need for alternative methods to quantify uncertainty. This section presents a range of uncertainty analysis techniques applicable to various procedures, such as the calculation of energy yield uncertainty. Power estimates are contrasted with in-situ measurements collected near the turbine. The uncertainty arises from the variability in these measurements rather than being evaluated statistically using the approaches described in this section. Although these methods won't be employed in this thesis, they still hold significance in the realm of uncertainty analysis.

2.6.1 Sensitivity Studies

Sensitivity studies are widely used to analyse how uncertainties in the output of numerical processes are linked to uncertainties in their inputs. Complex numerical processes or mathematical models can obscure the relationships between inputs and outputs, leading to models being treated as black boxes, where outputs are determined by opaque functions of inputs.

Importantly, uncertainties obtained from sensitivity studies are meaningful only when the model is well-validated. The focus is on understanding parameter sensitivity within the equation rather than its real-world sensitivity. Investigating individual parameter sensitivity loses relevance if the model is inaccurate or poorly represents reality. This highlights the necessity of accurate models that faithfully mirror reality, validated against real-world data.

Uncertainties often arise in model inputs due to factors like measurement errors, incomplete data, and a limited understanding of influencing factors. This uncertainty limits the confidence in the model's responses. When models involve input variables, sensitivity analysis becomes pivotal in uncertainty assessment. The choice of sensitivity analysis method is guided by problem constraints or settings. Common methods include:

- *Data from an unknown source*: Sensitivity analysis may involve data gathered from an external source, where the analyst cannot choose the model input values for each run.
- *Model interactions*: Interactions might occur within a model when two or more inputs cause variations in the output that are greater than the variations in each individual input.
- *Correlated inputs*: While many sensitivity analysis methods assume independence between model inputs, there can be strong correlations between inputs.
- *Multiple outputs*: While many sensitivity analysis methods assume independence between model inputs, there can be strong correlations between inputs.
- *Non-linearity*: Linear regression methods struggle to measure sensitivity accurately when the model's response is nonlinear with respect to inputs. Variance-based measures are more suitable in such cases.
- *Computational expense*: If running the model takes considerable time or the model has numerous uncertain inputs.

Various approaches are available for performing sensitivity analysis, many designed to address specific constraints. A typical sensitivity study follows these steps:

1. Identify the model outputs to analyse.
2. Run the model multiple times, varying input parameters for each iteration using an appropriate method based on input uncertainty.
3. Calculate the desired sensitivity measures using the resulting model outputs.
4. Quantify the uncertainty.

Local sensitivity analysis, a derivative-based approach, focuses on analysing the effect of one parameter while keeping others fixed. This technique only addresses chosen point estimates and not the entire parameter distribution. Sensitivity analysis often involves altering one variable or assumption at a time, although it can also encompass simultaneous variations of multiple variables to assess result robustness. A more comprehensive approach involves Monte Carlo techniques, detailed in Section 2.6.4.

2.6.2 Analysis of Residuals

Another approach to evaluating uncertainties involves examining the differences between predicted values (f_i) and actual measured values (y_i) of a variable, which are referred to as residuals. Several standard error measures from statistics can be employed to indicate the degree of uncertainty. These include:

- *Mean Absolute Error (MAE)*: This measures the proximity of predictions to actual measured data. It's computed by finding the residuals between the measured and model-predicted data and then calculating the average of these absolute errors. The formula is:2.39:

$$\text{MAE} = \frac{1}{n} \cdot \sum_{n-1}^{n} |f_i - y_i| \tag{2.39}$$

  where: n is the number of data points, f_i represents the predicted values, and y_i the measured values.
- *Mean Absolute Percentage Error (MAPE)*: This expresses prediction accuracy as a percentage. It's calculated by finding the absolute percentage difference between the measured and predicted values for each data point and then averaging these percentages. The formula is:

$$\text{MAPE} = \frac{1}{n} \cdot \sum_{n-1}^{n} \left| \frac{y_i - f_i}{y_i} \right| * 100 \tag{2.40}$$

- *Root Mean Squared Error (RMSE)*: This measures the differences between predicted and actual observed values, representing the sample standard deviation of the residuals. The formula for RMSE is:

$$\text{RMSE} = \sqrt{\frac{\sum_{t=1}^{n}(f_i - y_i)^2}{n}} \tag{2.41}$$

- *Coefficient of Determination (R^2)*: This value indicates how well data fits a statistical model. An R^2 of 1 indicates a perfect fit of the regression line to the data, while an R^2 of 0 indicates a poor fit. The formula to calculate R^2 is:

$$R^2 = 1\frac{\sum_i (y_i - f_i)^2}{\sum_i (y_i - \bar{y}^2} \tag{2.42}$$

2.6.3 Jack-Knife Method

The jack-knife procedure, initially designed to gauge the bias of an estimator, later extended its application to estimate variance. Named after its versatility, the technique can serve as a rapid and practical substitute for more intricate tools. This iterative method involves initially estimating an output using the entire dataset, then sequentially excluding different data subsections to create partial estimates (jack-knife replications). The difference between the complete estimate and these partial estimates yields a pseudo-value.

In the wind industry, the jack-knife method can assess the uncertainty of an analysis process by partitioning a complete dataset into subsections, as depicted in Figures 2.34 and 2.35. The representation of time-series data as bars signifies that the entire dataset contributes to the analysis.

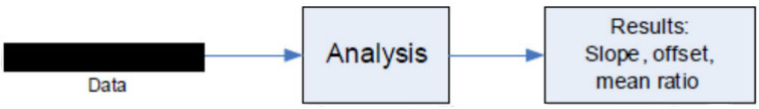

Figure 2.34: Visual representation of the standard analysis process.

The jack-knife variance estimate quantifies analysis result uncertainty by evaluating how outcomes vary when specific subsets of data are excluded, as shown in Figure 2.35. Here, six distinct results are derived, each from a different 5/6 portion of the complete dataset. The vacant areas indicate the omitted data subsections. Result uncertainty is subsequently inferred from the disparities between these results.

Figure 2.35: Visual representation of the jack-knife method for uncertainty determination.

In wind energy yield analysis, the jack-knife method can gauge uncertainty in long-term predictions by assessing the correlation between short-term site data and long-term reference data using the Measure Correlate Predict (MCP) process. The MCP calculates the long-term mean wind speed for various data subsets, and the variance in the output results determines the uncertainty.

Variance is computed by comparing the known mean wind speed with the estimated speeds from the jack-knife subset. The total jack-knife variance (σ_{jk}) is determined using Equation 2.43:

$$\sigma_{jk} = \frac{N-1}{N} \cdot \sum_{n=1}^{n} (\bar{v} - \bar{x}_n)^2 \tag{2.43}$$

where N represents the total number of jack-knife subsets, $\bar{v}$ is the mean long-term flow speed using the whole data set, and $\bar{x}$ is the mean long-term flow speed using the jack-knife subset n of the full data set.

The uncertainty (u_{jk}) can be calculated using the total variance as defined in Equation 2.44.

$$u_{jk} = \frac{\sqrt{\sigma_{jk}}}{\bar{v}} \tag{2.44}$$

2.6.4 Monte Carlo Analysis

Monte Carlo analysis (MCA) finds utility across various industries such as finance, project management, energy, manufacturing, research and development, insurance, transportation, and the environment. It addresses complex problems by employing random and probabilistic methods. The methodology involves generating a large number of random samples, wherein variables interact within a simulation structure to yield a probability distribution of potential outcomes. The approach identifies key variables governing the experiment's outcome and assigns probability distributions through numerous iterations. This process reiterates deterministic calculations but incorporates stochastic input variables. As the number of iterations increases, the resulting distribution converges toward an analytical solution [113].

While there exist variations of Monte Carlo sampling, some of which offer more efficient output distribution statistics estimation (e.g. Latin hypercube [114], importance sampling [115]), these methods face the challenge of dimensionality [116]. Conventional random Monte Carlo sampling remains the prevailing method for reporting uncertainties in metrology (the science of measurement) [107].

Monte Carlo analysis is pivotal in evaluating measurement uncertainty [107]. Given its computational demands, this method is frequently executed across multiple processes in a distributed memory environment, like a multi-node cluster or supercomputer.

In practical applications, Monte Carlo analysis offers a significant advantage by propagating distributions through functional relationships instead of relying on standard uncertainties. It surpasses the limitations of deterministic methods, as discussed in ISO-GUM guidelines [107], since it does not necessitate assumptions regarding distribution shapes and correlations. Shah [110] outlines a Monte Carlo analysis framework for assessing annual yield uncertainty in tidal energy and compares it to the ISO-GUM method. Nonetheless, a drawback of Monte Carlo analysis, aside from its time-intensive nature, is its provision of statistical estimates rather than exact results, rendering it as accurate as the data model and its interactions.

Ensemble modelling is another variation of Monte Carlo analysis, often used in weather forecasting and climate predictions [117]. Instead of relying on a single weather model, an ensemble of predictions is generated. This ensemble approach offers insights into the potential range of future atmospheric outcomes. Employing multiple simulations helps mitigate uncertainties in:

- Errors stemming from the utilisation of imperfect initial conditions, further magnified by the inherent chaotic behaviour of the atmosphere [118].

- Errors arising due to imperfections in the model formulation, including the mathematical techniques employed to solve the governing equations [119].

Ideally, verified future atmospheric conditions align with the predicted ensemble range, where the range's extent reflects the forecast's uncertainty. This probabilistic approach is applicable beyond weather predictions and can be employed for various dynamic systems [120, 121].

Sampled Distributions

A Monte Carlo uncertainty analysis can be applied to the following transformation, for example:

$$Y = g(X)$$

where g is a transformation of input quantity X, often considered a random variable, into quantity of interest Y, also a random variable. Here the uncertainty in X is specified as:

$$X \sim f_x(X)$$

where $f_x(X)$ is a probability distribution of X. The Monte Carlo method proceeds by sampling $f_x(X)$ to obtain an input Monte Carlo sample:

$$(x_n)_{n=1}^N$$

evaluating the transformation g on these samples to obtain a Monte Carlo sample of y:

$$(y_n)_{n=1}^N$$

where:

$$y_n = g(x_n), \text{for } n = 1...,N \tag{2.45}$$

The distribution of the Monte Carlo sample $(y_n)_{n=1}^N$ approximates the probability distribution of Y due to variability in X. This sampling distribution can be used in uncertainty analysis to estimate the expected value and variability in the quantity of interest Y. The input sample distribution, here $(x_n)_{n=1}^N$, is typically formed by using a pseudorandom number generator (PRNG), which generates a sequence of pseudorandom numbers with a discrete distribution that agrees with, in some measure, that of the specified distribution.

2.6.5 Guide to the Expression of Uncertainty in Measurement: ISO-GUM

The principles of the calculus of small changes can be utilised to analyse a function that connects multiple input variables to an output variable. This technique helps in estimating the range of uncertainty in the output variable caused by uncertainties in the input variables. In the context of a quantity y that is determined by a function involving $x_1, x_2, ...x_n$:

$$y = f(x_1, x_2, ...x_n) \tag{2.46}$$

The variation in y caused by variations in x_i can be formulated as:

$$\delta y = fx_1 \delta x_1 + fx_2 \delta x_2 + ... + fx_n \delta x_n \tag{2.47}$$

The ISO-GUM (Guide to the Expression of Uncertainty in Measurement) methodology provides valuable guidance for uncertainty analysis, but there are certain limitations related to input uncertainties that are worth noting:

- *Assumption of Independence: ISO-GUM often assumes that input uncertainties are independent. In reality, variables can be correlated, leading to a potential underestimation or overestimation of the overall uncertainty if correlations are not properly considered.*
- *Linearity Assumption:* ISO-GUM guidelines are most straightforward for linear models. In cases where the relationship between inputs and outputs is nonlinear, the methodology may not accurately capture the true uncertainty propagation, potentially resulting in unreliable uncertainty estimates.
- *Complexity of Combined Uncertainties:* The combined uncertainty calculation can become intricate when multiple sources of uncertainty are combined, especially if they have different distributions or correlation structures.

In summary, while ISO-GUM offers a solid foundation for uncertainty analysis, its assumptions and limitations should be considered. Users should be aware of these limitations and consider more advanced methods when the input uncertainties or the model's complexity require a more accurate representation of uncertainty propagation.

The establishment of the function connecting the input variables to the output is crucial. In many instances, this functional relationship can be intricate and might necessitate simplifying assumptions to formulate a workable functional model. Consider an output variable y that is dependent on input variables x_i, as depicted in Equation 2.46. If the standard uncertainty in the input variables is denoted as u_{xi}, then the standard uncertainty in y, denoted as u_y, can be expressed using Equation 2.48 [107]:

$$u_y = \sqrt{\sum_{i=1}^{N} \left(fx_i \right)^2 \cdot u_{xi}^2 + 2 \sum_{i=1}^{N-1} \sum_{j=i+1}^{N} fx_i fx_j \cdot u(x_i, x_j)} \tag{2.48}$$

Here, $u(x_i, x_j)$ represents the covariance between x_i and x_j. If the assumption is made that all variables are independent and uncorrelated, meaning $u(x_i, x_j) = 0$, then Equation 2.48 simplifies to Equation 2.49, as illustrated:

$$u_y = \sqrt{\sum_{i=1}^{N} \left(fx_i \right)^2 \cdot u_{xi}^2} \tag{2.49}$$

The assumption is that the uncertainty in y is suitably characterised by a Normal distribution. This is generally accurate, largely due to the central Limit Theorem (CLT). However, there might be instances where this assumption proves less precise, especially when dealing with a limited number of uncertainties or when a small number of substantial non-Gaussian uncertainties hold more significance [107]. With the presumption of a normal distribution, it follows that there is a 68% likelihood for the true value, y_{true}, to be described by Equation 2.50.

$$y_{\text{true}} = y_{\text{mean}} \pm u_y \tag{2.50}$$

2.7 Power Performance Assessment for Tidal Energy Converters

The purpose of a PPA for a TEC is crucial for its development and successful deployment. Primarily, a PPA provides a standardised approach to evaluate how efficiently the device converts the kinetic energy of tidal currents into electrical energy under various conditions. This verification of performance is essential for bench marking the device against industry standards and optimising its design and operational procedures.

Furthermore, reliable data from PPAs boost investor confidence by demonstrating the technological viability and economic potential of tidal energy converters. This aspect is pivotal for attracting the necessary investments and funding for further development. Additionally, PPAs often fulfill regulatory requirements, helping to ensure that devices meet specific safety and performance standards before commercial deployment.

Data gathered through PPAs also support extensive research and development activities, offering valuable insights that can improve efficiency, durability, and environmental compatibility. Moreover, understanding the power performance enables developers to assess the environmental impact of the device, ensuring operations within acceptable limits to minimise disruption to marine ecosystems.

IEC TS 62600-200 Technical Specification

The IEC TS 62600-200 TS is a standard developed by the IEC that specifically addresses the PPA of TECs. This standard plays a crucial role in the tidal energy industry by providing a structured framework and guidelines for evaluating the performance of these devices. Its importance can be understood from several perspectives:

- *Industry Consistency:* The IEC TS 62600-200 establishes a common methodology and terminology for assessing the power performance of TECs. This standardisation promotes consistency across the industry, allowing for fair and accurate comparisons between different tidal energy devices and projects. It provides a basis for reliable decision-making in investment, procurement, and regulatory processes.
- *Quality Assurance:* The standard ensures that the PPA process is conducted using recognised and validated procedures. This leads to higher levels of confidence in the accuracy and reliability of the assessment results. It helps developers, operators, investors, and regulators make informed decisions based on sound technical information.
- *Optimisation and Innovation*: By adhering to the guidelines of IEC TS 62600-200, developers and researchers can better understand the factors influencing power production in TECs. This knowledge facilitates continuous improvement in design, operational strategies, and technology innovation. It promotes the development of more efficient and reliable tidal energy systems.
- *Investment Confidence and Risk Mitigation:* Investors and financing institutions often seek assurance that the anticipated energy production of a tidal energy project is based on rigorous and standardised assessments. Adhering to IEC TS 62600-200 enhances the credibility of the performance predictions and can attract more investment to the sector. It also supports identifying potential risks and uncertainties associated with TEC operation. Understanding the expected energy production helps developers plan for contingencies and mitigate financial and operational risks.

While this TS is valuable for establishing a common framework and methodology for assessing TEC performance, it is worth noting that it does not extensively address uncertainties associated with these assessments. This lack of emphasis on uncertainties can have implications for the accuracy, reliability, and overall credibility of the assessment results. Uncertainties in PPAs are essential to provide a comprehensive understanding of the

potential variability in the outcomes. TEC performance can be influenced by a wide range of factors, including environmental conditions, device design, and operational strategies. Ignoring uncertainties can lead to overly optimistic or pessimistic predictions, which may impact investment decisions, project planning, and regulatory compliance.

Site conditions - bathymetry

In the context of the TS, considering the site conditions and bathymetry at a tidal test site is of paramount importance. The standard outlines the rules and guidelines for the PPA of TECs, and this includes taking into account the specific characteristics of the site where the assessment is conducted.

Site conditions and bathymetry refer to the physical characteristics of the location where a TEC is deployed. These factors play a significant role in determining the performance and efficiency of TECs. The bathymetry of the TEC test site needs to undergo a thorough survey to ascertain its suitability for conducting tests. This survey ensures that there are no obstacles or irregular topography that could potentially impact both the performance of the TEC and the quality of local tidal currents. Specifically, a designated section of the TEC test site, extending 10 equivalent diameters (10x the rotor diameter of the TEC to be deployed) upstream and downstream of the TEC's location, as well as 5 equivalent diameters on each side, should be subjected to the survey.

This defined area spans dimensions of 20 equivalent diameters (20x the rotor diameter of the TEC to be deployed) and adheres to the standards outlined in the International Hydrographic Organisation (IHO) order 1a for hydrographic surveys [34]. The survey conducted within this specified area guarantees that the bathymetric conditions are accurately assessed, ensuring the TEC's optimal functioning and the reliability of the local tidal current characteristics.

Prediction of the power curve from measurements

The power curve is a graphical representation where the recorded power production (y-axis) is plotted against the incident current resource (x-axis). This power production encompasses the reduction in transmission due to factors like drive train efficiency and other device equipment contributions. When direct power measurement at the TEC's output point is not feasible, measuring power at a suitable location, such as the onshore substation, is recommended. To account for losses through cables, transformers, and power conditioning, accurate measurements must be taken and incorporated.

The tidal current records, which serve as the resource, should be available at intervals of 10 minutes or similar, with a spatial resolution of 1 meter or finer. These records should span the water column from the seabed upward. To derive the power-weighted rotor average (PWRA) velocity for constructing the power curve, the vertical variation of the tidal current at each time interval is integrated across the power capture area. This approach is visually represented in Figure 2.36 [30] and follows the method of bins as described in Equation 2.51:

$$\hat{U}_{i,j,n} = \left[\frac{1}{A} \sum_{k=1}^{S} U_{i,j,k,n}^{3} \cdot A_k \right]^{\frac{1}{3}} \quad A = \sum_{k=1}^{s} A_k \tag{2.51}$$

where: $\hat{U}_{i,j,n}$, is the instantaneous PWRA velocity, A_k is a depth bin over the swept area of the TEC rotor, $u_{i,j,k,n}^{3}$ is the velocity in the relative bin, and i, j, k, are index numbers for the velocity bin (increments of 0.1 m·s^{-1}), time instant of the measurement and the current depth bin across the projected capture area respectively.

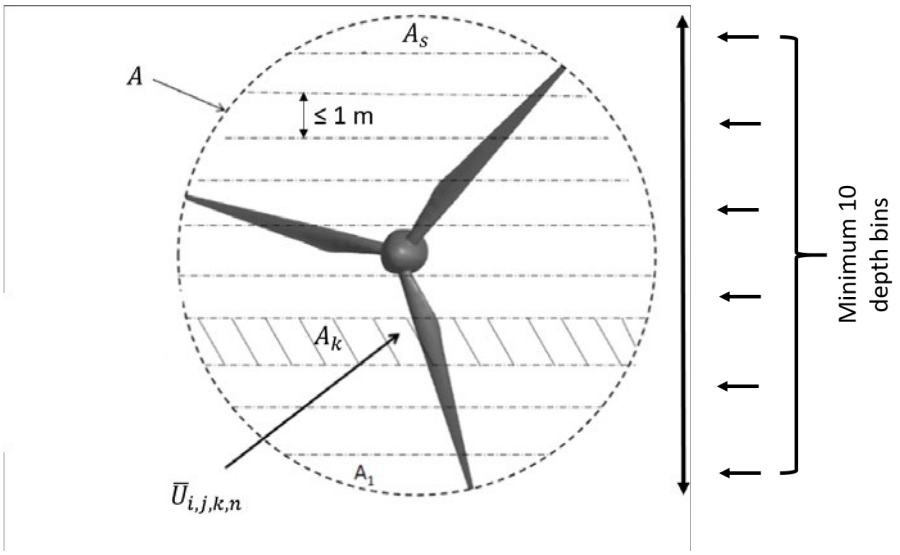

Figure 2.36: Vertical variation of tidal currents across the projected capture area. Image revised from IEC.

The instantaneous PWRA velocity calculated in Equation 2.51 should then be averaged by an divisor of 10 minutes. Equation 2.52 computes the temporal average of $\hat{U}_{i,j,n}$, yielding the mean power-weighted tidal current velocity $\bar{U}_{i,n}$. This value becomes a data point in the dataset for a specific current velocity bin i. Correspondingly, the averaged active power and reactive power output for that velocity bin should also be determined over the same time frame, as outlined in Equations 2.53 and 2.54.

The measured power curve is obtained by employing the method of bins on the current velocity data, with bin increments of 0.1 m·s^{-1}. This involves calculating the mean values of the current resource across the power capture surface and the device's power output for each current resource bin, as described below:

$$\bar{U}_{i,n} = \left[\frac{1}{L} \sum_{j=1}^{L} \hat{U}_{i,j,n}^{3} \right]^{\frac{1}{3}} \tag{2.52}$$

$$\bar{P}_{i,n} = \frac{1}{L} \sum_{j=1}^{L} P_{(i,j,n)} \tag{2.53}$$

$$\bar{Q}_{i,n} = \frac{1}{L} \sum_{j=1}^{L} Q_{(i,j,n)} \tag{2.54}$$

where: L is the number of samples in the defined averaging period, and $\bar{U}_{i,n}$ is the mean PWRA velocity in velocity bin i for data point n in m·s^{-1}. $\bar{P}_{i,n}$ represents the mean recorded TEC active power in velocity bin i for data point n, $P_{i,j,n}$ is the magnitude of the total instantaneous active electrical power from the TEC, $\bar{Q}_{i,n}$ is the mean recorded TEC reactive power in velocity bin i for data point n, and $Q_{i,j,n}$ is the magnitude of the total instantaneous reactive electrical power from the TEC.

Calculation of the TEC overall efficiency

In accordance with IEC TS 62600-200, the calculation of the turbine's overall efficiency involves assessing its performance across a range of operational conditions. This assessment aims to provide a comprehensive understanding of how efficiently the turbine converts tidal energy into electricity, considering both design and real-world variations.

The overall efficiency of an operating TEC should include the power at its output terminals in the test results. For each velocity bin i, the TEC's overall efficiency should be calculated using the measured power curves for both flood and ebb tides, according to the specified equation 2.55:

$$\eta_{\text{system},i} = \frac{\bar{P}_i}{\frac{1}{2} \cdot \rho \cdot A \cdot \bar{U}_i^3} \tag{2.55}$$

where: A represents the projected capture area of the TEC (m^2), $\bar{P}_i$ is the mean recorded TEC active power in velocity bin i, $\bar{U}_i$ is the mean tidal current velocity in velocity bin i ($m \cdot s^{-1}$), $\eta_{\text{system},i}$ is the TEC overall efficiency in velocity bin i, and ρ is the density of water (kg/m^3).

Levels of uncertainty

It should be noted that the value of $\bar{P}_{i,n}$ for each bin, is a mean, or expected value based upon an ensemble average of the collected values in that bin. Consequently, a distribution of values will be scattered randomly around the mean value given in Equation 2.52, with a standard deviation attached to that distribution, relating to that bin. The standard deviation on each bin in the power curve will provide one of the levels of uncertainty associated with the behaviour of the device at the site.

The standard deviations for each velocity bin are the best estimates of the true standard deviation, which will possess a distribution and become increasingly accurate as the number of points in the bin increases. The duration of the test period is, therefore, likely to influence the level of uncertainty attached to the expected performance of the device at that site.

Annual energy production

In compliance with IEC TS 62600-200, the calculation of the AEP for TECs involves estimating the amount of energy that the device is expected to generate over the course of a year under realistic operating conditions. This assessment is crucial for evaluating the economic feasibility and performance of tidal energy projects.

The AEP calculation takes into account various parameters, including the device's power curve, the tidal resource at the installation site, and the device's availability and downtime. These factors are integrated to determine the total energy output that can be expected from the TEC over a year and can be estimated using the following Equation 2.56:

$$\text{TEC}_{AEP} = \text{N}_\text{h} \cdot \text{TEC}_A \cdot \sum_{i=1}^{\text{N}_\text{B}} \bar{P}_i \cdot f_i(\bar{U}_i) \tag{2.56}$$

where: TEC_A represents the predicted availability of the TEC, TEC_{AEP} is the expected annual power production in kWh, N_B is the total number of velocity bins set in increments of 0.1 $m \cdot s^{-1}$, in the device power curve, N_h is the number of hours in one year (8760). $\bar{P}_i$ Represents the power in kW generated by velocity bin i of the power device curve, $\bar{U}_i$ is the average performance current velocity of bin i of the power device curve, f_i is the proportion of time during the year for which the average performance current velocity occupies a value within velocity bin i.

It's worth emphasising that the anticipated AEP serves as a robust estimator of the projected power output. However, this estimation is accompanied by a degree of uncertainty linked to each of the velocity bins (N_B) representing tidal current velocities at the testing site. While the AEP can often be extrapolated to another site using the known set of $f_i(U_{\text{perf}(i)})$, it's essential to present the AEP along with a specified margin of error, capturing the range around the mean value.

To clarify, estimates of AEP uncertainty can be calculated using upper and lower confidence limits ($P_{(i)} \pm E_{(i)}$) for each velocity bin. Here, $E_{(i)}$ represents the confidence increment specific to bin i. It's important to note that the uncertainties considered in the AEP calculation pertain solely to factors stemming from the power performance test. Other crucial uncertainties beyond this test should also be disclosed in the report. If necessary, these factors should be accounted for and appropriately communicated, especially when addressing allowances or providing context in the test report. Practical forecasting of AEP should encompass these additional uncertainties, incorporating considerations like the TEC's availability influenced by environmental factors such as storm damage, biofouling, and other influences (which are captured in the value of TEC_A) in equation 2.56.

2.8 Summary of Theory in the Context of the Thesis

This chapter has covered several key aspects related to tidal energy, including the formation of tides, the measurement of tidal energy resources, methods for harnessing tidal energy with a focus on horizontal axis tidal turbines, and techniques for assessing uncertainty using field measurements. The forthcoming thesis will be centred on in-situ flow measurements collected through ADCP deployments as part of the ReDAPT project [122] in the Fall of Warness, located in Orkney, Scotland. This near rectangular full-scale tidal test site is situated between Eday and Muckle Green Holm, a small outcrop southwest of the island, and experiences semi-diurnal tides.

While this section has provided a comprehensive listing and explanation of various methods of uncertainty assessment, the primary focus of this thesis centres around the estimation of power output from an operational HATT and two further modelled HATTs that occupy different regions in the water column, aiming to explore the spatial and temporal uncertainties derived from in-situ measurements.

The absence of uncertainty quantification in the standard can be attributed to several factors, including the complexity of uncertainty analysis, the diversity of TEC technologies, and the evolving nature of the tidal energy industry. However, the omission of uncertainties has implications for both the accuracy of reported results and the comparability of different performance assessments. Without considering uncertainties, the reported metrics might present an incomplete picture of the TEC's performance and reliability, potentially leading to misleading conclusions.

Efforts are underway to develop supplementary guidance, best practices, and standards that address uncertainty analysis in the context of TEC testing. By incorporating uncertainty quantification into the assessment process, the tidal energy industry can provide more accurate, reliable, and comprehensive information about the performance of TECs, fostering growth and confidence in this promising renewable energy sector.

Chapter 3

State of the Art Review - In-situ measurements and Tidal Devices

3.1 Chapter Overview

This section provides a detailed examination of two essential components in tidal energy technology. Section 3.2 focuses on the design, mounting, and hardware configurations of acoustic instruments, further elaborated in Sections 3.2.1, 3.2.2, and 3.2.3. The chapter then shifts to tidal turbine installation methods, categorising them as surface-piercing systems in Section 3.3.1, gravity-based systems in Section 3.3.2, and floating systems in Section 3.3.3. This structured approach clarifies complex topics, facilitating a comprehensive understanding of current tidal energy technologies.

3.2 Tidal Energy Site Measurement Campaigns

Tidal energy resource assessments using ADCPs involve measuring water currents and velocities in tidal environments to estimate the available kinetic energy that can be harnessed for electricity generation. These assessments provide valuable information for project developers, policymakers, and researchers to understand the energy potential of tidal sites. Tidal current energy resource investigations have been conducted in many regions, including sites or areas in the US [123, 124, 125], UK [44, 126, 127], Canada [128, 129, 130, 131], France [132, 133], Mexico [134], Spain [135], Brazil [136, 137], Australia [138, 139, 140], Japan [141, 142], Malaysia [143], Korea [144, 145].

The thorough characterisation of a tidal energy site revolves around acquiring precise insights into water velocity across various spatial and temporal dimensions that hold paramount significance for the designers and operators of TECs. This undertaking spans from comprehending variations across annual and seasonal time frames to capturing rapid velocity fluctuations occurring at sub-second intervals. Diverse scales of motion are acknowledged to exert varying influences on the efficiency of energy extraction devices [146].

Equally significant is the awareness of how flow parameters exhibit spatial variations, encompassing a wide spectrum. This spectrum ranges from scales of tens of blade diameters, which are crucial for tasks such as power curve development [147], to variations at the level of meters and even smaller scales, which are vital for investigating device loading, blade fatigue [148, 149], and power quality [150]. Currently, there is no single instrument system that offers a cost-effective means to comprehensively gather the necessary measurements

that account for the multi-scale nature of tidal flows. Consequently, the central aim of these flow characterisations shifts towards identifying pivotal velocity measurements and metrics. These must not only be achievable and reliable but also representative of the intricate flow conditions and possess a significant impact on TEC design, operational performance, and overall reliability.

Table 3.1 provides a detailed overview of specific measurement campaigns conducted at the full-scale tidal test site, Fall of Warness (FoW). It is important to note that the data utilised in this thesis is sourced from the FoW and this site will be the focus of the thesis. Also included in Table 3.1 are campaigns aimed at carrying out a PPA in accordance with the IEC TS 62600-200.

3.2.1 ADCP: Design Considerations

Pressure vessel for communications and power

When integrating systems, a robust approach for incorporating subsea power, communications, and control mechanisms becomes essential. In instances where these systems cannot be accommodated within the existing infrastructure due to logistical, financial, risk-related, project, or technical limitations, the utilisation of a pressure vessel emerges as a necessary solution to house the integrated controller systems [47].

The design of the pressure vessel is contingent upon several critical factors, including its projected operational lifespan, internal volume prerequisites, attachment methodology, connector dimensions, and the installation depth. A comprehensive evaluation of these considerations is imperative to ensure optimal performance and longevity. [156, 157].

Turbine Monitoring

The presence of a TEC extracting energy creates a dynamic interplay between the machinery and the flow. The inherent fluid structures — flow speed, shear, turbulence, and eddies - directly influence the turbine's behaviour. Simultaneously, the turbine obstructs the incoming flow, harnesses energy, and alters fluid structures at its location and downstream, owing to blade tip vortices and wake effects [47].

Understanding this interaction and leveraging site characterisation for turbine design and site development necessitates quantifying the turbine's behaviour. Crucially, machine data originates from sensors embedded within TEC structures and systems. An exemplar of a comprehensively instrumented TEC system is showcased in the ReDAPT MC7.3 report [158].

Installation and recovery methods

The deployment and recovery methods of ADCPs for tidal PPAs involve careful planning and execution to ensure accurate data collection. Below are general steps for installation and recovery:

- *Site Selection*: Choose a suitable location with consistent tidal flow for accurate performance assessment [159].
- *Mooring Design*: Design a mooring system to secure the ADCP in place. This could involve buoys, anchors, and ropes/chains [160].
- *Sensor Depth*: Determine the appropriate sensor depth based on the expected tidal variations. Attach the ADCP to the mooring system using specialised mounting hardware.
- *Calibration*: Calibrate the ADCP to ensure accurate measurements.
- *Scheduled Recovery*: Plan a schedule for ADCP recovery based on the data logger's capacity and the assessment period.

Table 3.1: Summary of measurement campaigns from the Fall of Warness, Orkney, Scotland.

Title	Authors	Year	Key Findings
On the Variation of Turbulence in a High-Velocity Tidal Channel [71]	C. Greenwood, A. Vogler, V. Venugopal.	2019	The disparity in turbulence levels among the deployment sites highlights a substantial variability occurring over relatively short distances. This variability introduces uncertainty into the precision of turbulence measurements conducted using ADCPs.
Capture and simulation of ocean environment for offshore renewable energy [151]	S. Draycott, B. Sellar, T. Davey, D.R. Noble, V. Venugopal, D.M. Ingram.	2019	This work showcases a significant evolution in available approaches and tools, underscoring the recent capability to accurately simulate the complexities of the real-world ocean environment through physical means.
Structure of turbulent flow in EMEC's tidal energy test site [52]	E. Osalusi, J. Side, R. Harris.	2009	This study discovered that the flow velocity at a specific location can exhibit substantial variations across the turbine's actuator area. Such disparities could result in notable fluctuations in loading across the actuator, potentially giving rise to issues related to fatigue and vibrations.
High-resolution velocimetry in energetic tidal currents using a convergent-beam acoustic Doppler profiler [152]	B. Sellar, S. Harding, M. Richmond	2015	A groundbreaking sensor array comprised of convergent acoustic Doppler velocity profilers was demonstrated to enhance the spatial and temporal resolution of underwater velocimetry, specifically tailored for applications within the marine energy sector.
Initial flow characterisation utilising turbine and seabed installed acoustic sensor arrays [153].	D. RJ. Sutherland, B. Sellar, S. Harding, I. Bryden.	2013	The study has revealed that the most prominent twist in the depth profile and directional changes occur at the lowest flow speeds. Notably, there is an increase in mean turbulence intensity near the surface, even though there is no substantial decline in mean velocity. This trend is especially pronounced during the ebb tide, suggesting that wave orbital motion might contribute to the near-surface fluctuations.
Measuring and modelling the power curve of a commercial-scale tidal turbine [147].	J. Mcnaughton, R. Sinclair, B. Sellar.	2015	In this study, an evaluation was conducted to gauge the influence of instrument placement on the power curve. The results indicated a close alignment between the power curves generated from Tidal Bladed predictions and those derived from ADCPs measurements.

- *Boat and Crew*: Prepare a boat and crew capable of safely recovering the ADCP. Accurately position the boat over the mooring location using GPS [159].

Table 3.2: Summary of literature conducting a PPA as per the IEC/TS 62600-200 .

Title	Authors	Year	Key Findings
Tidal energy site characterisation at the fall of warness, EMEC, UK [122].	B. Sellar, D. Sutherland.	2015	This concise twelve-page summary serves as a brief introduction to the ReDAPT project, offering contextual information for understanding the individual work packages. This approach highlights the significant interdependence among project partners' endeavours. Additionally, the summary offers a succinct overview of the key outcomes stemming from the field measurement campaign conducted by the University of Edinburgh, followed by subsequent data analysis.
Initial operation power curve [154]	J. Mcnaughton	2014	This document unveils the power curve computed for DEEP-Gen IV, a horizontal axis TEC. The test procedure was conducted as part of the ReDAPT project, coinciding with the deployment of the TEC in the fourth quarter of 2013 at the Fall of Warness site within the EMEC.
Field performance testing of a floating tidal energy platform - Part 1: power performance [23]	R. Starzmann, I. Goebel, O. Jeffcoate.	2018	The test site located downstream from the Falls of Lora exhibits pronounced spatial and temporal fluctuations in inflow speed, marked by mean turbulence intensities of 40% at a velocity of 2 $m \cdot s^{-1}$. When relying on a single velocity measurement location, the spatial disparities in inflow bring about alterations in the performance curves of individual turbines, contingent upon their proximity to the velocity measurement point.
PPA of the tidal turbine Sabella D10 following IEC62600-200 [155]	S. Paboeuf, P. Yen Kai Sun, L. Macadre.	2016	This analysis highlights the need for clarification and interpretation of the equations of the IEC62600-200 standard. Indeed, equations used to plot the power curve have been rewritten for this application. The final result is the same as IEC however, the methodology has been clarified. Moreover, the sensitivity study validates the parameters, velocity bin step and time averaging proposed by IEC62600-200

- *Recovery Process*: Use winches or cranes to carefully raise the ADCP and mooring system to the surface. Retrieve the data logger for analysis [159].
- *Sensor Maintenance*: Inspect the ADCP for any damage and perform necessary maintenance.

Remember that specific guidelines may vary based on equipment models, study objectives, and local conditions. Always refer to manufacturer's manuals and relevant literature for detailed instructions tailored to the ADCP system being used [67, 161].

Meteorology

To ensure accurate and site-specific meteorological information for informing instrument recovery, it's crucial to collect meteorological data as close as possible to the TEC site. This practice offers a realistic representation of local meteorological conditions. The following key data points are essential from a weather station [47]:

- *Wind Speed and Direction:* Accurate wind speed and direction measurements provide insight into the prevailing wind patterns at the site. This data is vital for understanding potential impacts on instrument recovery operations.
- *Wind Gustiness:* Measuring wind gusts helps assess sudden changes in wind intensity, providing valuable information for safe instrument recovery procedures.
- *Surface Pressure:* Surface pressure readings offer insights into atmospheric conditions, aiding in predicting weather changes and their potential effects on recovery activities.

While traditional weather stations are typically positioned on land, moored weather buoys can also provide meteorological measurements. However, it's important to note that buoyed weather stations have limitations, particularly in high-flow regions. These limitations restrict their deployment to providing measurements from a far-field perspective, offering a broader understanding of the site's meteorological conditions [47].

3.2.2 ADCP: Mounting Solutions

Acoustic instruments are versatile tools used to measure water velocities in various marine applications, including tidal energy assessment. To effectively integrate ADCPs into these systems, various mounting solutions have been proposed. These solutions range from traditional mooring systems and bottom-mounted configurations to more innovative approaches like buoy-mounted and turbine-mounted setups. Mooring systems provide stable deployment in deep waters and have been used extensively for oceanographic studies [162]. Bottom-mounted ADCPs are fixed to the seabed and offer continuous measurements of tidal flows [163]. Buoy-mounted configurations utilise surface buoys to deploy ADCPs in shallower waters, facilitating adaptable data collection [164]. Turbine-mounted ADCPs enable localised flow measurements near TECs, aiding in PPA [165]. These mounting solutions underscore the flexibility and potential of ADCPs in monitoring and assessing marine environments. The subsequent sections offer valuable insights into the benefits and constraints associated with different mounting solutions, elucidating their intended roles in facilitating PPAs of TECs.

Seabed Gravity frames

Seabed gravity frames and boat-mounted systems are designed for remote measurements within the mid-depth range. A seabed gravity frame is a substantial non-buoyant structure engineered to ensure its frictional force surpasses the flow-induced drag force. Refer to Figure 3.1 for a visual representation of an ADCP mounted on a gravity base. In certain cases, instruments are positioned on a two-axis rotation gimbal to maintain horizontal alignment on an uneven seabed. However, a trade-off arises, as the turbulent fluid forces within the boundary layer can result in significant pitching and tilting of the sensor. The rigidity of gimbals [166], subject to potential biofouling during prolonged deployments, becomes crucial. However, the effects of minor dynamic pitching and tilting on velocity measurements can be rectified during post-processing if accurately recorded and within acceptable ranges, their correction hinges on their precise measurement.

This method has been employed and has effectively characterised mean flow conditions and energy flux at various sites for TEC installations [38, 167, 168, 169].

These frames provide notable advantages but also have inherent limitations. This method is acknowledged in literature for several distinct advantages:

- *Stability and Precision*: Seabed gravity frames provide a stable and precise mounting platform for ADCPs, minimising instrument movement and ensuring accurate velocity measurements in turbulent tidal flows [170].
- *Versatility*: These frames can be designed and configured to accommodate various instrument types, enabling the deployment of multiple sensors simultaneously for comprehensive data collection [171].
- *Minimised Vibration*: Being anchored to the seabed, gravity frames minimise the vibration caused by surface waves or boat traffic, which can negatively impact the accuracy of velocity measurements [172].
- *Long-Term Monitoring*: Seabed gravity frames are suitable for long-term monitoring, allowing researchers to capture temporal variations in tidal currents and related parameters [173].

Nevertheless, this approach is not without its limitations, including:

- *Site Specificity*: The deployment of seabed gravity frames requires appropriate seabed conditions, and they may not be feasible in all types of substrates or terrains [174]
- *Installation Complexity*: Deploying seabed gravity frames can be complex and time-consuming, involving specialized equipment and expertise for installation and recovery [175].
- *Maintenance Challenges*: Periodic maintenance and retrieval of instruments from seabed gravity frames can be challenging, especially in harsh marine environments with strong currents and sediment transport [176].
- *Instrument Accessibility*: Accessibility to instruments mounted on seabed frames for real-time data retrieval or adjustments may be limited, depending on the deployment depth.

These references provide insights into the use, advantages, and limitations of seabed gravity frames for ADCP deployments in tidal environments.

For PPA purposes, strict placement guidelines are enforced for seabed fixed ADCPs based on the turbine's equivalent diameter (D_E). The 'in-line orientation' requires positioning the ADCP between 2 and 5 D_E upstream and downstream of the TEC location, and within 1/2 D_E laterally from the rotor centerline respectively [30]. Alternatively, the 'adjacent orientation' allows ADCP placement between 1 and 2 D_E on either side of the TEC, within 1/2 D_E off the lateral centerline, perpendicular to the TEC [30]. For turbines with smaller rotor diameters, such as the SCHOTTEL Tidal Generator (STG) [177], complying with these guidelines becomes more challenging. The STG necessitates a 4 m lateral range for ADCP installation [23]. This challenge is heightened if the TEC is situated on a floating platform subject to surge and sway motions, leading to a reduction in the feasible ADCP placement area [178].

Autonomous Underwater Vehicle

An Autonomous Underwater Vehicle (AUV) presents an alternative method for installing flow measurement equipment. Nevertheless, its application is restricted to environments with relatively low flow speeds. AUVs have emerged as valuable tools for deploying ADCPs in underwater environments. Examples of these mounting systems are shown in Figure 3.2. This method provides notable advantages but also has inherent limitations. This method is acknowledged in literature for several distinct advantages:

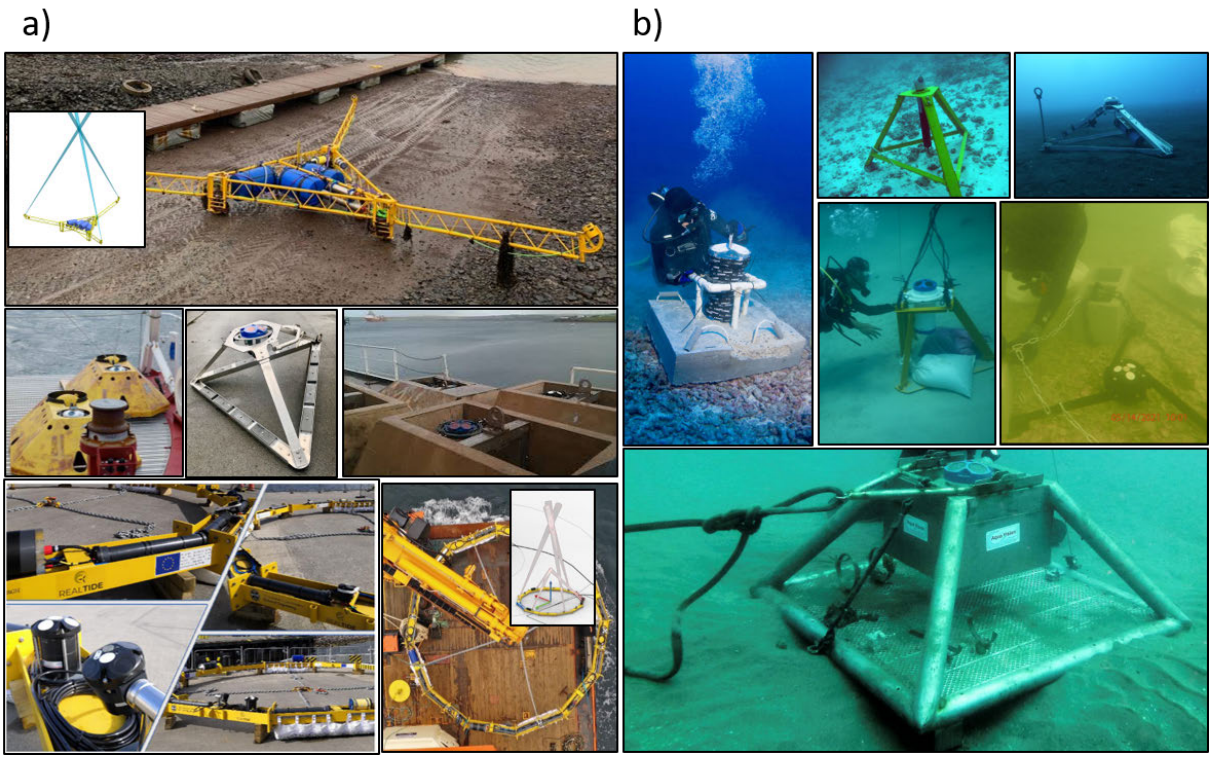

Figure 3.1: Gravity-based ADCP frames: a) Prior to ADCP deployment, and b) Seabed-mounted ADCPs during deployment/retrieval.

- *Flexibility and Mobility*: AUVs provide flexibility in choosing deployment locations and can navigate through complex and remote areas, enabling data collection in previously inaccessible regions [179].
- *High-Resolution Data*: AUVs can operate at varying depths, allowing them to capture high-resolution data across vertical profiles, which is crucial for accurately assessing tidal currents [180].
- *Reduced Infrastructure*: AUV deployments eliminate the need for dedicated structures or platforms, reducing deployment costs and logistics [179].
- *Real-Time Data Transmission*: Some AUVs offer real-time data transmission capabilities, enabling researchers to monitor and analyze data remotely [181].

Nevertheless, this approach is not without its limitations, including:

- *Limited Payload*: AUVs have limited space for instrument payloads, which might constrain the number of sensors or types of measurements that can be collected simultaneously [181].
- *Operational Complexity*: Deploying and recovering AUVs can be operationally complex, requiring specialized training and equipment, especially in challenging environmental conditions [179].
- *Power and Endurance*: AUVs have finite battery life, limiting their operational endurance and coverage area, which might require careful mission planning [180].
- *Risk of Loss or Damage*: AUVs operating in harsh underwater environments face risks such as collisions, entanglements, or system failures, which could result in the loss or damage of expensive equipment [182].

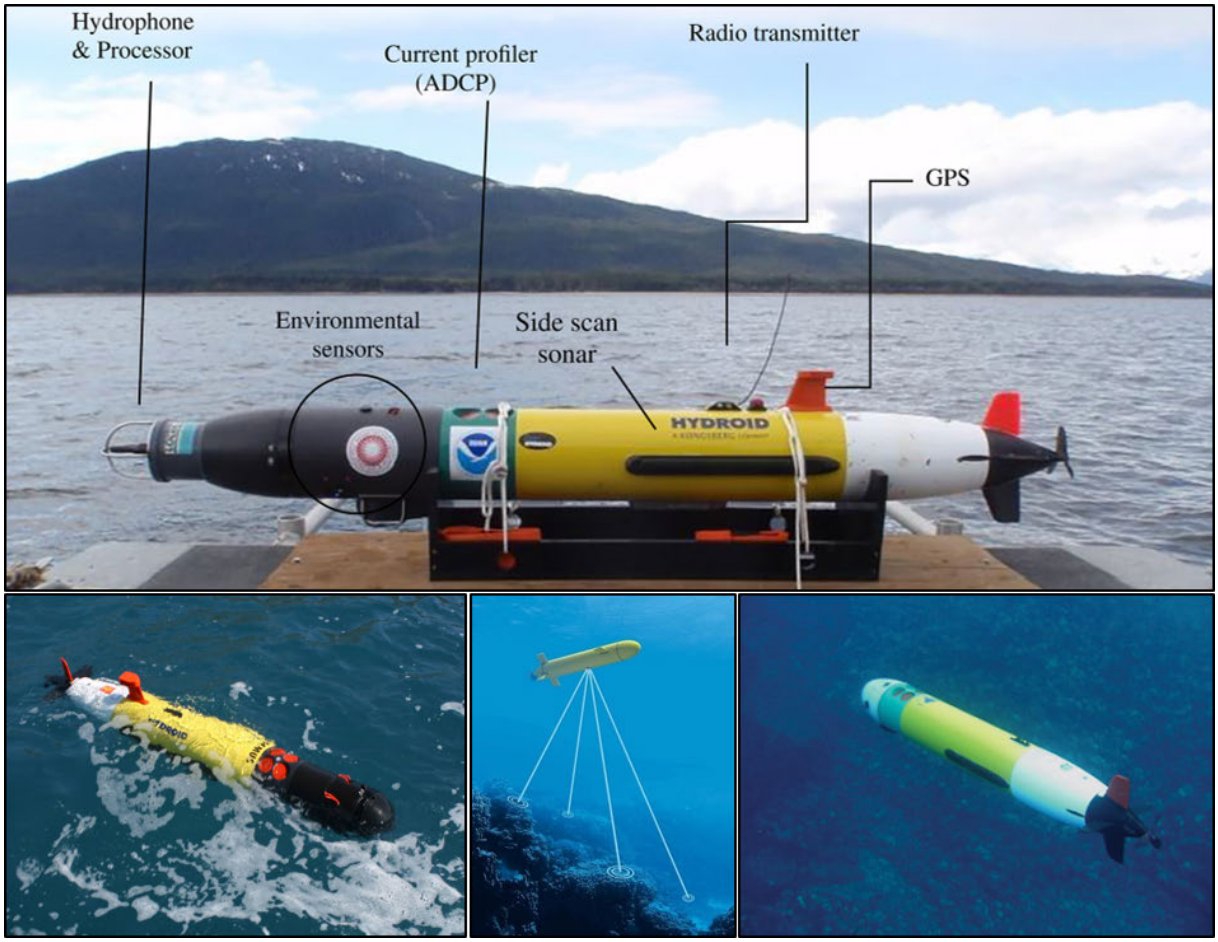

Figure 3.2: AUV equipped with a ADCP for surface tracking and flow velocity measurements.

AUVs offer great potential for assessing the power performance of TECs due to their ability to gather data in challenging underwater environments. However, there are several reasons why AUVs might not be extensively utilised for this purpose. Firstly, the deployment and operation of AUVs can be costly and technically complex, potentially limiting their widespread use in PPA [183]. Additionally, the specific requirements for accurately measuring the power output of TECs, including precise positioning and velocity measurements, might demand specialised sensors and equipment that could add to the complexity and cost associated with AUV deployments [184]. Furthermore, the variability of underwater conditions and the dynamic nature of tidal flows could pose challenges for consistent and reliable data collection using AUVs. Despite these potential hurdles, ongoing advancements in AUV technology and research might gradually overcome these limitations, leading to more frequent and effective utilisation of AUVs for PPA of TECs [185].

Vessel Mounted

Mounting ADCPs on vessels offers a promising means of capturing both mean and turbulence characteristics along a water column profile. These instruments facilitate the collection of multi-component instantaneous velocities with relative ease, enhancing the ability to understand flow dynamics. Refer to Figure 3.3 for a visual representation of an ADCP integrated onto a vessel.

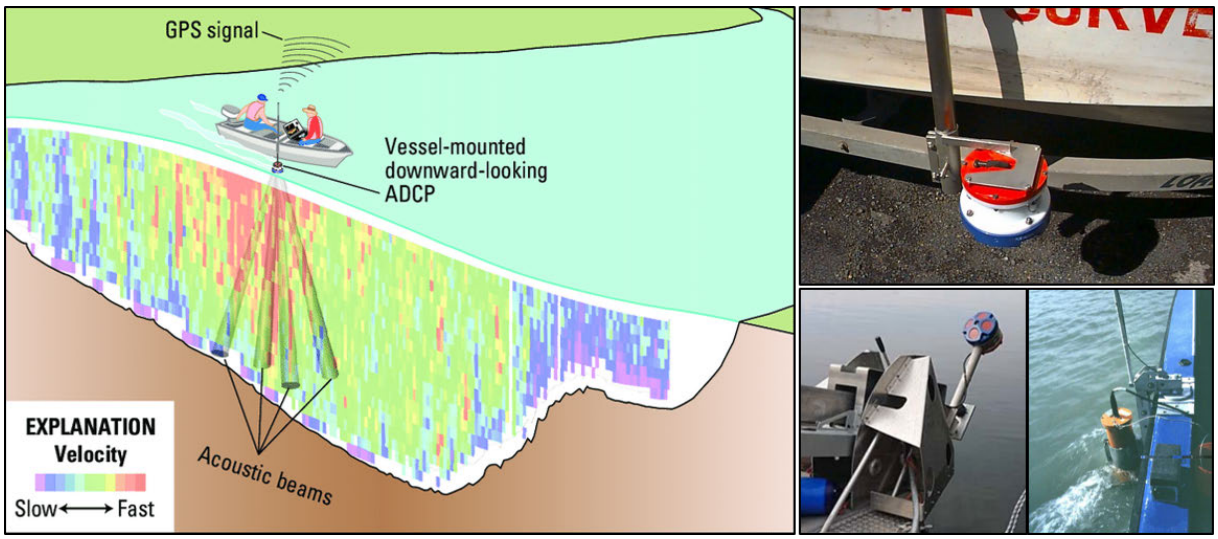

Figure 3.3: Vessel mounted ADCPs.

However, employing vessel-mounted sensors necessitates corrections for the vessel's pitch, roll, and yaw, akin to those required for seabed gravity frames. Additionally, a crucial step involves measuring and subtracting the vessel's own velocity to ensure accurate measurements. Notably, small boat designs can also be tethered to a mooring system, serving as a surface measurement platform for hydrodynamic data collection.

This method provides notable advantages but also has inherent limitations. This method is acknowledged in literature for several distinct advantages:

- *Mobility and Coverage*: Vessel-mounted ADCPs provide the capability to collect data across extensive spatial scales as vessels traverse different areas, enabling comprehensive coverage of a study region [186, 187].
- *Dynamic Measurements*: Real-time data acquisition is possible due to the dynamic nature of vessel-mounted deployments, allowing insights into temporal variations and flow dynamics [188].
- *Rapid Deployment*: The quick setup of vessel-mounted ADCPs makes them suitable for capturing transient events or surveying different areas within relatively short timeframes [187].
- *Adaptability*: Vessel-mounted ADCPs can be used on various types of vessels, including research vessels and commercial ships, expanding their potential applications [188].

Nevertheless, this approach is not without its limitations, including:

- *Vessel Interference*: The movement, speed, and interactions of the vessel with the water can influence the accuracy of hydrodynamic measurements, necessitating careful data correction [188].
- *Mounting Challenges*: Precise installation of ADCPs on vessels is critical to ensure accurate measurements while minimizing vibrations and interference from the vessel's structure [187].
- *Logistical Complexities*: Coordinating vessel schedules, availability, and equipment setup can present operational challenges, impacting data collection timing and scope [187].
- *Interference*: The presence of other equipment or structures on the vessel might interfere with the acoustic signals used by the ADCP for velocity measurements [188].

While ADCPs mounted on vessels offer an initial assessment of spatial variation at a site, they are typically not employed as the primary resource measurement method. The utilisation of vessel-mounted ADCPs introduces additional uncertainties stemming from both temporal and spatial resolution, as well as potential discrepancies between the boat's speed and the current speed [31, 189]. The latter concern is commonly addressed through bottom-tracking techniques [67, 190], which, unfortunately, can be negatively impacted by significant amounts of material like clay, sand, or vegetation that move near the seabed [191].

To address these challenges, a framework has been established to estimate the uncertainties associated with vessel-mounted ADCPs [31]. This framework highlights the potential for evaluating certain uncertainties using available information. Furthermore, IEC standards focused on tidal energy resource assessment and characterisation provide guidelines for best practices in conducting vessel-mounted studies [59]. These standards offer valuable insights into ensuring the reliability and accuracy of data acquired through vessel-mounted ADCPs.

At present, vessel-mounted ADCPs are acknowledged by the IEC/TS 62600-200 standard as a valid measurement method [30]. However, employing such instruments on a platform or vessel for extended periods and measuring flow while the TEC operates may introduce inherent uncertainty. This uncertainty arises due to potential interactions between the vessel's motion and the flow, as well as adherence to the existing data collection guidelines.

Buoy Mounted

A wave buoy stands as a pivotal tool for oceanographers, serving as a key instrument for data collection. The early 2000s marked a significant development with the introduction of commercially available Downward-Looking ADCPs, which opened the enticing possibility of augmenting wave-buoy datasets with current profile measurements. Refer to Figure 3.4 for a visual representation of an ADCP integrated onto a buoy.

For many, utilising a wave buoy equipped with an ADCP, rather than deploying an ADCP on the seabed, offered compelling advantages. These advantages encompassed easier accessibility, simplified power requirements, streamlined maintenance, and the ability to gather real-time data via radio telemetry systems. The amalgamation of real-time wave and current data collection at a single location bears operational benefits across various applications, spanning from climate studies to offshore energy endeavours.

Mounting ADCPs on buoys offers a distinct approach to hydrodynamic data collection. This method comes with specific advantages and limitations that need to be considered:

- *Elevated Positioning*: Buoys provide an elevated platform, enabling ADCPs to capture water column characteristics from a higher vantage point, which can yield insights into surface and subsurface flow dynamics.
- *Minimized Vessel Interference*: Buoy-mounted ADCPs eliminate vessel-induced disturbances, ensuring cleaner and less perturbed measurements of water currents [192].
- *Long-Term Deployment*: Buoys can be deployed for extended periods, facilitating continuous data collection and enabling the capture of longer-term flow patterns [193].
- *Reduced Bottom Interference*: Buoy-mounted ADCPs avoid the potential challenges associated with bottom interference, which can affect measurements close to the seabed [192].

Nevertheless, this approach is not without its limitations, including:

- *Deployment Challenges*: Deploying and maintaining buoys can be complex, requiring careful consideration of factors such as buoy stability, mooring design, and navigational safety [193].
- *Spatial Constraints*: Buoys have limited space for instrument deployment, which can limit the number of sensors or measurement types that can be accommodated.

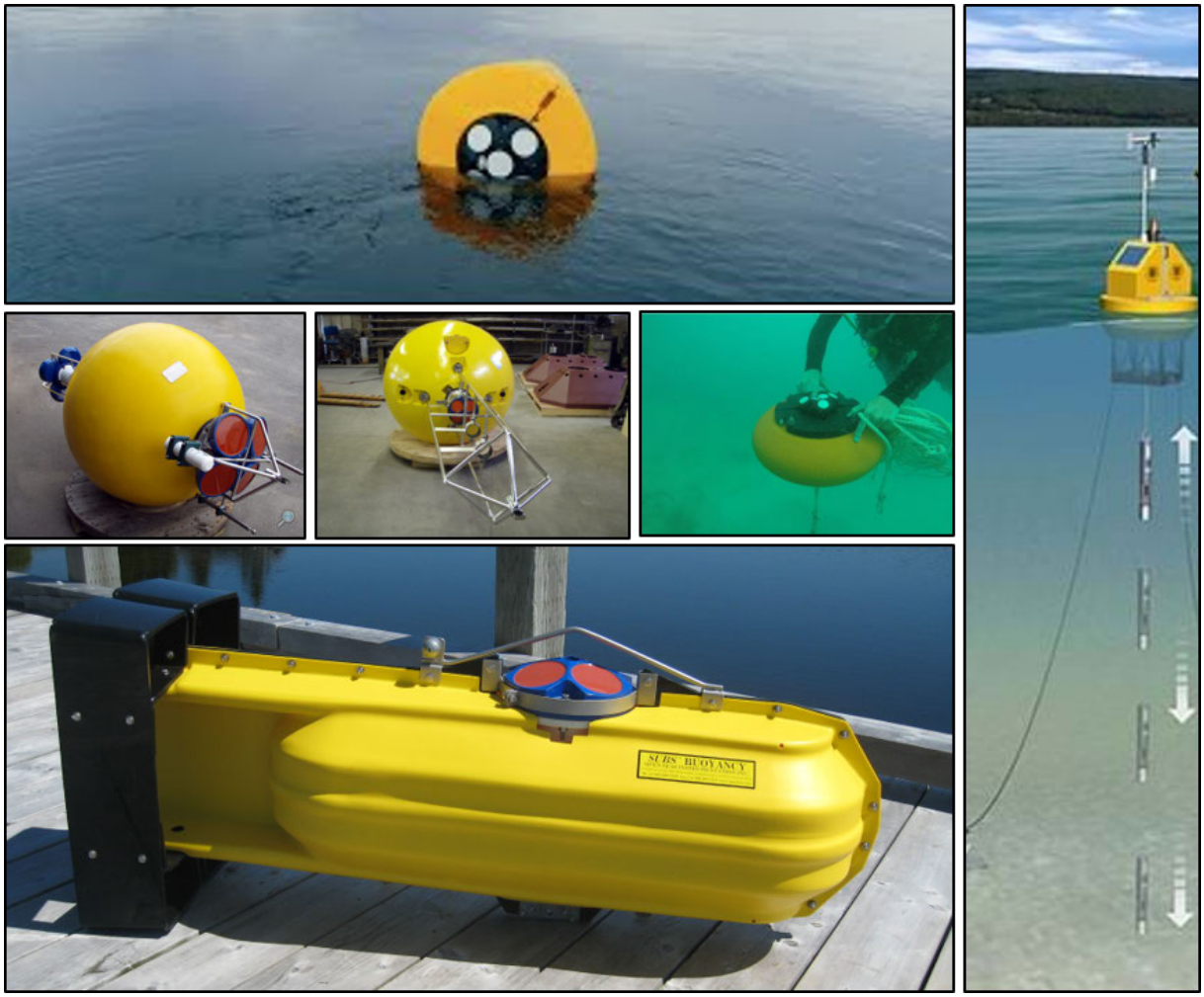

Figure 3.4: Buoy mounted ADCPs.

- *Maintenance and Accessibility*: Periodic maintenance and servicing of buoy-mounted ADCPs can be challenging due to their offshore location and exposure to harsh environmental conditions [192].
- *Data Quality*: Buoy motions and vibrations caused by waves or currents can impact the quality of collected data, necessitating post-processing corrections.

Turbine Mounted Instruments

Currently, the IEC/TS 62600-200 also does not recognise forward-facing ADCPs that profile in the horizontal plane and can be installed on the turbine. This arrangement, therefore, does not require any additional costly offshore work to deploy ADCPs on the seabed. Recent interest in using ADCPs mounted on the turbine has demonstrated their capabilities in profiling the rotor approach flow [194, 195, 166, 196]. Magnus Harrold et al. [195] evaluated the TEC-mounted instrument's merits by measuring the tidal turbine's performance relative to this reference and a conventional seabed placed ADCP, which adhered to the IEC/TS 62600-200 where possible. It was observed that the TEC-mounted ADCP provided a better reference of the free-stream conditions, evident from an improved agreement with theoretical predictions of device performance and a reduced amount of variation in the results [195].

This new method could reduce the costs and uncertainty of existing performance assessment best practices. Despite the results, further work was recommended to compare a TEC-mounted ADCP with an upstream-positioned ADCP [195]. Work by James McNaughton [147] did just that, considering two types of acoustic sensors for flow characterisation, ADCPs positioned on the seabed and a forward-facing Single Beam Doppler (SBD) mounted on the TEC, see Figure 3.5. Several locations of the ADCPs were considered, largely influenced by recommendations in the IEC/TS 62600-200. The study revealed that the SBD recorded a significant reduction in flow upstream of the rotor plane. Initial conclusions suggest that this observation is likely due to the specific configuration, including the operating frequency of the device, and the unique environmental conditions at the Fall of Warness. These findings underscore the importance of considering both device settings and local hydrodynamic conditions in assessing the performance and impact of such technologies [147].

Figure 3.5: TEC mounted ADCPs.

- *Operational Feedback*: Hydrodynamic data collected from turbine-mounted sensors can serve as operational feedback for optimising TEC design, placement, and performance [197].
- *Direct Flow Measurement*: Turbine-mounted ADCPs and SB-ADPs provide direct measurements of flow velocities within the vicinity of the TEC, offering insights into the flow conditions that directly impact the TEC's performance [195, 166, 74, 147].
- *Comprehensive Data*: Data collected from turbine-mounted sensors provide a comprehensive understanding of flow patterns, turbulence, and interactions between the TEC and its surrounding environment [195, 197, 166, 74].
- *In-Situ Observations*: The deployment of ADCPs and SB-ADPs on turbines allows for in-situ observations, minimising uncertainties associated with spatial variations and flow interference [197, 166, 198].

Nevertheless, this approach is not without its limitations, including:

- *Instrument Integration*: Integrating ADCPs or SB-ADPs onto turbines requires careful design and engineering to ensure proper alignment, minimal interference, and accurate measurements [197, 74].
- *Maintenance Challenges*: Accessing turbine-mounted instruments for maintenance can be complex and require specialised procedures, especially in challenging offshore conditions [197, 74].

- *Data Compatibility*: Turbine-induced motions can introduce complexities in data processing, requiring advanced correction techniques to ensure accurate measurements [197, 74, 198].
- *Resource Limitations*: Deploying instruments on turbines limits the number of locations available for hydrodynamic measurements, potentially affecting the representatives of the collected data [195].

Turbine-mounted ADCPs offer a direct and localised approach for assessing the power performance of TECs by measuring water velocities near the turbine. However, their application for this purpose might be limited due to technical challenges and operational considerations. Turbine-mounted ADCPs require integration into the turbine structure, which can be complex and potentially disruptive to ongoing operations [199]. Additionally, the close proximity to the turbine blades might introduce flow disturbances that could affect the accuracy of velocity measurements. Furthermore, the interpretation of velocity data from turbine-mounted ADCPs into meaningful power performance metrics would necessitate intricate modelling and analysis to account for flow variations caused by the turbine's operation [165]. Despite these challenges, ongoing research aims to refine and optimize the use of turbine-mounted ADCPs for accurate and practical PPA of TECs [200].

In summary, the deployment of ADCP instruments in various configurations, such as seabed-placed ADCPs, ADCPs mounted on AUVs, vessel-mounted ADCPs, buoy-mounted ADCPs, and tidal turbine-mounted ADCPs/SBDs, plays a crucial role in enhancing the precision and scope of marine data collection. Each configuration offers unique advantages tailored to specific research needs and operational conditions, thus ensuring comprehensive coverage and high-resolution data. These setups contribute significantly to advancing marine science by providing accurate, consistent, and reliable measurements of water currents. This detailed understanding supports more informed decision-making and a deeper comprehension of complex oceanic dynamics. The complete list of ADCP configurations and their specific applications relevant to this thesis is detailed in Chapter 5 Section 5.2, providing essential insights into their roles and effectiveness in field research.

3.2.3 ADCP: Hardware, Software and Configuration

The selection of appropriate ADCP hardware, software, and configurations plays a crucial role in accurately assessing the power performance of TECs.

The hardware components encompass range, frequency, beam configuration, and the potential for sensor integration. The required range and frequency for capturing current flow across diverse depths and resolutions are dictated by site-specific requirements. ADCPs offer multiple beam configurations, with a pertinent choice aiding precise flow velocity measurement, particularly in regions with intricate flow patterns around tidal energy systems. These ADCPs can also integrate with additional sensors, including those for turbulence and temperature, furnishing a more holistic comprehension of flow conditions encompassing the tidal energy converter [47, 201, 202].

The software encompasses data processing and QC procedures, data visualisation techniques, and cross-data correlation. Effective ADCP data processing and QC are imperative for converting raw data into meaningful insights. Ensuring accurate and reliable data for PPAs, proper processing and QC is essential. The availability of software with clear and informative data visualisation tools empowers researchers and engineers to interpret collected data efficiently, aiding the understanding of flow patterns, turbulence levels, and velocity profiles within the tidal flow interaction [203]. Performance assessments of TECs often require correlating ADCP data with variables like power output and structural behaviour. For this purpose, the software should seamlessly facilitate the integration and correlation of disparate data sets [204].

ADCP configuration hinges on deployment depth, location, sampling interval, and measurement plan. Strategically selecting ADCP deployment depth and location is pivotal to capturing flow conditions pertinent to tidal energy converter operation, encompassing varied depths for a comprehensive flow overview. The sampling interval governs data point collection frequency, necessitating a balance between high sampling rates and data storage capacity to capture swift flow changes while ensuring sufficient data collection duration [205]. Essential to the process is a well-structured measurement plan, which captures tidal flow variations, turbulence, and other pertinent parameters over time, ultimately yielding a precise representation of device performance [206].

3.2.4 Quality Assurance of Real-Time Oceanographic Data: QARTOD

QARTOD, which stands for "Quality Assurance of Real-Time Oceanographic Data," is a framework that encompasses a set of QC checks designed to ensure the accuracy, reliability, and consistency of oceanographic data collected from various in-situ instruments, including ADCPs. These QC checks are crucial for maintaining the integrity of collected data, enabling researchers, scientists, and decision-makers to make informed conclusions and decisions based on accurate information [207].

ADCPs are instruments used to measure ocean currents by emitting acoustic pulses and analysing the Doppler shift in the returning signals to calculate water velocity at different depths, as discussed previously in Section 2.3.2 and here within Sections 3.2.1 and 3.2.2. However, since ADCP data collection involves various environmental and instrumental factors that can introduce errors or anomalies, implementing QC measures is essential to ensure data reliability [208].

The importance of QARTOD QC checks for in-situ ADCP measurements can be summarised as follows [207]:

- *Data Accuracy:* QARTOD checks help identify and correct inaccuracies in ADCP measurements. These inaccuracies can arise from sensor drift, signal noise, biofouling, and other sources. By detecting and correcting such errors, researchers can rely on more accurate data for their analyses.
- *Data Consistency:* Long-term oceanographic studies require consistent data over time. Inconsistent or spurious data points can lead to incorrect conclusions. QARTOD checks can identify outliers or data points that deviate significantly from expected patterns, allowing researchers to either correct or remove them.
- *Model Validation:* Oceanographic models rely on accurate and consistent input data. By applying QARTOD checks to ADCP data, researchers can improve the validation of models, leading to more reliable predictions and assessments.
- *Resource Management:* Many important decisions, such as coastal infrastructure planning, marine resource management, and disaster response, depend on accurate oceanographic data. Ensuring the quality of ADCP data through QARTOD checks enhances the reliability of these decisions.
- *Scientific Integrity:* High-quality data is the foundation of rigorous scientific research. By implementing QARTOD QC checks, researchers uphold the integrity of their findings and contribute to the overall advancement of oceanography and related fields.

In summary, QARTOD QC checks play a vital role in maintaining the reliability and accuracy of in-situ ADCP measurements. By ensuring data accuracy, completeness, consistency, and comparability, these checks contribute to better scientific research, more informed decision-making, and a deeper understanding of our oceans and their complex dynamics [207]. The complete list of QC checks relevant to this thesis is provided in Chapter 5 Section 5.4.

3.3 Tidal Energy Site Exploitation Devices

Tidal Range

Tidal range technologies employ a barrage, a structural barrier such as a dam, to harness energy derived from the vertical disparity between high and low tides [209]. This potential energy is transformed into electricity using tidal turbines, often adapted from hydropower designs like bulb turbines, positioned within the barrage structure. The commercial viability of these technologies has been firmly established through operational facilities in France (240 Megawatts), Canada (20 MW), China (approximately 5 MW), and Russia (0.4 MW) dating back to the 1960s and 1970s. South Korea introduced the largest and most recent tidal barrage, with a capacity of 254 MW, in 2011/2012 [14]. Still in full operation today, The La Rance tidal barrage, has an installed capacity of 240 MW, from its twenty-four 10 MW bulb turbines, generating around 500 GWh/yr [210]. Advancements in tidal range power generation encompass emerging technologies such as tidal lagoons, tidal reefs, underwater fences, and low-head tidal barrages.

Tidal Currents

Tidal currents that are suitable for extraction are often found in areas where the flow is constricted through narrow passages, causing an acceleration in velocity. A range of conceptual designs for tidal stream turbines have been developed, which are elaborated upon below:

3.3.1 Seabed fixed: Surface Piercing TEC Concepts

The pioneering venture in harnessing marine currents on a commercial scale was the SeaFlow project, established in 2003 near Lynmouth along England's north Devon coast [211]. Engineered by Marine Current Turbines (MCT), this endeavour introduced a 300 kW HATT with a 2-bladed rotor spanning 11 meters in diameter. The distinctive feature of SeaFlow was its novel installation on a steel monopile embedded into the seabed socket, enabling the turbine's rotor, gearbox, and generator to be vertically moved along the monopile for maintenance purposes [211] (see Figure 3.6a). While SeaFlow operated effectively during its deployment, power fluctuations ranging from 30 kW to 50 kW were noted. Insights derived from this project illuminated that the monopile positioned behind the turbine led to immediate current deceleration ahead of it, causing the current to bifurcate around it. Moreover, the two-bladed rotor intersected the monopile approximately every 2 seconds, resulting in periodic variations in captured power [211]. Remarkably, SeaFlow not only achieved its stipulated 300 kW power rating but also exhibited a peak rotor efficiency of approximately 43%, a figure favourably comparable to contemporary wind turbines [212, 211].

The valuable insights collected from the SeaFlow project drove the evolution of the megawatt-scaled commercial SeaGen device. Differing significantly from SeaFlow, SeaGen employs two 16-meter diameter rotors while integrating full blade pitch control to eliminate the need for yaw control, similar to SEAFLOW [212]. In 2009, the SeaGen unit was installed in Strangford Narrows, Northern Ireland, marking a groundbreaking milestone as a dual HATT with a collective capacity of 1.2 MW, designed for current flows surpassing 2.4 $m \cdot s^{-1}$ [150] (Figure 3.6b). These rotors are strategically positioned on opposing sides of the monopile, mitigating the impact of monopile wake during downstream tidal operation. Moreover, the streamlined cross arm, drawing insights from SeaFlow, not only captures double the energy but also generates considerably less disruptive wake than the monopile [213]. SeaGen triumphed in meeting design objectives, achieving peak efficiencies of 52% for both rotors on both sides and exporting over 11 GWh of power during its lifecycle. Building upon this triumph, MCT Atlantis Resources developed the SeaGen S, an advancement featuring twin 1 MW powertrains and a 20-meter rotor diameter [37].

Founded in 2005, Open Hydro also embraced monopile-foundation development [214, 211, 215]. Their initial achievement involved the deployment of a 250 kW bidirectional open-centred TEC with a 6-meter rotor diameter in 2006 at the Fall of Warness, Orkney [214]. Open Hydro holds the distinction of being the first to undergo full-scale testing at EMEC's tidal test site, successfully feeding electricity to the national grid in 2008 [216, 217] (Figure 3.6c). As they expanded their presence, Open Hydro contributed to demonstration projects in Canada (2 MW installed) and France (an array of two 16-meter diameter devices, adding 1 MW to the grid capacity) [218, 219]. Concurrently, Open Hydro continually advanced its TEC technology, introducing subsequent generations for testing on the EMEC test rig [214, 215].

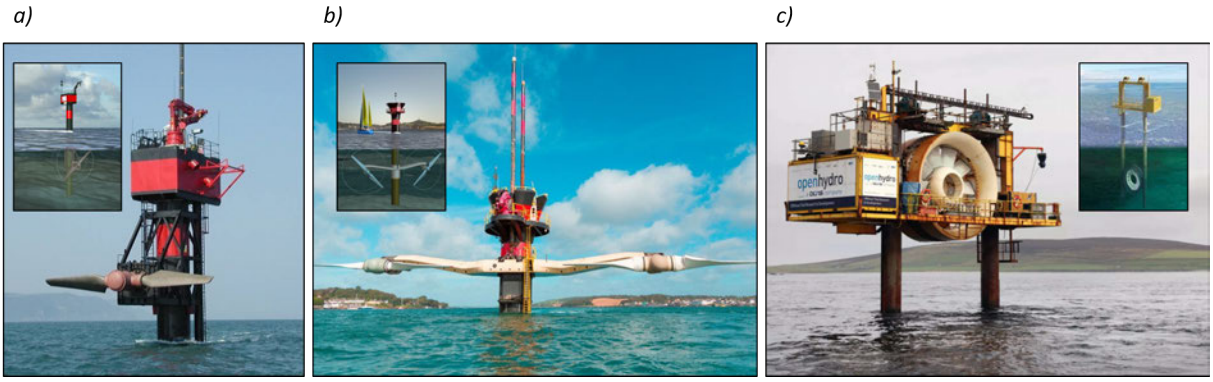

Figure 3.6: Types of tidal stream devices utilising seabed-fixed monopile foundation: a) 300 kW SeaFlow, b) 1.2 MW SeaGen, and c) 250 kW OpenHydro.

3.3.2 Seabed fixed: Gravity Based TEC Concepts

Verdant Power played a pivotal role in the creation, testing, and deployment of the Gen4 tidal turbine for the Roosevelt Island Tidal Energy (RITE) Project, marking the first-ever grid-connected tidal turbine array operation in the US [220]. The initial installation, dating back to 2005, featured 3 Kinetic Hydropower Systems (KHPS) turbines affixed to a single gravity-based triframe. These HATTs featured 3-bladed rotors and collectively offered a capacity of 105 kW [221]. Accumulating over 9,000 operational hours, Verdant Power refined its design approach and transitioned to the RITE East Channel Pilot. This progression led to the installation of the next-generation Gen5 turbine in 2020, boasting an improved capacity of 187.5 kW (Figure 3.7a).

Andritz Hydro Hammerfest (AHH) entered the tidal energy sector by creating and deploying the HS300 prototype, the world's initial tidal turbine linked to the Norwegian grid in 2003 [222]. This HATT, boasting a 300 kW capacity and a 20-meter rotor diameter, laid the foundation for the subsequent full-scale HS1000 development (1 MW, 21 m rotor diameter). The HS1000 successfully commenced operations at EMEC's full-scale tidal test site in 2011 [214, 222, 223, 224] (Figure 3.7b). Following HS1000 testing, AHH actively participated in the Meygen tidal array project situated in the Pentland Firth, Scotland [225]. This 6 MW demonstration array incorporates four 1.5 MW turbines, with three of these being AHH's upscaled HS1500 HATT, featuring a rated capacity of 1.5 MW at 3 $m{\cdot}s^{-1}$ and an 18-meter rotor diameter [225, 226] (Figure 3.7c).

The Energy Technology Institute's (ETI) ReDAPT initiative introduced an innovative 1 MW buoyant tidal generator, Alstom's DEEP-Gen IV turbine, deployed at EMEC's full-scale tidal test site in 2013 [214, 122] (Figure 3.7d). The DEEP-Gen IV turbine is a 3-bladed HATT with a 1 MW capacity at rated flow conditions of 2.7 $m{\cdot}s^{-1}$ with a 257 m^2 capture area, encompassing an 18-meter rotor diameter [122, 213]. This project effectively demonstrated the

turbine's performance across diverse operational scenarios, aiming to improve public and industry confidence in tidal turbine technologies [158]. The initiative achieved this through the provision of comprehensive environmental impact and performance data, while also showcasing a novel and reliable turbine design [194, 158, 166, 213, 227, 228].

In France, the Ushant Island tidal initiative accommodated Sabella, where the D10 TEC was set up within the Fromveur Passage in 2015 [213]. This island-linked TEC possesses a 1 MW capacity and adheres to the traditional HATT design, featuring 6 blades that contribute to a 10-meter rotor diameter. Notably, the D10 represented a milestone as the first French TEC to generate electricity and connect to the electrical grid. Sebella's entry into the tidal industry commenced with their prototype D03, which was installed in 2008. Positive outcomes and recognition from French public authorities prompted the evolution of the D10 iteration [155, 213] (Figure 3.7e).

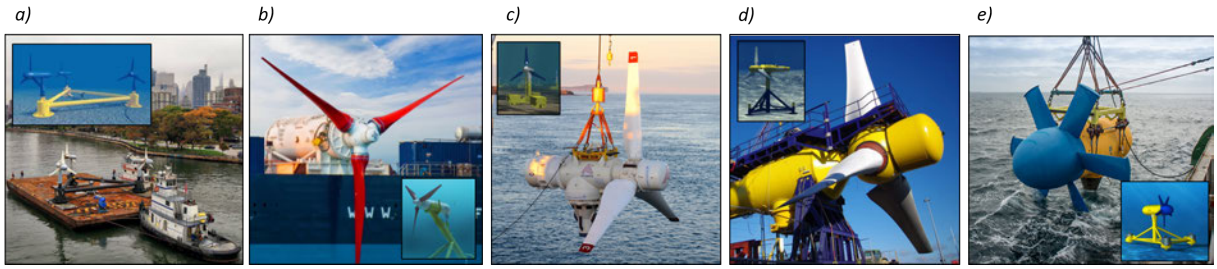

Figure 3.7: Variants of seabed gravity-based tidal stream devices: a) 187.5 kW Gen5, b) 300 kW HS300, c) 1 MW HS1000, d) 1 MW DEEP-Gen IV, and e) 1 MW D10.

3.3.3 Sea Surface: Floating TEC Concepts

Sustainable Marine introduced the PLATform for Inshore Energy (PLAT-I) at Connel, Oban in 2018, a pioneering floating TEC system and the world's first of its kind [229]. The initial model, the first-generation SCHOTTEL Instream Turbine (SIT), features a HATT design with a 4-meter rotor diameter and a 250 kW capacity at 2.75 $m{\cdot}s^{-1}$ flow velocity. The PLAT-I comprises a three-hulled platform accommodating SIT250 turbines, usually four, identified as SIT1 to SIT4. Employing a turret mooring configuration, the platform enables weather-vaning with river flow [23, 229]. Rigorous testing encompassed full-scale pushing trials in Rotterdam harbour [177, 230], moored assessments using a floating platform at Queen's University Belfast's tidal test site in Strangford Lough, and power performance evaluations for both steady and turbulent tidal conditions at Connel, Oban [23, 230]. Subsequent deployments in Scotland and Nova Scotia spurred the development of PLAT-I 6.40 (Figure 3.8a), housing six improved SIT250 turbines with a capacity of 70 kW each, collectively amounting to 420 kW. Tailored for the Fundy Ocean Research Centre for Energy (FORCE) project, this iteration boasts 50% more power generation than its predecessor [231].

Magallanes Renovables devised a floating system by retrofitting an old vessel with a submerged monopile hosting two counter-rotating rotors, formally known as Atir [232, 233]. The platform, depicted in Figure 3.8b, employs four mooring lines to anchor to the seabed, reducing installation and maintenance costs associated with traditional seabed-mounted TECs [228]. Featuring twin HATT with a collective 1.5 MW capacity (750 kW each) and a 19-

meter rotor diameter [234], the variable pitch of both rotors allows them to alter rotation direction for energy harvesting from both tide directions while remaining stationary [232, 234]. After rigorous testing at EMEC's full-scale tidal test site in 2017, the capacity of Atir was enhanced to 2 MW (1 MW per power train), followed by redeployment in 2019 and further optimisation in 2021 at EMEC [214, 232].

Tocardo developed two tiers of tidal turbines: T-1 and T-2 [235, 236]. The T-1, initially proven in 2008 during tests within the Dutch Afsluitdijk sluice, generates 50 kW to 100 kW power. In 2013, it underwent trials in Marsdiep, known for strong currents, attached to a motorised barge acting as a floating foundation. The T-2, an advancement of the T-1, scales up power generation, providing 100 kW to 250 kW. In 2015, five T-2 TECs were successfully arrayed within the Eastern Scheldt Storm Barrier, delivering a combined peak power output of approximately 1.2 MW at 4 $m \cdot s^{-1}$ flow velocity, effectively proving performance under varied velocity conditions [235, 236].

Scotrenewables introduced an innovative floating tidal stream turbine turbine, SR250 (250 kW with two 8 m rotors) in 2011 [237]. Installed at EMEC's full-scale tidal test site and connected to the grid, the design is similar to Atir (Magallanes 1.5 MW Device) in that the two rotors are submerged and connected to two monopiles [237]. The SR250 achieved over 4,000 hours of operation over three years, it became the first floating TEC to transfer electricity to the UK national grid [237]. The main technical features are the floating design, compliant mooring system, and passive yaw system with fixed pitch rotor blades for reducing system complexity and cost [224, 237].

Following SR250's triumph, the SR2000, commercialised in 2016, scaled up power generation to 2 MW. The 64-meter-long floating hull accommodates two 16-meter diameter rotors with a rated capacity of 1 MW each, totalling 2 MW at 3 $m \cdot s^{-1}$ flow velocity, making it the most powerful tidal turbine of its time [178]. Designed for cost-effective electricity production throughout its lifecycle, its 6-meter transport draught and turret-style mooring system simplify installation, operation, and maintenance [228]. After generating over 3,250 MWh of electricity, the SR2000 was decommissioned in 2020. Evolving from its lessons, the 02, depicted in Figure 3.8c, was designed to increase yield by 35% at EMEC [238], subsequently installed in 2021 [214].

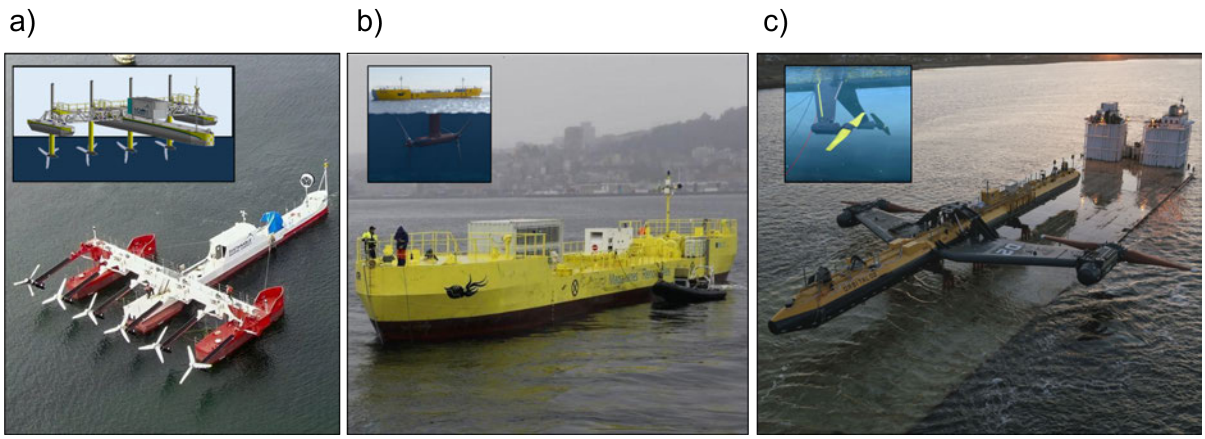

Figure 3.8: Variations of floating tidal stream devices: a) PLAT-I 6.40, b) 1.5 MW Magallanes, and c) 2 MW O2 Device.

Tidal Commercial Arrays

The UK holds a considerable share of Europe's exploitable tidal resources, with a substantial portion located in the Pentland Firth. Situated at the northern end of Scotland, this area separates the Orkney Islands from the mainland to the south (Figure 3.9). Renowned for its swift tidal currents, the Pentland Firth has garnered substantial interest as a potential location for deploying tidal stream generators [51, 239].

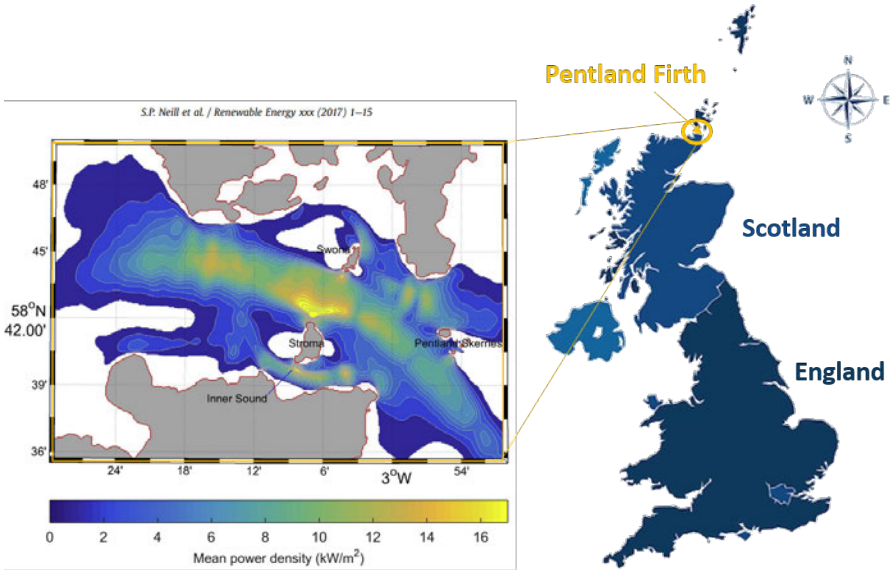

Figure 3.9: Pentland Firth location in Scotland, UK.

Simec Atlantis Energy, as the lead developer of the MeyGen project, is situated along a 3.5 km stretch in the Pentland Firth between the island of Stroma and mainland Scotland [240]. Positioned just 2 km away from Scotland's northeastern tip, the site lies on a natural channel through which water flows between the North Sea and the Atlantic Ocean, boasting an average tidal current of 4.4 $m{\cdot}s^{-1}$—among the swiftest currents in the UK [217, 240]. As the world's largest planned tidal stream project, MeyGen is divided into three phases, reaching a capacity of 6 MW in 2018 and with a planned ultimate capacity of 398 MW [217, 240].

The MeyGen project currently encompasses four 1.5 MW turbines mounted on gravity turbine support structures, three of which are Andritz Hydro Hammerfest's HS1500 turbines, contributing a total of 4.5 MW to the array [225]. The fourth turbine, the AR1500 from Atlantis Resources, also rated at 1.5 MW and with a rotor diameter of 18m, was installed [225]. Simec Atlantis holds the necessary permissions to further expand the grid capacity, with plans to add an additional 49 turbines (73.5 MW total), increasing Phase 1's capacity to 86 MW [225].

In Scotland, Nova Innovation achieved a significant milestone by developing the world's first fully operational offshore tidal energy array connected to the grid at Bluemull Sound in the Shetland Islands [217, 241, 242] (see Figure 3.10). In 2014, they deployed their first community-owned tidal turbine, the Nova 30, in Bluemull Sound, with a generating capacity of 30 kW [243]. This pilot deployment demonstrated the feasibility of rapid, cost-effective installation using local work boats and marked success by delivering power to the grid. The following years saw the deployment of the Nova M100 devices (with an installed capacity of 300 kW), reaching over 17,000 generating hours in 2019. The M100-D TEC, featuring a rotor diameter of 8.5m, produces up to 100 kW in currents of 2 $m{\cdot}s^{-1}$ [243].

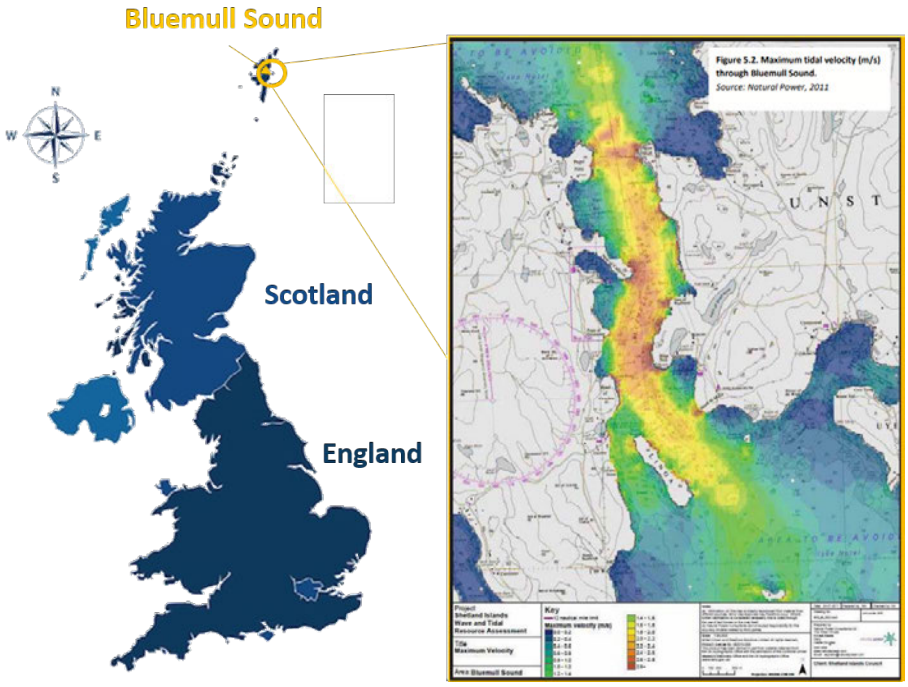

Figure 3.10: Bluemull Sound location in Shetland, Scotland, UK.

In 2018, Nova Innovation secured licenses to expand the tidal array to include six turbines, effectively increasing the capacity to 600 kW, and reconfiguring the arrangement of turbines within the array. Collaborating with Tesla in the same year, they integrated energy storage into their tidal technology, leading to the creation of the world's first grid-connected tidal power station capable of providing baseload power and delivering energy on demand to meet consumer requirements [243]. In August 2020, a fourth 100 kW turbine, representing the next generation of Nova's M100 turbine with a direct drive mechanism (no gearbox), was incorporated into the array. This was followed by the installation of two more 100 kW turbines in 2021, bringing the total to six. Furthermore, a reconfiguration of the array's TECs was conducted to gather insights into array effects and optimise layout design [241, 243].

Perpetuus Tidal Energy Centre (PTEC) Limited is an independent company collaborating with The EMEC in Orkney, in partnership with leading turbine operators, to implement tidal stream energy solutions within the next four years. PTEC's objective is to establish a 30 MW commercial demonstration facility for tidal stream projects, positioned off the southern coast of the Isle of Wight (see Figure 3.11) [244].

PTEC's goal is to expedite the path to full commercialisation for tidal technologies. It aims to achieve this by offering a pre-consented facility that enables tidal developers to transition from testing individual tidal devices to installing and optimising the performance, operation, and maintenance of small arrays of tidal devices under real-world conditions. This pioneering initiative, the first of its kind globally, is situated in a highly significant market. PTEC's mission encompasses the operation of tidal arrays, examination of their interaction with the marine environment, emission-free energy generation, as well as contributing to employment, skills, education, and investments for the Isle of Wight community [244].

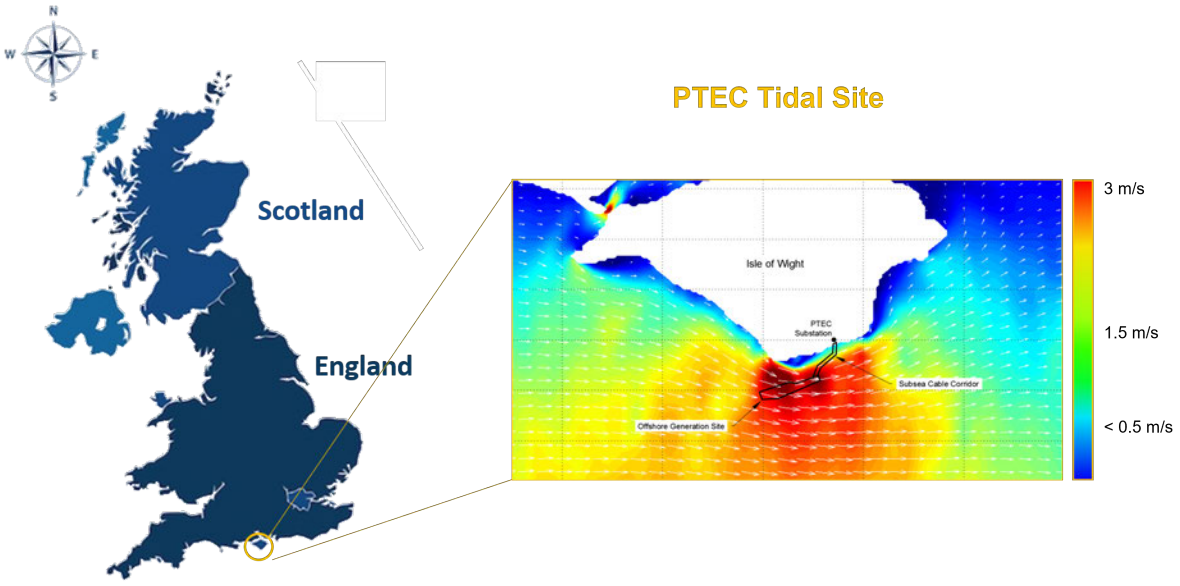

Figure 3.11: PTEC tidal test site located south from the Isle of Wight.

Chapter 4

Uncertainties in the power Performance Assessment

4.1 Chapter Overview

This chapter examines uncertainties in tidal energy technology in line with IEC TS 62600-200 standards. Section 4.2 introduces these standards, followed by tailored guidance for the tidal energy sector in Section 4.2.1. Section 4.3 compares methodologies for wind and tidal energy, detailing wind-specific procedures in Section 4.3.1 and tidal-specific ones in Section 4.3.2. The chapter then identifies uncertainties within the IEC standards in Section 4.3.4 and provides acoustic instrument guidance for power curve measurement in Section 4.3.5. It concludes by pinpointing uncertainties related to instrumentation, data processing, and spatiotemporal variations in Sections 4.4.1, 4.4.2, and 4.4.3. This chapter serves as a comprehensive guide for those seeking to understand the complexities and uncertainties in tidal energy performance assessments.

4.2 Power Performance Assessment as per IEC

In the pursuit of harnessing tidal energy as a viable renewable resource, the assessment of power performance in tidal turbine deployments becomes a critical factor. Uncertainties inherent in this assessment process hold considerable significance due to their potential impact on energy yield estimates and project viability [2, 245]. Accurate power performance assessment requires a comprehensive understanding of various parameters, including flow patterns, underwater topography, and the dynamic behaviour of turbines within tidal environments.

Research by Evans and Palmer [246] emphasises the necessity of a thorough comprehension of flow patterns and their interaction with underwater topography for effective site characterisation. This understanding lays the foundation for a robust assessment of potential impacts. Site measurements emerge as a pivotal tool in this process, serving to gauge the energy resource available, assess fluid flow's spatial and temporal variations, and evaluate the implications of flow dynamics on turbine performance and reliability within tidal locations [47, 246].

As PPA evolves as a crucial component of tidal energy development, it becomes evident that uncertainties are intertwined with this evaluation. These uncertainties encompass a range of factors, including measurement inaccuracies, variations in flow behaviour, and complexities arising from the interaction of turbines with dynamic underwater conditions. Recognising and quantifying these uncertainties is indispensable for refining the accuracy and reliability of PPAs, thereby enhancing decision-making, optimising project planning, and instilling confidence in the tidal energy sector's growth [47, 246].

In the context of PPA for tidal turbines, the IEC TS 62600-200 plays a pivotal role by providing guidelines and recommendations for performance testing and data analysis [155]. This TS offers a structured framework for evaluating the energy production and efficiency of TECs, ensuring a consistent and reliable assessment methodology across the industry [155, 195].

Just like the wind industry, the tidal energy sector has established standards through TC114, as outlined in Section 4.2.1. One significant standard is the IEC TS 62600-200, which addresses the evaluation of the power performance of TECs [30].

In the evolving landscape of tidal energy technology, it's essential for developers to showcase the real-world power performance of tidal turbines. However, due to their novelty, only a limited number of full-scale prototypes have undergone sea trials, with an even smaller fraction integrated into the power grid. Given this scenario, the IEC TS 62600-200, titled "Electricity producing TECs — Power performance assessment," has been applied only to a handful of turbines. The scarcity of operational TECs generating electricity has hindered the widespread adoption of this specification by both industry stakeholders and certification bodies [155].

Notably, the IEC TS 62600-200 standard has been employed to evaluate the performance of seabed-mounted tidal turbines in various regions, including the UK [150, 212, 195, 23, 154], France [155, 247], and the US [248].

Type certification of the turbine

Evaluating the power performance of a tidal turbine involves establishing a connection between the incoming water current conditions and the turbine's generated power, resulting in the creation of a power curve based on actual measurements. This process is commonly carried out as a pivotal phase towards obtaining the turbine's type certification [48]. It forms the foundation for assuring the device's power output to various stakeholders, including customers, investors, and insurers.

Validation of models

Another rationale behind generating the power curve lies in the validation of tools employed by turbine designers. The validation of theoretical forecasts for tidal turbine performance against real-world measurements remains relatively scarce, as evident in only a handful of studies [194, 195, 227]. Nonetheless, there exists a considerable body of scale-model investigations [249, 250]. Throughout the turbine development design phase, techniques such as blade-element momentum models and model scale tank tests find widespread utilisation [251].

Design verification

Beyond model validation and type verification, the continuous monitoring of turbine performance offers operators the means to evaluate the device's state [252]. This practice aids in the early detection of faults and malfunctions, enabling timely maintenance interventions to prevent the escalation of issues and potential serious failures.

4.2.1 Relevant Guidance and Standards for Tidal Energy

The IEC Technical Committee 114 (IEC/TC 114) was established with the aim of advancing marine energy technology, specifically focusing on wave, tidal, and other water current converters. Since its inception in 2007, IEC/TC 114 has been instrumental in developing a series of standards and best practices to drive the progress of marine energy technology. These standards and guidelines, listed in Figure 4.1, serve as crucial tools for promoting the growth and reliability of this evolving field [1].

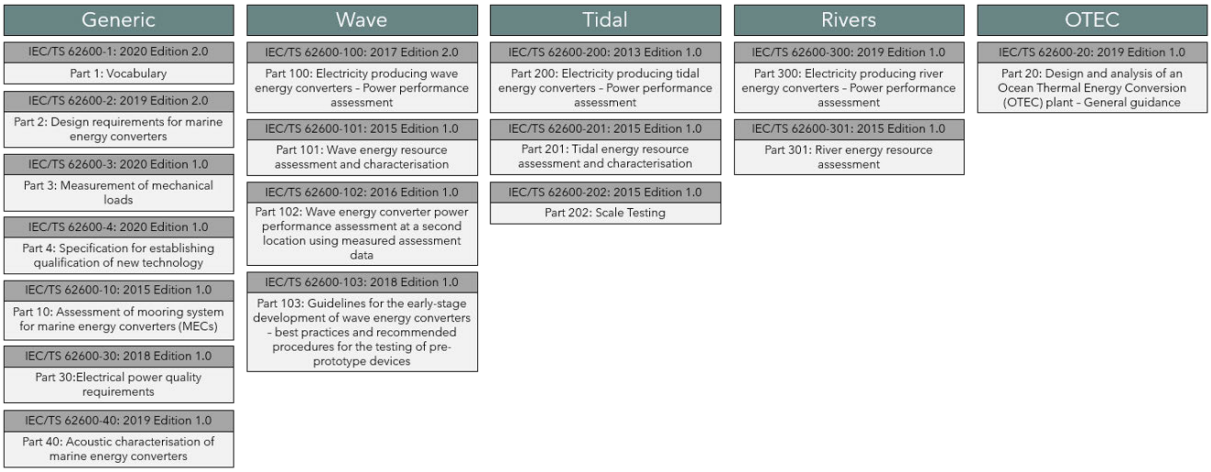

Figure 4.1: IEC/TC 114: Marine Energy - Wave, tidal and other water current converters. List of standards and best practices published since 2007 to support the progression of marine technology [1].

Table 4.1 offers a comprehensive overview of the two primary industry standards and best practices that outline the flow measurement requisites relevant to tidal stream energy, which are integral to the scope of this thesis [70]. The focus of this research predominantly centers on the IEC TS 62600-200 standard, a pivotal framework wherein the implications of uncertainties on PPAs are still undergoing refinement.

Table 4.1: Overview of industrial standards and best guidance containing flow measurement requirements applicable to tidal stream energy, relevant to this thesis.

Standard	Stated Purpose
IEC TS 62600-200:2013 [30] Electricity producing TECs - Power Performance Assessment.	This TS offers a structured approach for systematically assessing the power performance of TECs that generate electricity for both utility-scale and localised grids. This TS encompassed defining TEC-rated power and rated water velocity, establishing methodologies to construct power curves for the considered TECs, and providing a framework for result reporting. Developers are directed to IEC 61400-12 for effectively quantifying uncertainties associated with PPAs.
IEC TS 62600-201:2015 [59] Marine energy: Wave, tidal and other water current converters. Tidal energy resource assessment and characterisation.	A segment of IEC 62600, is dedicated to marine energy, specifically focusing on wave, tidal, and other water current converters. This TS, titled Tidal energy resource assessment and characterisation, establishes a systematic framework to analyse and report the theoretical tidal current energy resource across oceanic regions, including estuaries up to the limit of tidal influence. The aim is to identify suitable areas for the deployment of arrays of TECs. This TS proves valuable at various stages of project life cycles, providing accurate estimates of tidal resources necessary for calculating projected AEP at each TEC location, in tandem with IEC 62600-200.
IEC TS 61400-12:2005 [31] Wind energy generation systems - Power performance measurements of electricity producing wind turbines.	This TS offers a systematic methodology for evaluating the power performance of wind energy converters contributing to the grid. This standard derives the wind turbine's power performance characteristics through a combination of measured power curves and estimates of AEP.

In this context, it's worth noting that the IEC 61400-12:2005, a wind industry standard, finds significant referencing within the existing IEC TS 62600-200 standard, particularly in the context of quantifying uncertainties. As such, the inclusion of this wind standard in Table 4.1 is warranted.

The insights garnered from this research endeavour are poised to enrich these established standards. This valuable contribution will, in turn, provide robust support to the sector and developers in their pursuit of crafting accurate power curves for their type certification certificates.

Certification serves as a pivotal mechanism in mitigating both real and perceived risks associated with technology, encompassing performance and structural reliability. This validation process plays a significant role in attracting commercial investments and facilitating global trade. Currently, the IEC is actively enhancing a certification scheme tailored for marine energy converters, engaging all stakeholders in a continuous dialogue to establish international consensus [253]. The development of international standards and certification frameworks emerges as a key catalyst for expediting the progress of marine energy technologies, a principal recommendation from the ocean energy forum's strategic road map [254]. The vitality of this process lies in its practical application and the iterative feedback loop, funnelling experiential insights back to the entities refining specifications and certification paradigms.

Incorporating these standards and certification mechanisms into real-world projects serves as a dual-purpose approach: not only does it subject technology to real-world trials, but it also gathers indispensable feedback to enhance the effectiveness of IEC guidelines. This dynamic process is poised to yield a resilient and globally recognised certification framework tailored for the sector, thereby ameliorating both the tangible and perceived risks intertwined with marine energy ventures [29, 254].

Resource Assessment - IEC TS 62600-201

Initiating progress towards the commercial implementation of tidal stream array sites requires robust resource assessments [46]. When gauging the power potential from rivers and tidal test locations, accounting for uncertainties that can impact the accuracy of resource estimations becomes crucial. Such uncertainties can originate from imprecise specifications of physical parameters (like bed roughness, flow geometry, turbine drag, tidal components, etc.), mathematical modelling parameters (encompassing model assumptions, approximations, boundary conditions), and numerical parameters (encompassing grid resolution, time step).

Estimates of the tidal power that can be extracted at a given site are subject to significant uncertainty, with estimates sometimes more than an order of magnitude apart [4]. Of the many sources of uncertainty, sea bed friction can be considerable due to unknown and spatially varying bed conditions. It's noteworthy that various bed friction models may yield the same predictions [4, 255, 256].

Kreitmair [4] has examined the effect of bed roughness uncertainty on power estimates from a numerical model of the Pentland Firth, U.K. regarding the change in expected power and standard deviation. The effect of uncertainty in bed roughness coefficient was explored using the expansion method applied to the following three analytic models available in the literature for tidal stream resource assessment: (1) the quasi-steady state channel model of [257, 258] (GC05) where a fence of tidal turbines completely spans the flow; (2) a relaxation of the steady-state assumption of GC05 where the inertial term is retained in the governing equation, and an approximate solution found by [259] (V10); and (3) the laterally unconfined model of [260] (GC13) where a circular tidal turbine farm in free shallow flow is modelled as a circular patch of enhanced friction. All three models exhibited increased standard deviation and a shift in mean (expected) power upon introducing uncertainty. Clayton [2] also found that uncertainties in bed roughness affect the predicted flow velocity and TEC power. The bed roughness could be calculated by evaluating the seabed geology and assessing the shear profile of the flow [2].

In addition to the uncertainty in bed roughness coefficient, Kreitmair [4] assessed the impact of uncertainty in correctly parameterising the turbine drag. the following conclusions were drawn. For small-scale turbine deployment (i.e. mean turbine drag smaller than bed friction), turbine drag uncertainty would reduce the expected power. It could do so by as much as -6% for small, friction-dominated channels. For significantly under-designed channels (mean turbine drag approaching zero), the power standard deviation could reach 41%. However, it would drop off rapidly as more turbines are added, the deterministic optimum is approached, and the standard deviation in power drops to zero [4].

Power Performance Assessment IEC TS 62600-200

The PPA holds an important position between resource assessment and energy yield evaluation. Its primary objective is to gauge the performance of a tidal turbine against the available tidal resource [155], facilitating the subsequent estimation of energy yield at a designated site. This is achieved by correlating incoming current conditions with the resulting power output of the tidal turbine, leading to the construction of a measured power curve [195]. This essential process is typically a crucial stage within the turbine's journey toward achieving type certification, a pivotal certification that serves as a cornerstone for assuring the device's power performance to stakeholders such as clients, investors, and insurers [48]. The entirety of the methodology involved in the PPA of tidal turbines is illustrated comprehensively in Figure 4.2.

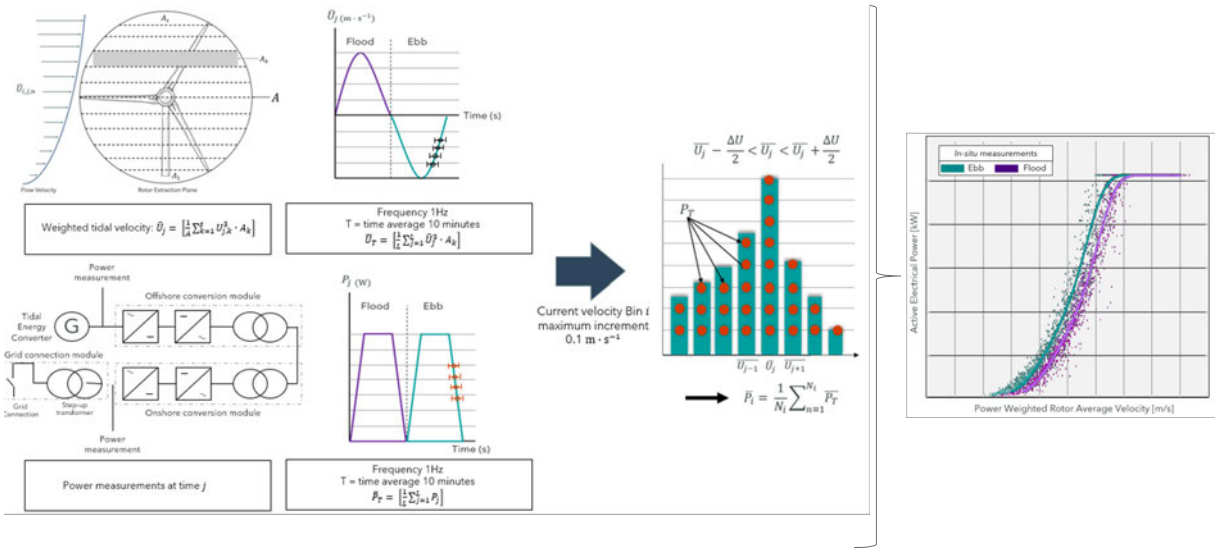

Figure 4.2: Overview of the methodology for assessing the power performance of tidal turbines.

Beyond confirming the validity of specific power curves and verifying the type of turbines, consistent monitoring of turbine performance emerges as an essential strategy for operators. This practice allows for timely assessments of the device's condition [252], facilitating the detection of potential faults and enabling proactive maintenance to avert critical failures.

The preliminary annual energy yield estimate for a tidal energy venture stands as a critical metric for investment decisions. This estimation involves integrating the project's long-term site resource with the power performance attributes of the technology in use. Both datasets are rooted in measurements, models, and assumptions that inherently harbour uncertainties. The resultant uncertainty in the annual yield significantly contributes to the overall risk assessment of a standard tidal energy project [2, 29, 261]. Recognised as a reference document for the industry, the "guide to the expression of uncertainty in measurement" (ISO-GUM) method has been recommended for tackling annual yield uncertainty in tidal energy [107, 245].

The measurement of uncertainty within the tidal industry often appears to be an afterthought, resulting in an incomplete understanding of how to effectively address this critical aspect. Notably, the ongoing revision of the IEC TS 62600-200:2013 TS for PPA in TECs has garnered attention [2, 31]. This specification defines the categories of error, yet the listed parameters represent only a fraction of those found within the wind industry's extensive collection. Notably, the current uncertainty annex guides developers to utilise the IEC TS 61400-12:2005 power performance standard for wind turbines, further highlighting the knowledge gap in uncertainty quantification within the tidal sector [30, 31]. See Table 4.2 for a list of uncertainty parameters currently considered in the uncertainty analysis as part of a PPA [30, 70].

Table 4.2: Summary of industrial Technical specifications and best guidance for Flow measurement requirements applicable to tidal stream energy. Refer back to section 2.5.1 for category explanation.

Measured parameter	Uncertainty component	Uncertainty category
Electric power	Current transformers	B
	Voltage transformers	B
	Power transducer or power measurement device	B
	Variability of electric power	A
Current speed	Current profiler accuracy	B
	Depth measurement relative to performance surface	B
	Misalignment of performance surface with principle flow direction	B
Data Acquisition	Singal transmission	B
	System accuracy	B
	Signal conditioning	B

A better understanding of uncertainty in power performance at this stage will better prepare developers for producing an accurate power curve for their TEC device. Additionally, it will help locate areas of large uncertainty to aid future work on reducing these quantities and increase confidence in the industry [2, 110].

As tidal turbines are emerging technologies, demonstrating and validating the power performance in real conditions are vital for designers and moving forward towards commercialisation for the tidal energy sector [23]. This includes performance prediction during the design phase and field measurements. Few full-scale prototypes have been tested at sea and even fewer have been integrated into the electricity grid. Due to this context, the IEC TS 62600-200 has been applied only to a few turbines. Therefore, due to the limited number of TECs installed on site and producing electricity, the application of the TS by industrials and certification bodies remains limited so far [155].

The IEC TS 62600-200 TS has been used previously to assess the performance of seabed-mounted tidal turbines [155, 195, 154, 221, 227, 262]. But before its publication in 2013, developers followed the methodology outlined by EMEC [263]. This document provided recommendations for data measurement, test equipment, prediction of the power curve from measurements and a methodology of reporting the results. This allowed developers to be consistent when testing their tidal devices.

A number of companies already manufacture tidal turbines to harness the energy provided by tidal streams, a summary of TEC developers is provided in Table 4.3 (relative references for: (1) [150, 212], (2) [248], (3) [155], (4)[194, 158], (5) [195], (6) [23]), including the specifications, deployment location, year deployed and their compliance with the IEC TS 62600-200 to date.

Energy Yield Assessment

As the industry moves towards commercialisation and array scale deployment, there is an opportunity to better understand the uncertainties around energy yield assessments [2, 264]. Energy yield predictions for wind and tidal are made by combining a power curve with the long-term resource. Energy yield assessments are used widely in the wind industry to evaluate the potential energy production from a prospective project. One key challenge is quantifying and reducing uncertainty in energy yield assessment [2, 29, 264]. Clayton, [2] evaluated the wind and tidal energy yield assessment process, highlighting where synergies can be used to increase understanding of uncertainty for the nascent tidal industry [2]. Clayton, [2, 264] found the process differed in evaluating the long-term variations, in that assessments of tidal variations over longer periods utilise harmonic analysis. This can deconstruct the individual astronomical variations of the tide and reconstruct them to predict future variations [2, 265]. Despite harmonic analysis being able to determine the astronomical effects of the tide, there are uncertainties in the measurements of tidal flow, which are associated with non-astronomical effects. Effects such as turbulence introduce uncertainty when evaluating measured tidal data [2, 29].

Statistical methods were applied to the harmonic analysis to assess the level of uncertainty in long-term predictions of tidal variations by Clayton, [2]. In addition, Clayton, carried out an investigation into how uncertainty in bed friction affects hydrodynamic modeling, and the consequent impact on the predicted power output from a theoretical array of tidal turbines spanning a tidal channel. The methodology is based on first conducting sensitivity studies by varying a parameter in the model and calculating the power. Then using a mean and standard deviation for the input parameter, the impact of the uncertainty can be transferred to the power estimate. Results indicated that a larger uncertainty associated with the bed roughness tends to over predict the power estimation [2, 265].

Uncertainty is present whenever a measurement or a prediction is made. When seeking finance for renewable energy projects, an understanding of uncertainty in energy yield assessment allows financiers to decide on project funding. The tidal industry is currently building towards commercialisation, and there is an opportunity to increase the understanding of energy yield uncertainty to inform tidal resource assessment [2, 110, 265].

Work carried out by Sunny Shah [110] focused on increasing investor confidence by improving the uncertainty analysis methods used to quantify the overall uncertainty in key investment decision metrics, such as; energy yield, levelised cost of energy (LCOE) and internal rate of return (IRR) [110]. A Monte Carlo Analysis (MCA) framework for tidal energy annual yield uncertainty analysis was developed and compared to the currently recommended ISO-GUM method [107]. It was shown that key assumptions implicit in ISO-GUM are inaccurate for most realistic projects. Crucially, the resultant error provides an overly optimistic view of a project's P90 energy yield. P90 is a conservative statistical measure indicating a 90% probability that the actual energy yield of a project will meet or exceed this level, commonly used to manage risk in energy production forecasts.

TEC Name	Deployment Location / Year	Rated Vel/Pow & rotor diameter	Company / Image	IEC 62600-200:2013 PPA
SeaFlow	North Coast Devon – 2003	300 kW	Marine Current Turbines (MCT)	x
SeaGen (1)	Strangford Lough Northern Ireland – 2008	2.4m/s, 2 x 600 kW		✓ : EMEC Standard
OpenHydro	EMEC, FoW - 2006	250 kW	Open Hydro *www.emec.org.uk*	x
OpenHydro	EMEC, FoW - 2014	1000 kW		x
HS300	Kvalsudet Norway – 2003	300 kW	SIMEC Atlantis *www.simecatlantis.com*	x
HS1000	EMEC, FoW – 2011	1000 kW		x
Verdant Power	East River New York – 2006	175 kW	Verdant Power *www.verdantpower.com*	x
Verdant Power (2)	Roosevelt Island -2020	2.5 m/s, 187 kW		✓ : 2020 – 2021
HydroQuest	Brittany Painpal Breheat – 2019	1000 kW	Hydroquest *www.hydroquest.fr/en/*	x
M30	Bluemull sound Shetland – 2014	30 kW	Nova Innovation *www.novainnovation.com*	x
M100-D	Bluemull sound Shetland – 2016/2017	3 x 100 kW		x
AR500	Nagasaki Japan (Naru Strait) – 2021	500 kW	SIMEC Atlantis *www.simecatlantis.com*	x
Sabella	Brest, Odet esturary – 2008	10 kW	Sabella *www.sabella.bzh/en*	x
Sabella (3)	Fromveur Passage – 2015	1000 kW		✓ : 2015 - 2016
OpenHydro	EMEC, FoW – 2008	1000 kW	Open Hydro *www.emec.org.uk*	x
OpenHydro	Paimpal Breheat, France – 2011	500 kW		x
DEEP-Gen IV (4)	EMEC, FoW – 2012/2015	1000 kW	Alstom *www.alstom.com*	✓ : 2013 – 2015
Ocean Kite	Venice lagoon - 2012	100 kW	SeaPower *www.seapowerscrl.com/ocean-and-river-system/gem*	x
RivGen	Kvichak river, Igivgig – 2019	500 kW	ORPC *www.orpc.com*	x
Delta Stream (5)	Ramsey Sound, Wales – 2015/2016	2.7m/s, 400 kW, 12m	Tidal Energy Ltd www.tidalenergy.com.au	✓ : 2015 - 2016
DG100	Faroe Islands – 2020	100 kW	Minesto *www.minesto.com*	x
AR-1000	EMEC, FoW – 2011	2.65m/s, 1000 kW	SIMEC Atlantis *www.simecatlantis.com*	x
AR-1500	MeyGen, Pentland Firth – 2016	3m/s, 1500 kW		x
T1	Den Oever – 2008	100 kW	Tocardo *www.tocardo.com*	x
T2	Eastern Scheldt Storm Barrier – 2015	250 kW		x
PLAT-I SIT250 (6)	Rotterdam Harbour & Connel, Oban – 2014/2017 - 2018	4 x 50 kW	Tocardo *www.tocardo.com*	✓ : 2018
SR250	EMEC, FoW – 2011	250 kW	Orbital Marine Power *orbitalmarine.com*	x
SR2000	EMEC, FoW – 2016	2 x 1000 kW		x
02	EMEC, FoW – 2021	2 x 1000 kW		Planned 2023
ATIR	EMEC, FoW – 2019	2 x 750 kW	Magallanes Renovables *www.magallanesrenovables.com*	Planned 2023

Figure 4.3: Summary of TEC developers and PPAs carried out. Light grey, blue and dark blue represent tidal turbines fixed to pile foundations, the seabed (gravity-based) and floating concepts.

By modelling a range of realistic projects, it was shown that the ISO-GUM P90 yield overestimate exceeds 2% for a maximum resource uncertainty between 4% and 11%, depending on the project, with increasing uncertainty leading to larger errors [107, 110].

The ISO-GUM method has been recommended for propagating tidal energy yield uncertainties in recent industry guidance documents. Still, no comprehensive evidence of its validity can be found in the literature. Based on an analysis of a typical tidal energy project, the fundamental ISO-GUM assumption of linear variation in annual yield with change in resource was shown to be not always valid [110].

4.3 Comparison of Wind and Tidal Energy Performance Methodology

Analysing the power performance methodologies of wind and tidal energy systems offers insight into the similarities and differences between these two renewable energy sectors. This comparison, based on the practices established by industry standards and technical specifications, provides an overview of how each sector assesses and quantifies its energy conversion capabilities. The following methodologies are compared at a high level with regards to the IEC methodologies for developers [30, 31].

Measurement Approach

Wind turbines' power performance is assessed by measuring the actual power output under varying wind conditions. This is typically done using anemometers and other meteorological instruments to record wind speed, direction, and other relevant parameters. The data collected over a specific period is used to calculate performance metrics such as capacity factor and energy production. TECs' performance is assessed by measuring the electricity generated as the devices harness kinetic energy from tidal currents. This involves monitoring the electrical output over time to quantify the energy produced under different tidal flow conditions which are measured by acoustic instruments.

Resource Assessment

Resource assessment in wind energy involves characterising the wind regime at a specific site, considering factors like wind speed distribution and turbulence intensity. This information helps determine the potential energy yield and feasibility of wind turbine installations. Similar methods are used for tidal energy, where tidal flow patterns, velocities, and water depths at a particular location are analysed. This data is used to estimate the available kinetic energy in the tides and assess the site's suitability for tidal energy extraction.

Uncertainty Quantification

The IEC standard IEC TS 61400-12 provides guidelines for assessing power performance in wind turbines, including uncertainty quantification. A range of uncertainty parameters such as measurement errors, instrument calibration, and data analysis techniques are considered. The IEC TS 62600-200 outlines guidelines for assessing power performance in TECs. While uncertainty parameters are acknowledged, the scope of uncertainty treatment is currently narrower compared to the wind energy standard. This may reflect the relatively early stage of development in the tidal sector.

Operational Challenges

Turbulent atmospheric conditions and variable wind speeds pose challenges in accurately predicting wind turbine power output. Maintenance and repair activities at heights also present operational challenges. Whereas, harsh underwater environments, corrosion, fouling, and the complex nature of tidal flows can affect the performance and maintenance of TECs.

Environmental Impact

Environmental considerations in the wind sector primarily involve the potential impact on bird and bat populations, as well as visual and noise concerns. Tidal energy projects need to address potential impacts on marine ecosystems, including changes in water flow patterns, sediment transport, and potential effects on marine life. These factors become more important as the wind industry moves further offshore with floating platforms requiring mooring systems.

Transferring Wind Industry Expertise to the Tidal Stream Industry

The integration of expertise and methodologies from the wind industry into tidal stream technology represents a strategic advancement in renewable energy. This approach leverages decades of wind sector innovation and operational experience to accelerate the development and optimisation of tidal stream systems. By adopting proven strategies, such as turbine design improvements and maintenance protocols, the tidal sector can enhance efficiency, reduce costs, and overcome technical challenges more effectively.

Transferring knowledge and experience from the mature wind industry to the emerging tidal sector involves several challenges and considerations. The following points highlight these challenges:

- *Resource Disparities*: The wind industry has evolved over time, accumulating knowledge, infrastructure, and established supply chains. In contrast, the tidal industry lacks such resources, making direct knowledge transfer complex and requiring adaptation for differing contexts [266].

- *Technology Differences*: Tidal and wind energy technologies have distinct operational principles, infrastructure requirements, and maintenance considerations. Transferring experience requires accounting for these differences and adapting strategies accordingly [267, 268].

- *Site-Specific Dynamics*: Tidal energy sites exhibit unique characteristics such as varying flow patterns, depths, and seabed conditions. Lessons from wind projects need to be carefully tailored to suit these site-specific dynamics in tidal environments [269].

- *Uncertainty and Risk*: The tidal energy industry faces higher uncertainties due to limited operational experience and the complex nature of ocean environments. Transferring knowledge must encompass strategies for addressing and identifying and quantifying uncertainties.

- *Environmental Impact*: Tidal energy systems can have different ecological impacts compared to wind turbines. Effective knowledge transfer should include understanding and mitigating potential environmental effects specific to tidal energy installations [269, 270].

- *Regulatory Frameworks*: Regulatory processes and permitting requirements can differ significantly between wind and tidal energy projects. Adapting regulatory strategies and engaging with relevant authorities are crucial aspects of knowledge transfer [268, 271].

- *Supply Chain and Infrastructure*: The well-established wind industry benefits from an established supply chain and infrastructure. In the tidal sector, building a functional supply chain and suitable infrastructure presents a challenge that requires attention.

- *Operational Experience*: Wind energy has accumulated decades of operational experience, leading to refined maintenance practices. Transferring this experience to the tidal sector involves adapting operational strategies to the unique challenges of underwater installations.

- *Investment and Funding*: The wind industry's maturity offers a more attractive investment landscape compared to the emerging tidal sector. Knowledge transfer should address funding challenges and involve stakeholders in building confidence in tidal energy's potential [272].

- *Public Perception and Acceptance*: Public acceptance of wind energy has grown over time due to familiarity. Transferring knowledge requires addressing potential concerns and educating the public about the benefits and impacts of tidal energy [273].

- *Collaboration and Communication*: Effective knowledge transfer requires collaboration among experts from both industries and clear communication channels. Lessons learned and best practices should be shared to accelerate the learning curve in the tidal sector [2, 264].

4.3.1 Wind Energy Measurement Campaign Procedure

The accurate assessment of power performance is a critical aspect of wind energy projects, ensuring that the actual energy output aligns with pre-construction predictions. Wind measurement campaigns play a pivotal role in gathering essential data to validate energy yield estimates and inform project feasibility studies. This procedure involves a structured approach to measuring and analysing wind conditions at the proposed site [274]. By adhering to industry best practices and recognised standards, developers can enhance the reliability of their PPAs and optimise project outcomes [31].

The initial step involves choosing a suitable site for placing wind measurement equipment, taking into account factors such as terrain, distance from potential obstructions, and proximity to the wind turbine installation site. Subsequently, meteorological instruments like anemometers, wind vanes, and temperature sensors are deployed at designated heights to collect comprehensive wind data [275]. Choosing appropriate locations for wind farm installation involves more complexity than merely raising turbines in regions with consistently high wind speeds. Factors like the distance to grid transmission lines [276, 277], the ruggedness of the terrain [278], the existence of fragile flora and fauna [279, 280, 281], and the closeness to existing infrastructure [282, 283, 284] can significantly escalate the costs, difficulties, or potential hazards associated with establishing commercial wind farms.

During the data collection phase, wind-related information should be gathered over an extended time frame, usually spanning between 6 to 12 months, to accommodate seasonal fluctuations. This involves consistent and frequent recording of wind speed, direction, and other pertinent meteorological factors. The pivotal factor for turbine power generation is the measurement of wind speed at the hub height. Accurate prediction of wind speed aids in precisely calculating the wind turbine's power output. Turbulence intensity (TI) is computed to classify turbulence's impact on the wind turbine [285]. Two prevalent techniques are employed to forecast wind speeds at different heights from designated reference locations. The primary method, known as the power law, relies on an exponent-based approach, with the exponent referred to as the wind shear coefficient (WSC) or wind shear exponent (WSE) [286, 287]. This coefficient is instrumental in computing wind speed and direction at varying heights based on reference measurements [288].

In Figure 4.4, the standard setup of a met mast is depicted. Cup anemometers are commonly employed throughout the wind industry for wind speed measurement [289]. These anemometers typically comprise three hemispherical or conical cups organised in a horizontal rotor pattern around a vertical shaft, generating signals as they turn. They offer effective mean wind speed measurement across diverse terrains, offering a cost-effective and sturdy option compared to alternative instruments [5].

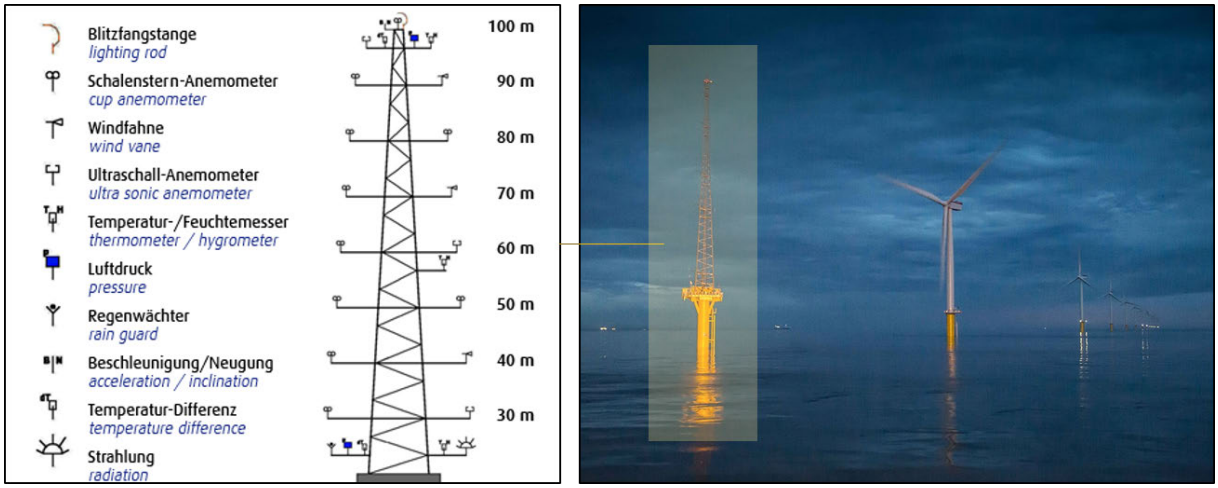

Figure 4.4: Wind measurement techniques - Met mast configuration.

During the data Quality Control (QC) stage, stringent procedures are put in place to detect and rectify inaccurate data. This encompasses evaluating data consistency, calibrating sensors, and identifying anomalies such as icing or equipment malfunctions [290].

In the data analysis phase, statistical techniques and data analysis tools to process the amassed wind data are employed, encompassing the computation of crucial parameters like mean wind speed, wind rose diagrams, and Weibull distribution parameters. These metrics offer valuable insights into the wind patterns of the site and the prospective energy output [291, 292]. As the wind industry has progressed, wind turbines have grown considerably in size, featuring longer blades and consequently taller hubs. This necessitates taller met masts, which can be cumbersome and costly to install, particularly in regions characterised by mountainous or intricate terrain. For precise measurements of the incoming wind for the increasingly large turbines being deployed, comprehensive wind speed and wind shear characterisation across the entire rotor plane necessitate multi-point, multi-height wind measurements. Achieving this involves the utilisation of remote sensing tools like SODAR (Sonic Detection and Ranging) or LIDAR (Light Detection and Ranging), as illustrated in Figure 4.5 [293].

In the uncertainty assessment stage, quantifying the uncertainties linked to measurement equipment, data processing methods, and other variables that could impact the outcomes. This process guarantees the incorporation of the uncertainty range into the power performance evaluation [294].

Using the gathered wind data and computed metrics, the estimate of the anticipated energy output of the proposed wind turbine across various operational scenarios can be analysed. This crucial information serves as the basis for financial projections and project planning [295]. Additionally, research endeavours have explored enhancing energy production through techniques such as optimising pitch control using fuzzy logic [296] and hybrid controllers [297], as well as optimising yaw control employing the parametric model for wake effects [298] and the k-NN classifier [299].

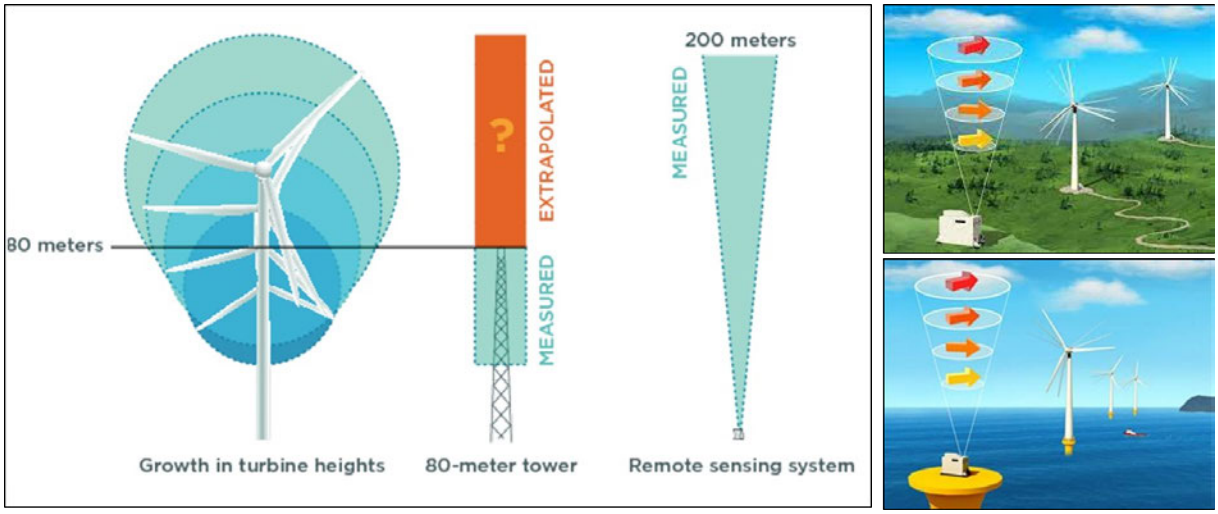

Figure 4.5: Wind measurement techniques - LIDAR & SODAR applicability for onshore and offshore wind farms.

In the validation and reporting phase, comparisons between the projected energy yield and the turbine's manufacturer power curve to validate the accuracy of the predictions are carried out. Comprehensive reports that outline the measurement campaign, the methodology used for data analysis, the assessment of uncertainties, and the outcomes of energy yield estimation are assessed [300].

4.3.2 Tidal Energy Measurement Campaign Procedure

When undertaking any measurement campaign, it is imperative to adhere to important industry guidelines or specifications, should they be accessible. This practice is essential to uphold results within acceptable realms of uncertainty. Deviating from established industry standards will lead to an increase in uncertainty. The IEC TS stipulates a minimum criterion for tidal resource assessment [59], mandating a 35-day flow measurement if the data is employed for calibrating or validating a hydrodynamic model. For tidal power performance evaluation as per IEC TS 62600-200, a data collection period of at least 15 days is prescribed [30]. Both of these data requisites encompass a representative spring and neap tidal cycle, recurring roughly twice per month. This primary data can then be extended over longer time frames through the application of harmonic analysis.

Tidal currents are usually assessed with an ADCP or a velocimeter, comparable to a wind anemometer [67, 161]. ADCPs are oceanographic tools that gauge water velocity within the water column [168, 301]. Furthermore, new technologies like the Barnacle represent a novel type of marine sensor that presents an economical substitute for the ADV in oceanographic applications, including locations such as tidal power sites, where turbulence measurements are essential [302]. Nonetheless, ADCPs are the primary instruments utilised for collecting flow data at tidal sites, specifically in the context of a PPA, which forms the central focus of this thesis.

ADCPs are favoured for measuring current flow due to several reasons. Firstly, they provide a comprehensive and detailed picture of current velocities throughout the water column. Unlike surface measurements, ADCPs offer information from various depths, which is crucial for understanding vertical variations in current speed [122, 303]. Secondly, ADCPs have non-intrusive measurement capabilities. They use sound waves to assess current velocities, eliminating the need for physical contact with the water. This non-intrusive nature reduces the impact on the environment and minimises disturbance to aquatic life [304]. Moreover, ADCPs can be positioned at fixed

locations, such as being bottom-mounted on seabed structures, offering consistent measurements at specific points. Additionally, they can be deployed on vessels, enabling mobile analysis over larger areas [305, 306]. This versatility allows researchers to gather data from various locations, providing a broader understanding of current patterns.

The ADCP measures water currents by transmitting sound waves and measuring the Doppler shift in the frequency of reflections from water-suspended particulates, which are assumed to act as Lagrangian tracers [67, 307]. This method contrasts with other devices like velocimeters, which measure flow speed at a specific location [308]. Unlike single-point velocimeters, ADCPs can assess the entire water column.

Each transducer on an ADCP emits and captures its own Doppler shift pulse, measuring velocity perpendicular to its head. To ascertain overall velocity, data are combined from multiple beams set at different angles, which spread apart as they move away from the device. Current ADCP data processing techniques assume a uniform flow between these radial velocity components [170, 190, 306, 309], a simplification that, while often debated, remains standard practice [310].

ADCPs operate by emitting acoustic "pings" to generate velocity profiles across sequential depth cells. Research has shown that individual ADCP pings can vary significantly in accuracy, with uncertainties as high as 45% [309]. However, averaging multiple pings can reduce this variability and mitigate random errors, but does not affect the bias, as seen in Figure 4.6 though it does not eliminate systematic biases [67].

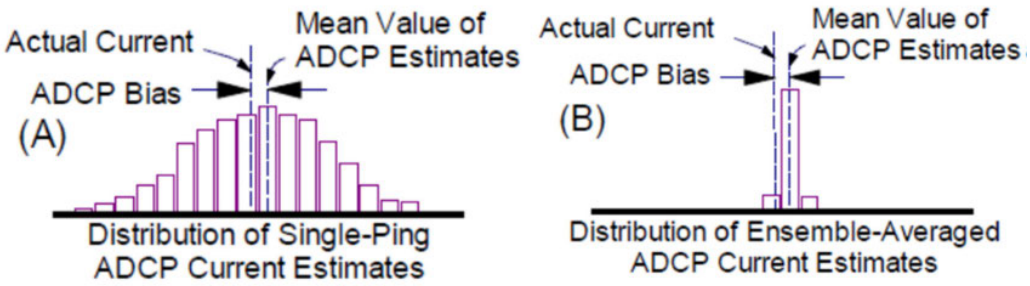

Figure 4.6: The distribution of measurements. (a) single-ping data. (b) Measurements averaged over 200-pings.

Through this averaging process, the standard deviation of velocity error is reduced by a factor of $N^{-0.5}$, where N represents the number of pings averaged together. It's important to note that ensemble averaging assumes the velocity field remains constant throughout the averaging period. However, this might lead to extended data periods smoothing out actual fluctuations in the measured current.

Similar to wind data, the measured data from ADCPs also necessitate post-processing. An essential element of this analysis involves the elimination of erroneous data. Several factors linked to ADCPs can compromise data quality, including:

- *Side-lobe interference:* Refers to a phenomenon where a small portion of the emitted acoustic energy leaks out in directions other than the intended measurement direction [67, 161]. This leaked energy can interact with boundaries or surfaces before the primary energy has completed its round trip, leading to unwanted echoes that contaminate the desired measurement signal. Particularly troublesome when weak signals reach the water's surface directly, these echoes interfere with the accurate measurement of currents

and water velocities. The angle between the main measurement beam and the leaked energy (commonly known as the side lobe), typically ranges from 30° to 40°, contributing to the distortion of measurements and requiring consideration during data analysis and interpretation. Equation 4.1 gives an approximate estimate of the amount of near-surface contamination:

$$\mathrm{R}_{max} = \mathrm{D} \times cos(\theta) \tag{4.1}$$

where R_{max} signifies the range of reliable data, D is the distance from the ADCP to the surface or bottom (as appropriate), and θ represents the beam angle relative to the vertical. For a transducer angled at 20°, echoes from the side lobe directed at the surface align with the main lobe echo, occurring at 94% of the distance to the surface. As a result, data within the final 6% of the range to the surface may be tainted. This principle also holds for when a 25° and 30° beam angle is used, with contamination encompassing 10% and 15% of the range respectively [161].
Side lobe interference often leads to a bias favouring the velocity of the boundary causing interference. Near the bottom, this bias tends to favour zero velocity (unless the bottom is in motion), while at the surface, it hinges on the sea state or wind conditions. When reviewing data, it's advisable to pay special attention to the vertical velocity (Z) in this region. It should ideally register close to zero. If it doesn't, it might be an outcome of interference effects.

- *Transducer ringing:* Ringing refers to the phenomenon where energy from the transmitted pulse persists even after the transmission has ended. In the absence of ringing, the transducer could swiftly pick up echo signals right after transmitting. However, since echo signals are delicate, even a slight amount of ringing can corrupt them. Consequently, the ADCP needs to wait until the ringing subsides before it can listen to and analyze the echoes. This interval of waiting is termed the blanking period. Table 4.3 presents standard ringing durations, which are approximately equivalent to the default blanking period [67, 74, 161].

Table 4.3: Typical ringing times, denoted as distances ahead of the transducer.

Frequency (kHz)	75	150	300	600	1200
Ringing Distance (m)	6	4	2	1	0.5

- *Non-homogeneous flow:* Manufacturer-stated uncertainties of ADCPs are rooted in the assumption of uniform flow across consistent depth layers. However, real-world conditions often entail spatial variations due to shear. The instrument's uncertainty doesn't encompass the error arising when distinct beams detect spatially differing flows [31]. Nonetheless, ADCPs provide an "error velocity," offering a means to assess the validity of assuming non-uniform flow, a crucial built-in feature for assessing data quality. Similar challenges arise in wind industry LIDAR applications within intricate terrain, where measurements can validate models by comparing shear across larger areas [311]. While this approach might extend to tidal currents eventually, it's essential to underline that models shouldn't be employed to adjust measured data.

- *Positional uncertainty:* When deploying an ADCP, the intended device location can shift due to installation conditions and external environmental influences. Consequently, the ADCPs position may alter as it is lowered through the water column. Therefore, confirming the actual deployment point on the sea bed becomes vital, as it diverges from the intended location. While this doesn't directly induce measurement uncertainty, it can impact the interpolation of findings, leading to a spatial extrapolation uncertainty.

- *Pitch and Roll:* In an ADCP, pitch (tilting forward and backward in the horizontal plane) significantly influence the accuracy of velocity and depth measurements. These movements alter the orientation of the ADCP beams relative to the water flow, leading to misalignment and reduced precision in velocity readings. Pitch changes can cause beam angles to deviate from the desired direction, affecting the accuracy of current measurements [312]. Similarly, roll-induced changes in the beam pattern can result in the detection of unintended flow components, distorting the recorded velocities. Correcting for pitch and roll effects is crucial for obtaining reliable current data and ensuring the data's quality and applicability.

- *Proximity to ferrous materials:* The magnetic properties of ferrous materials can interfere with the magnetic field used by ADCPs for compass and tilt measurements, introducing errors in orientation data. Therefore, proximity to ferrous materials requires careful consideration during ADCP deployment to ensure accurate data collection. The way to mitigate this issue is to calibrate the device before the survey, whilst it is mounted in the deployment frame [59], and also cross-check the compass calibration when the survey is completed.

- *Tidal shear in tidal channels:* Similar to how wind resources fluctuate with altitude above the ground, tidal resources exhibit variations along the water column's depth. This phenomenon arises from the frictional interaction between water and the seabed, causing a deceleration of flow nearer to the seabed. Generally, this yields a power or logarithmic profile across the water column, as depicted in Figure 4.7

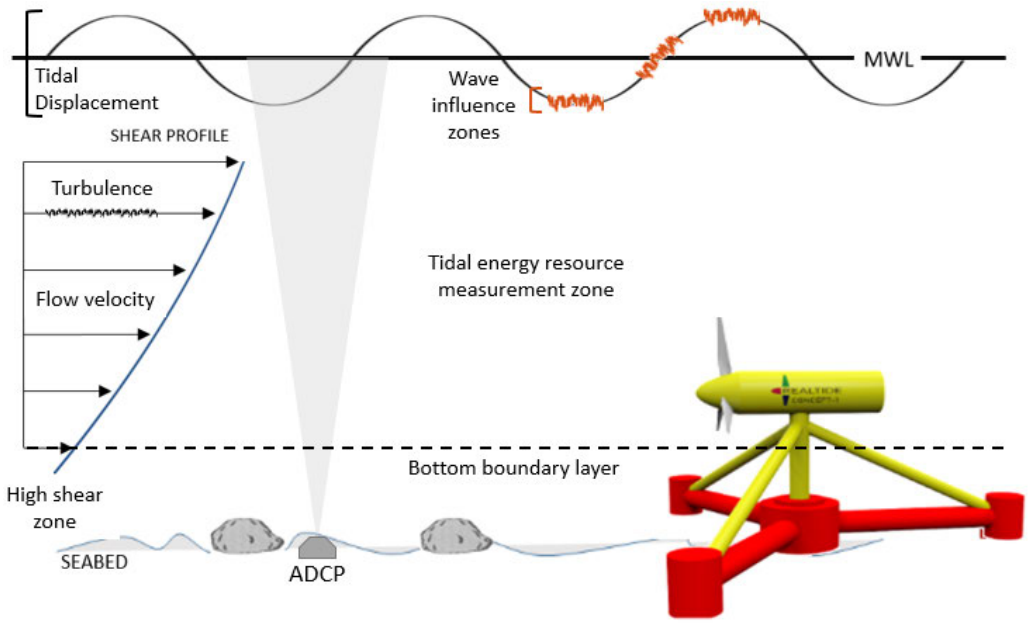

Figure 4.7: Schematic depicting the vertical current velocity profile observed at a standard tidal energy site.

The fastest tidal currents occur near the upper section of the water column, gradually diminishing as depth increases. Ideally, the optimal location for a tidal turbine would be within a flow zone characterised by a relatively linear and vertical profile, avoiding the lower boundary layer where flow is significantly slower due to friction with the seabed [313]. Additionally, the region near the sea surface experiences wave and wind influences, potentially leading to undesirable forces on the device. Consequently, ensuring that the turbine is situated away from both these areas serves to minimise variations in flow speed along the turbine blades, which theoretically results in a more consistent power output [44, 50].

- *Turbulence:* Turbulence in current flow increases the variability of the resource and introduces uncertainty in ADCP measurements due to its impact on the accuracy and reliability of velocity data. Turbulence generates fluctuations in the water velocity field, causing variations in the Doppler shift signals received by the ADCPs transducers. These fluctuations can lead to erratic measurements and increased random errors, especially in regions with high turbulence intensity. The uncertainty arising from turbulent flow is documented in studies such as the work by Clark et al. [314], where the effects of turbulence on ADCP measurements in the oceanic boundary layer were investigated. This turbulence-induced uncertainty underscores the importance of carefully interpreting ADCP velocity data in regions where turbulence plays a significant role.//
  While extensive research has been conducted on the influence of turbulence on various aspects such as blade loads, power performance, and the uncertainty of measurements, It's worth highlighting that this thesis primarily centres on a different aspect. Consequently, the in-depth exploration of turbulence-related topics is not within the scope of this study.

4.3.3 Resource and Power Performance Procedure Analogies

Both wind and tidal energy industries rely on comprehensive measurement campaigns to gather essential data for their respective resource assessments and power performance evaluations. While the energy sources differ, the methodologies exhibit noteworthy similarities.

In the wind industry, met masts equipped with cup anemometers are comparable to ADCPs used in tidal energy assessments. Met masts incorporate cup anemometers to measure wind speed across various heights, mirroring ADCPs capability to gauge water flow velocity at multiple depths. The met mast configuration captures vertical wind speed gradients, similar to ADCPs capturing velocity profiles across the water column [293, 161].

Similarly, both industries adhere to established industry guidelines for measurement campaigns. The IEC offers technical specifications (e.g., IEC 61400-12 [31] for wind and IEC/TS 62600-201 [59] and 62600-200 [30] for tidal) outlining data collection requirements, including duration and frequency. These guidelines ensure that data collection aligns with industry standards, minimising uncertainty in resource assessments and power performance evaluations [315].

Moreover, post-processing is crucial in both fields. Wind measurements undergo data validation and corrections to eliminate outliers and erroneous values. Similarly, ADCP data processing involves removing contaminated data caused by beam patterns and external factors, enhancing data quality [315].

However, just as differences exist between wind and tidal energy, unique challenges arise in measurement procedures. Wind speed measurements are influenced by turbulence due to terrain, while tidal flow measurements face complexities from underwater terrain and varying currents [316].

4.3.4 Uncertainty Categorisation: Knowledge Exchange from the Wind Sector

The gross energy yield value represents a hypothetical situation where all the turbines are performing at 100% all the time. In reality, this will never be the case. The solution is to apply corrections and losses to account for energy lost during the operation of the technology. The corrections and losses outlined in the subsequent section are taken from the DNV KEMA [317] categorisation document and the wave and tidal energy yield uncertainty from the ORE catapult [29]. They are site-specific and some are calculated, and others are estimated based on experience. This section will highlight the uncertainty components addressed in the wind industry as part of a PPA.

Energy yield predictions are only useful if their uncertainty is well-defined. Uncertainties play an important role in financing renewable projects. Unless the energy yield assessment can offer a degree of confidence to the resource prediction, it is not possible to construct a sound financial model for project investment. Financial models depend on understanding and capturing risk. For a renewable energy project, risk depends strongly on the uncertainty in the resource. Table 4.4 outlines the uncertainties that are typically included in a wind energy yield assessment, categorised into the four main areas: Site measurement, Temporal extrapolation, spatial extrapolation, and losses [2, 317, 29].

Analogies Between Wind and Tidal Uncertainty

While the nature of uncertainties varies between tidal and wind PPAs, both fields share the challenge of accurately quantifying and minimising these uncertainties to improve the reliability of energy yield estimations. References for these uncertainties can be sourced from relevant research articles and industry standards within the tidal and wind energy sectors.

In terms of measurement uncertainty, parallels exist between the wind and tidal sectors. Despite the distinctive instruments employed for resource assessment, both fields rely on the precision of the instrument, determined by manufacturing specifications [318, 319]. ADCP technical specifications commonly cite velocity measurement inaccuracies ranging from 0.3% to 1.0% in flow speed [67, 161]. Nonetheless, empirical assessment of ADCP accuracy, based on two laboratory and two field tests, indicates a higher uncertainty of 4.55% and 5.24%, respectively [320]. These uncertainties, derived from standard deviations of Flow Tracker ADV and Stream Pro ADCP mean values, pertain specifically to lower flow speeds (0.12 – 0.50 $m \cdot s^{-1}$). The study also dissects the factors influencing ADCP accuracy, including resolution, operational conditions, and sampling time. Notably, the foremost contributors to overall ADCP measurement uncertainty are mean velocity accuracy (32%) and depth measurement accuracy (49%), yielding an approximate combined standard uncertainty of 2.15%.

Measurement interference is commonly induced by installation methods, impacting both wind and tidal sectors. In the wind, the mast's influence on anemometer readings is a key example. In the tidal domain, several factors contribute to interference, encompassing ADCP site arrangement, installation, and specific challenges like side lobe interference inherent to acoustic flow velocity measurement, this is discussed further in Chapter 6. A prevalent approach involves minimising affected data during analysis through robust QC checks throughout post-processing procedures.

Table 4.4: Uncertainty categories for wind and tidal (with indicative values for wind and predicted change for tidal). Taken from Clayton et al [2].

Energy Yield Uncertainty Categories		Wind Uncertainty Range (%)	Tidal Uncertainties Comparison
Site Measurement	Instrument Accuracy	1.5 - 3.0	Similar
	Measurement Interference	0.5 - 1.0	Higher
	Data Synthesis	0.0 - 1.5	Similar
	Data Quality and Metadata	0.0 - 2.0	Similar
Temporal Extrapolation	Historic Variation	1.0 - 4.0	Similar
	Future Variation	0.0 - 2.5	Higher
	Climate Change	0.5 - 1.0	Similar
Spatial Extrapolation	Model Inputs	0.0 - 3.0	Higher
	Horizontal Extrapolation	1.0 - 5.0	Higher
	Vertical Extrapolation	0.0 - 3.0	Similar
Device Performance & Losses	Availability	0.5 - 3.0	Higher
	Array Interactions	0.3 - 0.5	Higher
	Power Performance	3.0 - 5.0	Similar
	Electrical Losses	0.1 - 3.0	Similar
	Performance Degradation	0.0 - 2.0	Higher
	Curtailment	0.0 - 2.0	Similar

Complete removal of all disrupted data might not always be feasible. For instance, in wind analysis, when a lone anemometer is employed, it can be obscured by the mast in a specific direction, which is typically not aligned with the prevailing wind. Addressing this shadowing effect is challenging with a single anemometer, leading to data elimination from a directional sector that may not accurately represent conditions. In some scenarios, distorted data from certain directions are retained if they belong to non-prevailing wind sectors. This approach, although affecting overall wind speed readings and yielding a more cautious estimation, might be deemed acceptable when data removal would otherwise introduce substantial uncertainty.

In the context of wind analysis, various long-term reference data sources can be employed to anticipate prolonged fluctuations in the wind resource. Nevertheless, such resources do not exist for tidal assessments. Given the deterministic behaviour of tides, harmonic analysis stands out as a potent technique for estimating tidal variations over extended intervals. Consequently, the approach used to predict uncertainties in this aspect of assessment in wind analysis cannot be directly applied to tidal evaluations. Attaining a more profound comprehension of harmonic analysis and its applicable tools is essential to assess the uncertainty inherent in these methods for tidal analysis.

Uncertainties related to climate change are also taken into account when predicting wind resource, contributing a minor degree of uncertainty to yield assessments [321]. However, the understanding of local and global climate change patterns in the context of tidal flow remains incomplete. The dynamics of sea level rise can impact tidal hydrodynamics by altering tidal ranges, surge heights, and the submergence of current shorelines. Furthermore, it holds the potential to reshape circulation and sediment transport patterns, consequently affecting habitats and their ecosystems. While increased tidal ranges might amplify tidal current velocities [322], the quantification of such effects remains challenging. At present, there is no evidence suggesting that climate change will exert a significant impact on tidal resources. Research has explored climate change's influence on sea-level rise and storm surge occurrences, with the UK Climate Impacts Programme 2009 [323] projecting potential absolute sea-level rises of 100 mm to 300 mm by 2030 and an escalation in extremely high sea levels, leading to heightened storm events. Although this might potentially influence the energy yield of tidal devices through reduced availability, this aspect of uncertainty lacks comprehensive understanding. Consequently, the implications of climate change on the future variability of tidal resources are not delved into further in this discussion but are noted as a secondary matter for readers' awareness.

Wind and tidal modelling methods share numerous similarities. The primary objective of creating models is to analyse the spatial dynamics of fluids, be it air or water. This process entails extrapolating measured data from established points to other significant positions within the model, typically the designated turbine sites. Though the methodologies for modeling wind and tidal flows may vary, the uncertainties they entail are interchangeable. These uncertainties encompass model inputs, boundary conditions, and user-defined parameters like resolution and domain configuration. Validation with multiple measurement devices allows for the quantification of these uncertainties.

The wind industry calculates turbine power performance uncertainty using the testing procedures outlined in the IEC standard for power performance measurement of wind turbines 61400-12-1-2005 as previously mentioned [31]. This standard provides a methodology to measure both overall uncertainty and specific parameters to assess. Turbine performance testing usually occurs under typical operational conditions, accounting for wind shear, turbulence intensity, and temperature variations. This methodology can be directly applied to tidal energy and has influenced the development of the TS used for testing tidal turbines [30].

Similarities in loss uncertainties exist between wind and tidal energy, and they can be regarded as percentages of overall losses. However, the factors influencing performance degradation differ for wind and tidal energy. Wind turbines face challenges like blade degradation due to soiling and extreme weather, while tidal turbines contend with marine growth and bio-fouling [324, 325, 326]. Effective corrosion protection is vital to counteract seawater-induced degradation. Quantifying this loss is challenging, and the associated risk is often shifted to turbine suppliers, who must conduct thorough inspections and blade cleaning to uphold the warranted power curve.

4.3.5 ADCP specific guidance: Measured Power Curve

Guidance tailored to the utilisation of ADCPs in PPAs for tidal turbine deployments involves several key aspects [30]. As such, the instrument chosen for data collection should be able to:

- Capture an uninterrupted sequence of time-stamped data comprising tidal current velocities, direction, pitch, and roll.
- Obtain a vertical profile by measuring within the projected rotor plane of the TEC, ensuring a maximum vertical distance of 1 meter between depth bins (with a minimum of 10 vertical depth bins).
- Capture data with a sampling frequency of at least 1 Hz.

Measurements conducted must conform to the following criteria: [155, 30]:

- The range for recording velocities should encompass the maximum and minimum current speeds determined during the Tidal Resource Assessment stage, and the resolution should exceed $\pm$ 0.05 m·s^{-1}.
- The geographic position during deployment needs to be determined with a system possessing accuracy equal to or exceeding that of a Differential GPS, ensuring precise identification of the final current profiler placement. In cases where deployment is from a vessel, the measurement system must be positioned directly above the davit arm or block.

The data collection phase should encompass at least one spring-neap cycle (approximately 15 days). It is probable that the test duration will extend beyond 15 days to guarantee ample data recording. The test availability should surpass 80% throughout this 15-day testing period. If any instrument is employed for the measurement campaign, it must undergo calibration as necessary by an entity adhering to ISO/IEC 17025 standards [111]. The power curve derived from measurements should be based on data collected during the regular operation of the TEC device, following the guidelines outlined in the TEC operations manual.

When computing the mean flow velocity for each depth bin in the calculated power curve, the data points and resultant datasets should be founded on a 10-minute averaging interval obtained from continuous data samples. An additional dataset, with an averaging interval shorter than 10 minutes yet equal to or exceeding 2 minutes, may also be processed and reported optionally. It is recommended to employ an integer divisor of 10 minutes or 600 seconds. The test data should consist of two distinct datasets, one corresponding to flood operation and the other to ebb operation. These selected datasets should be organised using the method of bins procedure as outlined in [155].

Incident Resource Measurement

The placement of the measurement instruments should be strategically selected to ensure accurate measurement of tidal current conditions (both magnitude and direction) experienced during TEC operation. It's essential to report the distance from the seabed to the centre of each ADCP depth bin, at the location of the ADCP deployment.

The positioning of the ADCP should capture the natural ambient current behaviour without being influenced by the proximity of the TEC, yet still be sufficiently near the TEC to represent the local current patterns accurately. The deviation in total water depth between the sampling site and the TEC location should fall within $\pm$ 10% of the water depth with respect to a known chart datum. The upper and lower bounds for distances between the recording device and the TEC should be determined based on the suitable equivalent diameter for the specific TEC. These instruments should be deployed in either orientation A (in-line) or B (adjacent), with a strong preference for orientation A due to potential effects related to blockage, horizontal shear, and variations in bathymetry.

NOTE **A - In-line**: Two measurement devices need to be positioned in alignment with the TEC, with one placed upstream of the TEC extraction plane during the flood tide and the other upstream during the ebb tide, as depicted in Figure 4.8a. These instruments should be situated in a way that ensures the distance from the nearest outer surface of the measurement area to the projected area where the TEC extraction takes place is always greater than 2 equivalent diameters (2_{D_E}) but less than 5 equivalent diameters (5_{D_E}), as shown in Figure 4.8b. Moreover, these instruments should be positioned within a range of $1/2_{D_E}$ of the primary flood and ebb direction streamlines, which align with the vertical centre line of the TEC extraction plane [30].

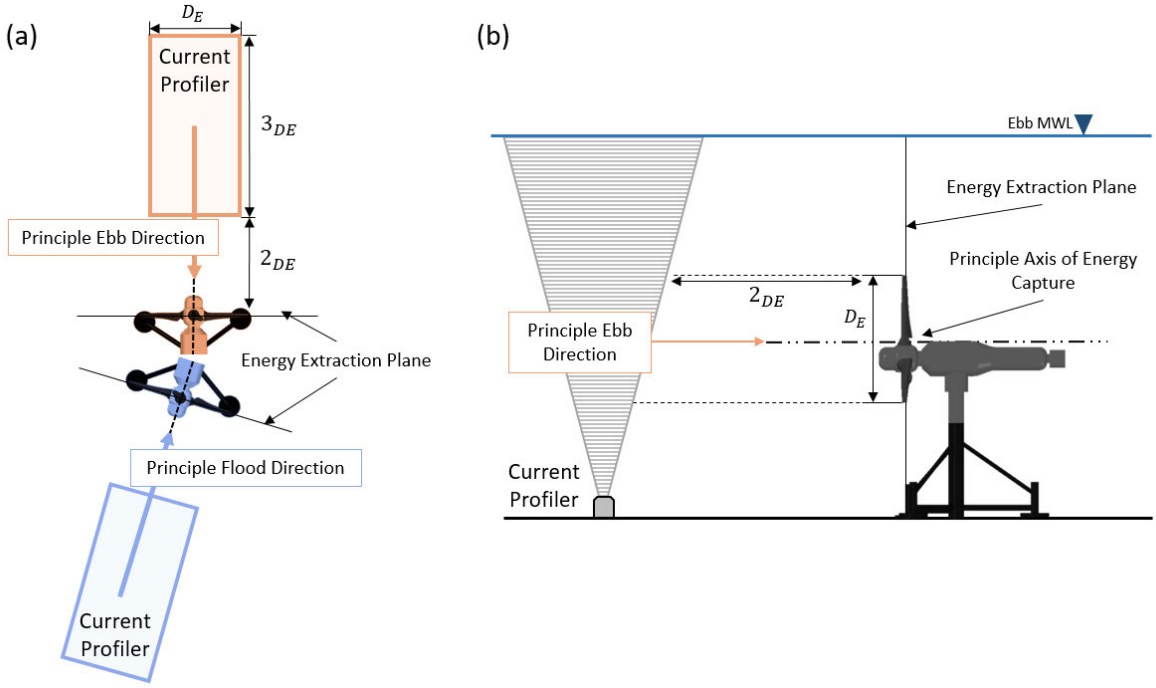

Figure 4.8: ADCP positioning adheres to Orientation A (in-line), wherein: a) the ADCPs plan view shows its placement between 2_{D_E} and 5_{D_E} from the TEC, and b) the section view of the ADCPs measuring volume indicates the distance involved. Figure adapted from IEC 62600-200.

NOTE **B - Adjacent**: Two measurement devices should be situated adjacent to the TEC, with one positioned on the starboard side and the other on the port side of the TEC extraction plane. These devices should be positioned in a way that the closest external surface of their measuring volume remains at a distance greater than 1_{D_E} yet less than 2_{D_E} from the TEC extraction plane's lateral extent, as depicted in Figure 4.9a. Additionally, their placement should adhere to the principle of being within $1/2_{D_E}$ of the TEC extraction plane's lateral centre line, illustrated in Figure 4.9b. To ensure accuracy, the linear average should be computed between any two measured values at equivalent water depths, provided they possess identical measurement bin heights. For the linear average to be a reliable approximation of the flow at the energy extraction plane, the variation in measured axial velocity between the two measuring devices should be less than 10%.

In the context of a floating TEC concept operating on a compliant mooring, the flow measurement instruments should be utilised as follows:

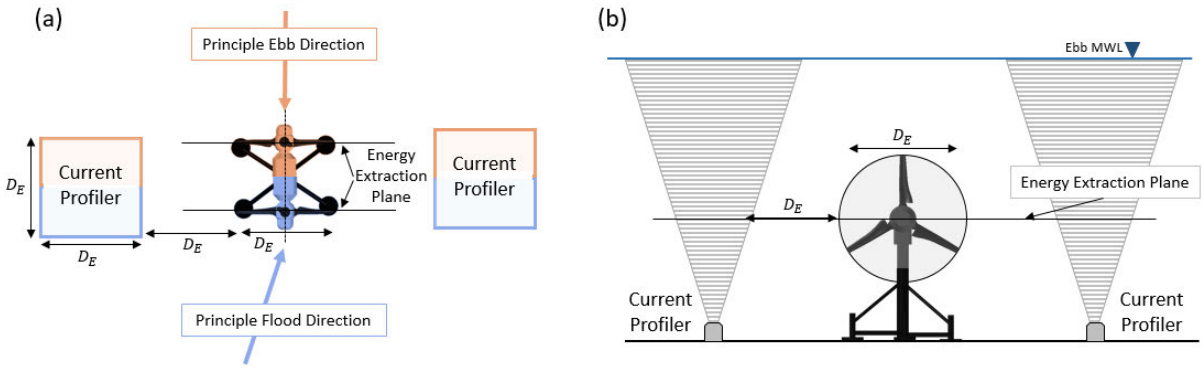

Figure 4.9: ADCP positioning adheres to Orientation B (adjacent), wherein: a) the ADCPs plan view shows its placement between 1_{D_E} and 2_{D_E} from the TEC, and b) the section view of the ADCPs measuring volume indicates the distance involved. Figure adapted from IEC 62600-200.

- An instrument attached to the TEC itself that measures the conditions ahead of the turbine (in a similar orientation to that described in A or B) at a suitable distance to be considered a true representation of the flow.
- A bottom-mounted instrument on both ebb and flood tides positioned strategically to ensure that the footprint (the area formed by the intersection of the energy extraction plane and the principal axis of energy capture) remains within the dimensions outlined in Figure 4.10.
- If none of these deployment orientations can be achieved, an array of bottom-mounted instruments may be considered. In such cases, a correction methodology should be developed and substantiated, ensuring that the instruments capture the ambient current behaviour without being influenced by the proximity of the TEC. Justification for the methodology could involve conducting a site calibration as one possible approach.

Contribution to uncertainty

Although turbulence and wave interaction with the tidal flow could notably impact TEC power performance, it is advised not to apply corrections for these effects in the reported PPA. These aspects remain subjects of active research, and the associated uncertainty has yet to be quantified.

4.4 Sources of Uncertainty

At its fundamental essence, uncertainties represent a reflection of the data quality being reported. Even after accounting for all measurement errors, a degree of inevitable uncertainty persists concerning how faithfully the measurement truly represents the measured quantity. To establish the comprehensive uncertainty of the results, all potential sources of uncertainty that could influence the measurement need to be quantified. These sources encompass factors such as the specifications or tolerances of the standard employed, the calibration uncertainties associated with the certifying vendor, the repeatability and reproducibility of the measurement procedure, environmental influences, the device under test's resolution, and more, contingent on the equipment type utilised.

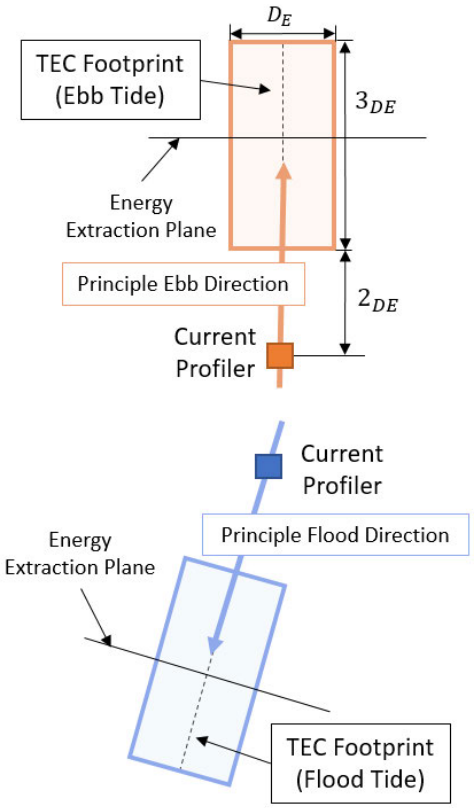

Figure 4.10: ADCP positioning with respect to a floating TEC from a plan view perspective. Figure adapted from IEC 62600-200.

Once these sources are identified, they are integrated based on their anticipated impact on the total uncertainty, accomplished through an analysis known as an uncertainty budget. This entails assessing and amalgamating all the uncertainty factors within a table to deduce the resultant combined uncertainty value. This process is intricate, entailing the thorough evaluation and consolidation of all the uncertainty components to yield a comprehensive picture.

Comprehensive guidelines for conducting resource assessment and power performance predictions in the realm of tidal energy systems are being developed by the IEC. Specifically, the draft IEC TS 62600-201 [59] outlines a two-tiered approach to assessment:

1. *Stage 1 - Feasibility*: This phase investigates the energy resource's scope and attributes within a designated study area. By estimating the 'undisturbed site resource', it evaluates the feasibility of establishing tidal energy arrays at various sites within the study area.

2. *Stage 2 - Layout Design*: Centred on generating detailed, precise information about the tidal energy resource within a specific region, this stage determines the AEP and supports the layout design of a tidal array. It might also encompass the impacts of energy extraction on the project's scale. Stage 2 studies factors in the installation technology and deployment locations of TECs to estimate AEP with reduced uncertainty.

Additionally, a standardised framework for categorising uncertainties related to marine energy yield has been proposed by OREC [29]. This framework presents a breakdown of uncertainty categories and recommends processes for quantifying each uncertainty, which are concisely summarised in Table 4.5. The significance of each uncertainty category, as evaluated by OREC [29] through a literature review, is also taken into consideration.

Table 4.5: Categorisation of yield loss domains as suggested by ORE.

Uncertainty Category	Sub-Category [327]	Quantification process [328]	Importance [29]
1) Site Measurement	1a) Instrument Accuracy	Provided by device manufacturer	Low
	1b) Measurement Interference	Avoided by good practice and error-checking	Low
	1c) Short-term site data synthesis	Not specified	Low
	1d) Data quality and metadata	Guidance in IHO [34] to be followed	Low
2) Temporal Variation	2a) Historic resource estimation	Guidance in IEC [59]	Low/Medium
	2b) Future resource variability	Sensitivity analysis on different meteorological inputs to the resource model for non-astronomical variations	Medium/High for exposed site
	2c) Climate change	No evidence of a significant effect of climate change on future tidal currents	Low
3) Spatial Variation	3a) Model inputs	Validation of the 2D model	Medium
	3b) Horizontal and vertical extrapolation	Sensitivity analysis on model inputs or use of additional ADCP dataset	Medium/High (Horizontal) Low/Medium (Vertical)
4) Performance and Losses	4a) Availability	Sensitivity studies using stochastic availability model	Medium/High for early arrays
	4b) Resource-array interactions	Sensitivity analysis on wake parameters of hydrodynamic model	Low/Medium for small arrays, high for large
	4c) Device performance	Guidance in IEC TS 626200-200 [30]	Medium
	4d) Electrical losses	Specified by manufactures	Low
	4e) Performance degradation	Assumed impossible to quantify, but empirical data over time should provide guidance	Medium
	4f) Curtailment	Depends on the terms of the power performance agreement	Low

4.4.1 Sensor Characteristics and Performance

Measurement uncertainty in current velocities arises from a mixture of random errors and bias. Random errors emerge from Doppler noise and turbulence variations, which can be mitigated by averaging multiple readings or "pings." As the number of measurements increases, the cumulative impact of these random errors tends to diminish. Conversely, bias errors, originating from the device itself, persist regardless of the quantity of data points. They often stem from uncertainties in beam direction due to manufacturing tolerances. Detecting bias errors is challenging, and they typically cannot be eliminated [58].

Manufacturers typically offer information about uncertainties, and here are a couple of examples (bias and single ping error, respectively):

- *Nortek Signature 500*: The accuracy of speed measurements is specified as 1% $\pm$ 0.5 cm·s^{-1}, The accuracy of direction measurements is specified as 2°
- *Teledyne Workhorse Sentinel*: The accuracy of speed measurements is specified as 0.5% $\pm$ 0.5 cm·s^{-1}, The accuracy of direction measurements is specified as 2°

The single ping random error can range from a few millimetres per second (mm·s^{-1}) to as much as 0.5 mm·s^{-1}. Increasing the number of data points leads to a reduction in random error following $N^{-1/2}$, where N represents the data points. Typically, the bias in current speed is reported to be under 10 mm·s^{-1} [191]. For a current speed of 1 m·s^{-1}, this translates to an uncertainty of 1%, which broadly aligns with the manufacturers' specifications.

Tidal site characterisation places significant emphasis on mitigating instrument-related uncertainties. Inherent errors are intrinsic to measurements, but the utilisation of acoustic instruments adds distinct complexities. ADCP measurements entail errors stemming from both internal instrument factors and external field conditions [67, 329]. These errors primarily manifest as random fluctuations around the mean and systematic biases where the measured mean deviates from the true value [107]. Given the inherent noise in acoustic technology and the significance of capturing mean fluctuations in this context, the identification and reduction of random errors become paramount.

Measurement uncertainty (refer back to 2.5.2) in current velocities arises from the interplay of random error and bias. Random errors originate from factors like Doppler noise and turbulence fluctuations, which are effectively diminished through the practice of averaging multiple readings, or "pings" [29, 330]. Across numerous measurements, the cumulative impact of these random errors approaches zero. On the other hand, bias errors stem from inherent device characteristics and persist even with an increasing volume of data points. These biases often emerge due to uncertainties in beam direction influenced by manufacturing tolerances and interactions with structures, surfaces, or other acoustic instruments. Detecting and mitigating bias errors pose challenges and generally entail their retention within the data [29, 58, 330].

Relevant sources of errors, encompassing both random and systematic components, pertinent to the operation and measurements of acoustic instruments are outlined below. Achieving dependable data interpretation demands familiarity with these sources and, when feasible, their quantification, albeit acknowledging that the comprehensive computation of error for ADCP measurements remains a subject of ongoing discussion [331]. The ensuing overview draws from [67, 161, 329, 331].

1. Instrument

- *Distance from transducer*: As the distance from the transducer increases in a conventional divergent ADCP, the beam spread widens. This expansion in beam spread amplifies the error magnitude linked to disparities in the orthogonal velocity components at the measurement locations of each bin. Consequently, the assumption of homogeneity across the beam spread becomes less valid.

- *Sample volume*: Reducing measurement cell sizes results in larger standard deviations and lower signal-to-noise ratios, thereby increasing the level of uncertainty.

- *Beam alignment*: The uncertainty in the beam direction introduces bias to velocity measurements, altering the conversion from beam to earth coordinates through the coordinate transformation matrix.

- *Transducer ringing*: The residual energy from the transmission, known as the ringing signal, does not undergo Doppler shifting and consequently introduces a bias towards zero in velocity measurements. This phenomenon is influenced by both the transducer characteristics and the instrument electronics.

- *Instrument noise*: The characteristics of the ringing signal are affected by factors such as the transmit frequency, power, and pulse length. In continuous measurement under burst mode, the resulting single ping data exhibits elevated uncertainty (noise) on a per-ping basis. This is primarily due to a significant proportion of the total pulse volume comprising new scatterers entering the measurement volume, while other scatterers have exited it.

- *Speed of sound*: Variations along a measurement profile impact both the determination of the instrument's measurement range and the positioning of depth cells. The influence of temperature (T in °C) on the speed of sound (denoted as C in m·s^{-1}) is more pronounced than that of salinity (S in parts per thousand), as indicated previously by Equation 2.5 [201].
  In turbulent tidal environments, where thorough mixing is assumed, variations in the speed of sound across the profile are typically neglected, particularly in comparison to potentially more significant effects in highly stratified environments [329].

- *Instrument calibration*: Sensors like pressure and heading/pitch/roll sensors necessitate regular calibration to prevent drift effects that could introduce biases into the results.

- *Side-lobe interference*: ADCPs emit sound not only through their main beam but also through side lobes, which can interfere with measurements. Reflections from these side lobes, especially when oriented at angles of 20° or 30°to the main beam, can contaminate up to 6% or 15% of the water column, respectively. For further details, see sections 2.3.2 and 4.3.2.

- *Positional uncertainty*: As ADCPs are deployed into the water, they can be influenced by currents, leading to potential differences between their seabed and sea surface locations. While this doesn't inherently introduce measurement uncertainty, it can impact result interpretation and lead to spatial extrapolation uncertainties.

- *Proximity to ferrous materials*: The presence of ferrous materials can impact the accuracy of ADCPs internal magnetic compasses, potentially leading to directional measurement biases. To address this, a calibration of the unit while mounted within the deployment frame before the survey, as well as compass calibration checks upon survey completion, can effectively mitigate these biases.

2. Process/environment driven
   - *Particles*: Scattering material is essential to reflect the acoustic signal in ADCP measurements. The concentration of scatterers directly influences the measurement range, with higher concentrations leading to reduced range capabilities. Conversely, a minimum concentration is necessary for maintaining an acceptable correlation. During field operations, variations in scatterer concentration may arise due to shifts in the tidal cycle and changes in light levels within the water column, as phytoplankton tend to move vertically toward sources of light.

   - *Boundaries*: The return signal strength from boundaries like the sea surface or sea bed is notably stronger compared to that from scatterers. It is crucial to eliminate this data from the dataset to prevent any biasing effect on the measured velocity, which could lead to erroneous results.

   - *Obstructed Measurements*: Data can become contaminated when there are obstructions situated in front of the transducer and within a cone-shaped volume around it. Similarly, if objects of substantial size, like marine debris, fish, or marine mammals, traverse through the beam, contamination can occur. The detection of object movement within the beams can be recognised and subsequently eliminated during the post-processing phase.

   - *Air bubbles*: Air bubbles have the potential to distort or even absorb the returned signal. Due to their positive buoyancy, their velocity often does not accurately reflect that of the surrounding water.

   - *Turbulence fluctuations*: In flowing water, turbulence is inherently random and lacks predictability, but it can be quantified statistically over extended time periods with stationary statistics [332]. In the context of mean velocity measurements, turbulence introduces noise and uncertainty. The impact of turbulence on energy yield manifests in three key ways:
     (a) It influences the kinetic energy flux through the turbine, consequently altering the turbine's apparent power curve.
     (b) Turbulence accelerates the process of wake recovery.
     (c) Turbulence typically serves as the primary driver of fatigue loads experienced by the device, thereby impacting the cost and availability of tidal energy devices.

Considering the sources of error and uncertainty in acoustic velocimetry outlined above, the error analysis presented in this thesis encompasses the entirety of the measurements' error. While a comprehensive breakdown of the individual sources contributing to this overall error lies outside the scope of this study, a qualitative exploration of potential contributors to the cumulative error is provided. This examination takes into account the field conditions in which the experiments were carried out.

Tidal Surface Elevation

The spatial and temporal fluctuations in surface elevation caused by tidal propagation around the Earth are influenced by local factors such as land boundaries and seabed topography. Tide gauges, commonly situated near coastal regions, operate in major ports and harbours. These measurements encompass the local coastal

effects on tides, potentially differing from what transpires at a turbine site. To ensure accuracy in tidal resource assessments and the validation of regional models, elevation data should be gathered across the site [333]. For this purpose, two established methods are utilised for in situ surface elevation measurement: upward-looking acoustic instruments, as discussed earlier, or pressure sensors mounted on fixed structures.

In the case of acoustically derived elevation measurements, it's crucial to ascertain the instrument's depth, orientation, and precise spatial coordinates. Utilising a surface tracking mode, the instrument can ascertain the position of the water-air interface and subsequently adjust range-gating to a higher resolution mode. In cases where the instrument lacks a surface tracking mode, the precision of surface elevation data is constrained by the relatively larger bin sizes employed for current profiling. Nonetheless, this elevation data still provides valuable insights, especially in situations involving energetic wave conditions [333].

When utilising elevation data obtained from a pressure gauge, it's essential to ensure the sensor is zeroed prior to deployment, with the concurrent recording of the atmospheric pressure during zeroing. The pressure sensor's record will encompass fluctuations in atmospheric pressure, necessitating their removal or at least their identification as an additional source of error. Depending on the sensor's sensitivity and relative depth, the pressure record will encompass a certain degree of uncertainty when measuring the sea surface [333].

4.4.2 Data Quality Control

To ensure the usability of data stored in a database for future applications, it's essential to implement and thoroughly document QC procedures. Established standards that encompass acoustic velocimeter data comprise resources such as the British Oceanographic Data Centre [334], the Marine Environmental Data and Information Network [335], and the Quality Assurance of Real-Time Oceanographic Data [208]. These standards play a crucial role in maintaining the reliability and consistency of the data for various applications.

Data integrity and validity increase after carrying out relevant QC. Data integrity entails verifying that the expected volume of data has been received in the correct format, while data validity involves identifying and addressing instances of duplicate or anomalous data. Achieving this requires the careful selection of QC parameters related to sensor health, signal quality, current velocity, and overall profiles. These checks, when applied to the data, result in the inclusion of flags based on predetermined thresholds. These flags provide subsequent users with insight into the quality of the data, all without altering the data points themselves. Given the substantial volume of data typically generated during measurement campaigns spanning weeks to months, the automation of QC processes becomes an imperative focus [208].

4.4.3 Spatial and temporal scales of heterogeneity in tidal stream sites

In cases where no modelling is employed to anticipate the spatial variance of the resource, the uncertainty is defined by the potential flow changes across the span between the measurement site and the turbine's actual position. For instance, at selected sites within Puget Sound, the spatial variance in energy forecasts concerning a reference site was assessed, resulting in uncertainty values of 10% at 50 meters, 15% at 150 meters, and 20% at 250 meters for an ideal turbine.

In the context of the ReDAPT project, a 3D hydrodynamic model of the Falls of Warness was validated using three ADCPs. This was summarised through methods of validation, which included time-domain and spectral analysis [336]. In both analyses, the model demonstrated an exceptional alignment with the ADCP data. The highest absolute bias between the model and measurements was 0.13 $m \cdot s^{-1}$ for speed and 8.1° for direction.

In many open marine environments, the assumption of horizontal homogeneity in current velocity is often reasonable [161]. However, marine sites suitable for tidal stream TEC deployment are characterised by their high energy levels, leading to significant spatial and temporal flow heterogeneity [197, 332]. Such sites typically feature water depths between 25 and 45 meters, peak spring tide velocities of at least 3 $m{\cdot}s^{-1}$, and accessibility to an electrical grid [337].

Spatial variations in flow arise due to various factors, including the presence of headlands, islands, and sudden changes in bathymetry. These variations can occur over a range of spatial scales, from kilometres (large-scale eddy structures) down to blade lengths and even smaller scales (microscale eddies). Site-specific topography can lead to the shedding of eddy structures [32, 338]. Non-uniform flow fields can also result from influences like high shear in velocity profiles, surface waves, interactions between waves and currents, changes in seabed roughness, and turbulence [58, 146].

Temporal variations in flow occur over timescales that span from years [32] to mere seconds (turbulent gusts). An illustrative example of spatial heterogeneity at a tidal site is depicted in Figure 4.11. This figure showcases streamwise velocity data collected during ebb tides at two vertical depth profiles positioned 80 meters apart (points 6a and 6b in Figure 4.11a). The distortion observed in the upper half of the water column at point 6a is unique to the ebb tide and may stem from the nearby presence of a headland [197, 166].

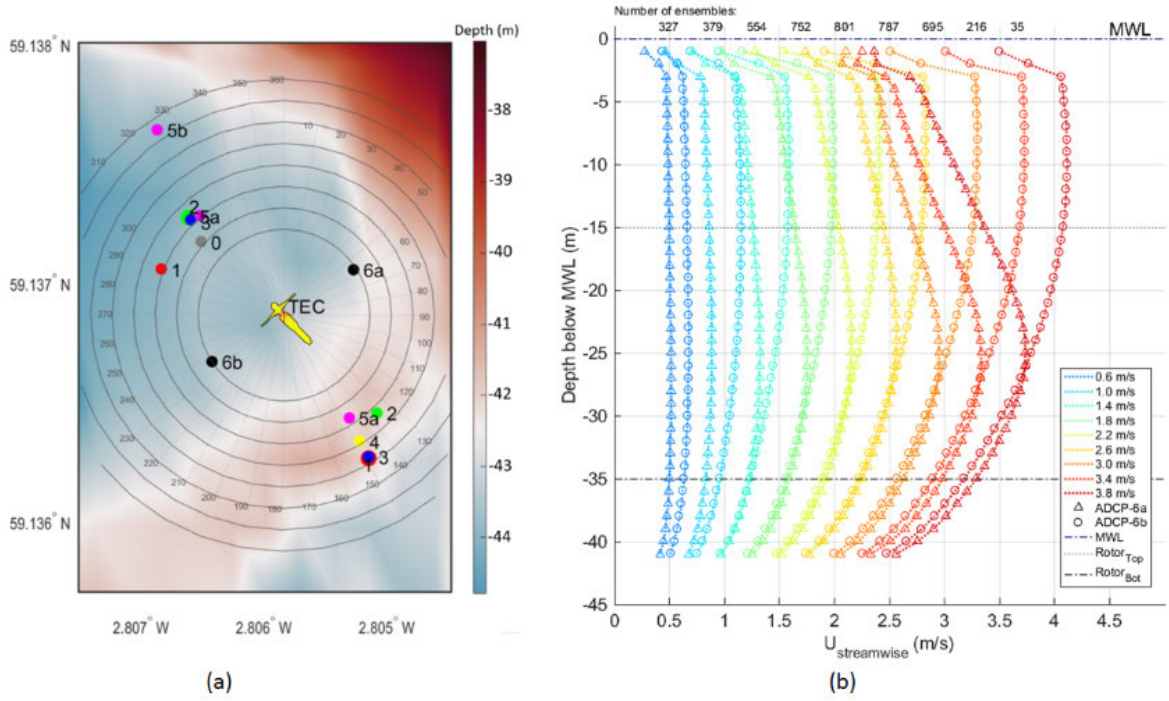

Figure 4.11: Vertical variation in streamwise current velocity was measured at two locations, 6a and 6b, within the Falls of Warness region in Orkney as part of the ReDAPT project. (a) illustrates the deployment positions of selected instruments, including ADCPs situated at 6a and 6b. (b) Depth profiles of streamwise velocities from the instruments at locations 6a and 6b is depicted, showcasing 5-minute ensemble averages juxtaposed with a reference velocity averaged over the rotor plane. Each line on the graph corresponds to a velocity bin width of 0.4 $m{\cdot}s^{-1}$, encompassing velocities ranging from 0.6 $m{\cdot}s^{-1}$ to 3.8 $m{\cdot}s^{-1}$.

Large-scale Flow Structures

The configuration of the tidal channel along with the underlying bathymetry introduces significant localised flow patterns that exhibit spatial variations throughout the tidal cycle. These intricate flow phenomena are primarily triggered by specific mechanisms, namely headland eddies [339, 340] and island wakes [341, 342]. In addition, the seabed's bathymetric features, such as sills and channels, contribute to the generation of localised vertical flow instabilities. These instabilities arise due to the detachment of vortex structures from the seabed when flow velocities reach a point where boundary layers separate (typically exceeding 1 $m{\cdot}s^{-1}$) [333].

When the TEC is positioned within the influence zone of these flow separations caused by the bathymetric features, the velocity profile structures become notably intricate. Consequently, this complexity gives rise to diverse loading conditions and available energy levels throughout a tidal cycle. This stands in contrast to regions experiencing "clean" flow, where the flow patterns are less influenced by these bathymetric effects.

Evident within satellite imagery, the distinct horizontal eddy patterns linked with island wakes and headlands often become discernible. As exemplified in Figure 4.12, a Sentinel 2 image of the Iroise Sea captured during an ebb tide showcases these phenomena. The pronounced phytoplankton bloom serves to accentuate the prominent large-scale eddies that materialise due to the flow separations induced by the presence of channels and islands. These eddies manifest across a horizontal spectrum, spanning from tens of meters to kilometres.

The influence of substantial eddy structures of this type becomes apparent when observing the depth profile of flow across a tidal cycle, as depicted in Figure 4.11b. Here, the disparity between two sensors positioned 90 meters apart becomes increasingly evident, exhibiting marked variations in form. However, capturing the complete spatial extent and intricacies of these structures through on-site measurements necessitates an extensive array of stationary instruments or a dedicated survey conducted via vessel.

For a more resource-efficient approach to quantifying these features and gauging their impact on tidal flow, a well-calibrated and validated regional model offers a pragmatic solution. Such a model presents a cost-effective means of assessing the spatial scales and associated dynamics of these eddy structures.

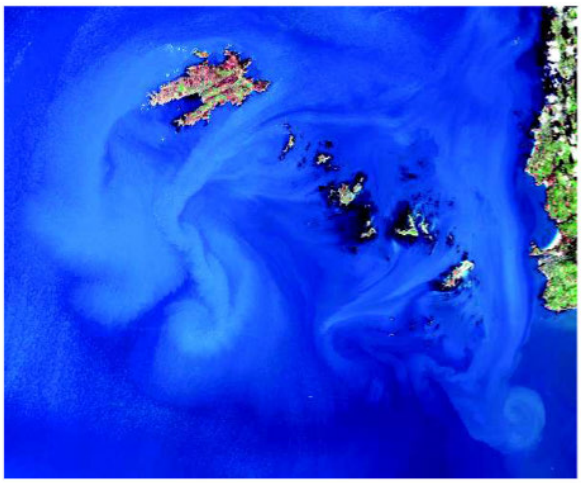

Figure 4.12: Satellite imagery depicting expansive flow patterns within and around a tidal channel.

Limited studies have examined spatial variation in energetic tidal flow using multiple instruments [194, 158, 122, 177]. During the 1 MW DEEP-Gen IV McNaughton et al. [194], assessed the impact of measurement location on the power curve. Greater differences appeared at the power curve's foot, suggesting more variation at lower velocities. Sensitivity within $1D_E$ was also explored, yielding notably distinct power curves, limited by acknowledged measurement bias [194].

In the Strangford Narrows, Torrens-Spence [343] synchronised instruments on separate barges 500 m apart. Varied flow characteristics due to a rocky outcrop caused substantial variation between flood and ebb tides [343], aligning with findings within work carried out by B. Sellar [197, 166].

Variations in current velocity measurements indirectly affect turbine performance, especially when these measurements are influenced by flow variations such as eddy structures or are not taken in close proximity to the TEC, thus failing to accurately represent the flow directed towards the TEC. Such discrepancies can significantly impact the creation of power curves, which are crucially correlated with the turbine's active power performance [23, 230]. Four SCHOTTEL Instream Turbine (SIT) were tested in Connel, Oban. For each SIT(1-4), distinct power curves were presented [23, 230]. Electromagnetic Current Metres (ECMs) measured velocity upstream from SIT2. The starboard turbines (SIT3 and SIT4) yielded considerably less power than port side turbines (SIT1 SIT2) due to the platform's off-centre position relative to the Falls of Lora jet [23, 230].

Conclusively, single-point velocity measurements cause shifts in performance curves based on proximity. SIT2's performance perfectly matched semi-empirical predictions using the blade-element momentum method (BEM), whereas the performance curves for SITs 1,3 and 4 diverged due to the greater distance between the turbine extraction plane and the point at which velocity was measured.

Free Stream Flow - Vertical Variation

Tidal turbine research commonly employs scaled tank experiments or device-scale hydrodynamic numerical models [54, 344]), with parameterised oceanographic conditions [345]. Variations in the velocity profile have demonstrated their impact on the loading of both tidal turbine support structures and gearboxes [344, 346], as well as the overall performance of tidal energy devices [347]. Consequently, uncertainties in velocity profile shapes at tidal stream energy sites pose challenges to the development of resilient, efficient, and globally applicable devices [50].

This complexity is amplified for floating TECs due to wave interactions. Surface waves significantly alter the mean velocity profile in coastal waters [348]. The presence of waves opposing the flow direction leads to increased upper water-column velocities (higher velocity shear), while waves propagating in the same direction as tidal flow result in the opposite effect [349, 350]. Thus, accurate characterisation of the velocity profile and velocity shear becomes crucial [53, 347, 351].

M. Lewis et al. [50] depicted velocity profile uncertainty using a range of power-law - α and β - coefficients within Equation 2.2. Additionally, Equation 4.2 was utilised to further illustrate:

$$P = \sum_{z_0}^{z_1} [\frac{1}{2} \cdot \rho \cdot A_z \cdot \delta Z \cdot (u_z)^3] \tag{4.2}$$

where the velocity (u_z) and the swept turbine width at height above the bed z (A_z, discretised heights, δz, 0.1 m was used) were used to estimate the theoretical instantaneous power (P). It was found the tidal energy resource varied by $\pm$ 8% (when decreasing the α from 7 to 5) to -4% (by increasing α from 7 to 9, with changing β from 0.32 to 0.4 decreasing the power by 9%) for various velocity profiles [50].

Turbulence Effect on Velocity Spatial Variation

Turbulence arises from shear instabilities both along physical boundaries and within the fluid interior, particularly in swift flows. These dynamic structures can span the dimensions of tidal channels. Through frictional dissipation, energy cascades from larger to smaller eddies until it dissipates as heat at molecular levels. The vigour, spatial dimensions, and spatiotemporal consistency of turbulence significantly influence structural loads and component fatigue.

Turbulence is an integral facet of the velocity field and is thus inherently embedded within velocity data. It's generally characterised statistically, exhibiting dominant length scales linked to energy-containing eddies that adapt based on the velocity field's state. The mean energy attributed to turbulence can be quantified as turbulence intensity, a critical parameter in TEC design.

Turbulence raises questions of homogeneity, isotropy, and coherency. By examining homogeneity, isotropy, and coherency, we gain valuable insights into the shape and behavior of turbulent flows, providing a deeper understanding of their complex dynamics. Coherency relates to upstream turbulent instabilities, triggered by growing and bursting phenomena often associated with bathymetric structures. Comprehending these generative mechanisms informs optimal TEC placement.

Though turbulence intrinsic to tidal flow potentially impacts TEC power performance, any PPAs conducted under IEC TS [30] guidelines shouldn't incorporate turbulence corrections. Consequently, due to the limited understanding of turbulence's precise effect on TEC performance, uncertainties surrounding this matter remain unquantified.

Measurement of Direction

Tidal energy extraction sites typically feature flow constriction, inducing localised acceleration in flow speeds from which energy is harnessed. This constriction often steers the flow away from a simple rectilinear pattern; in other words, the peak flow during flood tide isn't aligned with the peak flow during ebb tide. Such deviation from rectilinear flow bears significant consequences for TECs that lack the capacity to adjust their rotor plane (yaw), leading to reduced energy availability. Properly quantifying this effect becomes crucial, whether to account for decreased energy extraction in fixed-yaw devices or to anticipate movement in yaw-capable devices. Employing techniques to map this phenomenon across a site would prove invaluable to site developers and tidal array designers.

To gauge the expected misalignment at tidal sites, resource assessment techniques can be tailored to provide a comprehensive overview of flow angles during ebb and flood. Understanding the attributes of tidal stream sites remains an ongoing process. It's imperative to identify directional variations for yaw control systems and off-axis power projection in cases involving fixed-yaw turbines [45, 58].

Frost et al. [45] delved into the non-dimensional performance traits of a tidal stream turbine and their response to shifts in flow direction. The study advocated for integrating a yaw mechanism that reorients the turbine to face the flow during both flood and ebb phases. This, in operational contexts, is expected to enhance the longevity of turbine components like blades, thrust bearings, and gearboxes which are prone to fatigue failure due to dynamic loads. Frost et al. [45] considered flow misalignment conditions that involved yawing a TEC away from the primary flow by angles of 0, $\pm$10, $\pm$15, and $\pm$20 degrees. The study revealed that higher yaw angles led to diminished

non-dimensional performance attributes for the TEC. Notably, under extreme misalignment angles (α=$\pm$20), both C_p and C_Θ dropped by up to approximately 11%. It was suggested that developers of bi-directional devices without blade pitch adjustment to counteract flow misalignment should not target sites featuring symmetrical ebb-flood cycles [45].

Bathymetry

The bathymetric configuration significantly impacts the local tidal flow pattern and its symmetry. The morphology and dimensions of surface features play a crucial role in shaping the vertical velocity profile and giving rise to large-scale turbulent formations. Consequently, the strategic placement of TECs hinges on factors like seabed evenness, as well as the extent of horizontal and vertical variations such as sills, mounds, and hollows. The scales of these spatial variations also dictate the optimal positioning of instruments within seabed frames. To provide essential guidance for both developers and modellers, detailed bathymetric data should be readily available within the area of interest. Ideally, this data should boast a spatial resolution of at least 10 meters or finer.

Seabed Composition

The composition of the seabed plays a pivotal role in determining surface roughness metrics and the corresponding boundary friction. In regions with robust tidal currents, fine sediment is often scarce, revealing underlying bedrock. The specific type of rock and geological processes that have shaped the seabed introduce a range of formations and depressions that influence the structure of the flow boundary layer and the occurrence of eddy-shedding processes. It's imperative to comprehend how bathymetric features influence downstream flow patterns, especially when interpreting in situ flow measurements and estimating the variability in flow dynamics.

Given that seabed composition can exhibit spatial variations across a site, the resulting alterations in bed friction lead to spatial variability in the vertical flow structure. This spatial variability influences the tidal flow's spatial arrangement and has direct implications for the positioning of TECs and the deployment of data collection instruments.

Wave Environment

Frictional wind stress acting at the water-air interface initiates the generation of ocean surface gravity waves. Most TEC sites encounter local wind-induced waves with limited reach, while some also contend with open-ocean swells originating remotely from storms with basin-scale propagation. The local wave dynamics exhibit intricacies shaped by the nearby topography (diffraction, refraction, reflection) and bathymetry (wave-breaking), interacting non-linearly with the adjacent velocity field. These surface gravity waves convey energy horizontally, influencing the vertical flow that diminishes with depth, contingent on wave amplitude and wavelength.

The depth of wave energy penetration is closely tied to the wavelength. Generally, a common assumption is that significant wave effects on flow attributes persist to depths equivalent to half the wavelength. Consequently, the site's location (whether exposed to open-ocean swell or channelled constriction), the overall water depth at the site (relative to the longest wavelengths), and the turbine's depth (distance from the water surface to rotor plane) collectively dictate the degree of influence exerted by waves on a turbine's performance.

Though wave interaction with tidal flow potentially wields a substantial impact on TEC power output, PPAs conducted under IEC TS [30] guidelines should not involve corrections for wave effects. Hence, owing to the limited understanding of how the wave environment precisely affects TEC performance, the uncertainty concerning this matter remains unquantified.

Combined Wave-Current Environment

The interaction between waves and currents holds significant implications for both the fluid environment and the loading experienced by TEC systems. Notably, waves' presence can introduce errors in estimates of turbulent parameters, potentially leading to an overestimation of TI. This interaction operates as a two-way exchange: tidal flow's presence alters the characteristics of surface waves—such as steepness, frequency, and direction—while surface waves, in turn, modify the magnitude and direction of tidal flow with depth.

Efforts are underway to disentangle wave and turbulence signals from in situ data, although these observations are currently limited to point measurements across specific regions. To gain a more comprehensive grasp of the intricate wave-current interplay, the need arises for a meticulously tuned and thoroughly validated coupled wave-current regional model. The collected data must encompass a spectrum of wave-current states to effectively support the validation of these models. Such a coupled wave-current model stands to serve as an instrument for interpreting in situ measurements, as well as for forecasting the implications of extreme waves on local tidal flow patterns, the structural loads experienced by TECs, and TEC power generation.

Marine Energy Converter Power Performance

Two primary uncertainties relate to the performance of the TEC:

1. *Uncertainty in Full-Scale Performance Testing Results*: This relates to uncertainties within the outcomes of comprehensive full-scale performance testing, which is employed to establish a rated power performance curve for the device.
2. *Uncertainty upon Deployment at Project Location*: This additional uncertainty arises where the device is positioned at the designated project site. It emerges from site-specific influences such as current shear, wave interactions, and turbulence.

The procedural guidelines for full-scale testing are delineated in the PPA IEC TS [30]. Within this TS, a minimum roster of uncertainty parameters that should be incorporated in the assessment is outlined—covering aspects like electric power, current speed, and data acquisition. However, the TS doesn't prescribe a specific approach for quantifying the comprehensive uncertainty enveloping the measured power curve, unlike its wind equivalent standard, IEC 61400-12 [31].

Turbine performance models, exemplified by tools like Tidal Bladed, facilitate the anticipation of how turbine performance reacts to turbulence and wave conditions. These tools can serve as a foundational resource for initiating an evaluation of the linked uncertainty. Addressing this concern is the aim of projects like PeraWatt, focused on generating validated tools for forecasting energy yields at tidal sites, and ReDAPT, which offers test data garnered from a full-scale turbine. These endeavours collectively contribute toward refining our understanding and mitigation of uncertainties associated with TEC performance assessments.

4.5 Summary and elements carried forward in this Thesis

Uncertainty assessment plays a pivotal role in the robust evaluation of tidal energy systems. The PPA framework, in accordance with the IEC TS, delineates the testing and uncertainty considerations to characterise device performance. However, while this standard offers guidance on incorporating specific uncertainties, it doesn't prescribe a comprehensive approach for quantifying the overall uncertainty associated with measured power curves, a divergence from the equivalent wind standard.

The methodology comparison between wind and tidal energy performance underscores the unique challenges faced by the latter due to complexities in flow patterns, boundary conditions, and environmental interactions. These disparities emphasise the need for a tailored approach to tidal energy uncertainty estimation. The sources of uncertainty, stemming from variables like wave-current interactions, seabed composition, and local turbulence, further accentuate the intricate web of factors affecting performance predictability. Moreover, the spatial and temporal scales of heterogeneity within tidal stream sites highlight the necessity of capturing fine-grained variations to mitigate uncertainty impact on site-specific TEC performance estimates. A comprehensive understanding of these uncertainties and their complex interplay is essential to ensure the credibility and reliability of tidal energy extraction endeavours.

This chapter has underlined the drivers for tidal energy extraction and the challenges surrounding this emerging technology. It has also detailed why site characterisation in this field is important and challenging. The strengths of ADCPs for measuring the velocities at such sites have been argued. The metrics that can be utilised at these sites are cited, including results from previous characterisation work at the Fall of Warness.

A fishbone diagram, is a visual tool used to systematically identify and present the possible causes of a specific problem or effect. The diagram resembles the skeleton of a fish, with the main problem at the head and the causes extending out like bones from the spine. It is particularly useful in quality control and process improvement to brainstorm and categorise potential sources of variation or issues.

The uncertainty fishbone diagram illustrated in Figure 4.13 holds a pivotal role within the realm of PPAs for TECs, effectively categorising and quantifying uncertainties. This fishbone diagram highlights the various factors contributing to the combined uncertainty in power performance assessment for Tidal Energy Converters. It categorizes these factors into current speed, data acquisition, instrument uncertainties, and electrical power uncertainties, each with specific elements that need to be controlled or mitigated to ensure accurate and reliable power measurements. This inclusive approach aids researchers and practitioners in recognising and tackling critical factors that could sway the precision of their evaluations. Once the uncertainties are pinpointed, the subsequent chapters delve into their quantification across different dimensions—such as cross-talk, ADCP placement, and TEC extraction plane misalignment. This essential step is instrumental in comprehending the scope of uncertainties and their potential repercussions on the accuracy of PPAs.

The work presented in chapters 6, 7, and 8 quantifies uncertainties in the following crucial areas:

1. *Cross-talk between two proximal acoustic instruments*: The performance of a multi-instrument ADCP campaign targeting IEC TS 62600-200 guidelines was investigated. This thesis was the first to uncover the occurrence of acoustic cross-talk throughout the measurement campaign and quantify its subsequent effects on AEP estimates.

2. *Spatial variation in flow velocity from various acoustic references relative to a operational tidal turbine*: Two measurement campaigns - featuring a total of 6 acoustic instruments - are used to assess the impact of velocity measurements from 6 locations around the TEC on the estimates of power and AEP.

3. *Spatial and temporal variation in current flow directionality*: The flow direction naturally evolves over a tidal cycle resulting in non-yawing (nacelle rotation mechanism) TEC concepts being susceptible to off-axis currents. A sensitivity study to misalignment between the principle flow direction and TEC yaw angle was conducted to analyse the impact on the power and AEP estimates from misalignment.

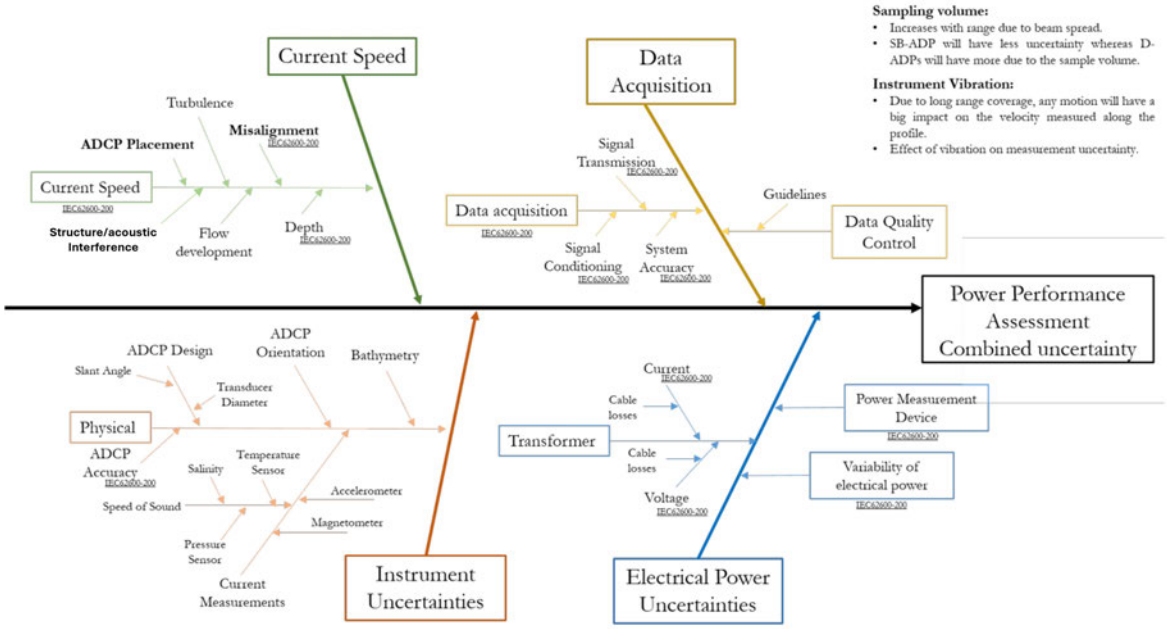

Figure 4.13: Fishbone of uncertainties associated with a tidal stream PPA.

These specific uncertainties collectively contribute to the broader realm of the instrument and current speed uncertainties, as illustrated in Figure 4.13. The examination and quantification of these uncertainties stand as essential steps in comprehending their potential impact on the accuracy of the overall assessment.

Chapter 5

Full-Scale Turbine Data and Proximal Flow Data (ReDAPT data set)

5.1 Chapter Overview

This chapter sets the foundation for analyses in chapters 6, 7, and 8. It begins by detailing the measurement campaigns and instrumentation features in Section 5.2, followed by their spatial configurations relative to the deployed tidal turbine in Section 5.3. Section 5.4 outlines quality assurance protocols for data filtration. Instrumentation and post-processing uncertainties are addressed in Section 5.5. The chapter concludes with operational details of the tidal turbine in Section 5.6 and its theoretical maximum power curve in Section 5.7. This arrangement provides a detailed introduction to the data sets and methodologies used in subsequent chapters.

5.2 Instrument Specification: Measurement campaign

The assessment of power performance for tidal turbines heavily relies on in-situ data, typically gathered by local ADCPs or recently adopted turbine-mounted acoustic instruments. This thesis is dedicated to quantifying uncertainties within the various steps of this procedure, encompassing measurement, processing, and analysis. This is accomplished through a meticulous analysis of in-situ datasets obtained from tidal energy sites, particularly the Fall of Warness in Orkney, Scotland. This chapter meticulously outlines the data employed, offering insight into the instrumentation, and experimental design of the original measurement campaigns, as well as the quality control and post-processing methodologies applied in this research.

The dataset selected for this study originates from the ReDAPT (Reliable Data Acquisition Platform for Tidal) project, chosen due to its comprehensive and distinct multi-sensor deployments within a tidal energy site. All data utilised in this thesis originates from the ReDAPT project. This UK-based consortium was commissioned and funded by the Energy Technologies Institute (ETI), with Alstom Ocean Energy at its helm, and collaboration from institutions are listed, the University of Edinburgh, Plymouth Marine Laboratory, Electricite de France (EDF) Energy, Det Norske Veritas - Germanischer Lloyd (DNV GL), E.ON, and EMEC. The principal objective of the ReDAPT project was to assess a 1 MW commercial-scale prototype tidal turbine, providing extensive insights into its performance and environmental interactions. This turbine, crafted by Alstom, was installed at the EMEC full-scale tidal test site in the Fall of Warness, Orkney, as depicted in Figure 5.1.

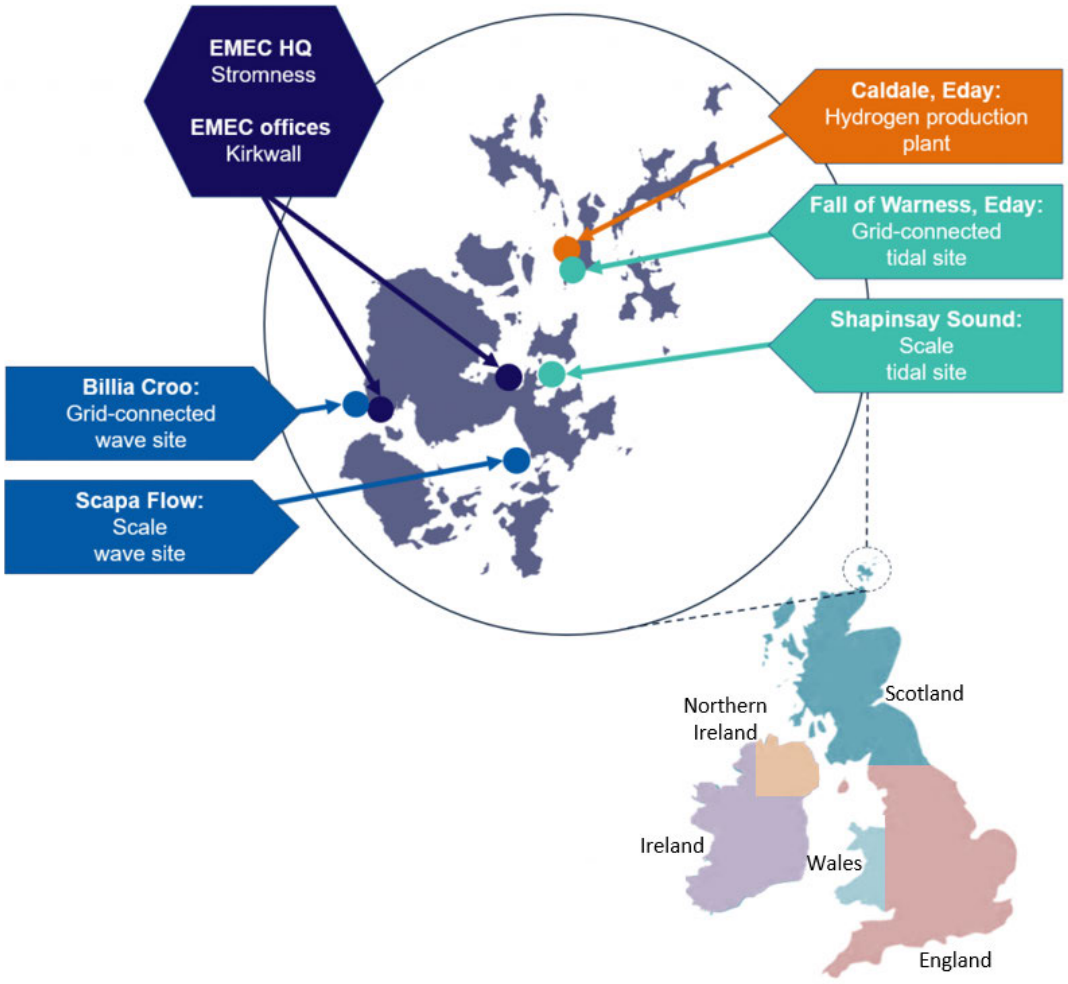

Figure 5.1: Geographical position of EMEC tidal and wave test sites: The Alstom DEEP-Gen IV 1 MW turbine was positioned at the Eday grid-connected tidal test site.

Three distinct case studies have been conducted utilising diverse datasets sourced from both the seabed-placed ADCPs and the turbine-mounted SB-ADPs deployed at berth 2 of EMEC's full-scale tidal test site, as visualised in Figure 5.2 [214]. The organisation of this section is as follows: Section 5.2 furnishes an overview of the instrumental apparatus employed in the measurement campaigns. Section 5.3 illustrates the precise positioning of these instruments in relation to the turbine's location. Subsequently, Section 5.4 comprehensively outlines the sequence of QC measures undertaken to assess the data quality, categorising them as 'good' or 'bad', and quantifying the degree of their quality. Furthermore, Section 5.6 delves into the detailed characteristics of the DEEP-Gen IV turbine—installed during the measurement campaigns—alongside two additional horizontal axis variants (modelled turbines for comparison). The power curve data, fundamental for analysis, is presented in Section 5.7.

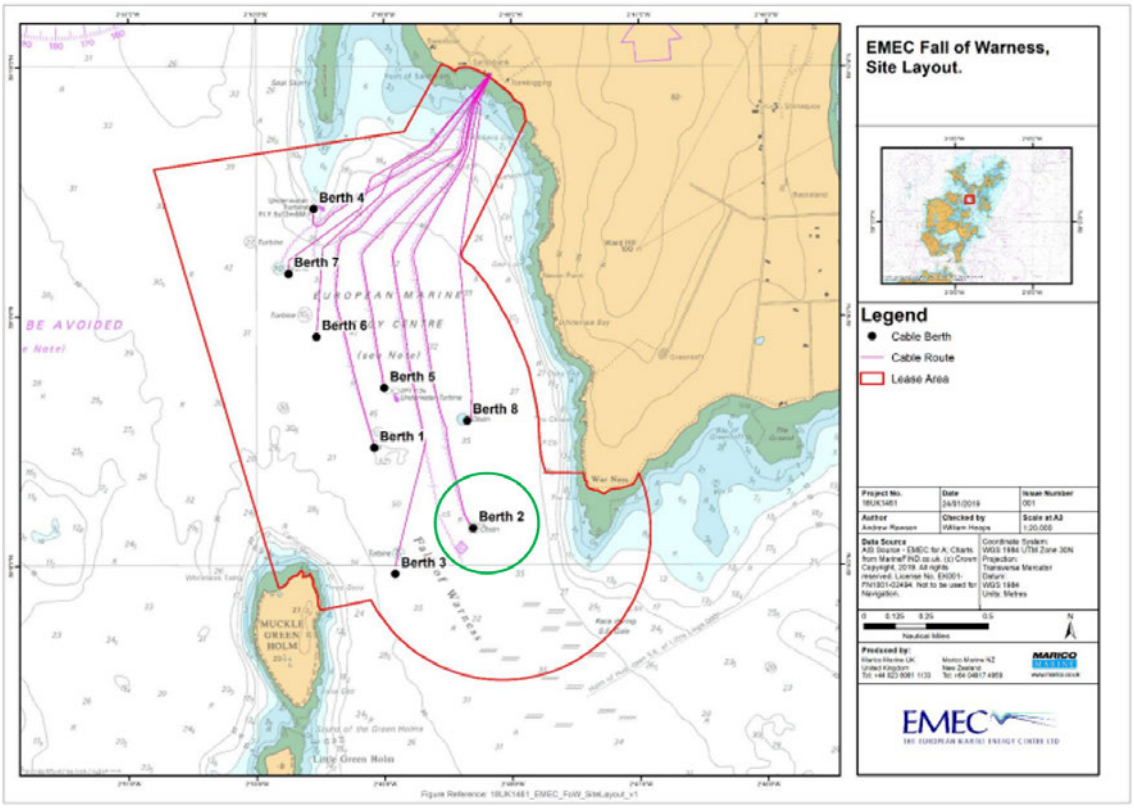

Figure 5.2: Test site layout at Fall of Warness. The DEEP-Gen IV and all relevant instrumentation over the measurement campaigns were deployed at Berth 2 (green circle).

From 2011 to 2015, the ReDAPT project amassed an extensive dataset exceeding 1 terabyte, encompassing in-situ measurements such as flow velocities, wave heights, and power output (recorded from the rotor shaft). These recordings stemmed from a total of seven distinct measurement deployments, a few of which employed as many as twenty-two Doppler profilers. All relevant acoustic instruments available for this work are presented in Table 5.1. Within this spectrum, three out of the seven measurement campaigns were chosen for inclusion in this thesis, strategically positioned within the two specified zones advocated by the IEC TS 62600-200 (refer back to Figure 4.8 and 4.9). These zones ensure measurements encompass both flood and ebb tides, maximising the comprehensive insight. Moreover, the arsenal includes both rotor-attached and rear hub-attached SB-ADPs, facilitating velocity measurements along the beam axis. Notably, the SB-ADPs boast an effective range of approximately 20 meters, whereas the ADCPs were configured to profile the vertical water column, with a range spanning around 45 meters. Employed in this context are Nortek AD2CP Signature1000s, operating at a carrier frequency of 1 MHz, with a broad-band signal processing technique. A singular ping entails the synthesis of two chirp-modulated acoustic pulses, culminating in a refined measurement methodology. By synthesising two chirp-modulated acoustic pulses in a singular ping, ADCPs can achieve higher resolution, better SNR, deeper penetration, and more accurate Doppler measurements than with conventional single-frequency pings.

Table 5.2 lists the key parameters of the acoustic instruments used in the project. To date, the IEC TS 62600-200 does not recognise TEC-mounted instruments that profile in the horizontal plane. Instruments mounted on TECs could limit the requirement for seabed ADCPs for PPAs, thus providing flexibility for these assessments and reducing additional costs of offshore deployments. Two data sets acquired from SB-ADPs mounted on the TEC

Table 5.1: Instrumentation Summary.

ADCP Campaign ID	Date Deployed	Date Recovered	Location UTM 30N East (m)	Location UTM 30N North (m)	Depth (m)	Label
ADCP01-NW-Dep5	19/06/2014	03/08/2014	511072	6555354	45	A_1
ADCP02-NW-Dep5	06/07/2014	17/08/2014	511052	6555394	45	A_2
ADCP03-SE-Dep5	19/06/2013	03/08/2013	511142	6555260	45	A_3
ADCP01-NW-Dep1	18/02/2013	20/03/2013	511054	6555328	44	A_4
ADCP02-SE-Dep1	17/02/2013	20/03/2013	511151	6555241	45	A_5
ADCP01-NE-Dep7	17/09/2014	11/12/2014	511141	6555333	43	B_2
ADCP02-SW-Dep7	17/09/2014	27/11/2014	511083	6555288	43	B_1
SBD01-rotor	23/06/2014	21/12/2014	511111	6555307	19	C_1
SBD16-rear	22/02/2013	22/10/2014	511111	6555307	19	C_2

(rotor-attached, C_1, and rear hub-attached, C_2, profiling the approaching flow in the horizontal plane) are used in this work. Mounting sensors on a turbine presents advantages over a standard seabed-mounted deployment. The turbine itself is installed $\approx$ 20 m deep in a $\approx$ 45 m depth channel. Instrumentation mounted on the nacelle is all within the swept plane of the turbine and thus takes measurements representative of the flow the blades are experiencing. This combined with the turbine's ability to yaw through 360°, allows the acoustic instruments to be oriented at a variety of angles to the approaching flow. The turbine's power and communications infrastructure also allows instruments to be hard-wired with power and Ethernet. However, the effects of electrical noise and turbine vibrations, particularly during the generating periods, were an unquantified source of uncertainty.

In addition to the turbine-mounted SB-ADPs instruments, seabed-placed ADCPs were deployed in gravity bases mounted in a gimbal to mitigate any offset angle of the gravity base from horizontal. Small offsets in pitch and roll were still possible. These instruments allowed the flow conditions to be measured for the full depth profile from the seabed to the surface at a distance great enough to avoid any impeding effects of the turbine on the flow.

Table 5.2: Key operating parameters of acoustic profilers used in the flow characterisation.

Identification/s	A_1,A_2,A_3,A_4,A_5,B_1,B_2	C_1, C_2
Instrument	WHS	AD2CP
Manufacturer	RDI	Nortek
Acoustic frequency	600 kHz	1000 kHz
Type	ADCP	SB-ADP
Sample rate	1 Hz	2 Hz
Quantity	5	1
Location	Seabed	RA (C_1), RHA (C_2)
No. operating beams	4	1
Bin length	1 m	0.4 m

RA = Rotor-Attached; RHA = Rear hub-Attached;

5.3 Instrument Specification: Location

Three measurement campaigns are considered in this project to assess and re-inform the current use of the IEC TS 62600-200 standard. The uncertainty associated with in-situ measurements is the main focus. The ADCPs deployed at the same time-stamp are grouped by colour, where yellow, green, and orange beams (Fig 5.3) correspond to Dep1, Dep5 and Dep7 (Table 5.1). The turbine-mounted SB-ADPs (represented by the blue beam in Fig 5.3) were installed during the three measurement campaigns back in July 2013 to December 2014. Instruments placed in-line, adjacent or mounted on the turbine are denoted as "A", "B", and "C" respectively. The seabed-placed ADCPs were placed - aligned with the expected principal direction of the flow through the channel - at a minimum and maximum of 32 m and 106 m from the turbine location respectively. Table 5.3 provides the distance of each seabed instrument used in the project. Figure 5.3 depicts the instrument position relative to the turbine location.

Table 5.3: Key parameters of acoustic profilers used in the flow characterisation. The visual representation is shown in Figure 5.3.

ADCP distance from TEC location (m)								
A_1	A_2	A_3	A_4	A_5	B_1	B_2	C_1	C_2
61	106	54	63	60	34	32	12	12

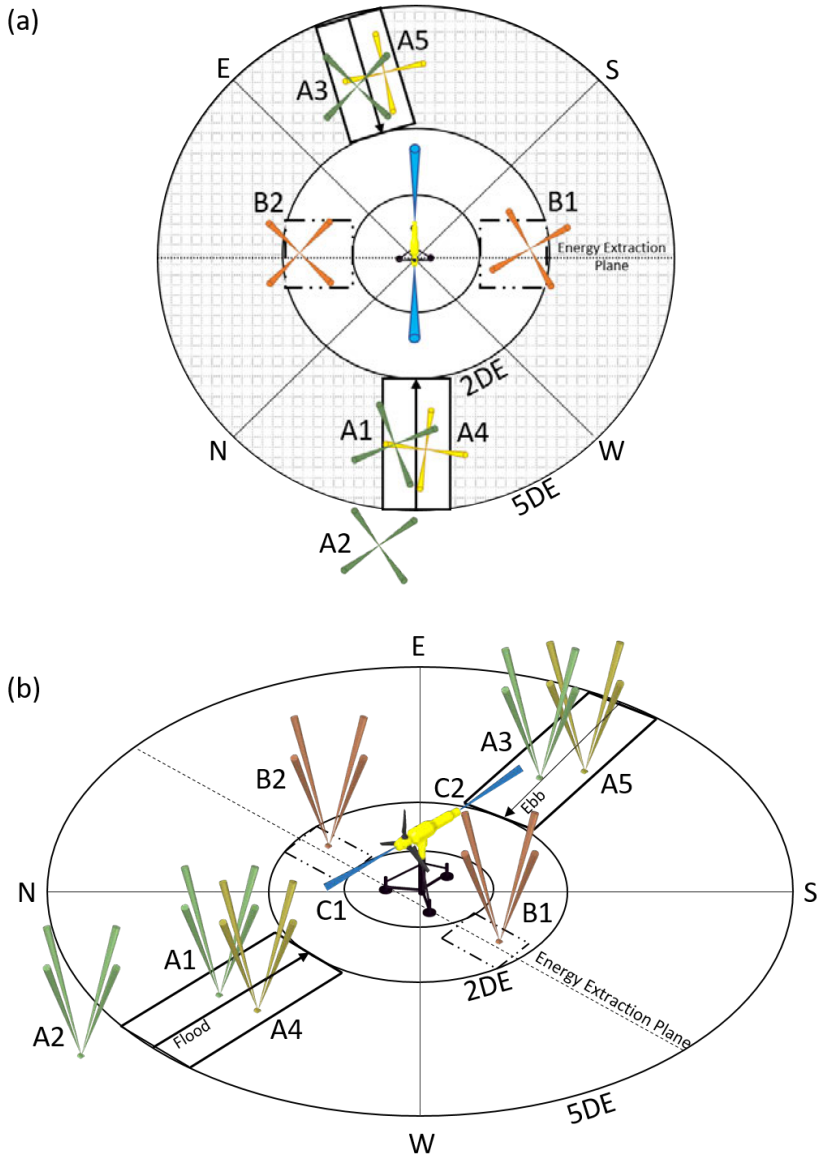

Figure 5.3: Instrument placement for Deployments 1, 5 and 7 showing distance (D_E) from the DEEP-Gen IV TEC, relative to North. Instrument locations from Deployment 5 are identified as A_1, A_2 and A_3 (green beam) targeting ambient conditions on the flood and ebb tides respectively. Deployment 6 featured B_1, B_2 data-sets (orange beam) targeting ambient flows on both the flood and ebb tide. Deployment 1 featured A_4 and A_5 (yellow beam) targeting ambient flow conditions on the flood and ebb tide. The rotor-attached and rearhub SB-ADP C_1, C_2, measured both flood and ebb tide (hence yawing with the TEC).

Illustrated in Figure 5.4 is a comprehensive display of the raw velocity data measured from each individual instrument deployed. Specifically, the ADCPs denoted A_1 and A_2 are the focal points of chapter 6. The x-axis features the measured velocity (in m$\cdot$ s^{-1}), turbine yaw angle (divided by 100) and the turbine power (in MW). In chapter 7, the attention shifts to datasets $A_{1,2,3}$, $B_{1,2}$, and C$_{1,2}$. Finally, datasets A_4 and A_5 are used in chapter 8. This delineation efficiently directs attention to the specific datasets relevant to each chapter, facilitating a clear overview of the research segmentation.

The ADCPs positions were established with precision to the nearest metre, relying on their UTM coordinates recorded at the location of the vessel when deploying the instruments as tabulated in Table 5.1. However, there exists an inherent level of uncertainty when the instrument is lowered into the dynamic tidal race. Using a bathymetric map in conjunction with each ADCPs pressure data, it was feasible to gauge their respective depths relative to the TEC, with a resolution aligned to the instrument's 1-metre resolution. All the instruments and the TEC were deployed in Berth 2 at the FoW, at a depth of $\approx$ 43-46 m. The bathymetry of a TEC test site must be surveyed to ensure that it is free from obstacles and topography that could affect the performance of the TEC. The berth locations at the Fall of Warness site have been extensively surveyed (10 D_E x 20 D_E) throughout the years of site operation for the purpose of a PPA as per the IEC TS 62600-200, see Figure 5.5 ('Contains Maritime and Coastguard Agency data © Crown Copyright' [352]).

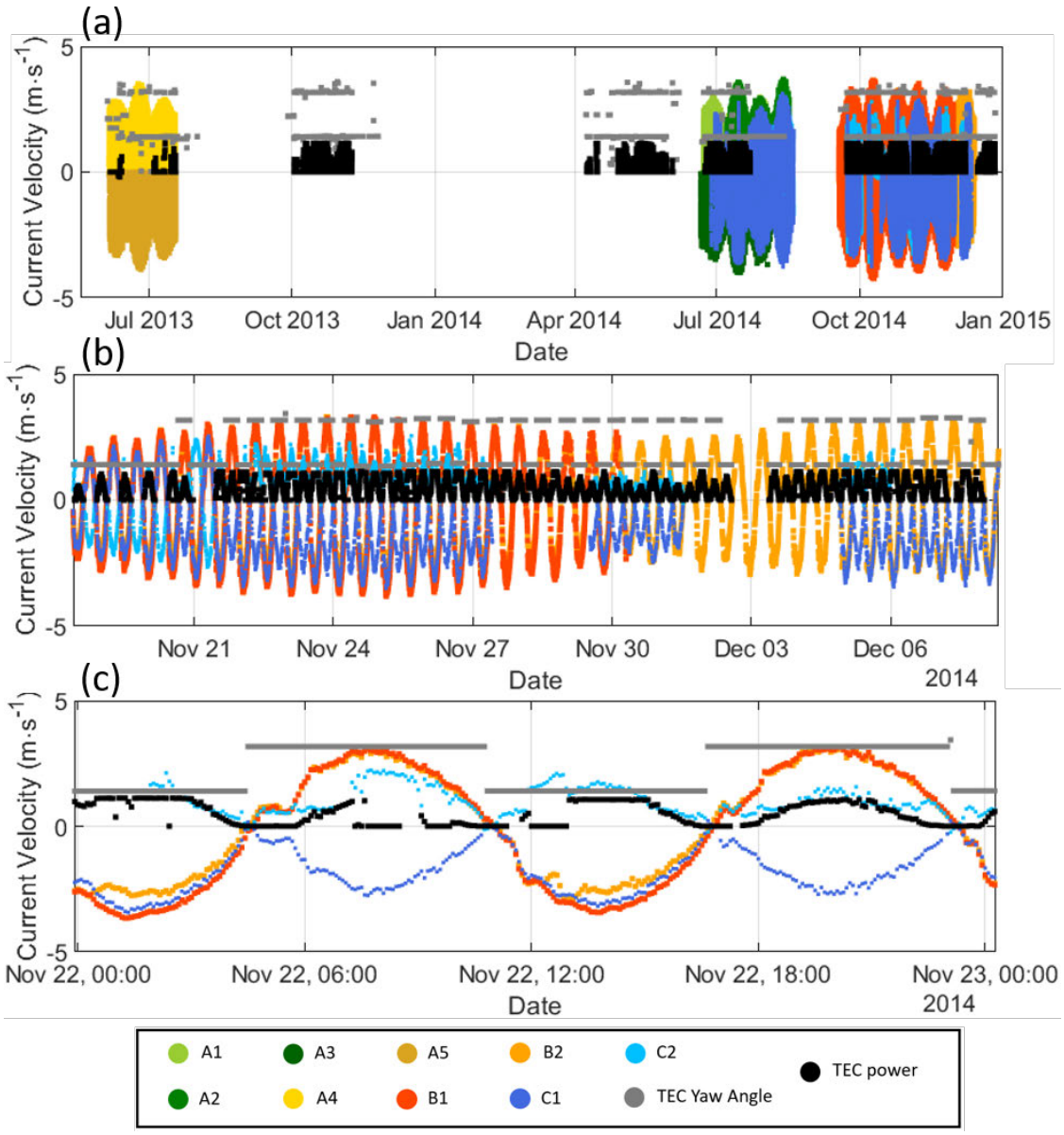

Figure 5.4: Instantaneous current velocities were measured at various locations at berth 2 within the Fall of Warness site. (a) Current velocities captured by ADCPs positioned at A_{1-5}, B_{1-2}, and upstream and downstream from the TEC-mounted SBD (C_1 and C_2), along with the actual TEC yaw angle (/100) and power between June 2013 and Jan 2015. (b) A two-week focused view of deployment B (B_1 and B_2) with corresponding TEC yaw and power data. (c) A one-day detailed view of deployment B.

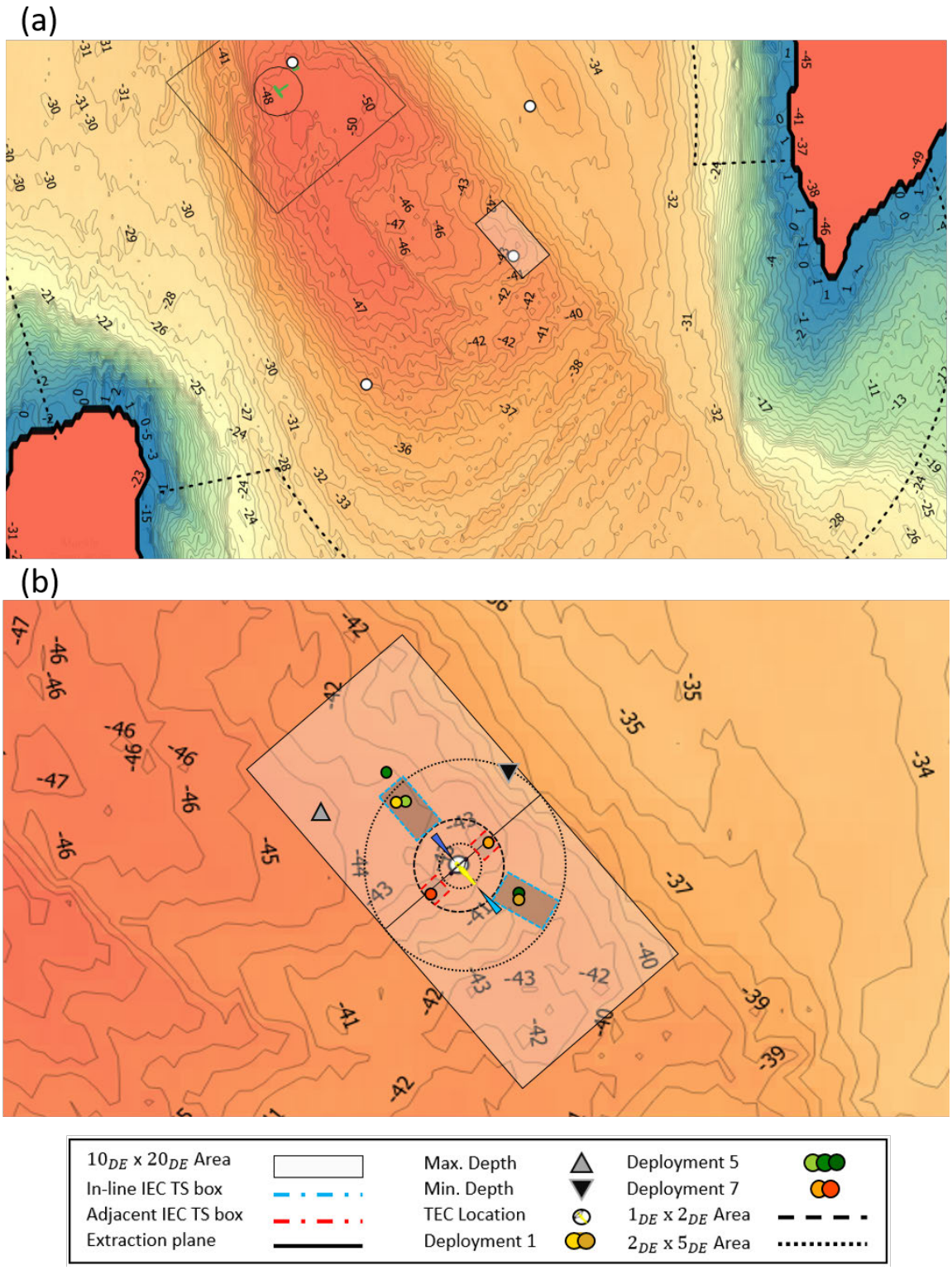

Figure 5.5: Bathymetry in the vicinity of the turbine, with a) showing the 10 D_E x 20 D_E area of interest (solid black rectangle within highlighted grey squared) at the Fall of Warness, and b) a closer view at the depth around the DEEP-Gen IV and IEC TS target locations with ADCP layouts.

The depth within the 10 D_E x 20 D_E area ranges from 46 m (grey triangle fig 5.5b) northwest of the turbine, to 39 m (black triangle fig 5.5b) near the east side of the area of interest. The latter is considered far enough from the turbine to not create any significant disturbance in the turbine flow.

5.4 Data Post-Processing: Quality Control

5.4.1 Seabed Placed Profilers

Data are evaluated using QC checks, and the results of those checks are recorded by inserting flags in the data files. Table 5.4 provides a simple set of flags and associated descriptions that have been used in the data post-processing phase. For example, if the data failed the current speed test by exceeding the upper limit, a 'failed high' flag may indicate that the values were higher than the expected range.

Table 5.4: Flags from in-situ data from ADCPs.

Flag	ID	Description
Pass	1	Data have passed critical QC checks and are deemed adequate for use as preliminary data.
Not evaluated	2	Data has not been QC-tested, or the information on quality is not available.
Suspect or of high interest	3	Data are considered to be either suspect or of high interest to the user. They are flagged suspect to draw further attention to them.
Fail	4	Data are considered to have failed one (or more) critical QC check. If they are disseminated at all, it should be readily apparent that they are not of acceptable quality.
Missing data	9	Data are missing, used as a placeholder.

A comprehensive compilation of twenty QC checks is necessary and strongly recommended for assessing in-situ currents. These checks, delineated in Table 5.5, specifically apply to current observations procured from ADCPs. The array of checks is strategically categorised into four groups: sensor health, signal quality, current velocity, and overall profile.

The precise selection of appropriate thresholds, as these thresholds fundamentally influence the efficacy of the QC process, are significant in the QC process. While thresholds can be derived from historical insights or statistics gleaned from recent data acquisitions, their establishment should not be arbitrary. Rather, they should be thoughtfully determined to ensure the utmost accuracy and reliability of the QC evaluation.

All data post-processing adhered to the guidelines outlined in IEC/TS 62600-200 [30]. A consistent suite of processing methods was applied to each instrument (as depicted in Table 5.5), with recommended thresholds determined in alignment with internationally recognised QARTOD guidelines (as depicted in Table 5.5) and ADCP manufacturer's best practices [67, 69, 207]. Any measurements that deviated beyond these thresholds were identified and flagged, as detailed in Table 5.4, and subsequently excluded from the analysis.

Table 5.5: QC checks that have been used to filter the in-situ data from the fixed current profilers.

Test Type	Test Name	Status
Sensor Health	Battery Voltage (Test 1)	Strongly Recommended
	Check Sum (Test 2)	Required
	Sensor Tilt (Test 3)	Required
	Speed of Sound (Test 4)	Required
Sensor Quality	Noise Floor (Test 5)	Strongly Recommended
	Signal Strength (Test 6)	Required
	Signal-to-Noise (Test 7)	Strongly Recommended
	Correlation Magnitude (Test 8)	Strongly Recommended
	Percent Good (Test 9)	Strongly Recommended
Current Velocity	Current Speed (Test 10)	Required
	Current Direction (Test 11)	Required
	Horizontal Velocity (Test 12)	Required
	Vertical Velocity (Test 13)	Strongly Recommended
	Error Velocity (Test 14)	Strongly Recommended
	u, v Rate of Change (Test 15)	Strongly Recommended
	u, v Spike (Test 16)	Strongly Recommended
	Flat Line (Test 17)	Required
Overall Profile	Echo Intensity (Test 18)	Required
	Echo Intensity Drop-off (Test 19)	Strongly Recommended
	Current Gradient (Test 20)	Strongly Recommended

Figure 5.6 illustrates a comparative assessment of 5-minute and 15-minute ensembles against the IEC TS 62600-200 recommended 10-minute ensemble length. The IEC recommends ensemble lengths ranging from 2 to 10 minutes. In this project, a 5-minute averaging period was employed for the datasets. The impact of ensemble length on the power curve was found to be more pronounced at lower velocities. Empirical findings from Thomson et al. [58], based on data collected at two tidal sites in Puget Sound, Washington, determined that a stable mean and variance were achieved with a 5-minute ensemble. Likewise, for the ReDAPT project, Sellar et al. [122] also identified a 5-minute ensemble as the most appropriate choice.

Initially, a stringent tilt threshold (Test 3 as presented in Table 5.5), ranging from $<$-15° to $>$15°, was employed to assess the pitch and roll data for each seabed-placed ADCP. Figure 5.7 focuses on ADCP positioned at A_2 to illustrate this procedure, as it exhibited the most significant movement among the seabed-deployed ADCPs. Subsequently, a threshold for the SoS (Test 4 as shown in Table 5.5) was established, with values set to be within $<$1470 m·s^{-1} and $>$1570 m·s^{-1}. Notably, the measured SoS values obtained from both seabed ADCPs and turbine-mounted SB-ADPs fell within the stipulated SoS thresholds.

In line with these QC measures, all measurements of SoS from the seabed ADCPs and turbine-mounted SB-ADPs adhered to the prescribed thresholds. Furthermore, a signal correlation threshold (Test 8 in Table 5.5) was implemented, where values corresponding to a correlation below 70% were identified and flagged. To detect velocity outliers, a rate-of-change and spike test was carried out (Tests 15 and 16 in Table 5.5), flagging values displaying a change of 1 m·s^{-1} between consecutive samples. The rate-of-change test identifies gradual, consistent changes in data over time, while the spiking test detects sudden, isolated deviations from expected values. It's noteworthy that this threshold led to the removal of less than 0.5% of data from each utilised ADCP.

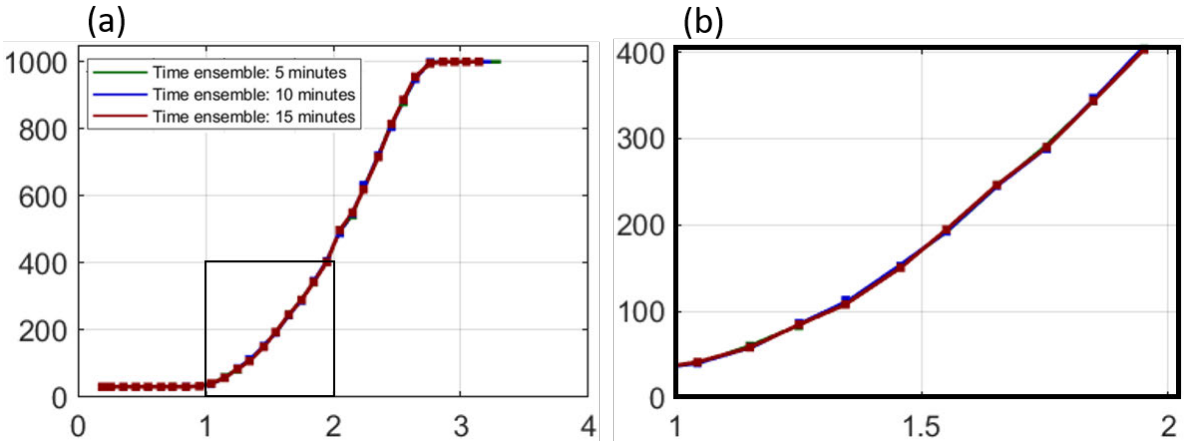

Figure 5.6: Power Curves plotted by time averaging ensemble of 5, 10 and 15 minutes. (a) Full power curve. (b) Higher resolution.

Data measurements acquired close to the acoustic emitter are adversely affected by both "ringing" and sensor-induced local flow disturbance. For effective mitigation of ringing, manufacturer-recommended "blanking distances" of 2.0 m and 0.4 m were implemented for seabed ADCPs and turbine-mounted SB-ADPs respectively. To ensure data quality, a correlation threshold of 50% ([67, 161]) was applied for data filtering, resulting in less than 1% flagged data. The correlation test examines the relationship between two or more variables to determine if and how strongly they are related, in this case the transmitted and returned signal are analysed.

Furthermore, the Phase Space Thresholding (PST) technique was employed to eliminate spikes within the velocity time series (Test 10 in Table 5.5). These spikes, arising from factors like flow-interrupted bubbles or prior pulse reflections from boundaries, were effectively addressed using this method. If the current speed exceeds a reasonable maximum value (threshold set of 250 cm$\cdot$ s^{-1}), the measurement is flagged as suspect and potentially removed.

The effective range of an ADCP is influenced by oceanic conditions, particularly particle density affecting backscattering. In the case of the ADCP signal, originating from the seabed, its strength was generally robust until within 5 m of the water's surface. Consequently, data within this 5 m range were excluded from the analysis. On the other hand, the quality of the return signal from the seabed-attached ADPs diminished gradually with distance, introducing a bias towards lower measured velocities. To address this, a decision was made to implement signal strength metrics for filtering (Test 6 in Table 5.5), rather than employing a predetermined cut-off distance.

Signal-to-noise ratio (SNR), quantifying the signal's amplitude in relation to the background noise level, was used for filtering (Test 5 in Table 5.5). To further mitigate measurement bias, amplitude and correlation were leveraged by setting thresholds. Specifically, an amplitude threshold (Tests 18 and 19 in Table 5.5) was established, with 64 dB and 30 dB applied to seabed ADCPs and turbine-mounted SB-ADPs, respectively. The interplay between amplitude, correlation, distance, and the resulting filtered data is depicted in Figure 5.9 for SB-ADPs, and in Figure 5.8 showcasing the mean amplitude profile for the chosen ADCP (located at A_1 for illustration).

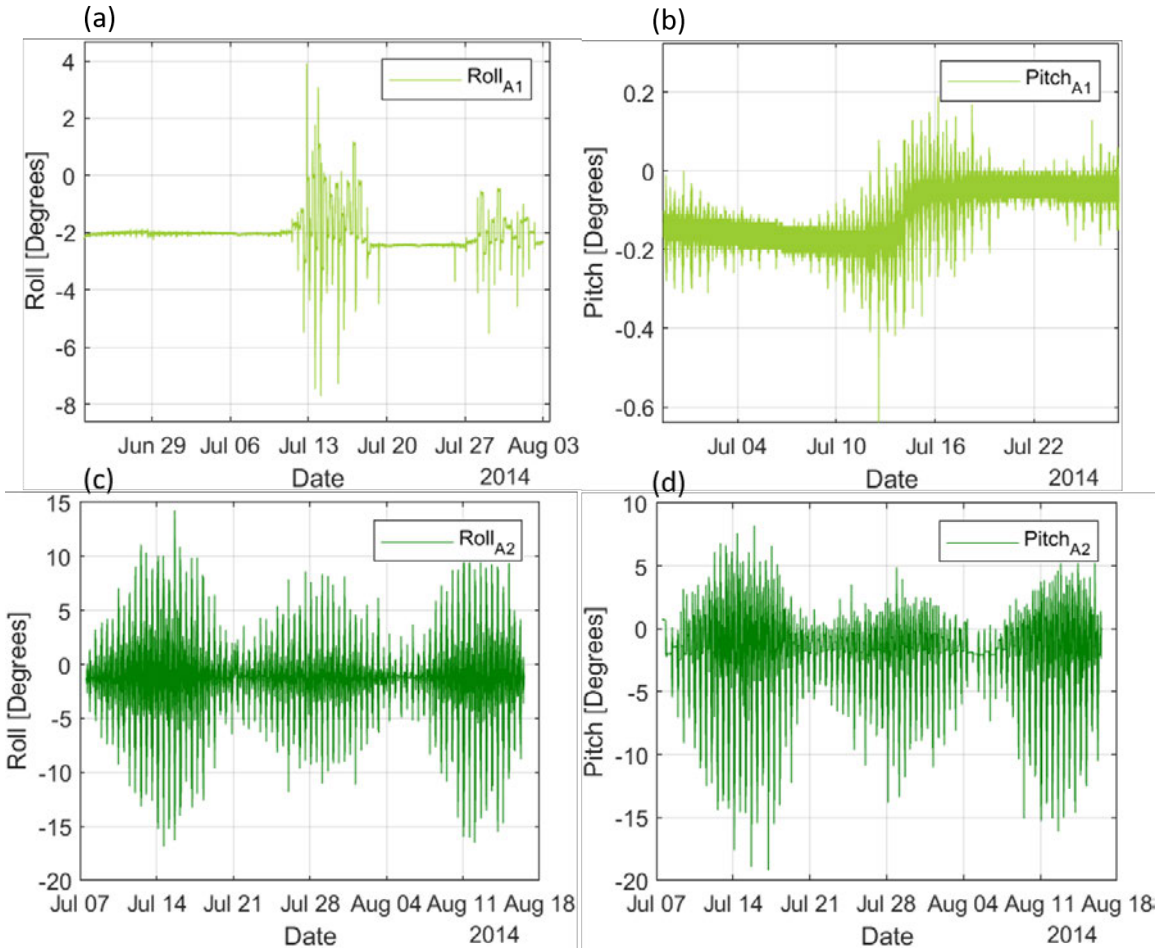

Figure 5.7: Instrument stability measured by ADCP$_{A1}$ (a and b) and ADCP$_{A2}$ (c and d). Roll (a and c) and pitch (b and d) for two instruments, where one instrument is stable (A_1) and the other is unstable (A_2).

In consideration of each spatial bin (corresponding to the velocity measurements within the instrument's range interval), the number of data samples passing the signal strength requirement was aggregated for each ensemble (Test 9 in Table 5.5). This test was based on having enough data samples to ensure negligible random error. Figure 5.10 illustrates the typical variation in the count of "good samples" with respect to beam range, indicating the number of instantaneous samples deemed acceptable per depth bin before being averaged into a 5-minute averages per depth bin demonstrated using SB-ADP C_1 as an illustrative example.

All data that did not satisfy the relevant thresholds during the quality assurance process were flagged as "4" and subsequently replaced with "not a number" (NaN) to prevent any influence on subsequent analyses.

The depths at which further characterisation was performed are detailed in Table 5.6. However, the SB-ADPs mounted on the turbine achieved sensing ranges lower than initially anticipated. Therefore, a reliable profiling range of 5 and 15 meters was chosen, ensuring a robust signal strength while maintaining an adequate distance from the turbine structure. For the SB-ADPs, data were discarded beyond a range of 25 meters.

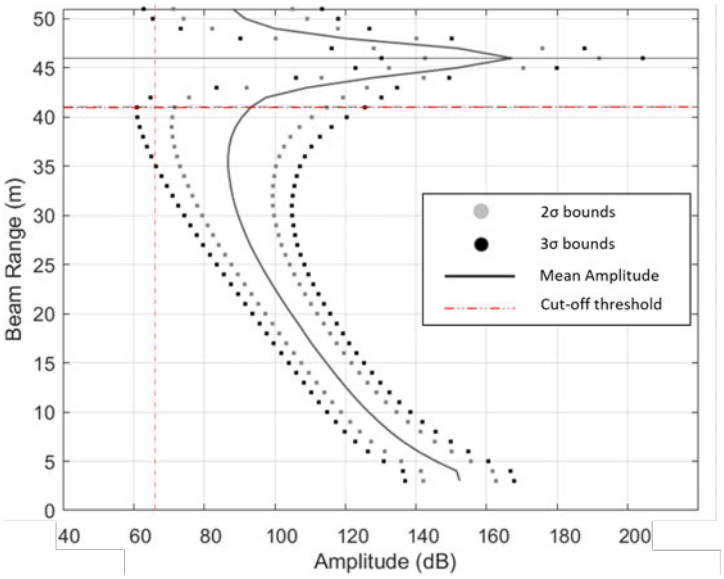

Figure 5.8: Amplitude vs distance along the water column from the ADCP (upward from the seafloor to surface). The distribution is shown in terms of standard deviations from the mean, σ.

Table 5.6: Spatial averaging regions in the vertical direction for three TEC installation types and a narrow mid-depth sampling regime. Distance are relative to the seabed.

Turbine Installation Type	Range from Seabed	Rotor Diameter	ID
TEC_{T2} (Bottom Third)	6 - 18 (m)	12 (m)	$A_{1...5}$, $B_{1,2}$
TEC_{T1} (Mid-depth)	9 - 27 (m)	18 (m)	$A_{1...5}$, $B_{1,2}$
TEC_{T3} (Upper Third)	20 - 40 (m)	20 (m)	$A_{1...5}$, $B_{1,2}$
TEC_{T1} Channel Mid-Depth	19 (m)	N/A	C_1, C_2

Due to the varying bathymetry, the ADCPs are situated at locations with differing depths (up to 3 m) compared to the turbine's position (see Fig 5.5). This introduces complexity in establishing the hub height location for the method of bins, which calculates the flow velocity for the PWRA. To address this, the surface is chosen as the reference depth, and the hub height is measured downward from this reference point. An additional challenge arises from the 2-degree tilt of the DEEP-Gen IV turbine's tripod. Consequently, during a flood tide, the turbine is positioned higher in the water column than the assumed hub height, while during an ebb tide, it is positioned lower. Refer to Figure 5.11 for a visualisation of this tilt.

The 2-degree tilt at the TEC's base also influences the horizontal bin ranges of C_1 and C_2. Notably, at a depth of 12 meters, a maximum deviation of 0.42 meters was observed. Additionally, in conjunction with the TEC's tilt, manual adjustments were made to the turbine's yaw orientation to align with the incident flow direction; however, this process was not entirely precise. Considering that C_1 and C_2 were oriented in line with the TEC's yaw angle (with C_2 profiling at -180 degrees to C_1), this tilt meant that the SB-ADPs measured not a purely horizontal velocity component but one that includes a fractional vertical component.

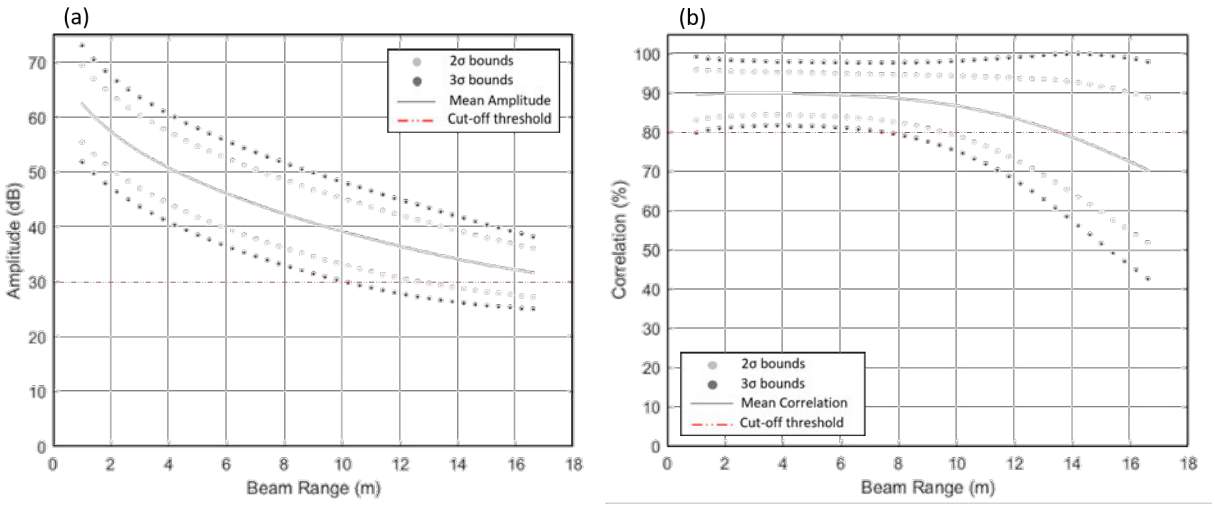

Figure 5.9: Amplitude (a) and correlation (b) vs distance upstream from the SB-ADP mounted on the TEC. The distribution is shown in terms of standard deviations from the mean, σ. The sea surface is depicted as a grey line.

5.4.2 Turbine Mounted Single Beam Profilers

The SB-ADPs C_1 and C_2 were employed to measure the current flow along the beam. The manually set speed of sound values were 1470 m·s^{-1} and 1490 m·s^{-1} for C_1 and C_2 respectively, as depicted in Figure 5.12. However, to align with the measurements from the seabed-placed ADCPs, particularly A_1 for the in-line orientation and B_1 for the adjacent orientation (the two closest ADCPs to the TEC location), an SoS correction was necessary for the SB-ADPs. This correction was integrated into the data processing through scaling, illustrated by equation 5.1 (where C_1 serves as an example):

$$u_{C1} = u_{C1_{(org)}} \cdot \frac{S_{A1}}{S_{C1}} \tag{5.1}$$

where u_{C1} represents the corrected instantaneous velocity, $u_{C1(org)}$ stands for the uncorrected instantaneous velocity measured by C_1, S_{A1} denotes the instantaneous SoS reported by the ADCP, and S_{C1} represents the manually set SoS for the single-beam ADP.

The two SB-ADPs were utilised to monitor the flow approaching the rotor of the TEC. During periods when the TEC remained stationary, the rear hub-attached SB-ADP was employed to gauge the in-flow current. Notably, a relatively stable longitudinal flow velocity was observed within the range of approximately 10 to 12 metres for both C_1 and C_2. As the flow interacts with the rotor, it experiences deceleration closer to the TEC, and beyond the 17 metre mark, a significant reduction in flow magnitude becomes evident. This behaviour is a direct consequence of the instrument's range limitations, where the SNR improves. Within the region of highest data reliability, spanning from 10 to 12 metres, the longitudinal velocities u_{C1} and u_{C2} were spatially averaged, denoted as $\bar{u}_{C1}$ and $\bar{u}_{C2}$ respectively. These averaged velocities serve as reference values for the TEC-mounted instruments' longitudinal velocity measurements.

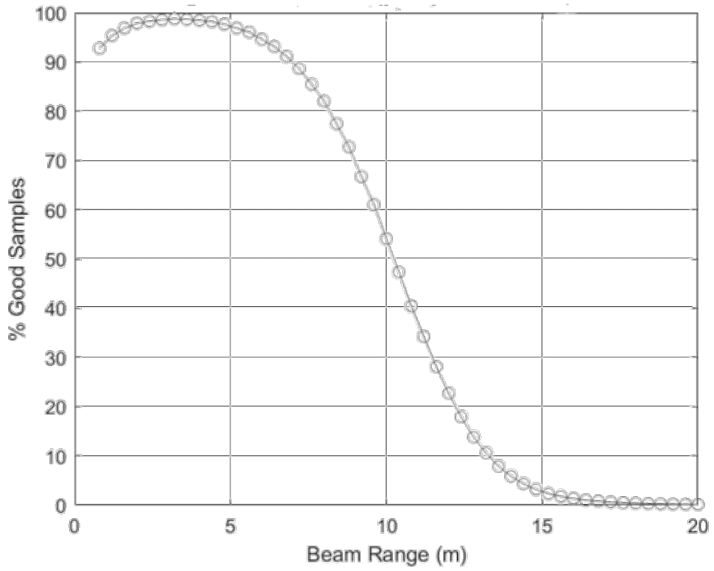

Figure 5.10: Mean number of samples passing signal strength filter vs distance upstream of the rotor-attached SB-ADP C_1.

Flow Angle

In order to facilitate a precise comparison between the velocities measured by the SB-ADP and ADCP, it was necessary to align the data according to the same flow direction. The ADCPs captured data along Cartesian dimensions, where the streamwise velocity was aligned with the principal angle. The principal angle was determined by analysing the dominant flow direction, typically by averaging the flow direction from the ADCP upstream of the TEC (deemed to be the most representative of the flow conditions near the TEC) over a significant period to identify the most consistent direction of the current. The true flow direction in relation to the principal angle was determined using Equation 5.2:

$$\alpha = \arctan \frac{u_{\text{transverse}}}{u_{\text{streamwise}}} \tag{5.2}$$

The velocity along the true flow direction was simply the magnitude, calculated using Equation 5.3

$$u = \sqrt{u^2_{\text{streamwise}} + u^2_{\text{transverse}}} \tag{5.3}$$

This correction carried significant importance, particularly at lower velocities, where the flow direction, as illustrated in Figure 5.13, could deviate by more than $\pm$ 35° from the principal angle.

The SB-ADP attached to the rotor faced the same direction as the turbine's yaw angle, while the rear-hub attached SB-ADP was positioned 180° from this direction. Although the turbine was manually adjusted around its yaw axis to align with the incident flow direction, this approach was discovered to be imprecise. The divergence between the flow direction (measured at A_1) and the TEC yaw angle is depicted in Figure 5.14 and diagrammatically illustrated in Figure 5.15.

The resulting error in the SB-ADP measuring the velocity upstream of the TEC was corrected using Equation 5.4:

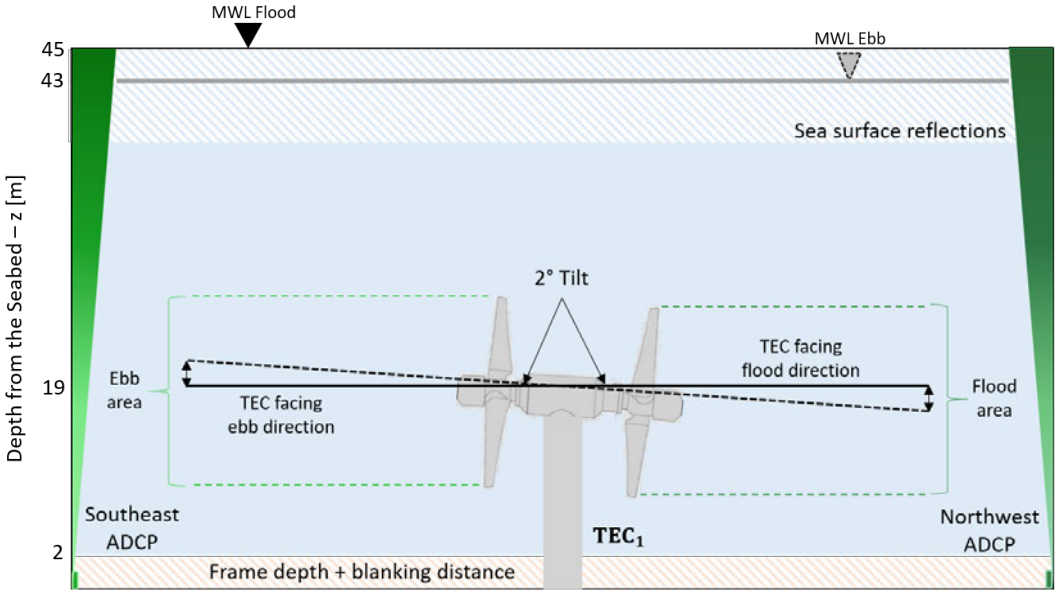

Figure 5.11: Flood and ebb areas used in the method of bins, where ADCPs A_1 (Northwest) and A_2 (Southeast) are used as an example. Turbine tilt included. Not to scale.

$$u_{\text{corrected}} = \frac{u_{\text{uncorrected}}}{\cos\alpha} \tag{5.4}$$

This correction used the flow direction calculated from the ADCPs located at A_1 for the inline and B_1 for the adjacent configuration and therefore was based on the assumption that the flow direction does not change on approaching the SB-ADP.

5.5 Instrument Uncertainty

In order to enhance the comprehensiveness of a TEC power curve, it is imperative to incorporate an assessment of the associated measurement uncertainties. When conducting a PPA, it is essential to furnish the uncertainty estimates, budgets, and expanded uncertainties for key measurable quantities pertinent to incident TEC power, output electrical power, and TEC performance metrics. This entails encompassing uncertainties that emanate from multiple facets including tidal resource measurement, electrical components, and data acquisition. The framework for uncertainty analysis should encompass a range of potential uncertainties encountered throughout the measurement campaign and the requisite minimum uncertainties to be included in the analysis are outlined in Figure 4.13.

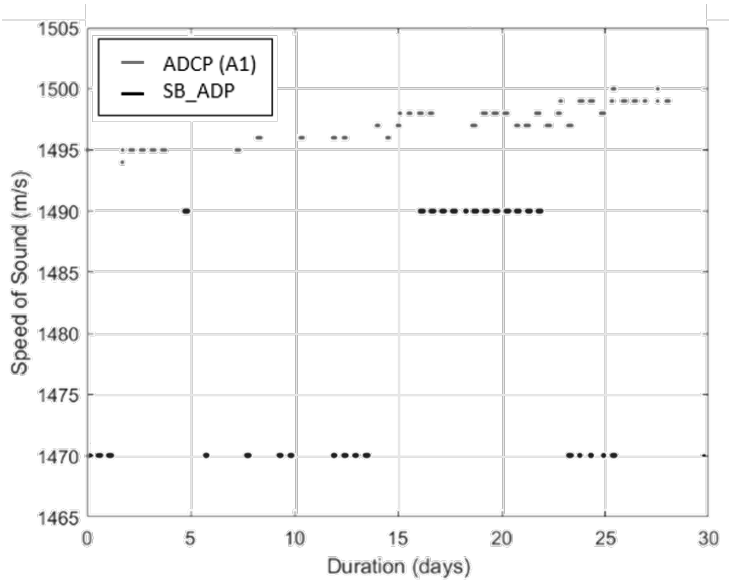

Figure 5.12: Comparison of the ADCP (A1 used for example) and the TEC rotor-mounted SB-ADP speed of sound during Deployment 5.

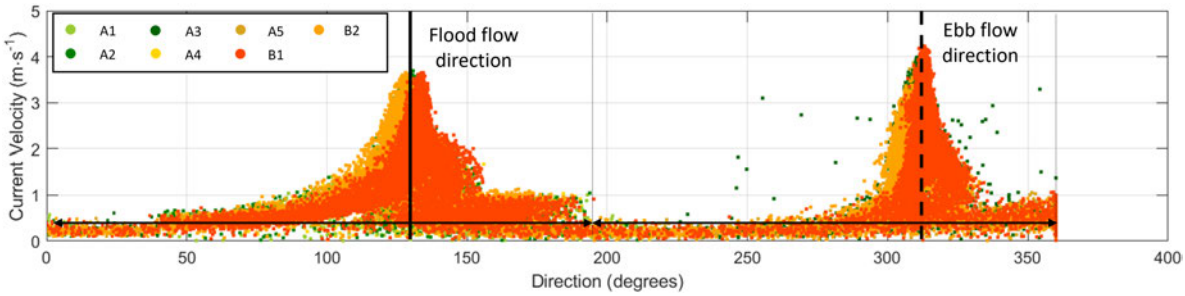

Figure 5.13: Variation in flood and ebb direction at seven individual locations in close proximity to the DEEP-Gen IV. DEEP-Gen IV aligned to $\approx 133^{\circ}$ and 312° for the flood and ebb tide respectively. ADCP locations are depicted in Figure 5.3.

5.5.1 Electrical Test Equipment

The principal measurands for the electrical test equipment are electrical phase currents and phase voltages. The measurement location is generally the generator terminal or the Point of Common Coupling (PCC). As the electrical equipment performance was out of the scope of this project, the relevant references included in the IEC TS 62600-200 are included. The following quantities should be derived:

- Active power (MW);
- Reactive power (MVar);
- Power factor;
- Frequency (Hz).

The determination of the TEC net electrical power should be predicated on the measurement of current and voltage across all three phases of Alternating Current (AC). In instances where measurement is conducted for only two phases, the computational methodology should be explicitly outlined. In cases where the TEC is integrated into a network, the recorded voltage and frequency values should accurately reflect the conditions

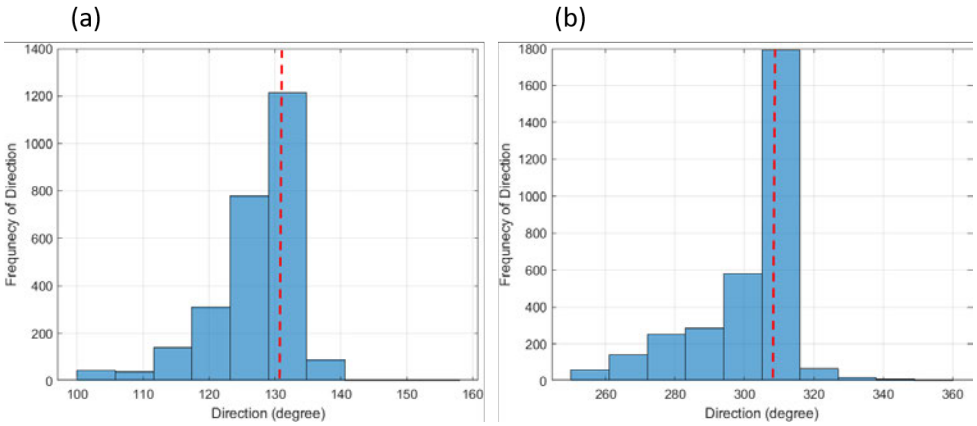

Figure 5.14: Histogram of the typical angle between flow direction and TEC yaw angle (red dashed line) for the (a) flood tides and (b) ebb tides.

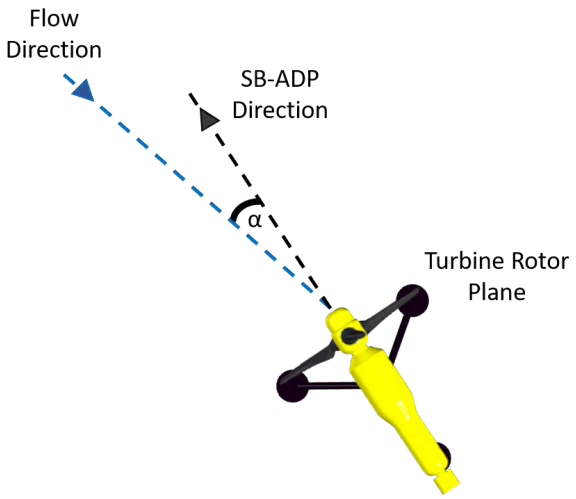

Figure 5.15: Plan view of the angle between flow direction and the DEEP-Gen IV yaw angle.

of the network at the measurement location. To ensure accuracy and reliability, the measurement instruments utilised must adhere to a classification of at least 0.5 (accuracy class of the measurement instruments, indicating that their measurement errors must not exceed 0.5% of the full-scale value) or superior, and they should possess a calibration record that is traceable to the applicable standard:

- Current transformers IEC 61869-2 [353];
- Voltage transformers IEC 61869-3 [354];
- Power transducer IEC 60688 [355].

As a guide, the operating range of the power transducer shall be at least:

- Export: 5% to 200% of TEC rated power;
- Import: -5% to -50% of TEC rated power.

5.5.2 Uncertainty of Ancillary sensors

This section discusses the propagation of instrument uncertainty through various calculations, including the transformation of data from beam coordinates to Earth coordinates. It also details how this uncertainty is quantified through the calibration of the Doppler instruments. The uncertainty script is a MATLAB toolbox containing a collection of functions that are used to perform calculations, and create uncertainty values related to the sensors used encased within ADCPs to be included within uncertainty budgets in the industry. Figure 5.16 labels some of the uncertainties that have been combined to provide guidance on the propagation of uncertainty (full uncertainty chain depicted in Figure 4.13).

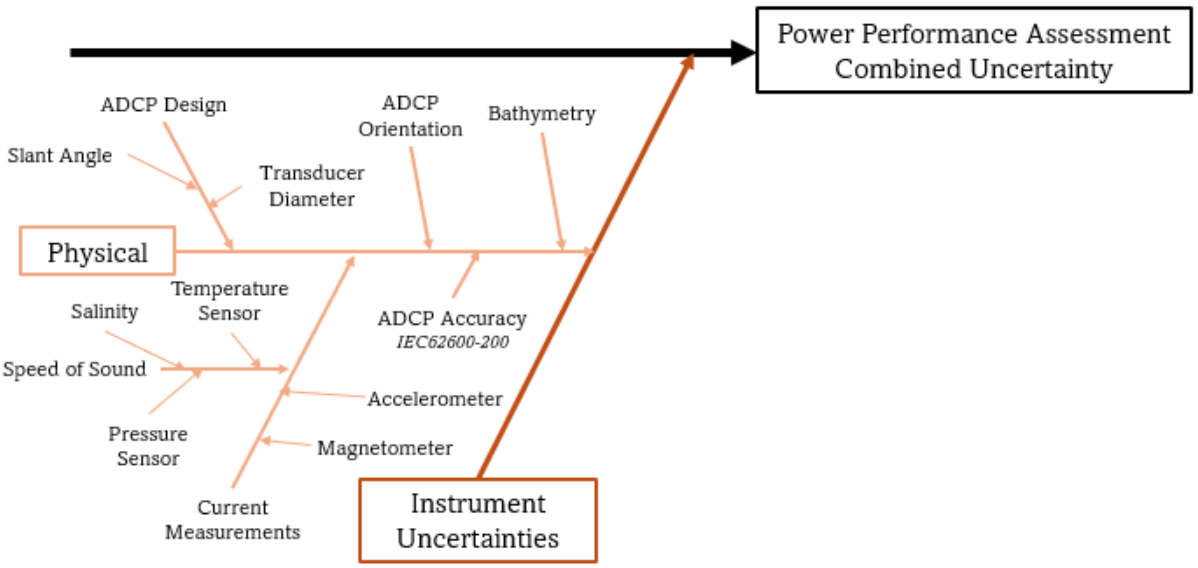

Figure 5.16: Contributors to uncertainty associated with the deployed instrument used to inform the power performance assessment.

The essential part of the uncertainty tool, is it contains the inputs for a specific deployment and will serve to provide accurate measures of uncertainty for the instrument used. The impact of the uncertainties within the individual ancillary sensors and their contributions to the system uncertainty were assessed for a Nortek 500 kHz 4 beam ADCP. The script produced is compliant to the guidelines of "Guide to the expression of uncertainty in measurement" [107].

Referring back to section 2.3.2, the coordinate transformation is described, here the uncertainty for the conversion is expressed. The maximum angular displacement from the ideal position is denoted $/Delta\ z$ and the radius of the transducer:

$$\tan\theta = \frac{\Delta z}{r} \tag{5.5}$$

$$\theta = \tan^{-1}\frac{\Delta z}{r} \tag{5.6}$$

The exact impact of the uncertainty of the Janus angle depends on the diameter of the transducer, meaning it is specific for each design. The tilt can however be in any direction, therefore the uncertainty "envelope" can be thought of as a cone extending outwards from the base of the transducer. A normal distribution with a coverage factor of 3 is therefore used, this gives a standard uncertainty as:

$$u_a = \frac{1}{3} tan^{-1} \frac{\Delta z}{r} \tag{5.7}$$

The beam angle will translate directly into the decomposition of the beam speed into horizontal and vertical components. Given an inbound velocity v_{ri}, where i notes the beam number and v is the shift in velocity along the beam axis, the instrument body velocity (assumed to be zero) can be found from:

$$v = T \cdot v_r \tag{5.8}$$

where T is the transformation matrix expressed in Table 2.2. In which a_i, for the i'th beam is:

$$\alpha_i = \alpha_j + u_\alpha \tag{5.9}$$

where α_i is the Janus angle, also sometimes referred to as the slant angle, and u_α is the uncertainty related to the transducer mounting angle. Since all the heads are inspected at the supplier before shipment, 99.73% confidence is assumed.

5.5.2.1 Pressure Sensor

Piezoresistive pressure sensors are commonly employed for pressure measurements. These sensors are adopted by manufacturers and are supplied with a characterised sensitivity and a calibrated linearisation. Pressure sensors are crucial for this work because they help determine the depth of the ADCPs, allowing us to accurately measure water currents at different depths. As an illustrative instance, the Keller piezoresistive pressure sensor, a component used in Nortek Signature ADCP series [356], can be considered. Illustrated in Figure 5.17, the +OUT and -OUT terminals are connected to an Analogue-to-Digital Converter (ADC), which transforms the voltage at the centre of the bridge into a digital format. After the signal has undergone digital conversion, it is presumed to remain constant without introducing additional uncertainties.

The pressure sensors specification indicates a potential measurement error of 0.25%, as detailed in Table 5.7 [356]. This interpretation signifies that the measurement error is consistently 0.25% or less of the sensors full range. Given that these sensors undergo testing before being dispatched to Nortek, it is reasonable to consider a 99.73% confidence interval (3σ). Consequently, this results in a standard uncertainty of:

$$u(p) = \frac{0.25 \cdot R_p}{3}$$

where: $u(p)$ represents the standard uncertainty for the pressure sensor, R_p is the nominal resistance for the pressure sensor. R_p has a nominal value of 453Ω with a tolerance of $\pm$0.1% which translates to $\pm$0.453Ω.

The variance is found to be $\frac{a^2}{3}$, therefore the standard uncertainty becomes:

$$u(p) = \frac{0.453}{\sqrt{3}} = 0.261\Omega$$

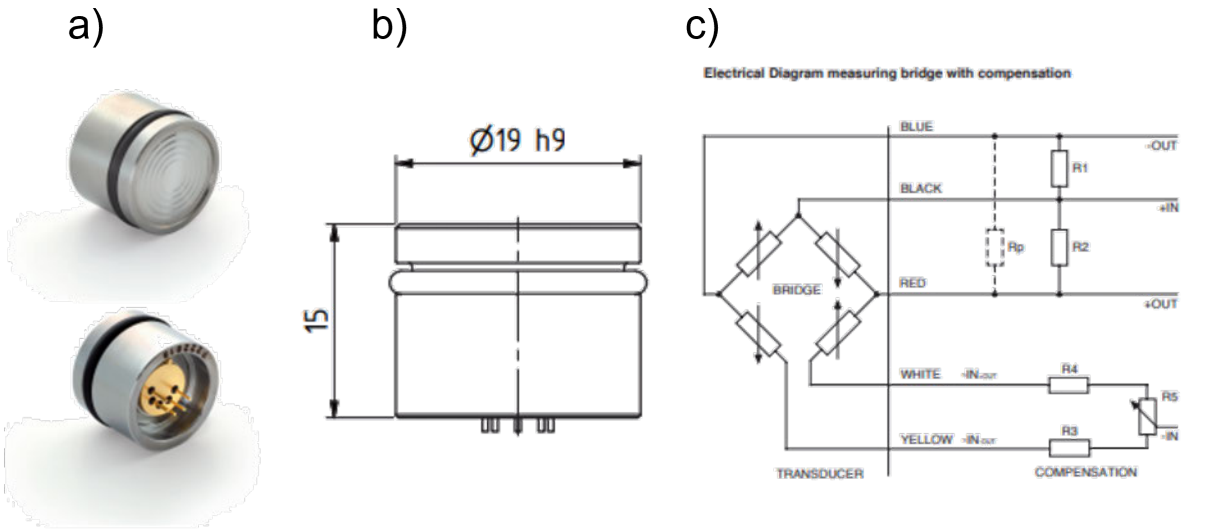

Figure 5.17: Keller piezo resistive pressure sensor. (a) 10L series design (b) Sensor dimensions. (c) electrical diagram measuring bridge with compensation.

Table 5.7: Pressure sensor datasheet accuracy.

Accuracy	$\pm$ 0.25 %
Long Term Stability	$\pm$ 0.15 %
Dimensions	ϕ 19 mm by 15 mm
Temperature Range	-40:125 $^{\circ}C$

5.5.2.2 Temperature Sensor

Nortek ADCPs employ Negative Temperature Coefficient (NTC) thermistors as temperature sensors. The data sheet does not explicitly provide their inaccuracy but rather defines it implicitly as being better than 0.1°C. This implies a rectangular distribution, and considering the units are screened, it is reasonable to adopt a 99.7% confidence interval. Given that the thermistor operates in conjunction with other analogue components, it's important to consider its baseline accuracy cautiously. However, it's crucial to include the uncertainty associated with the other analogue components engaged in the circuit prior to the signal's digitisation. The sensor's output is expressed by the supplier through the following equation, referencing the R16 (high-precision resistor screened at the factory before shipment).

$$T = \frac{1}{a + b log_{10}\frac{Rt}{R_{16}} + c(log_{10}\frac{R_t}{R_{16}})^2 + (log_{10}\frac{R_t}{R_{16}})^3} - 273$$

Assuming a rectangular distribution with a stated tolerance of 0.1% for $R16$ with a nominal value of 10 kΩ, the variance is $\frac{a^2}{3}$, therefore the following equation is employed for the standard uncertainty of the temperature sensor:

$$u(t) = \frac{0.1 \cdot 10,000}{\sqrt{3}} = 5.77\Omega$$

5.5.2.3 Tilt Sensor

Nortek utilises low-frequency accelerometers manufactured using Micro Electromechanical Systems (MEMS) technology. The tilt sensor employed by Nortek is subjected to validation. Prior to shipping, each sensor undergoes a characterisation process, which is carried out in the following manner:

- The sensor is positioned within a custom-designed rotary table utilising a fixture that precisely aligns the axis of rotation with the accelerometers position.
- The rotary table is then oriented to ensure its upper surface is within 0.05° of horizontal, employing a Digi-pas leveller.
- For systems in which accuracy is influenced by resolution, the standard variance is $\frac{a2}{12}dx$, where dx represents the step resolution, giving rise to a rectangular distribution and a standard uncertainty as follows:

$$u_{a_{init}} = \sqrt{\frac{dx^2}{12}} = \frac{0.05}{\sqrt{12}}$$

- Subsequently, the sensor is incrementally tilted within the range of $\pm$ 30°, and output readings are captured from both the rotary table and the instrument's accelerometer.
- The angular position of the rotary table is determined via a decoder on the step motor responsible for its control, with a resolution of 360/10000. This leads to an angular uncertainty given by:

$$u_a = \frac{0.036}{\sqrt{12}}$$

The combined uncertainty is obtained by adding the initial uncertainty of the rotary table to the uncertainty arising from the encoder resolution. This characterisation is carried out under room temperature conditions because the uncertainty can increase with different operating temperatures (typically, manufacturers provide specifications for temperature-related uncertainty changes (e.g., ±0.01% ℃)). In the FoW, where temperatures can vary widely, the uncertainty could increase by approximately 0.2% due to temperature induced changes in material dimensions and electronic component behavior. The remaining standard uncertainty is determined as follows:

$$u_{a_{tot}} = \sqrt{u_{a_{init}}^2 + u_a^2} = 0.017^\circ$$

5.5.2.4 Magnetometer

Nortek employs a Honeywell 3-axis digital compass IC HMC5983. The magnetometer outputs the magnitude of the magnetic field along the three axes (x, y, z). It's important to note that the compass data isn't used in calculating water speed. The specified inaccuracy is 2°. The validation of performance is assumed to involve normal distribution and factory screening. As a result, a 99.7% confidence level is adopted, leading to a variance of $\frac{a^2}{9}$. Consequently, the standard uncertainty is 2/3, in accordance with the manufacturer's datasheet.

5.5.3 Propagation of Uncertainty

To compute the magnitude of velocity, both velocity components are obtained by taking the square root of the sum of squared velocity components (u, v):

$$u_{mag} = \sqrt{u^2 + v^2}$$

When transforming the uncertainty to be proportional to the magnitude, a crucial rule comes into play: if the quantity x is measured with an uncertainty θx, and the measured value is employed to calculate the power $q = x^n$, the fractional uncertainty in q becomes n times that in x.

$$\frac{\theta q}{|q|} = n\frac{\theta x}{|x|}$$

Therefore the uncertainty will follow the equation expressed below:

$$\theta u_{mag} = \sqrt{\left(\frac{u\theta u}{u_{mag}}\right)^2 + \left(\frac{v\theta v}{u_{mag}}\right)^2}$$

he inputs to the MATLAB tool is depicted in Figure 5.18, where HT is the head tolerance of the transducers, TD is the transducer diameter, Aj is the angle of beam (Janus configuration used for 4 beam), dp is the Doppler shift, the pressure and temperature uncertainty is in percentage (%), and the magnetometer reading from the deployment area along with the accelerometer data (x, y, z). The inputs are gathered from the specific deployment of the ADCP (predominately averages).

The inputs are passed through the model along with the beam speed measurements from the specific deployment - where the transformation and propagation of uncertainty (based on the described formulas outlined in section 2.5.3) is carried out - the model then provides the mean and maximum uncertainty associated with different velocity bin edges (which are defined as per tidal site characteristics), see Table 5.19

5.6 Turbine Specification: Operational Characteristics

Alstom deployed the DEEP-Gen IV 1 MW tidal turbine, as illustrated in Figure 5.20, at the EMEC test site within the framework of the ReDAPT project. This turbine is a bottom-mounted, pitch-regulated, variable-speed design featuring three blades. It features a rotor diameter of 18 m and a hub height of 19 m above the seafloor. Additional essential parameters can be found in Table 5.8. The turbine commonly underwent yawing between flood and ebb tides, essentially rotating during slack tides. This yawing ensured that the energy extraction plane was perpendicular to the predominant flow direction, known as the principle flow direction. For the ensuing chapters, the DEEP-Gen IV turbine will be denoted as TEC_{T1}.

To evaluate the influence of vertical misalignment on power performance metrics, we introduce two additional turbine configurations designated as TEC_{T2} and TEC_{T3}. Unlike the DEEP-Gen IV (TEC_{T1}) which relied on measured power, TEC_{T2} and TEC_{T3} employ modelled power data. These turbines, representative of horizontal axis tidal turbines, are situated at distinct depths within the water column, as depicted in Figure 5.21.

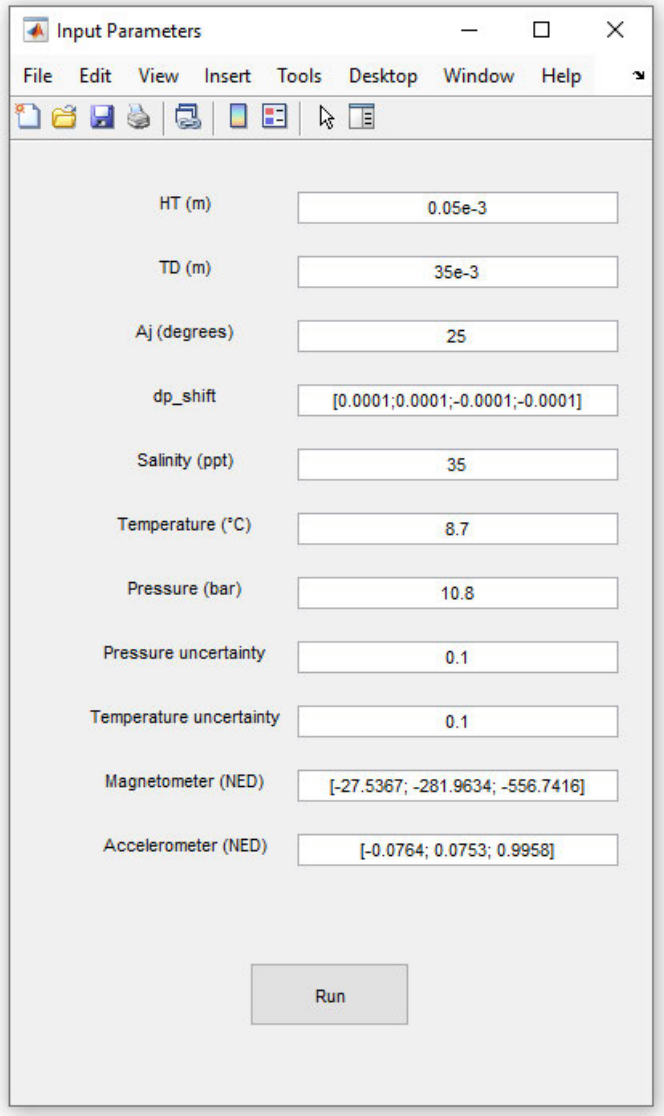

Figure 5.18: Input characteristics for the calculation of the combined uncertainty per ADCP deployment.

These configurations draw from insights gained through the RealTide project [357], and their fundamental characteristics are outlined in Table 5.9. Here, z denotes the hub height of each turbine above the seabed, while C-S signifies the cross-sectional area of their respective rotors. By considering three turbines with varying degrees of shear within the water column, we can evaluate the effects of vertical misalignment between the instrument and TEC hub-height.

Bin edges	Mean Uncertainty	Maximum Uncertainty	Bin edges	Mean Uncertainty	Maximum Uncertainty
0.1	0.0000715	0.0001447	2.4	0.0033557	0.0034619
0.2	0.0002229	0.0002927	2.5	0.0035421	0.0036746
0.3	0.0003626	0.0004249	2.6	0.0036684	0.0038247
0.4	0.0005029	0.0005663	2.7	0.0038118	0.0039852
0.5	0.0006427	0.0007116	2.8	0.0039664	0.0041096
0.6	0.0007995	0.0008844	2.9	0.0041876	0.0042740
0.7	0.0009423	0.0010498	3	0.0043399	0.0044447
0.8	0.0010965	0.0011548	3.1	0.0043925	0.0044852
0.9	0.0012145	0.0012750	3.2	0.0045834	0.0047556
1	0.0013702	0.0014698	3.3	0.0047506	0.0049945
1.1	0.0015192	0.0015891	3.4	0.0048798	0.0051307
1.2	0.0016894	0.0017819	3.5	0.0049424	0.0050743
1.3	0.0017989	0.0019584	3.6	0.0050983	0.0052929
1.4	0.0019566	0.0020248	3.7	0.0053649	0.0055883
1.5	0.0021131	0.0022362	3.8	0.0053773	0.0054955
1.6	0.0022501	0.0023039	3.9	0.0055439	0.0057552
1.7	0.0023598	0.0024703	4	0.0056826	0.0058313
1.8	0.0025062	0.0026251	4.1	0.0058723	0.0060734
1.9	0.0026771	0.0027701	4.2	0.0060824	0.0062794
2	0.0028117	0.0029789	4.3	0.0061109	0.0064339
2.1	0.0030085	0.0031373	4.4	0.0062551	0.0064937
2.2	0.0031022	0.0032150	4.5	0.0064989	0.0068308
2.3	0.0032640	0.0033739			

Figure 5.19: Average and maximum expected uncertainty per velocity bin - from the in house ancillary sensors. Note this does not account for all uncertainties external to the ADCP.

5.7 Turbine Specification: Power Curve

This section elucidates the data utilised for the subsequent power curve generation. In instances where actual TEC power data is not accessible, the power curve provided by Alstom (Appendix 1 10.1) is employed for the DEEP-Gen IV, utilising the flow velocities recorded by the corresponding seabed-placed ADCPs. It's important to note that Section 8.3 of the IEC TS Guidelines [30] stipulates the collection of data across a minimum of 15 days to encompass a spring-neap cycle, with a maximum allowable duration of 90 days.

Furthermore, data availability over the test period should exceed 80%. Data is exclusively presented on the power curve when the minimum power exceeds zero. The division into flood and ebb datasets is predicated on the flow direction. For instance, flood data is selected when the flow speed of the seabed placed ADCPs is positive, whereas ebb data is chosen when the flow speed is negative. The calculated time for flood or ebb instances is presented for each case study (1-3) in Table 5.10.

It's worth noting that the IEC TS guidelines [30], Section 8.7, outline that the velocity range should span from 50% of cut-in velocity (i.e., 0.5 m·s^{-1} for TEC$_{T1}$) to 120% of rated velocity (i.e., 3.25 m·s^{-1} for TEC$_{T1}$). Furthermore, each velocity bin should encompass a minimum of 30 minutes of data, and the complete dataset should cover 180 hours. The power and velocity measurements for the actual measured power curve of the Alstom DEEP-Gen IV 1 MW TEC are tabulated and provided in Appendix 1 (Figure 10.1).

Figure 5.20: Alstoms DEEP-Gen IV 1 MW tidal turbine, deployed for seven separate measurement campaigns over 4 years (Jan 2011 to Jan 2015).

Table 5.8: Key parameters of the DEEP-Gen IV TEC.

Description	Units	TEC_{T1} spec
Type	-	3-Blade HATT
Foundation	-	Piled tripod
Production year	-	2011
Distance above seabed	m	18 (hub-height)
Blade radius	m	9
Projected capture area	m^2	256.74
Rated output power	MW	1
Cut-in	$m{\cdot}s^{-1}$	1
Rated speed	$m{\cdot}s^{-1}$	2.7
Nominal rotor speed	rpm	13.78
Maximum rotor speed	rpm	19.29

The measurement campaigns utilised for case studies 1-3 encompassed periods where the DEEP-Gen IV did not generate power or displayed inconsistent power generation. This resulted in a reduced amount of comparable data. Consequently, during periods of no TEC power, power was computed using the published power curve furnished by Alstom (for TEC_{T1}). Each velocity measurement was assigned an active power value from the predefined power curve for the DEEP-Gen IV 1 MW TEC (Appendix 1 Fig 10.1) [154]. Additionally, two distinct power curves were generated to simulate power production for the 0.25 MW (TEC_{T2}) and 2 MW (TEC_{T3}) turbine concepts. Figure 5.22 visually represents the theoretical power curves for each TEC in this project, where TEC_{T2} is anchored in real-world power data. The methodology employed to compute power for TEC_{T1} and TEC_{T3} is elucidated in Equation 5.10:

$$P_{\text{active}} = P_{\text{rated}} \cdot \left(\frac{U^2 - U_{ci}^2}{U_r^2 - U_{ci}^2} \right) \tag{5.10}$$

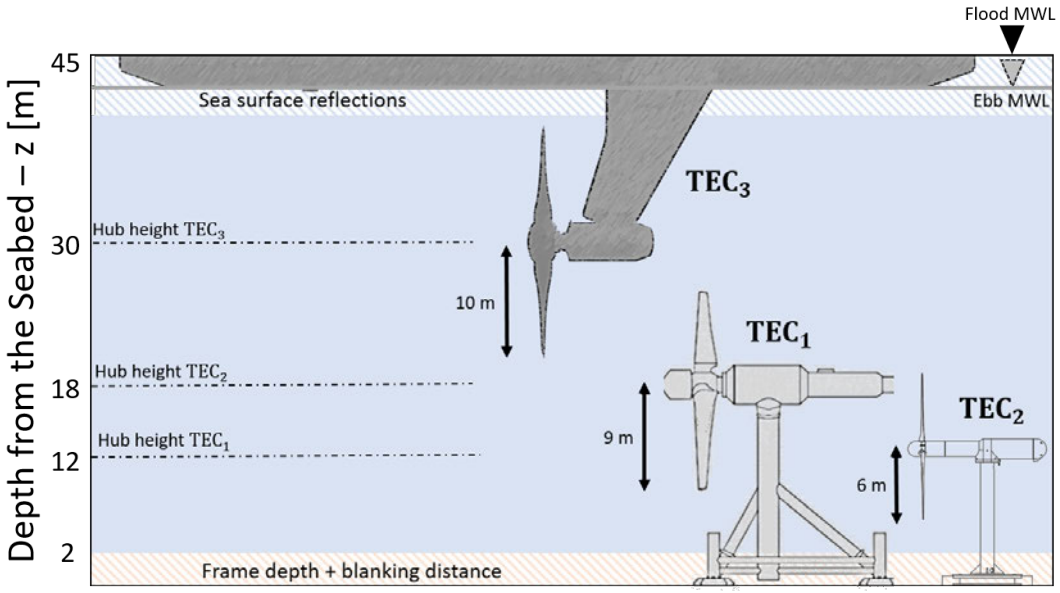

Figure 5.21: Vertical position of TEC$_{T1}$, TEC$_{T2}$ and TEC$_{T3}$ in the water column.

Table 5.9: Generic types of tidal energy converter parameters.

TEC Characteristics	Units	TEC$_{T2}$	TEC$_{T3}$
z	m	12	34
Rotor Diameter	m	12	20
C-S Area	m^2	113.1	314.2
Rated Power	MW	0.25	2
Cut-in	m·s^{-1}	0.75	1.2
Rated velocity	m·s^{-1}	1.8	3.1
Cut-out	m·s^{-1}	3.5	4.5

z: Hub-height reference above the seabed;
C-S: Cross-sectional area of the rotor;

where P_{rated} is the predefined rated power, U is the in-situ velocity measurement from the instrument used in m·s^{-1}, U_{ci} is the cut-in velocity for the proposed TEC, and U_r is the rated flow velocity for peak power production. Velocity measurements that fall beneath the cut-in are rejected, and above the rated are equal to the rated power defined.

Subsequently, the PWRA technique is employed to compute the power for the two bottom-fixed TEC concepts (as the upper depth bins lacked sufficient data to facilitate this approach, thus the hub height value was used as a reference) by applying Equation 2.51. This method was coupled with the corresponding power output. The subsequent procedures were executed using the bin methodology:

1. Calculate the instantaneous PWRA velocity, using Equation 2.51, where $\hat{U}_{i,j,n}$, is the instantaneous PWRA flow velocity, A_k is a profiler bin over the swept area of the TEC and $U_{i,j,k,n}$ is the velocity in the relative instrument depth bin, see Figure 5.23 for visual representation.
2. Calculate the mean value of the velocity, $\bar{U}_i$ and the respective data sources (TEC power), $\bar{P}_{\text{active},i}$ as,

Table 5.10: Overview of sampled data used for power curve creation, shown as a percentage of the total amount of the data-sets.

case study 1	26	Days	
A_1, A_2	Flood	Ebb	Total
Tide by ADCP direction	46%	53%	99%
Time at slack (U $<$ 0.5 m·s^{-1})	11%	13%	24%
Minimum Power $>$ 0	11%	14%	25%
Minimum Power $>$ 0 + Slack	23%	26%	50%
case study 2a	15	Days	
A_1, A_2, C_1, C_2			
Tide by ADCP direction	53%	46%	99%
Time at slack (U $<$ 0.5 m·s^{-1})	14%	11%	25%
Minimum Power $>$ 0	14%	12%	26%
Minimum Power $>$ 0 + Slack	25%	23%	48%
case study 2b	57	Days	
B_1, B_2, C_1, C_2			
Tide by ADCP direction	51%	48%	99%
Time at slack (U $<$ 0.5 m·s^{-1})	12%	13%	25%
Minimum Power $>$ 0	12%	13%	25%
Minimum Power $>$ 0 + Slack	24%	26%	50%
case study 3	32	Days	
A_4, A_5			
Tide by ADCP direction	50%	50%	100%
Time at slack (U $<$ 0.5 m·s^{-1})	12%	13%	25%
Minimum Power $>$ 0	13%	12%	25%
Minimum Power $>$ 0 + Slack	25%	25%	50%

$$\bar{U}_i = \left[\frac{1}{N_i} \cdot \sum_{n=1}^{n_i} \cdot \hat{U}_{i,n}^3] \right]^{\frac{1}{3}} \tag{5.11}$$

Where N_i is the number of samples in the defined averaging period which produces data point n.

$$\bar{P}_{\text{active},i} = \frac{1}{N_i} \cdot \sum_{n=1}^{n_i} \cdot \bar{P}_{\text{active},i,n} \tag{5.12}$$

3. Sort values into the corresponding flow velocity bins - increments of 0.1ms^{-1}.

The list of flow current velocity parameters used throughout this work is shown in Table 5.11

The energy production can be estimated from available time series power data (produced using the flow velocities from each instrument). This will be derived via the trapezoidal method, which computes the approximate power integral. The energy can then be multiplied by the deployment campaign's ratio to the year's length, see the following Equation 5.13:

$$\text{AEP} = R \cdot \Sigma_{t1}^{t2} \cdot \bar{P} dt \tag{5.13}$$

where: AEP is the expected AEP, in MWh, R is the ratio of the number of days a year over the duration of the deployment, $\bar{P}$ is the mean calculated TEC power, t_1 is the index number defining the time start, and t_2 is the index number of the end time interval.

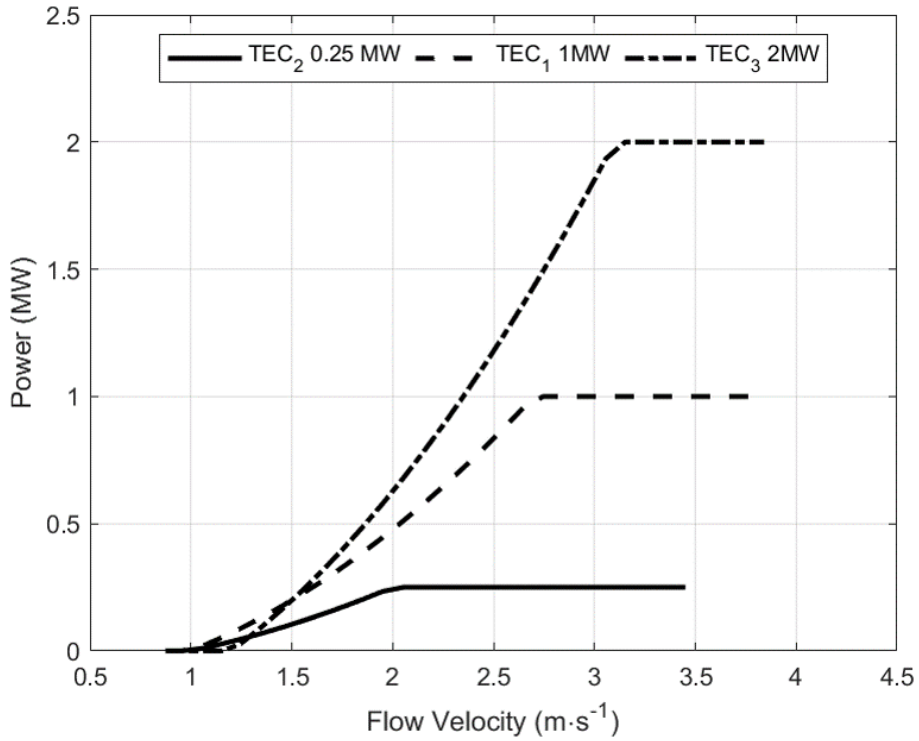

Figure 5.22: Therotical power curve for the three TEC concepts used in the project where the DEEP-Gen IV 1 MW TEC is based on real-world power and TEC_{T1} and TEC_{T3} are based on modelled data.

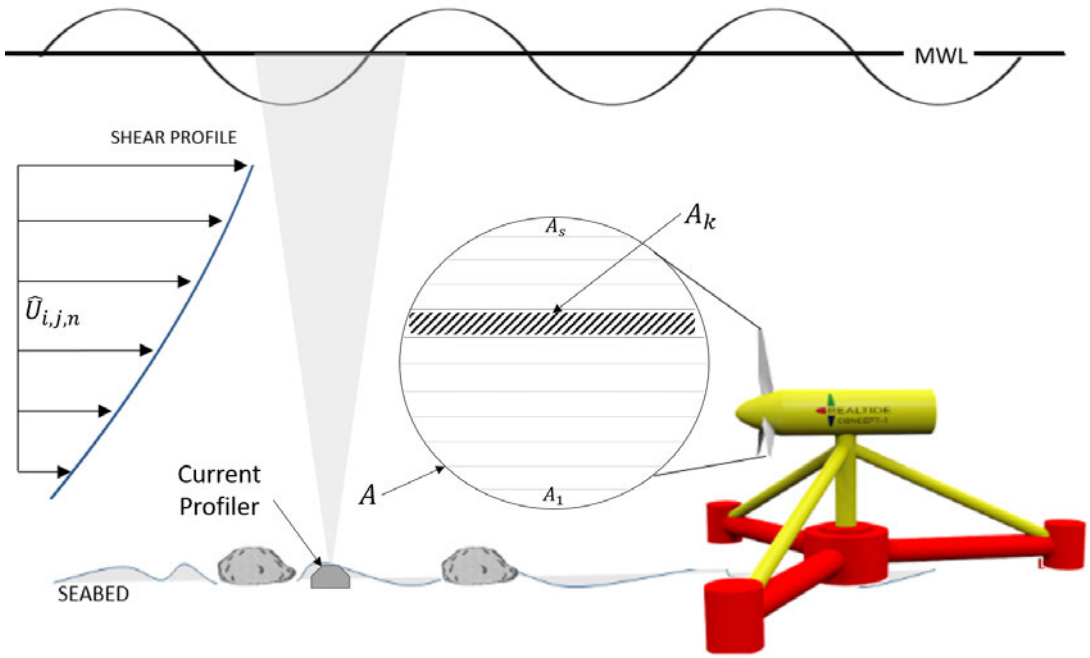

Figure 5.23: Power weighted rotor average velocity example.

Table 5.11: Flow current parameter list.

Instrument Location	Streamwise Component ($m \cdot s^{-1}$)	Magnitude ($m \cdot s^{-1}$)	Instantaneous PWRA ($m \cdot s^{-1}$)	Average PWRA ($m \cdot s^{-1}$)
A_1	u_{A1}	U_{A1}	$\hat{U}_{A1}$	$\bar{U}_{A1}$
A_2	u_{A2}	U_{A2}	$\hat{U}_{A2}$	$\bar{U}_{A2}$
A_3	u_{A3}	U_{A3}	$\hat{U}_{A3}$	$\bar{U}_{A3}$
A_4	u_{A4}	U_{A4}	$\hat{U}_{A4}$	$\bar{U}_{A4}$
A_5	u_{A5}	U_{A5}	$\hat{U}_{A5}$	$\bar{U}_{A5}$
B_1	u_{B1}	U_{B1}	$\hat{U}_{B1}$	$\bar{U}_{B1}$
B_2	u_{B2}	U_{B2}	$\hat{U}_{B2}$	$\bar{U}_{B2}$
C_1	u_{C1}	-	-	-
C_2	u_{C2}	-	-	-

Chapter 6

Cross-talk Between Multiple Acoustic Instruments Measuring Concurrently

6.1 Chapter Overview

The use of ADCPs as part of arrays of acoustic sensors provides potential advantages over single sensor deployments in flow characterisation work. One problem that can frequently occur when deploying multiple acoustic instruments in close proximity is cross-talk. This occurs when pulses interact with each other, resulting in unwanted consequences. In order to use multiple sensors in close proximity the effects of cross-talk must be understood so that they can be: identified, predicted and mitigated. Cross-talk is a prevalent occurrence where a transmission system's signal emitted on one channel has an unwanted effect when received by another channel. It is known that the acoustic pulses from sub-sea Doppler sensors interact, but the degree of interaction varies depending on the pulse frequency, sensor angle, separation, water depth and turbidity. This chapter explores this phenomenon through an examination of echo amplitude and flow velocity before identifying and removing the corrupted measurements as part of the quality control process. Furthermore, the study aims to detect measurement interference and subsequently assess its impact on both the measured power curve and annual energy estimates.

This chapter is structured as follows: Section 6.2 introduces the method used to split the data set into flood and ebb flow measurements. Section 6.3 introduces cross-talk between co-located acoustic instruments; Section 6.4 outlines the identification of interference; while Section 6.5 presents the consequences of interference of performance metrics of an operational TEC and two further theoretical variants; The detection algorithm is outlined in Section 6.6, and a plausible treatment that can be applied to remaining gaps in the data after the removal of interference features is presented in Section 6.6.1. Section 6.7 discusses the results with the key findings outlined in the conclusion Section 6.8.

6.2 Flood and Ebb Conditions

When analysing ADCP data, it is common to categorise the data into flood flow and ebb flow phases, with an additional consideration for slack tide conditions. These categories can be distinguished using various methods such as the direction of flow, slack tide velocities, or water acceleration.

- Firstly, the flood tide is the period when the tide is rising, and water is flowing inland from the sea. The flood flow is characterised by water moving in the direction of the incoming tide, typically towards the coast or up an estuary.
- Secondly, the ebb tide is the period when the tide is falling, and water is flowing back out to the sea. The ebb flow is characterised by water moving away from the coast or down an estuary.
- And lastly the period of slack water refers to the period of relatively still water occurring at the turn of the tide. During slack tide, the velocity of the water flow is minimal as the direction of the tide is changing. It occurs at the transition between flood and ebb tides.

When splitting the data into the respective flood and ebb data sets different methods can be utilised, these are:

- By monitoring the direction of water movement, the data can be categorised as flood flow (inland movement) or ebb flow (seaward movement).
- During slack tide, the velocities are close to zero, marking the transition between the flood and ebb phases.
- Changes in water acceleration can also indicate transitions between flood and ebb tides, with minimal acceleration corresponding to slack tide.

The acceleration method was used to split the data set in this chapter. This method provides a sophisticated approach to distinguish between flood and ebb tides by calculating the rate of change in water velocity over time. During flood tide, acceleration values will generally be positive as the water speed increases inland, while during ebb tide, the values will be negative as the water speed increases seaward. The slack tide, characterised by minimal or near-zero acceleration, indicates the transitional period where the flow direction changes and water velocity stabilises before reversing. By precisely identifying these changes in acceleration, the data was accurately segmented into flood and ebb phases.

6.3 Cross-talk - Data Featuring Interference Characteristics

To address the objectives of this project, in-situ data was required. Data from the ReDAPT project was chosen as a rich data resource (with unique multi-sensor deployments at a tidal energy site) that was available through the ReDAPT data exchange. This work forms an entirely new investigation - targets a not-previously investigated research question - focusing on data obtained from instruments placed at locations A_1 and A_2 as outlined in Section 5.3 (see Table 5.1) to assess the impact of measurement bias from features of cross-talk.

Figure 6.1 depicts the uncertainty chain related to the flow characteristics (full uncertainty chain depicted in Figure 4.13). Uncertainties associated with interference, ADCP placement, and the depth bin of the ADCP/interference features, are focused on in this chapter. These elements, in accordance with IEC62600-200 standards, play a critical role in the accurate assessment of power performance. Understanding and mitigating these uncertainties are essential for enhancing the reliability of power performance assessments in marine energy systems.

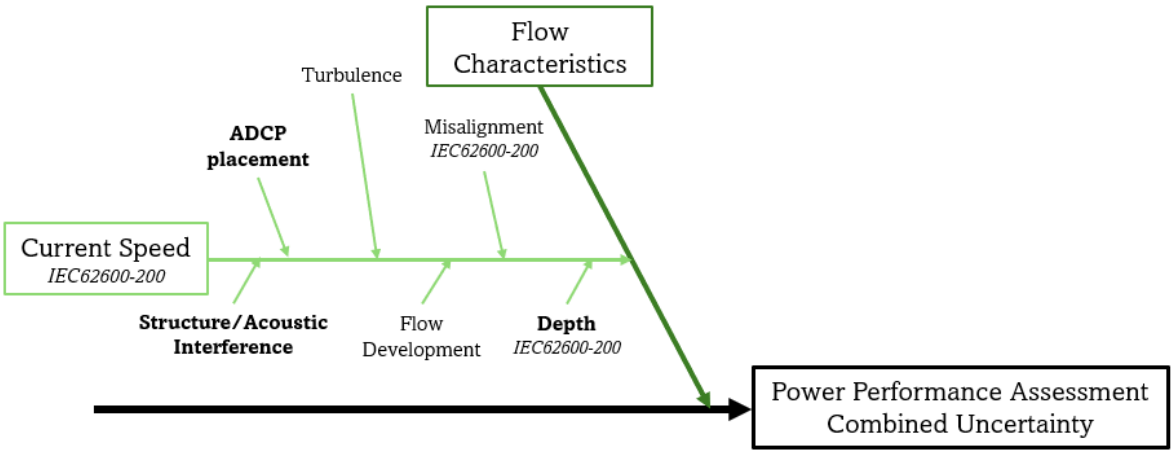

Figure 6.1: Contributors to uncertainty associated with the placement of multiple ADCPs and potential interference features in the measurements used to inform the uncertainty in a power performance assessment.

Doppler technology-based instruments use frequency shifts in transmitted and received signals to estimate flow current. These signals are received from water-borne particulates' backscattering. ADCPs sample the water column remotely over ranges/depths of tens to hundreds of meters without interfering with fluid flow. A former comparison study of two seabed-placed ADCPs separated by 45 m was carried out at the Fall of Warness in the Orkney Islands. This study aimed to assess the spatial variation in velocity between two locations (61 m and 106 m upstream of the DEEP-Gen IV) to inform the IEC TS 62600-200 on instrument placement. The single-ping data collected from these two ADCPs revealed the presence of interference. The interference is shown to contaminate the measurements of echo amplitude and flow velocity. This would result in a variation in the measured power curve if not removed prior to carrying out a PPA.

This chapter focuses on in-situ measurements obtained in July 2014 by two co-located ADCPs A_1 and A_2 as shown in Figure 5.4 and Figure 5.3. The data sets are presented in detail in Figure 6.2, where the streamwise velocity component (Fig 6.2a), velocity magnitude (Fig 6.2b), and flood tide data set with the difference between the two co-located instruments (Fig 6.2c) is shown.

One of the possible effects of cross-talk is that two sending and receiving sensors will measure the same flow component but receive the reflection meant for the other instrument. As the ADCPs were of the same configuration the pulse transmitted is identical across the instruments. Therefore, both ADCPs are able to process the signal of the neighbouring instrument's signal as it would its own. One commonly used method is to control timing/triggering [74, 122]. Due to operational constraints at the site, triggering was not controlled on this data set under study. Using triggering to mitigate these issues was not viable due to the complexity of synchronisation, increased power consumption, operational overhead, and potential data gaps in the short time frame this deployment was planned and deployed.

Vertically mounted sensors present a special case in cross-talk analysis in sub-sea acoustic sensors. When an acoustic pulse reaches a change of medium, there is a very strong reflection. This means that even horizontally mounted sensors may experience interference from vertically mounted sensors if the range of the instruments permits it. Figure 6.3 shows a high-level example of this process for two seabed-placed ADCPs separated by

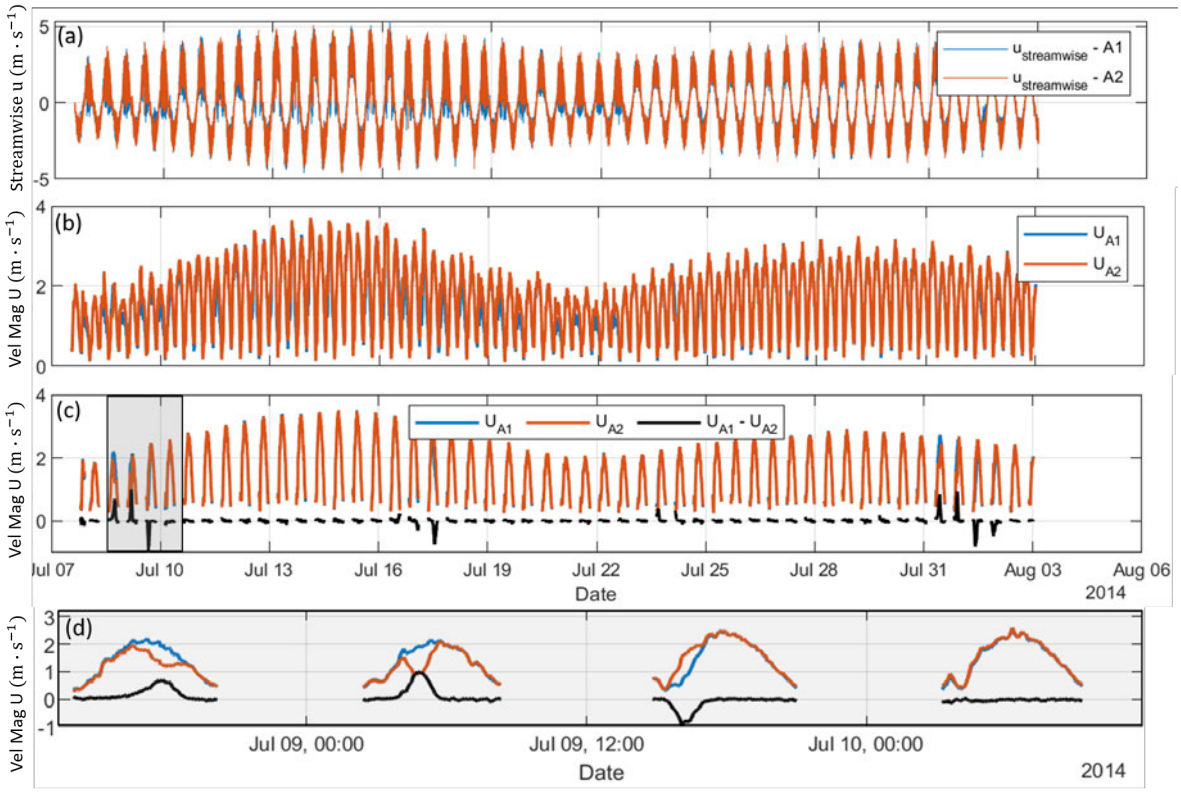

Figure 6.2: Data obtained from two ADCPs positioned upstream from the DEEP-Gen IV turbine at a distance of 61 m (A_1) and 106 m (A_2). (a) Instantaneous streamwise flow speed. (b) Averaged (5 minute) velocity magnitude. (c) Flood tide measurements with periods of a large difference between the two close-proximity ADCPs (black spikes), the grey box outlines a section of data that is zoomed into. (d) Zoom in to the flood tide measurements from ADCP$_{A1}$ and ADCP$_{A2}$ that feature interference characteristics.

45 m. It shows that the signal from the source sensor reaches the measurement column, and part of the pulse is reflected at an angle [67]. This reflected pulse will experience a Doppler shift due to its interaction with the free-stream velocity, u. The frequency shift observed in the ADCP measurement is related to the angle between the two sensor beams, which bisects the angle of the reflected pulse.

For multi-instrument deployments, considering the distance between locally placed ADCPs is important due to beam spread over range, which can cause alike instruments to listen to each other. Beam spreading is represented as an increasing separation between beam sample locations with greater distance from the sensor. It's associated with a loss in echo intensity, where echo intensity is measured in dB. Objects inside the main lobe width can block the main lobe path and create beam distortion, and as a result, the entire measured depth profile may be affected.

The presence of interference when plotted as a contour image using parameters time, depth and velocity (or echo amplitude) presents itself as vertical, horizontal or diagonal lines. The interference is typically associated with a reduced flow velocity or increased echo amplitude measured by the instrument refer to Figure 6.4 for a visual representation of interference structures [358].

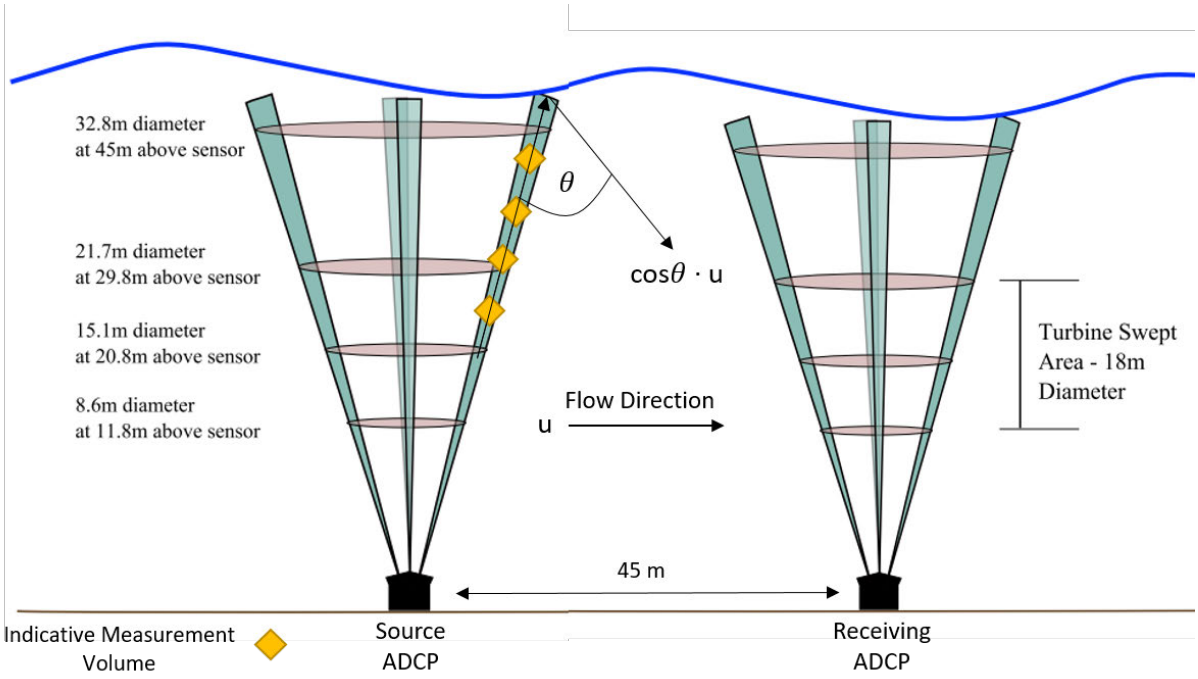

Figure 6.3: Illustration of the theory of two angled sensors measuring a component of the free stream velocity along the angle intersecting the two beams. NOTE the rhombus volumes represent the ADCP weighting as per user manuals where the depth cell is most sensitive to velocities at the centre of the cell.

The features of interference caused by other acoustic instruments can be seen in the data sets used in Figure 6.5. Shown in Figure 6.5 the four beams of ADCP$_{A2}$ featured data with characteristics of interference depicted as diagonal lines, most pronounced in beams 2 and 3. This indicates the interference originates in the direction of these beams (which is directly positioned toward ADCP$_{A1}$ as shown in Figure 6.6). However, beams 1 and 4 show signs of interference during the same period. This implies that the two beams (1 and 4) facing away from ADCP$_{A1}$ still receive some reflections of the transmission signals from ADCP$_{A1}$.

To assess the impact of interference on the measured power curve at different depths, two further horizontal-axis turbines are introduced, labelled TEC$_{T2}$ and TEC$_{T3}$ (Section 5.6) using modelled power (as opposed to measured power as was the case with the DEEP-Gen IV - TEC$_{T1}$). The turbines used for TEC$_{T2}$ and TEC$_{T3}$ are based on deployed variants of horizontal-axis turbines that occupy different regions in the water column. The depth bins used to calculate the PWRA velocity for each position of the three turbines stated above will be denoted as z_{T1}, z_{T2} and z_{T3} for the measurements between 6 - 18 m, 9 - 27 m and 20 - 40 m respectively.

Figure 6.6 illustrates the position, orientation and distance of A_1 and A_2 relative to the DEEP-Gen IV. The main lobe transmitted from the transducers is depicted as the solid beams, and the clearance zone is shaded and extended out a further 11° from the main lobe. In this Figure (6.6a), the zero along the vertical axis represents the first bin measured by the ADCPs (including the blanking distance of 2.08 m). The orientation of the two instruments was identified through the measured heading (for RDI WH instruments the main beam used to determine the heading is beam 3). Beam 4 faces 180° to beam 3, and beams 1 and 2 are at 90° and 270° to beam 3.

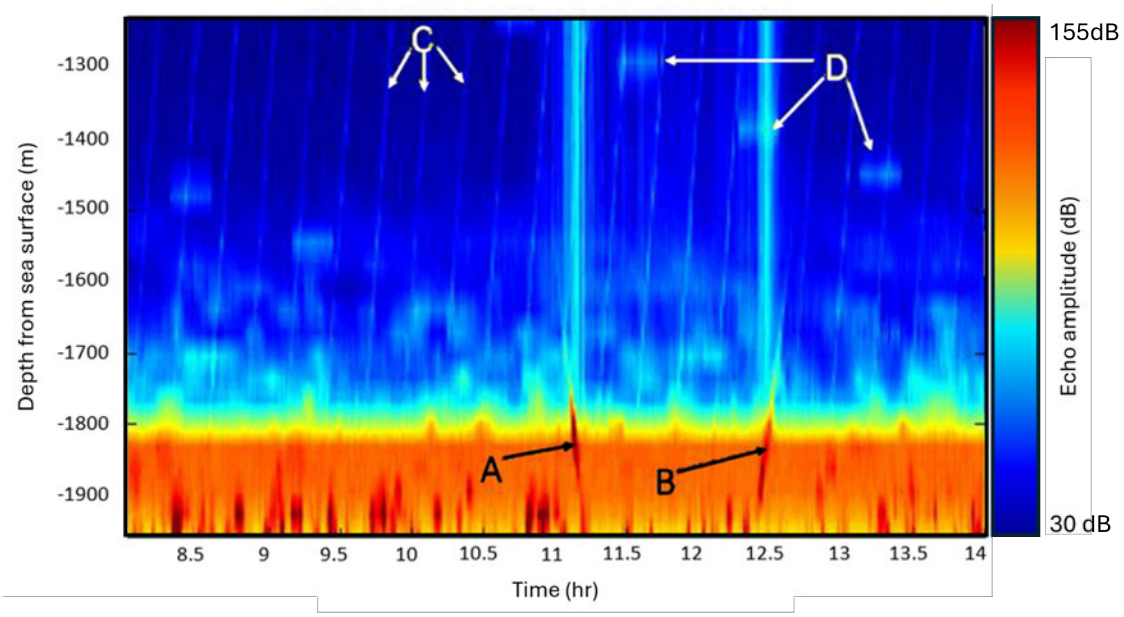

Figure 6.4: Example of seabed mounted ADCP echo amplitude measurements featuring interference characteristics, where A and B markers are strong vertical lines associated with the desent and as cent of a deployed remote-operated vehicle respectively. Markers C and D are diagonal and horizontal lines associated with interference from other acoustic instruments.

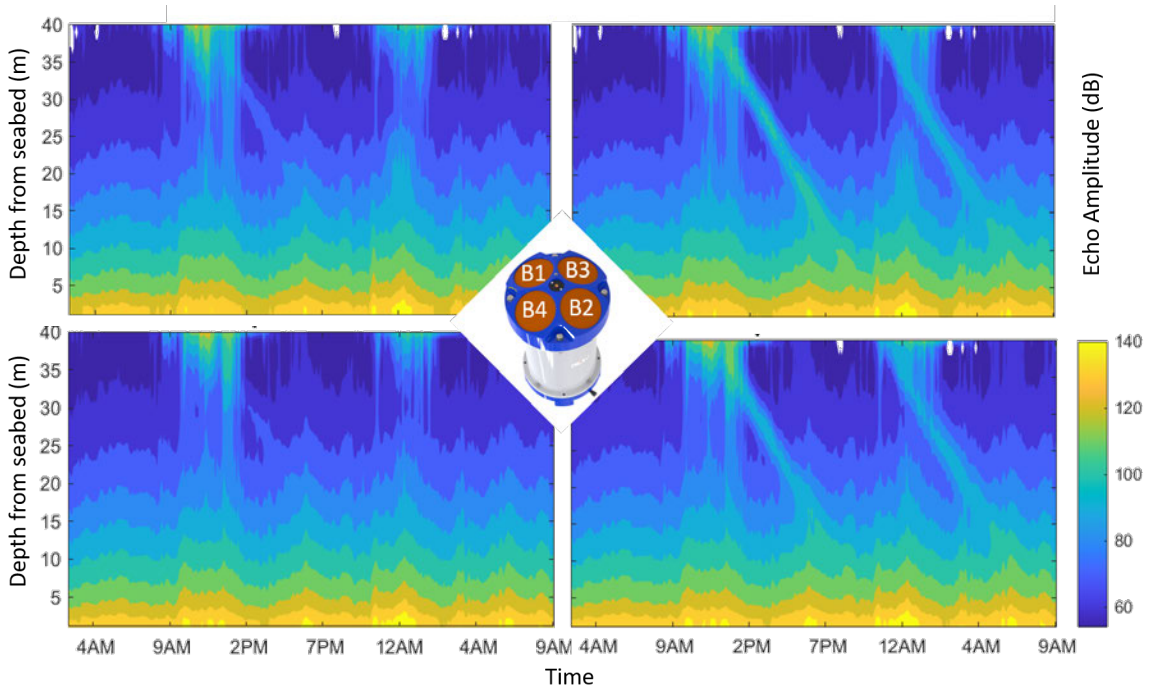

Figure 6.5: The four beam transducers located at A_2 measuring echo amplitude along the water column, with features of interference illustrated at the diagonal lines. Beams 3 and 2 (top and bottom right) show a significant increase in the echo amplitude, implying the interference is toward this location.

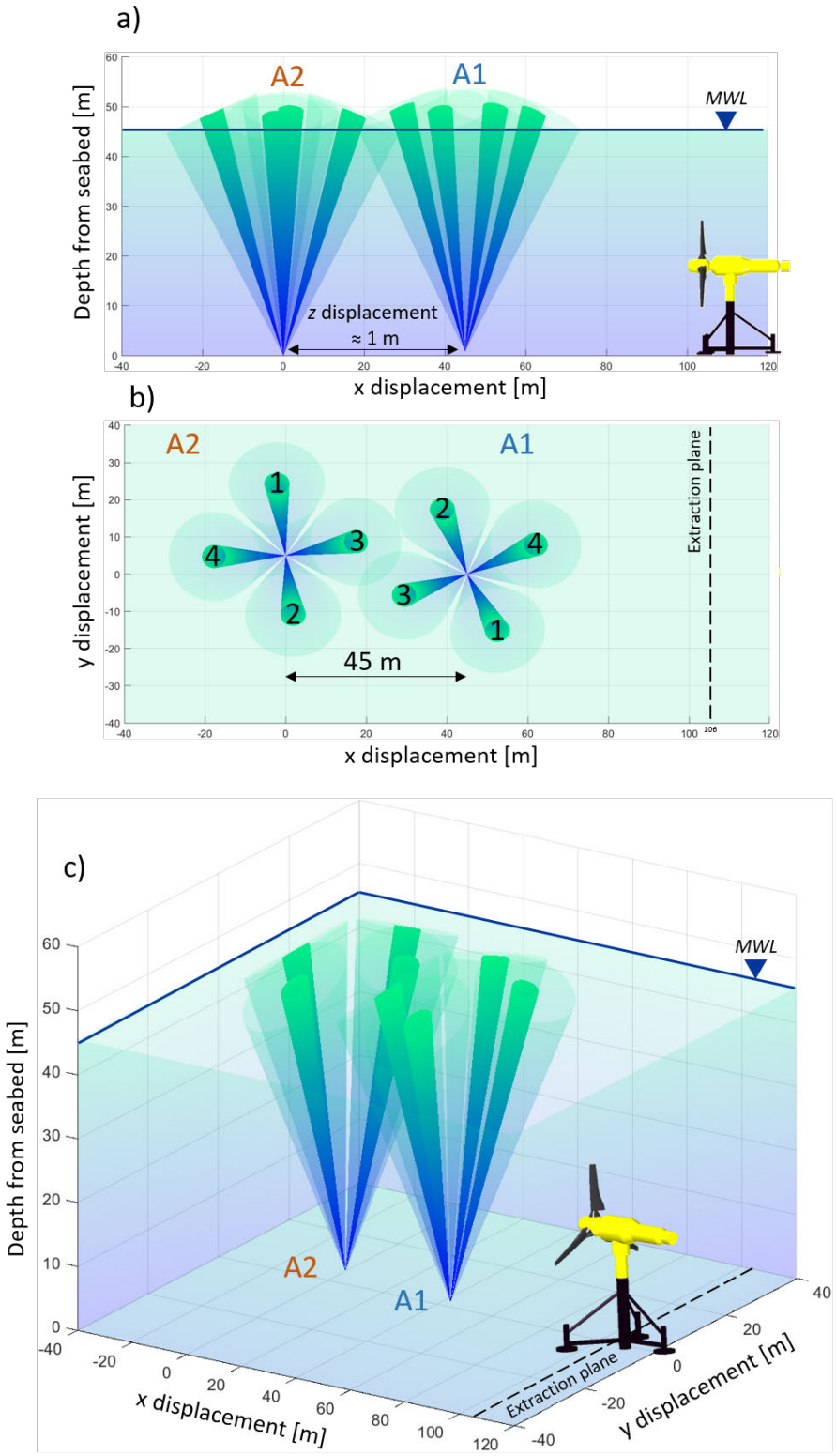

Figure 6.6: RDI WH 600 kHz ADCPs, A1 and A2 which are 61 m and 106 m northeast of the TEC location (upstream on a flood tide), respectively. (a) Side profile showing the vertical displacement between A1 and A2. (b) Showcases the top-down view of A1 and A2 beam paths and the clearance zones. (c) Illustration of the main lobes (solid), clearance zones (shaded), and the orientation of the two bottom-mounted ADCPs.

The clearance zone is recommended to be free from any objects or other acoustic instruments. As shown in Figure 6.6b, it is clear that the clearance zones of beam 3 for instrument A1 & beam 3 for instrument A2 overlap. This is more apparent under periods of significant movement in pitch and roll observed in the instantaneous measurements from ADCP$_{A2}$, as seen previously (Fig 5.7c, 5.7d). Figure 6.7 shows the 5-minute averaged time series of ADCP A_1 and A_2 stability during the measurement campaign carried out from June to July 2014.

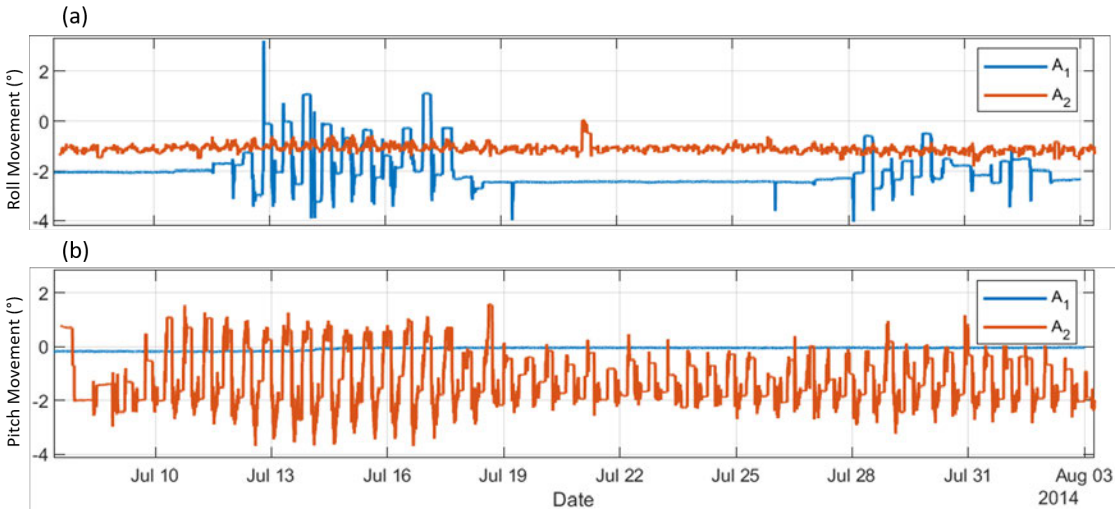

Figure 6.7: Averaged (5-min) in-situ measurements of instrument stability by the two ADCPs located at A_1 and A_2. (a) Time series of pitch measurements by ADCP$_{A1}$ and ADCP$_{A2}$. (b) Time series of roll measurements ADCP$_{A1}$ and ADCP$_{A2}$.

Representative amplitude returns for an RDI WH 600 kHz ADCP deployed in a depth of $\approx$ 45 m, with no evidence of interference over a 1 day period, positioned upstream of the DEEP-Gen IV at location A_1 is given in Figure 6.8a. The flow velocity profile is given in Figure 6.8b to illustrate the average profile without interference.

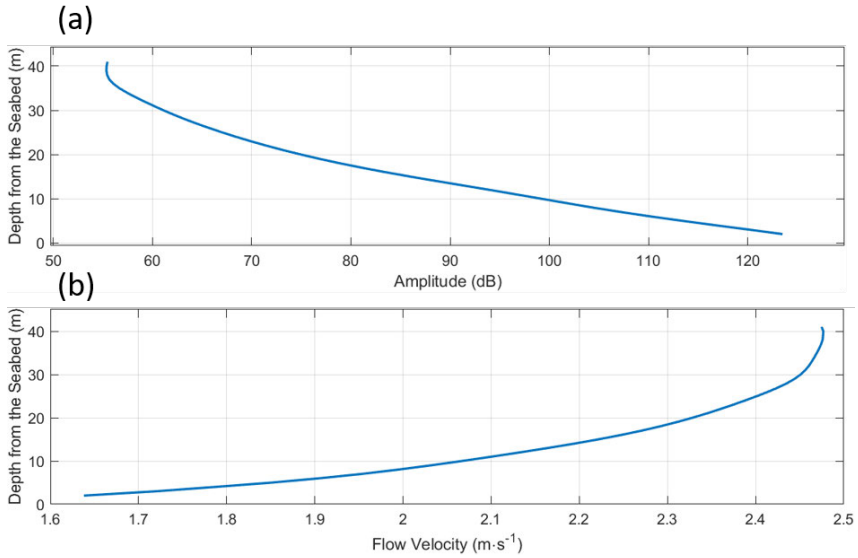

Figure 6.8: Representative amplitude (a) and flow velocity (b) for ADCP measurements without interference features.

It was found that the two ADCPs interfered with one another, causing the echo amplitude signal to increase and the current flow measurement to be misrepresented. A combined total of 33% of the cycles (both flood and ebb) measured at locations A_1 and A_2 were contaminated by interference effects. Only flood cycles were analysed to assess the impact this instrument interference had on the PPA procedure due to the wake effects impacting the flow measurements when the DEEP-Gen IV faced the ebb tide. The flood cycles affected by interference represented 15% of the cycles from the total data set.

Figures 6.9a, 6.9b and 6.9c depict the effect interference has on the measured flow velocity at a specific bin height (25 m), and along the water column from ADCP located at A_1 and A_2 respectively.

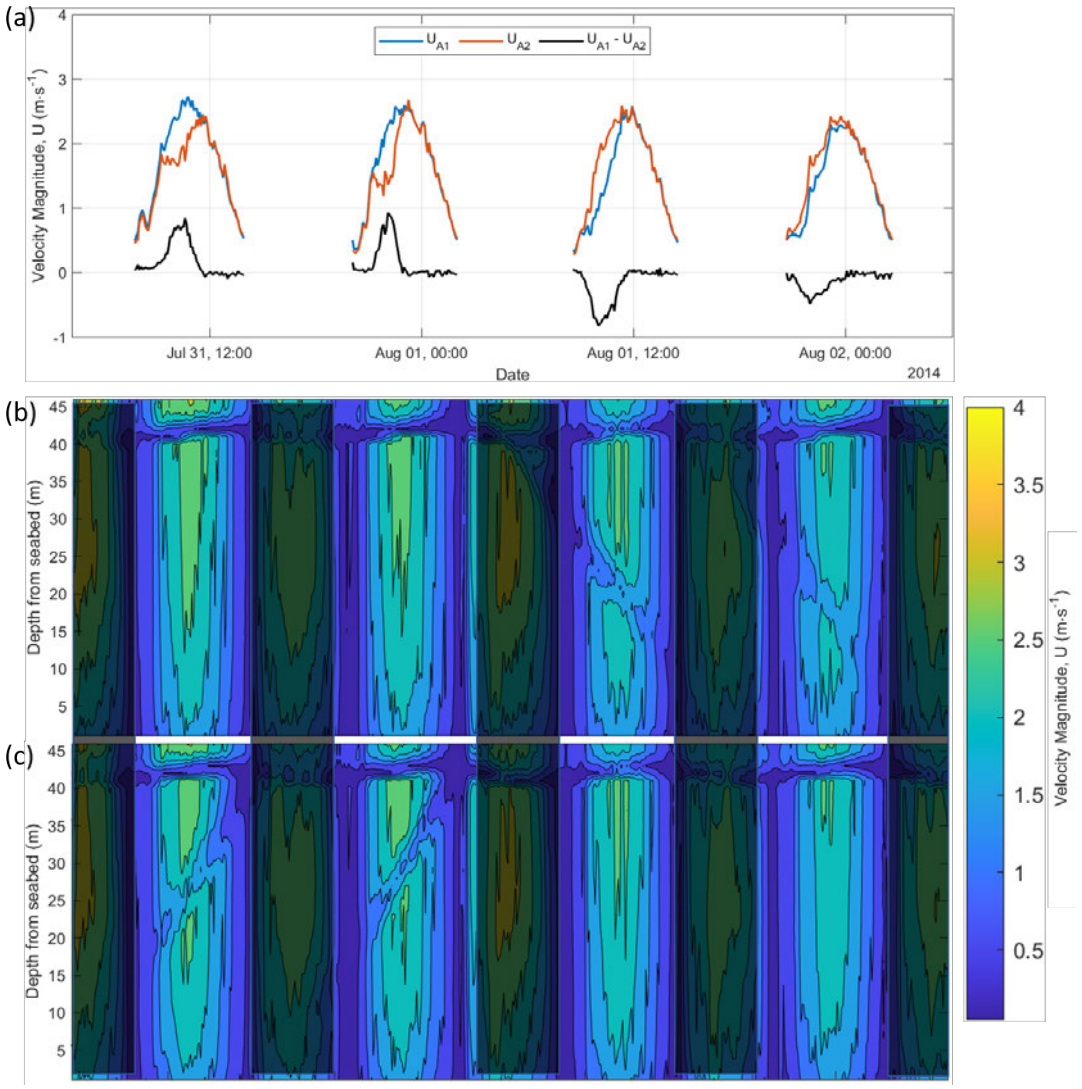

Figure 6.9: Velocity for ADCP located at A_1 and A_2 showing indications of interference for four consecutive flood cycles. (a) Flow velocity time-series for ADCPs located at A_1 and A_2 and the difference between them (black line). Contour plot of the 5-minute averaged measurements across the water column measured by ADCPs located at (b) A_1, and (c) A_2. Ebb tidal cycles are removed.

6.3.1 Data restrictions and quality control

Individual instrument settings for the analysis are listed in the previous section (section 5.2). The two ADCPs used in the identification and treatment of interference are A_1 and A_2 (listed in Table 5.1), all the data was collected over turbine deployment 5. The data were collected over a range of tide and flow conditions which were assumed not to affect the results of the instrument interaction analysis. QC was undertaken as per other sections (section 5.4). Velocities exceeding the ambiguity range are removed as are data points with sensor errors and measurements with non-unique timestamps. Gaps of up to two points are not replaced by linear interpolation due to the IEC TS 62600-200 requirements. Upon retrieval of acoustic instruments, the clock drift is analysed, as although ADCP$_{A1}$ and ADCP$_{A2}$ were not exactly synced by timestamps the difference in the instantaneous data was so minuscule that after averaging was negligible. Therefore, the two ADCPs had data with common timestamps and could be passed for processing and comparison analysis.

6.4 ADCP: Identification of Interference Features

To determine the possible advantages of having multiple acoustic sensors operating in close proximity, it is essential to examine and, if feasible, remove or replace measurements associated with cross-talk.

Thorough visual data processing after following the quality controls checks outlined in section 5.4 were carried out, peaks in the amplitude and velocity profiles were identified. Figures 6.10a and 6.10b present the mean amplitude and mean velocity profiles of each ADCP for simultaneous measurements respectively.

Figures 6.10a and 6.10b enable us to distinguish interference caused indirectly by the acoustic instruments in close proximity, one flood cycle apart due to not displaying the interface at the same time during the deployment. In the echo amplitude signal, interference appears as a rise in mean amplitude in a typically decreasing profile. In the velocity signal interference features can appear as a rise or drop in magnitude. The interference appeared at different depths in the water column, the interference characteristics were more pronounced in the upper region of the water column ($>$ 25 m from the sea bed). The interference characteristics were present in both data sets from ADCP$_{A1}$ and ADCP$_{A2}$. However, the interference never appeared simultaneously for both instruments. This is evident in the flow velocity time series presented in Figure 6.11.

The velocity time series was split into 1 hour 30-minute slots to show how the measurement interference shifts along the water column. The bounds of the DEEP-Gen IV swept area were used for depth bins to show the variation in velocity measurements that would be considered when calculating the PWRA velocity. The echo amplitude depth profiles were used to pinpoint these periods of interference. The echo amplitude is significantly greater at the boundary layers (5 bins upward from the seabed and downward from the sea surface is removed to limit the peaks identified). Therefore, the measurements required manipulation to locate the periods of interference correctly.

Figures 6.12a, 6.12b, and 6.12c show the correlation of the measured flow velocities (U_{A1} and U_{A2}) across the rotor plane of TEC$_{T1}$, TEC$_{T2}$ and TEC$_{T3}$ respectively. The power-weighted flow velocity is compared including periods of interference across the depth bins used in the power-weighted calculation. A linear trend line is fitted to the data with an R^2 goodness of fit value of 0.99, 0.98 and 0.97, representing the best goodness of fit across the flow velocity measured along the rotor plane for TEC$_{T1}$, TEC$_{T2}$ and TEC$_{T3}$ respectively. The linear model coefficients (with 95% confidence bounds) and the sum of squared error (SSE) are presented in Table 6.1. Where

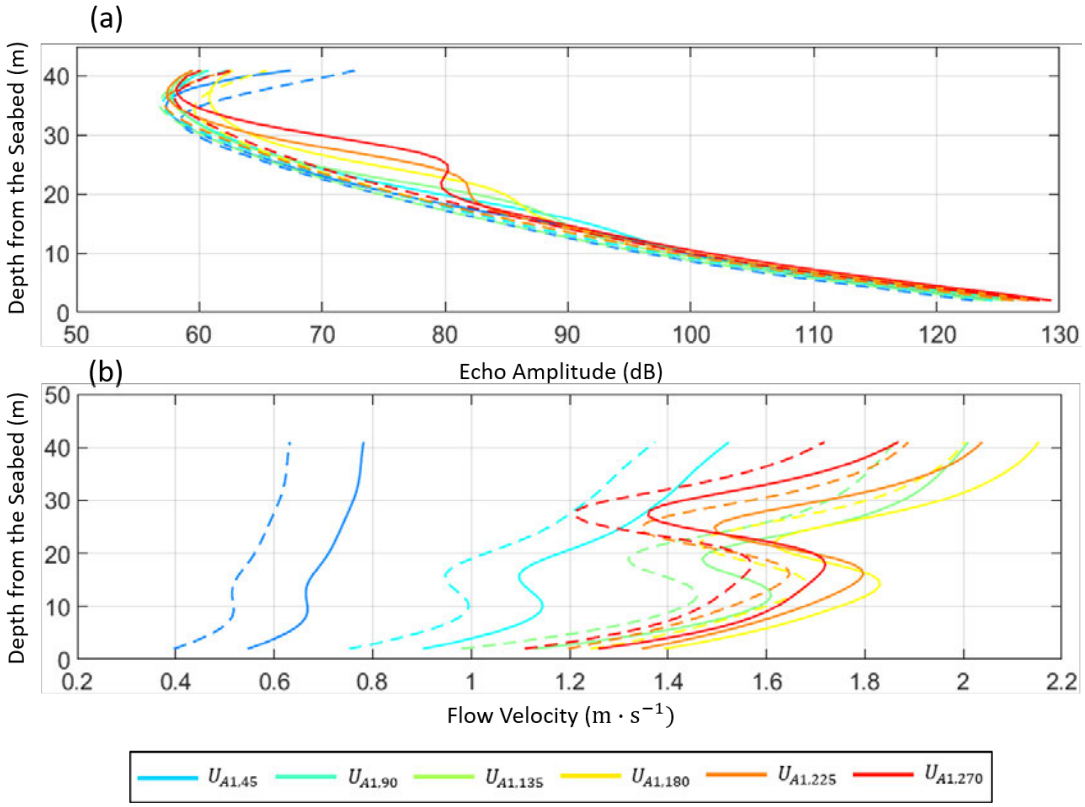

Figure 6.10: Echo amplitude and velocity depth profile from ADCP$_{A1}$ (solid lines) and ADCP$_{A2}$ (dashed lines) averaged at intervals of 45 minutes to illustrate the movement of the interference feature one flood cycle apart. (a) Amplitude showing indications of interference at different heights from the seabed as the flood tide develops. (b) Effect on velocity measurement.

$z_{T...}$ is representative of the bin depths used across the rotor diameter of TEC$_{T1}$, TEC$_{T2}$ and TEC$_{T3}$. Figure 6.12 shows that at higher depth bins, the impact of interference is more significant. An object inside the clearance zone will bias the velocity estimation in the depth bin that the object corresponds to. Additionally, it can also bias the depth bins on either side of the depth bin the object is in. The data indicates that the interference starts high in the water column for A2's measurements, as seen in Figures 6.5 and 6.9. However, it is not necessarily stronger higher up, as interference can also begin lower in the water column at certain times, as shown in Figure 6.11c. This suggests that the region where the measurement interference first occurs can vary before it attenuates both upward and downward. The interference affects the velocity between 1 m·s^{-1} and 3 m·s^{-1}.

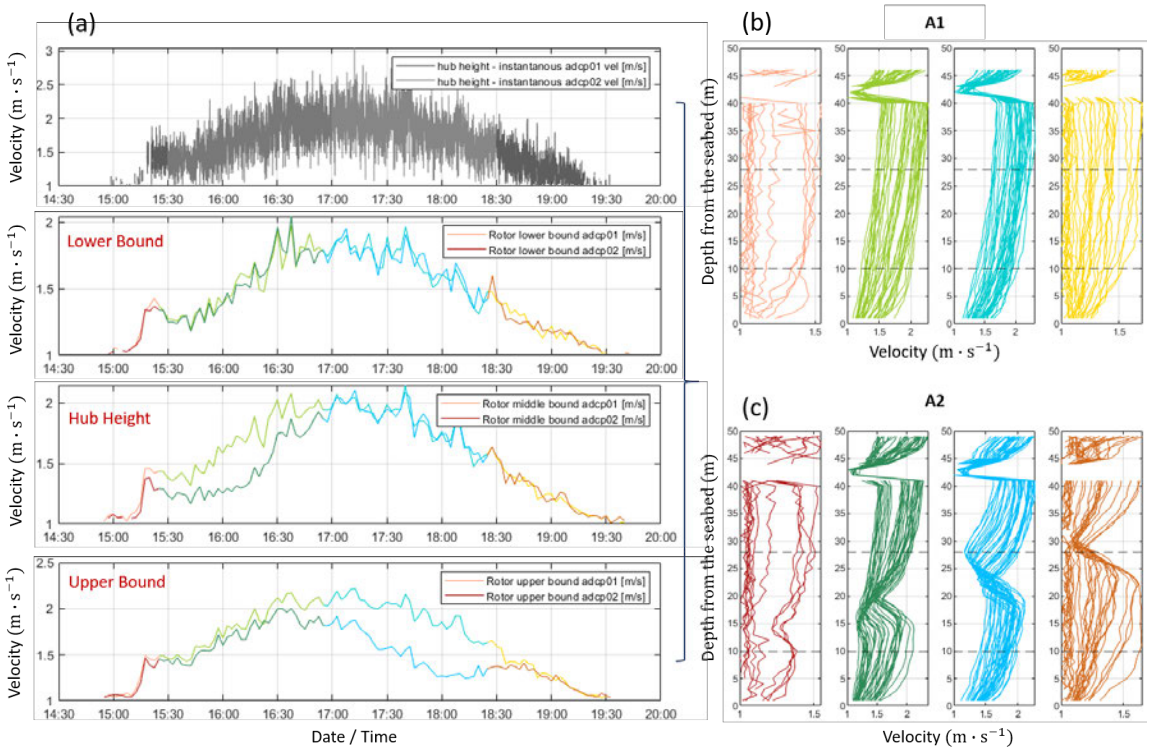

Figure 6.11: (a) Simultaneous velocity time series for measurements at A_1 and A_2, segmented to 1.5 hours with slack water removed (velocities < 1 m·s^{-1}). The upper, hub height and lower bound represent the swept area of the DEEP-Gen IV (TEC$_{T1}$) at a height of 9, 18 and 27 m respectively. Velocity depth profile for ADCP$_{A1}$ (b) and ADCP$_{A2}$ (c).

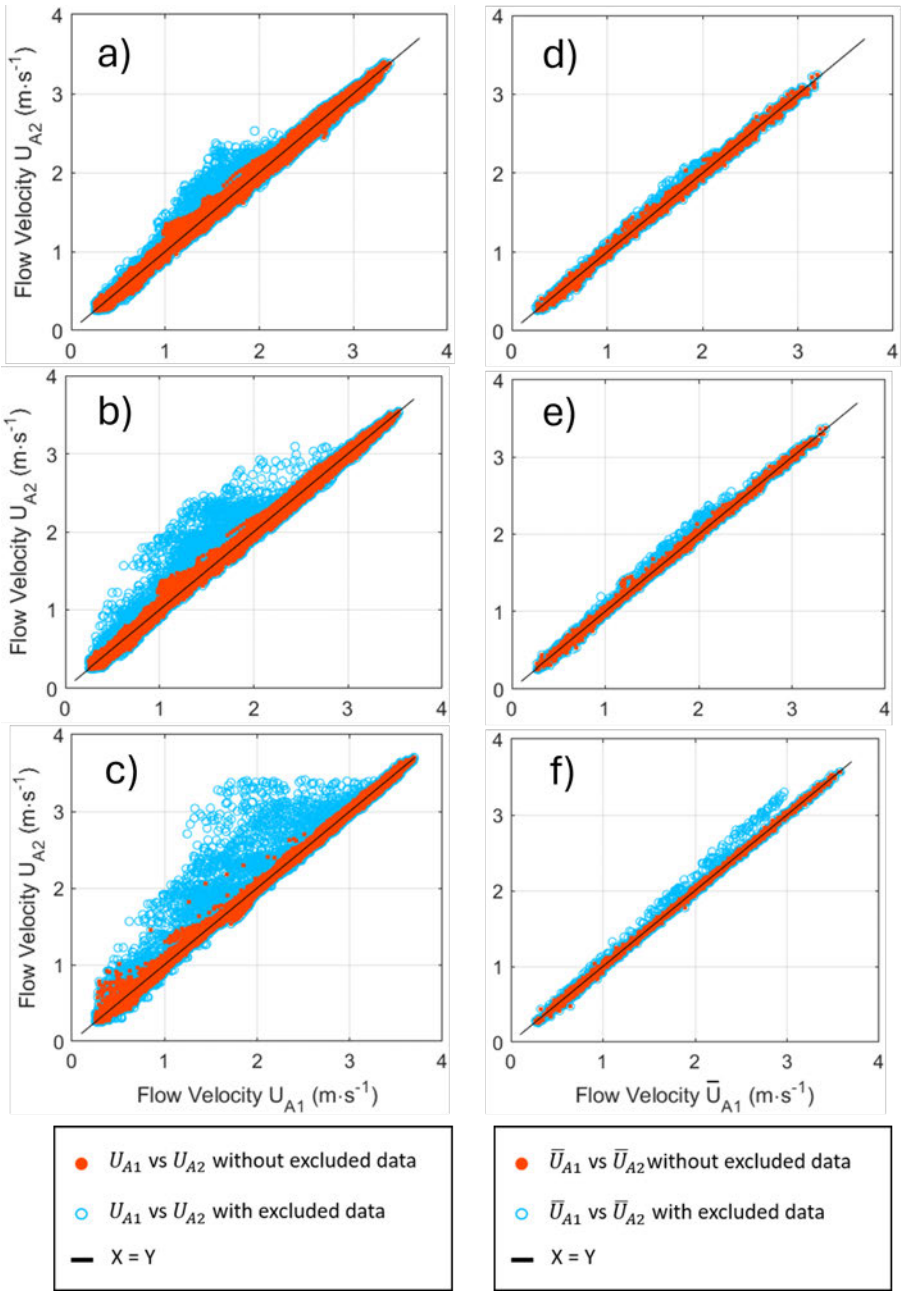

Figure 6.12: Correlation between flow velocities measured across the swept area of TEC_{T2}, TEC_{T1} and TEC_{T3} displayed in (a), (b) and (c) respectively, for data with (blue) and without (orange) features of interference. Correlation between the calculated PWRA velocities - weighted average of measurements taken across the rotors of TEC_{T2}, TEC_{T1} and TEC_{T3} - from ADCPs at locations A_1 and A_2 illustrated in (d), (e) and (f) for data with (blue) and without (orange) features of interference. Perfect correlation is illustrated as a the black line of 1-1 (x = y).

Table 6.1: Correlation parameters between concurrently measuring ADCPs located at A_1 and A_2. Velocities representative of the depth bins across the swept area of TEC_{T2}, TEC_{T1} and TEC_{T3} given by (a), (b) and (c) respectively. Correlation between PWRA velocities - calculated using depth bins across TEC_{T2}, TEC_{T1} and TEC_{T3} - with and without features of interference provided in (d), (e) and (f).

	Statistics	z_{T2}	z_{T1}	z_{T3}
U_{A1} vs U_{A2}		(a)	(b)	(c)
	P1	0.999	0.996	0.998
	P2	0.003342	0.009526	-0.007145
	SSE	223	663	1465
	R^2	0.9908	0.9834	0.9722
	RMSE	0.0677	0.0965	0.1364
$\bar{U}_{A1}$ vs $\bar{U}_{A2}$		(d)	(e)	(f)
	P1	1.002	1.002	1.006
	P2	-0.005135	-0.005498	-0.02074
	SSE	10.3	14.27	24.85
	R^2	0.994	0.9932	0.991
	RMSE	0.05242	0.06167	0.08134

6.5 Interference Impact on the Measured Power Curve

The primary goal of investigating cross-talk is its effect on velocity measurements, subsequently the impact of data featuring interference characteristics on the estimated power metrics of a turbine. This will impact the PPA when not identified and removed. The power extracted from TECs is based on the principle that power (P) is a function of the cube of the volumetrically averaged current velocity (u) over the rotor swept area (A), turbine power coefficient (Cp) and seawater density (ρ):

$$P = \frac{1}{2}\rho CpAu^3$$

The measured power produced by TEC_{T1} was evaluated against the velocity measured from the two individual ADCPs, A_1 and A_2 (Fig 5.3). A tidal ellipse of data used for the measured power curve production is presented in Figure 6.13. Note that the bin data is 5-minute PWRA velocities (calculated from measurements over the rotor area of TEC_{T1}) used as an example.

Figure 6.13 also shows the orientation of the two ADCPs A_1 (blue lines) and A_2 (black lines), where the solid line represents the measured beam heading - beam 3 for a four-beam RDI WH ADCP). An important factor for cross-talk analysis is understanding the beam trajectory of all four transducers. $ADCP_{A1}$ is positioned $\approx$ 45 m from A_2 and beams 2 and 3 of the instrument pair face toward one another (refer to Fig 6.6).

Figure 6.14 illustrates the proximity of the beams as they diverge upward in the water column. This causes the beams to be closer to one another in the upper region of the water column, increasing the chances of cross-talk through sea surface reflections.

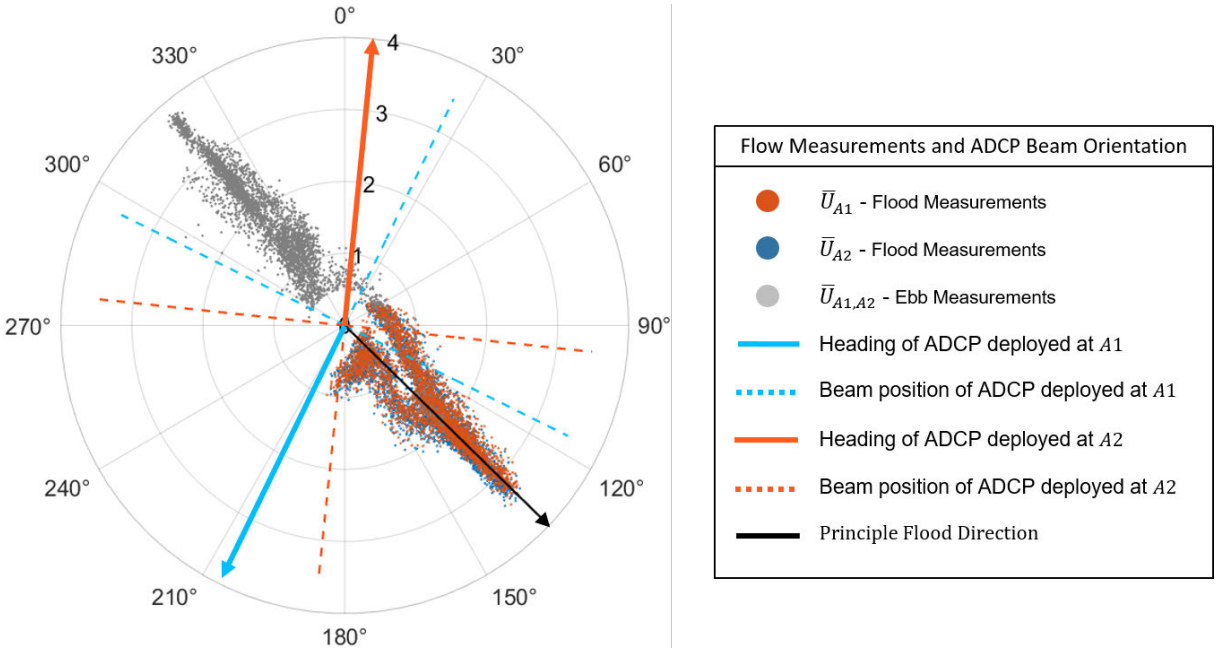

Figure 6.13: Tidal ellipse for the flood tide PWRA flow velocities $\bar{U}_{A1}$ (orange dot) and $\bar{U}_{A2}$ (blue dot), with the beam orientation of both instruments (solid line representing main beam heading - angle of beam 3 for RDI WH ADCPs) and the principle flood flow direction is shown as the black line. Ebb data (grey dot) is not used in this analysis.

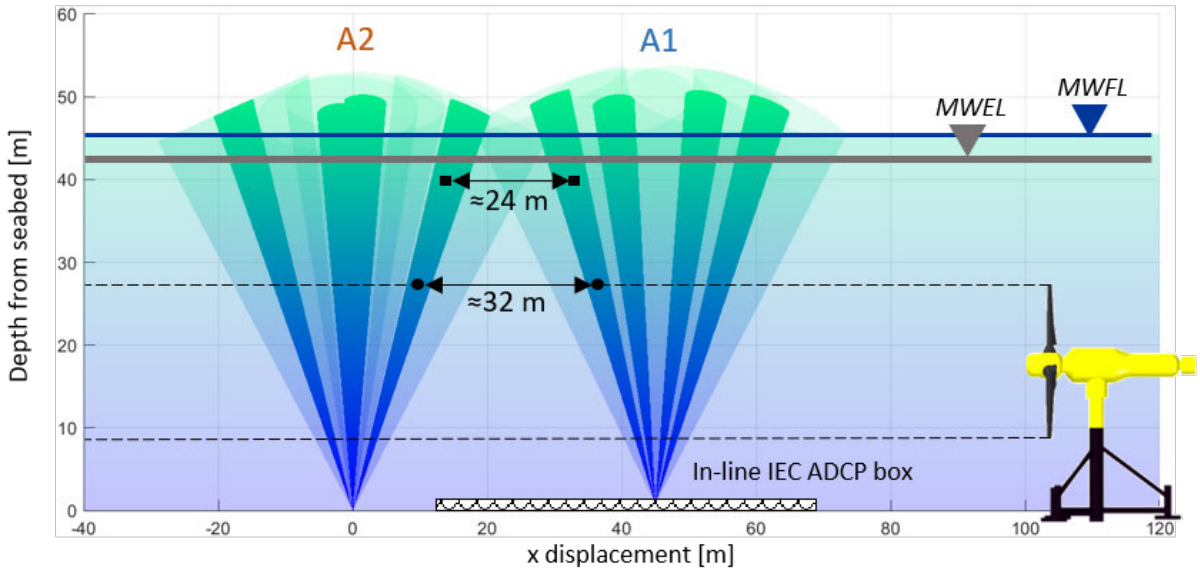

Figure 6.14: Distance between neighbouring beam trajectories from ADCP$_{A1}$ and ADCP$_{A2}$. Beam distance at the upper rotor bound (circle) and close to the sea surface (square) and the mean water level for the flood (blue triangle) and ebb (grey triangle). IEC TS 62600-200 instrument target box is included as the lined box.

However, as previously stated the data set had $\approx$ 15% of the total flood cycles measured in this campaign containing interference features. This means that the remaining data measured was usable, and the causality and specific conditions causing interference are further work. Additionally, placing two instruments in close proximity (in this case $\approx$ 45 m) is just achievable at this depth. However, if deployed in greater depths will cause the beams to be too close in the upper region and the measurements will be void unless the instruments are configured correctly.

If not identified and removed, the effect of this interference (before applying any spatial averaging and considering flood and ebb tides separately) can provide a misrepresented velocity estimate for use in the measured power curve. Figure 5.21 displays the three TEC rotor positions in the water column that are used to assess the impact of interfered velocity measurements on the measured power curve. Figure 6.15 illustrates three consecutive flood cycles indicating the presence of interference varying in location along the water column (dashed lines) alongside the following three consecutive flood cycles with no interference (solid lines), measurements were taken from location ADCP$_{A1}$. The PWRA velocity is calculated for the measurements obtained across the swept area of the three turbines denoted as a square, triangle and circle symbol for TEC$_{T3}$, TEC$_{T1}$ and TEC$_{T2}$ respectively. The filled symbols represent velocity measurements without bias from interference ($\bar{U}_{A1}$), whereas the unfilled symbols show how measurement bias from interference would be included in the calculation of the PWRA velocity ($\bar{U}_{A1,wi}$). The bias is significantly greater in the upper region of the water column (position of TEC$_{T3}$). This implies the region where the cross-talk is most evident before attenuating down the water column, with the velocity measured at 10 m from the seabed still measuring a slight bias. The impact on the PPA and AEP estimates can be analysed with the regions of interference identified and defined.

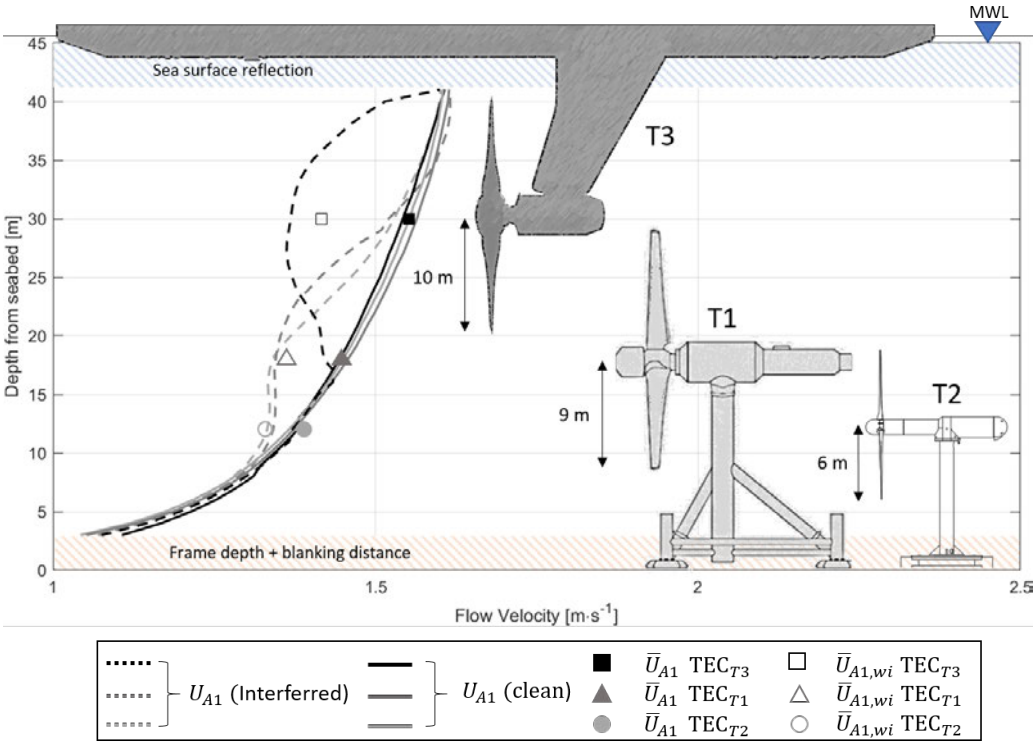

Figure 6.15: Six consecutive flood tide depth profiles measured from location ADCP$_{A1}$ featuring interference effects (dashed lines) and *clean* profiles (solid lines). The position of three variants of TECs are overlaid (T1,T2, and T3) with symbols showing corresponding interfered (unfilled) and *clean* (filled) PWRA velocities.

Figure 6.16a shows the generated power output for each 5-minute measurement against the flood tide velocity component approaching the DEEP-Gen IV, TEC$_{T1}$. The flow velocity measurements containing features of interference are presented as blue dots. This expresses the variation in velocity when two ADCPs cross-talk. Additionally, the flow velocity measurements with 90% of the interference features removed are presented as orange dots. Figure 6.16b illustrates the variation in the mean PWRA velocity (black dash line) for measurements with and without interference features. The PWRA velocity shown combines measurements taken across z_{T1}, the

swept area of TEC$_{T1}$. At the lower flow velocities, more obvious differences exist between the curves presented in Figure 6.16b. The velocity differed by 0.5 to 2.5% between 1 - 1.5 m·s^{-1} and 1.5 - 2.0 m·s^{-1} (where the interference occurs during the depth bins used in the calculation on the PWRA velocity) respectively. Had the interference not been identified and removed the power curve would shift to the left, making it more favourable as lower flow velocities are paired with the power produced by the DEEP-Gen IV. This difference represents the shift for $\approx$ 15% of the total flood cycles, including interference features. The variation in flow velocity changes along the depth of the water column. Therefore, the interference's impact on the measured power curve could be more significant depending on the depth bins used.

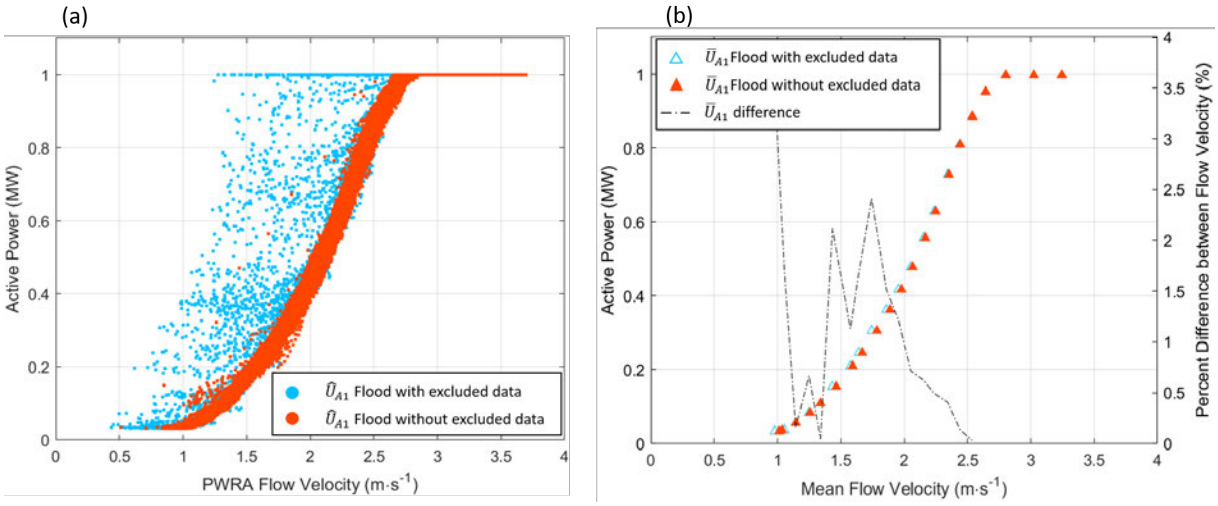

Figure 6.16: The effect of ADCP interference on the measured power curve for the averaged 5-minute PWRA velocities in increments of 0.1 m·s^{-1}. (a) Blue dots represent the flood tide measurements for ADCP A_1 ($\hat{U}_{A1}$) with features of interference from interacting with ADCP A_2, the orange dots represents data with interference features removed. (b) The mean PWRA velocity from ADCP A_1 ($\bar{U}_{A1}$) with (blue triangle) and without (orange triangle) features of interference in the 5-minute averaged measurements.

This is shown in Figure 6.17 when using the depth bins relative to the swept area of TEC$_{T3}$ in the upper region on the water column (z_{T3}). Here the interference features are more pronounced and significantly reduce the measured velocity (refer back to Figure 6.15). The flow velocity (including the 15% contaminated flood cycles) when averaged and used to produce the power curve was found to be on average around $\approx$ 6% lower than data used without interference. Failing to identify and remove the interference features in the post-processing phase of the data can alter the power curve for the device undergoing a performance review. This can also cause the annual energy estimate to be misrepresented.

Using the two velocity time series measured by ADCPs positioned at A_1 and A_2 alongside the power produced by TEC$_{T1}$, the AEP can be calculated. For periods of interference - happened in one instrument at any given time - the other instrument could be used to estimate the AEP. This allowed the impact of the interference to be analysed in terms of AEP. Accounting for $\approx$ 15% of the flood cycles being contaminated, results show a difference in estimates of AEP of up to 4%. The difference in AEP varied when using different depth bins as the reference. The effect on the velocity measures due to interference was greater in the upper region (z_{T3}) of the water column. This resulted in differences in AEP of up to $\approx$ 7%. The lowest difference in AEP with and without interference features was in the lower region of the water column (z_{T2}), where the difference was 2%. However, this implies an area of uncertainty when inspecting the data used for the purpose of a PPA or annual yield assessment.

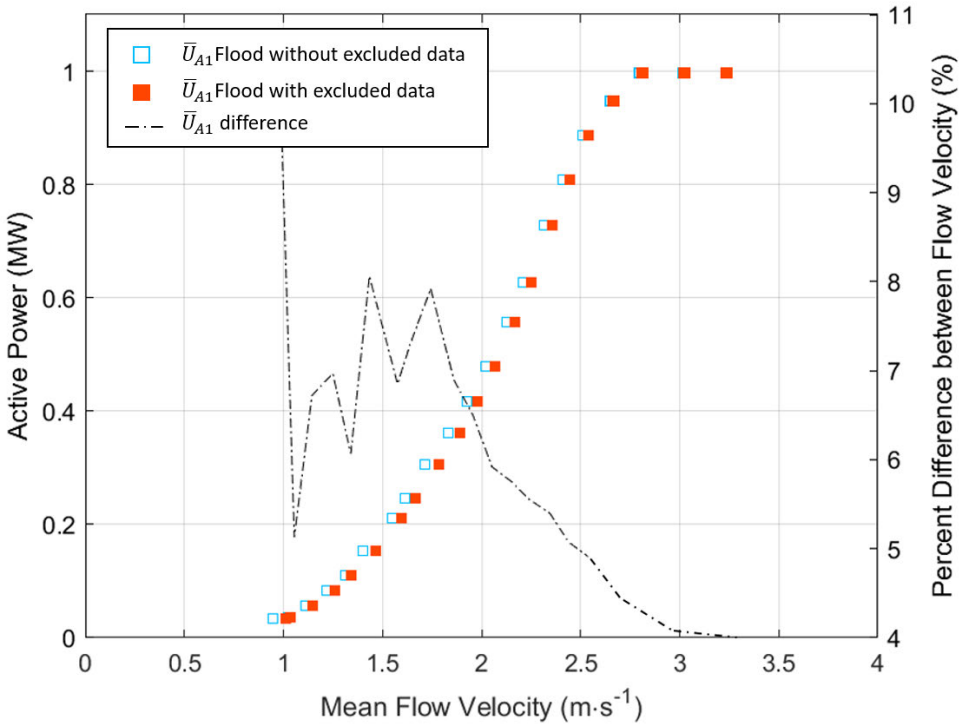

Figure 6.17: The mean PWRA velocity from ADCP A_1 ($\bar{U}_{A1}$) with (blue square) and without (orange square) features of interference in the 5-minute averaged measurements across the rotor span of TEC$_{T3}$ (z_{T3}).

6.6 Post-processing data sets: Interference Detection Algorithm

In the case of an ocean deployment of multiple ADCPs, there is often no access to monitoring the data from the shore until the instruments are retrieved. The environment is complex, showing multiple features from fauna and turbulence. It is difficult to separate the inter-instrument contamination from the rest of the measured profiles. An interference detection algorithm has been developed in order to flag the measurement containing interference features. The algorithm looks for interference features in the contaminated averaged amplitude and time-averaged velocity profiles. Through data manipulation, the peaks in echo amplitude were identified. The interference detection algorithm in amplitude does the following:

1. The 5-minute averaged echo amplitude profiles are separated out individually to be assessed for indications of interference (see Figure 6.18a).
2. The amplitude profile was detrended, subtracting the line of best fit (typically known as $y = mx + b$) from each profile (see Figure 6.18b).
3. The profile was then smoothed to remove small measurement fluctuations and distinguish the large peaks (see Figure 6.18c).
4. Finally, the profile is then multiplied by negative one to identify the primary peak (eliminating the peak found at the lower and most upper region of the water column) to allow correct identification of the peak on either side of the biased measurement. The peaks were identified using the "findpeaks" function from the Curve Fitting Toolbox in MATLAB. The identified peaks had a prominence of at least 5 counts after detrending the data. (see Figure 6.18d).

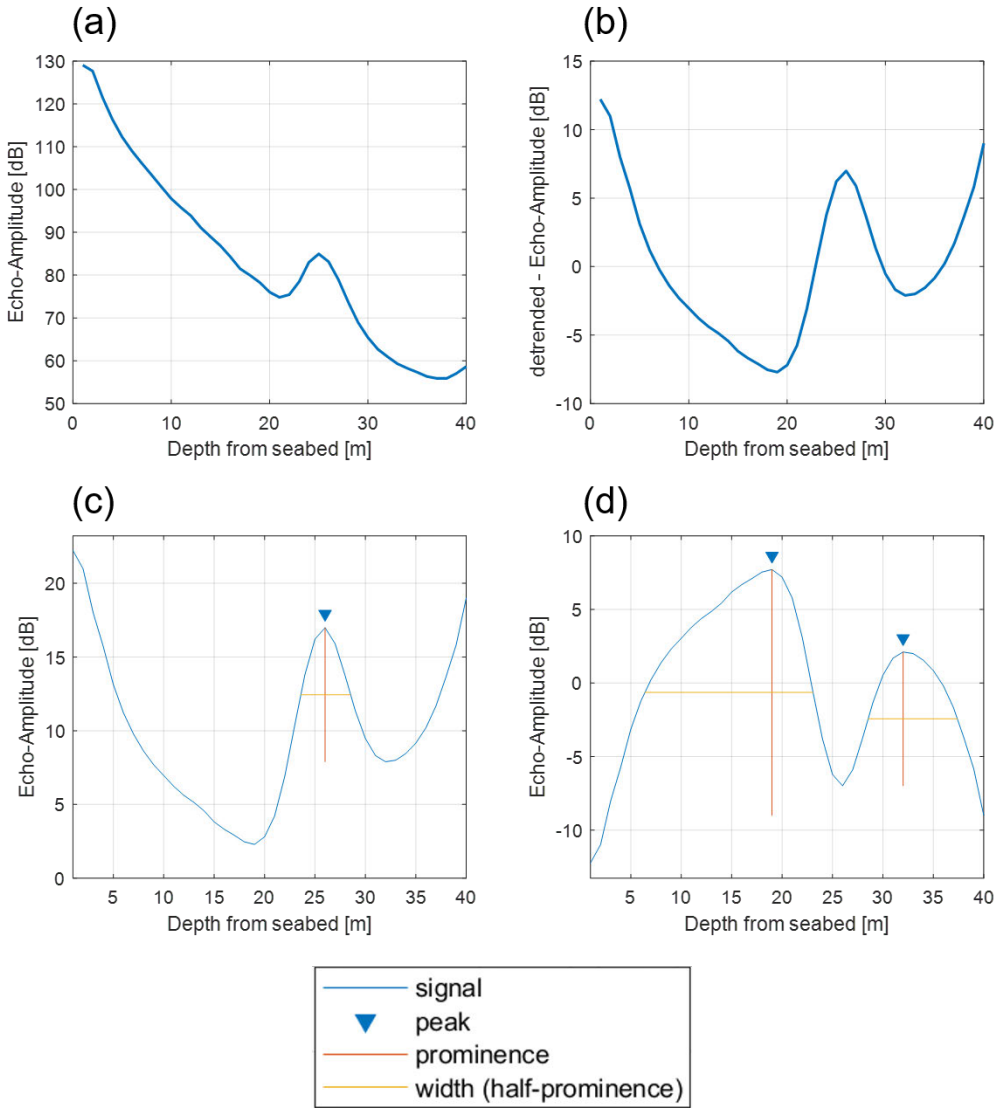

Figure 6.18: Echo-Amplitude Depth Profile: (a) A data sample displaying a prominent peak in echo amplitude within the upper portion of the water column. (b) The amplitude profile detrended by subtracting the line of best fit. (c) The profile is then smoothed to remove multiple mini-peaks and then multiplied by negative one to identify the primary peak (d) The algorithm effectively identifies the peak (indicated by a triangle) within the data sample, while also eliminating measurements between the designated square markers that represent bias from cross-talk features.

Removing the trend allowed the focus on the large fluctuations in the signal to be analysed. Due to the nature of the interference, two peaks were consistently identified using this method. A series of QC factors were introduced based on the number of peaks in the signal. The QC factors were simple to implement due to only one peak being present in the depth profiles during periods of interference. The QC factors are as follows and flagged with the relevant guidance from QARTOD (as stated in Section 5.4.1):

- if $N_p <= 1$: flag data *1*;
- if $N_p = 2$: flag data *4* between the two peaks;

- if $N_p > 2$, the trough between the number of peaks is checked, and the peaks on either side of the largest trough are flagged *4*

where N_p is the number of peaks, measurements that have been flagged as containing interference have been removed from the analysis. Figure 6.19a and 6.19b shows the mean amplitude and averaged velocity profiles of the data that have passed the interference detective algorithm. It can be seen that the algorithm has enabled the removal of the measurements that the boundary reflections have contaminated. It can be seen that no good measurement has been removed.

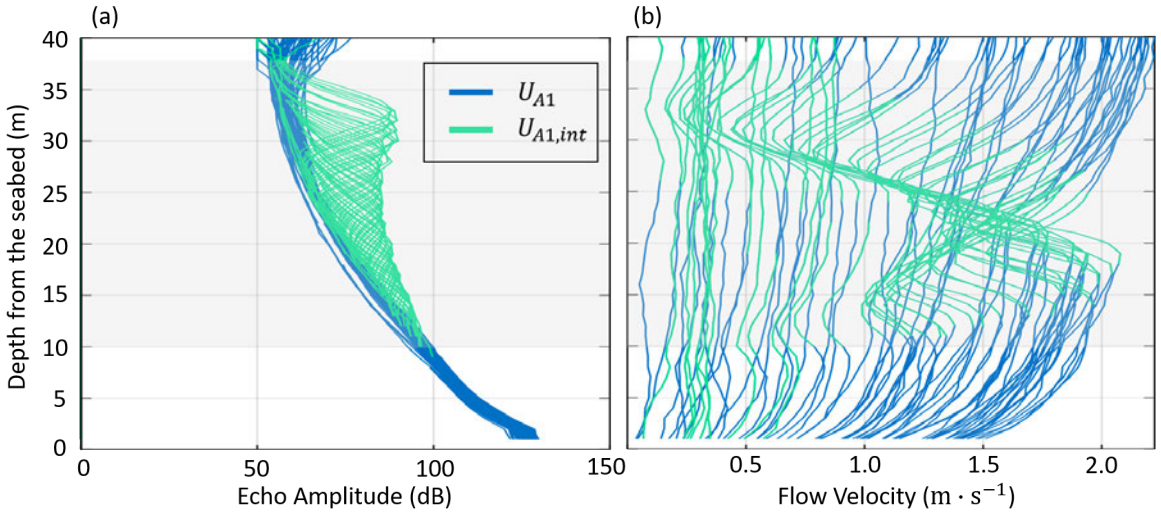

Figure 6.19: An area of interference is identified and highlighted in the grey box, and the good measurements (U_{A1}) and flagged contaminated measurements ($U_{A1,int}$) are given for one flood cycle. (a) Mean echo amplitude measurements in dB. (b) Mean flow velocity profile in $\mathrm{m \cdot s^{-1}}$.

Figure 6.20 presents velocity profiles along the measured water column in 45-minute intervals during a specific flood tide cycle, with panels (a) and (c) showing data with interference features and panels (b) and (d) displaying data after interference removal. Panel (a) illustrates the acceleration phase of the flood tide, where velocity profiles transition from purple to cyan, representing the progression from 0 to 135 minutes. Panel (b) shows the same acceleration data with interference removed, resulting in cleaner profiles but with some residual noise near the sea surface, indicated by the red circle. Panel (c) depicts the deceleration phase with velocity profiles transitioning from yellow to green, covering 135 to 270 minutes. Panel (d) presents these deceleration profiles post-interference removal, significantly reducing noise but still exhibiting some interference near the boundary layers. The method described effectively cleans most of the noise, particularly in the main water column, though some interference persists near the boundary layers due to the inherent turbulence and noise in these regions, making it challenging to completely remove all relevant data.

Table 6.2 provides a detailed summary of the total samples available, flagged, and removed during flood tides over a 26-day measurement period for two ADCPs. It highlights the number of samples impacted by interference and the subsequent removal percentages, emphasising the rigorous data processing steps taken to ensure only high-quality, timestamp-matching samples were used in the final analysis.

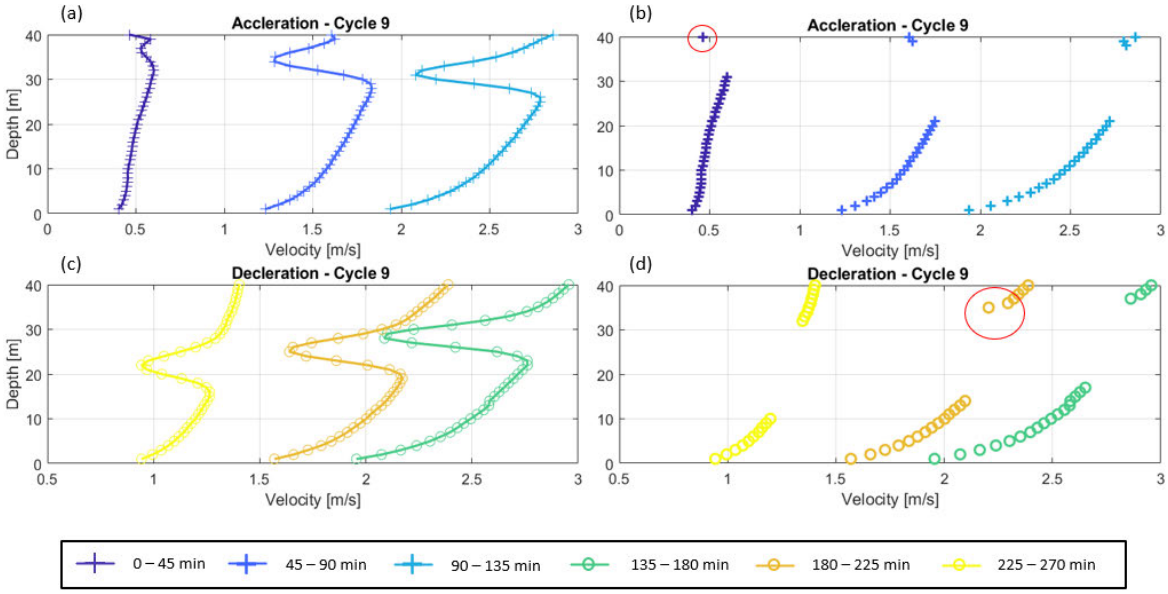

Figure 6.20: Interference features identified throughout the averaged flow velocity profiles (by time on a flood cycle in intervals of 45 minutes). (a) Acceleration of the flood tide with interference features high up in the water column. (b) Interference features removed from the acceleration section of the data set, with a leftover sample close to the boundary layer. (c) Deceleration of the flood tide with interference features high up in the water column. (d) Interference features removed from the deceleration section of the data set, with a leftover sample close to the removed section.

Table 6.2: Overview of total samples available, flagged, and removed during flood tides over a 26-day (days of overlap between the co-located ADCPs) measurement period. Note that only samples with matching timestamps were included in the analysis for comparison. The table summarises the total number of samples.

ADCP ID	A_1	A_2
No. 5 min samples	3744	3801
No. interfered samples	562	646
No. samples removed	507	588
% removed	90.2	91.0
No. remaining 5 min samples	3237	3213
No. samples used in analysis	3213	3213

Initially, cross-talk was identified through a detailed comparison of the velocity time series plots, as shown in Figure 6.21a, these plot allowed for a direct comparison between the two ADCPs. The analysis revealed periods where each instrument took turns measuring a significantly lower velocity than the other at various periods in the deployment. Upon closer examination, it became clear that the interference was not simultaneous across both instruments, but rather exhibited a delayed response, with only one instrument being affected at a time. Following identification, the methodology previously outlined was employed to flag and subsequently remove the contaminated measurements. This approach proved effective in removing up to 90% of the samples that were influenced by interference, see Figure 6.21b. The remaining data that passed through were from regions close to boundary layers, where accurately locating a peak proved challenging.

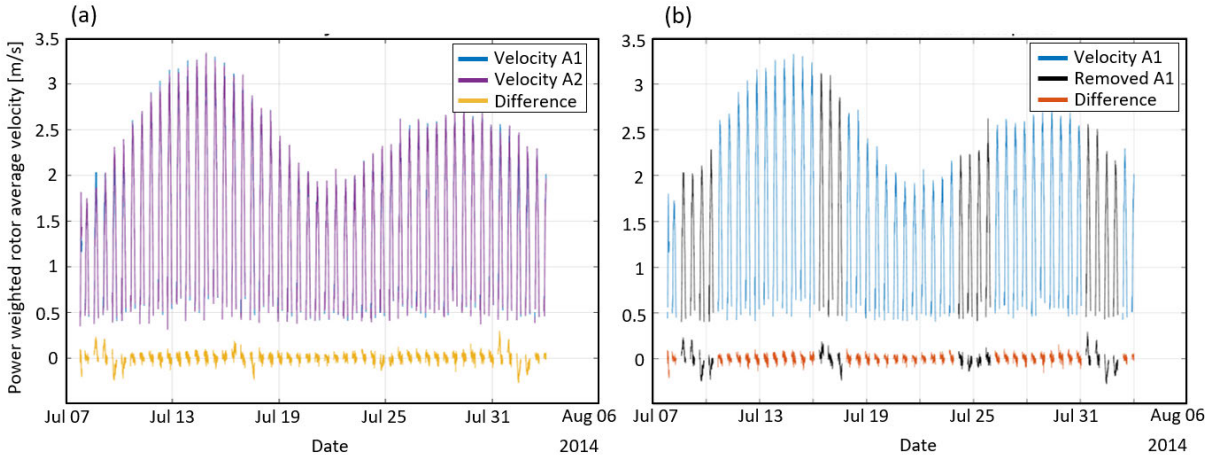

Figure 6.21: (a) Time series comparison of power-weighted rotor average velocities from ADCPs A_1 and A_2, focusing on the TEC$_{T2}$ rotor. The yellow line represents the difference between the two measurements. (b) Power-weighted rotor average velocity time series from ADCP A_1, highlighting flagged data influenced by interference (black line). The difference between ADCP A_1 and A_2 measurements is also depicted.

6.6.1 Data Treatment Post Interference Removal

Acoustic instrument deployments at tidal test sites are associated with substantial costs, and data analysis is possible only after the instrument is recovered. Consequently, any disruption to the measurements remains unknown until post-retrieval analysis. In instances where corrupted measurements render the dataset unusable, techniques could be applied to fill in and restore the gaps with plausible measurements based on reliable data obtained during the measurement campaign. This approach would alleviate the necessity for redeployment and minimise the overall expenses. Even though the IEC TS 62600-200 discourages repairing flagged and removed bad data for the purpose of a PPA, such data can still provide valuable insights into local resource characteristics, flow patterns, and more.

The power law (as discussed in Section 2) is described in Equation 6.1:

$$U_z = \left(\frac{z}{\beta h}\right)^{\frac{1}{\alpha}} \bar{U} \tag{6.1}$$

where the velocity profile (the velocity at height z above the seabed U_z) is described using a power law (α) and bed roughness (β) coefficient with water depth (h) and depth averaged velocity ($\bar{U}$). At each 5-minute time step in the data sets, when the depth averaged tidal velocity exceeded 1 m·s^{-1} (cut-in velocity of the DEEP-Gen IV), the tidal velocity profile form Equation 6.1 was calculated. To calculate the tidal velocity profile from of Equation 6.1, the power law coefficient (α) was iterated through a range of values, the bed roughness coefficient (β) remained constant at 0.32 (typically used in shelf-sea oceanographic research). However, the bed roughness coefficient may be incorrect at tidal energy sites because seabed sediment is likely to be much coarser, or bed forms that give higher bed roughness values (β), in areas of fast tidal currents.

Before constructing the velocity shear profiles using the four beams of the ADCPs, each individual beam was assessed. As shown in Figure 6.5, interference was present in all four beams, albeit with varying intensities. Although eliminating interference at this stage could mitigate its impact on the final deployment results, the variability made it challenging to isolate and remove interference from any single beam. Consequently, all four beams were used to construct the current velocity profile. By addressing the combined interference effect, the overall impact became clearer, and the algorithm processing time for removing each individual interference case was significantly streamlined.

Removing interference features left large gaps in the measured velocity profiles. Interpolation can be used for the purpose of a PPA when the number of data points in a velocity bin is insufficient and prevents the completion of a measurement campaign. The values in an empty velocity bin can be estimated by linear interpolation from the two adjacent completed bins. However, it is not permissible to interpolate a velocity bin with an incomplete adjacent velocity bin. Therefore, interpolating could be used to recover the contaminated data removed. Although extrapolating data during the processing stage is not permitted for a PPA, it can aid measurement campaigns for different purposes. To use extrapolation, the $1/7^{\text{th}}$ power law was compared against other exponent values. Figure 6.22a, 6.22b and 6.22c depicts a velocity profile with the interference spike removed and a comparison of power law exponents to replace the corrupted data for further use. Figure 6.22d, 6.22e and 6.22f shows another profile with missing data at a different depth - due to interference varying with depth - where the required power law exponent is different for representing velocity profile between the good measurements.

Figure 6.23 provides an enhanced resolution of the tested power law coefficients. Figure 6.23 highlights that the velocity profile, featuring remaining reliable data (at depths below 9 m and above 30 m) can be substituted with the calculated power law curve utilising an α exponent of 9.2. However, it's important to note that this exponent doesn't remain consistent for individual 5-minute averaged profiles. When enabling the power-law fitting algorithm to determine the optimal fit, the coefficient exhibited variations depending on the available data within each velocity profile. This highlights that the velocity profile can be effectively processed with suitable values by allowing the power-law algorithm to tailor the best fit for each individual profile.

When including data that has been replaced - in this case extrapolated - the data should be flagged with the QARTOD representative QC flag of *3* (see section 5.4). This highlights that the data is suspect and draws attention to this data. Making comparisons with and without using data flagged as *3* can help the user understand if the data can be used or should be removed from further analysis.

6.7 Discussion

Previous knowledge of acoustic velocity sensors suggested that interference from one beam would adversely affect velocity measurements in another [72]. As the ADCPs both transmit an identically coded pulse at the same carrier frequency the likelihood of cross-talk affecting velocity measurements was relatively high for the two ADCPs separated by 45 m. This chapter has presented clear evidence that acoustic sensors operating in $\approx$ 45 m proximity will operate and collect usable measurements. However, periods of acoustic interference that negatively affected velocity measurements were also found during the measurement campaign. The evidence suggests that interference is strongest and most detrimental at the range corresponding to the measurement volume potentially measured by the two concurrent instruments via sea surface reflections. However, the interference features were

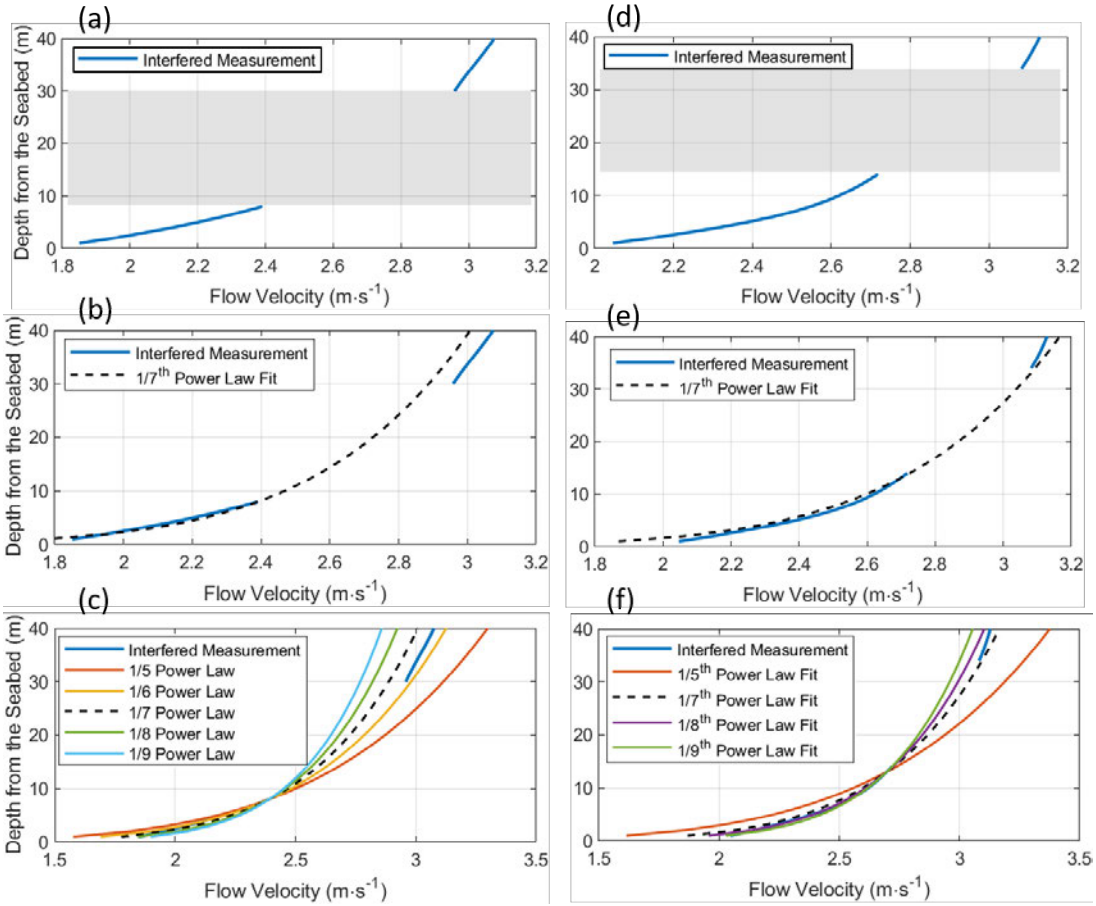

Figure 6.22: Utilising the power law calculation for data gap restoration. (a, d) Display of two velocity profiles indicating gaps (grey area) at distinct depths. (b, e) Frequently used $1/7^{th}$ velocity profile, anchored on the final velocity bin with reliable data (9 m and 13 m for b and e, respectively). (c, f) Visualisation of power law fits, showcasing different coefficients of α.

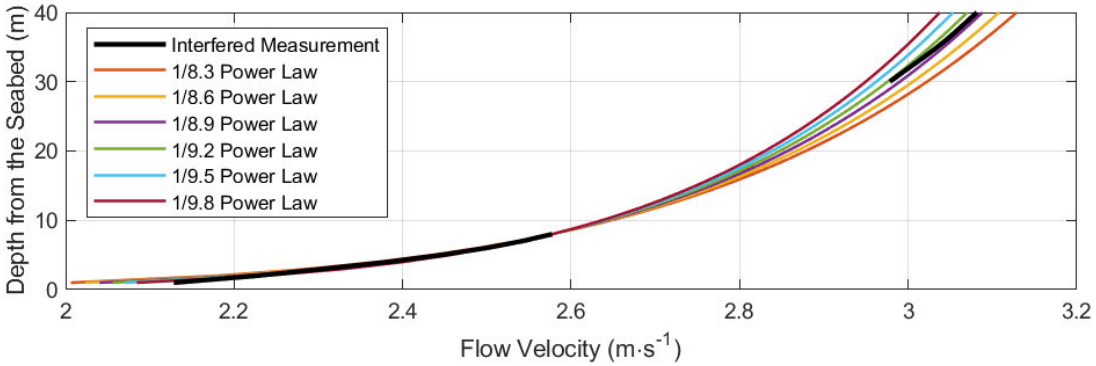

Figure 6.23: Velocity profile variability due to the power law exponent α chosen to represent the corrupted data removed for assumed conditions present at the Falls of Warness.

apparent in one instrument alone before switching to another. This feature made it difficult to identify the causality for this interference successfully. The availability of the flood data was greater than 80% for the measurement campaign, which suggests that two acoustic profilers mounted on the seafloor profiling the vertical plane can be positioned at a distance of the profiling range (in this case $\approx$ 45 m).

One of the notable effects of cross-talk between the two ADCPs is that the interference location (peak) changes frequently as shown in Figure 6.10. There is a biasing towards zero for the measured velocity at the locations of the echo amplitude spikes which is most pronounced in the upper region of the water column ($>$ 30 m from the seabed). In the region beyond the spike, there is little evidence of the velocity measurement changing due to interference. Visual checks on data acquired from ADCPs should be mandatory for multi-instrument deployments, this can increase the chance of identifying anomalies in the data.

This work has explored the sensitivity of the tidal turbine power-production performance to the flow velocity of two individual ADCPs located upstream on a flood tide. The power curve presented followed the methodology of the IEC TS 62600-200. The real-world power measurements from the DEEP-Gen IV were time matched to the PWRA velocity calculated for two seabed ADCPs across different depths. Two curves have been presented - with/without interference characteristics included - had the interference not been identified, the corrupted velocity measurements along the swept area of the DEEP-Gen IV would have been used to calculate the PWRA velocity. This value would significantly increase if the number of flood cycles featuring interference characteristics was greater. This indicates that a small amount of corrupted data passing through the data QC checks can have a significant impact on the averages calculated. The impact of interference was more significant when using measurements at higher-depth bins. This indicates that the interference is more prominent in the upper water column before attuning downward.

To identify and remove the features of interference an algorithm was developed. Each 5-minute sample was filtered for characteristics of interference. Upon analysing the results $\approx$ 90% of the corrupted measurements were removed using the detection algorithm. The remaining 10% of the data were close to the sea surface where there is an increase in echo amplitude due to the medium change. Although data were removed in the most upper-depth bins ($>$ 40 m in this case), the interference occasionally occurred at a depth of 35 - 40 m from the seabed. This meant that only one peak occurred close to the boundary and the data was flagged as good. This highlights an area of further work to improve the algorithm for features of interference. However, for the purpose of this work, the consequence of corrupted measurements passing through QC checks was presented on the measured power curve and AEP estimates.

When planning multi-instrument deployments, the range the instruments are separated by should be considered. For deployments where the possibility of cross-talk is high, efforts can be made to reduce the amount of gaps in the data after post-processing checks have been carried out. To meet data criteria (hours, days or weeks of measurements required), data can be repaired. Removing the features of interference left large gaps in the velocity depth profiles, this can have an effect on the average profile and measurements per velocity increments at heights associated with interference. Here, the 1/7th power law (typically used to characterise the velocity profile in tidal energy) was examined for the purpose of treating gaps in the data. The measurements missing were greater than two or three depth bins, therefore interpolation was not feasible, for this reason, extrapolation was used. The remaining good measurements were used as a reference when applying a 1/7th power law. This coefficient was found to provide an inconsistent profile which failed to fit between the good data provided in the lower and upper bounds of the velocity depth profile. Therefore, coefficients other than α = 7 were examined for different velocity profiles. Individual 5-minute velocity profiles with varying gaps in the velocity depth profile were found to have different coefficients of α when attempting to restore bad data. The power-law profile varied

from the good measurements (Fig 6.22) when the velocity from a selective depth bin was used in the power law calculation (Equation 6.1). This method should only be used as a guide and the treated data should be flagged as suspect data for further analysis. Although it's currently unsuitable to restore data deemed unusable according to the IEC TS 62600-200 guidelines for PPA, valid data can offer valuable insights into data restoration methods.

6.8 Conclusions

This chapter assessed the DEEP-Gen IV 1 MW tidal turbine's power performance using data from seabed-based ADCPs, ADCP$_{A1}$ and ADCP$_{A2}$, placed at 61 m and 106 m from the TEC in accordance with IEC TS 62600-200 guidelines. One of the key challenges confronted was acoustic cross-talk affecting the data.

A systematic approach for identifying and removing cross-talk features from ADCP measurements is introduced. Despite efforts to remove inadequate data using industry standards and best practices, this new method proved to be effective in flagging and removing unreliable data points. If necessary, the flagged data points are replaced with plausible measurements but remain marked as suspect for further analysis.

The presence of acoustic cross-talk impacted around 15% of the entire set of flood tide cycles. These disturbances varied across the water column, impacting velocity measurements by up to 2.5% across the DEEP-Gen IV rotor plane and by 6% in the upper-most 20-40 m depth bins.

It also examined how cross-talk features affect AEP estimates. The data revealed considerable sensitivity to changes in velocity measurements, with variations in AEP estimates ranging from 2% to 7% depending on the depth of the measurement. This highlights the sensitivity of AEP estimates to changes in velocity measurements.

Given the high costs associated with each deployment—covering equipment, ship time, and human resources—making the most out of each data point is imperative. The power law was explored for replacing flagged data, with coefficients optimised for each unique velocity profile. The algorithm effectively determined the best fit for each velocity profile, filling in the gaps but also indicating the level of uncertainty introduced by such replacements.

Despite the challenges posed by acoustic cross-talk, the bulk of the data—over 80%—remained usable. To further improve data quality, it's recommended to stagger the duty cycle of concurrently deployed ADCPs, thereby avoiding overlapping signal pings.

The measured power curve and AEP estimates are highly sensitive to changes in velocity caused by acoustic cross-talk. However, more than two-thirds of the data was usable, this justifies further work in this area to find the causality of acoustic cross-talk. This will be particularly useful for turbines with smaller rotor diameters, where the instrument will be placed closer to the turbine location.

In summary, acoustic cross-talk in ADCP measurements can significantly impact PPAs for tidal turbines. It is crucial to develop methods to identify and remove cross-talk features from data to ensure the accuracy of power curve generation and AEP estimates. In this scenario, two ADCPs operated simultaneously, positioned 45 meters apart at the same depth, yielding reliable measurements for more than 80% of the campaign. Despite the undetermined cause of cross-talk, the study indicates that ADCPs can operate successfully at a function of their operating range - in this case, a depth of 45 m and both separated by 45 m (as seen in Fig 6.14) - from each other and obtain accurate measurements.

Chapter 7

Uncertainty in Power Estimates due to Spatial Variability in Flow Velocity

7.1 Chapter Overview

Demonstrating power performance in real conditions is vital for verifying tidal turbine design. The International Electrotechnical Commission's Technical Specification IEC TS 62600-200 provides guidance for tidal developers to evaluate machine performance. This chapter evaluates the performance of the operational 1 MW DEEP-Gen IV commercial-scale tidal turbine deployed during the ReDAPT project at the European Marine Energy Centre's tidal test site in Orkney, Scotland. IEC TS 62600-200 states that the power performance should be measured relative to two independently located current profilers deployed in one of two orientations; 'in-line' (preferred) or 'adjacent' (least preferred), relative to the turbine. Two measurement campaigns are used to assess the impact of instrument placement on the measured power curve and annual energy production. The ambient current flow and vertical profile form differed at each current profiler location (due to topography and bathymetry), leading to AEP variability.

An additional analysis assesses the sensitivity of AEP estimates on the vertical alignment of the flow profiles with rotor positioning. For this, three turbine scenarios were investigated: the DEEP-Gen IV and two modelled turbine rotors occupying different regions in the water column. Results show that for regions of high vertical shear, AEP estimates can be misrepresented under an imposed vertical misalignment. This chapter aims to quantify, at this site (specific tidal berth), the variation in AEP estimates from different flow measurement campaigns informed by IEC TS 62600-200 and has shown the need to ensure good vertical alignment between measurements and turbine rotor positioning. Findings from the results can help inform future deployments at different tidal test sites.

Multiple instrument deployments are becoming more common as we aim to gather more in-situ data at tidal test sites to understand the flow characteristics better. In addition, TEC-mounted instruments are being implemented to analyse their capabilities for performance monitoring, with comparisons against traditional seabed-placed instruments considered as the reference. Findings from unique measurement campaigns with standardised placed instruments and an operating full-scale commercial TEC can help provide insights and re-inform standardised methods.

Many TEC designs exist, all having different characteristics (e.g. rated power and rated velocity) and deployed at different depths (z) along the water column. For turbines that float, the motion from mooring cables, in addition to the flow velocity in the upper regions of the water column, adds further complexity to carrying out a PPA. The floating TEC concept is likely exposed to further tidal flow variation due to wind-induced flow and wave-current

interaction, and measured flow data is frequently removed close to the surface. This can impact the calculation of the power-weighted rotor average (PWRA) velocity, recommended in the IEC TS 62600-200. Furthermore, capturing the orientation and location of the current profiler becomes difficult once it is lowered into the water. Increasing the accuracy of sensor deployment position and orientation comes with additional costs and can involve further dedicated sub-systems and complex installation techniques. As such, quantifying the impact of spatial variability and verifying the use of TEC-mounted measurements can help expand the acceptable PPA instrument configurations.

This chapter is structured as follows: Section 7.2 provides a test overview of the installation site, tidal turbine, the suite of instruments relative to this chapter, and the post-processing of the in-situ measurements; Section 7.2.1 and 7.2.2 reports on the key results obtained for the spatial variation in velocity in the horizontal and vertical plane respectively; Section 7.3 discusses these key findings in the context of existing best practices. Section 7.4 concludes the chapter.

7.2 Instrumentation Configuration and Deployment

The uncertainties discussed in this chapter include the ADCP placement, the alignment of ADCP bins to the hub height of the deployed TEC in situ (refer back to 6.1). The resulting uncertainties in velocity measurements due to these factors will be examined in detail, providing critical insights into optimising ADCP deployment for reliable power performance assessments.

All the instruments and the TEC were deployed in Berth 2 at the FoW, at a depth of $\approx$ 43-46 m, see Figure 5.2 for a high-level location of the tidal test site and Figure 5.3 for a plan view of the measurement campaigns. The bathymetry of a TEC test site must be surveyed to ensure that it is free from obstacles and topography that could affect the performance of the TEC and the measurements from deployed instruments. Figure 5.5b highlights the maximum and minimum depth recorded at berth 2. This also aids in post-processing data sets when matching the depth bins of the acoustic instruments to the hub height of the TEC. The bathymetry varies by up to a maximum of 3 m, therefore will not cause any effect on the measurements. The instruments used in this chapter are positioned at locations A_1, A_2 and A_3 (in-line with the TEC), B_1 and B_2 (adjacent to the TEC) and C_1, C_2 attached to the rotor and rear hub of the DEEP-Gen IV (TEC$_{T1}$), refer back to Table 5.1 and 5.2 for instrumentation details and Figure 5.3 for a visual representation.

The velocity time-series data sets are presented in Figure 7.1. Tidal cycles (June to July 2014) are shown for the in-line instruments and (October to December 2014) for the adjacent instruments. Figure 7.1a and 7.1b depict the flood and ebb data sets from the in-line measurement campaign respectively, whereas Figure 7.1c and 7.1d depict the flood and ebb for the adjacent measurement campaign respectively. The directionality and strength of typical tidal currents (from the five seabed-placed instruments) at the deployment location are shown in Figure 7.2

The tidal currents at the site are predominantly bi-directional with an offset of $\approx 45^{\circ}$ from North/South. The ebb tide is stronger at this location, reaching mean flows up to 4 m·s^{-1}, whereas the flood tide reaches $\approx$ 3.5 m·s^{-1}. The ebb tide is also much more turbulent due to the flow being disturbed by several features of the site bathymetry and local islands, which have been reported on by others.

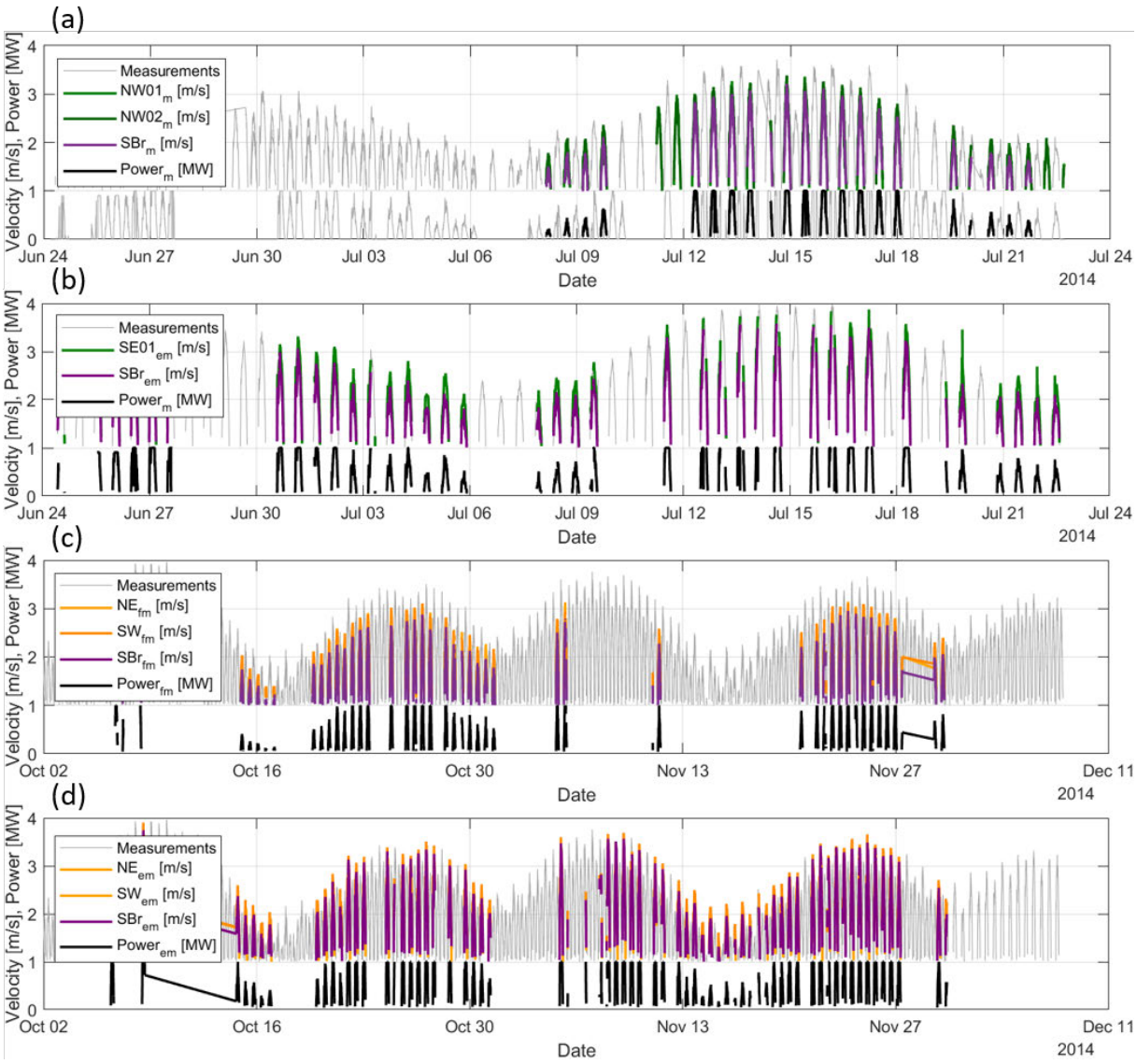

Figure 7.1: Velocity time-series of data sets: (a) flood tide measurements from ADCPs deployed at A_1 (NW01), A_2 (NW02), TEC rotor-attached SB-ADP C_1 (SB$_r$) matched with the power produced by the DEEP-Gen IV T_2. (b) Ebb tide measurements from an ADCP placed at A_3 (SE01), rotor-attached SB-ADP C_1 (SBr) matched with the TEC power generated. (c) Flood tide measurements from ADCPs placed at B_1 (SW$_{fm}$), B_2 (NE$_{fm}$) and the rotor-attached SB-ADP C_1 (SBr) matched with the TEC power generated. (d) Ebb tide measurements from ADCPs placed at B_1 (SW$_{em}$), B_2 (NE$_{em}$) and the rotor-attached SB-ADP C_1 (SBr) matched with the TEC power generated. 5-minute averaged data from the campaigns are highlighted as grey lines.

The tested turbine was the DEEP-Gen IV 1 MW-rated machine with a traditional horizontal axis three-blade design of 18 m rotor diameter, further key details on the DEEP-Gen IV can be found in Table 5.8 and visual representation in Figure 5.20.

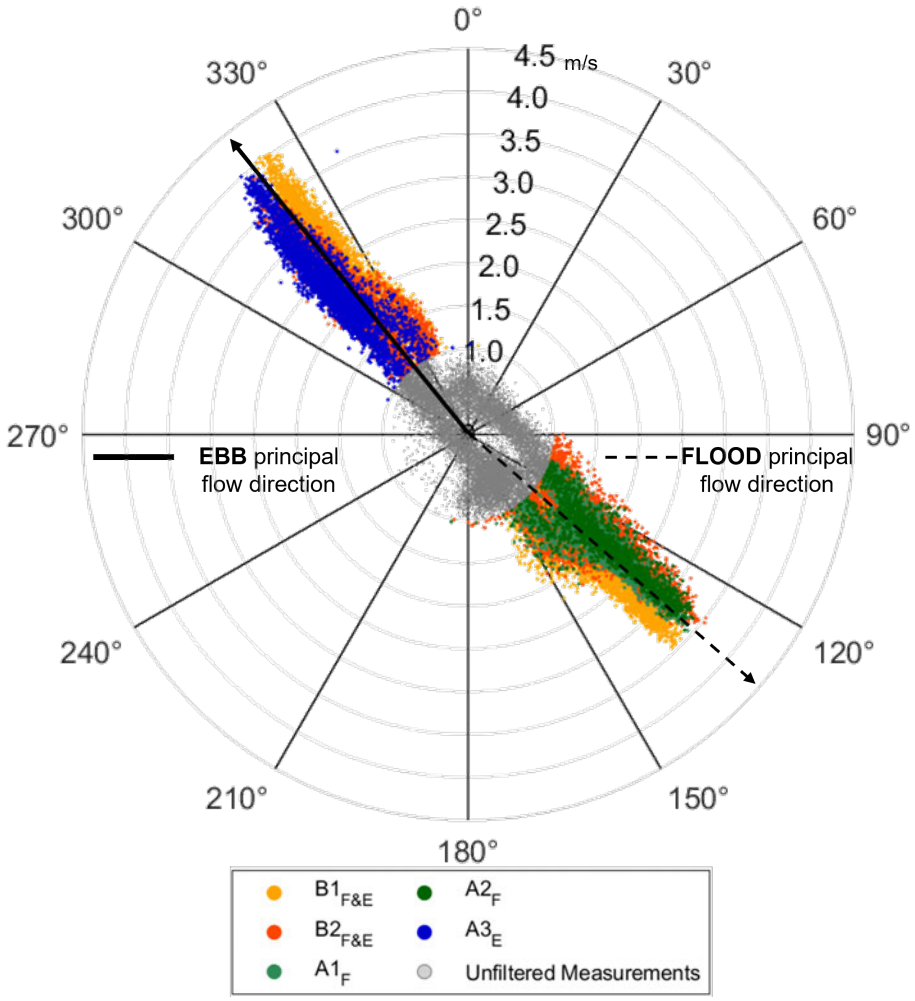

Figure 7.2: Directionality and strength of the flood and ebb tidal characteristics at Fall of Warness at each instrument location used in the analysis.

The SB-ADPs were used throughout both deployments (deployment 5, ADCPs located at A and deployment 7, ADCPs located at B), attached to the DEEP-Gen IV rotor (C_1) and rearhub (C_2). These data sets allow comparison between the two IEC TS recommended orientations to a TEC-proximal location. Orientation A had two ADCPs (A_1, A_2) measuring concurrently at locations upstream of the TEC (on a flood tide), separated by $\approx$ 45 m. The SB-ADP measurements were compared with the seabed ADCPs to assess the capabilities for performance assessments. Data collected from the two deployments (A and B) included periods of spring and neap tides. The data used in the analysis for type A and B are $\approx$ 15 and 57 days long respectively. The reduction in the amount of usable data compared to the full measurement campaigns was primarily due to decreased data quality during turbine operation, especially when instruments were positioned in the wake. This was further compounded by interference between co-located instruments and the overall measurement quality of the SB ADP.

Table 7.1 illustrates the inter-instrument comparison and the number of 5-minute samples available after QC and filtering the data for periods of no power generated by the DEEP-Gen IV. The instruments used for the flood tide comparison are as follows: A_1, A_2, C_1 and C_2 for the in-line measurements, and B_1, B_2, C_1 and C_2 for the adjacent. Instruments used for the ebb tide comparison are as follows: A_3, C_1 and C_2 for the in-line measurements, and B_1, B_2, and C_1 for the adjacent. Instruments located at A1, A2, measuring the ebb tide and A3 measuring the flood tide experience significant wake effects from the DEEP-Gen IV turbine during operation, and thus their data has been excluded from the analysis.

Table 7.1: Inter-instrument comparison table showing the available 5-minute ensembles, where colours correspond directly to instruments depicted in Figure 5.3. The light grey shaded region corresponds to flood conditions with data relating to ebb shown diagonally opposite.

Velocity Spatial Variation: Chapter 5										
ADCP ID	A1	A2	A3	A4	A5	B1	B2	C1	C2	Ebb Conditions
A1	**x**	x	x	x	x	x	x	x	x	
A2	2172	**x**	x	x	x	x	x	x	x	
A3	x	x	**x**	x	x	x	x	4579	2192	
A4	x	x	x	**x**	x	x	x	x	x	
A5	x	x	x	x	**x**	x	x	x	x	
B1	x	x	x	x	x	**x**	8458	8458	2214	
B2	x	x	x	x	x	9646	**x**	8458	2214	
C1	2172	2172	x	x	x	9646	9646	**x**	x	
C2	724	724	x	x	x	2512	2512	x	**x**	
Flood Conditions										

In order to assess the impact of vertical misalignment on energy production, two further turbine types are introduced, labelled T_2 and T_3, using modelled power (as opposed to measured power as was the case with the DEEP-Gen IV T_1). The TEC parameters are provided in Table 5.9 and visually represented in Figure 5.21.

7.2.1 Horizontal Variation in the Measured Flow Velocity

Preliminary Analysis of the ADCPs

Five tidal ellipses were produced (refer back to Figure 7.2 and respective instrument location in Figure 5.3) to show how the strength and direction of the flow vary per instrument location. As can be seen in Figure 7.2 at this location the ebb tides are faster than the flood tides by $\approx$ 0.8 m·s^{-1} and the tides are $\approx 10^{\circ}$ off from being rectilinear. There is some disagreement in the principal flow direction amongst the ADCPs. In the flood tide, these disagree by as much as 10°, whilst the difference is closer to 5° in the ebb direction. The calculation of PWRA velocities is insensitive to flow direction since they involve velocity magnitudes. However, for other applications, e.g., turbine operation and control, directionality should be considered.

Inter-instrument Comparison

The current velocity measurements at a range of heights covering the TEC rotor plane from instruments placed at locations A and B (refer back to Figure 5.3) are presented in Figure 7.3.

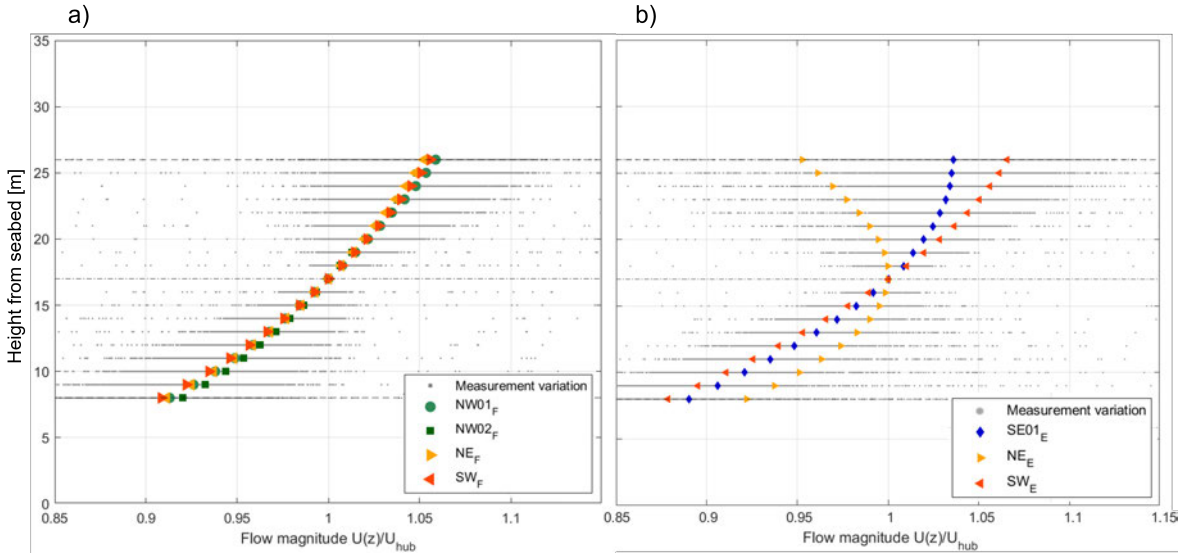

Figure 7.3: Velocity magnitude - long-term average (coloured) and individual 5 minute averaged measurement (grey) - along the rotor of the DEEP-Gen IV turbine from various nearby locations (a) Flood tide measurements from A_1 (NW01), A_2 (NW02), B_1 (NE$_F$) and B_2 (SW$_F$). (b) Ebb tide measurements from A_3 (SE01), B_1 (NE$_E$) and B_2 (SW$_E$). Averages are calculated using the entire dataset collected at each location around the TEC.

Velocities were normalised by hub-height velocities (18 m above the seabed for the DEEP-Gen IV TEC). These are compared against a mean velocity profile. The instruments were compared based on placement and tidal cycle. The in-line measured current velocity U$_{A1}$, and U$_{A2}$ varied by $\approx$ 0.75% at the lower bounds, and $\approx$ 0.35% at the upper bounds. Similarly, U$_{B1}$ and U$_{B2}$ differed by alike margins during the flood tide, Figure 7.3a. In contrast, the ebb tide revealed a substantial variation along the rotor plane, where U$_{B1}$ and U$_{B2}$ record significantly different current velocities in both the most-lower bound and most-upper bound, differing by $\approx$ 5%, and $\approx$ 12% respectively. Similar velocity reductions have been found in the upper region of U$_{A3}$, see Figure 7.3b.

Figure 7.4 displays the correlation between time-matched PWRA velocities for each instrument pairing, where the in-line instruments A_1, A_2 are $\approx$ 45 m apart, and the adjacent instruments B_1 and B_2 are $\approx$ 70 m apart. Periods of interference were removed from the analysis, resulting in a standard dataset with the interference excluded and not treated, as treated data should not be used for power performance assessments. The sum of square error (SSE) and the root mean squared error (RMSE) of the relationship between compared instruments are shown in Figure 7.4. Figure 7.4b compares the streamwise velocity component measured by the SB-ADP C_1 with the PWRA velocity reference positioned in-line with the TEC (thus SB-ADP).

The flood tide velocity measurements $\bar{U}_{A1}$, $\bar{U}_{A2}$ and $\bar{U}_{B1}$ $\bar{U}_{B2}$ show high correlation. However $\bar{U}_{B1}$ and $\bar{U}_{B2}$ contain a lot more data scatter with a larger SSE when compared with $\bar{U}_{A1}$ and $\bar{U}_{A2}$ as shown in Figure 7.4a. Unlike the flood tide, the ebb tide, on deployment 5, was measured by a single ADCP, A_3. This was compared with C_1, indicating a strong correlation (with an RMSE comparable with the other in-line instruments A_1, and A_2 measuring

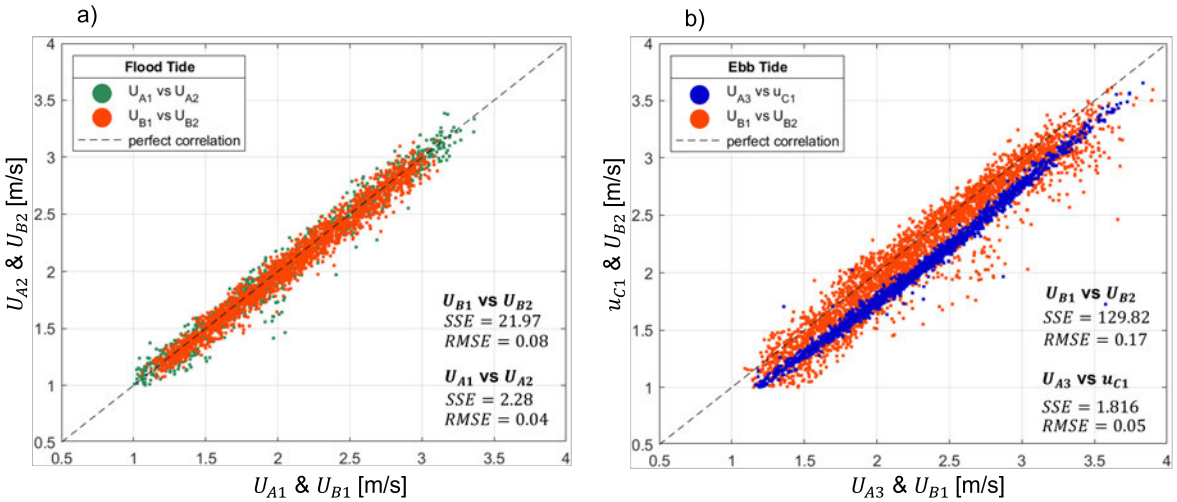

Figure 7.4: a) Inter-instrument correlation for the flood measurements, PWRA velocities $\bar{U}_{A1}$ vs $\bar{U}_{A2}$ (green) and $\bar{U}_{B1}$ vs $\bar{U}_{B2}$ (orange). b) Ebb tide correlation, for $\bar{U}_{A3}$ and $\bar{u}_{C1}$ (blue), and $\bar{U}_{B1}$ vs $\bar{U}_{B2}$ (orange).

the flood tide). However, a clear bias is present, where C_1 consistently underestimates the velocity compared with the traditional seabed-placed A_3. The ebb tide velocity scatter from B_1 and B_2 comparisons is also shown in Figure 7.4b, with greater variation than the equivalent comparison on the flood tide. This scatter increases further at higher velocities, where B_2 measurements also trend towards slower velocities.

Spatial Variation in Velocity

Velocity profiles were produced to analyse how the flow changes with depth. The measurements of velocity from instruments in both configurations A and B, were split by flood and ebb tides and subdivided into velocity bins (related to the depth bin aligned to the DEEP-Gen IV hub height) in increments of 0.3 m·s^{-1}. It can be seen in Figure 7.5a that the difference between U_{A1} and U_{A2} at hub-height and the speed of rated power (1 MW) is 0.5% for the instruments placed in-line measuring the flood tide. Figure 7.5b shows larger differences between the equivalent measurements for the $B1$ and $B2$ pairing, at 3.1%.

The velocity measured by the rotor-attached hub-height SB-ADP, $\bar{u}_{C1}$, is shown as a filled circle. The instrument measured a reduced velocity, commonly close to $\approx$ 0.15 m·s^{-1} slower than U_{A1}, U_{A2}, U_{B1} and U_{B2} during the flood tide.

Ebb tide data presented in Figure 7.6b shows a larger discrepancy between U_{B1} and U_{B2}. Differences increase with higher velocity and height above the seabed. At the rated-power velocity of 2.7 m·s^{-1} differences ranged from 2.1 - 19.4% from the bottom-most and top-most locations respectively of the rotor plane. $\bar{u}_{C1}$, shown as filled circles, corresponds closely with U_{B2} for the ebb tide measurements.

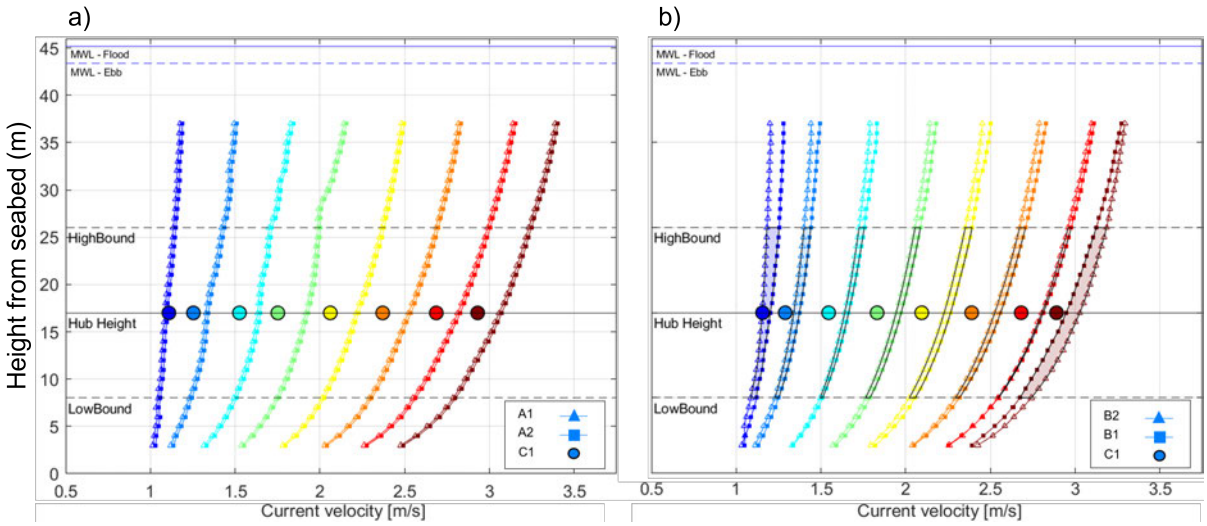

Figure 7.5: Velocity depth profile for flood tide measurements for a) in-line ADCP pair A_1 and A_2, compared against the rotor-attached instrument C_1 (filled circle marker at hub-height, 18 m). b) Velocity measurements from the adjacent locations to the TEC B_1 and B_2, the rotor-attached SB-ADP C_1 is depicted as a filled circle at hub-height.

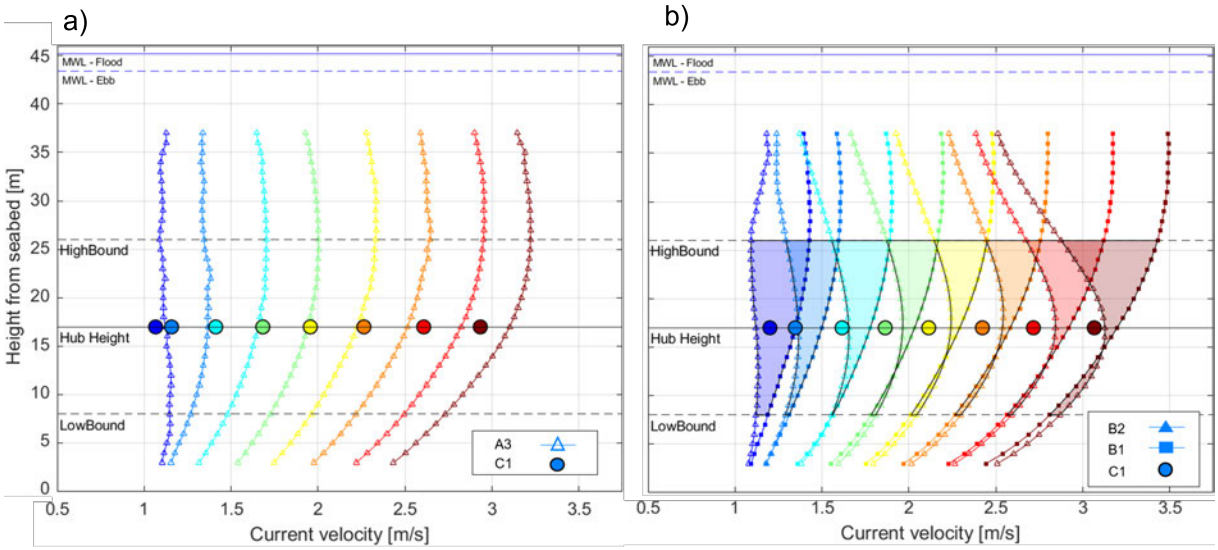

Figure 7.6: Velocity depth profile for ebb tide velocity measurements for a) in-line ADCP A_3, and SB-ADP C_1 (filled circle marker at hub-height of 18 m). b) Velocity measurements from the adjacent locations to the TEC, B_1 and B_2, and the rotor-attached SB-ADP C_1.

Power Curve and AEP Comparison

The PWRA velocities from each seabed ADCP and the streamwise velocity from the rotor-attached SB-ADP were paired with the real-world power measurements from the DEEP-Gen IV, and then sorted into velocity bins in increments of 0.1 m·s^{-1} in accordance with the IEC TS 62600-200. The mean velocity flow and power within each bin were then calculated. Figure 7.7 presents the final power curves for the flood and ebb tide. The black solid line shows the power curve provided by the DEEP-Gen IV operator, Alstom 10.1 [358].

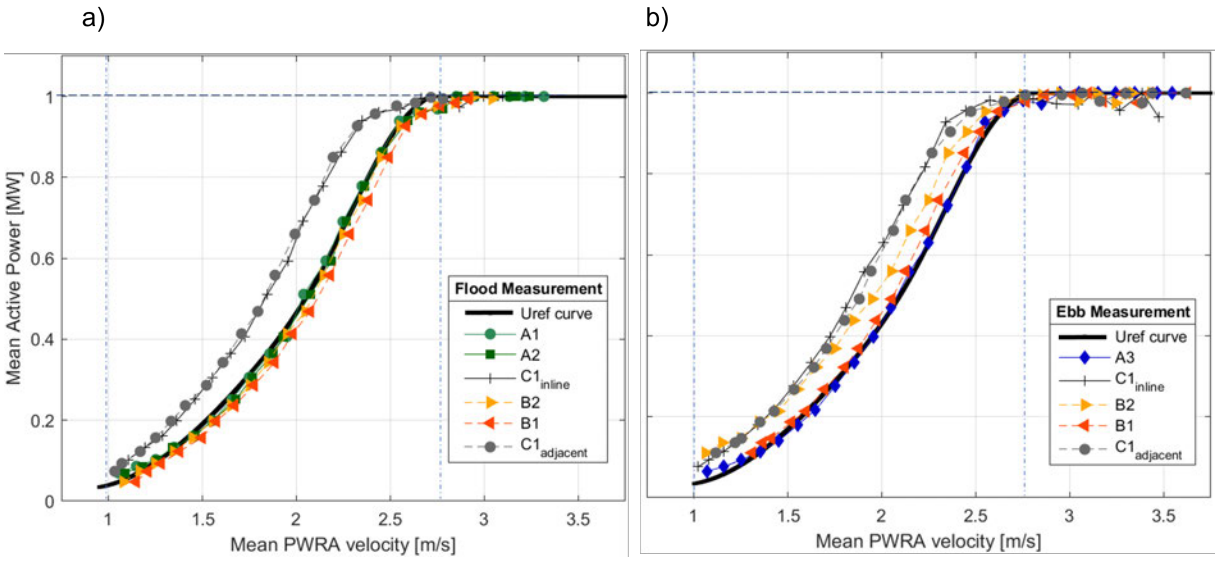

Figure 7.7: The effect of ADCP placement - per IEC TS 62600-200 - on measured power curve for the averaged 5-minute velocities in increments of 0.1 m·s^{-1}. a) The flood tide measurements from the in-line ADCP pair $\bar{U}_{A1}$ and $\bar{U}_{A2}$, the adjacent pair are included $\bar{U}_{B1}$ and $\bar{U}_{B2}$. b) The ebb tide measurements from the rotor-attached SB-ADP, $\bar{u}_{C1}$ and $\bar{U}_{A3}$, and the adjacent pair $\bar{U}_{B1}$ and $\bar{U}_{B2}$. The black line represents the published power curve of the DEEP-Gen IV.

The measured power curve was produced with reference to the velocity measured at C_1. This curve implies the DEEP-Gen IV produced more power under slower flow velocity conditions when compared with velocity measurements at the seabed-placed ADCP locations. However, the velocity measured by the rotor-attached SB-ADP was shown to underestimate the flow approaching the rotor (Fig 7.4b and 7.5). Therefore, the power curve is misleading and implies the SB-ADP provides a more favourable power curve from a developer's perspective.

A key part of this study is to assess the impact of using ADCPs around the extremities of the guidance provided by the IEC TS target locations. For this, the measured power curves for the flood tide measurements are shown in Figure 7.7a. The mean PWRA velocity at rated power (1 MW) for ADCP pair $\bar{U}_{A1}$ and $\bar{U}_{A1}$ (approximately 3.4 D_E and 5.5 D_E from the rotor centre respectively) differ by 0.6%. Whereas, the mean PWRA velocity at rated power for ADCP pair $\bar{U}_{B1}$ and $\bar{U}_{B2}$ (located 32 m southwest and 34 m northeast of the rotor centre) differed by 1.1%.

The ADCP pair positioned in-line A_1 and A_2, measure a slightly lower PWRA velocity compared with the ADCPs positioned adjacently B_1 and B_2. From a developer perspective, this results in a seemingly more efficient power curve when a lower mean velocity, U_{A1}, is compared with the higher mean velocity, U_{B1}, for the equivalent power. Figure 7.7b shows the power curves for the mean velocities measured for the ebb tide by: in-line ADCP A_3; adjacent ADCP pair B_1 and B_2; and the rotor-attached SB-ADP C_1. At the lower velocity values ($<$ 2 m·s^{-1}) there are more obvious differences between B_2 and the other two ADCPs (B_1 & A_3) produced from $\bar{U}_{B2}$, $\bar{U}_{B1}$ and $\bar{U}_{A3}$. However, A_3 and B_1 curves almost collapse on to one another for PWRA $<$ 2 m·s^{-1}, there are clearer differences between all ADCPs for PWRA $>$ 2 m·s^{-1}. This is likely due to a combination of faster accelerations in this regime and a spatial variation in the measured velocity on the ebb tide. At rated power, the ebb tide curves produced by $\bar{U}_{B1}$ and $\bar{U}_{B2}$ differ by 4.3%.

In terms of the flow references measured by ADCP pairs A_1 and A_2, and B_1 and B_2, a better agreement with the predicted curve is found using the ADCPs placed in-line to the TEC. This is shown for the ebb tide power curves, where A_3 is placed in-line and closely matches the predicted curve of the DEEP-Gen IV. It is likely that these findings highlight that there are periods in which the seabed ADCPs placed adjacent do provide a good reference velocity (velocity increments < 1.5 m·s^{-1}), but differences grow between ADCP pair placed in-line and ADCP pair placed adjacent as the mean velocity increases at the site.

In addition to the measured power curves generated from seabed ADCPs, the SB-ADP flow measurements are used to assess the power curve. Unlike the ADCP datasets however, there is no accounting for the vertical variation or directionality in the flow and so the SB-ADP represents a hub-height speed along the axis of rotation. Velocities for each seabed ADCP were compared against the velocity measured at C_1. The velocity differed by up to $\approx$ 8% when compared with ADCPs positioned in-line A_1 and A_2, and 11% when compared with ADCPs positioned adjacently B_1 and B_2.

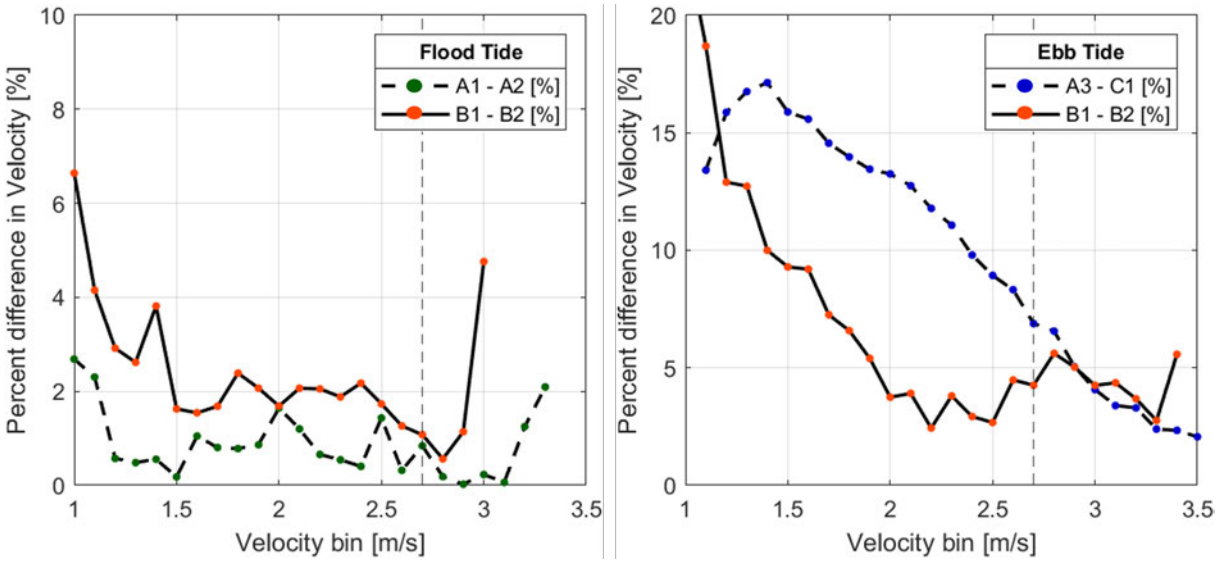

Figure 7.8: In-line placed ADCPs (black dashed line) A_1, A_2, A_3 and adjacent placed ADCPs B_1, B_2 (black solid line) and their calculated PWRA velocity in increments of 0.1 m·s^{-1}. a) Flood tide PWRA velocity difference between pair: $\bar{U}_{A1}$ and $\bar{U}_{A2}$, and pair $\bar{U}_{B1}$ and $\bar{U}_{B2}$. b) Average velocity difference between $\bar{u}_{C1}$, $\bar{U}_{A3}$, and the PWRA velocity difference between $\bar{U}_{B1}$ $\bar{U}_{B2}$.

AEP was estimated using the pre-defined power curve provided by Alstom for the 1 MW DEEP-Gen IV. The PWRA velocities, measured at locations A and B relative to the TEC location and hub-height, were paired with the corresponding power via a look-up table to form a power time-series. In terms of the two orientations - in-line and adjacent - a better agreement between ADCP pair A_1 and A_2 was found. Figure 7.8 shows the variation in velocity between instrument pairs calculated at various velocity bins. It can be seen that differences reduce during faster flows (where the turbine generates most of its power). The AEP differed by 1.2% between A_1 and A_2, and 2.6% between B_1 and B_2 for the flood tide. The ebb tide, measured by ADCPs at B_1 and B_2 differed by 7.3%.

7.2.2 Vertical Variation in the Measured Flow Velocity

An additional analysis on the impact of flow measurement vertical misalignment was conducted on three types of TEC: the ReDAPT commercial-scale tidal turbine, and two further variants of horizontal axis tidal turbines (selected as representative of current technologies), which operate in different locations of the water column. Since the measurements used for this case study focus on the instruments placed adjacent (B) to the DEEP-Gen IV location, DEEP-Gen IV does not affect the measurements collected. Therefore, the two additional turbines T_2 and T_3 will be "in theory" at the same location as the DEEP-Gen IV. The impact of vertical alignment between the instrument and the height of the TEC hub can then be assessed for three turbines that experience different variations of shear in the water column.

Figure 7.9 illustrates the velocity profiles for the flood and ebb tides measured at locations B_1 and B_2. The location of the turbine of T_1, T_2 and T_3 is also shown in Figure 7.9. These two instruments were selected because the profiles differ significantly, potentially representing conditions at different sites. This provided an opportunity to assess the extreme effects of misaligning the bin depth with the proposed hub height of a deployed TEC.

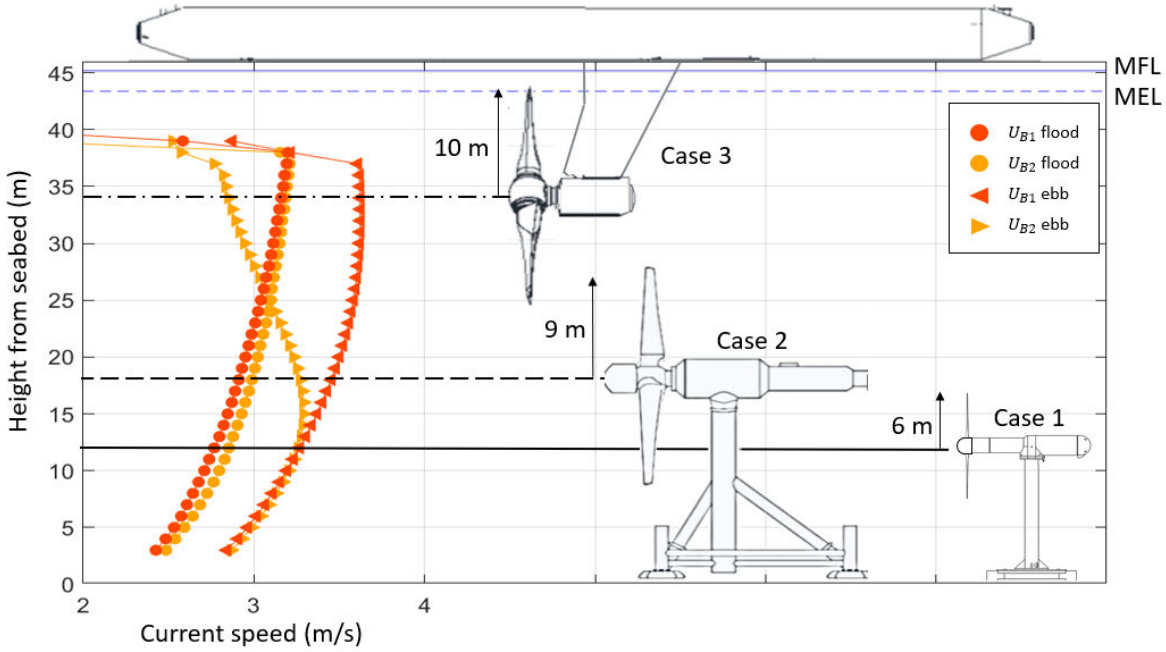

Figure 7.9: Three TEC concepts are placed accordingly to their hub-height reference. U_{B1} and U_{B2} represent the peak rated velocity for the flood and ebb tide. The mean water level for the flood (MFL) and ebb (MEL) tide is represented by the blue solid and dashed line respectively. NOTE rotor diameter to scale, TEC dimensions are not to scale.

Impact on the Measured Power Curve from Vertical Misalignment

Figure 7.10 illustrates the measurements that contribute to the measured power curve, included are the mean performance curves produced from data sets up to ± 2 m from the DEEP-Gen IV hub height - 18 m.

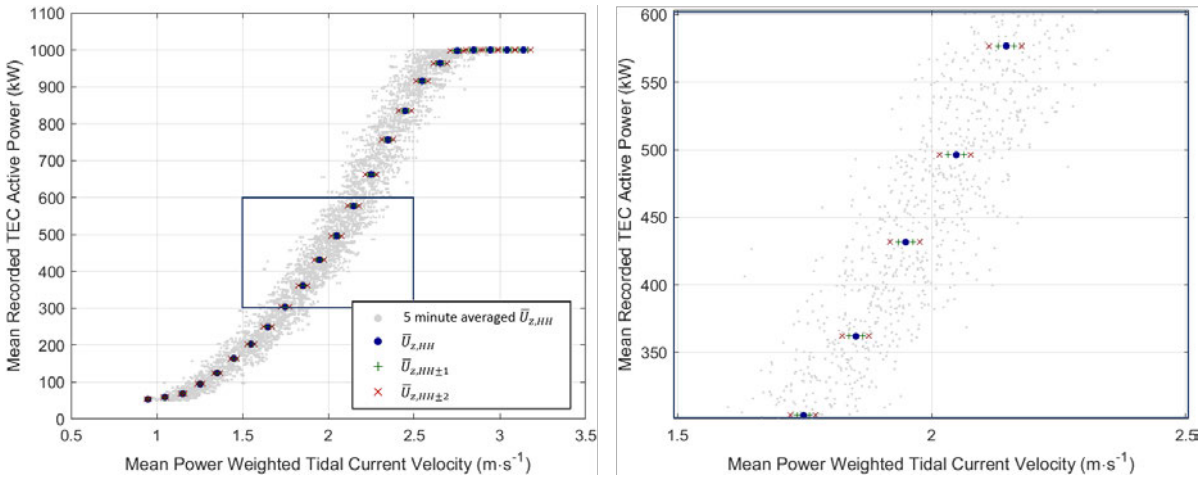

Figure 7.10: Presentation of the power curve for flood tide measurements at location B_1, showing the variation in mean velocity $\bar{U}_{B1}$ when the incorrect depth bin is paired with the TEC hub height.

Figure 7.11 shows the variation in velocity between instrument pairs calculated at various velocity bins. It is evident that the difference in velocity increases when the depth bins of the ADCP are misaligned with the TEC hub height, especially when a bin depth lower than the actual hub height is chosen.

The whole TEC system efficiency is defined by (previously stated in Equation 2.55):

$$\eta = \frac{P}{\frac{1}{2} \cdot \rho \cdot A \cdot U^3}$$

where P is turbine power in watts, ρ is the seawater density (1027 kgm^{-3}), A is the rotor area of the DEEP-Gen IV (257 m^2) and U is the flow velocity in m·s^{-1} at the acoustic instrument location. This is shown in Figure 7.12, the maximum efficiency for the flood tide is 0.442. This can be misrepresented by ≈2.2% and 4.8% if the vertical alignment between the instrument and TEC swept area by ± 1 and 2 m respectively.

TEC efficiency should not be confused with the rotor power coefficient which is a measure of the rotors hydrodynamic efficiency. This TEC efficiency includes all the mechanical and electrical losses in the whole system and so the rotor power coefficient is always larger than TEC efficiency.

Impact on the Annual Energy

To determine the estimated yearly energy output in kWh of a device with a specific power curve, it is necessary to merge the power curve with a probability distribution of flow velocity close to the TEC location, the following formula is used (previously stated in Equation 2.56):

$$\mathrm{TEC_{AEP}} = \mathrm{N}_h \cdot \mathrm{TEC_A} \cdot \sum_{i=1}^{N_B} \bar{P}_i \cdot f_i(\bar{U}_i) \cdot 1000$$

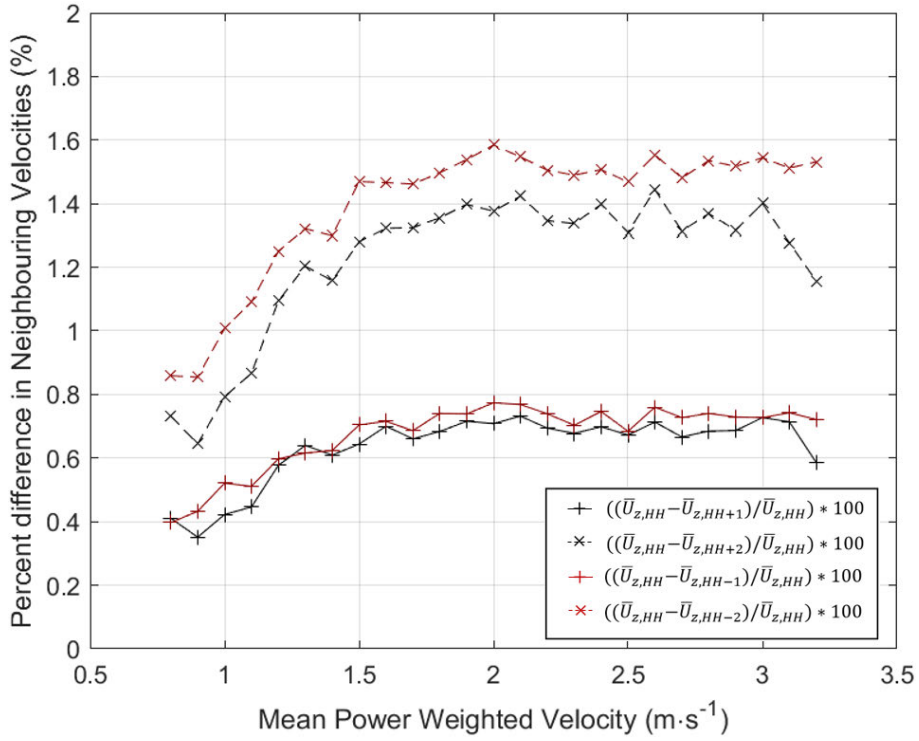

Figure 7.11: Adjacent placed ADCP (B_1) PWRA velocity in increments of 0.1 m·s^{-1}. Difference between PWRA velocity taken at hub height reference ($\bar{U}_{z,HH}$ where HH is 18 m and rotor diameter is 18 m) and an imposed misalignment of up to 2 m ($\bar{U}_{z,HH\pm2}$).

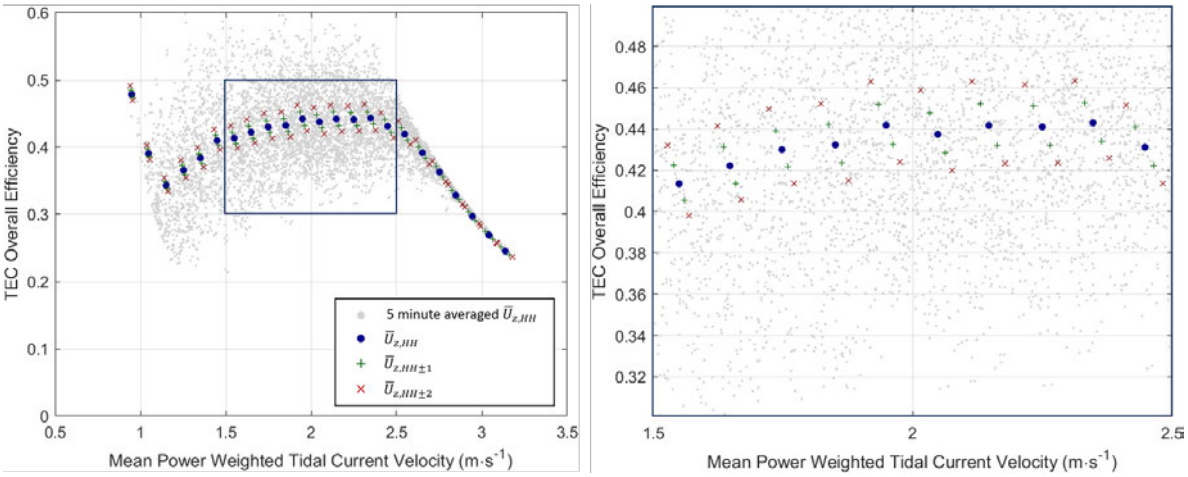

Figure 7.12: Presentation of the overall efficiency of the TEC for flood tides using measurements taken at B_1, showing the variation in TEC efficiency η when the incorrect depth bin is paired with the TEC hub height.

where: TEC_A is the predicted availability of the TEC; TEC_{AEP} is the expected annual power production in kWh; N_B is the total number of velocity bins set in increments of 0.1 m·s^{-1} in the device power curve; N_h is the number of hours in one year (8760); $\bar{P}_i$ is the power in kW generated by velocity bin i of the power device curve; $\bar{U}_i$ is the average PWRA velocity (bins 9 to 27 m for TEC_{T1}, 6 to 18 m for TEC_{T2} and 27 to 39 m for TEC_{T3}) of bin i of the power device curve; f_i is the proportion of time during the year for which the average performance current velocity occupies a value within velocity bin i.

The ADCPs placed adjacently - B_1 and B_2 - to the DEEP-Gen IV are used to assess the sensitivity of the estimated TEC_{AEP} to the vertical alignment for both the flood and ebb velocity profile, see figure 7.9 and Table 7.2.

Table 7.2: Sensitivity to the vertical misalignment of profiler depth bin to the proposed TEC hub-height, where each bin's mean velocity (U) is used. Values refer to the averaged velocity profile produced for each seabed instrument, where the profile for $B1$ is depicted in Figure 7.9. Diff refers to the percent difference between the hub-height AEP estimate and the estimate from an depth offset.

TEC Lcoation and Type		T_2			T_1			T_3		
SW ADCP (B1)										
	D offset [m]	U [m/s]	AEP* [GWh]	Diff [%]	U [m/s]	AEP [GWh]	Diff [%]	U [m/s]	AEP* [GWh]	Diff [%]
FLOOD	2	2.01	0.82	**3.8%**	2.11	8.95	**2.1%**	2.28	19.80	**1.1%**
	1	1.99	0.81	**2.0%**	2.09	8.87	**1.2%**	2.27	19.68	**0.5%**
	HH	1.97	0.79	**0.0%**	2.08	8.76	**0.0%**	2.27	19.58	**0.0%**
	-1	1.95	0.77	**2.3%**	2.06	8.61	**1.7%**	2.26	19.44	**0.7%**
	-2	1.93	0.76	**4.5%**	2.05	8.53	**2.7%**	2.25	19.28	**1.6%**
EBB	2	2.22	1.41	**4.3%**	2.37	15.54	**2.8%**	2.49	32.56	**0.0%**
	1	2.19	1.38	**2.2%**	2.35	15.30	**1.3%**	2.49	32.58	**0.0%**
	HH	2.16	1.35	**0.0%**	2.33	15.10	**0.0%**	2.49	32.58	**0.0%**
	-1	2.13	1.32	**2.3%**	2.30	14.90	**1.3%**	2.50	32.62	**0.1%**
	-2	2.10	1.28	**5.5%**	2.28	14.70	**2.7%**	2.50	32.62	**0.1%**
NE ADCP (B2)										
FLOOD	2	1.99	0.81	**3.6%**	2.08	8.830	**2.3%**	2.23	19.84	**0.7%**
	1	1.96	0.80	**1.9%**	2.06	8.730	**1.1%**	2.22	19.80	**0.5%**
	HH	1.94	0.79	**0.0%**	2.04	8.630	**0.0%**	2.22	19.70	**0.0%**
	-1	1.92	0.77	**2.2%**	2.03	8.520	**1.3%**	2.21	19.63	**0.3%**
	-2	1.90	0.75	**4.7%**	2.01	8.400	**2.7%**	2.20	19.58	**0.6%**
EBB	2	2.2	1.39	**2.9%**	2.21	14.10	**0.7%**	1.91	21.12	**3.2%**
	1	2.18	1.38	**2.2%**	2.21	14.20	**0.0%**	1.94	21.51	**1.3%**
	HH	2.15	1.35	**0.0%**	2.22	14.20	**0.0%**	1.95	21.80	**0.0%**
	-1	2.13	1.33	**1.5%**	2.22	14.20	**0.0%**	1.98	22.20	**1.8%**
	-2	2.11	1.30	**3.8%**	2.21	14.10	**0.7%**	2.01	22.60	**3.5%**

HH: represents 12, 18 and 34 for T_2, T_1 and T_3 respectively.
D: depth.
*: represents the estimated AEP using the pre-defined power curves for a 0.1 MW (T_2) and a 2 MW (T_3) concept

The streamwise velocity varies with increasing height from the seabed, typically following a logarithmic curve. The hub-heights for each TEC (refer to Table 5.9 and visually Figure 7.9) were used as the base case, and depth bins (ranging in 1 m) up to $\pm$ 2 m from the hub-height were assessed. The difference from a positive shift (toward the sea surface) in the bin resulted in an overestimation of AEP. On the contrary, a negative shift (toward the sea floor) is related to underestimating the total AEP. The results are summarised below:

1. With an imposed vertical misalignment of 2 metres between measurement locations and modelled rotor plan differences for flood and ebb tides, respectively, are up to 4.5% and 5.5%.
2. The variation in AEP estimated from the flood tide velocity measurements were similar at locations B_1 and B_2 for a misalignment up to 2 m, implying that the vertical variation in U_{B1} and U_{B2} for the flood tide are similar across a distance of $\approx$ 70 m.
3. Misalignment in the negative (towards sea-bed) direction (-1, -2 m) compared to a positive misalignment (towards sea-surface) has a greater impact on the estimated AEP for the flood and ebb tide across all three TEC cases.
4. The TEC placed in the lower region (T_2) of the water column experiences greater variation in AEP under the modelled vertical misalignment, compared with results for T_1 and T_3.

5. Due to the greater occurrence of faster flows measured in the ebb tide compared to the flood tide, the AEP on ebb tides are greater.
6. In the upper region of the water column AEP estimates from measurements made at B_2 during the ebb tide differed by up to 3.4% when compared with measurements made at B_1.
7. For an imposed misalignment of 2 metres the AEP estimated during ebb tides from measurements at mid-depth (T_1) from B_1 and B_2 locations differed/differ by less than 1%.
8. There is a noticeable increase in power output for turbine T_3 when it experiences a negative displacement during ebb flows.

7.2.3 Calculating Combined Uncertainties for Spatial variance in Velocity

To articulate how the 2.6% uncertainty in AEP from two velocity measurements by two independent ADCPs (B_1 and B_2) could be potentially cancel out halfway between them (at the location of the TEC), with B_1 being +1.3% and B_2 being -1.3% uncertainty, and then how to combine this with the vertical misalignment uncertainty of the two instruments for the three positions in the water column (this method assumes that the vertical bin chosen is consistent at both instrument locations and that the velocity difference between the two instruments remains constant), the following steps are carried out using the RMS method:

- Horizontal uncertainty for flood tide: $\pm$ 2.6 (assuming $+1.3\%$ for B_1 and -1.3% for B_2 as B_1 contained higher velocities consistently over B_2)
- Horizontal uncertainty for ebb tide: $\pm$ 7.6 (assuming $+3.8\%$ for B_1 and -3.8% for B_2 as B_1 contained higher velocities consistently over B_2)

Combining uncertainties for the flood tide measurements using the variation from instrument placement and an offset vertically of 2 m as an example:

$$\text{Total uncertainty } (B_1) = \sqrt{(3.8)^2 + (1.3)^2}$$

$$\text{Total uncertainty } (B_1) = \sqrt{14.44 + 1.69} \approx 4.0\%$$

$$\text{Total uncertainty } (B_2) = \sqrt{(3.6)^2 + (1.3)^2}$$

$$\text{Total uncertainty } (B_2) = \sqrt{12.96 + 1.69} \approx 3.83\%$$

Combining uncertainties for the ebb tide measurements using the variation from instrument placement and an offset vertically of 2 m as an example:

$$\text{Total uncertainty } (B_1) = \sqrt{(4.3)^2 + (3.8)^2}$$

$$\text{Total uncertainty } (B_1) = \sqrt{18.49 + 14.44} \approx 5.7\%$$

$$\text{Total uncertainty } (B_2) = \sqrt{(2.9)^2 + (3.8)^2}$$

$$\text{Total uncertainty } (B_2) = \sqrt{8.41 + 14.44} \approx 4.8\%$$

The following Tables 7.3 and 7.3 includes the combined uncertainty using the flood and ebb tide measurements respectively.

Table 7.3: The combined uncertainty of the two variables during the flood tide: instrument placement relative to the operational TEC and vertical misalignment of the hub height and ADCP bins.

Depth offset (m)	U ($m \cdot s^{-1}$)	Diff offset (%)	Diff location (%)	Comb. uncertainty (%)
		B_1 flood		
+ 2	2.01	3.8	1.3	4.0
+ 1	1.99	2.0	1.3	2.4
0 (HH)	1.96	0.0	1.3	1.3
- 1	1.95	2.3	1.3	2.6
- 2	1.95	4.5	1.3	4.7
		B_2 flood		
+ 2	1.99	3.6	1.3	3.8
+ 1	1.96	1.9	1.3	2.3
0 (HH)	1.94	0.0	1.3	1.3
- 1	1.92	2.2	1.3	2.6
- 2	1.90	4.7	1.3	4.9

Table 7.4: The combined uncertainty of the two variables during the ebb tide.

Depth offset (m)	U ($m \cdot s^{-1}$)	Diff offset (%)	Diff location (%)	Comb. uncertainty (%)
		B_1 ebb		
+ 2	2.22	4.3	3.8	5.7
+ 1	2.19	2.2	3.8	4.4
0 (HH)	2.16	0.0	3.8	3.8
- 1	2.13	2.3	3.8	4.4
- 2	2.10	5.5	3.8	6.7
		B_2 ebb		
+ 2	2.20	2.9	3.8	4.8
+ 1	2.18	2.2	3.8	4.4
0 (HH)	2.15	0.0	3.8	3.8
- 1	2.13	1.5	3.8	4.1
- 2	2.11	3.8	3.8	5.4

Accurately assessing uncertainties in AEP for tidal energy converters using ADCPs is crucial. This assessment considered vertical misalignment (differences in velocity readings at various depths relative to the hub height) and horizontal spacing (variability due to a 70-meter separation between two ADCPs - TEC placed in the middle). Vertical misalignment uncertainties were analysed at hub height and ± 1 meter and ± 2 meters above and below the hub height. Horizontal uncertainties were set at 1.3% (2.6% total between the two instrument locations) for flood tides and 3.8% (7.6% total between the two instrument locations) for ebb tides to be representative of no uncertainty if the instrument was placed directly at the TEC location. Combined uncertainties were calculated using the root-mean-square (RMS) method to provide a comprehensive assessment. This highlights the importance of ensuring the data collected is robust and accurate.

7.3 Discussion

This work explores the sensitivity of tidal turbine power-production performance to the flow velocity reference used. The spatial variation in the flow measurements from ADCPs placed as per the IEC TS 62600-200 guidelines is found to impact the measured power curve. Furthermore, the vertical misalignment between the depth bin and the three modelled TECs of varying hub heights affects the estimate of AEP.

The current velocity and direction measured by the five seabed-placed ADCPs differ based on location and tidal cycle. The tidal ellipse (Fig 7.2) shows the velocity magnitude (as a radius) and direction (as a compass heading transformed to a radial coordinate) in polar coordinates. The difference in the established flow direction between the five seabed ADCPs is likely due to the combination of inaccuracies in the ADCPs internal compass (due to insufficient calibration), but could also be due to localised bathymetric effects. The velocity measurements from ADCPs placed in orientation B (U_{B1} and U_{B2}) differed significantly in the ebb tide (Fig 7.3b, 7.4b and 7.6b). This is likely due to a flow structure - trapped eddy - forming on the ebb tides off the local island Eday. Furthermore, ADCP placed at A_3 measured a reduced flow velocity in the upper region of the water column (Fig 7.3b and 7.6a), suggesting the flow structure extends into this location.

The rotor-attached SB-ADP (C_1) measured velocity at hub-height along the heading of the TEC. The only ADCP found to measure similar velocities was at B_2. However, compared to the other ADCPs B_2 measurements appeared significantly lower at the hub-height of the DEEP-Gen IV, especially at lower velocity bins (< 2 m·s^{-1}). The discrepancy between the measured velocity at location C_1 and the five seabed ADCPs placed around the TEC may be due to several possible causes. First, as the flow decelerates upstream of the turbine (velocity reference taken at 10 - 12 m) the flow may already be significantly decelerated, this is commonly known as the induction zone. Secondly, the hardware and calibration, including a limit on the maximum sensor range of the SB-ADP, could cause differences in the measured velocity.

The power curves presented follow the methodology of the IEC TS 62600-200 [30]. The real-world power measurements from the DEEP-Gen IV is time-matched with the PWRA velocity calculated for the five seabed ADCPs. In addition, the velocity measured at hub-height from the SB-ADP was used to produce an additional non-PWRA power curve. During the flood tide measured by the in-line ADCP pair A_1 and A_2 (inside and close to the IEC TS target location respectively), the closer ADCP A_1 measured a slightly reduced flow. This would make the power curve appear seemingly more efficient for a developer, due to a lower velocity $\bar{U}_{A1}$ being compared against a larger velocity $\bar{U}_{A2}$ for the equivalent power measurement. The impact of this is small with a difference of $\approx 0.6\%$ between $\bar{U}_{A1}$ and $\bar{U}_{A2}$, when the DEEP-Gen IV was operating at rated power. The difference potentially arises from a push-back on the flow when the TEC is operational or the variation in bathymetric conditions northwest of ADCP A_2 (Fig 5.5).

On the contrary, the current flow does not appear to be effected by the TEC at the locations B_1 and B_2. The velocity measurements U_{B1} and U_{B2} are significantly different between the flood and ebb tide, this is evident in Figure 7.5b. The velocity measured at B_1 and B_2 differed by 1.4% and 4.3% when the DEEP-Gen IV operated at rated power during the flood and ebb tide respectively (Fig 7.8a and 7.8b), producing four different power curves (Fig 7.7a and 7.7b). Due to the flow structure forming off the headland, the flow velocity measured at location B_2 was lower when compared with measurements from the instrument placed upstream of the turbine (A_1). This results in the power curve appearing seemingly more efficient when using measurements from instrument B_2.

The effect of ADCP placement on the estimated AEP is assessed. Based on the velocity variation between instrument locations A and B, the AEP differed by 1.2% and 2.6% when comparing ADCP pairs A_1 and A_2, and B_1 and B_2 respectively, for the flood tide measurements. For the ebb tides, the large variation between $\bar{U}_{B1}$ and $\bar{U}_{B2}$ resulted in a 7.3% difference between AEP estimates. According to the IEC TS 62600-200 the linear average velocity should be calculated when using the adjacent orientation B at equivalent water depths. For the linear average to be considered a valid approximation of the flow at the energy extraction plane, the variation in the instantaneous velocities u_{B1} and u_{B2} should be less than 10%. Figure 7.6b illustrates how the mean velocity binned by increments of 0.3 m·s^{-1} can vary by more than 10%, and the instantaneous velocity measurements significantly more. The study suggests that for a TEC located in the lower region of the water column ($<$ 20 m) the adjacent orientation ADCPs can be used for PPAs. However, as seen in Figure 7.6b, the variation in velocity upward of 20 m from the seabed exceeds the threshold required for a linear average calculation to be valid. For this reason, this instrument orientation should not be considered for a PPA at this specific location for a TEC deployed in the upper region of the water column. These findings highlight the importance of studying the form of the velocity-binned depth profiles (before applying any spatial averaging and considering flood and ebb tides separately), in particular, checking for forms that suggest the presence of large-scale flow features, e.g., eddies (as shown in Figures 7.3b, 7.6b and 7.9). The results from implementing an IEC Type B campaign have shown at this site a significant variation in velocity on either side of the turbine location. However, this instrument layout might be suitable for PPAs at other test locations where the turbine and flow sensors are situated further away from flow-affecting channel features e.g., upstream headlands. The study has shown that the suitability of an IEC Type B campaign for PPA is dependent on specific turbine size and positioning in a particular channel.

The consequence of estimating AEP from flow data that might feature significant vertical misalignment between the ADCP depth bin and the rotor swept area is assessed for the DEEP-Gen IV and two further variants of horizontal axis tidal turbines. This misalignment could occur due to numerous reasons. First, differences in the estimated depth may occur due to different pressure gauge specifications and/or varying states of calibration - including human operator error or poor data traceability in terms of zero-ing of sensors. In addition, incorrect post-processing of the data and mis-matching the depth bin to the hub-height (including the blanking distance and the starting position of the first measured bin) of the turbine, can lead to inaccuracies in the measured performance. Finally, the instrument stability (pitch and roll) should be considered as this can change the depth bin between beam pairs.

The AEP was estimated using the velocity measurements at three proposed hub-heights, where a misalignment between neighbouring depth bins up to $\pm$2 m was analysed. Results indicate the AEP was sensitive to the tidal cycle because the flood and ebb exhibit different shear profiles. It was found that a more gradual velocity profile (typically a flood tide, refer to Fig 7.9) has a lower impact on the estimated AEP, when flow data features a misalignment of 2 m. The results show (Table 7.2) that for regions of high vertical shear, AEP estimates become increasingly sensitive to imposed vertical misalignment.

7.4 Conclusions

This chapter examines how the placement of ADCPs and a rotor-attached SB-ADP influences the power performance of the DEEP-Gen IV 1 MW tidal turbine. Using IEC TS 62600-200 guidelines, the ADCPs were strategically located around the turbine. The ADCP closer (A_1) to the tidal turbine measured a lower velocity than A_2 (placed 45 m further upstream from the TEC). Despite this, both ADCPs corresponded to the same power output from the turbine. While the lower velocity reading from the closer ADCP may suggest a more efficient power curve when plotted, this can be misleading as it doesn't necessarily indicate better turbine performance.

It was found that ADCPs can be deployed outside the IEC TS recommended zone and still provide a true representation of the flow approaching the turbine. This indicates the possibility of more flexible instrument placement for flow measurements for the purpose of a power performance assessment.

Flow differences between adjacent locations (B_1 and B_2) exceeded the 10% limit set by IEC guidelines, particularly in the upper water column. This difference affected the AEP estimate by 7.3%. The study suggests that for this site, adjacent instruments placed as per IEC TS guidelines should not be used for PPAs. It should be noted, however, that for alternate TEC designs situated lower in the water column, the rotor-adjacent measurement method may be acceptable.

As for the rotor-attached SB-ADP, it does offer practical benefits like continuous power supply and remote control but falls short in accurate flow measurement. This is due to the turbine's impact on the flow within the instrument's measurement range. Without further corrections, this setup fails to meet the requirements of representative flow measurements for performance assessments, although the practical benefits warrant continued research.

Additionally, the impact of vertical misalignment between flow data and turbine rotor position on AEP estimates was evaluated. Three turbines were analysed: the commercial-scale DEEP-Gen IV and two other horizontal-axis models. The results indicated up to a 5.5% discrepancy in AEP estimates, with the largest variance observed at the lowest hub height under an imposed vertical misalignment of 2 metres. Those using IEC TS guidelines should understand that sensor placement for power assessments is influenced by spatial variations in flow, both horizontally and vertically.

In summary, this chapter highlights the importance of proper ADCP placement for accurate power curves and AEP estimates. It suggests that ADCPs can be placed outside the IEC TS recommended zone, but careful consideration is needed for adjacent instruments. The use of rotor-attached SB-ADP requires further work to address the turbine's impact on flow measurements. Additionally, the study emphasises the sensitivity of AEP estimates to vertical misalignment, which should be considered when using IEC TS guidelines for PPAs.

Chapter 8

Uncertainty in Power Estimates due to the Spatial Variability in Flow Direction

8.1 Chapter Overview

Tidal turbines are developed to face perpendicular to the oncoming tidal current to harness the energy passing through the rotor's swept area. Turbines that are designed with no yaw (rotation of the nacelle) control may have difficulty responding to changes in the current direction. Developers have started implementing bi-directional blades to capture energy from symmetrical tidal straits. However, when deployed in tidal races that are not symmetrical a misalignment between the current flow and the TEC rotor extraction plane occurs. Despite that, resource assessments commonly assume that the proposed TEC will always be aligned with the instantaneous tidal flow. Additionally, resource assessment inaccuracies can cause misalignment if developers are informed of the incorrect principle flow direction. The impact will be continued in the power performance where in-situ flow measurements are paired with the power produced from the TEC without considering the reduction in the velocity component when the TEC is not perpendicular to the flow.

As part of the ReDAPT project, the objective was to assess the flow characteristics and evaluate in-situ measurements for the power performance of the DEEP-Gen IV 1 MW tidal turbine. Part of this work identified a twist in the flow along the water column, where the direction could change by as much as 8° across an 18 m Rotor. The current direction has changed significantly through the water column by as much as 11° from the calculated mean used to inform developers. At present, the flow direction measured by the ADCP depth bin relative to the proposed TEC should be reported as per IEC TS 62600-200. Flow velocity and direction vary with depth - from bathymetry, seabed friction and interactions from the wind and waves. If this variation could be captured along the rotor plane of a TEC, a more accurate representation of the established flow could be estimated. This is done for the flow velocity magnitude using the PWRA method. The flow direction evolves over a tidal cycle. For non-yawing turbines, the impact on the measured power curve and AEP estimate has not yet been quantified.

This chapter primarily aims to quantify the three following aspects directly related to the measurement of flow direction and turbines that cannot adapt to changes in the current direction:

1. the impact of miscalculating the established flow direction - which is the direction of assumed maximum energy yield;
2. to define a methodology for estimating the established flow direction to help interpret performance results more accurately and inform developers on turbine installation design criteria;
3. the impact on power generated and AEP estimations from turbines positioned off-axis to the established flow direction.

Three variants of horizontal axis tidal turbines, which operate in different locations of the water column were examined for each aim listed above; one uses measured data (TEC_{T1}), and the other two are modelled through power curves (TEC_{T2} and TEC_{T3}). Flow direction is crucial in determining tidal energy production by non-yawing horizontal axis tidal turbines. Even small variations in flow can significantly impact AEP, emphasising the need for careful consideration in site design and performance evaluation.

This chapter is structured as follows: Section 8.2 provides a test overview of the suite of instruments relative to this chapter; Section 8.3 reports key results obtained for the spatial variation in the measured direction in the horizontal plane and how different estimates of direction can be calculated (8.3.1); Section 8.4 and 8.5 focus on the impact of misalignment between the TEC rotor extraction plane and the flow direction on the power performance and annual energy estimates; Section 8.6 analyses the flow twist along the measured water column; Section 8.7 identifies and quantifies the effect the tidal phase has on power production of a TEC; while Section 8.8 and 8.9 discuss the key results obtained and conclude the chapter respectively.

8.2 Instrumentation Configuration and Deployment

The uncertainties related to ADCP placement and the variation in flow direction measured at different locations around the DEEP-Gen IV in situ (refer back to Figure 6.1). Also considered is the flow development and changes in direction of the flow over a tidal cycle, and the impact of a TEC being off-center relative to the calculated principal flow. By examining these factors in detail, critical insights into optimising ADCP deployment for reliable power performance assessments can be analysed and used to inform future deployments.

A measurement campaign was devised to assess the DEEP-Gen IV 1 MW tidal turbine performance using two ADCPs (A_4 and A_5 with instrumentation configurations and specifications presented in Table 5.1 and 5.2) over June and July 2013 at the FoW (Fig 5.3 and 5.4). Figure 8.1 presents a plan view of the channel bathymetry and instrument locations.

The tidal current flows southeast and northwest throughout the flood and ebb tide, respectively. The strength in the ebb tide is larger and less spatially varied, reaching a peak flow of 4 m·s^{-1} in this measurement campaign with a flow direction spread of $\approx 35^\circ$ from the ramping up of the tide to the waning down phase. The flood tide reached a peak flow of $\approx$ 3.2 m·s^{-1} with a much larger flow direction spread of $\approx 75^\circ$. The data sets are presented in detail in Figure 8.2, the PWRA velocity is shown for the flood and ebb tide (Fig 8.2a), and the measured directional data over the duration of the measurement campaign (Fig 8.2b). Directional data corresponding to velocities below 1 m/s were removed due to significant variation in flow direction at low velocities.

8.3 Horizontal Variation in the Measured Flow Direction

For the following performance assessment, results obtained in both the flood and ebb tidal cycles are considered as the flow direction spread differs between tidal cycles. The flow direction is not symmetrical from the ramping up (first two hours of the tide) phase to the peak flow (two-hour period at the middle of the tide) phase and further during the waning down (final two hours of the tide) phase. Therefore, the analysis considers both positive $(+\alpha)$ and negative $(-\alpha)$ rotations of the TEC yaw - clockwise and anti-clockwise from the established flow direction - to the established flow estimate (θ) as shown in Figure 8.1b and 8.3.

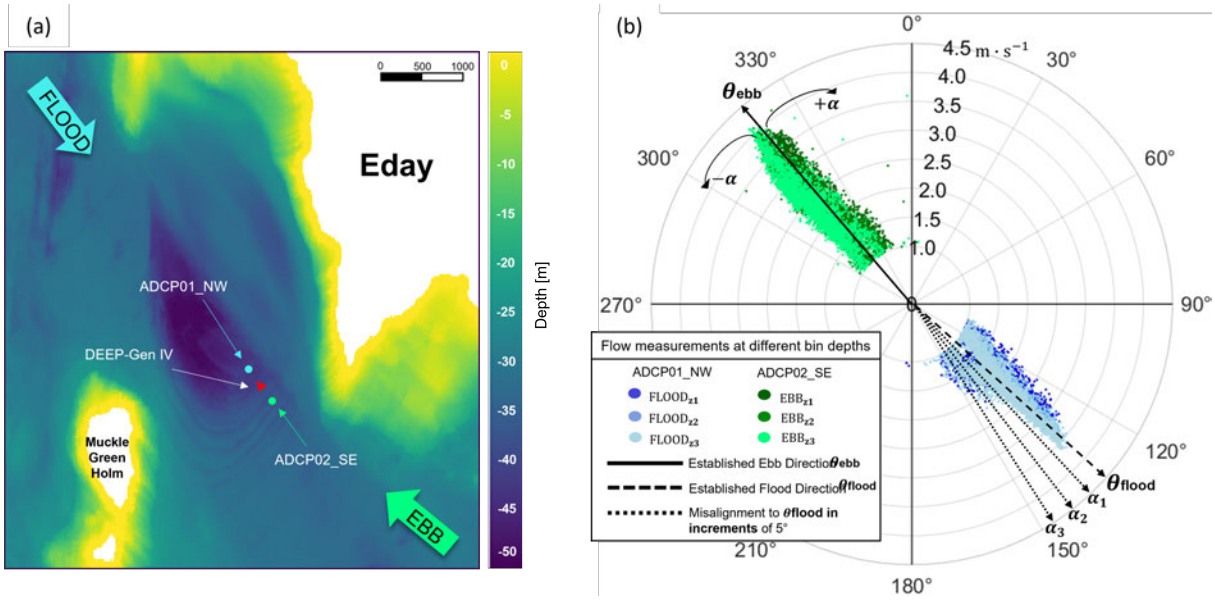

Figure 8.1: (a) Channel bathymetry and ADCP locations relative to the DEEP-Gen IV at the FoW tidal test site. (b) Tidal ellipse for three bin depths, where z_1, z_2 and z_3 represent 15, 25, and 33 m above the seabed. The generic established flow direction for both flood and ebb is presented. TEC yaw heading rotations used throughout the analysis is illustrated, where both clockwise and anticlockwise rotations are considered ($\pm\alpha$). NOTE measurements shown indicate flow travelling toward that direction.

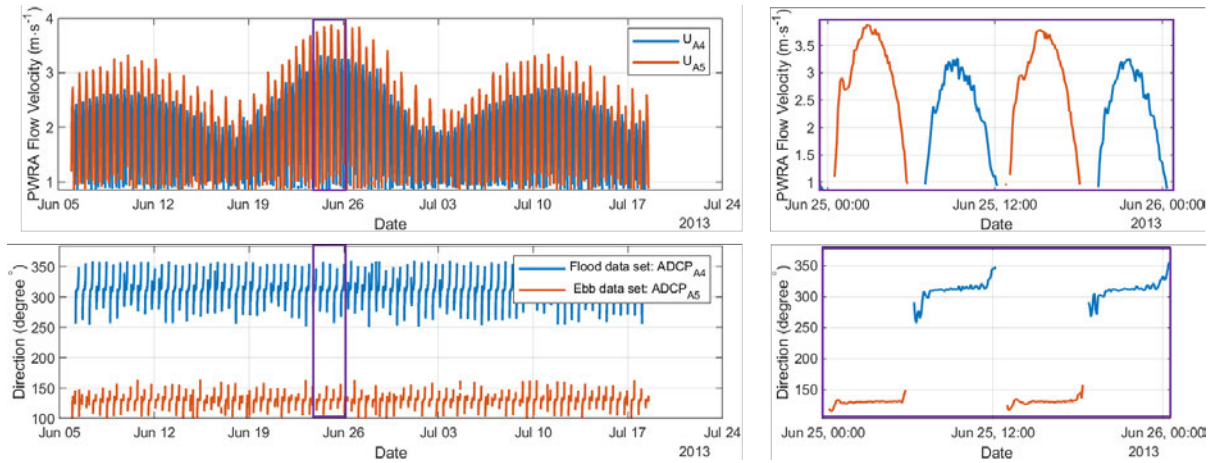

Figure 8.2: Data obtained from two ADCPs positioned upstream (A_4) and downstream (A_5) from the DEEP-Gen IV turbine at a distance of 63 m and 53 m respectively. (a) 5-minute averaged flow velocity data sets for the flood (A_4) and ebb (A_5) tide measurements. (b) 5-minute averaged flow direction data sets. The purple box shows the velocity and direction data in detail.

In addition to asymmetrical tides (refer to section 2.2.2), the flow direction changes during the different phases of the tide. Figure 8.3 illustrates the flow direction variation in 30-minute intervals on the flood tide (direction measurements are subject to variation based on instrument location) in the Fall of Warness. For non-yawing TEC concepts, the ability to capture the largest amount of energy will only take place once the TEC is positioned perpendicular to the flow. This variation in direction results in a reduced velocity passing through the TEC rotor capture area. Hence flow direction must be considered when evaluating and producing a measured power curve.

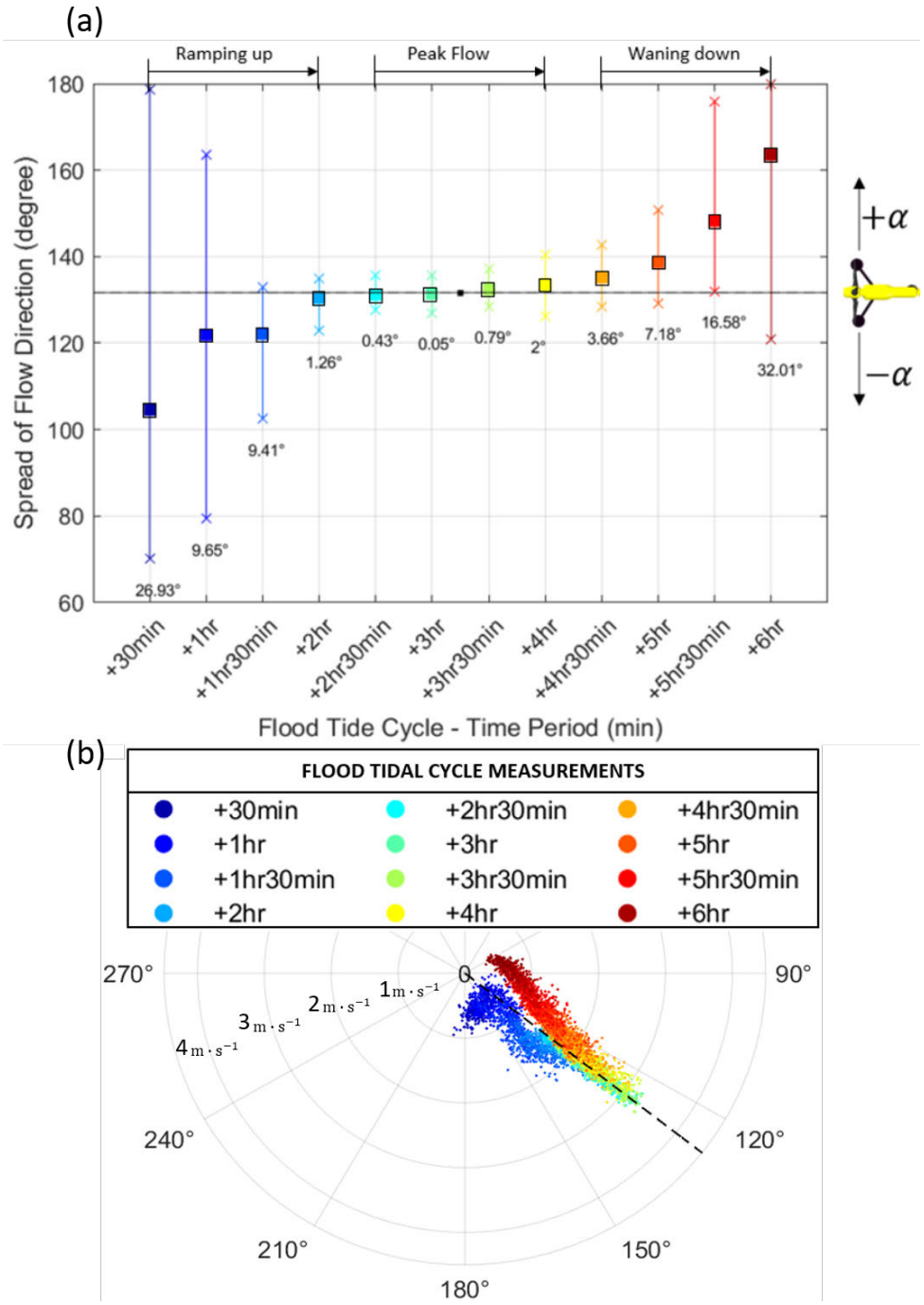

Figure 8.3: Flow direction variation over a flood tide at the FoW, where a) the flow direction mean (square markers) of 30-minute periods throughout the flood cycle, the TEC yaw heading (solid black line), and the min and max (crosses) variation in direction. b) The tidal ellipse for the flood measurements at a chosen hub height (18 m), the black dashed line represents the TEC yaw heading.

The measured flow evolves and a non-yawing TEC positioned toward the established flow direction will be susceptible to off-axis currents throughout each tidal cycle. Equation 8.1 describes the inflow velocity (U_{inflow}) at the instrument location, and the velocity at the TEC location (U_{rotor}) when the turbine's rotor heading is perpendicular to the free stream flow at all times ($\alpha = 0$), thus capturing the maximum amount of energy available. In misalignment circumstances, the inflow velocity becomes a component of the velocity, and the parameter α quantifies the difference between U_{inflow} and U_{rotor}. The impact of misalignment can be described using a simple trigonometric cosine relationship [45], as shown in Equation 8.2:

$$U_{\text{rotor}} = U_{\alpha=0} = U_{\text{inflow}} \tag{8.1}$$

$$U_{\text{rotor},\alpha} = U_{\alpha\neq0} = U_{\text{inflow}} \cdot cos\alpha \tag{8.2}$$

Alternatively, the turbine's swept area can be considered when misalignment is introduced and it changes from a circle to an ellipse. The vertical radius of the ellipse will remain the same, and the horizontal radius will decrease as the yaw angle increases from the established flow direction. The resulting equation for a turbine's projected area in aligned and misaligned flow is described by Equation 8.3 and 8.4, respectively, as shown below:

$$A_{\text{rotor}} = A_{\alpha=0} = \pi \cdot r^2 \tag{8.3}$$

$$A_{\text{rotor},\alpha} = A_{\alpha\neq0} = \pi \cdot r^2 \cdot cos\alpha \tag{8.4}$$

where r is the radius of the turbine and α is the misalignment in degree between the U_{inflow} and U_{rotor}.

It is expected that either one of these two corrections, when applied to the theoretical maximum power equation, would estimate the performance drop due to misalignment. Tidal stream devices designed to react to tidal sites with symmetrical tides may lack sufficient ability to extract energy efficiently from off-axis currents. The maximum power can be calculated using Equation 8.5:

$$P = \frac{1}{2} \cdot \rho \cdot cp \cdot U^3 \cdot A \tag{8.5}$$

where P is the power produced in W, ρ is the density of water in kg·m^{-3}, C_p is the power coefficient, U is the instantaneous flow velocity in m·s^{-1}, A is the cross-sectional area of the TEC rotor in m^2.

8.3.1 Estimates of the established flow direction

Considering data only above the proposed TEC cut-in velocities showed a difference in the estimated flow direction. Using a Power Weighted Rotor Average (PWRA) method to obtain the established flow direction compared with the hub-height estimate has been analysed.

Table 8.1 shows the effect of inclusion of data measured beneath the cut-in speed when calculating the established flow direction. Differences of up to 4° can be seen without removing data under the proposed TEC cut-in speed. The estimate of the established flow calculated using flow direction measurements aligned to the rotor plane (rotor average), alongside the PWRA method showed less than 1.2° difference, when compared with the commonly used hub-height estimate. Also shown in Table 8.1, the estimate of the established flow direction varied across the three depths by up to 4°. This highlights an area where uncertainties may occur in using an ADCP for flow characterisation, causing potential issues, for example, if they are used to instruct turbine heading.

Table 8.1: Effect of pre-processing on the estimate of established flow direction.

TEC Concept	Method	EFD with all data (°)	EFD with speed $<$ cut-in removed (°)	Difference (°)
TEC_{T1}	θ_{HH}	130.7	133.8	3.1
	θ_{RA}	130.8	133.5	2.7
	θ_{PWRA}	129.9	133.1	3.2
TEC_{T2}	θ_{HH}	133.7	137.4	3.7
	θ_{RA}	133.2	136.8	3.6
	θ_{PWRA}	132.5	136.5	4.0
TEC_{T3}	θ_{HH}	134.7	138.6	3.9
	θ_{RA}	134.2	137.9	3.7
	θ_{PWRA}	134.4	137.8	3.4

EFD: Established Flow Direction;
HH: Hub-Height estimate;
RA: Rotor Average estimate;
PWRA: Power-Weighted Rotor Average estimate;

8.4 Impact of Misalignment on the Power Performance

8.4.1 Axial Rotation Impact

The probability density distribution of flow direction, as shown in Figure 8.4, provides a visual representation on how the flow direction changes over a tidal cycle. The density curves are right-skewed, with the mean estimation greater than the median. The flow direction spends the majority of the time clockwise from the established flow direction (toward the waning down phase) of the tide for both tidal cycles. This highlighted that a TEC positioned off-axis from the established flow by either a positive (clockwise) or negative (anti-clockwise) shift would not perform identically. A fixed offset angle relative to the mean flow angle across the entire phase was applied to the TEC to demonstrate this effect. As a result, if the tide spends more time flowing clockwise or counterclockwise relative to the calculated average, the losses will increase or decrease, depending on how far the flow deviates from the mean direction.

Figure 8.5 illustrates the peak velocity (where α = 0) recorded at the instrument location (A_4) during the neap (blue line) and spring (black line) tidal currents for both the flood (solid line) and ebb (dashed line) cycle. The percent difference in velocity is recorded as the TEC is positioned away from the principal flow. The velocity ($\alpha > 0$) then represents the component of flow passing through the swept area of the TEC. It can be seen for a misalignment of up to 25° the velocity is $\approx$ 10% reduced. The results in the graph significantly decrease beyond 25°, however this is not shown as our analysis is limited to results up to 25 degrees. If the TEC is rated at under the max velocity at the site by at least 10% then during peak tides the TEC could potentially operate at rated power when misaligned to the principal flow by up to 25°. However, during the periods when the flow is not at peak flow, the power production will be significantly greater.

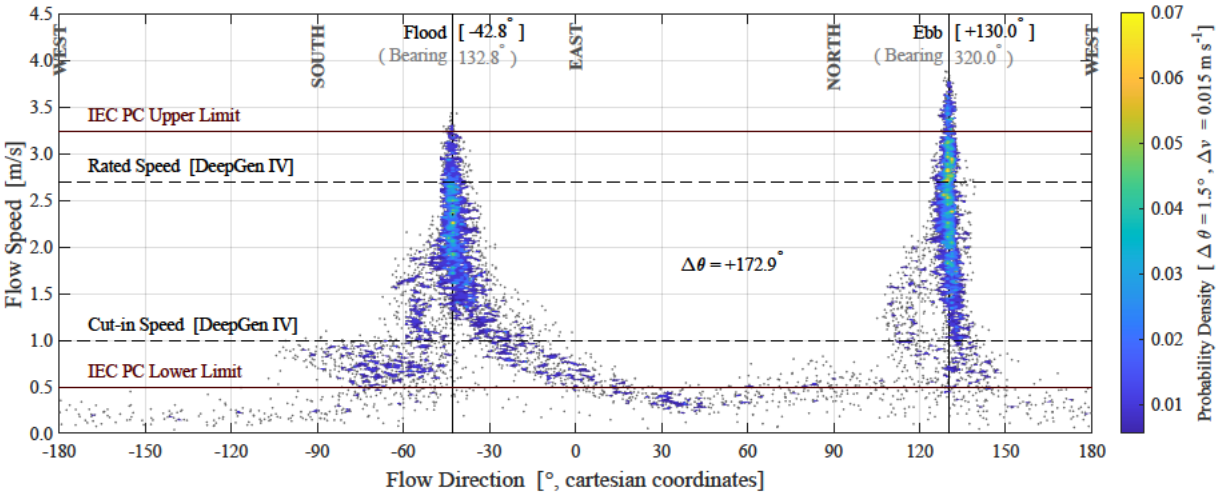

Figure 8.4: Probability density distribution for varying flow speeds and flow directions (in Cartesian coordinates) for flood and ebb tides. The data has been generated from hub-height measurements sampled by an ADCP deployed ≈ 40m southwest of the DEEP-Gen IV TEC (in a region of flow undisturbed by the presence of the turbine).

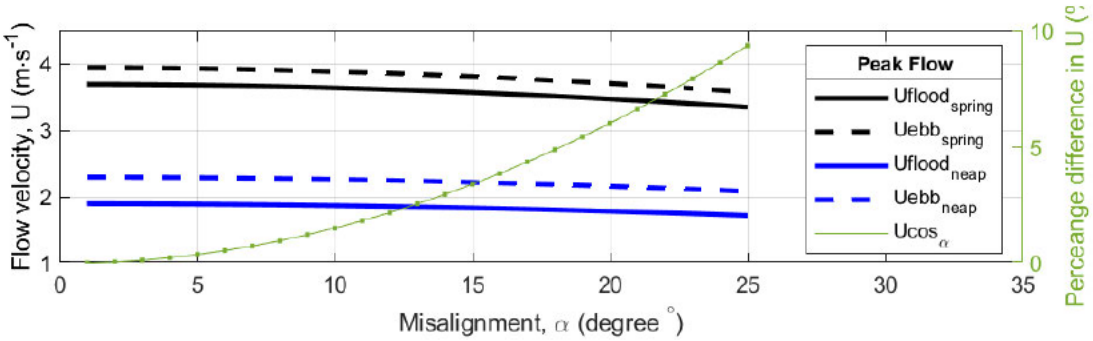

Figure 8.5: Peak flow velocity recorded at the FoW (instrument location A_4) for the flood and ebb (solid and dashed line respectively) cycle during a neap (blue) and spring tide (black). The percent difference in velocity from misalignment from the principle flow by α is given by the relationship (green line).

8.4.2 Power Performance Impact

Figure 8.6a shows the generated power output for each 0.1 m·s^{-1} velocity interval between 1 and 3.1 m·s^{-1} approaching the DEEP-Gen IV. The theoretical maximum power (red line) generated using the velocity magnitude U_{inflow} was compared with the velocity component $U_{\theta\pm\alpha}$, where α is the streamwise misalignment between the TEC heading and established flow estimate (θ) of 5°, 10° and 15°. As shown in Figure 8.6a, the DEEP-Gen IV curves differed by up to ≈ 1.5%, 4.9% and 10% at 2.5 m·s^{-1} for a misalignment of 5°, 10° and 15°. Figure 8.6b, 8.6c and 8.6d depicts the power loss for each TEC case when misaligned from the established flow, where the highest value of power lost per-velocity bin was measured from TEC_{T3}. At lower flow velocities, more obvious differences exist between the curves presented in Figure 8.6b, 8.6c and 8.6d. This is due to the variation between the 10-minute samples of flow direction and the averaged established flow direction θ_{HH} varying significantly more during low flow speeds, thus causing a greater misalignment.

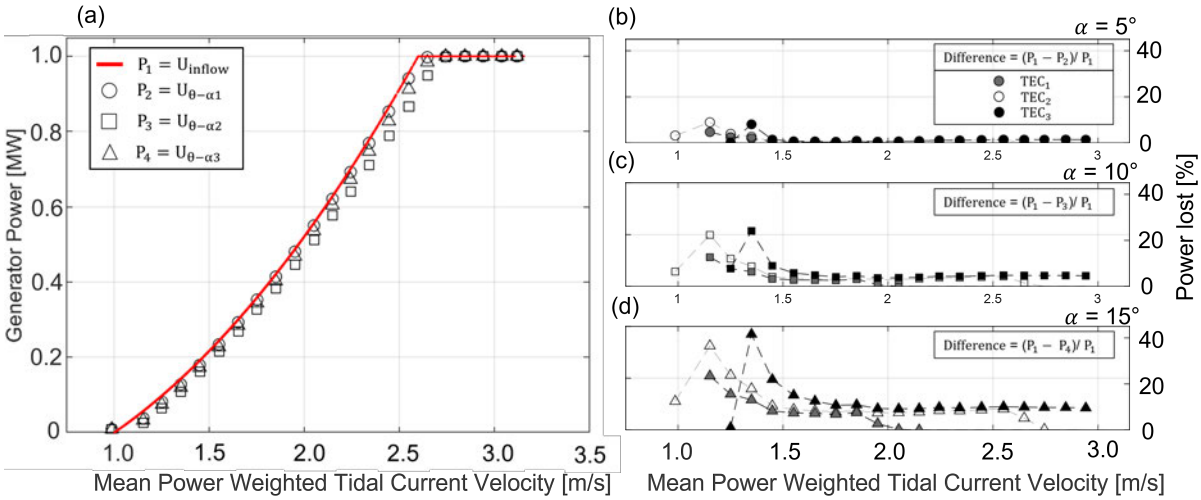

Figure 8.6: Comparison of theoretical maximum power generated using U_{inflow} (red line) and the realistic power generated using velocity component $U_{\theta-\alpha}$, where the TEC is misaligned to the established flood direction. The DEEP-Gen IV power curve is presented (a) by the unfilled symbols, where the circle, square and triangle represent a misalignment from the established flow of 5° (b), 10° (c) and 15° (d), respectively. Filled symbols represent the percentage lost in power when flow data used features misalignment for TEC_{T2} (filled grey) and TEC_{T3} (filled black).

The power lost from ebb measurements was lower than the flood measurements (Fig 8.6). This is due to the narrower flow direction spread ($\approx 35^{\circ}$) at this location and the greater occurrence of the flow velocity exceeding (3.9 m·s^{-1}), the TEC-rated velocities. However, due to this narrow flow direction spread, the impact on the power curve was more severe when flow data used was a velocity component due to misalignment from the established flow direction.

8.5 Consequence to Annual Energy Estimates

Figure 8.7 is a graphical representation of the difference in AEP estimates when changing the TEC heading away from the established flow direction. It can be seen that the introduction of misalignment reduces the total amount of energy captured and by different amounts when misaligned clockwise or anti-clockwise to the established flow direction. The greatest loss in AEP, when compared against the theoretical maximum, was found when the TEC was positioned clockwise from the established flow direction on the ebb tide. Results differed by up to 7.8%, 10.1% and 13.3% for TEC_{T2}, TEC_{T1} and TEC_{T3}, respectively. A summary of the AEP losses is provided in Table 8.2. The natural variation in flow direction measured on the ebb tide is closer to the established flow direction, resulting in a lower AEP loss of $\approx$ 0.7%, 0.8% and 1.1% when TEC_{T2}, TEC_{T1} and TEC_{T3} are accurately aligned with the established flow direction θ_{ebb}. However, when the TEC is not aligned to θ_{ebb}, the AEP losses are significantly greater when compared with a misalignment from θ_{flood} due to the narrow spread in the direction across the ebb cycle.

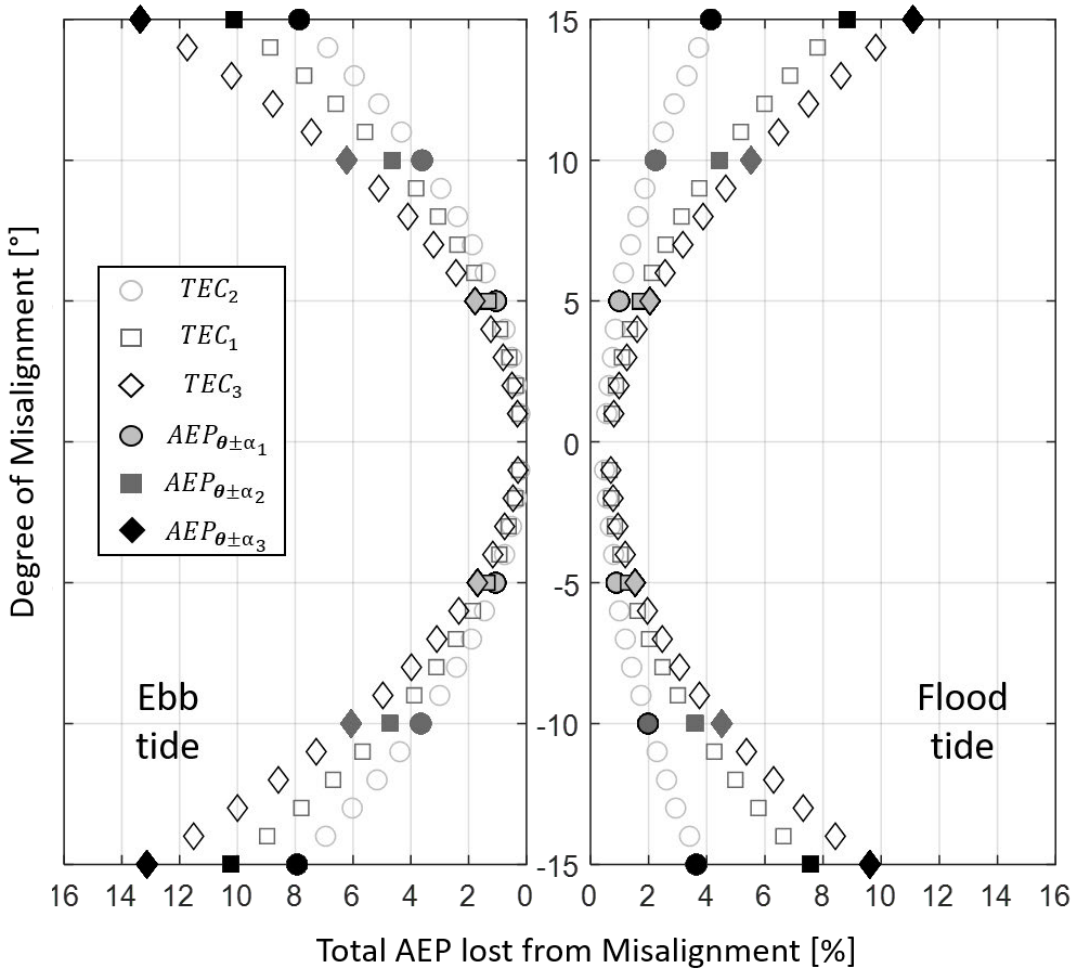

Figure 8.7: AEP loss based on flow velocity using U_α, where α changed in increments of 1° up to 15° (α_1, α_2 and α_3 represent 5°, 10° and 15° respectively). The flood (right) and ebb (left) tide AEP estimates with a clockwise and anti-clockwise shift from the established flow.

Table 8.2: AEP percentage loss from misalignment (α), where both flood and ebb tidal cycles were analysed for a clockwise and anti-clockwise shift for the three TEC concepts. NOTE θ is equal to the established flow direction.

	TEC_{T2}		TEC_{T1}		TEC_{T3}	
AEP cases	Flood	Ebb	Flood	Ebb	Flood	Ebb
U_θ	0.7	0.5	0.8	0.7	1.1	0.8
$U_{\theta+\alpha_1}$	0.9	1.1	1.7	1.2	2.1	1.8
$U_{\theta+\alpha_2}$	2.2	3.6	4.4	4.7	5.5	6.2
$U_{\theta+\alpha_3}$	4.2	7.8	8.8	10.1	11.1	13.3
$U_{\theta-\alpha_1}$	0.9	1.1	1.3	1.4	1.5	1.7
$U_{\theta-\alpha_2}$	1.9	3.7	3.6	4.8	4.6	6.0
$U_{\theta-\alpha_3}$	3.6	7.9	7.6	10.3	9.6	13.1

Figure 8.8 shows a time series of energy captured by TEC_{T1} for each tide across the measurement campaign, where the lower energy yields are directly related to lower velocities which occur during neap tidal cycles, experienced around periods June 12th-14th and June 24th-26th. During these periods of lower tidal flow speeds, we see the greatest energy lost due to the modelled misalignment. The energy lost over each tidal cycle varies, but was as high as 3%, 7% and 12% when the TEC is misaligned to the established flow direction by 5°, 10° and 15° respectively.

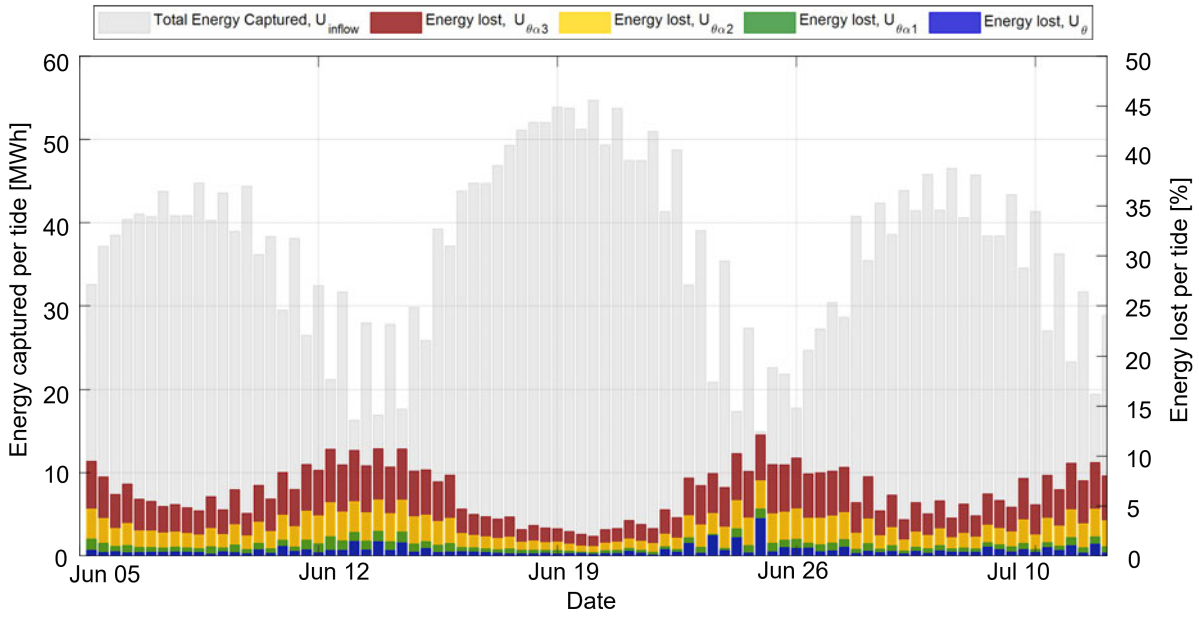

Figure 8.8: Energy lost when TEC_{T1} is misaligned to the flow, where the grey bar is the energy captured per tidal cycle. The blue, green, yellow and red bars represent the energy lost by the TEC facing the established flow θ, misaligned by α_1 (5°), α_2 (10°) and α_3 (°), respectively.

8.6 Vertical Variation in the Measured Flow Direction

The variation in flow direction at different heights above the seabed over each tidal cycle is dissimilar. Therefore, three TEC concepts that occupy different regions of the water column were chosen to assess the impact of power performance relative to the amount of time spent off-axis to the established flow. Figure 8.1b depicts the measurements along the water column at three depths.

The 10-minute averaged measurements were split by acceleration and deceleration of the tide and into velocity bin increments of 1 m·s^{-1}. Figure 8.9a and 8.9b shows a variation with depth in the flow direction along the measured water column of $\approx 8°$, and 13° for the ebb and flood tide at peak flow (3 - 4 m·s^{-1}), respectively. Also shown in Figure 8.9a and 8.9b, the estimate of θ_{HH} (solid red line) and θ_{PWRA} (red cross), differed by $\approx$ 0.9% at location TEC_{T1} (presented in Fig 8.9) and 1.7% and 0.4% at locations relative to TEC_{T2} and TEC_{T3} respectively.

Figure 8.9b depicts the variation in flow direction in the lower region ($<$ 15 m) as $\approx$ 11 - 13 °, compared to $\approx$ 5 - 7° in the upper region ($>$ 35 m from the seabed) on the flood tide. The ebb tide ranged from $\approx 6°$ down to 4° between the lower and upper region as shown in Figure 8.9a. This highlighted that the two tidal cycles have different flow direction characteristics and the acceleration and deceleration phases of the tide differ significantly between the flood and ebb tidal cycles.

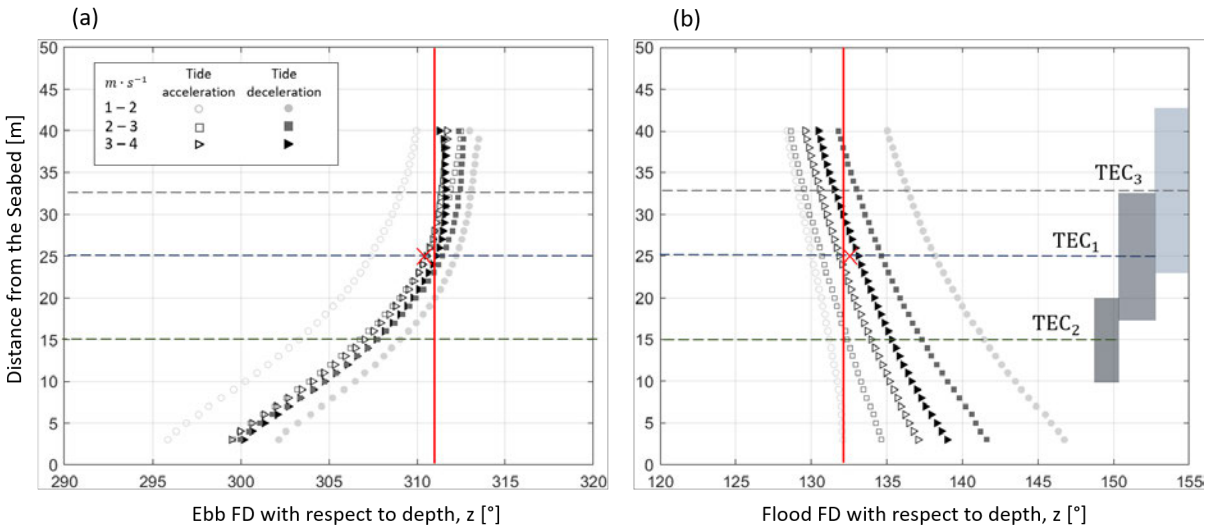

Figure 8.9: Flow direction variation along the measured water column (z) during the acceleration and deceleration phase of the tide for a) the ebb tide measurements and b) the flood tide measurements. The established flow direction estimate using θ_{HH} (solid red line) and θ_{PWRA} (red cross) methods are shown for TEC_{T1}. The position of all three TECs in the water column is shown in (b).

8.7 Flow direction variation across tidal phases

Characterising and defining sites for deploying available technologies are important for evaluating tidal energy use. Tidal characteristics of most coastal locations have been studied with a respective toward navigation safety. Tidal dynamics depend on both the global characteristics of the tide and regional and local geometry, which can lead to tidal resonance or flow constriction.

The lunar variability in the tides should be considered because the practical power generation varies considerably when large differences exist between spring and neap tides. The tides at the Fall of Warness differ by $\approx$ 0.5 m·s^{-1} between flood and ebb tides, the latter containing greater flow velocities. However, each tide is subject to fortnightly variation through the gravitational pull of the Moon and Sun. This effect causes the tides to vary in strength. During spring tides, there are large sea level variations, which can be associated with high tidal currents, particularly in narrow steps and shallow channels connecting different micro-basins. In contrast, during neap tides, sea level variations are relatively small, and tidal currents are drastically reduced. The flood tide at the Fall of Warness varies by $\approx$ 1.3 m·s^{-1} ($\approx$ 1.8 - 2.2 m·s^{-1} in a neap cycle and $\approx$ 3 - 3.4 m·s^{-1} in a spring cycle). Whereas the ebb tide varies by $\approx$ 1.7 m·s^{-1} ($\approx$ 2.0 - 2.4 m·s^{-1} in a neap cycle and $\approx$ 3.7 - 4.1 m·s^{-1} in a spring cycle). For the following performance assessment, results obtained in flood flows only are considered.

Figure 8.10a and 8.10b illustrates the tidal flow velocity and direction at the Fall of Warness spilt by tidal phase, neap (purple), intermediate (blue) and spring tidal (gold) respectively. The three phases were defined as follows: neap phase with flow speeds up to 2.25 m·s^{-1}, intermediate phase with flow speeds up to 2.75 m·s^{-1}, and spring phase with flow speeds up to and exceeding 3.25 m·s^{-1}.

The sea level elevation ranges at the Fall of Warness from 1.4 m in the neap tide, 2.2 m in the intermediate tide and 3.2 m in the spring tidal phase. Figure 8.11a, 8.11b and 8.11c illustrate the variation in tidal elevation during the neap, intermediate and spring tidal phases respectively.

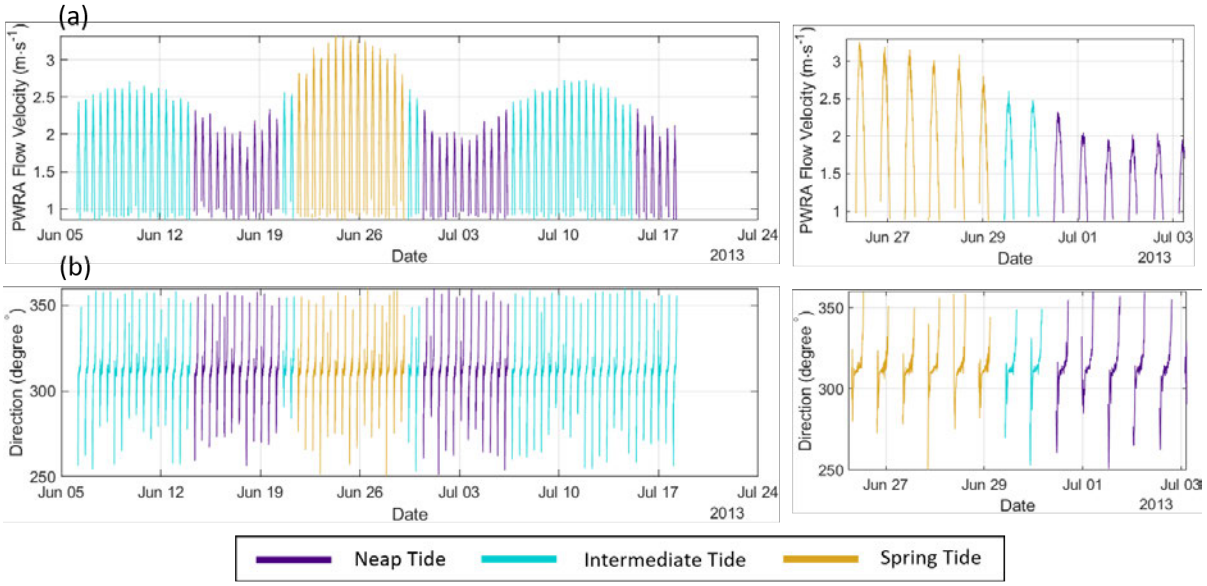

Figure 8.10: Flood time-series data set for (a) PWRA flow velocity and (b) direction measured by seabed mounted ADCP A_4 (refer to Fig 5.3). The neap (purple), intermediate (blue) and spring currents are shown over a fortnight at the Fall of Warness.

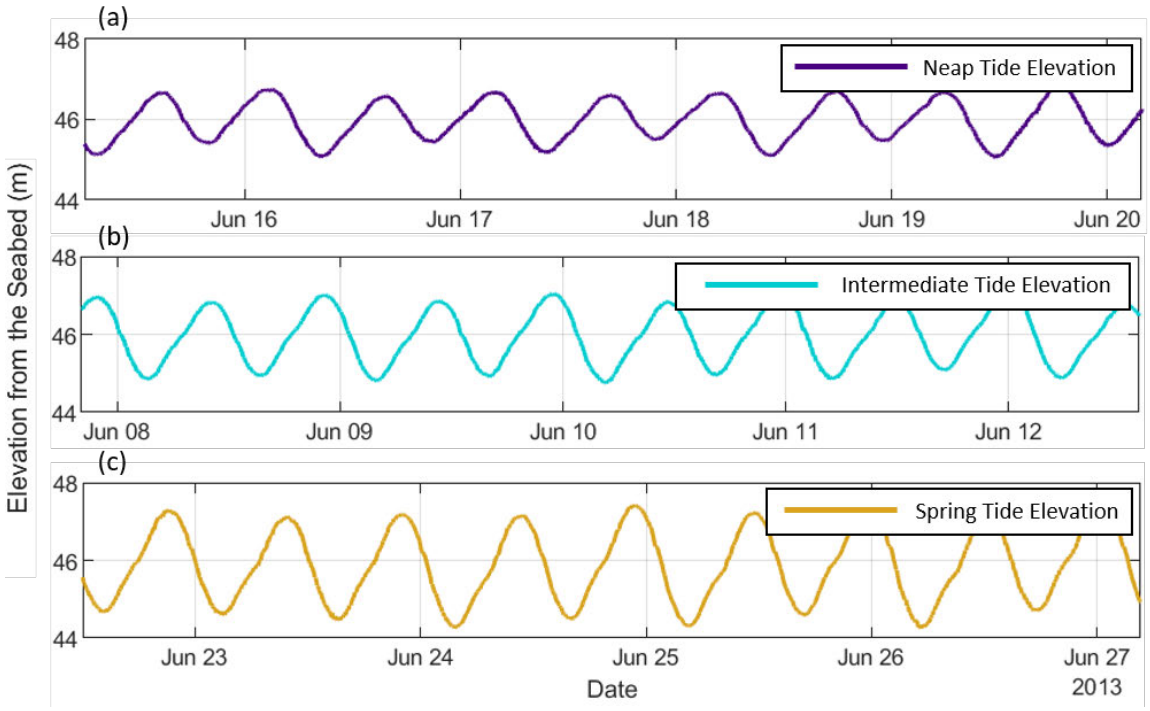

Figure 8.11: Sea level comparison between pressure measurements obtained from the seabed mounted ADCP located at A_4. (a) Neap tide elevation variation. (b) intermediate tide elevation variation. (c) Spring tide elevation variation.

This section highlights the consequences of not aligning with the main flow during different tidal phases. The neap tidal cycle - flood tide velocity measurements - at this location is $\approx$ 33 - 45% less than the spring tidal cycle. Therefore, a TEC not aligned with the approaching flow during this tidal phase will experience significantly higher losses since the flow velocity will not exceed the TEC-rated velocity. For TECs that lack yaw capabilities, it is imperative to position the TEC rotor towards the principal flow direction. However, it is worth noting that the flow direction estimate may vary throughout a fortnight period due to the differences in the tidal phase.

The directionality and strength of typical neap, intermediate and spring tidal currents at the turbine location are shown in Figure 8.12. The tidal ellipse illustrates the direction the flood flow velocity is coming from (Fig 8.12a). Figure 8.12b shows the current strength and directionality relative to the TEC characteristics - cut in and rated velocity - indicating that the TEC doesn't run optimally during neap and intermediate tides.

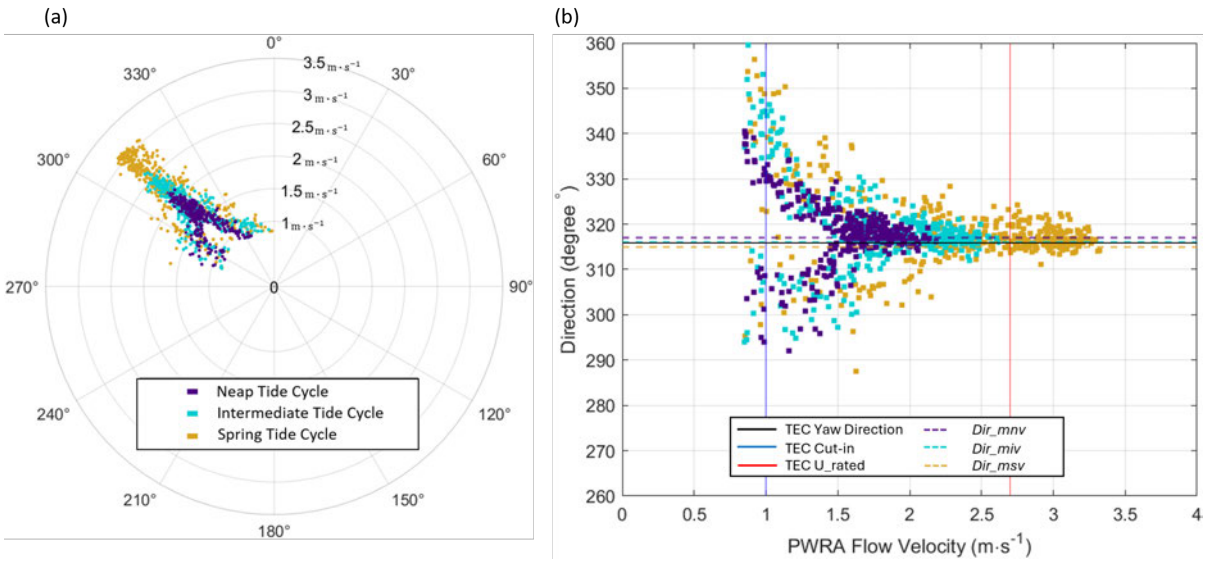

Figure 8.12: Typical directionality and strength of neap, intermediate and spring tidal currents on the flood tide at the Fall of Warness. (a) A tidal ellipse indicates the direction from which the flood tide flows. (b) Estimated mean flow direction based on tidal phase (dashed lines), showing $\frac{2}{3}$ of the tidal phases that don't reach the TEC-rated velocity.

Figure 8.13 illustrates the tidal flow direction variations during the three key phases throughout a fortnight period. As the mean direction is estimated from a full data set, this estimate informs TEC developers on turbine orientation, this is shown by the solid black line in Figure 8.13. The angle of off-axis separation between the TEC rotor extraction plane and the principle flow direction is presented at each 30-minute interval. During the two hours at mid-tide - where the current flow velocity is the greatest and direction is established - TECs produce the most energy. For non-yawing TEC devices, this region should be targeted. It can be seen in Figure 8.13, the misalignment between the TEC rotor extraction plane and the flow can be as high as 38° and 26° during a neap and spring tide respectively. The flow velocity relative to these direction increments of 30-minutes can be harnessed by a TEC with a cut-in velocity of 1 m·s^{-1} after 1 hour and 1 hour 30 minutes in a spring and neap tide respectively. Therefore, the impact of misalignment begins at different periods based on the operational characteristics of the TEC.

Figure 8.14 depicts the variation in flow direction along the measured water column as the flood tide progresses. The grey region highlights the swept area of the DEEP-Gen IV TEC. The mean flow direction is presented at each depth bin at 1 hour 30 minutes (circular symbol), mid-way (3 hours - square symbol) and approaching slack tide at 4 hours 30 minutes (triangle symbol). The variation between the neap and spring tide direction at a hub height of 18 m for the three intervals provided (Fig 8.14) is $\approx 4°$, 0.3° and 2.5° respectively.

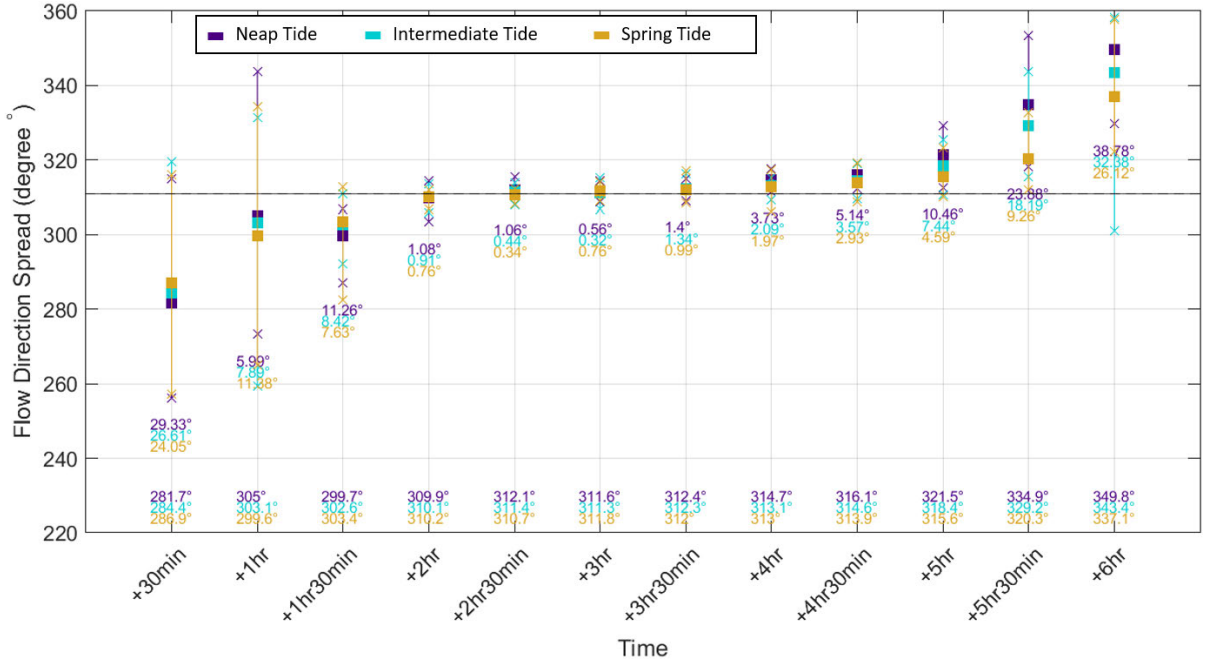

Figure 8.13: The flow direction mean (square markers) of 30-minute periods throughout the flood cycle, the TEC yaw heading (solid black line), and the min and max (crosses) variation in direction.

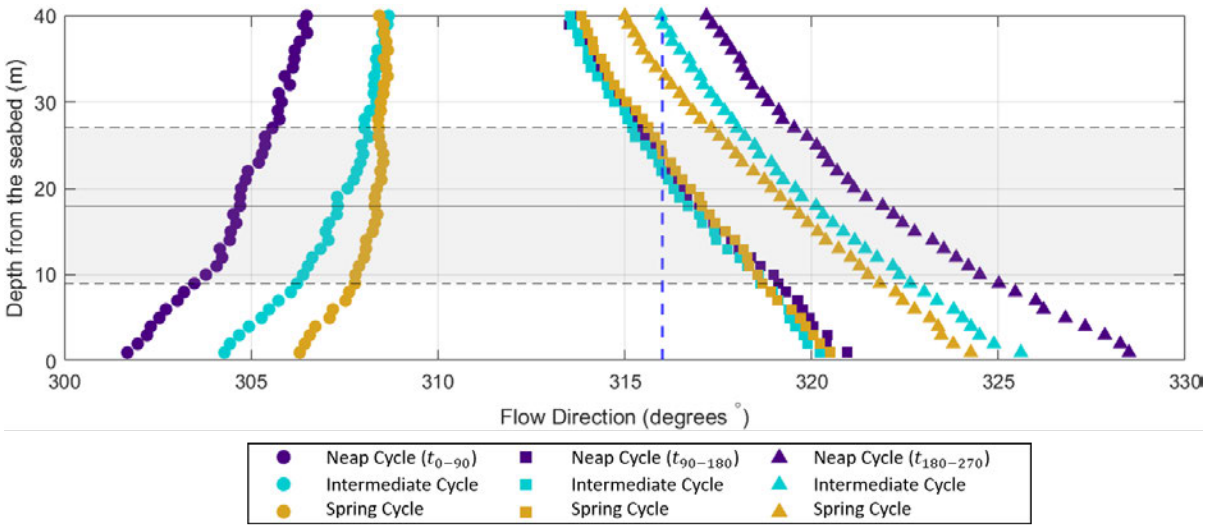

Figure 8.14: Flow direction variation along the measured water column (z) during the flood tide. The mean direction for the neap, intermediate and spring tide at a time (t) period of 1 hour 30 minutes, 3 hours and 4 hours 30 minutes into a flood tide. TEC swept area and yaw angle are defined by the grey box and blue dashed line respectively.

Figure 8.15 shows the generated power output for each velocity bin in increments of 0.1 m·s^{-1} for the neap, intermediate and spring tide measurements on a flood cycle. The black line represents the DEEP-Gen IV measured curve facing the flow direction 100% of the time (theoretical maximum possible). The difference presented in Figure 8.15 represents the natural misalignment between the DEEP-Gen IV when positioned toward the estimated established flow direction (in this case 316°) and the flow direction as it evolves over a tidal cycle.

The greatest variation exists during the periods of slower velocities - foot of the curve - where the variation between the mean flow direction and TEC yaw angle varies significantly more. In addition where the generated power is lower and therefore where the denominator of the percentage calculation is smaller. As Shown in Figure 8.15, the DEEP-Gen IV curves differed by up to $\approx$ 17%, 15% and 10% during the natural misalignment during a neap, intermediate and spring tide and the rotor extraction plane at velocities $<$ 1.5 m·s^{-1}. This reduces to < 1% for all the tide cycles at velocities $>$ 2.5 m·s^{-1}.

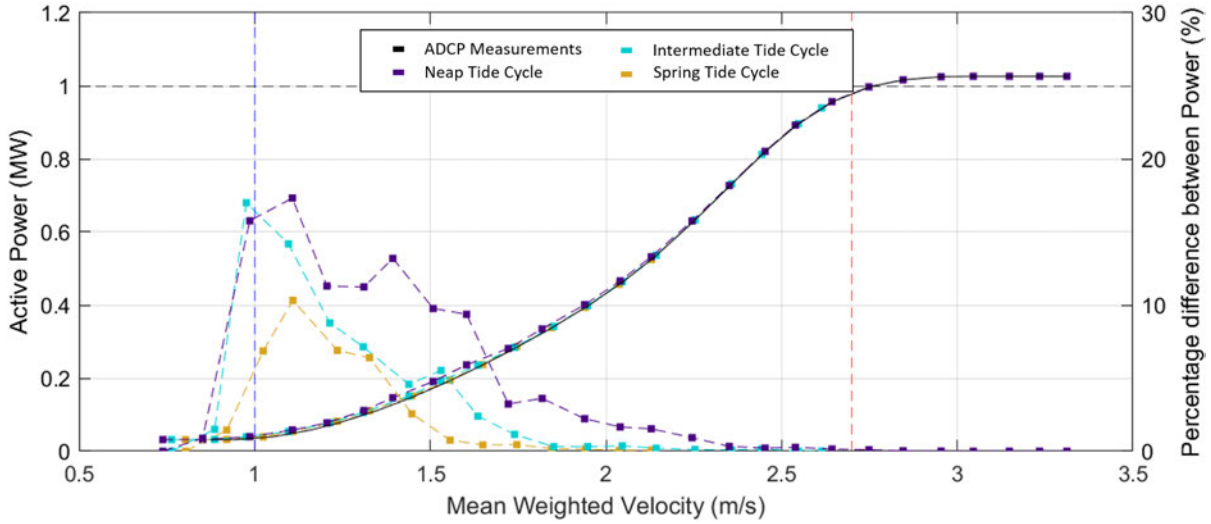

Figure 8.15: Comparison of theoretical maximum power generated assuming the DEEP-Gen IV is positioned to the flow direction (black line) at each time-stamp, and the realistic power generated using velocity components equal to the misalignment of the turbine from the established flow direction during the neap, intermediate and spring tides. The percentage difference in velocity is given by the natural misalignment between the flow direction and the turbine extraction plane during each tidal cycle.

Capturing this feature in the power performance can support developers in producing a more accurate measured power curve for their devices. Accounting for the component of velocity passing through the swept area under off-axis conditions will yield a more favourable power curve for a developer as the velocity at the TEC rotor is lower than what is measured at the instrument location. This result is based on the TEC facing the estimated flow direction based on previous data sets deployed in the same location. If the TEC is off-axis to the principle flow direction by a fixed degree this will change what velocity the calculated power should correspond to on the measured power curve as previously discussed in section 8.4 and the AEP estimates in 8.5.

8.8 Discussion

This chapter demonstrates the importance of accurately estimating the principle flow direction, but also defining the principle flow direction that correlates most closely to the swept area of the turbine in situ. First, it is shown that including data outside of the TECs operational limits can skew the established flow direction estimate by up to 4° (see Table 8.1). The greatest variation in flow direction is found when the tide changes between flood and ebb. The flow velocity and direction evolve over the tidal cycle; removing data beneath the cut-in speed of the TEC will remove the large variations in flow direction and provide a more accurate reference for TEC orientation.

In addition, the flow direction can vary up to 13° in the vertical plane of the measured water column. The rotor average and PWRA methods are used in this study to capture the variation in the direction along the rotor plane. Results differed by less than 1.2% when comparing the two methods against the averaged hub-height estimate. The work highlights that misalignment between the TEC extraction plane and the flow direction will impact the energy captured. Furthermore, aligning the depth bin from the ADCP to the proposed TEC hub height when estimating the established flow direction is key, and inaccuracies can impact the amount of energy captured when the TEC orientation is incorrectly informed. This was shown in Figure 8.9, where the flow direction varied with depth.

A key objective of this study was to assess the impact on power production when flow data used features misalignment from the TEC extraction plane. The flow direction evolves over a tidal cycle, making the TEC susceptible to off-axis currents, even when the TEC is aligned to the averaged (over a tidal cycle) flow direction. This is evidenced by the temporal variation in the flow direction, shown in Figures 8.1 and 8.3 and the vertical variation displayed in Figure 8.9. The AEP estimate calculated from assuming the TEC tracks the flow, compared with a fixed TEC heading toward the established flow angle, differed by up to 1%. This is site-specific and will be based on a tidal site's natural flow direction variation. The variation in the flood tide direction was $\approx 75°$, whilst the ebb tide direction varied by $\approx 35°$ (Fig 8.4), this resulted in the TEC being off-axis more frequently during the flood tidal cycles, thus the AEP losses were greater. Furthermore, if the TEC is misaligned with the established flow angle once deployed, the the actual annual power production will be less than estimated. For a non-yawing TEC the total AEP loss, as shown in Table 8.2, can be up to $\approx$ 2%, 6% and 13%, when the TEC is incorrectly aligned to the established flow by 5°, 10° and 15° respectively. This highlights an area of uncertainty when deploying a TEC at a tidal site. The accuracy of both the TEC heading and flow direction will reduce the uncertainty in the measured power curve and energy yield estimates.

A case study using three horizontal axis TECs rated at 0.25 MW, 1 MW and 2 MW and occupying the lower, mid and upper regions of the water column respectively, is presented. The 1 MW machine used real-world data as this was available. Figure 8.7 and Figure 8.9b show the position of the three TECs and the AEP loss when misaligned to the established flow direction respectively. Of the three TECs assessed, the 2 MW variant shows the greatest AEP losses under misalignment. This is a result of the operational characteristics of the TEC, where the rated velocity is 3.1 m·s^{-1}, and the flow velocity at the site on a flood tide was 3.2 m·s^{-1}. Whereas the smaller-scale TECs (TEC_1 and TEC_2) experience more frequent flows in excess of their rated velocity which mitigates the impact of misalignment. Overall, a tidal energy converter that has a rated velocity beneath the tidal site flow characteristics by $\approx$ 10% will operate at full capacity during peak flow conditions even during periods of excessive misalignment up to 25°, at the expense of capturing significantly less energy during times below peak flow conditions. On the other hand, TECs with a rated velocity over or close to the peak flow tidal conditions will suffer significantly if the flow velocity is lower than the rated. This is evident in Figure 8.8, where the AEP losses are greater under lower flow conditions, commonly referred to as neap cycles. An active yaw mechanism would be most efficient during periods of lower velocity, where the TEC operating characteristics are close to the flow characteristics at the tidal site, to maximise the energy captured and minimise losses.

This observed dependence of the impact of misalignment on the relative velocity of the tides means the impact will also vary with the spring/neap cycle. The lunar variability in the tides should be considered as the practical power generation varies considerably when large differences exist between spring and neap tides. The amount of energy extracted from the tide is proportional to the cubed flow velocity. Therefore a change in velocity will directly impact the power produced. For TEC devices with a high rated velocity (> 2.5 m·s^{-1}) will perform better

during spring tides that reach $>$ 3 m·s^{-1}, whereas the neap cycle has a maximum flow of around $\approx$ 30 - 40% of the spring tide (2.1 m·s^{-1}). It has been shown that the greatest variation between the TEC yaw angle and the flow direction (assuming the TEC is positioned toward the established flow direction) is at lower flow velocities where the flow direction varies significantly more. For a neap tidal cycle, the velocity variation differs by up to 17% at the lower flow velocities (TEC generates power in this region). This is due to the flow accelerating to a greater velocity at a slower rate when compared to a spring tide.

8.9 Conclusions

This chapter focuses on the need for precise flow direction estimates in tidal turbine installation and power performance assessments. Accurate flow direction is key to proper turbine setup and energy output calculations.

For precise flow direction estimates that inform turbine installation and power assessments, data processing should focus solely on conditions during the TECs active power production. Using rotor averaging methods led to flow direction variations up to 1.2°, while limiting data to operational turbine velocities showed deviations up to 4°.

Three horizontal-axis tidal turbines - which were theoretically positioned toward the principle flow direction and then shifted from this direction in increments of 1° - were examined to analyse the effects of yaw misalignment on AEP. This offset from the turbine when deployed becomes more important due to the natural flow direction varies greatly over a tidal cycle. When turbines were aligned with the established flow direction, AEP deviated by a maximum of 1.1% from a theoretically perfect yawing turbine. Misalignment significantly affected AEP, when misaligned by 5°, 10°, and 15° the AEP varied by 2%, 6%, and 13%, respectively.

The relationship between onsite flow velocity and the TECs rated velocity plays a significant role in the misalignment impact on AEP. Turbines rated close to or above the site's maximum flow velocity are particularly vulnerable to misalignment effects. In contrast, those rated at least 10% below the maximum flow can operate at full capacity even when misaligned by up to 25 degrees. However, the reduced velocities during neap tidal cycles negatively affect the turbine's operational time, particularly when misaligned, leading to less energy capture.

Accounting for tidal cycles is essential for precise TEC performance evaluation. The power output of a tidal turbine is a cubic function of flow velocity, making small velocity increases significantly boost power generation. At the studied site, neap tide velocities were 30-40% slower than those during spring tides, which not only lowers power output but can also cause generation to dip below the TEC's rated capacity, adversely affecting overall performance.

In summary, accurately estimating the flow direction and considering local conditions is crucial for optimising tidal turbine installation and power generation performance. Misalignment from the established flow direction can have significant effects on energy estimates and turbine operation - which is inevitable for non-yawing TECs - making it essential to account for these factors in tidal energy projects. Future research should focus on quantifying these uncertainties and comparing flow direction variability across different tidal sites.

Chapter 9

Industry Recommendations, Research Contributions and Final Work Conclusions

9.1 Recommendations for Tidal PPAs

Understanding uncertainty in tidal power performance assessments is pivotal for the tidal energy industry. Accurate performance metrics are critical for securing investment, optimising system designs, and ensuring long-term viability. Uncertainty in assessments can lead to either overestimation or underestimation of a system's capabilities, both of which have significant economic and operational implications. Overestimation can result in unmet production targets and financial shortfalls, while underestimation can lead to underutilised resources and missed opportunities. Therefore, a comprehensive understanding of uncertainty helps in risk mitigation, improving the reliability and credibility of tidal energy projects.

This thesis identifies new uncertainties in tidal power performance assessments, expanding the uncertainty budget for future power performance evaluations. Additionally, the work presents techniques to quantify and mitigate specific sources of uncertainty.

9.1.1 Acoustic Doppler Measurement Uncertainty

Uncertainty in ADCP Accuracy

Uncertainties in the accuracy of measurements from acoustic instruments arise from various factors including calibration errors, internal clock drift, Doppler noise, and multi-path interference. Additionally, environmental conditions such as water salinity, temperature, and pressure can impact sensor accuracy. To mitigate these uncertainties, it is recommended to conduct regular calibrations, employ optimal configuration settings, and validate against alternative measurement methods. Consultation with device-specific guidelines and manufacturer support is advised for best practices.

Consult device-specific guidance from companies such as Teledyne RD Instruments [359] and Nortek [360] for further information.

Cross-Talk Features in Acoustic Instrument Data: Implications for Signal Integrity and Interpretation

Cross-talk in acoustic instrument data refers to the unintended interference of signals between different channels or transducers. This phenomenon can compromise signal integrity, leading to erroneous measurements and potentially misleading interpretations. In ADCPs and similar acoustic devices, cross-talk can occur when multiple

transducers are in close proximity or when signals overlap in frequency or time. The implications are twofold: first, it can lead to an inaccurate representation of water current profiles, affecting the reliability of performance assessments; second, it can complicate data analysis, requiring additional signal processing steps to isolate and remove the noise generated by cross-talk.

To mitigate the impact of cross-talk, careful planning of sensor layout, frequency selection, and synchronisation protocols should be considered. Consult manufacturer guidelines for specific anti-cross-talk features and calibration methods to improve data quality.

Developers should enforce the practice of conducting visual inspections on data obtained from ADCPs (before and after data QC), particularly in scenarios involving multiple instrument deployments. This approach aids in recognising data anomalies, such as cross-talk patterns, thereby guaranteeing the integrity of the collected data. When planning multi-instrument deployments, consider the range at which ADCPs are separated to minimise the likelihood of cross-talk. Part of this work (Chapter 6) has demonstrated that two acoustic instruments can effectively operate within a function of their profiling range. For instance, in this specific case, with a 45 m profiling range, the instruments were deployed with a separation of 45 m and collected over 80% of valid data.

The current approach permits linear interpolation between adjacent bins if valid data exists. This can be iterated across multiple velocity bins, provided that the interpolated portion does not exceed 10% of the total number of bins. However, the data processing stage prohibits interpolation involving an incomplete adjacent bin or extrapolation between data points.

Chapter 6 presented instances where data was missing at various depths due to the elimination of cross-talk interference. Interpolation methods, such as power law calculations, were used to fill in these data gaps in the velocity-depth profiles. However, it is essential to flag any repaired data as suspect, in accordance with QARTOD guidelines, for subsequent analyses. Data repair is recommended under specific conditions: when the instrument deployment is expensive and the collected data is critically important. Utilising post-processing techniques to correct flawed data is crucial for preserving valuable insights, minimising data loss, and eliminating the need for costly re-deployments.

9.1.2 Estimation of Power Performance for a Tidal Device

Tidal Site Specific: Flow Velocity Variation

The PPA of a TEC was conducted in accordance with IEC TS 62600-200, using data from ADCPs placed both in-line and adjacent to the TEC. Chapter 7 demonstrated that flow velocity varied by 0.6% and 1.1% for in-line and adjacent placements, respectively. This resulted in an error in the estimated AEP of 1.2% and 2.6% during flood tide, and up to 4.3% during ebb tide. These findings support the IEC TS 62600-200 guidelines for instrument orientation, as in-line measurements yielded less AEP variation.

Before averaging spatial data, a visual examination of velocity-binned depth profiles for both flood and ebb tides is essential. Large-scale flow features like eddies, as identified in Chapter 7, should be detected and removed prior to analysis. Failing to identify these features before spatial averaging over the TECs rotor plane impacted the AEP estimate by 7.3% in this study. This impact would vary significantly if the TEC were located higher or lower in the water column at this site.

Aligning the ADCP depth bin with the rotor-swept area is critical for accurate PPAs. The work in Chapter 7 indicates that an alignment error of up to 2 meters could result in an estimated AEP deviation as high as 5.5%. These results emphasise that in regions exhibiting high vertical shear, the AEP is particularly sensitive to vertical misalignment. Therefore, meticulous checks should be conducted to align the ADCP bin with the TEC. Factors to consider before and after instrument deployment include:

- Calibration Errors: Inaccurate calibration of pressure sensors in the ADCP can lead to depth measurement errors. Factors contributing to these errors include variations in calibration coefficients, time-induced drift, and improper initial calibration.
- Zero Offset: Proper zeroing of pressure sensors at the surface before deployment is essential for compensating for atmospheric pressure. Inaccurate zeroing or shifts in zero offsets during deployment can cause discrepancies in depth measurements.
- Instrument Misalignment: Precise vertical alignment of the ADCP upon seabed deployment is critical. Errors in depth measurements can result from misalignment between the sensor and the actual seabed depth.
- Blanking distance: Consideration of the ADCP's blanking distance and the distance to the initial measurement depth bin is vital. These factors can vary based on the specific instrument used and should be accounted for to ensure accurate measurements.

With these checks implemented, the likelihood of inaccuracies in depth measurements can be reduced, thereby enhancing the reliability of data collection. This is particularly important for floating TEC concepts, which present additional complexities due to water column movement.

These guidelines underscore the need for meticulous data analysis, precise instrument calibration, and consideration of site-specific flow conditions in the evaluation of tidal turbine power performance. Adhering to these practices will result in more accurate and dependable power curve measurements and AEP estimates for TECs.

Tidal Site Specific: Flow Direction Variation

Accurate estimation of the principal flow direction is vital for both TEC installation and PPA. Chapter 8 demonstrated that errors of 5, 10, and 15° in the principal flow direction could result in errors of 2%, 6%, and 13%, in AEP respectively. Such errors are particularly likely when deploying non-yawing TECs based on incorrect post-processing data. Variability in the established flow direction can reach up to 1.2° using rotor averaging methods and 4° when restricting data to operational turbine velocities. Moreover, the flow direction naturally changes over a tidal cycle, contributing to an energy estimation error of up to 1.1% at this specific site when a non-yawing turbine is misaligned.

The vertical plane of the measured water column can show significant flow direction variations, as high as 13° at this site as shown in Chapter 8. Accurate depth bin selection during data post-processing is crucial; otherwise, it can introduce an uncertainty of up to 2° in the estimated flow direction and thereby affect calculated power metrics.

Misalignment between a non-yawing turbine's extraction plane and the flow direction is inevitable. TECs rated at velocities about 10% below site flow conditions can operate at full capacity even when misaligned by 25°. In contrast, TECs rated close to or above peak flow conditions may under perform if the flow velocity falls below the rated level. Active yaw mechanisms are most efficient during periods of lower velocity, aligning the TEC operating characteristics closely with site flow conditions to maximise energy capture and minimise losses.

The impact of misalignment varies between spring and neap tides due to differences in flow velocity and turbine characteristics. Since power generation is a cubic function of flow velocity, lunar variability should be taken into account. Real-world data can offer more accurate PPA results and improve our understanding of the impact of misalignment on TEC performance.

These guidelines underscore the importance of accurate flow direction estimation, meticulous data quality checks, and consideration of site-specific tidal characteristics for optimising TEC performance and energy capture.

Power Performance

The uncertainty in power performance should be calculated on a specific device basis. A PPA should be carried out at the site and the uncertainty should be calculated using the methodology provided by the IEC TS 62600-200. The uncertainty associated with a performance test has the potential to decrease over time with an increase in device performance validation. Other external factors will always exist (imposed misalignment between the measurement device and turbine rotor area, flow direction maturity and the spatial variation in velocity at the tidal site, etc). However, methods can be carried out to mitigate and reduce the magnitude of these uncertainties.

9.2 Research Contributions

9.2.1 Key Findings

The research presented in this thesis has contributed to the advancement of knowledge as follows:

Fish Bone Diagram

- Presented the first in-depth fishbone diagram (Fig 4.13) as a valuable tool for systematically addressing uncertainties. Decision-makers can use this diagram to prioritise their efforts and resources, focusing on the most critical factors first. This approach ensures that mitigation strategies are targeted at areas with the highest potential to improve assessment accuracy. As new data and insights emerge, the fishbone diagram can be updated to reflect the latest understanding of uncertainties. This facilitates continuous improvement in the PPA process and allows for iterative refinements in the future.

Impact of Acoustic Interference on Power Metrics: Chapter 6

- Proximal ADCPs (45 m apart) in energetic tidal channel without sampling synchronisation results in periods of data corruption. This Configuration yields valid data and provides insights for tidal energy and broader multi-sensor deployments (Section 6.3).
- AEP estimates for three turbine types showed 2-7% variation after anomalous data removal, more notably near the sea surface where the impact of cross-talk interference was more prominent (Section 6.5).
- Visual inspection revealed anomalies in auto-checked data. A developed algorithm identifies corrupted data with 90% accuracy (Section 6.6).
- It has been shown that a power law fit can be used to repair gaps in ADCP data. This mathematical model assumes a specific relationship between depth and flow velocity, often valid in uniform flow conditions. Using available data points, a power law equation can be fitted to approximate missing values. It should be noted that any data repaired in this manner should be flagged as suspect, in accordance with quality control guidelines like QARTOD, when used for further analyses (Section 6.6.1).

Uncertainty in Power Metrics from Flow Velocity Variation: Chapter 7

- During the flood tide, data from the in-line ADCP pair at 61 m and 106 m—located inside and near the IEC TS 62600-200 target location, respectively—indicated comparable measurements (Fig 7.4a and 7.5a). These findings suggest that ADCPs can be placed up to an additional 0.5D_E - 1D_E beyond the IEC-defined target area, offering more flexibility for instrument installation (Section 7.2.1).
- The IEC TS 62600-200 standard sets a maximum allowable variation of 10% between adjacent mean velocity estimates at a given depth. This limit was often surpassed in the upper water column regions northeast of the DEEP-Gen IV, suggesting that adjacently placed instruments, as advised by IEC TS 62600-200, may not be suitable for PPAs at this location. However, Figures 7.5b, 7.6b, and 7.9 show that for alternative TEC designs positioned lower in the water column, the rotor-adjacent measurement approach could be acceptable at this site (Section 7.2.1).
- Two upstream ADCPs, positioned 61 and 106 meters away from the DEEP-Gen IV turbine, displayed differences in flow velocity and AEP estimates of 0.6% and 1.2%, respectively. The closer ADCP showed marginally lower flow compared to its more distant counterpart. This variation could stem from flow push-back during TEC operation or bathymetric inconsistencies northwest of the distant ADCP, as indicated in Figure 5.5 (Section 7.2.1).
- During flood tide measurements, the AEP showed variations of 1.2% and 2.6% between in-line and adjacent ADCP pairs, respectively. In contrast, during ebb tides, the adjacent ADCP pair exhibited a 7.3% difference in AEP estimates (Section 7.2.1).
- An investigation into the sensitivity of AEP to vertical misalignment between flow data and modelled turbine rotor positioning revealed discrepancies of up to 2.3% and 5.5%. These occurred when the flow data used had a 1 and 2 m misalignment relative to the modelled rotor plane respectively, as shown in Table 7.2 (Section 7.2.2).

Uncertainty in Power Metrics from Flow Direction Variation: Chapter 8

- The established flow direction estimate, used to guide developers on TEC orientation, exhibited a variance of up to 1.2° with rotor averaging methods and 4° when data were restricted to operational velocities as shown in Table 8.1 (Section 8.3).
- Flow direction was observed to naturally evolve over a tidal cycle. For a non-yawing DEEP-Gen IV turbine aligned to this established flow direction, the AEP discrepancy at this site was 1.1%. In periods of misalignment, the generated power decreased and the AEP error increased. For misalignments of 5°, 10°, and 15°, the AEP diverged by 2%, 6%, and 13%, respectively (Section 8.4.1).
- The impact of misalignment on AEP is largely determined by the difference between the site's flow velocity and the TEC's rated velocity. Turbines with rated velocities at least 10% below the site's peak flow velocity will operate at full capacity during peak conditions, even with up to a 25° misalignment (Section 8.4.2 and 8.5).
- Figure 8.8 shows the periods of maximum energy loss for a TEC rated at 2.7 m·s^{-1}. An active yaw mechanism is most efficient during periods of lower velocity, specifically during neap cycles, to maximise energy capture and minimise losses (Section 8.5).
- As detailed in Section 8.7, tidal velocities at the Fall of Warness show approximately a 30% difference between neap and spring tides. The DEEP-Gen IV power curves (Figure 8.15) reveal variances of roughly 17%, 15%, and 10% for natural misalignment during neap, intermediate, and spring tides, respectively, at velocities below 1.5 m·s^{-1}. These differences diminish to less than 1% across all tidal cycles for velocities above 2.5 m·s^{-1} (Section 8.7).

This work holds significant importance as it explores various uncertainties in power metric estimations for PPAs, focusing on data quality, flow reference, and directional variations. Specifically, the thesis reveals the substantial impact of interference on power curve measurements and AEP estimates, emphasising the importance of interference-removal techniques. It also underscores the sensitivity of power curves and AEP estimates to the chosen flow reference. Regarding flow direction, the study demonstrates the need for precise determinations to optimise turbine performance and quantifies the AEP deviations due to natural flow direction changes and non-yawing turbines. Additionally, the work provides insights into the effects of tidal cycle variations on power curves, offering a holistic understanding of flow complexities that affect tidal energy performance assessments.

9.2.2 Commercial Impact

The EngD thesis is expected to bring substantial practical benefits to both the host company and the wider offshore renewable energy sector. The insights gained from this project are already being used to improve how EMEC assesses the performance of tidal stream deployments. EMEC's extensive knowledge in marine energy, particularly tidal and wave energy, positions the company to better account for uncertainties in evaluating the performance of TECs.

The methods and tools developed in the thesis have already proven effective in practical situations, as demonstrated by their successful use in the PPA for Verdant Power in 2021. Additionally, the findings from the thesis will directly shape the way EMEC calculates uncertainties in future PPAs planned for 2024.

Incorporating the interference algorithm into EMEC's in-house QC software is a significant advancement that enhances the dependability and precision of data processing for TECs. This algorithm allows the software to visually inspect data, identifying and excluding features caused by interference. By integrating the interference algorithm into the software, a consistent and standardised approach to recognising and addressing interference-related data is established, ensuring continuity across future projects.

9.2.3 Future Work Recommendations

The following topics are recommended for future work:

Cross-talk Between Multiple Acoustic Instruments Measuring Concurrently

1. Investigate the correlation between acoustic interference and environmental factors such as tidal conditions, water depth, seabed topography, and current-wave-wind interactions. This analysis could provide insights into potential patterns or triggers for interference events.
2. Understanding the cause to improve the identification of the interference characteristics. This would help refine the repair algorithm provided in this work so that we can support multi-ADCP deployments that suit accurate PPAs for tidal stream projects.

Uncertainty in Power Estimates due to Spatial Variability in Velocity

1. Addressing the limitations of turbine-mounted sensors, like the rotor-attached SB-ADP, could involve exploring correction factors or advanced techniques to enhance flow measurement accuracy in the turbine's presence, potentially rendering this configuration more suitable for PPAs.
2. Additionally, extending research to encompass long-term monitoring campaigns using ADCPs would provide insights into the temporal variability of flow conditions, enabling a better grasp of seasonal variations and their influence on power performance.

Uncertainty in Power Estimates due to the Spatial Variability in Flow Direction

1. The process of compass calibration for ADCPs is challenging and prone to failures when not carried out in a controlled environment, leading to unclear accuracy in measured directions. This study underlines the significance of directionality in shaping upcoming turbine deployments. A promising avenue to enhance accuracy involves investigating a directional frame concept, potentially reducing reliance on the onboard compass. This approach entails deploying the frame in a known orientation and subsequently processing the data to negate the need for the compass or to use it as a supplementary reference to the frame.
2. This study highlights the advantage of incorporating yaw capability into turbines. Yet, the introduction of yawing to turbines entails uncertain capital expenditure (CAPEX) and reliability implications, thereby influencing operational expenditure (OPEX). The demonstrated flow variability can serve as a valuable tool during the design phase to accurately assess the potential costs associated with non-yawing turbines.

9.3 Final Conclusions

In conclusion, this thesis provides essential insights into the impact of various uncertainties on tidal turbine power production and AEP estimates. Utilising a fishbone diagram as a structured tool for uncertainty assessment allows decision-makers to allocate resources to enhance assessment precision efficiently. The methodology proposed for mitigating acoustic interference in ADCP data is crucial for enabling reliable operations in close proximity, and enriching the dataset for spatial velocity and flow parameters.

The research emphasises the importance of accurate flow direction estimation for influencing turbine installation and PPAs. Misalignment, particularly in non-yawing turbines, notably affects AEP, especially when turbines are rated at or above maximum flow velocities. A thorough understanding of flow direction fluctuations over tidal cycles is critical for tidal energy system optimisation.

Spatial and vertical misalignment between ADCP measurements and rotor-swept areas affects both the power curve and AEP calculations. These considerations underscore the need for precise instrument placement and rigorous data analysis for reliable PPAs. Overall, the thesis offers invaluable contributions to the advancement and fine-tuning of tidal energy projects, stressing the importance of accurate flow measurement and judicious instrument placement.

Addressing these measurement uncertainties is key to the successful commercialisation of tidal energy systems. Adopting the recommended practices will improve data quality, accuracy, and reliability, thereby enabling more informed decision-making, superior performance evaluations, and increased investor trust in the tidal energy sector.

Bibliography

[1] International Electrotechnical Commission (IEC), "TC 114: Marine energy - Wave, tidal and other water current converters," pp. 2–13, 2021. [Online]. Available: https://www.iec.ch/ords/f?p=103:7:113537049471920::::FSP_ORG_ID,FSP_LANG_ID:1316,25

[2] R. Clayton, "Quantifying and reducing uncertainty in tidal energy yield assessments," 2020. [Online]. Available: https://ore.exeter.ac.uk/repository/handle/10871/122007?show=full

[3] H. Troup, "Electricity is on track for decarbonisation, but what about decarbonising heat?" *Renewable Energy Focus*, vol. 17, no. 5, pp. 178–179, 2016. [Online]. Available: https://www.sciencedirect.com/science/article/pii/S1755008416301016

[4] M. J. Kreitmair, "Uncertainty quantification in tidal energy resource assessment," 2018. [Online]. Available: https://era.ed.ac.uk/handle/1842/36084?show=full

[5] International Energy Agency, "IEA: Review 2021 assessing the effects of economic recoveries on global energy demand and C02 emissions in 2021 global energy," Tech. Rep., 2021. [Online]. Available: https://www.iea.org/reports/global-energy-review-2021

[6] ——, "IEA: World Energy Outlook 2022," p. 524, 2022. [Online]. Available: https://www.iea.org/reports/world-energy-outlook-2022

[7] H. Ritchie, M. Roser, and P. Rosado, "Our world in data," 2022. [Online]. Available: https://ourworldindata.org/energy

[8] K. W. Costello, "Electrification: The nexus between consumer behaviour and public policy," *The Electricity Journal*, vol. 31, no. 1, pp. 1–7, 1 2018. [Online]. Available: https://linkinghub.elsevier.com/retrieve/pii/S1040619018300010

[9] O. Ruhnau, S. Bannik, S. Otten, A. Praktiknjo, and M. Robinius, "Direct or indirect electrification? A review of heat generation and road transport decarbonisation scenarios for Germany 2050," *Energy*, vol. 166, pp. 989–999, 2019. [Online]. Available: https://www.sciencedirect.com/science/article/pii/S0360544218321042

[10] Z. Hausfather and P. Friedlingstein, "Global CO2 emissions from fossil fuels hit record high in 2022." [Online]. Available: https://www.carbonbrief.org/analysis-global-co2-emissions-from-fossil-fuels-hit-record-high-in-2022/

[11] United Nations: Climate change, "The paris agreement," 2020. [Online]. Available: https://unfccc.int/process-and-meetings/the-paris-agreement

[12] P. Gipe, "Wind energy comes of age California and Denmark," *Energy Policy*, vol. 19, no. 8, pp. 756–767, 10 1991. [Online]. Available: https://linkinghub.elsevier.com/retrieve/pii/030142159190045P

[13] M. J. Lewis, A. Angeloudis, P. E. Robins, P. S. Evans, and S. P. Neill, "Influence of storm surge on tidal range energy," *Energy*, vol. 122, pp. 25–36, 2017. [Online]. Available: https://www.sciencedirect.com/science/article/pii/S0360544217300683

[14] T. O'Doherty, D. M. O'Doherty, and A. Mason-Jones, "Tidal energy technology," *Wave and Tidal Energy*, pp. 105–150, 2017. [Online]. Available: https://onlinelibrary.wiley.com/doi/abs/10.1002/9781119014492.ch4

[15] T. Hooper, C. Hattam, A. Edwards-Jones, and N. Beaumont, "Public perceptions of tidal energy: Can you predict social acceptability across coastal communities in England?" *Marine Policy*, vol. 119, p. 104057, 9 2020. [Online]. Available: https://linkinghub.elsevier.com/retrieve/pii/S0308597X20303791

[16] E. O. E. Association *et al.*, “Industry vision paper, 2013,” *Brüssel. Online verfügbar unter http://www. oceanenergy-europe. eu/index. php/en/comm unification/publications*, 2013.

[17] “National Grid: Future energy scenarios,” 2020. [Online]. Available: https://www.nationalgrideso.com/future-energy/future-energy-scenarios

[18] A. J. MacGillivray, “Economically sustainable development of wave and tidal stream energy technologies,” 2016. [Online]. Available: http://hdl.handle.net/1842/25405

[19] J. V. Lamy and I. L. Azevedo, “Do tidal stream energy projects offer more value than offshore wind farms? A case study in the United Kingdom,” *Energy Policy*, vol. 113, pp. 28–40, 2 2018. [Online]. Available: https://linkinghub.elsevier.com/retrieve/pii/S0301421517306900

[20] UK government, “UK becomes first major economy to pass net zero emissions law,” 2019. [Online]. Available: https://www.gov.uk/government/news/uk-becomes-first-major-economy-to-pass-net-zero-emissions-law

[21] Scottish Renewables, “UK marine energy 2019,” *Marine Energy Council*, vol. 1, no. 1, pp. 3–18, 2019. [Online]. Available: https://www.scottishrenewables.com/publications/448-uk-marine-energy-2019-a-new-industry

[22] European Marine Energy Centre, “EMEC: Tidal developers,” 2023. [Online]. Available: https://www.emec.org.uk/marine-energy/tidal-developers/

[23] R. Starzmann, I. Goebel, and P. Jeffcoate, “Field Performance Testing of a Floating Tidal Energy Platform-Part 1: Power Performance,” Tech. Rep., 2018. [Online]. Available: https://tethys-engineering.pnnl.gov/sites/default/files/publications/AWTEC2018-320.pdf

[24] A. Garrad, “The lessons learned from the development of the wind energy industry that might be applied to marine industry renewables,” *Philosophical Transactions of the Royal Society A: Mathematical, Physical and Engineering Sciences*, vol. 370, no. 1959, pp. 451–471, 1 2012. [Online]. Available: https://royalsocietypublishing.org/doi/10.1098/rsta.2011.0167

[25] The Carbon Trust, “Performance assessment methodology,” 2007. [Online]. Available: https://www.zess.uni-goettingen.de/explics/Toulouse/anglais/KEYREPORTS/CTC724.pdf

[26] Hans-Wilhelm Schiffer, “World energy resources,” *World Energy Council*, pp. 27–29, 2016. [Online]. Available: https://www.worldenergy.org/assets/images/imported/2016/10/World-Energy-Resources-Full-report-2016.10.03.pdf

[27] Highlands and Islands Enterprise, “Marine Energy: Key steps to maintain a great british success story,” 2016. [Online]. Available: https://www.hie.co.uk/media/9857/marine-energy.pdf

[28] Deloitte, “Establishing the investment case wind power,” p. 27, 2014. [Online]. Available: https://www2.deloitte.com/content/dam/Deloitte/global/Documents/Energy-and-Resources/gx-er-deloitte-establishing-the-wind-investment-case-2014.pdf.

[29] ORE-Catapult, “Wave and tidal energy yield uncertainty literature review,” Tech. Rep., 2015. [Online]. Available: https://ore.catapult.org.uk/wp-content/uploads/2018/01/Wave-and-Tidal-Energy-Yield-Uncertainty-Literature-Review.pdf

[30] International Electrotechnical Commission (IEC), *IEC TS 62600-200:2013 BSI standards publication marine energy — Part 200: Electricity producing tidal energy converters — Power performance assessment*, 2013.

[31] BSI Standards Publication, “BS EN 61400-12-1:2017 Wind power generation systems - Part 12-1: Power performance measurement of electricity producing wind turbines,” 2017. [Online]. Available: https://webstore.iec.ch/publication/68499

[32] D. T. Pugh, “Tides, surges and mean sealevel,” pp. 1–486, 2006. [Online]. Available: https://eprints.soton.ac.uk/19157/1/sea-level.pdf

[33] D. Maradin, “Advantages and disadvantages of renewable energy sources utilisation,” *International Journal of Energy Economics and Policy*, vol. 11, no. 3, pp. 176–183, 2021. [Online]. Available: https://www.econjournals.com/index.php/ijeep/article/view/11027

[34] International Hydrographic Organisation, “IHO standards for hydrographic surveys,” *International Hydrographic Bureau*, 2008. [Online]. Available: https://repository.oceanbestpractices.org/handle/11329/388

[35] B. Polagye and J. Thomson, “Tidal energy resource characterisation: Methodology and field study in Admiralty Inlet, Puget Sound, WA (USA),” *Proceedings of the Institution of Mechanical Engineers, Part A: Journal of Power and Energy*, vol. 227, no. 3, pp. 352–367, 5 2013.

[36] Marine Alliance for Science and Technology in Scotland (MASTS), “TeraWatt position papers,” p. 166, 2015. [Online]. Available: https://www.masts.ac.uk/media/35656/position_papers_terawatt_e-book.pdf

[37] Marine Current Turbines, “MCT: SeaGen-S 2MW proven and commercially viable tidal energy generation,” Tech. Rep., 2016. [Online]. Available: https://atlantisresourcesltd.com/wp/wp-content/uploads/2016/08/SeaGen-Brochure.pdf

[38] I. Fairley, P. Evans, C. Wooldridge, M. Willis, and I. Masters, “Evaluation of tidal stream resource in a potential array area via direct measurements,” *Renewable Energy*, vol. 57, pp. 70–78, 2013. [Online]. Available: http://dx.doi.org/10.1016/j.renene.2013.01.024

[39] L. S. Blunden and A. S. Bahaj, “Initial evaluation of tidal stream energy resources at Portland Bill, UK,” vol. 31, pp. 121–132, 2006. [Online]. Available: https://www.sciencedirect.com/science/article/abs/pii/S0960148105002193

[40] R. Vennell, “Estimating the power potential of tidal currents and the impact of power extraction on flow speeds,” *Renewable Energy*, vol. 36, no. 12, pp. 3558–3565, 2011. [Online]. Available: http://dx.doi.org/10.1016/j.renene.2011.05.011

[41] Z. Defne, K. A. Haas, and H. M. Fritz, “Numerical modeling of tidal currents and the effects of power extraction on estuarine hydrodynamics along the Georgia coast , USA,” *Renewable Energy*, vol. 36, no. 12, pp. 3461–3471, 2011. [Online]. Available: http://dx.doi.org/10.1016/j.renene.2011.05.027

[42] S. P. Neill, E. J. Litt, S. J. Couch, and A. G. Davies, “The impact of tidal stream turbines on large-scale sediment dynamics,” *Renewable Energy*, vol. 34, no. 12, pp. 2803–2812, 2009. [Online]. Available: http://dx.doi.org/10.1016/j.renene.2009.06.015

[43] K. Hessner and P. S. Bell, “High resolution current & bathymetry determined by nautical X-band radar in shallow waters,” 2009. [Online]. Available: https://ieeexplore.ieee.org/document/5278333

[44] M. Lewis, S. P. Neill, P. E. Robins, and M. R. Hashemi, “Resource assessment for future generations of tidal-stream energy arrays,” *Energy*, vol. 83, pp. 403–415, 4 2015. [Online]. Available: https://www.sciencedirect.com/science/article/pii/S0360544215001930

[45] C. Frost, “Flow direction effects on tidal stream turbines,” Tech. Rep., 2016. [Online]. Available: https://orca.cardiff.ac.uk/id/eprint/98955/1/2017FrostCPhD.pdf

[46] M. Piano, S. P. Neill, M. J. Lewis, P. E. Robins, M. R. Hashemi, A. G. Davies, S. L. Ward, and M. J. Roberts, “Tidal stream resource assessment uncertainty due to flow asymmetry and turbine yaw misalignment,” *Renewable Energy*, vol. 114, pp. 1363–1375, 2017. [Online]. Available: https://www.sciencedirect.com/science/article/pii/S0960148117304081

[47] B. Sellar, C. Old, and P. McCallum, “RealTide D2.2: Advanced monitoring, simulation and control of tidal devices in unsteady, highly turbulent realistic tide environments,” Tech. Rep., 2021.

[48] DNV-GL, “DNV-SE-0163: Certification of tidal turbines and arrays,” 2015. [Online]. Available: https://www.dnv.com/energy/standards-guidelines/dnv-se-0163-certification-of-tidal-turbines-and-arrays.html

[49] European Marine Energy Centre, “Assessment of tidal energy resource,” Tech. Rep. [Online]. Available: https://www.emec.org.uk/assessment-of-tidal-energy-resource/

[50] M. Lewis, S. P. Neill, P. Robins, M. R. Hashemi, and S. Ward, “Characteristics of the velocity profile at tidal-stream energy sites,” *Renewable Energy*, vol. 114, pp. 258–272, 2017. [Online]. Available: https://www.sciencedirect.com/science/article/pii/S0960148117302884

[51] I. G. Bryden, S. J. Couch, A. Owen, and G. Melville, “Tidal current resource assessment,” *Proceedings of the Institution of Mechanical Engineers, Part A: Journal of Power and Energy*, vol. 221, no. 2, pp. 125–135, 3 2007. [Online]. Available: https://journals.sagepub.com/doi/10.1243/09576509JPE238

[52] E. Osalusi, J. Side, and R. Harris, “Structure of turbulent flow in EMEC’s tidal energy test site,” *International Communications in Heat and Mass Transfer*, vol. 36, no. 5, pp. 422–431, 5 2009. [Online]. Available: https://www.sciencedirect.com/science/article/abs/pii/S0735193309000530

[53] W. M. Batten, A. S. Bahaj, A. F. Molland, and J. R. Chaplin, “The prediction of the hydrodynamic performance of marine current turbines,” *Renewable Energy*, vol. 33, no. 5, pp. 1085–1096, 5 2008. [Online]. Available: https://www.sciencedirect.com/science/article/abs/pii/S0960148107002133

[54] L. E. Myers and A. S. Bahaj, “Experimental analysis of the flow field around horizontal axis tidal turbines by use of scale mesh disk rotor simulators,” *Ocean Engineering*, vol. 37, no. 2-3, pp. 218–227, 2 2010. [Online]. Available: https://www.sciencedirect.com/science/article/abs/pii/S0029801809002613

[55] A. O. D. M. E. P. S. W. C. F. F. I. O’Doherty, T. Mason-Jones, “Considerations of a horizontal axis tidal turbine.” *Proceedings of Institution of Civil Engineers: Energy*, vol. 163, pp. 119–130, 2010. [Online]. Available: https://doi.org/10.1680/ener.2010.163.3.119

[56] R. Soulsby, *Dynamics of marine sands*. R. L. Soulsby and Thomas Telford Services Limited, January 1998. [Online]. Available: https://www.icevirtuallibrary.com/doi/abs/10.1680/doms.25844

[57] S. C. Bailey, M. Vallikivi, M. Hultmark, and A. J. Smits, “Estimating the value of von Kármán’s constant in turbulent pipe flow,” *Journal of Fluid Mechanics*, vol. 749, pp. 79–98, 2014. [Online]. Available: https://www.cambridge.org/core/journals/journal-of-fluid-mechanics/article/abs/estimating-the-value-of-von-karmans-constant-in-turbulent-pipe-flow/F4836172669CBEB88639C6BA67CEC023

[58] V. J. Thomson, B. Polagye and M. C. Richmond, “Measurements of turbulence at two tidal energy sites in Puget Sound, WA,” *IEEE Journal of Oceanic Engineering*, vol. 37, no. 3, pp. 363–374, 2012. [Online]. Available: https://ieeexplore.ieee.org/document/6200383

[59] International Electrotechnical Comission, *IEC TS 62600-201:2015 BSI standards publication marine energy - Part 201: Tidal energy resource assessment and characterisation*, 2015. [Online]. Available: https://webstore.iec.ch/publication/22099

[60] Valeport, “Model 803 - ROV current meter,” 2020. [Online]. Available: https://www.valeport.co.uk/products/model-803-rov-current-meter/

[61] ——, “Model 106 current meter,” 2022. [Online]. Available: https://www.valeport.co.uk/products/model-106-current-meter/

[62] H. L. Grant, “The large eddies of turbulent motion,” *Journal of Fluid Mechanics*, vol. 4, no. 2, p. 149–190, 1958. [Online]. Available: https://www.cambridge.org/core/journals/journal-of-fluid-mechanics/article/abs/large-eddies-of-turbulent-motion/7BC1B52F5507DC9226B0F144857540F0

[63] D. Barratt, M. A. Nguepnang, and M. D. Atkins, “Chapter 4 - Fast-response velocity and shear stress measurements,” in *Application of Thermo-Fluidic Measurement Techniques*, T. Kim, T. J. Lu, and S. J. Song, Eds. Butterworth-Heinemann, 2016, pp. 101–123. [Online]. Available: https://www.sciencedirect.com/science/article/pii/B9780128097311000046

[64] Yokogawa, “ADMAG AXR two-wire magnetic flowmeter,” 2008. [Online]. Available: https://www.yokogawa.com/news/press-releases/2008/2008-11-21/

[65] F. D. Rowe and J. W. Young, “Ocean current profiler using Doppler sonar.” *Oceans Conference Record (IEEE)*, pp. 292–297, 1979. [Online]. Available: https://ieeexplore.ieee.org/document/1151265

[66] N. Pettigrew, J. Irish, and R. Beardsley, “Field evaluations of a bottom-mounted acoustic doppler profiler and conventional current meter moorings,” 1986. [Online]. Available: https://ieeexplore.ieee.org/document/1158487

[67] Teledyne RD Instruments, “Acoustic Doppler current profiler: Principles of operation, a practical primer.” vol. 01, no. January, p. 56, 2011. [Online]. Available: https://www.comm-tec.com/Docs/Manuali/RDI/BBPRIME.pdf

[68] A. Lohrmann, B. Hackett, and L. P. Røed, “High-resolution measurements of turbulence, velocity and stress using a pulse-to-pulse coherent sonar,” *Journal of Atmospheric and Oceanic Technology*, vol. 7, pp. 19–37, February 1990. [Online]. Available: https://journals.ametsoc.org/view/journals/atot/7/1/1520-0426_1990_007_0019_hrmotv_2_0_co_2.xml

[69] Teledyne RD Instruments, “RDI acoustic Doppler current profilers application note ADCP beam clearance area,” Tech. Rep., 2002. [Online]. Available: http://www.teledynemarine.com/Documents/BrandSupport/RDINSTRUMENTS/TechnicalResources/TechnicalNotes/ChannelMaster/FSA019.PDF

[70] Dorward, M, “Enabling tools for the development of marine renewable energy: a case study of wave energy converter ocean trials, and a novel sensor to measure energetic marine currents,” Tech. Rep., 2020. [Online]. Available: https://era.ed.ac.uk/handle/1842/37691

[71] C. Greenwood, A. Vogler, and V. Venugopal, “On the variation of turbulence in a high-velocity tidal channel,” *Energies*, vol. 12, no. 4, 2019. [Online]. Available: https://www.mdpi.com/1996-1073/12/4/672

[72] G. Appell, P. Bass, and M. Metcalf, “Acoustic Doppler current profiler performance in near surface and bottom boundaries,” *IEEE Journal of Oceanic Engineering*, vol. 16, no. 4, pp. 390–396, 1991. [Online]. Available: http://ieeexplore.ieee.org/document/90903/

[73] S. Rehman, M. A. Mohandes, and L. M. Alhems, “Wind speed and power characteristics using LiDAR anemometer based measurements,” *Sustainable Energy Technologies and Assessments*, vol. 27, pp. 46–62, 6 2018.

[74] D. R. J. Sutherland, “Assessment of mid-depth arrays of single beam acoustic Doppler velocity sensors to characterise tidal energy sites,” 2015. [Online]. Available: https://era.ed.ac.uk/handle/1842/19559?show=full

[75] O. O. F. Tides, “Chapter 9 Tides and Tidal Currents.”

[76] S. J. Couch and I. Bryden, “Tidal current energy extraction: Hydrodynamic resource characteristics,” *Proceedings of the Institution of Mechanical Engineers, Part M: Journal of Engineering for the Maritime Environment*, vol. 220, no. 4, pp. 185–194, 2006. [Online]. Available: https://doi.org/10.1243/14750902JEME50

[77] M. C. Easton, D. K. Woolf, and P. A. Bowyer, “The dynamics of an energetic tidal channel, the Pentland Firth, Scotland,” *Continental Shelf Research*, vol. 48, pp. 50–60, 2012. [Online]. Available: http://dx.doi.org/10.1016/j.csr.2012.08.009

[78] A. Cornett, “Guidance for assessing tidal current energy resources,” 2008. [Online]. Available: https://www.ocean-energy-systems.org/publications/oes-reports/guidelines/document/guidance-for-assessing-tidal-current-energy-resource-2008-/

[79] I. G. Bryden, S. Naik, P. Fraenkel, and C. R. Bullen, “Matching tidal current plants to local flow conditions,” *Energy*, vol. 23, no. 9, pp. 699–709, 1998. [Online]. Available: https://www.sciencedirect.com/science/article/abs/pii/S0360544298000218

[80] P. L. Fraenkel, “Underwater windmills – harnessing the world’s marine currents,” *Ingenia*, no. 46, 2011.

[81] I. A. Milne, R. N. Sharma, R. G. J. Flay, and S. Bickerton, “Characteristics of the turbulence in the flow at a tidal stream power site,” *Philosophical Transactions of the Royal Society A: Mathematical, Physical and Engineering Sciences*, vol. 371, no. 1985, p. 20120196, 2 2013. [Online]. Available: https://royalsocietypublishing.org/doi/10.1098/rsta.2012.0196

[82] F. Maganga, G. Germain, J. King, G. Pinon, and E. Rivoalen, “Experimental characterisation of flow effects on marine current turbine behaviour and on its wake properties,” *Renewable Power Generation, IET*, vol. 4, pp. 498–509, 2010. [Online]. Available: https://digital-library.theiet.org/content/journals/10.1049/iet-rpg.2009.0205

[83] L. Perez, R. Cossu, A. Grinham, and I. Penesis, “Tidal turbine performance and loads for various hub heights and wave conditions using high-frequency field measurements and Blade Element Momentum theory,” *Renewable Energy*, vol. 200, no. October 2021, pp. 1548–1560, 2022. [Online]. Available: https://doi.org/10.1016/j.renene.2022.10.058

[84] HydroQuest, “Look back at the demonstration project oceanquest.” [Online]. Available: www.hydroquest.fr/en/look-back-at-the-demonstration-project-oceanquest/

[85] D. Satrio, I. K. Utama, and M. Mukhtasor, “Vertical axis tidal current turbine: Advantages and challenges review,” 11 2016.

[86] Blue Energy, “Vertical axis hydro turbine,” 2016. [Online]. Available: https://www.bluenergy.com/technology_method_vaht.html

[87] New Energy Corporation, “The power of nature,” 2011. [Online]. Available: https://www.newenergycorp.ca/

[88] O. Conservancy, “Rising tidal energy: What fast company’s 8 “most innovative company in energy” learned from ocean planning.” [Online]. Available: https://oceanconservancy.org/blog/2013/03/01/risingtidal-energy-what-fast-companys-8-most-innovative-company-in-energy-learned-from-ocean-planning/

[89] INHABITAT, “Oxford unveils next-gen underwater turbines.” [Online]. Available: https://inhabitat.com/oxford-engineers-transverse-horizontal-axis-water-turbine/

[90] R. A. McAdam, “Studies into the technical feasibility of the transverse horizontal axis water turbine,” 2011. [Online]. Available: https://ora.ox.ac.uk/objects/uuid:6f48d5c6-14ce-4bba-b572-8c628155bb94

[91] P. Dixon, “Kepler energy,” 2016. [Online]. Available: http://keplerenergy.co.uk/press-release.html

[92] Hydrovolts, “Model C-12: Canal turbine,” 2012. [Online]. Available: https://www.scribd.com/document/534005358/Turbine-Hydrovolts-C-12

[93] European Marine Energy Centre, “Nautricity,” 2014. [Online]. Available: https://www.emec.org.uk/about-us/our-tidal-clients/nautricity/

[94] EMEC, “Nautricity.” [Online]. Available: www.emec.org.uk/about-us/our-tidal-clients/nautricity/

[95] Minesto, “Our technology: The future of renewable energy.” [Online]. Available: https://minesto.com/our-technology/

[96] Minesto, “Renewable energy from the ocean.” 2016. [Online]. Available: https://minesto.com/

[97] G. Kramm, G. Sellhorst, H. K. Ross, J. Cooney, R. Dlugi, and N. Mölders, "On the maximum of wind power efficiency," *Journal of Power and Energy Engineering*, vol. 04, no. 01, pp. 1–39, 2016. [Online]. Available: https://www.scirp.org/journal/paperinformation.aspx?paperid=62374

[98] G. A. Van Kuik, "The Lanchester-Betz-Joukowsky limit," *Wind Energy*, vol. 10, no. 3, pp. 289–291, 2007. [Online]. Available: https://onlinelibrary.wiley.com/doi/10.1002/we.218

[99] N. W. Cresswell, "The generation potential of diffuser augmented tidal stream turbines," Tech. Rep., 2015. [Online]. Available: http://etheses.dur.ac.uk/10980/

[100] J. Lee, Y. Kim, A. Khosronejad, and S. Kang, "Experimental study of the wake characteristics of an axial flow hydrokinetic turbine at different tip speed ratios," *Ocean Engineering*, vol. 196, no. November 2019, p. 106777, 2020. [Online]. Available: https://doi.org/10.1016/j.oceaneng.2019.106777

[101] S. R. Turnock, A. B. Phillips, J. Banks, and R. Nicholls-Lee, "Modelling tidal current turbine wakes using a coupled RANS-BEMT approach as a tool for analysing power capture of arrays of turbines," *Ocean Engineering*, vol. 38, no. 11-12, pp. 1300–1307, 2011. [Online]. Available: http://dx.doi.org/10.1016/j.oceaneng.2011.05.018

[102] A. J. MacLeod, S. Barnes, K. G. Rados, and I. G. Bryden, "Wake effects in tidal current turbine farms," *MAREC 2002, International Conference on Marine Renewable Energy - Conference Proceedings*, pp. 49–53, 2002. [Online]. Available: https://diving-rov-specialists.com/index_htm_files/os_22-wake-effects-tidal-current-turbine-farms.pdf

[103] W. Batten, M. Harrison, and A. Bahaj, "Accuracy of the actuator disc-RANS approach for predicting the performance and wake of tidal turbines," *Philosophical transactions. Series A, Mathematical, physical, and engineering sciences*, vol. 371, p. 20120293, 2013. [Online]. Available: https://royalsocietypublishing.org/doi/10.1098/rsta.2012.0293

[104] P. Ouro, L. Ramírez, and M. Harrold, "Analysis of array spacing on tidal stream turbine farm performance using Large-Eddy Simulation," *Journal of Fluids and Structures*, vol. 91, p. 102732, 2019. [Online]. Available: https://doi.org/10.1016/j.jfluidstructs.2019.102732

[105] The University of North Carolina, "Measurements and error analysis," pp. 1–20, 2011. [Online]. Available: http://www.webassign.net/question_assets/unccolphysmechl1/measurements/manual.html

[106] S. Bell, "Beginner's guide to uncertainty of measurement," *National Physical Laboratory*, p. 41, 2001. [Online]. Available: http://www.demarcheiso17025.com/private/A%20Beginner%92s%20Guide%20to%20Uncertainty%20of%20Measurement%20.pdf

[107] Joint Committee For Guides In Metrology, "Evaluation of measurement data — Guide to the expression of uncertainty in measurement," *International Organisation for Standardisation Geneva ISBN*, vol. 50, no. September, p. 134, 2008. [Online]. Available: http://www.bipm.org/en/publications/guides/gum.html

[108] Rumsey, Deborah J., *Statistics For dummies*, 2nd ed., 2016. [Online]. Available: https://www.wiley.com/en-us/Statistics+For+Dummies%2C+2nd+Edition-p-9781119293521

[109] H. Castrup, "Distributions for uncertainty analysis," Tech. Rep., 2007. [Online]. Available: http://www.isgmax.com/Articles_Papers/Distributions%20for%20Uncertainty%20Analysis%20-%20Revised.pdf

[110] S. Shah, "Improved uncertainty analysis for tidal energy project development," 2018. [Online]. Available: https://era.ed.ac.uk/handle/1842/31178

[111] British Standards Institution, *EN IEC 60598-2-1:2021 Luminaires - Part 2-1: Particular requirements - Fixed general purpose luminaires*, 2021. [Online]. Available: https://standards.iteh.ai/catalog/standards/clc/e7348b68-982a-451e-8411-ddd385f17ca4/en-iec-60598-2-1-2021

[112] J. R. Taylor, *An introduction to error analysis: The study of uncertainties in physical measurements, second editionn*, 2nd ed., 1997. [Online]. Available: https://uscibooks.aip.org/books/introduction-to-error-analysis-2nd-ed/

[113] R. Stammers, "Using monte carlo analysis to estimate risk," 2021. [Online]. Available: https://www.investopedia.com/articles/financial-theory/08/monte-carlo-multivariate-model.asp

[114] M. D. McKay, R. J. Beckman, and W. J. Conover, "Comparison of three methods for selecting values of input variables in the analysis of output from a computer code," *Technometrics*, vol. 21, no. 2, pp. 239–245, 1979. [Online]. Available: https://doi.org/10.1080/00401706.1979.10489755

[115] D. C. H. J. M. Hammersley, *Monte carlo methods*, 1st ed. Springer Dordrecht, 2011. [Online]. Available: https://link.springer.com/book/10.1007/978-94-009-5819-7

[116] N. R. Council, *Assessing the reliability of complex models: mathematical and statistical foundations of verification, validation, and uncertainty quantification*. Washington, DC: The National Academies Press, 2012. [Online]. Available: https://nap.nationalacademies.org/catalog/13395/assessing-the-reliability-of-complex-models-mathematical-and-statistical-foundations

[117] J. M. Murphy, D. M. H. Sexton, D. N. Barnett, G. S. Jones, M. J. Webb, M. Collins, and D. A. Stainforth, "Quantification of modelling uncertainties in a large ensemble of climate change simulations," *Nature*, vol. 430, no. 7001, pp. 768–772, 8 2004. [Online]. Available: http://www.nature.com/articles/nature02771

[118] F. P. Russell, P. D. Düben, X. Niu, W. Luk, and T. Palmer, "Exploiting the chaotic behaviour of atmospheric models with reconfigurable architectures," *Computer Physics Communications*, vol. 221, pp. 160–173, 12 2017. [Online]. Available: https://linkinghub.elsevier.com/retrieve/pii/S0010465517302564

[119] A. Miftakhova, K. L. Judd, T. S. Lontzek, and K. Schmedders, "Statistical approximation of high-dimensional climate models," *Journal of Econometrics*, vol. 214, no. 1, pp. 67–80, 1 2020. [Online]. Available: https://linkinghub.elsevier.com/retrieve/pii/S0304407619301083

[120] V. Nourani, H. Gökçekuş, and I. K. Umar, "Artificial intelligence based ensemble model for prediction of vehicular traffic noise," *Environmental Research*, vol. 180, p. 108852, 1 2020. [Online]. Available: https://linkinghub.elsevier.com/retrieve/pii/S0013935119306498

[121] R. S. Rao, T. Vaishnavi, and A. R. Pais, "PhishDump: A multi-model ensemble based technique for the detection of phishing sites in mobile devices," *Pervasive and Mobile Computing*, vol. 60, p. 101084, 11 2019. [Online]. Available: https://linkinghub.elsevier.com/retrieve/pii/S1574119219304493

[122] B. G. Sellar and D. R. Sutherland, "Tidal energy site characterisation at the Fall of Warness , EMEC , UK Energy technologies institute Redapt Ma1001 (Md3.8)," REDAPT, Tech. Rep. December, 2016. [Online]. Available: http://redapt.eng.ed.ac.uk

[123] Z. Defne, K. A. Haas, H. M. Fritz, L. Jiang, S. P. French, X. Shi, B. T. Smith, V. S. Neary, and K. M. Stewart, "National geodatabase of tidal stream power resource in USA," *Renewable and Sustainable Energy Reviews*, vol. 16, no. 5, pp. 3326–3338, 2012. [Online]. Available: https://www.sciencedirect.com/science/article/pii/S1364032112001554

[124] B. Polagye, M. Kawase, and P. Malte, "In-stream tidal energy potential of Puget Sound, Washington," *Proceedings of the Institution of Mechanical Engineers, Part A: Journal of Power and Energy*, vol. 223, no. 5, pp. 571–587, 2009. [Online]. Available: https://doi.org/10.1243/09576509JPE748

[125] Z. Yang, T. Wang, R. Branch, Z. Xiao, and M. Deb, "Tidal stream energy resource characterisation in the Salish Sea," *Renewable Energy*, vol. 172, pp. 188–208, 2021. [Online]. Available: https://www.sciencedirect.com/science/article/pii/S0960148121003827

[126] L. S. Blunden and A. S. Bahaj, “Initial evaluation of tidal stream energy resources at Portland Bill, UK,” *Renewable Energy*, vol. 31, no. 2, pp. 121–132, 2006. [Online]. Available: https://www.sciencedirect.com/science/article/pii/S0960148105002193

[127] S. Serhadlıoğlu, T. A. A. Adcock, G. T. Houlsby, S. Draper, and A. G. L. Borthwick, “Tidal stream energy resource assessment of the Anglesey Skerries,” *International Journal of Marine Energy*, vol. 3-4, pp. 98–111, 2013. [Online]. Available: https://www.sciencedirect.com/science/article/pii/S2214166913000404

[128] A. Cornett, N. Durand, and M. Serrer, “3D modelling and assessment of tidal current resources in the Bay of Fundy, Canada,” *3rd International Conference on Ocean Energy, 6 October, Bilbao*, 2010. [Online]. Available: https://tethys-engineering.pnnl.gov/sites/default/files/publications/Cornett_et_al_ICOE_2010.pdf

[129] R. H. Karsten, J. M. McMillan, M. J. Lickley, and R. D. Haynes, “Assessment of tidal current energy in the Minas Passage, Bay of Fundy,” *Proceedings of the Institution of Mechanical Engineers, Part A: Journal of Power and Energy*, vol. 222, no. 5, pp. 493–507, 2008. [Online]. Available: https://doi.org/10.1243/09576509JPE555

[130] J. T. Carlson and M. Adams, “Assessing the consistency of in-stream tidal energy development policy in Nova Scotia, Canada,” *Marine Policy*, vol. 113, p. 103743, 2020. [Online]. Available: https://www.sciencedirect.com/science/article/pii/S0308597X1930048X

[131] G. Sutherland, M. Foreman, and C. Garrett, “Tidal current energy assessment for Johnstone Strait, Vancouver Island,” *Proceedings of the Institution of Mechanical Engineers, Part A: Journal of Power and Energy*, vol. 221, no. 2, pp. 147–157, 2007. [Online]. Available: https://doi.org/10.1243/09576509JPE338

[132] N. Guillou, S. P. Neill, and P. E. Robins, “Characterising the tidal stream power resource around France using a high-resolution harmonic database,” *Renewable Energy*, vol. 123, pp. 706–718, 2018. [Online]. Available: https://www.sciencedirect.com/science/article/pii/S0960148117312375

[133] D. S. Coles, L. S. Blunden, and A. S. Bahaj, “Assessment of the energy extraction potential at tidal sites around the Channel Islands,” *Energy*, vol. 124, pp. 171–186, 2017. [Online]. Available: https://www.sciencedirect.com/science/article/pii/S0360544217301974

[134] C. J. Mejia-Olivares, I. D. Haigh, N. C. Wells, D. S. Coles, M. J. Lewis, and S. P. Neill, “Tidal-stream energy resource characterisation for the Gulf of California, México,” *Energy*, vol. 156, pp. 481–491, 2018. [Online]. Available: https://www.sciencedirect.com/science/article/pii/S0360544218306819

[135] J. M. González-Caballín, E. Álvarez, A. J. Guttiérrez-Trashorras, A. Navarro-Manso, J. Fernández, and E. Blanco, “Tidal current energy potential assessment by a two dimensional computational fluid dynamics model: The case of Avilés port (Spain),” *Energy Conversion and Management*, vol. 119, pp. 239–245, 2016. [Online]. Available: https://www.sciencedirect.com/science/article/pii/S0196890416303107

[136] E. González-Gorbeña, P. C. C. Rosman, and R. Y. Qassim, “Assessment of the tidal current energy resource in São Marcos Bay, Brazil,” *Ocean Engineering and Marine Energy*, vol. 1, 2015. [Online]. Available: https://link.springer.com/article/10.1007/s40722-015-0031-5

[137] M. Marta-Almeida, M. Cirano, C. Guedes Soares, and G. C. Lessa, “A numerical tidal stream energy assessment study for Baía de Todos os Santos, Brazil,” *Renewable Energy*, vol. 107, pp. 271–287, 2017. [Online]. Available: https://www.sciencedirect.com/science/article/pii/S0960148117300575

[138] P. Marsh, I. Penesis, J.-R. Nader, and R. Cossu, “Multi-criteria evaluation of potential Australian tidal energy sites,” *Renewable Energy*, vol. 175, pp. 453–469, 2021. [Online]. Available: https://www.sciencedirect.com/science/article/pii/S0960148121006133

[139] P. Marsh, I. Penesis, J. R. Nader, C. Couzi, and R. Cossu, “Assessment of tidal current resources in Clarence Strait, Australia including turbine extraction effects,” *Renewable Energy*, vol. 179, pp. 150–162, 2021. [Online]. Available: https://www.sciencedirect.com/science/article/pii/S0960148121010120

[140] P. Marsh, I. Penesis, J. R. Nader, R. Cossu, C. Auguste, P. Osman, and C. Couzi, “Tidal current resource assessment and study of turbine extraction effects in Banks Strait, Australia,” *Renewable Energy*, vol. 180, pp. 1451–1464, 2021. [Online]. Available: https://www.sciencedirect.com/science/article/pii/S0960148121012118

[141] P. Garcia Novo and Y. Kyozuka, “Tidal stream energy as a potential continuous power producer: A case study for West Japan,” *Energy Conversion and Management*, vol. 245, p. 114533, 2021. [Online]. Available: https://www.sciencedirect.com/science/article/pii/S0196890421007093

[142] H. Kuroda, T. Tanaka, S. Ito, and T. Setou, “Numerical study of diurnal tidal currents on the Pacific shelf off the southern coast of Hokkaido, Japan,” *Continental Shelf Research*, vol. 230, p. 104568, 2021. [Online]. Available: https://www.sciencedirect.com/science/article/pii/S0278434321002247

[143] Y. S. Lim and S. L. Koh, “Analytical assessments on the potential of harnessing tidal currents for electricity generation in Malaysia,” *Renewable Energy*, vol. 35, no. 5, pp. 1024–1032, 2010. [Online]. Available: https://www.sciencedirect.com/science/article/pii/S096014810900442X

[144] Y. H. Park, “Analysis of characteristics of Dynamic Tidal Power on the west coast of Korea,” *Renewable and Sustainable Energy Reviews*, vol. 68, pp. 461–474, 2017. [Online]. Available: https://www.sciencedirect.com/science/article/pii/S136403211630658X

[145] M. H. Nguyen, H. Jeong, H. H. Tran, J.-s. Park, and C. Yang, “Energy capture evaluation of tidal current turbines arrays in Uldolmok strait, South Korea,” *Ocean Engineering*, vol. 195, p. 106675, 2020. [Online]. Available: https://www.sciencedirect.com/science/article/pii/S0029801819307930

[146] I. A. Milne, A. H. Day, R. N. Sharma, and R. G. Flay, “The characterisation of the hydrodynamic loads on tidal turbines due to turbulence,” pp. 851–864, 4 2016. [Online]. Available: https://www.sciencedirect.com/science/article/pii/S1364032115013623

[147] J. Mcnaughton, R. Sinclair, and u. . h. i. . . i. . . p. . . a. . a. B. G. Sellar, number = October, “Measuring and modelling the power curve of a commercial-scale tidal turbine,” *Proceedings of the 11th European Wave and Tidal Energy Conference*, 2015.

[148] I. Milne, R. Sharma, R. Flay, and S. Bickerton, “The role of onset turbulence on tidal turbine blade loads,” 01 2010, pp. 444–447. [Online]. Available: https://www.semanticscholar.org/paper/The-role-of-onset-turbulence-on-tidal-turbine-blade-Milne-Sharma/9cc5d43a6cb7ab49ecedb6457f599e69ce952fa2

[149] T. Blackmore, L. E. Myers, and A. S. Bahaj, “Effects of turbulence on tidal turbines: Implications to performance, blade loads, and condition monitoring,” *International Journal of Marine Energy*, vol. 14, pp. 1–26, 6 2016. [Online]. Available: https://linkinghub.elsevier.com/retrieve/pii/S2214166916300297

[150] J. MacEnri, M. Reed, and T. Thiringer, “Power quality performance of the tidal energy converter, SeaGen,” in *Proceedings of the International Conference on Offshore Mechanics and Arctic Engineering - OMAE*, vol. 5, 2011, pp. 529–536.

[151] S. Draycott, B. G. Sellar, T. Davey, Noble, D. R., V. Venugopal, and D. M. Ingram, “capture and simulation of the ocean environment for offshore renewable energy,” *Renewable and Sustainable Energy Reviews*, vol. 104, pp. 15–29, 4 2019. [Online]. Available: https://www.sciencedirect.com/science/article/pii/S1364032119300115

[152] B. G. Sellar, S. Harding, and M. Richmond, “High-resolution velocimetry in energetic tidal currents using a convergent-beam acoustic Doppler profiler,” *Measurement Science and Technology*, no. July, p. 85801, 2015. [Online]. Available: http://dx.doi.org/10.1088/0957-0233/26/8/085801

[153] D. R. J. Sutherland, B. G. Sellar, S. H. Harding, and I. Bryden, “Initial flow characterisation utilising turbine and seabed installed acoustic sensor arrays,” *European Wave and Tidal Energy Conference*, pp. 1 – 8, 2013. [Online]. Available: https://www.researchgate.net/publication/282327510_Initial_Flow_Characterisation_Utilising_Turbine_and_Seabed_Installed_Acoustic_Sensor_Arrays

[154] J. Mcnaughton, R. Sinclair, S. Harper, D. Dobson P, and P. Chesman, “ReDAPT: Initial operation power curve (MC7.1),” 2014. [Online]. Available: https://redapt.eng.ed.ac.uk/?p=library_redapt_reports

[155] S. Paboeuf, S. Y. Yen, M. Pascal, and G. M. Laura-Mae, “Power performance assessment of the tidal turbine Sabella D10 following IEC62600-200,” ser. International Conference on Offshore Mechanics and Arctic Engineering, vol. Volume 6: Ocean Space Utilisation; Ocean Renewable Energy, 2016. [Online]. Available: https://doi.org/10.1115/OMAE2016-54836

[156] C. Ross, “Pressure vessels: External pressure technology,” 04 2011. [Online]. Available: https://www.sciencedirect.com/book/9780857092489/pressure-vessels

[157] &. G. J. B. Leão, J. F. B., “Pressure Vessels: Design and Practice.” Tech. Rep., 2007.

[158] J Harrison, “ReDAPT MC7.3 Public domain report: Final.” [Online]. Available: http://redapt.eng.ed.ac.uk/library/eti/reports/MC7.3OperationsFinalReport.pdf

[159] T. A. Smith and J. Rigby, “Underwater radiated noise from marine vessels: A review of noise reduction methods and technology,” Tech. Rep., 2022. [Online]. Available: https://www.sciencedirect.com/science/article/pii/S0029801822021461

[160] L. E. Jones, “Renewable energy integration: Practical management of variability, uncertainty, and flexibility in power grids.” [Online]. Available: https://books.google.co.uk/books?id=b_6pDQAAQBAJ&printsec=frontcover&source=gbs_ge_summary_r&cad=0#v=onepage&q&f=false

[161] Nortek, “Signature manual; Principles of operation,” Tech. Rep., 2018. [Online]. Available: https://www.nortekgroup.com/assets/software/N3015-011-SignaturePrinciples.pdf

[162] L. Chunyan and K. M. Boswell, “Estimating water transport from short-term vessel-based and long-term bottom-mounted acoustic doppler current profiler measurements in an arctic lagoon connected to the Beaufort Sea,” *Journal of Atmospheric and Oceanic Technology*, 2021. [Online]. Available: https://www.ncbi.nlm.nih.gov/pmc/articles/PMC8747608/

[163] P. K. Pandian, O. Emmanuel, J. P. Ruscoe, J. C. Side, R. E. Harris, S. A Kerr, and C. R. Bullen, “An overview of recent technologies on wave and current measurement in coastal and marine applications,” 2010, pp. 551–556. [Online]. Available: https://www.researchgate.net/profile/Cr-Bullen/publication/242571633_An_overview_of_recent_technologies_on_wave_and_current_measurement_in_coastal_and_marine_applications/links/00b7d52b1785d4f58a000000/An-overview-of-recent-technologies-on-wave-and-current-measurement-in-coastal-and-marine-applications.pdf

[164] H. S. J. Roe and Griffiths, G., “Biological information from an acoustic Doppler current profiler,” *Marine Biology*, pp. 126–137, 1993. [Online]. Available: https://link.springer.com/article/10.1007/BF00346352#citeas

[165] E. R. Funke, Y. Yu, X. Yu, L. Deng, and M. H. Patel, “Deployment and validation of an ADCP on a tidal turbine,” *Renewable Energy*, pp. 866–874.

[166] B. G. Sellar, G. Wakelam, D. R. Sutherland, D. M. Ingram, and V. Venugopal, “Characterisation of tidal flows at the european marine energy centre in the absence of ocean waves,” *Energies*, vol. 11, no. 1, pp. 1–23, 2018.

[167] J. Thomson, B. Polagye, M. Richmond, and V. Durgesh, “Quantifying turbulence for tidal power applications,” *IEEE Oceans 2010*, 2010. [Online]. Available: https://ieeexplore.ieee.org/document/5664600

[168] G. M. Lonneke, D K. Woolf, and M. C. Easton, “Current patterns in the inner sound (Pentland Firth) from underway ADCP data,” *Journal of Atmospheric and Oceanic Technology*, vol. 30, pp. 96–111, 2013. [Online]. Available: https://journals.ametsoc.org/view/journals/atot/30/1/jtech-d-11-00223_1.xml

[169] T. P. Rippeth, E. Williams, and J. H. Simpson, “Reynolds stress and turbulent energy production in a tidal channel,” *Journal of Physical Oceanography*, vol. 32, pp. 1242–1251, 2002. [Online]. Available: https://journals.ametsoc.org/view/journals/phoc/32/4/1520-0485_2002_032_1242_rsatep_2.0.co_2.xml

[170] Z. N. Zhu, X. H. Zhu, C. Zhang, M. Chen, M. Wang, M. Dong, W. Liu, H. Zheng, and A. Kaneko, “Dynamics of tidal and residual currents based on coastal acoustic tomography assimilated data obtained in Jiaozhou bay, China,” *AGU: JGR Oceans*, 2021. [Online]. Available: https://agupubs.onlinelibrary.wiley.com/doi/10.1029/2020JC017003

[171] C. Cao, F. Cai, H. Qui, Y. Zheng, and H. Lu, “Characteristics of underwater topography, geomorphology and sediment source in Qinzhou Bay,” *MDPI: water*, pp. 836–846, 2021. [Online]. Available: https://www.mdpi.com/2073-4441/13/10/1392

[172] W. J. Kirkwood, R. E. Harris, and J. S. Fisher, “Monitoring the tidal-stream energy resource in coastal waters: lessons learned from the Sound of Islay ADCP deployment.” *Journal of Marine Science and Engineering*, 2019.

[173] Y. Zheng, D. Liu, and J. Pan, “Comparative analysis of tidal current and its energy in the Bashi channel using data from ADCP gravity station style.” *Advances in Oceanography and Limnology*, pp. 36–44, 2020.

[174] S. Jones and J. D. Scourse, “A review of the Scottish marine climate in the vicinity of the Hunterston,” *Scottish Marine and Freshwater Science*, 2013.

[175] R. Duran, G. Caporossi, D. Tarchi, and M. Brocchini, “The Aquadopp ADCP: New challenges for coastal and estuarine applications,” *Ocean Engineering*, pp. 10–24, 2015.

[176] J. Agus and N. M. Zahari, “Deployment strategy of ADCP for measuring flow and sediment in a tidal coastal area.” *Marine Science and Technology Bulletin*, vol. 2020, pp. 16–21.

[177] P. Jeffcoate, R. Starzmann, B. Elsaesser, S. Scholl, and S. Bischoff, “Field measurements of a full scale tidal turbine,” *International Journal of Marine Energy*, vol. 12, pp. 3–20, 2015. [Online]. Available: http://dx.doi.org/10.1016/j.ijome.2015.04.002

[178] Orbital Marine Power, “Orbital-O2 2 MW tidal turbine,” 2018. [Online]. Available: https://www.orbitalmarine.com/technology/

[179] Y. Xie, N. Bore, and J. Folkesson, “Sidescan only neural bathymetry from large-scale survey,” *MDPI: Sensors*, p. 398, 2018. [Online]. Available: https://www.mdpi.com/1424-8220/22/14/5092

[180] R. B. Wynn, V. A. Huvenne, T. P. Le Bas, B. J. Murton, D. P. Connelly, B. J. Bett, H. A. Ruhl, K. J. Morris, J. Peakall, D. R. Parsons, E. J. Sumner, S. E. Darby, R. M. Dorrell, and J. E. Hunt, “Autonomous Underwater Vehicles (AUVs): Their past, present and future contributions to the advancement of marine geoscience,” *IEEE Journal of Oceanic Engineering*, pp. 109–118, 2018. [Online]. Available: https://www.sciencedirect.com/science/article/pii/S0025322714000747

[181] W. J. Kirkwood, R. E. Harris, and J. S. Fisher, “The use of an autonomous underwater vehicle for ADCP deployment in a tidal energy test site.” *Renewable Energy*, pp. 1148–1160, 2021.

[182] P. Hwang, G. Garcia-Medina, L. Whitcomb, L. Yoerger, D. R. Howland, and C. R. German, "Autonomous underwater vehicle dockside maintenance: A decade of lessons learned." *IEEE Oceans*, 2020.

[183] J. M. Hovem, A. F. Molland, D. Greaves, and G. Iglesias, "Tidal energy converter performance assessment using a numerical model and field measurements." *Renewable Energy*, pp. 1064–1078, 2018.

[184] A. Budiyono, "Advances in unmanned underwater vehicles technologies: Modeling, control and guidance perspectives," *Indian Journal of Marine Sciences*, vol. 38, pp. 282–295, 10 2009. [Online]. Available: https://www.researchgate.net/publication/228350056_Advances_in_unmanned_underwater_vehicles_technologies_Modeling_control_and_guidance_perspectives

[185] J. P. Panda, A. Mitra, and H. warrior, "A review on the hydrodynamic characteristics of autonomous underwater vehicles," *Journal of Engineering for the Maritime Environment*, vol. 235, pp. 38–52, 2021. [Online]. Available: https://journals.sagepub.com/doi/full/10.1177/1475090220936896

[186] A. S. Brierley, M. A. Brandon, and J. L. Watkins, "An assessment of the utility of an acoustic Doppler current profiler for biomass estimation," *Journal of Experimental Marine Biology and Ecology,*, pp. 171–179, 1998. [Online]. Available: https://www.sciencedirect.com/science/article/abs/pii/S0967063798000120

[187] A. J. Gotvald and K. A. Oberg, "Acoustic Doppler current profiler applications used in rivers and estuaries by the U.S. geological survey." *Journal of Hydraulic Engineering*, 2009. [Online]. Available: https://pubs.usgs.gov/fs/2008/3096/pdf/fs2008-3096.pdf

[188] D. S. Mueller and C. R. Wagner, "Measuring discharge with acoustic Doppler current profilers from a moving boat," 2009. [Online]. Available: https://pubs.usgs.gov/tm/3a22/pdf/tm3a22_lowres.pdf

[189] H. Huang, "Estimating random uncertainty of depth-averaged velocities measured by moving-boat acoustic Doppler current profilers," *Flow Measurement and Instrumentation*, vol. 14, no. 5, pp. 797–801, 2017. [Online]. Available: https://www.sciencedirect.com/science/article/abs/pii/S095559861730064X

[190] J. Epler, B. Polagye, and J. Thomson, "Shipboard acoustic Doppler current profiler surveys to assess tidal current resources," *IEEE*, vol. 2, no. 1, 2010. [Online]. Available: https://ieeexplore.ieee.org/document/5664387

[191] B. Gunawan and V. S. Neary, "ORNL ADCP post-processing guide and Matlab algorithms for MHK site flow and turbulence analysis," Tech. Rep., 09 2011. [Online]. Available: https://www.researchgate.net/publication/266470268

[192] Nortek, "Providing a higher level of accuracy with a buoy-mounted ADCP," 219. [Online]. Available: https://www.nortekgroup.com/knowledge-center/userstory/higher-level-of-current-data-accuracy-with-a-buoy-mounted-adcp

[193] H. E. Seim and C. R. Edwards, "Comparison of buoy-mounted and bottom-moored ADCP performance at Gray's Reef." *Oceanography in the 21st Century*, p. 270–284, 2007. [Online]. Available: https://journals.ametsoc.org/view/journals/atot/24/2/jtech1972_1.xml?tab_body=abstract-display

[194] J. Mcnaughton, R. Sinclair, and B. Sellar, "Summary for policymakers," in *Climate Change 2013 – The Physical Science Basis*. Cambridge University Press, 3 2014, no. October, pp. 1–30. [Online]. Available: https://research.tilburguniversity.edu/en/publications/summary-for-policymakers

[195] M. Harrold, P. Ouro, and T. O'Doherty, "Performance assessment of a tidal turbine using two flow references," *Renewable Energy*, vol. 153, pp. 624–633, 6 2020. [Online]. Available: https://doi.org/10.1016/j.renene.2019.12.052https://linkinghub.elsevier.com/retrieve/pii/S096014811931924X

[196] L. Myers and A. S. Bahaj, "Near wake properties of horizontal axis marine current turbines," in *Proceedings of the 8th European Wave and Tidal Energy Conference, Uppsala, Sweden*, 2009. [Online]. Available: http://homepages.ed.ac.uk/shs/Wave%20Energy/EWTEC%202009/EWTEC%202009%20(D)/papers/176.pdf

[197] B. G. Sellar, D. R. Sutherland, D. M. Ingram, and V. Venugopal, "Measuring waves and currents at the European marine energy centre tidal energy test site: Campaign specification, measurement methodologies and data exploitation," *OCEANS 2017 - Aberdeen*, pp. 1–7, 2017.

[198] L. Bolle, W. T. Smaal, J. A. Rynja, J. J. Nauw, and T. Ysebaert, "Deployment of an acoustic Doppler current profiler on a revolving tidal energy converter: First experiences." *Sensors*, 2017.

[199] M. C. Verbeek, R. J. Labeur, and W. S. J. Uijttewall, "The performance of a weir-mounted tidal turbine: Field observations and theoretical modelling," *Renewable Energy*, 2020. [Online]. Available: https://www.sciencedirect.com/science/article/pii/S0960148120301853

[200] H. C. L. K. M. S. &. S. H. Kühn, M., "Towards an acoustic Doppler current profiler (ADCP) based turbine performance monitoring system for a marine current energy converter." *Energy Procedia*, pp. 319–326, 2017.

[201] P. Spain, "Technology in focus: Acoustic Doppler current profilers (ADCP)," 2017. [Online]. Available: https://www.hydro-international.com/content/article/technology-in-focus-acoustic-doppler-current-profiler-adcp

[202] L. Kilcher, Z. Yang, and V. Neary, "Marine energy resource assessment and characterisation," *Ocean Engineering*, 2016. [Online]. Available: https://tethys-engineering.pnnl.gov/signature-projects/marine-energy-resource-assessment-characterization

[203] L. C. Bender and S. F. DiMarco, "Quality control analysis of acoustic Doppler current profiler data collected on offshore platforms of the Gulf of Mexico," *MMS: U.S. Department of the interior minerals management service gulf of Mexico OCS*, 2009. [Online]. Available: https://cdn.ioos.noaa.gov/media/2017/12/qc_analysis_acoustic_doppler_current_profiler_data.pdf

[204] J. S. Li, T. C. Ho, H. J. Tang, and S. J. Jan, "Flow visualisation of vertical axis tidal current turbine," 12 2011. [Online]. Available: https://www.researchgate.net/publication/303447108_Flow_Visualization_of_Vertical_Axis_Tidal_Current_Turbine

[205] Nortek., "Understanding vessel-mounted current measurement." [Online]. Available: https://www.nortekgroup.com/knowledge-center/wiki/understanding-vessel-mounted-current-measurement

[206] Pacific Northwest National Laboratory, "Tidal energy: what is tidal energy?" 2021. [Online]. Available: https://www.pnnl.gov/explainer-articles/tidal-energy

[207] Integrated Ocean Observing System, "Manual for real-time quality control of stream flow observations," 2019. [Online]. Available: https://repository.library.noaa.gov/view/noaa/21151

[208] M. Bushnell, K. Bailey, J. Bosch, E. Burger, J. Dorton, R. Easley, B. Heitsenrether, J. King, K. Grissom, M. Tamburri, and J. Thomas, "QARTOD - Prospects for real-time quality control manuals, how to create them, and a vision for advanced implementation," *U.S. IOOS Program Office*, pp. 1–22, 2020. [Online]. Available: https://repository.library.noaa.gov/view/noaa/27130

[209] A. Angeloudis, L. Mackie, and M. D. Piggott, "Tidal range energy," in *Comprehensive Renewable Energy*. Elsevier, 2022, pp. 80–103. [Online]. Available: https://linkinghub.elsevier.com/retrieve/pii/B9780128197271000935

[210] T. M. Moreira, J. G. de Faria, P. O. Vaz-de Melo, and G. Medeiros-Ribeiro, "Development and validation of an AI-Driven model for the La Rance tidal barrage: A generalisable case study," *Applied Energy*, vol. 332, p. 120506, 2 2023. [Online]. Available: https://linkinghub.elsevier.com/retrieve/pii/S0306261922017639

[211] European Communities. and European Commission. Directorate-General for Research., *SEAFLOW, world's first pilot project for the exploitation of marine currents at a commercial scale*. Publications Office, 2005. [Online]. Available: https://op.europa.eu/en/publication-detail/-/publication/36f20105-3d03-4324-8312-24405bdbd939

[212] P. L. Fraenkel, “SeaGen development and testing of 1.2MW TEC,” *ICOE conference*, 2010.

[213] J. Zhang, L. Moreau, M. Machmoum, and P. E. Guillerm, “State of the art in tidal current energy extracting technologies,” *2014 1st International Conference on Green Energy, ICGE 2014*, pp. 1–7, 2014. [Online]. Available: https://ieeexplore.ieee.org/document/6835388

[214] European Marine Energy Centre, “Grid-connected tidal test site,” 2022. [Online]. Available: https://www.emec.org.uk/facilities/tidal-test-site/

[215] N. J. Baker, S. Cawthorne, E. Hodge, and E. Spooner, “3D modelling of the generator for OpenHydro’s tidal energy system,” in *IET Conference Publications*, vol. 2014, no. 628 CP. Institution of Engineering and Technology, 2014. [Online]. Available: https://digital-library.theiet.org/content/conferences/10.1049/cp.2014.0386

[216] Tethys, “OpenHydro at EMEC,” 2019. [Online]. Available: https://tethys.pnnl.gov/project-sites/openhydro-emec

[217] S. P. Neill, A. Vögler, A. J. Goward-Brown, S. Baston, M. J. Lewis, P. A. Gillibrand, S. Waldman, and D. K. Woolf, “The wave and tidal resource of Scotland,” *Renewable Energy*, vol. 114, pp. 3–17, 2017. [Online]. Available: https://www.sciencedirect.com/science/article/pii/S0960148117302082

[218] Offshore Energy, “Muddy waters hold OpenHydro turbine broken at bay’s bottom,” 2018. [Online]. Available: https://www.offshore-energy.biz/muddy-waters-hold-broken-openhydro-turbine-at-bays-bottom/

[219] Renewables Now, “OpenHydro deploys 2nd turbine for EDF tidal project in France,” 2016. [Online]. Available: https://renewablesnow.com/news/openhydro-deploys-2nd-turbine-for-edf-tidal-project-in-france-526986/

[220] Verdant Power, “Pilot license application Roosevelt Island tidal energy project,” Tech. Rep., 2010. [Online]. Available: https://tethys.pnnl.gov/sites/default/files/publications/Verdant-Power-2010.pdf

[221] ——, “The rite project.” [Online]. Available: https://www.verdantpower.com/projects

[222] A. Hydro, “Andritz Hydro Hammerfest - Renewable energy from tidal currents,” Tech. Rep. [Online]. Available: https://www.andritz.com/hydro-en/hydronews/hn32/meygen-scotland

[223] Xodus Aurora, “HS1000 1 MW tidal turbine at EMEC: Supporting documentation,” Tech. Rep., 2010. [Online]. Available: https://tethys.pnnl.gov/publications/hs1000-1-mw-tidal-turbine-emec-supporting-documentation

[224] Z. Zhou, M. Benbouzid, J. F. Charpentier, F. Scuiller, and T. Tang, “Developments in large marine current turbine technologies – A review,” *Renewable and Sustainable Energy Reviews*, vol. 71, no. February, pp. 852–858, 2017. [Online]. Available: http://dx.doi.org/10.1016/j.rser.2016.12.113

[225] Tethys, “MeyGen tidal energy project - Phase I,” 9 2021. [Online]. Available: https://saerenewables.com/tidal-stream/meygen/

[226] Quoceant, “Andritz Hydro Hammerfest - First power generation for MeyGen,” 2016. [Online]. Available: https://www.quoceant.com/post/2016/11/22/congratulations-andritz-hydro-hammerfest-first-power-generation-for-meygen

[227] S. G. Parkinson and W. J. Collier, “Model validation of hydrodynamic loads and performance of a full-scale tidal turbine using Tidal Bladed,” *International Journal of Marine Energy*, vol. 16, pp. 279–297, 2016. [Online]. Available: http://dx.doi.org/10.1016/j.ijome.2016.08.001

[228] P. E. Robins, S. P. Niell, M. J. Lewis, and S. L. Ward, “Characterising the spatial and temporal variability of the tidal-stream energy resource over the northwest European shelf seas,” 2015. [Online]. Available: https://www.sciencedirect.com/science/article/pii/S0306261915003293

[229] Schottel, “Sustainable marine energy’s inshore platform PLAT-I powers up,” 2017. [Online]. Available: https://www.schottel.de/medien-events/presseinfos/press-detail/sustainable-marine-energys-inshore-platform-plat-i-powers-up#:~:text=PLAT%2DI%20is%20a%20multiple,in%20an%20on%2Dboard%20container.

[230] P. Jeffcoate and N. Cresswell, “Field performance testing of a floating tidal energy platform - Part 2: Load performance,” *In Proc. of the 4th Asian Wave and Tidal Energy Conference (AWTEC)*, 2018. [Online]. Available: https://www.researchgate.net/publication/326573036_Field_Performance_Testing_of_a_Floating_Tidal_Energy_Platform-Part_2_Load_Performance

[231] Sustainable Marine, “Sustainable Marine launches ‘next-gen’ floating tidal platform,” 2021. [Online]. Available: https://www.sustainablemarine.com/plat-i-6-40

[232] Magallanes Renovables, “Unlocking energy from tidal power,” 2009. [Online]. Available: https://www.magallanesrenovables.com/

[233] ——, “Floating energy generation platform.” [Online]. Available: https://marine.gov.scot/sites/default/files/project_environmental_monitoring_plan_0.pdf

[234] E. Díaz-Dorado, C. Carrillo, J. Cidras, D. Román, and J. Grande, “Performance evaluation and modelling of the Atir marine current turbine,” *IET Renewable Power Generation*, vol. 15, no. 4, pp. 821–838, 2021. [Online]. Available: https://digital-library.theiet.org/content/journals/10.1049/rpg2.12071

[235] Tocardo, “T-1: Community based tidal turbine.” [Online]. Available: https://www.tocardo.com/tocardo-t1/

[236] ——, “T-2: Suitable for industrial scale solutions.” [Online]. Available: https://www.tocardo.com/tocardo-t2/

[237] Scotrenewables and Orbital Marine Power, *Tidal power Ltd SR250 deployment Fall of Warness environmental statement*, 2010, vol. II, no. October. [Online]. Available: https://tethys.pnnl.gov/publications/scotrenewables-tidal-power-ltd-sr250-deployment-fall-warness-environmental-statement-0

[238] Orbital Marine Power, “Turning the tide on climate change.” [Online]. Available: https://orbitalmarine.com/

[239] T. A. Adcock, S. Draper, G. T. Houlsby, A. G. Borthwick, and S. Serhadlioğlu, “The available power from tidal stream turbines in the pentland firth,” *Proceedings of the Royal Society A: Mathematical, Physical and Engineering Sciences*, vol. 469, no. 2157, 9 2013. [Online]. Available: https://royalsocietypublishing.org/doi/10.1098/rspa.2013.0072

[240] Simec Atlantis Energy, “MeyGen tidal energy site.” [Online]. Available: https://simecatlantis.com/tidal-stream/meygen/

[241] H. Chen, T. Tang, N. Ait-Ahmed, M. E. H. Benbouzid, M. MacHmoum, and M. E. H. Zaim, “Attraction, challenge and current status of marine current energy,” *IEEE Access*, vol. 6, pp. 12 665–12 685, 2018. [Online]. Available: https://ieeexplore.ieee.org/document/8264692

[242] Nova Innovation, “Europe case study - Shetland tidal array,” 2022. [Online]. Available: https://www.novainnovation.com/markets/scotland-shetland-tidal-array/

[243] Marine Scotland, “Nova Innovation - Shetland Tidal Array,” 2020. [Online]. Available: http://marine.gov.scot/sma/assessment/case-study-nova-innovation-shetland-tidal-array

[244] Tethys, and Orbital Marine Power, “Perpetuus Tidal Energy Centre (PTEC),” 2023. [Online]. Available: https://tethys.pnnl.gov/project-sites/perpetuus-tidal-energy-centre-ptec

[245] R. Torr, “Wave and tidal energy yield assessment: a standard taxonomy for losses and uncertainties,” no. 2, 2016. [Online]. Available: https://tethys-engineering.pnnl.gov/sites/default/files/publications/Torr.pdf

[246] P. Evans, S. Armstrong, C. Wilson, I. Fairley, C. Wooldridge, and I. Masters, “Characterisation of a highly energetic tidal energy site with specific reference to hydrodynamics and bathymetry,” *European Wave and Tidal Energy Conference*, no. September, pp. 1–11, 2013.

[247] HydroQuest, “Power curve certification of the OceanQuest,” 2020. [Online]. Available: https://www.hydroquest.fr/en/lorem-ipsum-dolor-sit-amet-consectetur-adipiscing-elit/

[248] European Marine Energy Centre, “EMEC delivers world first international power performance assessment to verdant,” 2021. [Online]. Available: https://www.emec.org.uk/press-release-emec-delivers-worlds-first-internationally-recognised-power-performance-assessment-to-verdant-power/

[249] P. Ouro, M. Harrold, T. Stoesser, and P. Bromley, “Hydrodynamic loadings on a horizontal axis tidal turbine prototype,” *Journal of Fluids and Structures*, vol. 71, pp. 78–95, 2017. [Online]. Available: http://dx.doi.org/10.1016/j.jfluidstructs.2017.03.009

[250] A. Mason-Jones, D. M. O’Doherty, C. E. Morris, T. O’Doherty, C. B. Byrne, P. W. Prickett, R. I. Grosvenor, I. Owen, S. Tedds, and R. J. Poole, “Non-dimensional scaling of tidal stream turbines,” *Energy*, vol. 44, no. 1, pp. 820–829, 2012. [Online]. Available: http://dx.doi.org/10.1016/j.energy.2012.05.010

[251] N. Kaufmann, T. H. Carolus, and R. Starzmann, “An enhanced and validated performance and cavitation prediction model for horizontal axis tidal turbines,” *International Journal of Marine Energy*, vol. 19, pp. 145–163, 2017. [Online]. Available: https://doi.org/10.1016/j.ijome.2017.07.003

[252] Z. Hameed, Y. S. Hong, Y. M. Cho, S. H. Ahn, and C. K. Song, “Condition monitoring and fault detection of wind turbines and related algorithms: A review,” *Renewable and Sustainable Energy Reviews*, vol. 13, no. 1, pp. 1–39, 2009. [Online]. Available: https://www.sciencedirect.com/science/article/abs/pii/S1364032107001098

[253] P. Scheijgrond, A. Southall, C. Bittencourt, P. Davies, P. Mathys, and G. Germain, “Advancing IEC standardisation and certification for tidal energy convertors,” *ICOE*. [Online]. Available: https://tethys-engineering.pnnl.gov/sites/default/files/publications/Scheijgronde2018.pdf

[254] European Commission, “Ocean Energy Strategic Roadmap: Building Ocean Energy for Europe,” *Ocean Energy Forum*, p. 74, 2016. [Online]. Available: https://webgate.ec.europa.eu/maritimeforum/en/frontpage/1036

[255] M. J. Kreitmair, T. A. Adcock, A. G. Borthwick, S. Draper, and T. S. van den Bremer, “The effect of bed roughness uncertainty on tidal stream power estimates for the Pentland Firth,” *Royal Society Open Science*, vol. 7, no. 1, 2020. [Online]. Available: https://royalsocietypublishing.org/doi/epdf/10.1098/rsos.191127

[256] P. Evans, A. Mason-Jones, C. Wilson, C. Wooldridge, T. O’Doherty, and D. O’Doherty, “Constraints on extractable power from energetic tidal straits,” *Renewable Energy*, vol. 81, pp. 707–722, 2015. [Online]. Available: http://dx.doi.org/10.1016/j.renene.2015.03.085

[257] C. Garrett and P. Cummins, “The power potential of tidal currents in channels,” *Proceedings of The Royal Society A: Mathematical, Physical and Engineering Sciences*, vol. 461, pp. 2563–2572, 2005. [Online]. Available: https://www.researchgate.net/publication/258796084_Maximum_power_from_a_turbine_farm_in_shallow_water

[258] S. Draper, T. A. Adcock, A. G. Borthwick, and G. T. Houlsby, “A note on the power potential of tidal currents in channels,” *International Journal of Marine Energy*, vol. 6, pp. 1–17, 2014. [Online]. Available: http://dx.doi.org/10.1016/j.ijome.2014.05.001

[259] R. Vennell, “Tuning turbines in a tidal channel,” *Journal of Fluid Mechanics*, vol. 663, no. November 2010, pp. 253–267, 2010. [Online]. Available: https://www.cambridge.org/core/journals/journal-of-fluid-mechanics/article/abs/tuning-turbines-in-a-tidal-channel/B3D9CBDEDDB573C12EE87371A8DD4E44

[260] C. Garrett and P. Cummins, “Maximum power from a turbine farm in shallow water,” *Journal of Fluid Mechanics*, vol. 714, pp. 634–643, 2013. [Online]. Available: https://www.researchgate.net/publication/258796084_Maximum_power_from_a_turbine_farm_in_shallow_water

[261] Ocean Energy Europe, “2030 Ocean energy vision,” *Industry analysis of future deployments, costs and supply chains*, 2018. [Online]. Available: https://www.oceanenergy-europe.eu/wp-content/uploads/2020/10/OEE_2030_Ocean_Energy_Vision.pdf

[262] V. Ramos and G. Iglesias, “Performance assessment of tidal stream turbines: A parametric approach,” *Energy Conversion and Management*, vol. 69, pp. 49–57, 2013. [Online]. Available: http://dx.doi.org/10.1016/j.enconman.2013.01.008

[263] European Marine Energy Centre, “Assessment of performance of tidal energy conversion systems,” Tech. Rep., 2009. [Online]. Available: https://www.emec.org.uk/assessment-of-performance-of-tidal-energy-conversion-systems/

[264] R. Clayton, R. Fahey, A. Mortimer, H. Smith, A. Borthwick, and Q. Xiao, “Tidal energy yield uncertainties: Learning from the wind industry,” *Proceedings of the 12th European Wave and Tidal Energy Conference*, pp. 1–9, 2016.

[265] A. Kavousi-Fard, “A novel probabilistic method to model the uncertainty of tidal prediction,” *IEEE Transactions on Geoscience and Remote Sensing*, vol. 55, no. 2, pp. 828–833, 2017.

[266] Wind Europe, “Wind energy in Europe: 2021 Statistics and the outlook for 2022-2026,” 2021. [Online]. Available: https://windeurope.org/intelligence-platform/product/wind-energy-in-europe-2021-statistics-and-the-outlook-for-2022-2026/

[267] International Energy Agency: IEA, *Energy Technology Perspectives 2012*, 2019. [Online]. Available: https://iea.blob.core.windows.net/assets/7136f3eb-4394-47fd-9106-c478283fcf7f/ETP2012_free.pdf

[268] S. J. K. Wright, G.; Kerr, “Ocean energy: Governance challenges for wave and tidal stream technologies,” pp. 35–53, 2018. [Online]. Available: https://tethys.pnnl.gov/publications/ocean-energy-governance-challenges-wave-tidal-stream-technologies

[269] D. Ziviani and S. P. Neill, “Resource assessment for marine energy conversion: A review of numerical modelling approaches.” *Renewable and Sustainable Energy Reviews*, pp. 412–422, 2019.

[270] G. Duclos and M. Sylvander, “Assessing and mitigating the impacts of tidal stream energy extraction on hydro-environmental processes.” *Renewable and Sustainable Energy Reviews*, 2019.

[271] V. Stelzenmuller, D. Green, and R. Nativ, “Marine renewables and the European marine strategy framework directive: working together towards a common approach.” *Journal of Ocean and Coastal Economics*, pp. 1–17, 2014.

[272] International Renewable Energy Agency, “(IRENA): Renewable power generation costs in 2018.” Tech. Rep., 2019. [Online]. Available: https://www.irena.org/publications/2019/May/Renewable-power-generation-costs-in-2018

[273] P. Devine-Wright, “Place attachment and public acceptance of renewable energy: A tidal energy case study,” *Journal of Environmental Psychology*, vol. 31, no. 4, pp. 336–343, 12 2011. [Online]. Available: https://linkinghub.elsevier.com/retrieve/pii/S0272494411000417

[274] Measnet, “Power performance measurement procedure, version 5,” *Measurement*, no. December, pp. 1–12, 2009. [Online]. Available: http://www.measnet.com/wp-content/uploads/2011/06/power5.pdf

[275] J. J. Wimhurst, C. C. Nsude, and J. S. Greene, “Standardising the factors used in wind farm site suitability models: A review,” *Heliyon*, vol. 9, no. 5, p. e15903, 5 2023. [Online]. Available: https://linkinghub.elsevier.com/retrieve/pii/S2405844023031109

[276] C. Bohn and C. Lant, “Welcoming the wind? Determinants of wind power development among U.S.” *The Professional Geographer*, vol. 61, no. 1, pp. 87–100, 2 2009. [Online]. Available: http://www.tandfonline.com/doi/abs/10.1080/00330120802580271

[277] P. V. Gorsevski, S. C. Cathcart, G. Mirzaei, M. M. Jamali, X. Ye, and E. Gomezdelcampo, "A group-based spatial decision support system for wind farm site selection in Northwest Ohio," *Energy Policy*, vol. 55, pp. 374–385, 4 2013. [Online]. Available: https://linkinghub.elsevier.com/retrieve/pii/S0301421512010580

[278] T. S. Cunden, J. Doorga, M. R. Lollchund, and S. D. Rughooputh, "Multi-level constraints wind farms siting for a complex terrain in a tropical region using MCDM approach coupled with GIS," *Energy*, vol. 211, p. 118533, 11 2020. [Online]. Available: https://linkinghub.elsevier.com/retrieve/pii/S0360544220316418

[279] W. P. Kuvlesky, L. A. Brennan, M. L. Morrison, K. K. Boydston, M. Bart, and F. C. Bryant., "Wind Energy Development and Wildlife Conservation: Challenges and Opportunities," *Journal of Wildlife Management*, vol. 71, no. 8, pp. 2487–2498, 11 2007. [Online]. Available: http://www.bioone.org/doi/abs/10.2193/2007-248

[280] K. Barré, I. Le Viol, Y. Bas, R. Julliard, and C. Kerbiriou, "Estimating habitat loss due to wind turbine avoidance by bats: Implications for European siting guidance," *Biological Conservation*, vol. 226, pp. 205–214, 10 2018. [Online]. Available: https://linkinghub.elsevier.com/retrieve/pii/S0006320718305469

[281] D. Fernández-Bellon, M. W. Wilson, S. Irwin, and J. O'Halloran, "Effects of development of wind energy and associated changes in land use on bird densities in upland areas," *Conservation Biology*, vol. 33, no. 2, pp. 413–422, 4 2019. [Online]. Available: https://onlinelibrary.wiley.com/doi/10.1111/cobi.13239

[282] Y. Zhang, F. Kong, and R. Palmer, "Impacts of wind turbine siting on radar clutter mitigation," in *IET International Radar Conference 2013*. Institution of Engineering and Technology, 2013, pp. 0232–0232. [Online]. Available: https://digital-library.theiet.org/content/conferences/10.1049/cp.2013.0467

[283] N. Teschner and R. Alterman, "Preparing the ground: Regulatory challenges in siting small-scale wind turbines in urban areas," *Renewable and Sustainable Energy Reviews*, vol. 81, pp. 1660–1668, 1 2018. [Online]. Available: https://linkinghub.elsevier.com/retrieve/pii/S1364032117309024

[284] L. Cuadra, I. Ocampo-Estrella, E. Alexandre, and S. Salcedo-Sanz, "A study on the impact of easements in the deployment of wind farms near airport facilities," *Renewable Energy*, vol. 135, pp. 566–588, 5 2019. [Online]. Available: https://linkinghub.elsevier.com/retrieve/pii/S0960148118314691

[285] E. Külüm, M. S. Genç, and F. Karagöz, "Evaluation of wind measurement methods for determination of realistic wind shear: A case study in Aksaray, Turkey," *Flow Measurement and Instrumentation*, vol. 93, p. 102408, 10 2023. [Online]. Available: https://linkinghub.elsevier.com/retrieve/pii/S0955598623001048

[286] A. J. F. Manwell, J. G. McGowan, "Wind energy explained theory, design and application." *John Wiley & Sons*, 2009. [Online]. Available: http://ee.tlu.edu.vn/Portals/0/2018/NLG/Sach_Tieng_Anh.pdf

[287] M. S. Genç and M. Gökçek, "Evaluation of wind characteristics and energy potential in Kayseri, Turkey." *Journal of Energy Engineering*, pp. 33–43, 2009.

[288] "Evaluation of site-specific wind conditions," Tech. Rep., 2016.

[289] H. D. Garrad and D. Stein, "Meteorological measurements on the wind measuring mast of the FINO3 offshore research platform." [Online]. Available: https://www.fino3.de/en/research/meteorology.html

[290] G. Liang, Y. Su, X. Wu, J. Ma, H. Long, and Z. Song, "Abnormal data cleaning for wind turbines by image segmentation based on active shape model and class uncertainty," *Renewable Energy*, vol. 216, p. 118965, 11 2023. [Online]. Available: https://linkinghub.elsevier.com/retrieve/pii/S0960148123008716

[291] P. J. Axaopoulos and G. T. Tzanes, "Wind energy potential (measurements, evaluation, forecasting)," in *Comprehensive Renewable Energy*. Elsevier, 2022, pp. 79–103. [Online]. Available: https://linkinghub.elsevier.com/retrieve/pii/B9780128197271001515

[292] J. M. S. Velázquez, J.A. Carta, "Comparison between ANNs and linear MCP algorithms in the long-term estimation of the cost per kW h produced by a wind turbine at a candidate site: A case study in the Canary Islands." *Applied energy*, vol. 88, no. 11, pp. 3869 – 3881, 2011.

[293] offshoreWIND, "Mitsubishi electric's compact wind lidar," 2014. [Online]. Available: https://www.offshorewind.biz/2014/05/28/ecn-approves-mitsubishi-electrics-compact-wind-lidar/

[294] J. Yan, C. Möhrlen, T. Göçmen, M. Kelly, A. Wessel, and G. Giebel, "Uncovering wind power forecasting uncertainty sources and their propagation through the whole modelling chain," *Renewable and Sustainable Energy Reviews*, vol. 165, p. 112519, 9 2022. [Online]. Available: https://linkinghub.elsevier.com/retrieve/pii/S1364032122004221

[295] J. Dai, Y. Tan, and X. Shen, "Investigation of energy output in mountain wind farm using multiple-units SCADA data," *Applied Energy*, vol. 239, pp. 225–238, 4 2019. [Online]. Available: https://linkinghub.elsevier.com/retrieve/pii/S0306261919302284

[296] T. L. Van, T. H. Nguyen, and D. C. Lee, "Advanced pitch angle control based on fuzzy logic for variable-speed wind turbine systems." *IEEE Trans Energy Convers*, vol. 30, pp. 578–587, 2015.

[297] M. Q. Duong, F. Grimaccia, S. Leva, M. Mussetta, and E. Ogliari, "Pitch angle control using hybrid controller for all operating regions of SCIG wind turbine system." *Renewable Energy*, vol. 70, pp. 197–203, 2014.

[298] P. Gebraad, F. Teeuwisse, J. V. Wingerden, P. A. Fleming, S. Ruben, and J. Marden, "Wind plant power optimisation through yaw control using a parametric model for wake effects - a CFD simulation study." *Wind Energy*, pp. 95 – 114, 2016.

[299] M. Yesilbudak, S. Sagiroglu, and I. Colak, "A novel intelligent approach for yaw position forecasting in wind energy systems." *Electrical Power Energy Systems*, vol. 69, pp. 406 – 413, 2015.

[300] E. G. Torres, S. Aubrun, O. Coupiac, N. Girard, and M. Boquet, "Statistical characteristics of interacting wind turbine wakes from a 7-month LiDAR measurement campaign," *Renewable Energy*, vol. 130, pp. 1–11, 1 2019. [Online]. Available: https://linkinghub.elsevier.com/retrieve/pii/S0960148118306608

[301] Y. Lu and R. G. Lueck, "Using a broadband ADCP in a tidal channel. Part I: Mean flow and shear," *Journal of Atmospheric and Oceanic Technology*, vol. 16, no. 11 PART 1, pp. 1556–1567, 1999. [Online]. Available: https://doi.org/10.1175/1520-0426(1999)016<1556:UABAIA>2.0.CO;2

[302] A. M. Young, I. A. Benson, and L. Kregting, "The barnacle: A low-cost marine turbulence sensor," *Renewable Energy*, p. 119179, 8 2023. [Online]. Available: https://doi.org/10.1016/j.renene.2023.119179

[303] C. Mohn, A. Denda, S. Christiansen, M. Kaufmann, F. Peine, B. Springer, R. Turnewitsch, and B. Christiansen, "Ocean currents and acoustic backscatter data from shipboard ADCP measurements at three North Atlantic seamounts between 2004 and 2015," *Data in Brief*, vol. 17, pp. 237–245, 4 2018. [Online]. Available: https://doi.org/10.1016/j.dib.2018.01.014

[304] A. Trembanis, M. Lundine, and K. McPherran, *Coastal mapping and monitoring*, 2nd ed. Elsevier Ltd., 2020, vol. 6. [Online]. Available: http://dx.doi.org/10.1016/B978-0-12-409548-9.12466-2

[305] M. Muste, K. Yu, and M. Spasojevic, "Practical aspects of ADCP data use for quantification of mean river flow characteristics; Part I: Moving-vessel measurements," *Flow Measurement and Instrumentation*, vol. 15, no. 1, pp. 1–16, 2004. [Online]. Available: https://doi.org/10.1016/j.flowmeasinst.2003.09.001

[306] B. Vermeulen, M. G. Sassi, and A. J. Hoitink, "Improved flow velocity estimates from moving-boat ADCP measurements," *Water Resources Research*, vol. 50, no. 5, pp. 4186–4196, 2014. [Online]. Available: https://doi.org/10.1002/2013WR015152

[307] M. Mahdavimanesh, A. R. Noghrehabadi, M. Behbahaninejad, G. Ahmadi, M. Dehghanian, and M. L. Dehghanian, "Particle tracking: Model development," Tech. Rep. 8, 2013.

[308] H. Canilho, C. Santos, C. Taborda, I. Falorca, and C. Fael, "Measurements of suspended ashes concentration in turbulent flow with acoustic doppler velocimeter," *Flow Measurement and Instrumentation*, vol. 87, p. 102207, 10 2022. [Online]. Available: https://doi.org/10.1016/j.flowmeasinst.2022.102207

[309] B. Gnawan, V. Neary, and J. Colby, "Tidal energy site resource assessment in the East River tidal strait, near Roosevelt Island, New York," Tech. Rep. [Online]. Available: https://doi.org/10.1016/j.renene.2014.06.002

[310] m. . . p. . . v. . . u. . h. d. . C. i. . . R. F. Marsden, and R. G. Ingram, number = 9, "Correcting for beam spread in acoustic Doppler current profiler measurements," *Journal of Atmospheric and Oceanic Technology*, 2004.

[311] S. Bradley, A. Strehz, and S. Emeis, "Remote sensing winds in complex terrain - a review," in *Meteorologische Zeitschrift*, vol. 24, no. 6. Schweizerbart Science Publishers, 2015, pp. 547–555. [Online]. Available: http://dx.doi.org/10.1127/metz/2015/0640

[312] S. Ott, J, Berg, and M, Nielsen, "Linearised CFD models for wakes." Tech. Rep., 2011. [Online]. Available: https://backend.orbit.dtu.dk/ws/portalfiles/portal/6354851/ris-r-1772.pdf

[313] X. F. Qing, "Velocity and shear stress profiles for tidal effected channels," *Ocean Engineering*, vol. 101, pp. 172–181, 6 2015. [Online]. Available: https://doi.org/10.1016/j.oceaneng.2015.04.013

[314] T. Clark, "Turbulence in Marine Environments (TiME): A framework for understanding turbulence and its effects on tidal devices." Proceedings of the 11th European Wave and Tidal Energy Conference, 2015, pp. 1–10.

[315] A. Clément, "Tidal turbine power performance assessment and comparison using standard IEC 62600-200 and an alternative methodology." *Renewable Energy,*, vol. 78, pp. 218–227, 2015.

[316] A. Mérigaud and J. V. Ringwood, "Condition-based maintenance methods for marine renewable energy," *Renewable and Sustainable Energy Reviews*, vol. 66, pp. 53–78, 12 2016. [Online]. Available: https://doi.org/10.1016/j.rser.2016.07.071

[317] "DNV KEMA Energy & Sustainability Framework for the categorisation of losses and uncertainty for wind energy assessments," Tech. Rep., 2013. [Online]. Available: http://assets.fiercemarkets.net/public/sites/energy/reports/kemaloss.pdf

[318] B. Bailey, "The maximum Type 40 Anemometer calibration project, NRG systems." Tech. Rep., 1998. [Online]. Available: https://www.nrgsystems.com/assets/resources/lock40.pdf

[319] T. F. Pedersen, P. Busche, and J. A. Dahlberg, *ACCUWIND - classification of five cup anemometers according to IEC61400-12-1*. Risø National Laboratory, 2006. [Online]. Available: https://backend.orbit.dtu.dk/ws/portalfiles/portal/7703253/ris_r_1556.pdf

[320] K. Lee, H. C. Ho, M, Marian, and C. H. Wu, "Uncertainty in open channel discharge measurements acquired with StreamPro ADCP," *Journal of Hydrology*, vol. 509, pp. 101–114, 2 2014. [Online]. Available: https://doi.org/10.1016/j.jhydrol.2013.11.031

[321] European Commission, "Effect of Climate Change in the UK Wind Speeds." Tech. Rep., 2006. [Online]. Available: https://joint-research-centre.ec.europa.eu/system/files/2020-09/13_pesetaiv_windstorms_sc_august2020_en.pdf

[322] D. L. Passeri, S. C. Hagen, S. C. Medeiros, M. V. Bilskie, K. Alizad, and D. Wang, "The dynamic effects of sea level rise on low-gradient coastal landscapes: A review," *Earth's Future*, vol. 3, no. 6, pp. 159–181, 6 2015. [Online]. Available: http://doi.wiley.com/10.1002/2015EF000298

[323] G. Jenkins, M, Perry, and J. Prior, "The climate of the United Kingdom and recent trends." Tech. Rep., 200. [Online]. Available: https://www.ukcip.org.uk/wp-content/PDFs/UKCP09_Trends.pdf

[324] J. M. Walker, K. A. Flack, E. E. Lust, M. P. Schultz, and L. Luznik, "Experimental and numerical studies of blade roughness and fouling on marine current turbine performance," *Renewable Energy*, vol. 66, pp. 257–267, 6 2014. [Online]. Available: https://doi.org/10.1016/j.renene.2013.12.012

[325] S. Song, W. Shi, Y. Kemal, and M. Atlar, "The effect of biofouling on the tidal turbine performance," Tech. Rep. [Online]. Available: https://strathprints.strath.ac.uk/68418/

[326] A. Farkas, N. Degiuli, I. Martić, M. Barbarić, and Z. Guzović, "The impact of biofilm on marine current turbine performance," *Renewable Energy*, vol. 190, pp. 584–595, 5 2022. [Online]. Available: https://doi.org/10.1016/j.renene.2022.03.134

[327] DNV KEMA, "Framework for the categorisation of losses and uncertainty for wind energy assessments," no. July, p. 8, 2013. [Online]. Available: http://www.sgurrenergy.com/wp-content/uploads/2013/02/Loss-and-Uncertainty-Definitions-Report-05Feb2013.pdf

[328] ORE Catapult, "Wave and tidal energy yield uncertainty," no. July, 2015. [Online]. Available: https://ore.catapult.org.uk/wp-content/uploads/2018/01/Wave-and-Tidal-Energy-Yield-Uncertainty-Literature-Review.pdf

[329] M. Muste, K. Yu, J. A. Gonzalez-Castro, M. Ansar, and R. Startzman, "Methodology for estimating ADCP measurement uncertainty in open-channel flows," *Proceedings of the 2004 World Water and Environmetal Resources Congress: Critical Transitions in Water and Environmetal Resources Management*, vol. 40737, no. May 2016, pp. 2148–2160, 2004.

[330] Blue Ocean Consulting, "Recommended practices for acoustic Doppler current profiler deployment," pp. 1–69, 2022. [Online]. Available: https://www.iogp.org/bookstore/wp-content/uploads/sites/2/woocommerce_uploads/2022/03/607.pdf

[331] International Organization for Standardization., "Hydrometry — Acoustic Doppler profiler — Method and application for measurement of flow in open channels from a moving boat," 2021. [Online]. Available: https://www.iso.org/standard/70758.html

[332] Z. Yang and A. Copping, *Marine renewable energy: Resource characterisation and physical effects*. Springer International Publishing, 5 2017. [Online]. Available: https://link.springer.com/book/10.1007/978-3-319-53536-4

[333] C. Old, M. Dorward, B Sellar, E. Nicolas, J. Marcille, and J. E. Hanssen, "D2.1 Deployment and instrument specification for advanced flow characterisation," Tech. Rep., 2020.

[334] British Oceanographic Data Centre, "Submit your data," 2023. [Online]. Available: https://www.bodc.ac.uk/submit_data/submission_guidelines/

[335] B. Seeley, J. Rapaport, O. Merritt, and M. Charlesworth, "Guidance notes for the production of discovery metadata for the Marine Environmental Data and Information Network (MEDIN)," pp. 1–20, 2014. [Online]. Available: http://www.oceannet.org

[336] K. Gunn and C. S. Williams, "ETI ReDAPT - MA1001 PM14 MD5.2: Falls of Warness 3D model validation report," 2014. [Online]. Available: https://s3-eu-west-1.amazonaws.com/assets.eti.co.uk/legacyUploads/2014/03/MD5.2-with-ETI-Website-Disclaimer.pdf

[337] S. J. Couch and I. Bryden, "Tidal current energy extraction: Hydrodynamic resource characteristics," *Proceedings of the Institution of Mechanical Engineers Part M: Journal of Engineering for the Maritime Environment*, vol. 220, no. 4, pp. 185–194, 2006.

[338] B. Polagye and J. Thomson, "Tidal energy resource characterisation: Methodology and field study in Admiralty Inlet, Puget Sound, WA (USA)," *Proceedings of the Institution of Mechanical Engineers, Part A: Journal of Power and Energy*, vol. 227, no. 3, pp. 352–367, 2013. [Online]. Available: https://doi.org/10.1177/0957650912470081

[339] Q. Yu, Y. Wang, B. Shi, Y. P. Wang, and S. Gao, "Physical and sedimentary processes on the tidal flat of central Jiangsu Coast, China: Headland induced tidal eddies and benthic fluid mud layers," *Continental Shelf Research*, vol. 133, pp. 26–36, 2 2017. [Online]. Available: https://doi.org/10.1016/j.csr.2016.12.015

[340] D. R. Sutherland, D. R. Noble, J. Steynor, T. Davey, and T. Bruce, "Characterisation of current and turbulence in the FloWave Ocean Energy Research Facility," *Ocean Engineering*, vol. 139, pp. 103–115, 7 2017. [Online]. Available: https://doi.org/10.1016/j.oceaneng.2017.02.028

[341] L. Lieber, W. A. M. Nimmo-Smith, J. J. Waggitt, and L. Kregting, "Localised anthropogenic wake generates a predictable foraging hotspot for top predators," *Communications Biology*, vol. 2, no. 1, pp. 12–13, 2019. [Online]. Available: http://dx.doi.org/10.1038/s42003-019-0364-z

[342] B. Guo, R. Ahmadian, P. Evans, and R. A. Falconer, "Studying the wake of an island in a macro-tidal estuary," *Water*, vol. 12, no. 5, p. 1225, 4 2020. [Online]. Available: https://www.mdpi.com/2073-4441/12/5/1225

[343] H. S. Torrens, P. Schmitt, C. Frost, I, Benson, P. MacKinnon, and T, Whittaker, "Assessment of flow characteristics at two Locations in an energetic tidal channel," *Proceedings of the Twelfth European Wave and Tidal Energy Conference*, 2017. [Online]. Available: https://pureadmin.qub.ac.uk/ws/portalfiles/portal/134529503/HTS_FullPaper_Version4.pdf

[344] I. Afgan, J. McNaughton, S. Rolfo, D. D. Apsley, T. Stallard, and P. Stansby, "Turbulent flow and loading on a tidal stream turbine by LES and RANS," *International Journal of Heat and Fluid Flow*, vol. 43, pp. 96–108, 10 2013.

[345] P. A. Work, K. A. Haas, Z. Defne, and T. Gay, "Tidal stream energy site assessment via three-dimensional model and measurements," *Applied Energy*, vol. 102, pp. 510–519, 2013. [Online]. Available: https://doi.org/10.1016/j.apenergy.2012.08.040

[346] A. M. Jones, D. M. O'Doherty, C. E. Morris, and T. O'Doherty, "Influence of a velocity profile & support structure on tidal stream turbine performance," *Renewable Energy*, vol. 52, pp. 23–30, 4 2013. [Online]. Available: https://doi.org/10.1016/j.renene.2012.10.022

[347] A. S. Bahaj, A. F. Molland, J. R. Chaplin, and W. M. Batten, "Power and thrust measurements of marine current turbines under various hydrodynamic flow conditions in a cavitation tunnel and a towing tank," *Renewable Energy*, vol. 32, no. 3, pp. 407–426, 3 2007. [Online]. Available: https://doi.org/10.1016/j.renene.2006.01.012

[348] M. J. Lewis, S. P. Neill, M. R. Hashemi, and M. Reza, "Realistic wave conditions and their influence on quantifying the tidal stream energy resource," *Applied Energy*, vol. 136, pp. 495–508, 12 2014.

[349] S. Q. Yang, S. K. Tan, S. Y. Lim, and S. F. Zhang, "Velocity distribution in combined wave-current flows," *Advances in Water Resources*, vol. 29, no. 8, pp. 1196–1208, 8 2006. [Online]. Available: https://doi.org/10.1016/j.advwatres.2005.09.010

[350] S. C. Tatum, C. H. Frost, M. Allmark, D. M. O'Doherty, A. Mason-Jones, P. W. Prickett, R. I. Grosvenor, C. B. Byrne, and T. O'Doherty, "Wave-current interaction effects on tidal stream turbine performance and loading characteristics," *International Journal of Marine Energy*, vol. 14, pp. 161–179, 6 2016. [Online]. Available: https://doi.org/10.1016/j.ijome.2015.09.002

[351] S. Gooch, J. Thomson, B. Polagye, and D. Meggitt, "Site characterisation for tidal power," *MTS/IEEE Biloxi - Marine Technology for Our Future: Global and Local Challenges, OCEANS 2009*, no. November, 2009.

[352] M. Agency and Coastguard, "Guide to using the CHP Bathy Atlas," 2005. [Online]. Available: https://assets.publishing.service.gov.uk/government/uploads/system/uploads/attachment_data/file/296198/chp_bathy_atlas_guide.pdf

[353] International Electrotechnical Commission (IEC), "IEC 61869-2: Performance of line commutated converter high-voltage direct curren (HVDC) systems with line-commutated converters. Steady-state conditions," 2012. [Online]. Available: https://bsol-bsigroup-com.ezproxy.is.ed.ac.uk/Bibliographic/BibliographicInfoData/000000000030077990

[354] BSi, "BSI Standards Publication Instrument transformers inductive voltage transformers," 2011.

[355] International Electrotechnical Commission (IEC), "IEC 60688: Electrical measuring transducers for converting AC and DC electrical quantities to analogue or digital signals," 2012. [Online]. Available: https://bsol-bsigroup-com.ezproxy.is.ed.ac.uk/Bibliographic/BibliographicInfoData/000000000030431305

[356] Keller, "Keller," 2023. [Online]. Available: https://keller-druck.com/en/products/pressure-transducers/oem-pressure-transducers/series-10l

[357] BUREAU VERITAS SA, "RealTide: Advanced monitoring, simulation and control of tidal devices in unsteady, highly turbulent realistic tide environments," *H2020 Programme for Research and Innovation*, no. 727689, pp. 1–45, 2019. [Online]. Available: https://www.realtide.eu/

[358] J. Mullison and D. Symonds, "ADCP Deployments near Offshore Structures," in *OCEANS 2007*. IEEE, 9 2007, pp. 1–6. [Online]. Available: http://ieeexplore.ieee.org/document/4449258/

[359] "Teledyne Marine." [Online]. Available: https://www.teledynemarine.com/en-us

[360] "Teledyne Marine." [Online]. Available: https://www.nortekgroup.com/

[361] L. Evans, I. G. C. Ashton, and B. G. Sellar, "Tidal turbine power performance assessments following IEC TS 62600-200 using measured and modelled power outputs," *Renewable Energy*, vol. 212, no. May, pp. 138–150, 2023. [Online]. Available: https://doi.org/10.1016/j.renene.2023.05.031

[362] ——, "Impact on energy yield of varying turbine designs under conditions of misalignment to the current flow," *Energies*, vol. 16, no. 9, p. 3923, 5 2023. [Online]. Available: https://www.mdpi.com/1996-1073/16/9/3923

Chapter 10

Appendix for Chapter 5

10.1 DEEP-Gen IV Pre-defined Power Curve

The gathered data samples, as illustrated in the preceding section, are averaged and categorized into velocity bins of 0.05 m/s. These results are tabulated values in Figure 10.1. It's important to acknowledge that the IEC Guidelines (IEC, 2013), Section 8.7, stipulate the velocity range should span from 50% of the cut-in velocity (i.e., 0.5 m/s) to 120% of the rated velocity (i.e., 3.24 m/s). Furthermore, each velocity bin should encompass a minimum of 30 minutes' worth of data, while the complete dataset should span 180 hours.

The velocities presented (at the centre of each bin) fall within the ranges of 0.925 to 3.025 m/s for flood tides and 0.825 to 3.375 m/s for ebb tides. However, taking into account the requirement for a minimum of 30 minutes of sampled data per velocity bin (as outlined in Figure 10.1), these ranges are adjusted to 0.925 – 3.025 m/s and 0.975 – 3.325 m/s for flood and ebb tides, respectively. Consequently, the stipulated minimum velocity range isn't fully met. This could be attributed to the stringent exclusion of samples with minimum power values below zero (intended to remove shutdown events). It's also worth noting that instances of power observed below the cut-in velocity are likely to be recorded at the end of a tidal cycle when the flow is decelerating from higher values.

Velocity range [m/s]		Flood		Ebb	
Minimum	Maximum	Mean Power [kW]	No. data points (10 min sample)	Mean Power [kW]	No. data points (10 min sample)
0.800	0.849			0.91	2
0.850	0.899			33.73	1
0.900	0.949	23.99	4	29.22	1
0.950	0.999	30.02	4	44.39	4
1.000	1.049	38.04	9	50.39	6
1.050	1.099	45.11	10	59.99	3
1.100	1.149	53.07	25	72.62	7
1.150	1.199	63.40	15	68.60	10
1.200	1.249	77.44	21	78.22	4
1.250	1.299	93.04	19	98.84	10
1.300	1.349	105.83	20	116.98	7
1.350	1.399	120.76	17	130.75	18
1.400	1.449	141.81	21	134.06	14
1.450	1.499	154.53	23	153.28	19
1.500	1.549	174.07	21	170.03	19
1.550	1.599	194.07	22	198.37	12
1.600	1.649	221.29	18	217.26	20
1.650	1.699	246.74	16	242.32	21
1.700	1.749	269.59	26	264.32	16
1.750	1.799	301.64	17	294.23	14
1.800	1.849	325.79	22	306.78	15
1.850	1.899	354.63	21	341.85	15
1.900	1.949	386.89	15	377.83	24
1.950	1.999	416.03	20	402.33	16
2.000	2.049	458.69	19	420.32	17
2.050	2.099	484.21	18	475.45	20
2.100	2.149	521.26	12	484.93	15
2.150	2.199	565.35	11	551.67	12
2.200	2.249	615.45	15	607.12	13
2.250	2.299	639.90	13	618.18	16
2.300	2.349	679.29	12	685.17	11
2.350	2.399	740.50	14	693.99	11
2.400	2.449	794.68	16	758.28	10
2.450	2.499	842.42	6	807.67	9
2.500	2.549	876.52	11	883.60	11
2.550	2.599	920.69	8	903.76	9
2.600	2.649	946.63	10	925.96	11
2.650	2.699	971.34	14	992.87	5
2.700	2.749	996.58	10	1000.74	9
2.750	2.799	1006.14	6	1015.04	7
2.800	2.849	1012.74	5	1020.28	8
2.850	2.899	1019.27	9	1020.93	10
2.900	2.949	1022.87	5	1019.57	10
2.950	2.999	1020.85	1	1022.18	9
3.000	3.049	1024.34	2	1023.95	10
3.050	3.099			1022.84	11
3.100	3.149			1023.73	7
3.150	3.199			1022.81	11
3.200	3.249			1023.70	8
3.250	3.299			1022.76	8
3.300	3.349			1022.58	4
3.350	3.399			1022.13	1

Figure 10.1: Alstom DEEP-Gen IV 1 MW TEC Power Curve Data.

Chapter 11

Appendix for Chapter 6

11.1 On the utility of partially corrupted flow measurement data arising from adjacent acoustic Doppler current profilers for energy yield assessment.

Abstract: Recommended practice for quantifying the energy resource at a tidal energy site requires the use of multiple instruments deployed across the site. However, the instruments used work by emitting an acoustic pulse and instruments working at the same time have the potential to interfere with each other through a process known as 'cross-talk'. It is important to understand the impact of cross-talk on measurements and how this can be managed through data processing or suitable positioning of devices. The ReDAPT project conducted a measurement campaign using two Acoustic Doppler Current Profilers (ADCPs) placed upstream of an operational tidal turbine. This aimed to assess the 'in-line' instrument placement guidelines from IEC 62600-200 for Power Performance Assessment (PPA) in real-world conditions. Despite adhering to industry standards and best practices to eliminate unreliable data in the Quality Control (QC) checks, cross-talk was present in both concurrently measuring ADCPs at different time stamps in approximately 15% of the returned data. This resulted in average deviations of up to 6% in velocities above the rated turbines cut-in. Such deviations impacted the measured power curve and the estimation of Annual Energy Production showed a difference of 7% when data exhibiting interference were removed. The study introduces an approach to identify and remove the bias introduced by cross-talk. The algorithm effectively removed roughly 90% of the compromised measurements. Moving forward, multi-sensor deployments could use the algorithm described to double-check for interference within the data sets, although care should be taken to avoid this by choosing a suitable layout for deployment.

Keywords: Marine Renewable Energy; Tidal Energy; Acoustic Interference; Power Curve; Power Performance; Uncertainty; IEC TS 62600-200; Acoustic Doppler Profiler;

Submitted to: Measurements:Sensors, Elsevier.

Measurement: Sensors 35 (2024) 101293

Contents lists available at ScienceDirect

Measurement: Sensors

journal homepage: www.sciencedirect.com/journal/measurement-sensors

On the utility of partially corrupted flow measurement data arising from adjacent acoustic Doppler current profilers for energy yield assessment

Luke Evans [a,b,*], Ian Ashton [c], Brian Sellar [d]

[a] EPSRC and NERC Centre for Doctoral Training in Offshore Renewable Energy (IDCORE), The University of Edinburgh, Exeter and Strathclyde, Grant Institute Kings Buildings, W Mains Rd, Edinburgh, EH9 3JW, UK
[b] European Marine Energy Centre (EMEC), Research Engineer, Orkney, The Charles Clouston Building ORIC, Back Rd, Stromness, KW16 3AW, UK
[c] University of Exeter, College of Engineering Mathematics and Physical Sciences, Penryn, Cornwall, UK
[d] The University of Edinburgh (UoE), School of Engineering, Edinburgh, UK

ARTICLE INFO

Keywords:
Acoustic Doppler profiler
Power performance assessment
Power curve
Tidal stream energy
Tidal turbine
Energy yield
Acoustic interference

ABSTRACT

Recommended practice for quantifying the energy resource at a tidal energy site requires the use of multiple instruments deployed across the site. However, the instruments used work by emitting an acoustic pulse and instruments working at the same time have the potential to interfere with each other through a process known as 'cross-talk'. It is important to understand the impact of cross-talk on measurements and how this can be managed and through data processing or suitable positioning of devices. The ReDAPT project conducted a measurement campaign using two Acoustic Doppler Current Profilers (ADCPs) placed upstream of an operational tidal turbine. This aimed to assess the 'in-line' instrument placement guidelines from IEC 62600-200 for Power Performance Assessment (PPA) in real-world conditions. Consequently, the results within hold potential to support arguments for expanding these zones or adjusting their general dimensions. Despite adhering to industry standards and best practices to eliminate unreliable data in the Quality Control (QC) checks, in both concurrently measuring ADCPs at different time stamps in approximately 15 % of the returned data. This work identified for the first time interference throughout the campaign and quantified subsequent impact on estimates. A method to remove data anomalies caused by interference between closely positioned ADCPs has been developed and demonstrated, resulting in a 7 % variation in estimated Annual Energy Production (AEP). The algorithm effectively removed approximately 90 % of the corrupted measurements. Moving forward, multi-sensor deployments could use the algorithm described to double-check for interference within the data sets, although care should be taken to avoid this by choosing a suitable layout for deployment.

Nomenclature

i	Index related to velocity bin
j	Index related to time stamp
L	Number of samples in the defined averaging period
n	Index related to data point
S	Number of depth bins across projected area of tidal energy converter
$\overline{P_i}$	Mean calculated tidal energy converter power in velocity bin i
$\overline{U}$	Mean power weighted rotor average velocity, $m{\cdot}s^{-1}$
$\overline{u}$	Mean velocity, $m{\cdot}s^{-1}$
$\widehat{U}$	Instantaneous power weighted rotor average velocity, $m{\cdot}s^{-1}$
A	Type-A configuration, instrument location, A_1 and A_2
A_k	Depth bin over the swept area of the tidal energy converter, m^2
f_i	Proportion of time during an average year for which the mean current velocity occupies a value within velocity bin i

(*continued on next column*)

(*continued*)

N_B	Total number of velocity bins in the power curve
U	Mean velocity, $m{\cdot}s^{-1}$
u	Velocity magnitude, $m{\cdot}s^{-1}$
z	Height above seabed, m

1. Introduction

Tidal energy, a form of renewable energy, generates electricity from the cyclic rise and fall of ocean tides which are driven by interacting gravitational forces between the Earth, moon, and sun. Tidal energy produces minimal greenhouse gas emissions, thus aiding in reducing carbon footprints and combating climate change. To adopt tidal energy for a low-carbon future, a thorough understanding of the challenging

* Corresponding author. 3 Sunnvbank Drive, Stromness, Orkney, KW16 3HS, UK.
E-mail address: (L. Evans).

https://doi.org/10.1016/j.measen.2024.101293
Received 30 August 2023; Received in revised form 11 August 2024; Accepted 13 August 2024
Available online 19 August 2024
2665-9174/© 2024 The Authors. Published by Elsevier Ltd. This is an open access article under the CC BY license (http://creativecommons.org/licenses/by/4.0/).

ocean environment is crucial for efficient, cost-effective, and reliable tidal turbine systems [1]. To capture tidal flows, the commonly used acoustic Doppler current profiler (ADCP) remotely samples the water column over ranges/depths of tens to hundreds of meters without interfering with fluid flow [2–4]. ADCPs work by transmitting acoustic pulses into the water, which scatter off particles such as sediment and plankton. The transducers then receive the backscattered signals, and the frequency shift (Doppler shift) of these signals is analysed to determine water velocity [2–5].

ADCPs exhibit a range of configurations and transducer quantities, with the prevailing variant in the tidal industry being the four-beam divergent ADCP and its successor which includes an additional fifth-beam; a central vertically orientated transducer. These configurations allow us to capture different components of the water velocity vector. By combining data from multiple beams, we can reconstruct the three-dimensional velocity field. As the beam spread increases with the range from the instrument, sampling increasingly further away from the above-ADCP water column, it must be assumed that the flow is homogeneous between beams to determine flow profiles [2]. It is assumed that the velocity within each measurement cell (sample volume) along the profile is measured virtually simultaneously given the speed of sound in water (approximately 1500 m s ^{1}) relative to the speed of the sampled current. The beam path of each individual transducer is typically known as the *main lobe*. All transducers have a *side lobe* - a small amount of the transmitted energy falls outside the *main lobe* [6].

Instruments positioned near structures, cables, or other acoustic devices may encounter increased backscatter, not only from typical sources within the *main lobe* or *side lobe* regions but also from these adjacent objects [6], refer to Fig. 1. Such proximity can lead to signal contamination, distinct from cross-talk, which arises when the acoustic beams intersect fixed objects within their paths. This form of contamination often appears as horizontal lines in echogram representations, particularly if these objects remain static [2,6]. However, if these interfering objects move relative to the Doppler sonar, the resulting range of contamination can evolve over time. On the other hand, cross-talk specifically refers to interference between multiple sonar units, which typically manifests as diagonal lines in data visualisations due to variations in the internal clock speeds of the different units. Users must be vigilant and understand these potential complications to prevent biases in measurements, which can become evident as either reduced flow velocity or increased echo amplitude. In contour images that plot the relationship between time, depth, and variables like velocity or echo amplitude, these biases are often distinctly visible, helping to identify the nature and source of interference [7,8].

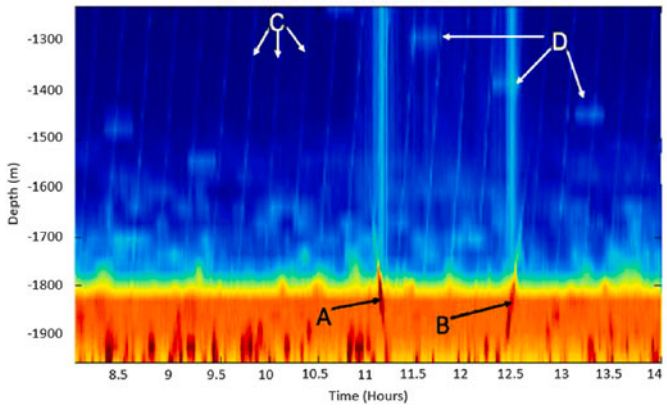

Fig. 1. Example of seabed mounted ADCP echo amplitude measurements featuring cross-talk characteristics, where A and B markers are strong vertical lines associated with the descent and ascent of a deployed remote-operated vehicle respectively. Markers C and D are diagonal and horizontal lines associated with cross-talk from other acoustic instruments [8].

Side lobe contamination from surface reflections and interference specific to a pair of ADCPs are distinct types of interference that affect ADCP data in different ways [9]. Side lobe contamination occurs when acoustic signals from an ADCP unit reflect off the water surface and return to the instrument, typically biasing the measured velocities to be lower than actual due to interference with the direct path signal, this has been comprehensively explored by Lentz, S.J [9]. The detection of this interference defines the extent of the contaminated surface region, which is influenced by factors such as water depth, beam angle, and bin size. It is crucial to note that this region has been excluded from the analysis, ensuring no overlap with the zone affected by cross-talk (interference specific to a pair of ADCPs). In contrast, cross-talk occurs when two units are deployed in close proximity and their acoustic signals interfere with each other. Cross-talk introduces erroneous data points and spikes, making velocity measurements unreliable. It is usually identified through comparative analysis between the two ADCPs, using methods like the spike test, a standardised test from the Quality Assurance of Real-Time Oceanographic Data (QARTOD), which is used to detect sudden, unexplained discrepancies.

Measurement campaigns must take into account the specific infrastructure that they are designed to measure. Numerous Tidal Energy Converter (TEC) designs exist and differ in characteristics like rated power, rated velocity, and deployment depths (z) in the water column. For floating turbines, assessing power performance becomes more complex due to motion from mooring cables and flow velocity variations in the upper water regions. Additionally, wind-induced flow and wave-current interaction further impact the floating TEC concepts of tidal flow variation. The removal of measured flow data near the surface can affect the calculation of the power-weighted rotor average (PWRA) velocity, a metric recommended in IEC TS 62600-200 [10]. Moreover, floating TEC concepts necessitate mooring systems that occupy the water column around the device, posing a challenge for ADCP placement. It becomes crucial to maintain a distance from potential cross-talk caused by the mooring system and device in the upper water column [6].

Within the Reliable Data Acquisition Platform for Tidal (ReDAPT) project [11], multiple ADCP deployments took place at the European Marine Energy Centre (EMEC) full-scale tidal test site at the Fall of Warness (FoW) between 2011 & 2015 (Fig. 2). The objectives were to evaluate flow characteristics and in-situ measurements for Alstom's DEEP-Gen IV 1 MW tidal turbines power performance. Recent studies indicate that spatial variations in current flow and direction significantly influence performance metrics [12,13]. One measurement campaign (out of seven) assessed the current flow variation upstream of the turbine using two concurrent flow sensors to comply with the guidelines set by the International Electrotechnical Commission (IEC) [12,14]. The IEC Technical Specification (IEC TS 62600-200) guides tidal developers in assessing machine performance [10]. According to this IEC TS, power performance should be measured relative to two independently located current profilers deployed in either 'in-line' (preferred) or 'adjacent' (least preferred) orientations at ranges based on the turbines diameter equivalent (D_E) [10].

This study investigates the impact of measurement cross-talk on the power performance assessment of an operational 1 MW tidal turbine and two modelled turbines. The analysis focuses on the effect of measurement bias on the power curve using in-situ data from two ADCPs located upstream on the flood tide of the DEEP-Gen IV at the Fall of Warness (Orkney, Scotland). This first-of-its-kind deployment at the site aimed to identify any near-machine upstream flow effects during the operation of the DEEP-Gen IV 1 MW tidal turbine and, on the alternate tide, wake effects. Despite passing the relevant QC checks outlined by QARTOD [15], this work identifies incidences of cross-talk between the two ADCPs, which would not be visible if adhering to the IEC 62600-200 (which requires a singular ADCP upstream of the TEC) by placing a second ADCP within 3 effective diameters of the first on the same side of the rotor.

However, this dataset is unique as it allows a review of data from two

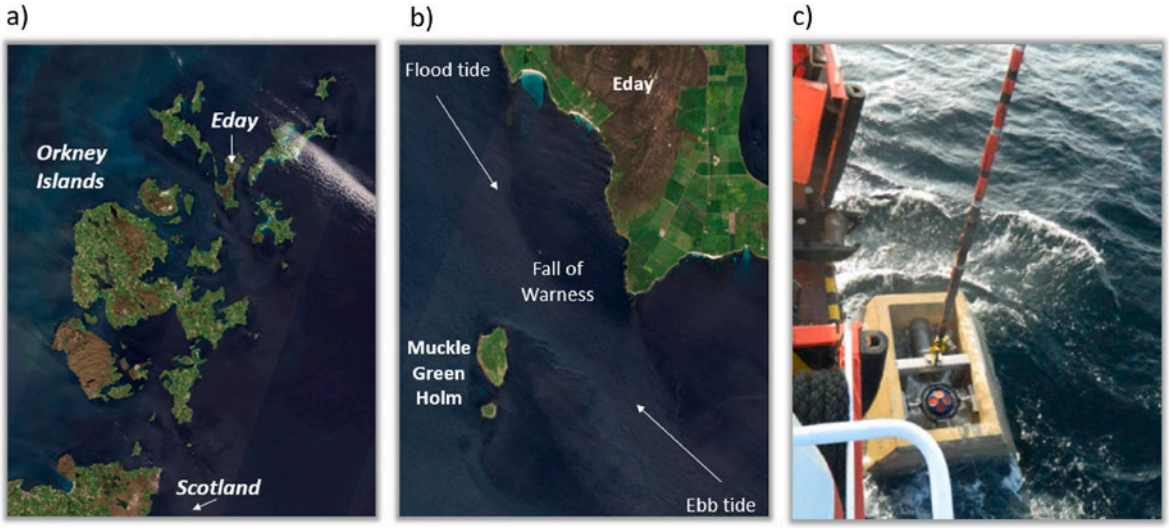

Fig. 2. Location of the study site. a) Orkney Islands location relative to Scotland; b) EMEC's full-scale tidal test site at the Fall of Warness, Eday; c) RDI ADCP in Gravity-based concrete frame being deployed. Image sourced from Ref. [11].

locations upstream of an operating turbine, enabling the conduction of two power performance assessments with more than 15 days of good data from both instruments, satisfying the IEC standard. Additionally, the study provides a robust method for removing interference from a dataset, offering valuable insights for deployments that encounter periods of interference and cannot afford to waste the collected data. This approach not only enhances the usability of contaminated datasets but also contributes to cost efficiency and knowledge transfer in ADCP deployments.

A methodology is proposed and demonstrated to identify and correct the interfered measurements, with a further study conducted to assess the impact of anomalous and filtered data on Annual Energy Production (AEP), a key techno-economic metric in the sector. Furthermore, the study addresses a key challenge of implementing IEC 62600-200 - deploying ADCPs within specified zones that are often small relative to water depth at deeper sites. The results advocate for expanding these zones or adjusting their dimensions.

The manuscript is structured as follows: Section 2 introduces the Fall of Warness tidal test site (Section 2.1), instrumentation relevant to this work (Section 2.2), turbine operational principles (Section 2.3), the modelled power for two other horizontal axis turbines (Section 2.4) and the power weighted rotor average method (Section 2.5). Section 3 outlines the methodology, the method for identifying the cross-talk (Section 3.1). The results are presented in Section 4, highlighting the difference between in-situ measurements between ADCPs (Section 4.1), impact on the power performance estimates (Section 4.2) and the variation in AEP estimates (Section 4.3) when data featured cross-talk characteristics. The results are discussed and concluded in Sections 5 and 6 respectively.

2. Test overview

2.1. Deployment site conditions

To ensure an obstacle-free environment, a rectangular area of 10 D_E x 20 D_E was surveyed for the power performance assessment (PPA) following IEC TS 62600-200 guidelines [10,12]. Fig. 3a depicts the survey area relative to the DEEP-Gen IV and the two ADCPs (known from here forward as A_1 and A_2 which are situated at 61 and 106 m

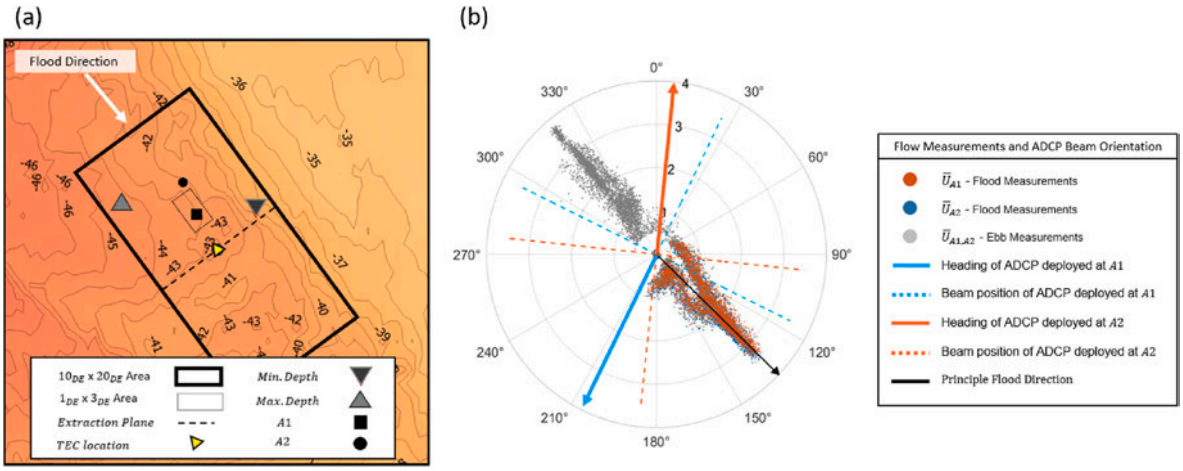

Fig. 3. Channel bathymetry and ADCP locations relative to the DEEP-Gen IV a t the FoW tidal test site. (a) The area of interest (solid black rectangle) showing the depth around the DEEP-Gen IV 'Contains Maritime and Coastguard Agency data © Crown Copyright' [16]. (b) Tidal ellipse for the flood tide PWRA flow velocities $\overline{U}_{A1}$ (orange dot) and $\overline{U}_{A2}$ (blue dot), with the beam orientation of both instruments (solid line representing main beam heading - beam 3 for RDI Work Horse (WH) ADCPs) and the principle flow direction is shown as the red line. Ebb data (grey) is not used in this analysis. Images adapted from [12,13].[12,13]. (For interpretation of the references to colour in this figure legend, the reader is referred to the Web version of this article.)

upstream of the DEEP-Gen IV respectively). For the purpose of a PPA the ADCP must be positioned within a rectangular area measuring 3 D_E long, 1 D_E wide and commencing at 2 D_E upstream of the turbine rotor. However, a significant challenge in implementing IEC 62600-200 has been effectively deploying ADCPs within the specified zones, particularly in deeper sites where these zones may be relatively small compared to the water depth. In this campaign, both ADCPs were deployed upstream of the turbine at distances of 3.4 D_E and 5.5 D_E exceeding the specified deployment zone outlined in IEC 62600-200.

The depth within this area varies from 46 m northwest of the turbine to 39 m near the east side. The typical flood tidal currents' directionality and strength at the deployment location are depicted in Fig. 3b. In a Janus configuration of a four-beam instrument like the Teledyne RDI ADCPs, the main heading is usually derived from the "forward-looking" beam. In this context, the ADCPs, labelled as A_1 and A_2, face approximately 206°and 6°, respectively. The forward-looking beam, oriented in the direction of the currents movement, serves as a crucial reference for determining the ADCPs' orientation relative to the flow direction and accurately calculating current velocities in various directions.

At this site, the flood tide reaches approximately 3.5 m s ^{1} with a direction offset of about 45° from the South. On the other hand, the ebb tide can reach up to 4 m s ^{1} and is known to feature higher turbulence, attributed to various features in the site bathymetry and nearby islands, as reported by others [17,18]. However, for this study, the ebb tide measurements were excluded since the instruments were placed in the wake of the TEC during this tide.

2.2. Instrumentation

Two RDI workhorse 600 kHz ADCPs (4 beams, 20-degree variant) were used, configured with 1 Hz sampling with a resolution of 1 m depth bins as specified in Table 1. Fig. 4 illustrates the displacement in the vertical and horizontal plane between the two deployed ADCPs A_1 and A_2 and the relative clearance zones (transparent cones around the transducers' main lobes). Instrument locations are specified in Table 2.

Fig. 5 illustrates a key scenario relevant to this study, involving two seabed ADCPs positioned 45 m apart. This figure shows how the signal from the source sensor spreads into the measurement column (vertical column that extends from the water surface to the seafloor). If the transducer beams of the two ADCPs are not perfectly aligned but remain relatively close, part of the signal pulse from the source sensor can reflect at an angle that matches the receiving ADCP's orientation. This misaligned reflection, interacting with the free-stream velocity component u, which causes an un-predictable pulse that arrives at the other co-located ADCP. This delay results in the second ADCP receiving the shifted signal later than expected, which introduces a measurement bias.

2.3. Turbine description

The operational TEC is a 1 MW rated machine featuring a traditional three-blade, horizontal axis design with an 18 m diameter rotor and variable-pitch control. The relevant turbine parameters are listed in Table 3. Throughout the study, this turbine will be referred to as TEC_{T2} (due to its position relative to the other two variants used in the analysis). To evaluate the impact of cross-talk on the measured power curve at different depths, two further variants of horizontal axis tidal turbines, which operate in different locations of the water column, were examined.

The designs of turbines TEC_{T1} and TEC_{T3} are based on deployed variants of horizontal-axis turbines. These designs were derived from the RealTide project [19], and their basic parameters are provided in Table 3.

Table 1
Instrument settings during the measurement campaign.

Specification	Unit	A_1 & A_2
Model		RDI WH 4 beam
Abbreviation		ADCP
Operating Frequency	kHz	600
Sample Rate	Hz	1
Cell Size	m	1
Beam Angle	°	20
Estimated Beam Width	°	2
Clearance Zone	°	11

2.4. Modelled power

The two separate power curves were created to simulate power production for the 0.1 MW and 2 MW TEC concepts. The power calculation method is illustrated by Equation (1):

$$P_{\text{active}} = P_{\text{rated}} \cdot \begin{pmatrix} U^2 & U_{ci}^2 \\ U_r^2 & U_{ci}^2 \end{pmatrix} \quad (1)$$

here, P_{rated} represents the predefined rated power, U is the in-situ velocity measurement in m·s ^{1}, U_{ci} is the cut-in velocity for the proposed TEC, and U_r is the rated flow velocity for peak power production. Velocity measurements below the cut-in velocity are rejected, and those above the rated velocity are set to the defined rated power. This method is beneficial because it directly incorporates the turbine specific parameters, providing a straightforward and realistic estimation of power output across a range of current velocities, which is adequate for our comparison purposes. The quadratic model was chosen over the cubic model because it can provide a more conservative and realistic representation of tidal turbine power output, particularly at lower velocities, accounting for mechanical and environmental factors that may prevent immediate efficiency gains and thereby better capturing the gradual power increase from cut-in to rated speeds. Energy production was calculated using available time series power data from each instrument. This was achieved through the trapezoidal method, which approximates the power integral. The resulting energy was then scaled by the campaigns deployment ratio relative to the length of a year, as depicted in Equation (2):

$$AEP = R \cdot \Sigma_{t1}^{t2} \cdot \overline{P} dt \quad (2)$$

where AEP represents the anticipated annual energy production in MWh, R is the ratio of the number of days in a year to the deployment duration, $\overline{P}$ signifies the calculated mean TEC power, t_1 denotes the index number marking the beginning of the time interval, and t_2 indicates the index number marking the end of the time interval.

2.5. Power weighted rotor average velocity

To comply with the guidelines of IEC/TS 62600-200 [10], the current flow was averaged directly over depth bins that corresponded to the positions and diameters of three rotors in the water column, following the method of bins. To calculate the power-weighted rotor average (PWRA) velocity for the two seabed-placed ADCPs, the velocity measurements from depth bins corresponding to the rotor plane were averaged [13]:

$$\widehat{U}_{i,j,n} = \left[\frac{1}{A} \Sigma_{k=1}^{S} U_{i,j,k,n}^3 A_k \right]^{\frac{1}{3}} \quad (3)$$

where i represents the index number defining the velocity bin, j represents the index number of the time instant at which the measurement is performed, k represents the index number of the current profiler bin across the projected capture area, S is the total number of current profiler bins across the projected capture area, $\widehat{U}_{i,j,n}$ denotes the instantaneous power-weighted tidal current velocity across the projected capture area in m·s ^{1}, $U_{i,j,k,n}$ represents the magnitude of the instantaneous tidal current velocity for time j, at current profiler bin k, in

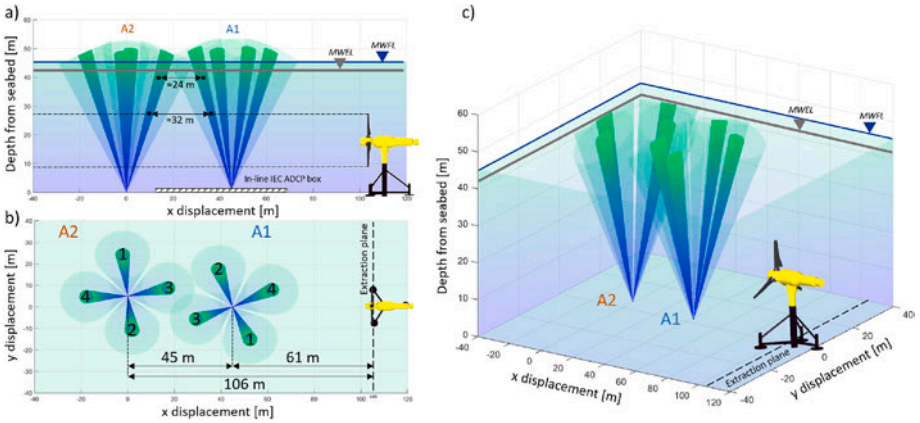

Fig. 4. RDI WH 600 kHz ADCPs, A_1 and A_2, which are 61 m and 106 m northeast of the TEC location (upstream on a flood tide), respectively. (a) Distance between neighboring beam trajectories from $ADCP_{A1}$ and $ADCP_{A2}$. Beam distance at the upper rotor bound (circle) and close to the sea surface (square) and the mean water level for the flood (blue triangle) and ebb (grey triangle). IEC TS 62600-200 instrument target box is included as the lined box. (b) Showcases the top-down view of A_1 and A_2 beam paths and the clearance zones. (c) Illustration of the main lobes (solid), clearance zones (shaded), and the orientation of the two bottom-mounted ADCPs. (For interpretation of the references to colour in this figure legend, the reader is referred to the Web version of this article.)

Table 2
Turbine proximal deployments of ADCPs showing unique campaign ID, date deployed (date format yyyy-mm-dd) and deployment duration. The coordinate system is in Decimal Degrees - WGS84.

ADCP ID	Campaign ID	Deployed	Recovered	Days	LN [°]	LW [°]
A_1	ADCP01-NWDep5	2014-06-22	2014-08-05	41	59.13726	2.80651
A_2	ADCP02-NWDep5	2014-07-07	2014-08-16	40	59.13764	2.80686
LN/LW: Location North/Location West						

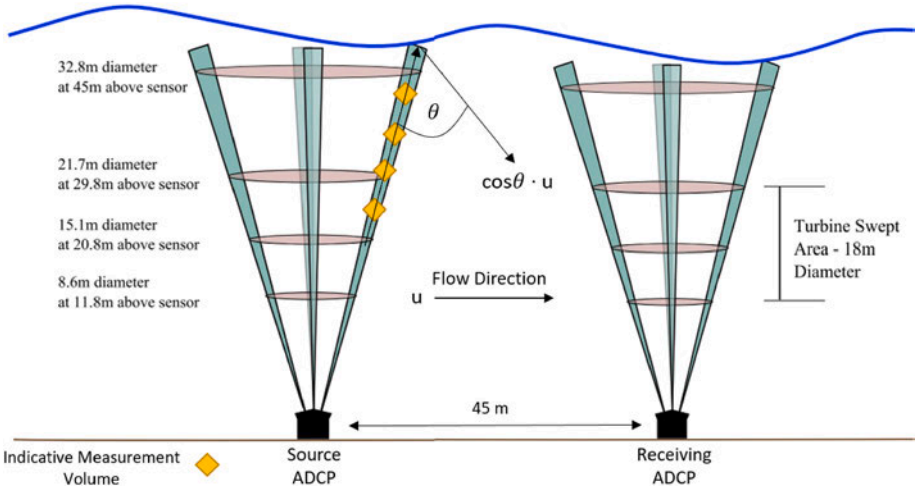

Fig. 5. Illustration of the theory of two angled sensors measuring a component of the free stream velocity along the angle intersecting the two beams. NOTE the rhombus volumes represent the ADCP weighting as per user manuals [2] where the depth cell is most sensitive to velocities at the centre of the cell.

Table 3
Key parameters of the DEEP-Gen IV TEC_{T2} and two further modelled variants, TEC_{T1} and TEC_{T3}.

Specification	Units	TEC_{T1}	TEC_{T2}	TEC_{T3}
Type	–	HATT	HATT	HATT
Distance above seabed	m	12	18	30
Blade radius	m	6	9	10
Projected capture area	m^2	113	256	314
Rated output power	MW	0.1	1	2
Cut-in	$m{\cdot}s^{-1}$	0.75	1	1.2
Rated speed	$m{\cdot}s^{-1}$	2.0	2.7	3.0

HATT: Horizontal-Axis Tidal Turbine.
NOTE: All turbines used in this study have 3 blades.

velocity bin i, for data point n in $m{\cdot}s^{-1}$, and A is the projected capture area of the proposed TEC in square meters.

The in-situ measurements were averaged by 5 min. Where $\widehat{U}_{i,j,n}$ should be averaged to calculate the mean PWRA velocity corresponding to the extraction plane of each rotor in the study. The averaging process is visually represented in Fig. 6 and expressed by Equation (4):

$$\overline{U}i, n = \left[\frac{1}{L}\sum_{j=1}^{L}\widehat{U}_{i,j,n}^{3}\right]^{\frac{1}{3}} \quad (4)$$

The measurements were grouped into velocity increments of 0.1 m s^{-1}, and the data within each bin were further averaged to obtain a single-point average. The study considers the PWRA velocity calculated

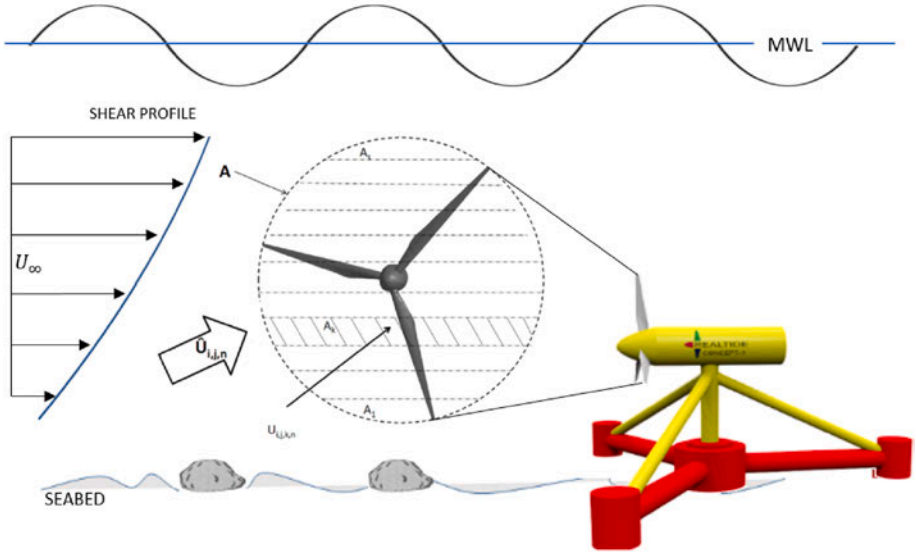

Fig. 6. The vertical variation of tidal current across the projected capture area - introducing the importance of the power PWRA technique. Image sourced from Ref. [13].

from instruments A_1 and A_2. For each turbine variant, the PWRA velocity from instrument A_1 is represented as $\overline{U}A_{1,T1}$, $\overline{U}A_{1,T2}$, and $\overline{U}A_{1,T3}$, while for instrument A_2, it is denoted as $\overline{U}A_{2,T1}$, $\overline{U}A_{2,T2}$, and $\overline{U}A_{2,T3}$.

3. Methodology

3.1. Identification and removal of the bias

Bias in ADCP measurements emerges as a consequence of the cross-talk between two instruments positioned in close proximity to each other. This cross-talk, often referred to as "acoustic interference," introduces distortions in the acquired data due to the overlap of acoustic signals emitted by one instrument and received by the other. The bias manifests as deviations from the true values, rendering the measurements susceptible to misinterpretation.

ADCP data typically undergoes rigorous quality checks to ensure that extreme outliers do not distort the analysis results. The QARTOD guidelines are highly recommended for quality control of ADCP data, as they provide both required and recommended checks, including setting appropriate thresholds. Key checks recommended by QARTOD guidelines that are relevant for detecting interference include the range test, which ensures data values are within expected ranges, and the flat line test, which identifies periods with no data variation. The spike test identifies data points that significantly deviate from the expected or neighboring values within a dataset, helping to detect and correct outliers or anomalies, while the attenuated signal test aims to flag issues with signal strength. Additionally, the surface echo test identifies interference from surface reflections. Together, these checks help mitigate the effects of interference and maintain the accuracy of the data analysis.

Table 4 provides a simple set of flags, as per guidance from QARTOD [15] - and associated descriptions that have been used in the data post-processing phase. For example, if the data failed the current speed test by exceeding the upper limit, a 'failed high' flag may indicate that the values were higher than the expected range.

Data anomalies passing through the quality control were then identified by the author as strong diagonal lines. This led to the development of an algorithm that could detect these features caused by acoustic cross-talk. The proposed method involves manipulating the data to locate the bias caused by cross-talk and disregard the corrupted measurements from further analysis.

To effectively identify cross-talk in echo amplitude profiles, data points were flagged for removal based on two key criteria: exceeding a prominence of 5 counts and containing two peaks in the detrended and smoothed amplitude profile. These conditions suggest potential acoustic cross-talk in this data set. Data with more than 5 counts but lacking two peaks were flagged, although not removed, due to limitations in the algorithms capacity to fully address complex cross-talk patterns near boundary layers. The algorithm assigns a flag of 4 to data that fail the check, indicating unacceptable quality. To quantify the total number of samples affected by cross-talk, the flagged data was summed for this quality control check and compared it to the overall data set.

Table 4
Assigning specific flags to data points that display potential anomalies or issues, helping to categorise and address the reliability of measurements, as per QARTOD.

Flag	ID	Description
Pass	1	Data have passed critical QC tests and are deemed adequate for use as preliminary data.
Not evaluated	2	Data has not been QC-tested, or the information on quality is not available.
Suspect or of high interest	3	Data are considered to be either suspect or of high interest to the user. They are flagged suspect to draw further attention to them.
Fail	4	Data are considered to have failed one (or more) critical QC check. If they are disseminated at all, it should be readily apparent that they are not of acceptable quality.
Missing data	9	Data are missing, used as a placeholder.

The algorithm examines the contaminated averaged echo amplitude and time-averaged velocity profiles to identify peaks in echo amplitude. The cross-talk detection algorithm in amplitude performs the following tasks:

1. The 5-min averaged echo amplitude profiles are separated out individually to be assessed for indications of cross-talk.
2. The amplitude profile was detrended, subtracting the line of best fit (typically known as $y = mx + b$) from each profile.
3. The profile was then smoothed - using the function in MATLAB

(*smoothdata(X)*, where X is the dataset) a moving average filter of 3 data points was used - to remove small measurement fluctuations and distinguish the large peaks.

4. Finally, the profile is then multiplied by negative one to identify the primary peak (eliminating the peak found at the lower and most upper region of the water column due to boundary layers) to allow correct identification of the peak on either side of the biased measurement. The peaks were identified using the "findpeaks" function from the Curve Fitting Toolbox in MATLAB. The identified peaks had a prominence of at least 5 counts after detrending the data.

By removing the trend from the signal, the analysis focused on studying the significant fluctuations caused by cross-talk. The cross-talk consistently led to the identification of two peaks using this method. To address this, a set of quality control factors was introduced based on the number of peaks in the signal. The quality control factors and their corresponding flag as per QARTOD guidance are as follows:

- if $N_p <= 1$: flag data *1*;
- if $N_p = 2$: flag data *4* between the two peaks;
- if $N_p > 2$, the trough between the number of peaks is checked, and the peaks on either side of the largest trough are flagged *4*

where N_p is the number of peaks, measurements that have been flagged as containing cross-talk have been removed from the analysis. It should be noted that data flagged as 4 can also be reclassified as 3 and used for further analysis. By representing this reclassified data with a different colour or symbol, we can effectively compare the data set with and without the flagged data, providing a more detailed and nuanced analysis.

3.2. Alternative approaches to mitigating cross-talk

While the algorithm developed in this study effectively detects data contamination in the presented example (see section 3.3), it is important to recognise its limitations. Specifically, the algorithms performance may vary under different contamination scenarios, such as those involving more complex noise patterns or more frequent levels of interference at the boundary layers. Additionally, the current algorithm may not be robust against all types of data anomalies, potentially limiting its applicability in diverse environments.

Alternative approaches to mitigating cross-talk contamination include altering ping rates, using interleaved sampling schedules, and employing parent-child arrangements. Adjusting the ping rates of nearby instruments can minimise data collection overlap, thereby reducing cross-talk, but this method requires careful coordination and calibration, increasing deployment complexity. Interleaving sampling schedules to prevent multiple instruments from sampling simultaneously can also avoid cross-talk, though this comes at the cost of losing synchronous data, which may be crucial for certain analyses. Finally, connecting instruments in parent-child configurations ensures synchronised transmission and avoids cross-talk, yet this approach can complicate the deployment and maintenance of the instrument network.

Each of these alternative solutions introduces a different type of complexity to the deployment process. For instance, altering ping rates and using interleaved sampling schedules require precise timing mechanisms and thorough testing to ensure accuracy and reliability. On the other hand, parent-child arrangements necessitate additional hardware and coordination, which could be prohibitive in large-scale or resource-limited deployments.

3.3. Removal of cross-talk features

A robust flow velocity measurement is crucial for accurate performance assessments. The presence of contaminated data, which passed the QC steps outlined by industry standards and instrument manufacturers can have a significant impact on the measured power curve and AEP estimates. To address this issue, a method is proposed in Section 3.1 to identify and remove the contaminated measurements, this is shown visually in Fig. 7. The method involved manipulating the data to highlight the contaminated sections and applying a flag to exclude them from further analysis. By implementing this approach, the study can compare the consequence of filtered/unfiltered data used in the measured power curve and AEP estimates.

During post processing the data set it was apparent that cross-talk interference impacted only one instrument at a time, rather than both simultaneously. This finding suggests that the interference source alternated between the two instruments, complicating the identification of the exact cause. One hypothesis for this intermittency could be related to the synchronisation of the ADCPs. It is possible that the ADCPs experience slight variations in synchronisation over time due to clock drift. As a result, one ADCP may briefly slip in and out of sync with the other, causing intermittent periods of cross-talk interference. During these periods, the ADCP that is slightly out of sync may inadvertently "listen" shortly after the other, leading to the observed alternating pattern of interference affecting only one instrument at a time. Fig. 8 depicts the interference from the two ADCPs by the diagonal lines (velocity reduction along the depth profile) and also presents that only one ADCP is affected at a time. While variations in clock speeds between separate instruments are beyond the users control, and perfect alignment or minimal differences could reduce the ability to remove contamination, this scenario is highly unlikely.

As the currents measured at the two ADCP locations were often similar and interference typically affected only one instrument at a time, the impact of interference on calculating the AEP can be accurately assessed by replacing measurements affected by cross-talk with the corresponding clean measurements from the other instrument, thereby obtaining the best-case scenario to compare against. However, it is important to note that this replacement approach is only valid when the currents are sufficiently homogeneous, such that the two instruments measure the same currents when there is no cross-talk. This method may not be applicable in regions of strongly sheared flow, where significant differences in measurements between the instruments could occur.

4. Results

4.1. Cross-talk impact: inter-instrument measurements

Initially, cross-talk was identified through analysis of velocity time series plots, as shown in Fig. 9a, allowing for a direct comparison between the two ADCPs. Following identification, the methodology previously outlined in section 3 was employed to flag and subsequently remove the contaminated measurements. This approach proved effective in removing up to 90 % of the samples that were influenced by interference, see Fig. 9b. The remaining data that passed through were from regions close to boundary layers, where accurately locating a peak proved challenging.

Fig. 10a and b highlight the individual mean velocity and echo amplitude profiles (dark blue) with features of cross-talk being removed (light blue) and have passed through the algorithm. Fig. 11a, b, and 11c show the correlation of the measured flow velocities (U_{A1} and U_{A2}) across the rotor plane of TEC_{T1}, TEC_{T2} and TEC_{T3} respectively.

Table 5 provides a detailed summary of the total samples available, flagged, and removed during flood tides over a 26-day measurement period for two ADCPs. It highlights the number of samples impacted by interference and the subsequent removal percentages, emphasising the rigorous data processing steps taken to ensure only high-quality, time-stamp-matching samples were used in the final analysis.

Fig. 11 provides an observation that underscores at higher depth bins, where signal levels from the profiler in question decrease while contaminating signal levels remain unchanged, the impact of cross-talk becomes more pronounced. This phenomenon highlights the initiation of measurement cross-talk at shallower depths, gradually diminishing in intensity with increasing depth. The cross-talk affects the velocity between 1 m s ^{1} and 3 m s ^{1}. The power-weighted flow velocity is

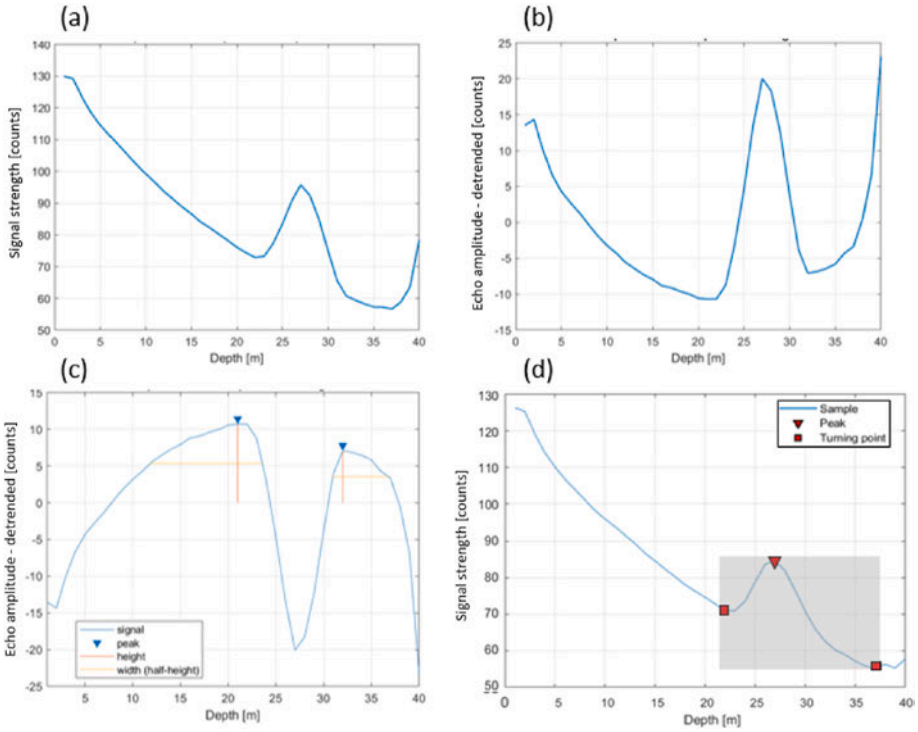

Fig. 7. Echo-Amplitude Depth Profile: (a) A data sample displaying a prominent peak in echo amplitude within the upper portion of the water column. (b) The amplitude profile detrended by subtracting the line of best fit. (c) The profile is then smoothed to remove multiple mini-peaks and then multiplied by negative one to identify the primary peak. (d) The algorithm effectively identifies the peak (indicated by a triangle) within the data sample, while also eliminating measurements between the designated square markers that represent bias from cross-talk features.

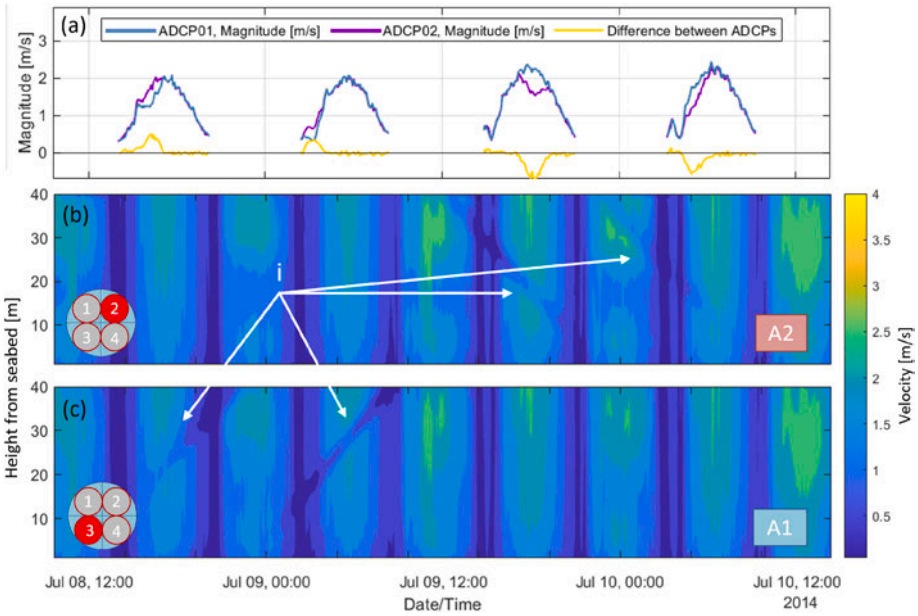

Fig. 8. (a) Velocity magnitude for A_1 (blue) and A_2 (purple) over four flood cycles, included is the difference between both velocity measurements (yellow). (b) Velocity depth contour for A_2 beam 2 (as depicted in the bottom left) where interference is identified as *i* - a diagonal line - for ADCP A_2. (c) Velocity depth contour for ADCP A_1 beam 3. (For interpretation of the references to colour in this figure legend, the reader is referred to the Web version of this article.)

compared, including periods of cross-talk across the depth bins used in the power-weighted calculation. The linear model coefficients (with 95 % confidence bounds) and the sum of squared error (SSE) are presented in Table 6. Where $z_{T\ldots}$ is representative of the bin depths used across the rotor diameter of TEC_{T1}, TEC_{T2} and TEC_{T3}. Also presented in Table 6 P1 and P2, these statistics represent correlation parameters between concurrently measuring ADCPs at A_1 and A_2. P1 assesses the alignment in magnitude of the measurements, while P2 evaluates the bias between them. These statistics are crucial for determining the agreement between the ADCPs.

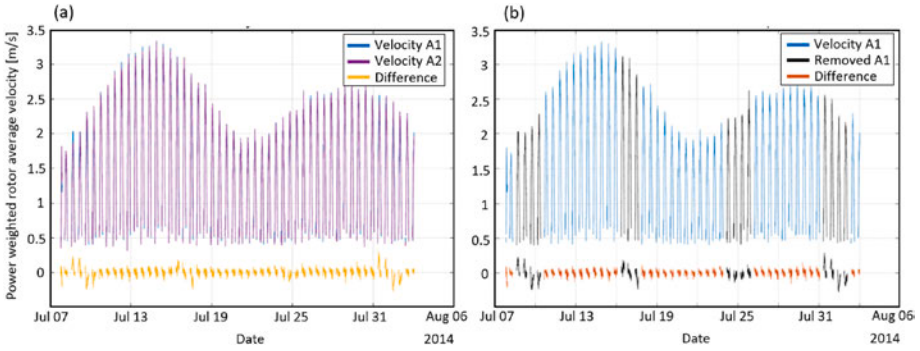

Fig. 9. (a) Time series comparison of power-weighted rotor average velocities from ADCPs A_1 and A_2, focusing on the TEC_{T2} rotor. The yellow line represents the difference between the two measurements. (b) Power-weighted rotor average velocity time series from ADCP A_1, highlighting flagged data influenced by interference (black line). The difference between ADCP A_1 and A_2 measurements is also depicted. (For interpretation of the references to colour in this figure legend, the reader is referred to the Web version of this article.)

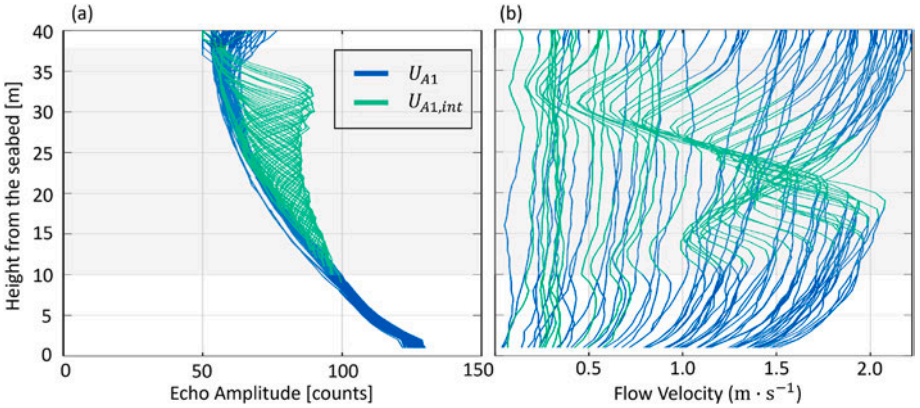

Fig. 10. An area of cross-talk is identified and highlighted in the grey box, and the good measurements (U_{A1}) and flagged contaminated measurements ($U_{A1,int}$) are given for one flood cycle. (a) Mean echo amplitude measurements in counts. (b) Mean flow velocity profile in m·s^{-1}.

4.2. Cross-talk impact: estimates of power performance

The main objective of this investigation is to analyze the impact of cross-talk on velocity measurements and its subsequent effect on estimated power metrics for a turbine. Fig. 12 presents three consecutive flood cycles, showing the varying locations of cross-talk along the water column (dashed lines), followed by three consecutive flood cycles with no cross-talk (solid lines). The PWRA velocity is calculated for measurements obtained across the swept area of three turbines represented by square, triangle, and circle symbols, corresponding to TEC_{T3}, TEC_{T2}, and TEC_{T1}, respectively.

In Fig. 13a, the generated power output for each 5-min measurement is plotted against the flood tide velocity component approaching the DEEP-Gen IV, TEC_{T2}. The flow velocity measurements containing cross-talk features are represented by blue dots, showcasing the variation caused by cross-talk between the two ADCPs. Additionally, the flow velocity measurements with 90 % of the cross-talk features removed are displayed as orange dots.

Fig. 13b illustrates the variation in the mean PWRA velocity (black dashed line) for measurements with and without cross-talk features. The PWRA velocity represents measurements taken across z_{T2}, the swept area of TEC_{T2}. At lower flow velocities, more noticeable differences are observed between the curves in Fig. 13b. The velocity differences range from 0.5 % to 2.5 % between flow velocities of 1–1.5 m s ^{1} and 1.5–2.0 m s ^{1} (where cross-talk occurs during the depth bins used for PWRA velocity calculation), respectively.

Had the cross-talk not been identified and removed, the power curve would shift to the left, favouring lower flow velocities when paired with the power produced by the DEEP-Gen IV. In the measurement campaign, 15 % of the flood tide data displayed significant interference features throughout the water column. The variation in flow velocity changes with depth, implying that the cross-talks impact on the measured power curve could be more significant depending on the depth bins used.

This effect becomes more evident when examining Fig. 14, where depth bins relative to the swept area of TEC_{T3} in the upper region of the water column (z_{T3}) are used. In this case, the cross-talk features are more pronounced, leading to a significant reduction in the measured velocity (as shown in Fig. 12).

The flow velocity, including the 15 % contaminated flood cycles, when used to generate the power curve, was found to be, on average, approximately 6 % lower than data unaffected by cross-talk. Neglecting to identify and remove these cross-talk features during the data post-processing phase can alter the power curve for the turbine under performance review, potentially misrepresenting the annual energy estimate. Hence, it is crucial to address cross-talk issues to ensure accurate and reliable turbine performance assessments.

4.3. Cross-talk impact: estimates of annual energy production

Using the velocity time series from ADCPs positioned at A_1 and A_2, along with the power produced by TEC_{T2}, the AEP can be calculated. During periods of cross-talk (which occurred in one instrument at any given time), the other instrument was used to estimate the AEP, allowing the impact of cross-talk to be quantified.

Considering the cross-talk affected approximately 15 % of the flood cycles, the results revealed a difference in AEP estimates of up to 4 %. The variability in AEP differences was observed when using different depth bins as the reference. The cross-talk effect on velocity

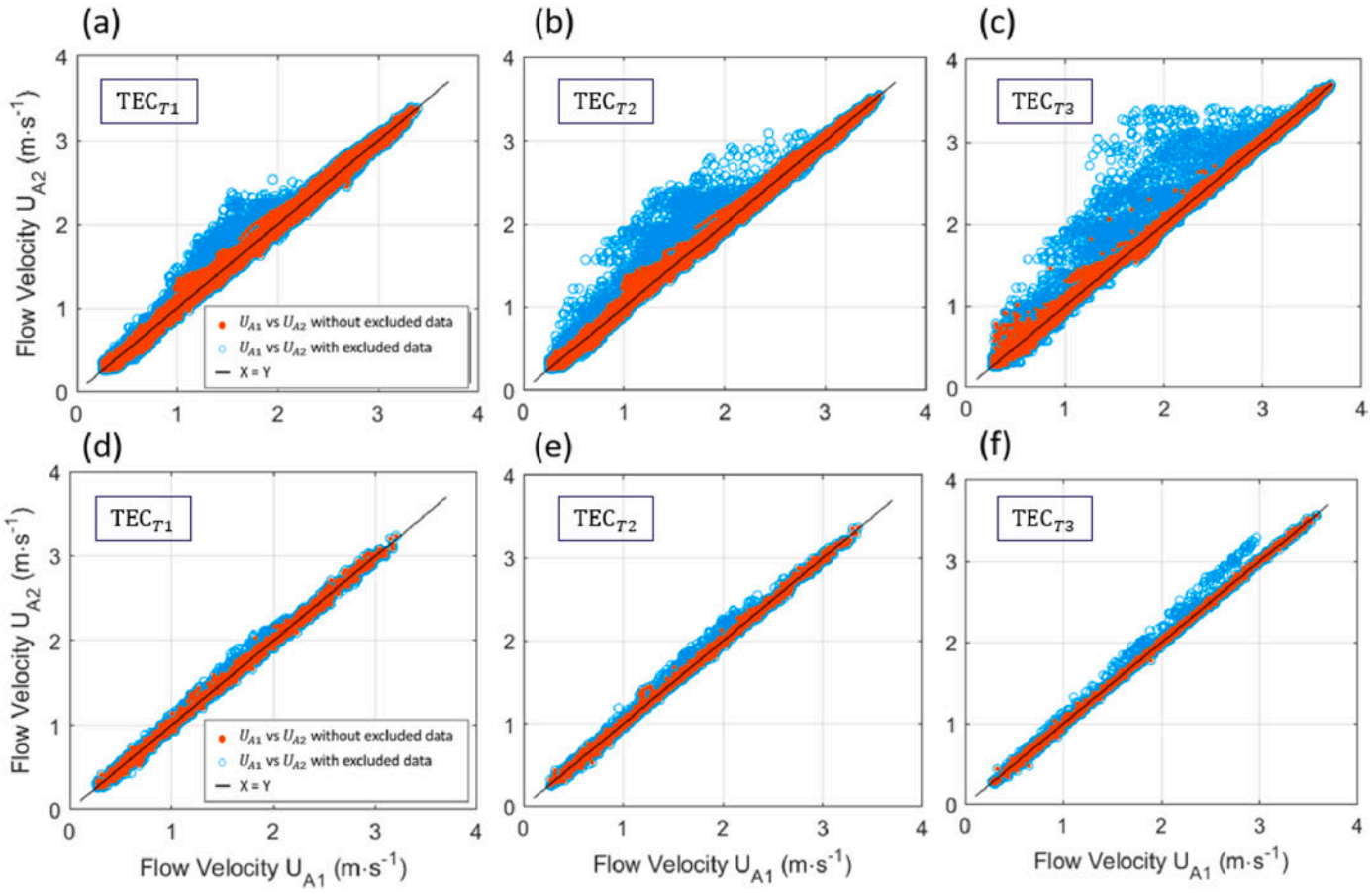

Fig. 11. Measurement correlation between flow velocities across the swept area of TEC_{T1}, TEC_{T2} and TEC_{T3} displayed in (a), (b) and (c) respectively, for data with (blue) and without (orange) features of cross-talk. PWRA velocity correlation across the swept area of TEC_{T1}, TEC_{T2} and TEC_{T3} illustrated in (d), (e) and (f) for data with (blue) and without (orange) features of cross-talk respectively. Perfect correlation illustrated as x y (black line). (For interpretation of the references to colour in this figure legend, the reader is referred to the Web version of this article.)

Table 5
Overview of total samples available, flagged, and removed during flood tides over a 26-day (days of overlap between the co-located ADCPs) measurement period. Note that only samples with matching timestamps were included in the analysis for comparison. The table summarises the total number of samples.

ADCP ID	A_1	A_2
No. 5 min samples	3744	3801
No. interfered samples	562	646
No. samples removed	507	588
% removed	90.2	91.0
No. remaining 5 min samples	3237	3213
No. samples used in analysis	3213	3213

Table 6
Correlation parameters between concurrently measuring ADCPs located at A_1 and A_2. Velocities representative of the depth bins across the swept area of TEC_{T1}, TEC_{T2} and TEC_{T3} given by (a, d), (b, e) and (c, f) respectively. Correlation between PWRA velocities - calculated using depth bins across TEC_{T1}, TEC_{T2} and TEC_{T3} - with (a, b, c) and without (d, e, f) features of cross-talk are provided.

	Statistics	z_{T1}	z_{T2}	z_{T3}
U_{A1} vs U_{A2}		(a)	(b)	(c)
	P1	0.996	0.999	0.998
	P2	0.009	0.003	0.007
	SSE	663	223	1465
	R^2	0.983	0.990	0.972
	RMSE	0.065	0.067	0.134
$\overline{U}_{A1}$ vs $\overline{U}_{A2}$		(d)	(e)	(f)
	P1	1.002	1.002	1.006
	P2	0.005	0.005	0.020
	SSE	14.272	10.331	24.853
	R^2	0.993	0.994	0.991
	RMSE	0.061	0.052	0.081

z: depth across swept area.

measurements was more significant in the upper region (z_{T3}) of the water column, resulting in differences in AEP of up to approximately 7 %. In contrast, the lowest difference in AEP with and without cross-talk features was found in the lower region of the water column (z_{T1}), where the difference was 2 %.

When cross-talk interference was absent, the measurements obtained at the two ADCP locations exhibited a high degree of similarity. This finding suggests the possibility of advocating for the expansion of these zones or the adjustment of their general dimensions, potentially by an additional 0.5 D_E, to accommodate more reliable data collection.

5. Discussion

In previous studies containing multiple acoustic velocity sensors, features of interference within the in-situ measurements were found to negatively affect the accuracy of velocity measurements. This study demonstrated that two ADCPs when placed close to each other (around 45 m apart), can still provide useful measurements. Nonetheless, this work identified for the first time interference throughout the campaign and quantified subsequent impact on AEP estimates. This interference was most pronounced at a certain range, where the possibility of the two

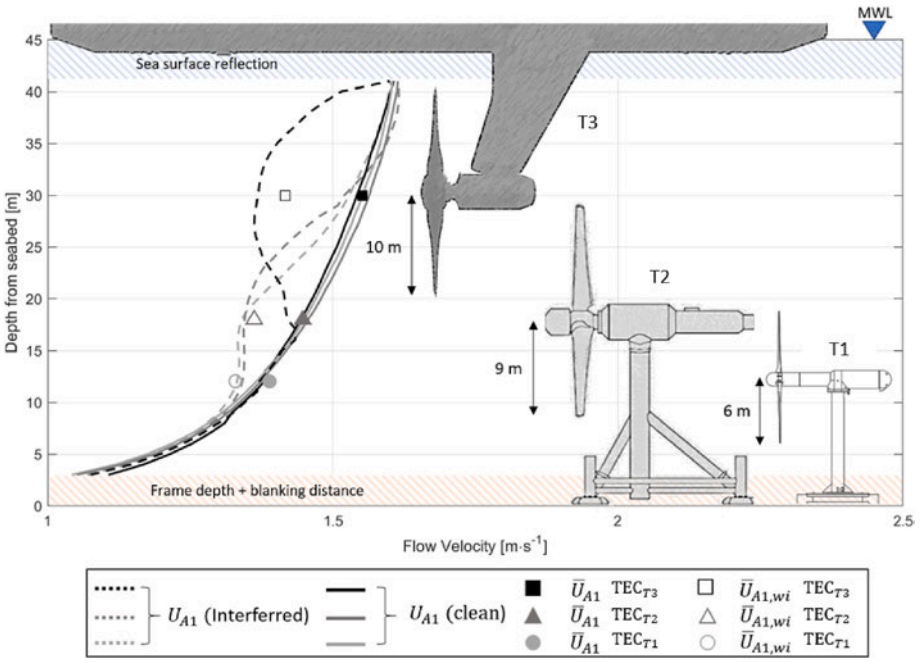

Fig. 12. Six consecutive flood tide depth profiles featuring cross-talk effects (dashed lines) and *clean* profiles (solid lines). The position of three variants of TECs are overlaid (*T*1, *T*2, and *T*3, at hub height 12, 18 and 30 m, respectively) with symbols showing corresponding interfered (unfilled) and *clean* (filled) PWRA velocities.

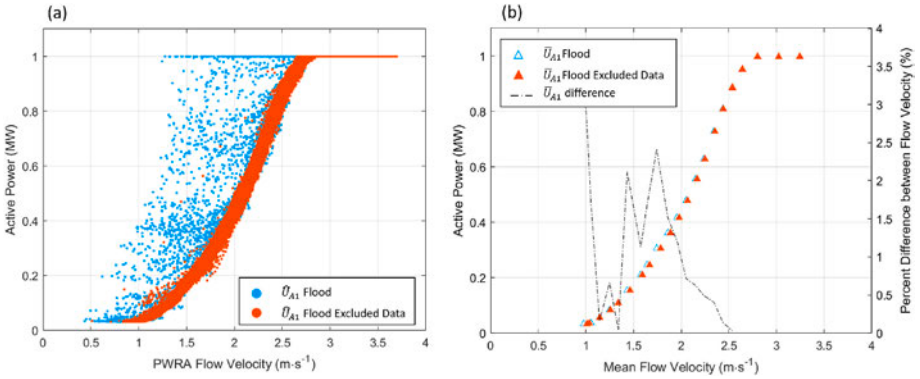

Fig. 13. The effect of ADCP cross-talk on the measured power curve - for TEC_{T2} - for the averaged 5-min PWRA velocities in increments of 0.1 m s^{-1}. (a) The flood tide measurements for ADCP A_1 ($\hat{U}_{A1}$) with features of cross-talk (blue dot) from interacting with ADCP A_2, the orange dot represents data with cross-talk features removed. (b) The mean PWRA velocity from ADCP A_1 ($\overline{U}_{A1}$) with (blue triangle) and without (orange triangle) features of cross-talk in the 5-min averaged measurements. (For interpretation of the references to colour in this figure legend, the reader is referred to the Web version of this article.)

ADCPs picking up signals reflecting off the sea surface was greater. This interference seemed to be associated with one sensor at a time, making it difficult to pinpoint the exact cause.

Despite the interference, we managed to obtain data valid (≈80 % of the campaign) for the purpose of a power performance assessment. This work suggests that It's is possible to position two ADCPs on the seabed for vertical profiling at a depth of 45 m, separated by 45 m, and obtain reliable results. Notably, the interference caused a frequent shift in the location of peak interference (measurements corrupted between 10 and 40 m from the seabed), with the most significant impact occurring in the upper part of the water column (over 25 m from the seabed). This led to a bias in the measurements, where the velocity data is reduced, but still appreciable, at points where interference was strong.

The interference primarily affects current velocity in the range of 1–3 m s ^{1} – a range crucial for applications like tidal energy. Since the interference happened at various depths simultaneously, it greatly distorted the calculation of the PWRA velocity. This bias in the PWRA velocity, when combined with the generated power from the TEC, was observed to lead to a misrepresentation of up to 8 % at velocities directly relevant to turbine operation. These findings highlight the significance of eliminating data that distorts the representation of flow characteristics. This observation is particularly relevant in the context of a data campaign in which 15 % of the data was compromised. In scenarios where this level of corruption is greater, the consequences would be even more substantial.

A method to remove data anomalies caused by interference between these closely positioned ADCPs has been developed and demonstrated, resulting in a 7 % variation in estimated AEP. The method involved data manipulation that successfully removed interference features with an accuracy of up to 90 %. However, addressing interference in the uppermost region proved to be more intricate, primarily due to the heightened variability in velocity measurements.

6. Conclusion

This study introduces a novel perspective on the deployment of

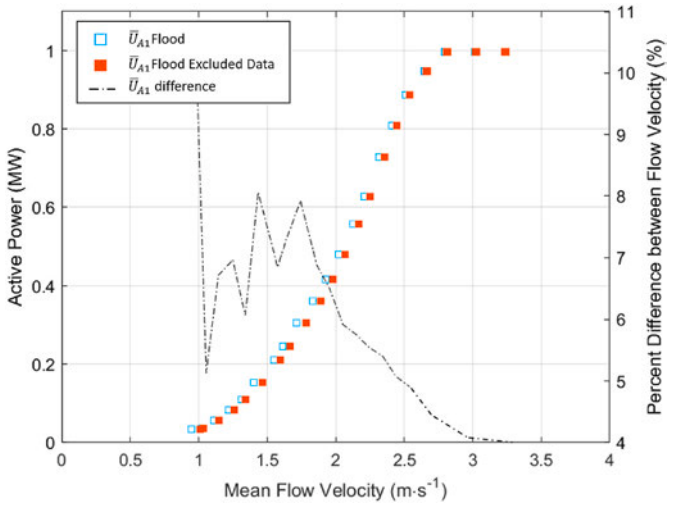

Fig. 14. The mean PWRA velocity from ADCP A_1 ($\overline{U}_{A1}$) with (blue square) and without (orange square) features of cross-talk in the 5-min averaged measurements across the rotor span of $TEC_{T3}(z_{T3})$. (For interpretation of the references to colour in this figure legend, the reader is referred to the Web version of this article.)

closely positioned ADCPs, demonstrating that two ADCPs placed 45 m apart can still provide valuable measurements, despite the challenges of interference (a consequence of not adhering to IEC 62600-200). For the first time, interference throughout the ReDAPT campaign was identified and quantified, revealing its significant impact on AEP estimates. The interference was most pronounced between 10 and 40 m from the seabed, affecting current velocities in the crucial range of 1–3 m/s for tidal energy applications.

Despite the interference, approximately 80 % of the data collected was valid and sufficient for accurate power performance assessment. This suggests that positioning two ADCPs 45 m apart on the seabed is viable for effective vertical profiling at a depth of 45 m. However, the interference introduced a bias in PWRA velocity calculations, leading to up to an 8 % distortion in velocities relevant to turbine operation.

To address this challenge, a method was developed to remove data anomalies with 90 % accuracy, resulting in only a 7 % variation in estimated AEP. This study underscores the importance of effective interference management and robust data cleaning techniques to ensure reliable turbine performance assessment and energy production estimates. These findings provide valuable insights for future research and practical applications, emphasising the need for accurate data in the context of tidal energy and other marine environments.

Against the backdrop of potential uncertainties, our findings highlight the resilience of the deployed ADCPs in capturing valid data for a PPA, despite interference. However, it is essential to recognise that the interference introduced a bias in PWRA velocity calculations, leading to up to an 8 % distortion in velocities directly relevant to turbine operation. Moreover, the resultant 7 % variation in estimated AEP underscores the importance of accounting for and mitigating the effects of interference in order to ensure accurate AEP estimates. By acknowledging these potential sources of uncertainty and their implications, our study contributes to a more comprehensive understanding of the challenges and opportunities in AEP estimation under real-world environmental conditions.

Data availability

To address the objectives of this project, in-situ data was required. Data from the ReDAPT project was chosen as a rich data resource (with unique multi-sensor deployments at a tidal energy site) that was available through the ReDAPT data exchange [20].

Author contributions

Luke Evans: Conceptualisation, Methodology, Formal analysis, Investigation, Writing – original draft, revision. Ian Ashton: Supervision and writing - review. Brian Sellar: Conceptualisation, Supervision, Writing – review.

Declaration of competing interest

The authors declare that they have no known competing financial interests or personal relationships that could have appeared to influence the work reported in this paper.

Data availability

Data will be made available on request.

Acknowledgments

The author gratefully acknowledges funding support from EPSRC and NERC for the Industrial CDT in Offshore Renewable Energy (IDCORE) (EP/S023933/1) and sponsorship by EMEC.

Abbreviations The following abbreviations are used in this manuscript:

TEC	Tidal Energy Converter
ADCP	Acoustic Doppler Current Profiler
PPA	Power Performance Assessment
AEP	Annual Energy Production
EMEC	European Marine Energy Centre
FoW	Fall of Warness
ReDAPT	Reliable Data Acquisition Platform for Tidal
DE	Equivalent Diameter
QC	Quality Control
PWRA	Power Weighted Rotor Average
QARTOD	Real-Time Quality Control of Stream Flow Observations

References

[1] M. J. Kreitmair, Uncertainty Quantification in Tidal Energy Resource Assessment.

[2] R.D.I. Teledyne, Acoustic Doppler Current Profiler: Principles of Operation, a Practical Primer, 2011, p. 56. P/N 951-6069-00. 00 (January), https://www.comm-tec.com/Docs/Manuali/RDI/BBPRIME.pdf.

[3] Nortek Manuals, Signature manual: principles of operation, Tech. rep. (2018). URL, https://www.nortekgroup.com/assets/software/N3015-011-SignaturePrinciples.pdf.
[4] Nortek Manuals, The comprehensive manual for ADCPs, J. Chem. Inf. Model. 53 (9) (2019) 1689–1699, https://doi.org/10.1017/CBO9781107415324.004.
[5] R.D.I. Teledyne, ADCP Coordinate Transformation, Formulas and Calculations 00 (July), 1997, p. 26. URL, www.rdinstruments.com.
[6] R.D.I. Teledyne, RD Instruments acoustic Doppler current profilers application: note ADCP beam clearance area, Tech. rep. (2002). URL, http://www.teledynemarine.com/Documents/BrandSupport/RDINSTRUMENTS/TechnicalResources/TechnicalNotes/ChannelMaster/FSA019.PDF.
[7] M. Jourdain De Thieulloy, M. Dorward, C. Old, R. Gabl, T. Davey, D.M. Ingram, B. G. Sellar, Single-beam acoustic Doppler profiler and co-located acoustic Doppler velocimeter flow velocity data, MD: Data 5 (3) (2020) 1–11, https://doi.org/10.3390/data5030061.
[8] J. Mullison, D. Symonds, ADCP Deployments Near Offshore Structures, Oceans Conference Record (IEEE)doi:10.1109/OCEANS.2007.4449258.
[9] R.D.I. Teledyne, A note on the depth of sidelobe contamination in acoustic Doppler current profiles, J. Atmos. Ocean. Technol. 00 (July) (2022) 31–35, https://doi.org/10.1175/jtech-d-21-0075.1.
[10] International Electrotechnical Commission (IEC), PD IEC/TS 62600-200 : 2013 BSI Standards Publication Marine Energy — Wave , Tidal and Other Water Current Converters Energy Converters — Power Performance.
[11] B. Sellar, D.R. Sutherland, Tidal energy site characterisation at the fall of warness , EMEC , UK energy technologies institute (ETI) ReDAPT MA1001 (MD3.8 release v4.0), Tech. rep. (2016) available at: http://redapt.eng.ed.ac.uk.
[12] L. Evans, I. Ashton, B. Sellar, Tidal turbine power performance assessments following IEC TS 62600-200 using measured and modelled power outputs, Renew. Energy 212 (2023) 138–150, https://doi.org/10.1016/j.renene.2023.05.031. URL, https://linkinghub.elsevier.com/retrieve/pii/S0960148123006547.
[13] L. Evans, I. Ashton, B.G. Sellar, Impact on energy yield of varying turbine designs under conditions of misalignment to the current flow, Energies 16 (9) (2023) 3923, https://doi.org/10.3390/en16093923. URL, https://www.mdpi.com/1996-1073/16/9/3923.
[14] J. Mcnaughton, R. Sinclair, B. Sellar, Measuring and modelling the power curve of a commercial-scale tidal turbine, Proceedings of the 11th European Wave and Tidal Energy Conference (October). doi:10.1017/CBO9781107415324.004. URL https://www.researchgate.net/publication/282327696.
[15] Integrated Ocean Observing System (IOOS), Manual for Real-Time Quality Control of Stream Flow Observations (QARTOD) v2.1 (July). doi:10.25923/sqe9-e310.
[16] Maritime, C. Agency, Guide to using the CHP Bathy Atlas. URL https://assets.publishing.service.gov.uk/government/uploads/system/uploads/attachment_data/file/296198/chp_bathy_atlas_guide.pdf.
[17] I. Afgan, J. McNaughton, S. Rolfo, D.D. Apsley, T. Stallard, P. Stansby, Turbulent flow and loading on a tidal stream turbine by LES and RANS, Int. J. Heat Fluid Flow 43 (2013) 96–108, https://doi.org/10.1016/j.ijheatfluidflow.2013.03.010.
[18] M. Lewis, J. McNaughton, C. Márquez-Dominguez, G. Todeschini, M. Togneri, I. Masters, M. Allmark, T. Stallard, S. Neill, A. Goward-Brown, P. Robins, Power variability of tidal-stream energy and implications for electricity supply, Energy 183 (2019) 1061–1074, https://doi.org/10.1016/j.energy.2019.06.181.
[19] RealTide Bureau Veritas, Advanced monitoring, simulation and control of tidal devices in unsteady, highly turbulent realistic tide environments, H2020 Programme for Research and Innovation 727689 (2019) 1–45. URL, https://www.realtide.eu/.
[20] B. Sellar, C. Old, D. Ingram, Dataset: field-measurements aligned to the implementation of a tidal energy converter's power performance assessment (IEC 62600-200 PPA Type B). https://doi.org/10.3390/en11010176, 2022.

Correspond author: Luke Evans will handle correspondence at all stages of refereeing and publication, also post-publication.

Chapter 12

Appendix for Chapter 7

12.1 Tidal turbine power performance assessments following IEC TS 62600-200 using measured and modelled power outputs

Abstract: Demonstrating power performance in real conditions is vital for verifying tidal turbine design. The International Electrotechnical Commission's Technical Specification IEC TS 62600-200 provides guidance for tidal developers to evaluate machine performance. This study evaluates the performance of the operational 1 MW DEEP-Gen IV commercial-scale tidal turbine deployed during the ReDAPT project at the European Marine Energy Centre's tidal test site in Orkney, Scotland. IEC TS 62600-200 states that the power performance should be measured relative to two independently located current profilers deployed in one of two orientations; 'in-line' (preferred) or 'adjacent' (least preferred), relative to the turbine. Two measurement campaigns are used to assess the impact of instrument placement on the measured power curve and annual energy production (AEP). The ambient current flow and vertical profile form differed at each current profiler location (due to topography and bathymetry), leading to AEP variability. The results reinforce the IEC TS preferred orientation for instrument placement, with inline measurements showing smaller variation in AEP estimates compared with adjacent measurements. An additional analysis assesses the sensitivity of AEP estimates on the vertical alignment of the flow profiles with rotor positioning. For this we consider three turbine scenarios: the DEEP-Gen IV and two modelled turbine rotors occupying different regions in the water column. Results show that for regions of high vertical shear, AEP estimates can be misrepresented by up to 5.5% under an imposed vertical misalignment of 2 m. This work has quantified, at this site, the variation in AEP estimates from different flow measurement campaigns informed by IEC TS 62600-200 and has shown the need to ensure good vertical alignment between measurements and turbine rotor positioning [361].

Keywords: Acoustic Doppler profiler; Power performance assessment; Power curve; Tidal stream energy; Tidal turbine; ReDAPT; Performance uncertainty; Energy yield; IEC TS 62600-200

ELSEVIER Renewable Energy Paper, Follow the link: Tidal turbine power performance assessments following IEC TS 62600-200 using measured and modelled power outputs

Renewable Energy 212 (2023) 138–150

Contents lists available at ScienceDirect

Renewable Energy

journal homepage: www.elsevier.com/locate/renene

Tidal turbine power performance assessments following IEC TS 62600-200 using measured and modelled power outputs

Luke Evans [a,b,*], Ian Ashton [c], Brian Sellar [d]

[a] EPSRC and NERC Centre for Doctoral Training in Offshore Renewable Energy (IDCORE), The University of Edinburgh, Exeter and Strathclyde, Grant Institute Kings Buildings, W Mains Rd, Edinburgh EH9 3JW, UK
[b] European Marine Energy Centre (EMEC), Research Engineer, The Charles Clouston Building ORIC, Back Rd, Stromness KW16 3AW, Orkney, UK
[c] University of Exeter, College of Engineering Mathematics and Physical Sciences, Penryn, Cornwall, UK
[d] The University of Edinburgh (UoE), School of Engineering, Edinburgh, UK

ARTICLE INFO

Keywords:
Acoustic Doppler profiler
Power performance assessment
Power curve
Tidal stream energy
Tidal turbine
ReDAPT
Performance uncertainty
Energy yield
IEC TS 62600-200

ABSTRACT

Demonstrating power performance in real conditions is vital for verifying tidal turbine design. The International Electrotechnical Commission's Technical Specification IEC TS 62600-200 provides guidance for tidal developers to evaluate machine performance. This study evaluates the performance of the operational 1 MW DEEP-Gen IV commercial-scale tidal turbine deployed during the ReDAPT project at the European Marine Energy Centre's tidal test site in Orkney, Scotland. IEC TS 62600-200 states that the power performance should be measured relative to two independently located current profilers deployed in one of two orientations; 'in-line' (preferred) or 'adjacent' (least preferred), relative to the turbine. Two measurement campaigns are used to assess the impact of instrument placement on the measured power curve and annual energy production (AEP). The ambient current flow and vertical profile form differed at each current profiler location (due to topography and bathymetry), leading to AEP variability. The results reinforce the IEC TS preferred orientation for instrument placement, with inline measurements showing smaller variation in AEP estimates compared with adjacent measurements. An additional analysis assesses the sensitivity of AEP estimates on the vertical alignment of the flow profiles with rotor positioning. For this we consider three turbine scenarios: the DEEP-Gen IV and two modelled turbine rotors occupying different regions in the water column. Results show that for regions of high vertical shear, AEP estimates can be misrepresented by up to 5.5% under an imposed vertical misalignment of 2 m. This work has quantified, at this site, the variation in AEP estimates from different flow measurement campaigns informed by IEC TS 62600-200 and has shown the need to ensure good vertical alignment between measurements and turbine rotor positioning.

1. Introduction

Tidal turbine technology is emerging, producing electricity using a renewable and predictable resource. The evaluation of the performance of the tidal turbine in real conditions is challenging and a key factor for the development of this industry to accelerate the commercialisation of current and tidal turbines [1]. The power performance assessment procedure has been described by the International Electrotechnical Commission (IEC) Technical Specification (TS) 62600-200, *"Electricity producing tidal energy converter - power performance assessment"* [2] issued in 2013. However, due to the limited number of tidal energy converters installed on site and producing electricity to the grid, the application of the technical specification by industrials and certification bodies remains limited. Large-scale deployments have occurred in the UK since 2003 [3–7], Northern Ireland in 2009 [8], and France since 2015 [1,9].

The power performance assessment (PPA) of a tidal turbine is a means of relating the current inflow conditions to the output power of the device, leading to the development of a measured power curve. Typically this procedure is undertaken as a key step in achieving type certification of the tidal energy converter (TEC) [4], providing a basis to guarantee the power performance of the device to interested parties, e.g. customers, investors and insurers. Another reason for measuring the power curve is to validate the tools used by turbine designers. Only a few studies have compared theoretical predictions of tidal turbine performance with full-scale measurements, e.g. ReDAPT 2010–2015 [10,11] Deltastreams 400 kW tested in 2015 [4], and Oceanflow

* Correspondence to: 3 Sunnybank drive, Stromness, Orkney KW16 3HS, UK.
E-mail address: (L. Evans).

https://doi.org/10.1016/j.renene.2023.05.031
Received 21 February 2022; Received in revised form 29 April 2023; Accepted 4 May 2023
Available online 12 May 2023
0960-1481/© 2023 The Author(s). Published by Elsevier Ltd. This is an open access article under the CC BY license (http://creativecommons.org/licenses/by/4.0/).

Nomenclature

i	Index related to velocity bin
j	Index related to time stamp
k	Index related to current at the depth bin
L	Number of samples in the defined averaging period
n	Index related to data point
S	Number of depth bins across projected area of TEC
z	height from the seabed [m]
$\bar{P}_i$	Mean calculated TEC power in velocity bin i
$\bar{U}$	Mean PWRA velocity, m s^{-1}
$\bar{u}$	Mean velocity, m s^{-1}
$\hat{U}$	Instantaneous PWRA velocity, m s^{-1}
A	Type-A configuration, instrument location, $A1$, $A2$ and $A3$
A_k	Depth bin over the swept area of the TEC, m^2
B	Type-B configuration, instrument location, $B1$, $B2$
C_1	Rotor-Attached instrument
c_s	Speed of sound, m s^{-1}
f_i	Proportion of time during an average year for which the mean current velocity occupies a value within velocity bin i
N_B	Total number of velocity bins in the power curve
U	Mean velocity, m s^{-1}
u	Velocity magnitude, m s^{-1}
z	Height above seabed, m

Energy's 1:10th scale Evopod model [12]. In addition to design verification, monitoring the performance will provide insights on design considerations – machine optimisation and performance deterioration – throughout the lifetime of the device [13,14].

The Reliable Data Acquisition Platform for Tidal (ReDAPT) project commissioned in 2011 provided an extensive amount of operational performance of a 1 MW – Alstom DEEP-Gen IV – full-scale tidal turbine [14,15]. The project objectives were to increase public and industry confidence in tidal turbine technologies by providing a wide range of environmental and performance information [14]. The DEEP-Gen IV performance was evaluated against guidelines published by the IEC TS 62600-200 over a series of deployments at the EMEC full-scale grid-connected tidal test site. This tidal test site has highly energetic tidal currents where the current narrows between the island of Eday and Muckle Green Holm, a small outcrop southwest of the island. The site is depicted in Fig. 1a [10].

The IEC TS 62600-200 [2] requires current velocities to be measured with an Acoustic Doppler Current Profiler (ADCP) during the power performance assessment. Among many configurations, the most common current profiler used in the tidal industry is a diverging beam ADCP in pairs of opposing beams. The position of instruments is to be placed at a large enough distance so that the flow is undisturbed from the operating TEC but not too far to ensure a true representation of the flow characteristics around the TEC location is observed. The position of these current profilers is clearly defined in the technical specification, and the initial influence of these positions has been analysed in Ref. [15]. It recommended further analysis to fully understand the impact of ADCP placement on the power curve.

The current profiler placement is based on a function of the diameter equivalent (D_E) relevant to the proposed TEC. This includes the preferred in-line configuration, which requires the current profiler to be placed between 2 D_E and 5 D_E upstream and downstream of the turbine, and within $\frac{1}{2}D_E$ of the rotor extraction plane centreline laterally, refer back to Fig. 1c. The other option is the adjacent configuration which requires the sensors to be placed between 1 D_E and 2 D_E towards the starboard and port of the turbine extraction plane, and within $\frac{1}{2}D_E$ of the rotor centreline laterally. These guidelines become challenging for turbines with smaller rotor diameters, where the instruments would be placed closer to the TEC, thus potentially observing the effects of pushback flow from the TEC. In extreme cases (5 m rotor diameter), the ADCP location could be close enough to experience interference from reflections of the tidal device. The placement is further complicated if the turbine is on a floating platform subject to sway and surge effects. These motions would reduce the size of the acceptable area in which the current profiler can be placed.

A limited number of studies have looked at the spatial variation in energetic tidal flow conditions using multiple instruments [7,14,16,17]. During the testing of the 1 MW DEEP-Gen IV [15], multiple ADCP campaigns were carried out over two years to measure performance. The results of the campaigns with instruments placed in-line with the TEC suggested that the location of these ADCPs had little significance on the measured performance, even in cases where the ADCP was located outside of the standardised deployment areas [2,14]. However, the deployment of the DEEP-Gen IV found a substantial spatial variation in the cross-stream direction at the Fall of Warness (FoW) [18]. Torrens-Spence [19] conducted a study in the Strangford Narrows (east coast of Northern Ireland), where two instruments were synchronised and attached to two different barges separated by 500 m. The results indicated that the flow characteristics vary significantly due to a rocky outcrop, and flow at each instrument location varied substantially between flood and ebb tides [19], which agrees with work carried out by [18].

Multiple instrument deployments are becoming more common as we aim to gather more in-situ data at tidal test sites to understand the flow characteristics better. In addition, TEC-mounted instruments are being implemented to analyse their capabilities for performance monitoring, with comparisons against traditional seabed-placed instruments considered as the reference. Findings from unique measurement campaigns with standardised placed instruments and an operating full-scale commercial TEC can help provide insights and re-inform standardised methods [4,10,15,20].

Many TEC designs exist, all having different characteristics (e.g. rated power and rated velocity) and deployed at different depths (z) along the water column. For turbines that float, the motion from mooring cables, in addition to the flow velocity in the upper regions of the water column, adds further complexity to carrying out a power performance assessment. The floating TEC concept is likely exposed to further tidal flow variation due to wind-induced flow and wave–current interaction, and measured flow data is frequently removed close to the surface. This can impact the calculation of the power-weighted rotor average (PWRA) velocity, recommended in the IEC TS 62600-200. Furthermore, capturing the orientation and location of the current profiler become difficult once it is lowered into the water. Increasing the accuracy of sensor deployment position and orientation comes with additional costs, and can involve the use of further dedicated sub-systems and complex installation techniques. As such, quantifying the impact of spatial variability and verifying the use of TEC-mounted measurements can help expand the acceptable PPA instrument configurations.

To date, the IEC TS 62600-200 does not recognise TEC-mounted instruments that profile in the horizontal plane. Harrold et al. [4] compared recorded power measurements with theoretically predicted measurements from Tidal Bladed. These predictions were compared using measurements from the rotor-attached single-beam acoustic Doppler

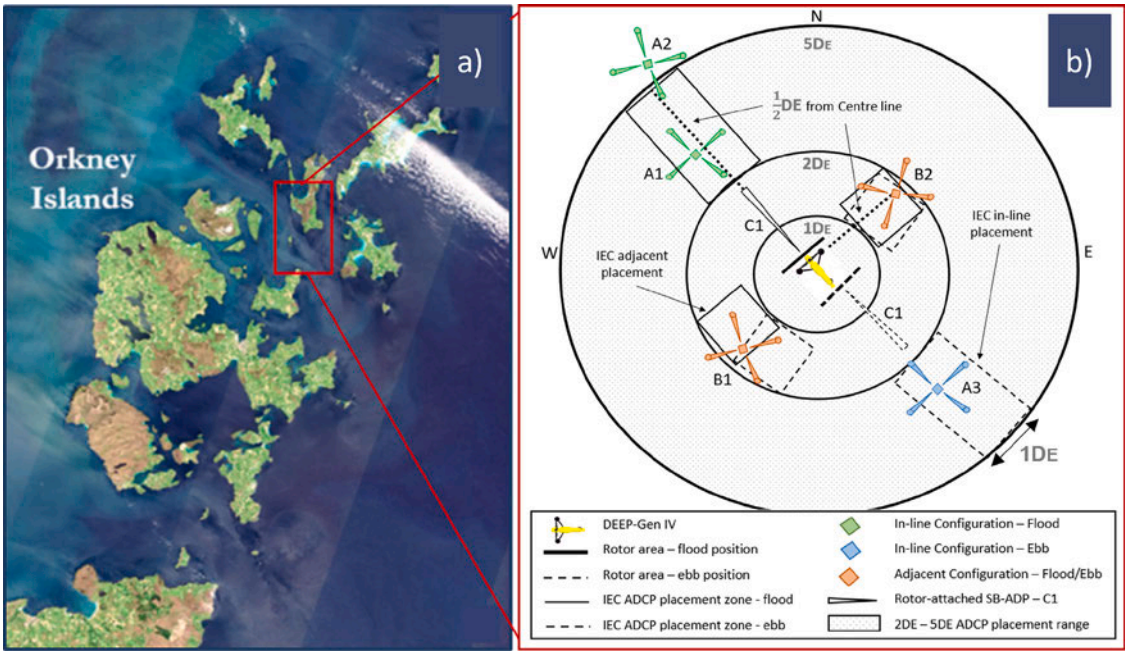

Fig. 1. Map showing (a) the Orkney Islands, Scotland, and the location of the European Marine Energy Centre (EMEC) tidal energy test site (red rectangle). The plan view of the measurement campaign is presented in (b), where the IEC TS 62600-200 highly influences the instrument placement and is placed relative to the DEEP-Gen IV [2]. A1, A2, A3, B1 and B2 are seabed current profilers, and C1 is a rotor-attached current profiler.

profiler (SB-ADP) and a seabed-mounted ADCP. The observations found that the TEC-mounted instrument corresponded closely to theoretical predictions from the industry standard tidal turbine modelling software Tidal Bladed, which provides accurate numerical load and performance estimates. However, the SB-ADP consistently measured weaker flows due to a spatial variation between instrument locations [4]. Instruments mounted on TECs limit the requirement for seabed ADCPs for power performance, thus providing flexibility for PPA and reducing additional costs of offshore deployments.

This paper aims to highlight the effect of ADCP placement (per the IEC TS 62600-200) on the power performance assessment of an operational 1 MW tidal turbine. We investigate the variation in velocity based on in-situ data obtained from two measurement campaigns – five separate current profilers – deployed at the FoW (Orkney, Scotland). The paper is structured as follows: Section 2 provides a test overview of the installation site, tidal turbine, the suite of instruments relative to this study, and the post-processing of the in-situ measurements; Section 3 reports on the key results obtained for the difference between an inter-instrument comparison (3.2), spatial variation in velocity (3.3) and the impact of instrument placement on the measured power curve 3.4. In addition, consideration of the vertical misalignment between the instrument measurement and the TEC hub-height and the effect this has on the estimated AEP is presented in (3.5). Section 4 discusses these key findings in the context of existing best practices; while Section 5 summarises this work to form a conclusion.

2. Test overview

2.1. Deployment site conditions

All the instruments and the TEC were deployed in Berth 2 at the FoW, at a depth of ≈ 43–46 m, see Fig. 1a for a high-level location of the tidal test site and 1b for a plan view of the measurement campaigns. The bathymetry of a TEC test site must be surveyed to ensure that it is free from obstacles and topography that could affect the performance of the TEC. Therefore, a rectangle box (10 D_E × 20 D_E) was surveyed for the PPA as per the IEC TS 62600-200, see Fig. 2a, b.

Table 1
Key parameters of the DEEP-Gen IV TEC.

Developer	Units	Alstom
Type	–	3-Blade HATEC
Foundation	–	Piled tripod
Production year	–	2011
Distance above seabed	m	18 (hub-height)
Blade radius	m	9
Projected capture area	m^2	256.74
Rated output power	MW	1
Cut-in	m s^{-1}	1
Rated speed	m s^{-1}	2.7
Nominal rotor speed	rpm	13.78
Maximum rotor speed	rpm	19.29

The depth within the 10 D_E × 20 D_E area ranges from 46 m northwest of the turbine, to 39 m near the east side of the area of interest. The latter is considered far enough from the turbine to create any significant disturbance in the turbine flow. The directionality and strength of typical tidal currents (from the five seabed placed instruments) at the deployment location are shown in Fig. 3.

The tidal currents at the site are predominantly bi-directional with an offset of ≈ 45° from North/South. The ebb tide is stronger at this location, reaching mean flows up to 4 m s^{-1}, whereas the flood tide reaches ≈ 3.5 m s^{-1}. The ebb tide is also much more turbulent due to the flow being disturbed by several features of the site bathymetry and local islands, which has been reported on by others [22,23].

2.2. Turbine description

The tested turbine is a 1 MW rated machine with a three-bladed, 18 m diameter, variable-pitch, horizontal-axis rotor. Other key parameters are presented in Table 1. The turbine typically yawed between flood and ebb tide (rotating during slack tides) so that the energy extraction plane is perpendicular to the established flow direction commonly refereed to as the principle flow direction. Outline turbine parameters are listed in Table 1.

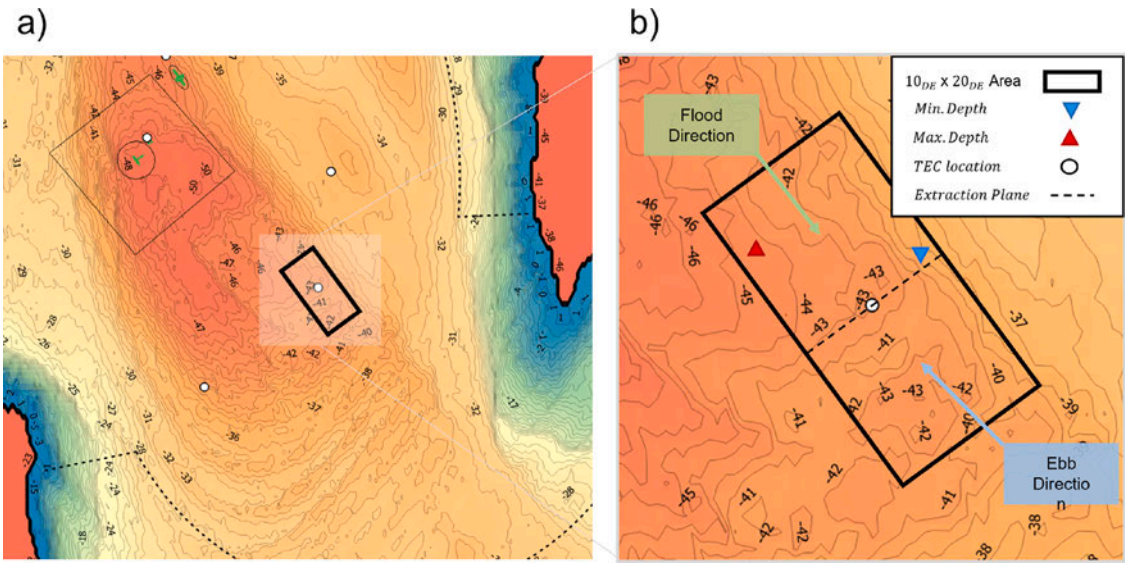

Fig. 2. Bathymetry in the vicinity of the turbine, with (a) showing the 10 D_E × 20 D_E area of interest (solid black rectangle within highlighted grey squared), and (b) a closer view at the depth around the DEEP-Gen IV. 'Contains Maritime and Coastguard Agency data © Crown Copyright' [21].

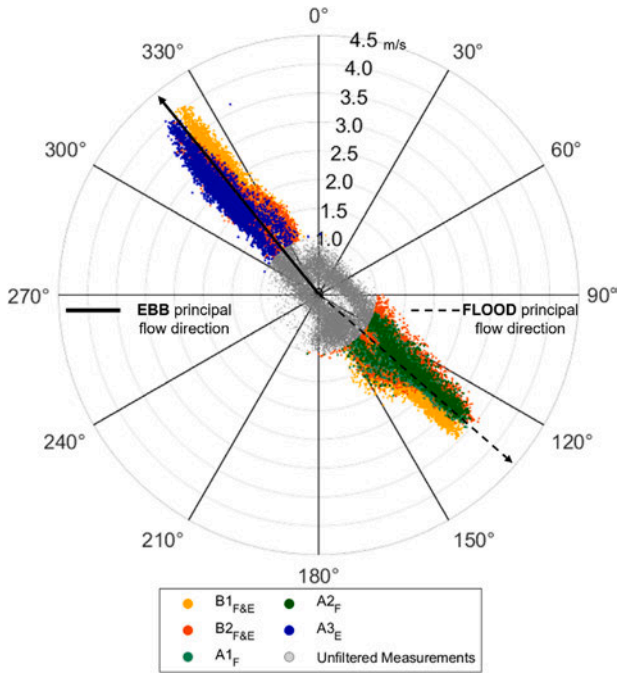

Fig. 3. Directionality and strength of the flood and ebb tidal characteristics at Fall of Warness at each instrument location used in the analysis.

Table 2
Key parameters of acoustic current Doppler profilers (ADCP) used in the flow characterisation.

Identification/s	*A*1, *A*2, *A*3 *B*1, *B*2	*C*1
Instrument	WHS	AD2CP
Manufacturer	RDI	Nortek
Acoustic frequency	600 kHz	1000 kHz
Type	ADCP	SB-ADP
Sample rate	0.5 Hz	2 Hz
Quantity	5	1
Location	Seabed	RA
No. operating beams	4	1
Bin length	1 m	0.5 m

RA = Rotor-Attached.

2.3. Instrumentation

A summary of the suite of instruments used is provided in Table 2, and their approximate locations are shown in Fig. 1c. Two measurement campaigns are considered, deployment 5 (in-line with TEC, denoted "*A*"), contains three seabed ADCPs, depicted as *A*1, *A*2, *A*3, and deployment 6 (adjacent to TEC, denoted "*B*"), contains two seabed ADCPs, *B*1 and *B*2, see Fig. 4 for a visual representation. These measurement campaigns are chosen as they are placed within the two stated zones recommended by the IEC TS, with the addition of an extra instrument placed in-line but just outside the IEC TS target placement zone.

The single-beam flow profiler (SB-ADP) was used throughout both deployments, attached to the Alstom DEEP-Gen IV's rotor (*C*1). This data set allows comparison between the two IEC TS recommended orientations to a TEC-proximal location. Orientation *A* had two ADCPs (*A*1, *A*2) measuring concurrently at locations upstream of the TEC (on a flood tide), separated by 45 m. The SB-ADP measurements were compared with the seabed instruments to assess the capabilities for performance assessments. Data collected from the two deployments (*A*&*B*) included periods of spring and neap tides. The data used in the analysis for type *A* and *B* are ≈ 15 and ≈ 57 days long, respectively. Table 3 provides relevant measurement campaign information.

The location of the ADCPs was known to the nearest metre based on their UTM coordinates, see Table 3. Using a bathymetric map in conjunction with each ADCP pressure data, their depths relative to the TEC were estimated to the nearest metre (as the instruments have a resolution of 1 m), see Fig. 1b. Velocity variation along the depth bins was analysed.

A 2° tilt on the TEC base led to a variation in depth which altered the horizontal bin ranges of *C*1. At 12 m, a maximum difference of 0.42 m was found. In addition to the TEC tilt, the turbine was manually rotated about its yaw axis to match the incident flow direction, but this process was inaccurate. As *C*1 faced the direction of the TEC yaw angle, it was often not aligned to the principal flow direction, thus measuring a minor component of the current velocity.

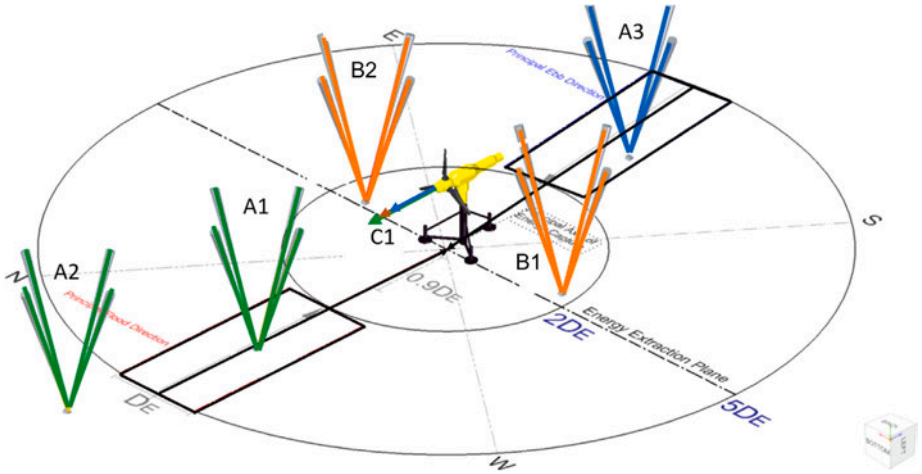

Fig. 4. Instrument placements for deployments 5 and 6 showing distance (DE) from the DEEP-Gen IV TEC, relative to North. Generated data-sets from Deployment 5 are identified as $A1$, $A2$ and $A3$ targeting ambient conditions on the flood (green beam) and ebb (blue beam) tides, respectively. Deployment 6 featured $B1$, $B2$ data-sets (orange beam) targeting ambient flows on both the flood and ebb tide. The rotor-attached (hence yawing with the TEC) single-beam instrument, $C1$, measured both flood and ebb tides.

Table 3
Turbine-proximal deployments of ADCPs showing unique campaign ID, date deployed (date format yyyy-mm-dd) and deployment duration. The coordinate system is WGS84.

ADCP ID	Seabed Campaign ID	Deployed	Recovered	Days	LocationNorth [°]	LocationWest [°]
A1	ADCP01_NW_Dep5	2014-06-22	2014-08-05	41	59.13726	2.80651
A2	ADCP02_NW_Dep5	2014-07-07	2014-08-16	40	59.13764	2.80686
A3	ADCP03_SE_Dep5	2014-07-07	2014-08-17	41	59.13643	2.80529
B1	ADCPTD7_01_Dep6	2014-09-17	2014-12-11	85	59.13705	2.80526
B2	ADCPTD7_02_Dep6	2014-09-17	2014-11-27	71	59.13667	2.80641
C1	SBD01	2014-06-23	2014-12-21	85	59.13685	2.80583

2.4. Instrument data processing

2.4.1. Data quality control (QC)

Data quality control (QC) was implemented on the ADCP and SB-ADP data. Recommended QC measures were based an internationally-recognised guideline, QARTOD, and instrument manufacturer recommendations, [24–26]. First, an excessive tilt threshold of <−15° and >15° was applied to both pitch and roll data. Secondly, a speed of sound (SoS) threshold of <1470 m s^{-1} and >1570 m s^{-1} was applied. The signal-to-noise (SNR) measures the signal's amplitude over the background noise level. Amplitude thresholds have been chosen to reject data from beyond the normal operating range of each instrument: a threshold of < 64 dB was applied for SNR based QC for the ADCPs. Lastly, a signal correlation threshold was applied. Values which correspond to a correlation <70% were flagged. A de-spiking algorithm was applied to detect velocity outliers, which flagged all values with a change of 1 m s^{-1} between consecutive samples. Data points that were flagged in these QC steps were removed.

During the processing stage, shear profiles were plotted for all five seabed-placed ADCPs. Data quality was found to deteriorate close to the sea surface. Therefore the top 6% of current depth bins were removed as recommended by RDI [25], for a 20° ADCP slant angle.

The SB-ADP measured the current flow along the beam with a manually set speed of sound value of 1470 m s^{-1} and required an SoS correction to match the seabed-placed ADCP, specifically $A1$ for the in-line orientation and B_1 for the adjacent orientation. This was accounted for during data processing via scaling, as per Eq. (1):

$$u_{C1} = u_{C1_{(org)}} \cdot \frac{S_{A1}}{S_{C1}} \tag{1}$$

where u_{C1} is the corrected instantaneous velocity, $u_{C1(org)}$ is the uncorrected instantaneous velocity measured by C_1, S_{A1} is the instantaneous SoS reported by the ADCP, S_{C1} is the manually set SoS for the single-beam ADP.

The difference in the measured current velocity between u_{C1} and U_{A1} due to TEC misalignment to the principle flow direction was considered negligible at less than 0.25%. In addition, the velocity measured along the SB_{C1} beam, with the horizontal axis tilt considered, was equivalent to the cosine of 2° and was also considered negligible at less than 0.1%.

2.4.2. Turbine mounted single beam profiler

The SB-ADP data was used to monitor the rotor approach flow using the approach carried out by [4,27]. Minimum variation in the longitudinal flow velocity was observed between ≈ 10–12 m for $C1$. Flow deceleration occurs closer to the TEC as the flow expands around the rotor, and at distances greater than 17 m severely decreased flow is observed. This is directly related to the instrument range capabilities, where the SNR increases. The region of highest data reliability was between 10–12 m, therefore, u_{C1} was spatially averaged, hereafter referred to as $\bar{u}_{C1}$, and representing the longitudinal velocity reference for the TEC mounted instrument ($C1$, refer to Fig. 4).

2.4.3. Power-weighted rotor average (PWRA) velocity

The instantaneous power-weighted rotor average (PWRA) velocity was calculated for the five seabed-placed ADCPs. This was achieved by averaging the velocity measurements from the 19 depth bins corresponding to the rotor plane. Greater weighting was applied to the bins closest to the rotor hub centre, where the swept cross-section area is the largest, as per Eq. (2):

$$\hat{U}_{i,j,n} = \left[\frac{1}{A}\Sigma_{k=1}^{S} u_{i,j,k,n}^{3} A_k\right]^{\frac{1}{3}} \tag{2}$$

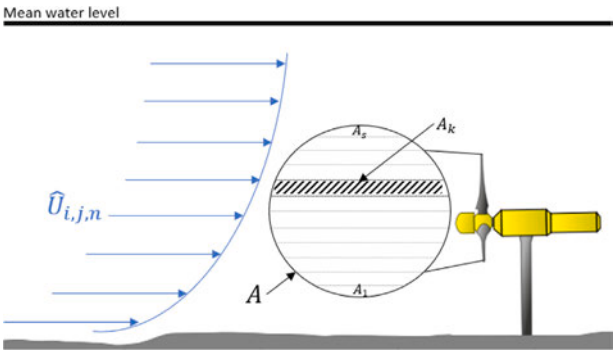

Fig. 5. Power weighted rotor average velocity example.
Source: Image adapted from [2,29].

where $\hat{U}_{i,j,n}$, is the instantaneous PWRA velocity, A_k is a depth bin over the swept area of the TEC rotor, $u^3_{i,j,k,n}$ is the velocity in the relative bin, and i, j, k, are index numbers for the velocity bin (increments of 0.1 m s^{-1}), time instant of the measurement and the current depth bin across the projected capture area, respectively, see Fig. 5 for visual representation. The in-situ measurements were then averaged by an integer divisor of 10 minutes, in this case, 5 minutes. Where $\hat{U}_{i,j,n}$ should be averaged to produce the mean PWRA velocity, as shown in Eq. (3) below:

$$\bar{U}_{i,n} = [\frac{1}{L}\Sigma_{j=1}^{L}\hat{U}^3_{i,j,n}]^{\frac{1}{3}} \quad (3)$$

where L is the number of samples in the defined averaging period, and $\bar{U}_{i,n}$ is the mean PWRA velocity in velocity bin i for data point n in m s^{-1}. The method of calculating the PWRA velocity can lead to inaccuracies if the wrong reference depth is chosen. This is not addressed in the current work. However, a detailed power curve of DEEP-Gen IV during the October 2013 campaign [28] showed that this accounts for approximately 2% uncertainty in the velocity. The current velocity data exceeded 15 days of measurements, where each velocity bin increment of 0.1 m s^{-1}, i, contained at least 30 minutes of in-situ data (as per IEC TS 62600-200).

2.4.4. DEEP-gen IV power data

Power measurements were available and used in this analysis for the DEEP-Gen IV (TEC case 2). The two deployment campaigns, A and B, featured periods with no generated power from the DEEP-Gen IV and periods of inconsistent power generation. The time-matched current velocities for these periods where the turbine produced no power were removed from the analysis.

Table 4 illustrates the inter-instrument comparison and the number of 5-minute samples available after QC and filtering the data for periods of no power generated by the DEEP-Gen IV. Instruments used for the flood tide comparison are as follows: $A1$, $A2$, and $C1$ for the in-line measurements, and $B1$, $B2$, and $C1$ for the adjacent. Instruments used for the ebb tide comparison are as follows: $A3$ and $C1$ for the in-line measurements, and $B1$, $B2$, and $C1$ for the adjacent.

2.4.5. Alternate turbine types

In order to assess the impact of vertical misalignment on energy production, two further turbine types are introduced, labelled case 1 and case 3, using modelled power (as opposed to measured power as was the case with the DEEP-Gen IV). The turbines used for case 1 and case 3 are based on deployed variants of horizontal axis tidal turbines that occupy different regions in the water column. They are informed by the RealTide project [30], with basic parameters provided in Table 5. Where z relates to the hub-height of each turbine above the seabed, and C-S is the cross-sectional area of their rotors. Since the measurements used for this case study focus on the instruments

Table 4
Inter-instrument comparison table showing number of available 5-minute ensembles, where colours correspond directly to instruments depicted in Fig. 4. The light grey shaded region corresponds to flood conditions with data relating to ebb shown diagonally opposite.

ADCP ID	A1	A2	A3	B1	B2	C1
A1	x	x	x	x	x	x
A2	2172	x	x	x	x	x
A3	x	x	x	x	x	4579
B1	x	x	x	x	8458	8458
B2	x	x	x	9646	x	8458
C1	2172	2172	x	9646	9646	x

Ebb Conditions

Flood Conditions

Table 5
Generic types of tidal energy converter parameters.

TEC characteristics	Units	Case 1	Case 2	Case 3
z	m	12	18	34
Rotor Diameter	m	12	18	20
C-S Area	m^2	113.1	254.5	314.2
Rated Power	MW	0.1	1	2

placed adjacent (B) to the DEEP-Gen IV location, the turbine does not affect the measurements collected. Therefore, the two additional turbines will be "in theory" at the same location as the DEEP-Gen IV. The impact of vertical alignment between the instrument and TEC hub-height can then be assessed for three turbines which experience different variations of shear in the water column.

The 5-minute time-average velocities U_{B1} and U_{B2}, were used to measure vertical misalignment error between the ADCP depth bin and the TEC rotor plane, as both instruments measured the flood and ebb tide. The current velocities taken at the hub-height of the proposed TEC concepts were used. Calculating the PWRA velocity was not possible for the floating TEC concept due to the removal of data in the upper region of the water column (refer back to Section 2.4.1). The alignment error was analysed in increments of 1 m up to ± 2 m from the hub-height.

2.4.6. Estimated annual energy production

The Annual Energy Production (AEP) estimates were derived using real world power generated from the DEEP-Gen IV, this is used in Sections 3.4 and 3.5 where the DEEP-Gen IV analysis forms case 2. The modelled power – produced from velocity measurements at locations B1 and B2 and theoretical turbine parameters – was used in Section 3.5 forming cases 1 and 3. Power data was time-integrated (using MATLAB trapezoidal method) and scaled by the ratio of measurement duration with respect to the number of days in a year, as per Eq. (4):

$$AEP = R \cdot \Sigma_{t1}^{t2}\bar{P}dt \quad (4)$$

where AEP is the expected annual energy production in MWh, R is the ratio of the number of days in a year over the duration of the campaign, $\bar{P}$ is the 5-minute averaged measured TEC power, t_1 is the index number defining the time start, t_2 is the index number of the end time interval.

For cases 1 and 3 (selected as representative of current technologies) which lack real-world data, two pre-defined power curves of rated power 0.1 MW and 2 MW were produced using Eq. (5):

$$\bar{P} = P_{rated} \cdot \left(\frac{V^2 - V_{ci}^2}{V_r^2 - V_{ci}^2}\right) \quad (5)$$

where P_{rated} is the predefined rated power, V is the velocity measurement, V_{ci} is the cut-in velocity for the proposed TEC, and V_r is the rated velocity for peak power production. In both cases power was capped at the corresponding rated power.

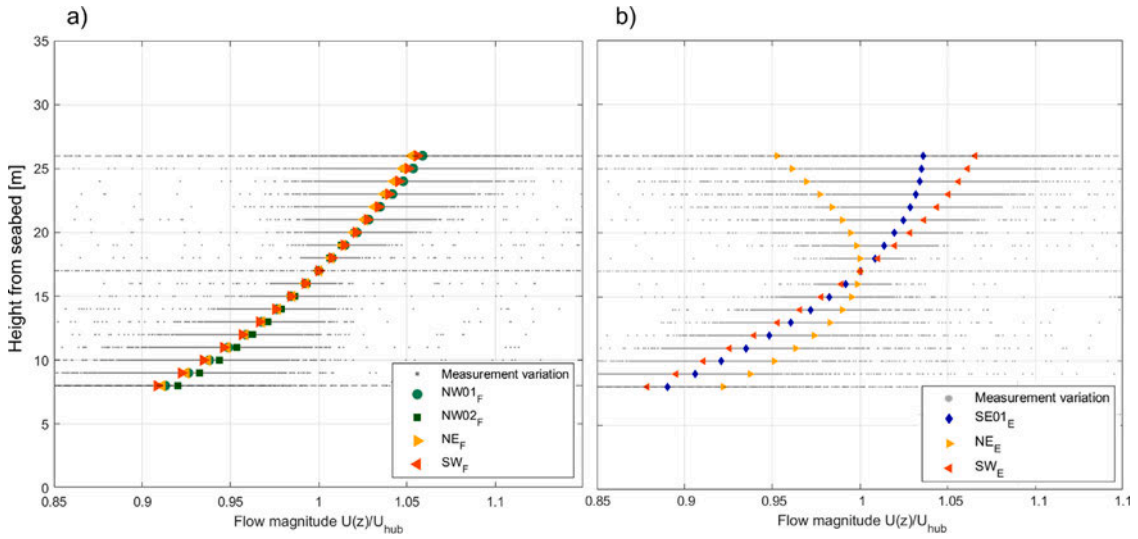

Fig. 6. Current velocity across the rotor plane for the DEEP-Gen IV, normalised by the hub-height at 18 m. The current velocity refers to the measurements captured for (a) flood tide, and (b) ebb tide. Approach adapted from Harrold et al. [4].

3. Results

3.1. Preliminary analysis of ADCPs

Five tidal ellipses were produced (refer back to Figs. 3, and 4) to show how the strength and direction of the flow vary per instrument location. As can be seen in Fig. 3 at this location the ebb tides are faster than the flood tides by ≈ 0.8 m s^{-1} and the tides are ≈ 10° off from being rectilinear. There is some disagreement in the principal flow direction amongst the ADCPs. In the flood tide, these disagree by as much as 10°, whilst the difference is closer to 5° in the ebb direction. The calculation of PWRA velocities are insensitive to flow direction since they involve velocity magnitudes. However, for other applications, e.g., turbine operation and control, directionality should be considered.

3.2. Inter-instrument comparison

The current velocity measurements at a range of heights covering the TEC rotor plane from instruments placed at locations A and B (refer back to Fig. 4) are presented in Fig. 6. Velocities were normalised by hub-height velocities (18 m above seabed for the DEEP-Gen IV TEC). These are compared against a mean velocity profile. The instruments were compared based on placement and tidal cycle. The in-line current velocity, measured by U_{A1} ($NW01_F$), and U_{A2} ($NW02_F$) varied by ≈ 0.75% at the lower bounds, and ≈ 0.35% at the upper bounds. Similarly, U_{B1} (SW_F) and U_{B2} (NE_F) differed by alike margins during the flood tide, Fig. 6a. In contrast, the ebb tide revealed a substantial variation along the rotor plane, where U_{B1} and U_{B2} record significantly different current velocities in both the most-lower bound and most-upper bound, differing by ≈ 5%, and ≈ 12% respectively. Similar velocity reductions have been found in the upper region of U_{A3}, see Fig. 6b.

Fig. 7 displays the correlation between time-matched velocities for each instrument pairing, where the in-line instruments A_1, A_2 are ≈ 45 m apart, and the adjacent instruments B_1 and B_2 are ≈ 70 m apart. The sum of square error (SSE) and the root mean squared error (RMSE) of the relationship between compared instruments is shown in Fig. 7.

The flood tide velocity measurements $\bar{U}_{A1}$, $\bar{U}_{A2}$ and $\bar{U}_{B1}$ $\bar{U}_{B2}$ show high correlation. However $\bar{U}_{B1}$ and $\bar{U}_{B2}$ contain a lot more data scatter with a larger SSE when compared with $\bar{U}_{A1}$ and $\bar{U}_{A2}$ as shown in Fig. 7a. Unlike the flood tide, the ebb tide was measured by a single ADCP, A_3. This was compared with C_1, indicating a strong correlation (with an RMSE comparable with the other in-line instruments A_1, and A_2 measuring the flood tide). However, a clear bias is present, where C_1 consistently underestimates the velocity compared with the traditional seabed-placed A_3, which is in agreement with previous work [15,27], refer to Fig. 7b. The ebb tide velocity scatter from B_1 and B_2 comparisons is also shown in Fig. 7b, with greater variation than the equivalent comparison on the flood tide. This scatter increases further at higher velocities, where B_2 measurements also trend towards slower velocities.

3.3. Spatial variation in velocity

Velocity profiles were produced to analyse how the flow changes with depth. The measurements of velocity from instruments in both configurations A and B, were split by flood and ebb tides and subdivided into velocity bins in increments of 0.3 m s^{-1}. It can be seen in Fig. 8a that the difference between U_{A1} and U_{A2} at hub-height and the speed of rated power (1 MW) is 0.5% for the instruments placed in-line measuring the flood tide. Fig. 8b shows larger differences between the equivalent measurements for the $B1$ and $B2$ pairing, at 3.1%.

The velocity measured by the rotor-attached hub-height SB-ADP, $\bar{u}_{C1}$, is shown as a filled circle. The instrument measured a reduced velocity, commonly close to ≈ 0.15 m s^{-1} slower than U_{A1}, U_{A2}, U_{B1} and U_{B2} during the flood tide.

Ebb tide data presented in Fig. 9b shows a larger discrepancy between U_{B1} and U_{B2}. Differences increase with higher velocity and height above the seabed. At the rated-power velocity of 2.7 m s^{-1} differences ranged from 2.1–19.4% from the bottom-most and top-most locations respectively of the rotor plane. $\bar{u}_{C1}$, shown as filled circles, corresponds closely with U_{B2} for the ebb tide measurements.

3.4. Power curve and AEP comparison

The velocities from each seabed ADCP and the rotor-attached SB-ADP were paired with the real-world power measurements from the DEEP-Gen IV, and then sorted into velocity bins in increments of 0.1 m s^{-1} in accordance with the IEC TS 62600-200. The mean velocity flow and power within each bin were then calculated. Fig. 10 presents the final power curves for the flood and ebb tide. The black solid line shows the power curve provided by the DEEP-Gen IV operator, Alstom [28]. The measured power curve was produced with reference to the velocity measured at C_1. This curve implies the DEEP-Gen IV produced more power under slower flow velocity conditions when

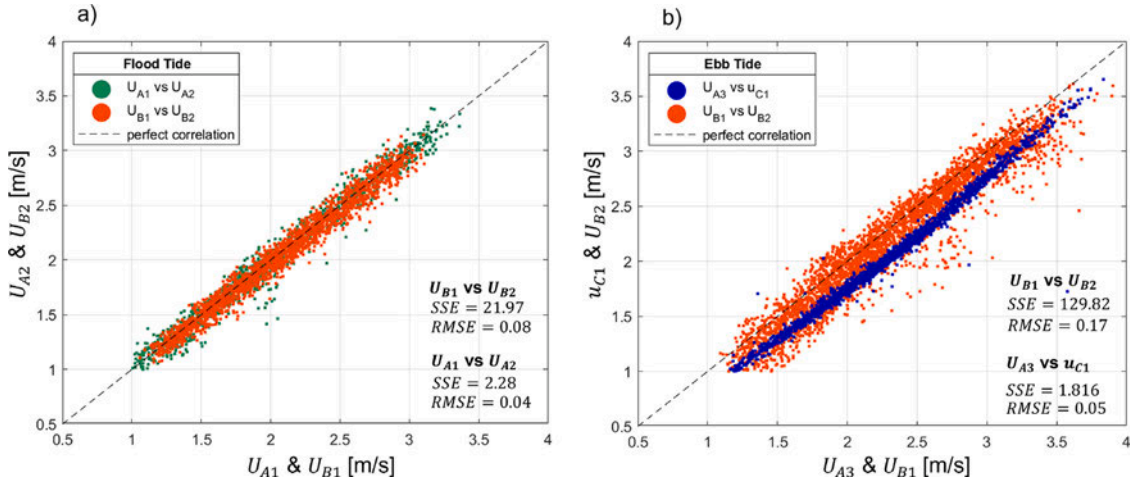

Fig. 7. (a) Inter-instrument correlation for the flood measurements, $\bar{U}_{A1}$ vs $\bar{U}_{A2}$ (green) and $\bar{U}_{B1}$ vs $\bar{U}_{B2}$ (orange). (b) Ebb tide correlation, for $\bar{U}_{A3}$ and $\bar{u}_{C1}$ (blue), and $\bar{U}_{B1}$ vs $\bar{U}_{B2}$ (orange).

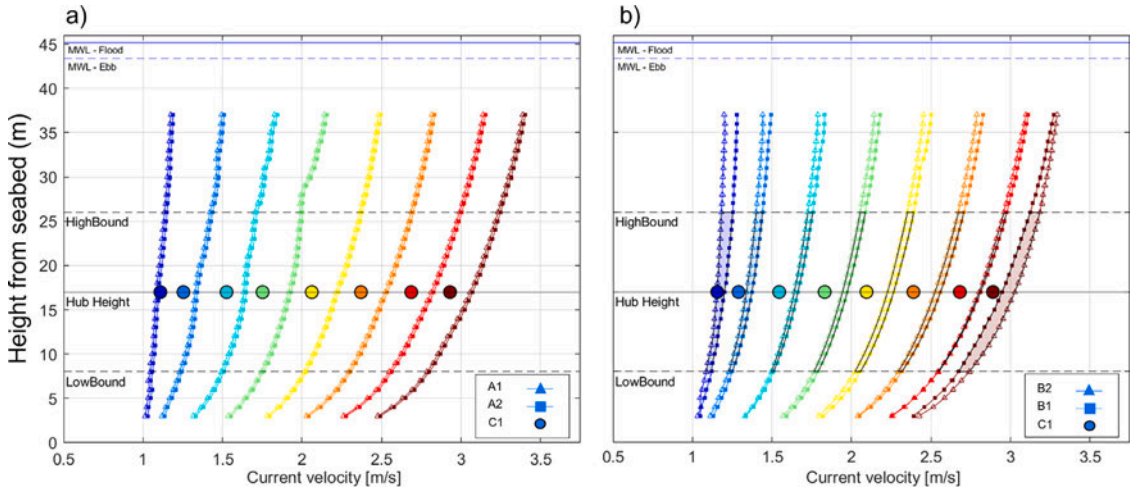

Fig. 8. Velocity depth profile for flood tide measurements for (a) in-line ADCP pair A_1 and A_2, compared against the rotor-attached instrument C_1 (filled circle marker at hub-height, 18 m). (b) Velocity measurements from the adjacent locations to the TEC B_1 and B_2, the rotor-attached SB-ADP C_1 is depicted as a filled circle at hub-height.

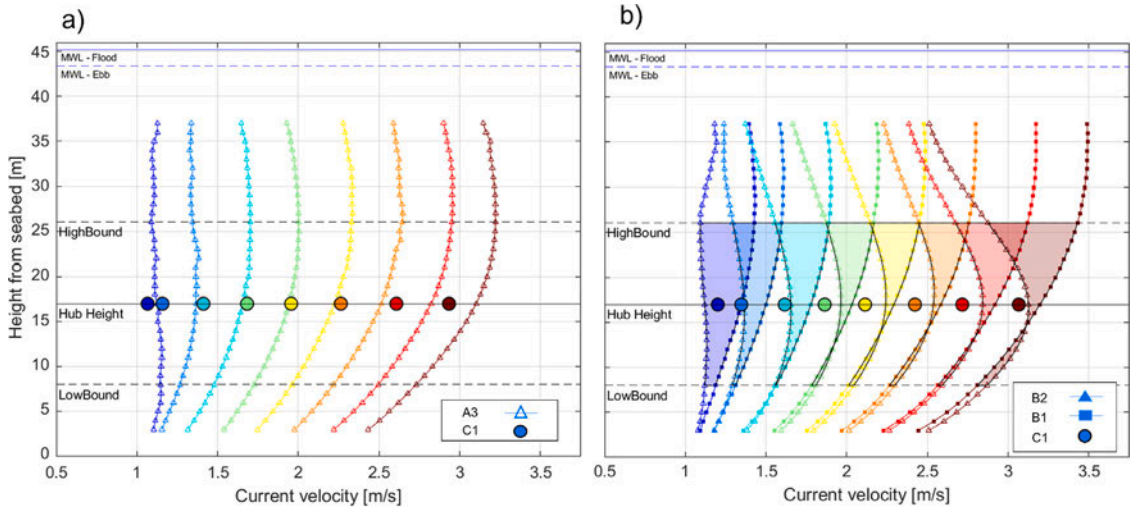

Fig. 9. Velocity depth profile for ebb tide velocity measurements for (a) in-line ADCP A_3, and SB-ADP C_1 (filled circle marker at hub-height of 18 m). (b) Velocity measurements from the adjacent locations to the TEC, B_1 and B_2, and the rotor-attached SB-ADP C_1.

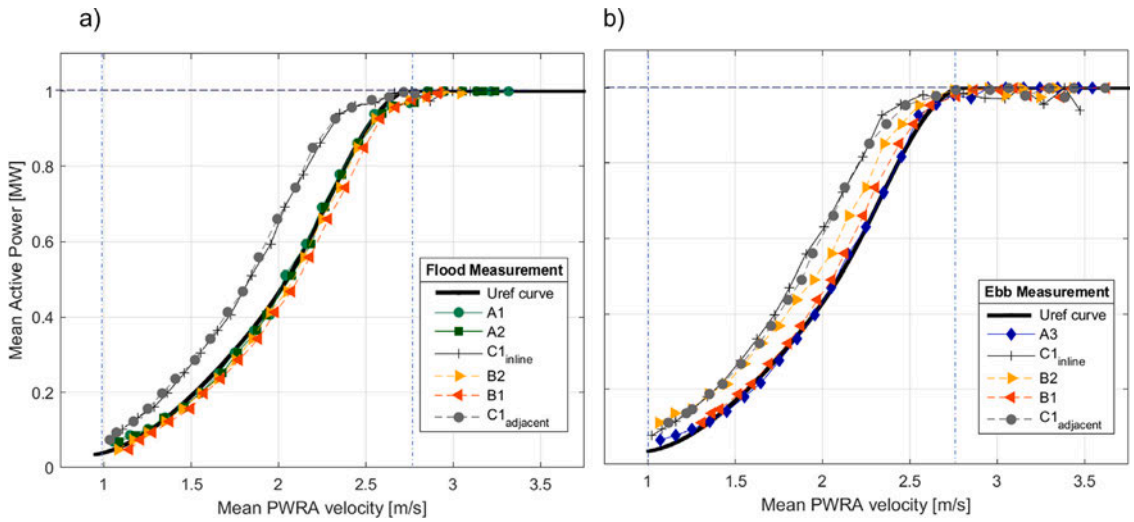

Fig. 10. The effect of ADCP placement – per IEC TS 62600-200 – on measured power curve for the averaged 5-minute velocities in increments of 0.1 m s^{-1}. (a) The flood tide measurements from the in-line ADCP pair $\bar{U}_{A1}$ and $\bar{U}_{A2}$, the adjacent pair are included $\bar{U}_{B1}$ and $\bar{U}_{B2}$. (b) The ebb tide measurements from the rotor-attached SB-ADP, $\bar{u}_{C1}$ and $\bar{U}_{A3}$, and the adjacent pair $\bar{U}_{B1}$ and $\bar{U}_{B2}$. The black line represents the published power curve of the DEEP-Gen IV [28].

compared with velocity measurements at the seabed-placed ADCP locations. However, the velocity measured by the rotor-attached SB-ADP was shown to underestimate the flow approaching the rotor (Figs. 7b and 8). Therefore, the power curve is misleading and implies the SB-ADP provides a more favourable power curve from a developers perspective. A key part of this study is to assess the impact of using ADCPs around the extremities of the IEC TS target locations. For this, the measured power curves for the flood tide measurements are shown in Fig. 10a. The mean velocity at rated power (1 MW) for ADCP pair $\bar{U}_{A1}$ and $\bar{U}_{A1}$ (approximately 3.4 D_E and 5.5 D_E from the rotor centre respectively) differ by 0.6%. Whereas, the mean velocity at rated power for ADCP pair $\bar{U}_{B1}$ and $\bar{U}_{B2}$ (located 32 m southwest and 34 m northeast of the rotor centre) differed by 1.1%.

The ADCP pair positioned in-line A_1 and A_2, measure a slightly lower velocity compared with the ADCPs positioned adjacently B_1 and B_2. From a developer perspective, this results in a seemingly more efficient power curve when a lower mean velocity, U_{A1}, is compared with the higher mean velocity, U_{B1}, for the equivalent power. Fig. 10b shows the power curves for the mean velocities measured for the ebb tide by: in-line ADCP A_3; adjacent ADCP pair B_1 and B_2; and the rotor-attached SB-ADP C_1. At the lower velocity increments (<2 m s^{-1}) there are more obvious difference between the three curves produced from $\bar{U}_{A3}$, $\bar{U}_{B1}$ and $\bar{U}_{B2}$. This is likely due to a combination of faster accelerations in this regime and a spatial variation in the measured velocity on the ebb tide. At rated power, the ebb tide curves produced by $\bar{U}_{B1}$ and $\bar{U}_{B2}$ differ by 4.3%.

In terms of the flow references measured by ADCP pairs A_1 and A_2, and B_1 and B_2, a better agreement with the predicted curve is found using the ADCPs placed in-line to the TEC. This is shown for the ebb tide power curves, where A_3 is placed in-line and closely matches the predicted curve of the DEEP-Gen IV. It is likely that these findings highlight that there are periods in which the seabed ADCPs placed adjacent do provide a good reference velocity (velocity increments < 1.5 m s^{-1}), but differences grow between ADCP pair placed in-line and ADCP pair placed adjacent as the mean velocity increases at the site.

In addition to the measured power curves generated from seabed ADCPs, the SB-ADP flow measurements are used to assess the power curve. Unlike the ADCP datasets however, there is no accounting for the vertical variation or directionality in the flow and so the SB-ADP represents a hub-height speed along the axis of rotation. Velocities for each seabed ADCP were compared against the velocity measured at C_1. The velocity differed by up to ≈ 8% when compared with ADCPs positioned in-line A_1 and A_2, and 11% when compared with ADCPs positioned adjacently B_1 and B_2.

Annual Energy Production was estimated using the pre-defined power curve provided by Alstom for the 1 MW DEEP-Gen IV. The PWRA velocities, measured at locations A and B relative to the TEC location and hub-height, were paired with the corresponding power via a look-up table to form a power time-series. In terms of the two orientations – in-line and adjacent – a better agreement between ADCP pair A_1 and A_2 was found. Fig. 11 shows the variation in velocity between instrument pairs calculated at various velocity bins. It can be seen that differences reduce during faster flows (where the turbine generates most of its power). The AEP differed by 1.2% between A_1 and A_2, and 2.6% between B_1 and B_2 for the flood tide. The ebb tide, measured by ADCPs at B_1 and B_2 differed by 7.3%.

3.5. Impact of vertical misalignment between measurements and TEC rotor plane

An additional analysis on the impact of flow measurement vertical misalignment was conducted on three types of TEC: the ReDAPT commercial-scale tidal turbine, and two further variants of horizontal axis tidal turbines (selected as representative of current technologies), which operate in different locations of the water column. The ADCPs placed adjacently - B_1 and B_2 - to the DEEP-Gen IV are used to assess the sensitivity to the vertical alignment, see Fig. 12 and Table 6.

The streamwise velocity varies with increasing height from the seabed, typically following a logarithmic curve. The hub-heights for each TEC (refer to Table 5) were used as the base case, and depth bins (ranging in 1 m) up to ± 2 m from the hub-height were assessed. The difference from a positive shift (towards the sea surface) in the bin resulted in an overestimation of AEP. On the contrary, a negative shift (towards the sea floor) is related to underestimating the total AEP. The results are summarised below:

1. With an imposed vertical misalignment of 2 metres between measurement locations and modelled rotor plan differences for flood and ebb tides, respectively, are up to 4.5% and 5.5%.
2. The variation in AEP estimated from the flood tide velocity measurements were similar at locations B_1 and B_2 for a misalignment up to 2 m, implying that the vertical variation in U_{B1} and U_{B2} for the flood tide are similar across a distance of ≈ 70 m.

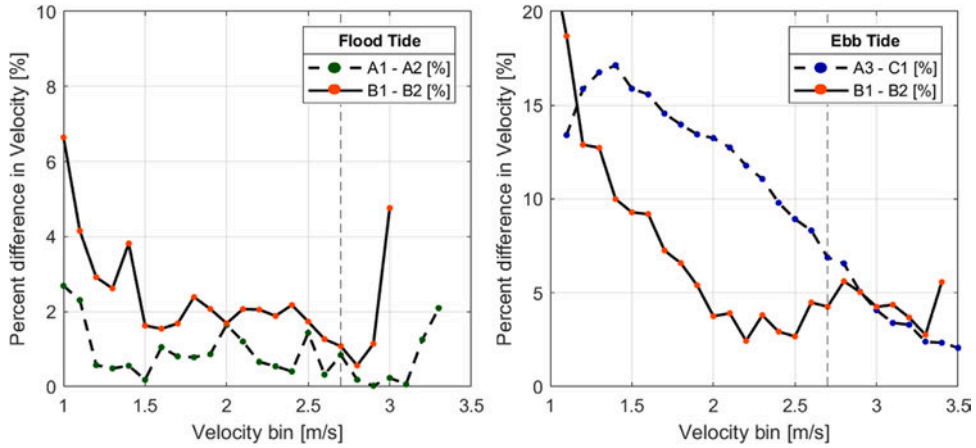

Fig. 11. In-line placed ADCPs (black dashed line) A_1, A_2, A_3 and adjacent placed ADCPs B_1, B_2 (black solid line) and their calculated PWRA velocity in increments of 0.1 m s^{-1}. (a) Flood tide PWRA velocity difference between pair: $\bar{U}_{A1}$ and $\bar{U}_{A2}$, and pair $\bar{U}_{B1}$ and $\bar{U}_{B2}$. (b) Average velocity difference between $\bar{u}_{C1}$, $\bar{U}_{A3}$, and the PWRA velocity difference between $\bar{U}_{B1}$ $\bar{U}_{B2}$.

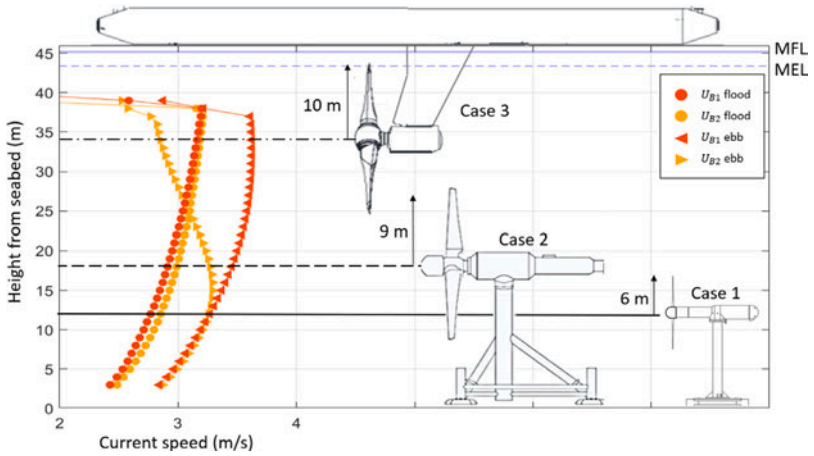

Fig. 12. Three TEC concepts are placed accordingly to their hub-height reference. U_{B1} and U_{B2} represent the peak rated velocity for the flood and ebb tide. The mean water level for the flood (MFL) and ebb (MEL) tide is represented by the blue solid and dashed line respectively. NOTE rotor diameter to scale, TEC dimensions are not to scale.

Table 6
Sensitivity to the vertical misalignment of profiler depth bin to the proposed TEC hub-height, where each bin's mean velocity (U) is used. Values refer to the averaged velocity profile produced for each seabed instrument, where the profile for $B1$ is depicted in Fig. 12. Diff refers to the percent difference between the hub-height AEP estimate and the estimate from an depth offset.

TEC Lcoation and Type		Case 1			Case 2			Case 3		
		SW ADCP (B1)								
	D offset [m]	U [m/s]	AEP* [GWh]	Diff [%]	U [m/s]	AEP [GWh]	Diff [%]	U [m/s]	AEP* [GWh]	Diff [%]
FLOOD	2	2.01	0.82	**3.8%**	2.11	8.95	**2.1%**	2.28	19.80	**1.1%**
	1	1.99	0.81	**2.0%**	2.09	8.87	**1.2%**	2.27	19.68	**0.5%**
	HH	1.97	0.79	**0.0%**	2.08	8.76	**0.0%**	2.27	19.58	**0.0%**
	-1	1.95	0.77	**2.3%**	2.06	8.61	**1.7%**	2.26	19.44	**0.7%**
	-2	1.93	0.76	**4.5%**	2.05	8.53	**2.7%**	2.25	19.28	**1.6%**
EBB	2	2.22	1.41	**4.3%**	2.37	15.54	**2.8%**	2.49	32.56	**0.0%**
	1	2.19	1.38	**2.2%**	2.35	15.30	**1.3%**	2.49	32.58	**0.0%**
	HH	2.16	1.35	**0.0%**	2.33	15.10	**0.0%**	2.49	32.58	**0.0%**
	-1	2.13	1.32	**2.3%**	2.30	14.90	**1.3%**	2.50	32.62	**0.1%**
	-2	2.10	1.28	**5.5%**	2.28	14.70	**2.7%**	2.50	32.62	**0.1%**
		NE ADCP (B2)								
FLOOD	2	1.99	0.81	**3.6%**	2.08	8.830	**2.3%**	2.23	19.84	**0.7%**
	1	1.96	0.80	**1.9%**	2.06	8.730	**1.1%**	2.22	19.80	**0.5%**
	HH	1.94	0.79	**0.0%**	2.04	8.630	**0.0%**	2.22	19.70	**0.0%**
	-1	1.92	0.77	**2.2%**	2.03	8.520	**1.3%**	2.21	19.63	**0.3%**
	-2	1.90	0.75	**4.7%**	2.01	8.400	**2.7%**	2.20	19.58	**0.6%**
EBB	2	2.2	1.39	**2.9%**	2.21	14.10	**0.7%**	1.91	21.12	**3.2%**
	1	2.18	1.38	**2.2%**	2.21	14.20	**0.0%**	1.94	21.51	**1.3%**
	HH	2.15	1.35	**0.0%**	2.22	14.20	**0.0%**	1.95	21.80	**0.0%**
	-1	2.13	1.33	**1.5%**	2.22	14.20	**0.0%**	1.98	22.20	**1.8%**
	-2	2.11	1.30	**3.8%**	2.21	14.10	**0.7%**	2.01	22.60	**3.5%**

HH : represents 12, 18 and 34 for Case 1, Case 2 and Case 3, respectively.
D : depth.
* : represents the estimated AEP using the pre-defined power curves for a 0.1 MW and a 2 MW TEC concept.

3. Misalignment in the negative (towards sea-bed) direction (−1, −2 m) compared to a positive misalignment (towards sea-surface) has a greater impact on the estimated AEP for the flood and ebb tide across all three cases.
4. The TEC placed in the lower region (case 1) of the water column experiences greater variation in AEP under the modelled vertical misalignment, compared with cases 2 and 3.
5. Due to the greater occurrence of faster flows measured in the ebb tide compared to the flood tide, the AEP on ebb tides are greater.
6. In the upper region of the water column AEP estimates from measurements made at B_2 during the ebb tide differed by up to 3.4% when compared with measurements made at B_1.
7. For an imposed misalignment of 2 metres the AEP estimated during ebb tides from measurements at mid-depth (case 2) from B_1 and B_2 locations differed/differ by less than 1%.

4. Discussion

This work explores the sensitivity of tidal turbine power-production performance to the flow velocity reference used. The spatial variation in the flow measurements from ADCPs placed as per the IEC TS 62600-200 guidelines is found to impact the measured power curve. Furthermore, the vertical misalignment between the depth bin and the three modelled TECs of varying hub-heights affects the estimate of annual energy production.

The current velocity and direction measured by the five seabed placed ADCPs differ based on location and tidal cycle. The tidal ellipse (Fig. 3) shows the velocity magnitude (as a radius) and direction (as a compass heading transformed to a radial coordinate) in polar coordinates. The difference in the established flow direction between the five seabed ADCPs is likely due to the combination of inaccuracies in the ADCPs internal compass (due to insufficient calibration), but could also be due to localised bathymetric affects. The velocity measurements from ADCPs placed in orientation B (U_{B1} and U_{B2}) differed significantly in the ebb tide (Figs. 6b, 7b and 9b). This is likely due to a flow structure – trapped eddy – forming on the ebb tides off the local island Eday. Furthermore, ADCP placed at A_3 measured a reduced flow velocity in the upper region of the water column (Figs. 6b and 9a), suggesting the flow structure extends into this location.

The rotor-attached SB-ADP (C_1) measured velocity at hub-height along the heading of the TEC. The only ADCP found to measure similar velocities was at B_2. However, compared to the other ADCPs B_2 measurements appeared significantly lower at the hub-height of the DEEP-Gen IV, especially at lower velocity bins (<2 m s^{-1}). The discrepancy between the measured velocity at location C_1 and the five seabed ADCPs placed around the TEC may be due to several possible causes. First, as the flow decelerates upstream of the turbine (velocity reference taken at 10–12 m) the flow may already be significantly decelerated, this is commonly known as the induction zone. Secondly, the hardware and calibration, including a limit on the maximum sensor range of the SB-ADP, could cause differences in the measured velocity.

The power curves presented follow the methodology of the IEC TS 62600-200 [2]. The real-world power measurements from the DEEP-Gen IV is time-matched with the PWRA velocity calculated for the five seabed ADCPs. In addition, the velocity measured at hub-height from the SB-ADP was used to produce an additional non-PWRA power curve. During the flood tide measured by the in-line ADCP pair A_1 and A_2 (inside and close to the IEC TS target location respectively), the closer ADCP A_1 measured a slightly reduced flow. This would make the power curve appear seemingly more efficient for a developer, due to a lower velocity $\bar{U}_{A1}$ being compared against a larger velocity $\bar{U}_{A2}$ for the equivalent power measurement. The impact of this is small with a difference of ≈ 0.6% between $\bar{U}_{A1}$ and $\bar{U}_{A2}$, when the DEEP-Gen IV was operating at rated power. The difference potentially arises from a push-back on the flow when the TEC is operational or the variation in bathymetric conditions northwest of ADCP A_2 (Fig. 2).

On the contrary, the current flow does not appear to be effected by the TEC at the locations B_1 and B_2. The velocity measurements U_{B1} and U_{B2} are significantly different between the flood and ebb tide, this is evident in Fig. 8b. The velocity measured at B_1 and B_2 differed by 1.4% and 4.3% when the DEEP-Gen IV operated at rated power during the flood and ebb tide respectively (Fig. 11a and 11b), producing four different power curves (Fig. 10a and 10b). Due to the flow structure forming of the headland, the flow velocity measured at location B_2 was lower when compared with measurements from the instrument placed upstream of the turbine (A_1). This results in the power curve appearing seemingly more efficient when using measurements from instrument B_2.

The effect of ADCP placement on the estimated AEP is assessed. Based on the velocity variation between instrument locations A and B, the AEP differed by 1.2% and 2.6% when comparing ADCP pairs A_1 and A_2, and B_1 and B_2 respectively, for the flood tide measurements. For the ebb tides, the large variation between $\bar{U}_{B1}$ and $\bar{U}_{B2}$ resulted in a 7.3% difference between AEP estimates. According to the IEC TS 62600-200 the linear average velocity should be calculated when using the adjacent orientation B at equivalent water depths. For the linear average to be considered a valid approximation of the flow at the energy extraction plane, the variation in the instantaneous velocities u_{B1} and u_{B2} should be less than 10%. Fig. 9b illustrates how the mean velocity binned by increments of 0.3 m s^{-1} can vary by more than 10%, and the instantaneous velocity measurements significantly more. The study suggests that for a TEC located in the lower region of the water column (< 20 m) the adjacent orientation ADCPs can be used for power performance assessments. However, as seen in Fig. 9b, the variation in velocity upward of 20 m from the seabed exceeds the threshold required for a linear average calculation to be valid. For this reason, this instrument orientation should not be considered for a power performance assessment at this specific location for a TEC deployed in the upper region of the water column. These findings highlight the importance of studying the form of the velocity-binned depth profiles (before applying any spatial averaging and considering flood and ebb tides separately), in particular, checking for forms that suggest the presence of large-scale flow features, e.g., eddies (as shown in Figs. 8, 9 and 12). The results from implementing an IEC Type B campaign have shown at this site a significant variation in velocity on either side of the turbine location. However, this instrument layout might be suitable for power performance assessments at other test locations where the turbine and flow sensors are situated further away from flow-affecting channel features e.g., upstream headlands. The study has shown that the suitability of an IEC Type B campaign for PPA is dependent on specific turbine size and positioning in a particular channel.

The consequence of estimating AEP from flow data that might feature significant vertical misalignment between the ADCP depth bin and the rotor swept area is assessed for the DEEP-Gen IV and two further variants of horizontal axis tidal turbines. This misalignment could occur due to numerous reasons. First, differences in the estimated depth may occur due to different pressure gauge specifications and/or varying states of calibration—including human operator error or poor data traceability in terms of zero-ing of sensors. In addition, incorrect post-processing of the data and mis-matching the depth bin to the hub-height (including the blanking distance and the starting position of the first measured bin) of the turbine, can lead to inaccuracies in the measured performance. Finally, the instrument stability (pitch and roll) should be considered as this can change the depth bin between beam pairs.

The AEP was estimated using the velocity measurements at three proposed hub-heights (refer to Table 5), where a misalignment between neighbouring depth bins up to ±2 m was analysed. Results indicate the AEP was sensitive to the tidal cycle because the flood and ebb

exhibit different shear profiles. It was found that a more gradual velocity profile (typically a flood tide, refer to Fig. 12) has a lower impact on the estimated AEP, when flow data features a misalignment of 2 m. The results show (Table 6) that for regions of high vertical shear, AEP estimates become increasingly sensitive to imposed vertical misalignment.

5. Conclusion

The power performance of the DEEP-Gen IV 1 MW tidal turbine relative to five seabed placed ADCPs and one rotor-attached SB-ADP has been evaluated. These ADCPs were placed in accordance with the IEC TS 62600-200, where A_1, A_2 and A_3 are in-line and B_1, B_2 are adjacent to the TEC rotor extraction plane. The study investigates the impact on the measured power curve and AEP estimates using different flow references.

The ADCP placed closer to the TEC (A_1, ≈ 61 m upstream of TEC) show a slightly reduced flow when compared with the ADCP further upstream (A_2, ≈ 106 m upstream of TEC). This result supposedly implies that the closer instrument (A_1) produces a more efficient power curve i.e. the velocity measured is lower when compared with the time-matched velocity measured at A_2 for the equivalent power measurement. As the ADCP placed at A2 is outside the IEC TS target box, measurements are comparable with the instrument located in the box. This suggests that instruments can be deployed outside the IEC TS recommended zone and be a true representation of the flow approaching the TEC.

The ebb tide measurements revealed a significant difference in the ambient flow conditions measured at locations B_1 and B_2, this affected the AEP estimate by 7.3% when comparing the two ADCPs. The IEC TS 62600-200 guidance imposes a limit of a maximum of 10% variation between two adjacent estimates of mean velocity at a particular depth. For this study this threshold is frequently exceeded in the upper regions of the water column. This suggests that at this site, the adjacently placed instruments informed by the IEC TS 62600-200 should not be considered for a power performance assessment. It should be noted, however, that for alternate TEC designs situated lower in the water column, the rotor-adjacent measurement method may be acceptable.

The rotor-attached SB-ADP measured a reduced flow compared to the five seabed ADCPs. This is because within the measurement range (limited by the instrument's acoustic frequency, water conditions and signal strength) of the SB-ADP the flow was affected by the turbine presence and induction zone when the turbine was generating power. Our findings suggest that without further work e.g., finding and applying correction factors (which is not done in this work), this instrument configuration is unsuitable for the specific role of power performance assessment in this case. However, the SB-ADP offers several practical advantages. By integrating the instrument with the turbine, the SB-ADP, unlike stand-alone seabed setups, can be continuously powered and remotely controlled. In addition, turbine-mounted instruments can provide in-situ measurements to users in real time. This study (alongside others) has proven instruments can reliably be mounted and operated on turbines to provide in-situ measurements of current flow at turbine hub-heights. Together these advantages justify further work in this area, particularly for turbines situated high in the water column or installed on non-fixed platforms.

An investigation of AEP sensitivity to the imposed vertical misalignment of flow data to turbine rotor positioning was conducted. Three turbines were assessed, namely the ReDAPT commercial-scale tidal turbine and two further variants of horizontal axis tidal turbines, which operate in different locations of the water column with varying rotor dimensions. Results show differences in estimates of Annual Energy Production of up to 5.5%. The largest difference was found for the lowest hub-height when flow data used featured a misalignment of 2 metres with respect to the modelled rotor plane. The user of the IEC TS guidelines should realise that the placement of current sensors used in the power assessment is affected by the spatial variation of the flow (horizontal and vertical).

CRediT authorship contribution statement

Luke Evans: Conceptualization, Methodology, Formal analysis, Investigation, Writing – original draft, Revision. **Ian Ashton:** Conceptualization, Methodology, Supervision, Writing – review, Editing & revision. **Brian Sellar:** Conceptualization, Methodology, Supervision, Writing – review, Editing & revision.

Declaration of competing interest

The authors declare the following financial interests/personal relationships which may be considered as potential competing interests: This research is Funded by the EPSRC and NERC for the Industrial CDT in Offshore Renewable Energy (EP/S023933/1) and sponsored by the European Marine Energy Centre.

References

[1] S. Paboeuf, P. Yen Kai Sun, L.-M. Macadré, G. Malgorn, Power Performance Assessment of the Tidal Turbine Sabella D10 Following IEC62600-200, in: International Conference on Offshore Mechanics and Arctic Engineering, vol. 6, 2016, http://dx.doi.org/10.1115/OMAE2016-54836.

[2] International Electrotechnical Commission (IEC), PD IEC / TS 62600-200 : 2013 BSI Standards Publication Marine Energy — Wave , Tidal and Other Water Current Converters Energy Converters — Power Performance, 2013.

[3] European Communities, European Commission. Directorate General for Research, SEAFLOW, World's First Pilot Project for the Exploitation of Marine Currents at a Commercial Scale, Publications Office, 2005, p. 33, URL https://op.europa.eu/en/publication-detail/-/publication/36f20105-3d03-4324-8312-24405bdbd939.

[4] M. Harrold, P. Ouro, T. O'Doherty, Performance assessment of a tidal turbine using two flow references, Renew. Energy 153 (2020) 624–633, http://dx.doi.org/10.1016/j.renene.2019.12.052.

[5] P. Scheijgrond, A. Southall, C. Bittencourt, P. Davies, P. Mathys, G. Germain, Advancing IEC Standardisation and Certification for Tidal Energy Convertors, Tech. rep., URL https://www.icoe-conference.com/documents.

[6] G. Mccann, Implications of Site-Specific Conditions on the Prediction of Loading and Power Performance of a Tidal Stream Device, Tech. rep., 2008, URL https://www.researchgate.net/publication/228402190.

[7] R. Starzmann, I. Goebel, P. Jeffcoate, Field Performance Testing of a Floating Tidal Energy Platform-Part 1: Power Performance, Tech. rep., URL https://tethys-engineering.pnnl.gov/sites/default/files/publications/AWTEC2018-320.pdf.

[8] J. MacEnri, M. Reed, T. Thiringer, Power quality performance of the tidal energy converter, SeaGen, in: Proceedings of the International Conference on Offshore Mechanics and Arctic Engineering - OMAE, Vol. 5, 2011, pp. 529–536, http://dx.doi.org/10.1115/OMAE2011-49549.

[9] J.-C. Allo, D. Dhomé, B. Battaglia, Feedback from Sabella D10 1 MW sea trials, Tech. rep..

[10] S.G. Parkinson, W.J. Collier, Model validation of hydrodynamic loads and performance of a full-scale tidal turbine using tidal bladed, Int. J. Mar. Energy 16 (2016) 279–297, http://dx.doi.org/10.1016/j.ijome.2016.08.001.

[11] B.G. Sellar, D.R. Sutherland, Tidal Energy Site Characterisation At the Fall of Warness , Emec , Uk Energy Technologies Institute Redapt Ma1001 (Md3.8), Vol. 1001, Tech. Rep., (December) REDAPT, 2016, URL http://redapt.eng.ed.ac.uk.

[12] M. Atcheson, P. Mackinnon, B. Elsaesser, A large scale model experimental study of a tidal turbine in uniform steady fl ow, Ocean Eng. 110 (2015) 51–61, http://dx.doi.org/10.1016/j.oceaneng.2015.09.052.

[13] Z. Hameed, Y.S. Hong, Y.M. Cho, S.H. Ahn, C.K. Song, Condition monitoring and fault detection of wind turbines and related algorithms: A review, Renew. Sustain. Energy Rev. 13 (1) (2009) 1–39, http://dx.doi.org/10.1016/j.rser.2007.05.008.

[14] J. Harrison, ReDAPT MC7 . 3 Public Domain Report : Final, http://redapt.eng.ed.ac.uk/library/eti/reports/MC7.3OperationsFinalReport.pdf.

[15] J. Mcnaughton, R. Sinclair, B. Sellar, Measuring and modelling the power curve of a commercial-scale tidal turbine, in: Proceedings of the 11th European Wave and Tidal Energy Conference, (October) 2015, http://dx.doi.org/10.1017/CBO9781107415324.004, URL https://www.researchgate.net/publication/282327696.

[16] P. Jeffcoate, N. Cresswell, Field performance testing of a floating tidal energy platform - Part 2: Load performance, in: Proc. of the 4th Asian Wave and Tidal Energy Conference (AWTEC), 2018, URL https://www.researchgate.net/publication/326573036_Field_Performance_Testing_of_a_Floating_Tidal_Energy_Platform-Part_2_Load_Performance.

[17] P. Jeffcoate, R. Starzmann, B. Elsaesser, S. Scholl, S. Bischoff, Field measurements of a full scale tidal turbine, Int. J. Mar. Energy 12 (2015) 3–20, http://dx.doi.org/10.1016/j.ijome.2015.04.002, URL http://dx.doi.org/10.1016/j.ijome.2015.04.002.

[18] B.G. Sellar, D.R. Sutherland, D.M. Ingram, V. Venugopal, Measuring waves and currents at the European marine energy centre tidal energy test site: Campaign specification, measurement methodologies and data exploitation, in: OCEANS 2017 - Aberdeen, Vol. 2017-Octob, 2017, pp. 1–7, http://dx.doi.org/10.1109/OCEANSE.2017.8085001.

[19] H. Torrens-Spence, P. Schmitt, C. Frost, I. Benson, P. MacKinnon, T. Whittaker, Assessment of flow characteristics at two locations in an energetic tidal channel, in: Proceedings of the Twelfth European Wave and Tdal Energy Conference, 2017, URL https://pureadmin.qub.ac.uk/ws/portalfiles/portal/134529503/HTS_FullPaper_Version4.pdf.

[20] B.G. Sellar, G. Wakelam, D.R. Sutherland, D.M. Ingram, V. Venugopal, Characterisation of tidal flows at the european marine energy centre in the absence of ocean waves, Energies 11 (1) (2018) 1–23, http://dx.doi.org/10.3390/en11010176.

[21] Maritime, C. Agency, Guide to using the CHP bathy atlas, 2005, URL https://assets.publishing.service.gov.uk/government/uploads/system/uploads/attachment_data/file/296198/chp_bathy_atlas_guide.pdf.

[22] I. Afgan, J. McNaughton, S. Rolfo, D.D. Apsley, T. Stallard, P. Stansby, Turbulent flow and loading on a tidal stream turbine by LES and RANS, Int. J. Heat Fluid Flow 43 (2013) 96–108, http://dx.doi.org/10.1016/j.ijheatfluidflow.2013.03.010.

[23] M. Lewis, J. McNaughton, C. Márquez-Dominguez, G. Todeschini, M. Togneri, I. Masters, M. Allmark, T. Stallard, S. Neill, A. Goward-Brown, P. Robins, Power variability of tidal-stream energy and implications for electricity supply, Energy 183 (2019) 1061–1074, http://dx.doi.org/10.1016/j.energy.2019.06.181.

[24] IOOS, Manual for real-time quality control of stream flow observations (qartod) v2.1, (July) 2019, http://dx.doi.org/10.25923/sqe9-e310.

[25] RDI, Acoustic Doppler current profiler: Principles of operation, a practical primer. P/N 951-6069-00. Teledyne RD instruments, poway, California, 00, (January) 2011, p. 56.

[26] RDI, RD Instruments Acoustic Doppler Current Profilers Application Note ADCP Beam Clearance Area, Tech. rep., 2002, pp. 1–7, http://www.teledynemarine.com/Documents/BrandSupport/RDINSTRUMENTS/TechnicalResources/TechnicalNotes/ChannelMaster/FSA019.PDF.

[27] D.R.J. Sutherland, Assessment of mid-depth arrays of single beam acoustic Doppler velocity sensors to characterise tidal energy sites, 2015, URL https://era.ed.ac.uk/handle/1842/19559?show=full.

[28] J. Mcnaughton, R. Sinclair, S. Harper, D. Dobson P, P. Chesman, ReDAPT: Initial operation power curve (MC7 . 1), 2014, URL https://redapt.eng.ed.ac.uk/?p=library_redapt_reports.

[29] S. Draycott, A. Nambiar, B. Sellar, T. Davey, V. Venugopal, Assessing extreme loads on a tidal turbine using focused wave groups in energetic currents, Renew. Energy 135 (May) (2019) 1013–1024, http://dx.doi.org/10.1016/j.renene.2018.12.075.

[30] European Commission, RealTide: Advanced monitoring, simulation and control of tidal devices in unsteady, highly turbulent realistic tide environments, H2020 Programme Res. Innov. (727689) (2019) 1–45, URL https://www.realtide.eu/.

Chapter 13

Appendix for Chapter 8

13.1 Impact on Energy Yield of Varying Turbine Designs under Conditions of Misalignment to the Current Flow

Abstract: Tidal energy resource characterisation using acoustic velocimetry sensors mounted on the seabed informs developers of the location and performance of a tidal energy converter (TEC). This work studies the consequences of miscalculating the established flow direction, i.e., the direction of assumed maximum energy yield. Considering data only above the proposed TEC cut-in velocities showed a difference in the estimated flow direction of up to 4°. Using a power weighted rotor average (PWRA) method to obtain the established flow direction resulted in a difference of less than 1° compared with the hub-height estimate. This study then analysed the impact of turbine alignment on annual energy production (AEP) estimates for a non-yawing tidal turbine. Three variants of horizontal axis tidal turbines, which operate in different locations of the water column, were examined; one using measured data, and the other two via modelled through power curves. During perfect alignment to the established flow direction, natural variations in flow meant that the estimate of AEP differed by up to 1.1% from the theoretical maximum of a fully yawed turbine. In the case of misalignment from the established flow direction, the difference in AEP increased. For a 15° misalignment, the AEP differed by up to 13%. These results quantify important uncertainties in tidal energy site design and performance assessment. [362].

Keywords: Marine Renewable Energy; Tidal Energy; Tidal Flow Asymmetry; Power Curve; Power Performance; Uncertainty; IEC TS 62600-200; Acoustic Doppler Profiler; Turbine Yaw Misalignment

MDPI Energies Paper, Follow the link: Impact on Energy Yield of Varying Turbine Designs under Conditions of Misalignment to the Current Flow

energies

MDPI

Article

Impact on Energy Yield of Varying Turbine Designs under Conditions of Misalignment to the Current Flow

Luke Evans [1,2,*], Ian Ashton [3] and Brian G. Sellar [4]

[1] EPSRC and NERC Centre for Doctoral Training in Offshore Renewable Energy (IDCORE), The University of Edinburgh, Edinburgh EH9 3DW, UK
[2] European Marine Energy Centre (EMEC), Research Engineer, Orkney, Old Academy Business Centre, Back Road, Stromness KW16 3AW, UK
[3] College of Engineering Mathematics and Physical Sciences, University of Exeter, Penryn Campus, Penryn TR10 9EZ, UK;
[4] School of Engineering, The University of Edinburgh (UoE), Edinburgh EH9 3DW, UK;
* Correspondence: ; Tel.: +44-793-5144-676

Abstract: Tidal energy resource characterisation using acoustic velocimetry sensors mounted on the seabed informs developers of the location and performance of a tidal energy converter (TEC). This work studies the consequences of miscalculating the established flow direction, i.e., the direction of assumed maximum energy yield. Considering data only above the proposed TEC cut-in velocities showed a difference in the estimated flow direction of up to 4°. Using a power weighted rotor average (PWRA) method to obtain the established flow direction resulted in a difference of less than 1° compared with the hub-height estimate. This study then analysed the impact of turbine alignment on annual energy production (AEP) estimates for a non-yawing tidal turbine. Three variants of horizontal axis tidal turbines, which operate in different locations of the water column, were examined; one using measured data, and the other two via modelled through power curves. During perfect alignment to the established flow direction, natural variations in flow meant that the estimate of AEP differed by up to 1.1% from the theoretical maximum of a fully yawed turbine. In the case of misalignment from the established flow direction, the difference in AEP increased. For a 15° misalignment, the AEP differed by up to 13%. These results quantify important uncertainties in tidal energy site design and performance assessment.

Keywords: marine renewable energy; tidal energy; tidal flow asymmetry; power curve; power performance; uncertainty; IEC TS 62600-200; acoustic doppler profiler; turbine yaw misalignment

check for updates

Citation: Evans , L.; Ashton, I.; Sellar, B.G. Impact on Energy Yield of Varying Turbine Designs under Conditions of Misalignment to the Current Flow. *Energies* **2023**, *16*, 3923. https://doi.org/10.3390/en16093923

Academic Editors: Doug Arent, Xiaolei Yang and Adam Warren

Received: 22 March 2023
Revised: 21 April 2023
Accepted: 27 April 2023
Published: 6 May 2023

Copyright: © 2023 by the authors. Licensee MDPI, Basel, Switzerland. This article is an open access article distributed under the terms and conditions of the Creative Commons Attribution (CC BY) license (https://creativecommons.org/licenses/by/4.0/).

1. Introduction

Tidal-stream energy, the extraction of kinetic energy from tidal currents to generate electricity, is becoming an increasingly attractive form of renewable energy due to the high predictability of the tides [1–3]. This resource has the potential to provide energy security and support a renewable grid network shift to decarbonised energy generation. Initial feasibility studies and characterisation of high energy sites often focus on peak velocity (>2.5 m·s^{-1}) and a restricted range of water depths (25–50 m) [1,4,5]. However, peak values do not accurately indicate the potential power production due to fine-scale temporal and spatial variability in the flow. Therefore, gathering additional information from site resource characterisations, while using Acoustic Doppler Current Profilers (ADCPs), is vital for understanding the potential uncertainties. In addition to quantifying the available resource, evaluating the tidal energy converters' (TECs) performance in natural conditions is challenging. Still, it remains an essential aspect of accelerating the tidal industry to the commercialisation phase [6].

Most TECs frequently developed do not have the ability to actively respond to changes in the current direction [7]. Thus, are of a non-yawing (no rotation in the nacelle) horizontal

axis design, [8–13], some designs yaw ≈ four times a day to face perpendicular to the established flow direction, e.g., the 1 MW DEEP-Gen IV from Alstom [14,15]. However, the tidal current magnitude and direction are typically asymmetric in highly energetic tidal test sites [3,4,16,17], particularly in nearshore environments where the topography and bathymetry vary significantly [4,5]. Despite that, resource assessments commonly assume that the proposed TEC will always be aligned with the instantaneous tidal flow [4,5].

The International Electrotechnical Commission (IEC) Technical Specification (TS) on Power Performance Assessment (PPA) [18] provides guidance for collecting potential uncertainties associated with the measurement of current and power produced by TECs [18]. However, due to the limited number of grid-connected commercial-scale TECs deployed (in the UK [6,10,19], France [8,12] and the US [12,20]), the standard IEC62600-200 has been applied only to a limited number of turbines and, as a consequence, industry has limited feedback on the use of the IEC62600-200. Typically, a PPA is undertaken as a key step towards achieving type certification of the TEC [6], providing a basis to guarantee the power performance of the device to interested parties, e.g., customers, investors and insurers [21].

As part of the Reliable Data Acquisition Platform for Tidal (ReDAPT) project [22], multiple ADCP deployments took place at the European Marine Energy Centre (EMEC) full-scale tidal test site at Eday, the Fall of Warness (FoW), between 2011 and 2015. The aims were to assess the flow characteristics and evaluate in situ measurements for the power performance of the DEEP-Gen IV 1 MW tidal turbine. The location of the tidal test site is presented in Figure 1a,b. Part of this work identified a twist in the flow along the water column, where the current direction changed significantly through the water column by as much as 10° from the calculated mean [14]. At present, the flow direction measured by the ADCP depth bin relative to the proposed TEC should be reported as per IEC62600-200 [18]. Figure 1c presents the typical flow conditions at the tidal test site situated at the FoW, taken from one of the ReDAPT measurement campaigns [19]. Flow velocity and direction vary with depth—from bathymetry, seabed friction and interactions from the wind and waves. If this variation could be captured along the rotor plane of a TEC, a more accurate representation of the established flow could be estimated. This is performed for the flow velocity, using the power-weighted rotor average (PWRA) method [18], as shown in Figure 2.

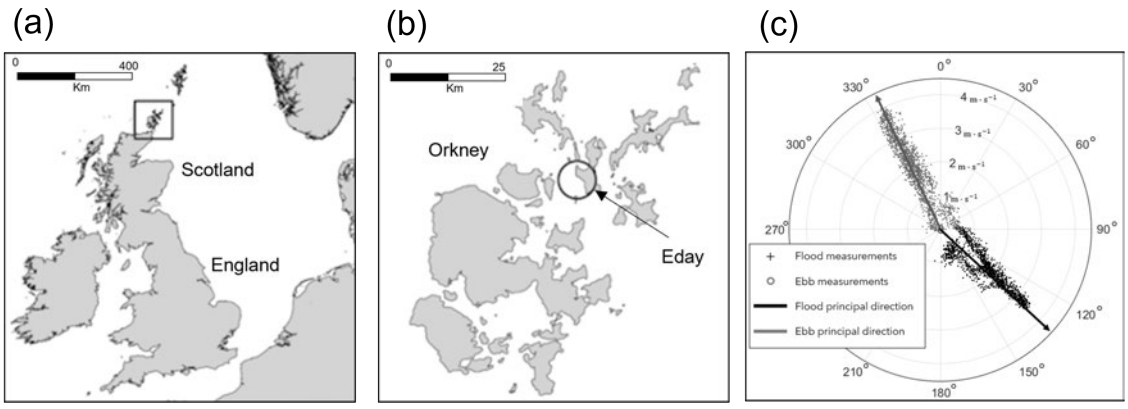

Figure 1. Location of the study site. (**a**) Orkney location relative to the UK [23]; (**b**) The Orkney Islands with Eday and the falls of Warness full-scale tidal energy test site highlighted [23]; (**c**) Tidal ellipse of data used from one instrument deployed at the FoW, flood (black marker) and ebb (grey marker) flow directions are shown.

Studies have analysed the impact of flow misalignment on tidal turbines. For example, Polagye and Thomson [24] used observations from an ADCP on a single point mooring to assess individual locations within Admiralty Inlet (Puget Sound, Washington, WA, USA) and estimated that the mean potential power generated by the non-yawing device may

be, at most, 5% lower than for a passive yaw device at the same site. It was observed that the penalty for using non-yawing devices increases as directional variation in the flow increases [24], which agrees with work from Galloway and Frost et al. [4,25], where they suggest that power reductions may only become apparent above a certain threshold of misalignment (>7.5° with an approximately 7% reduction of peak power at ±10° directional misalignment, and a 20% reduction at 22.5°. Frost et al. [4] found that asymmetrical regimes (difference in peak velocity between the flood and ebb tidal cycle) lead to unequal power generation during the two tidal cycles. Since turbine power output is proportional to the cube of the flow velocity, even a slight difference in the velocity magnitude between tides can lead to a significant alteration in the power generated [26]. In addition, Piano et al. [5] found that optimising turbine orientation to specific flow dynamics could reduce the potential losses by up to 2% where strong asymmetry occurs and as low as 0.25% for ideal symmetrical conditions when considering a non-yawing TEC. However, tidal characteristics are dissimilar across sites and have the potential for increased losses in annual energy yield, exceeding 2% where the optimal orientation of non-yawing devices is ignored [5].

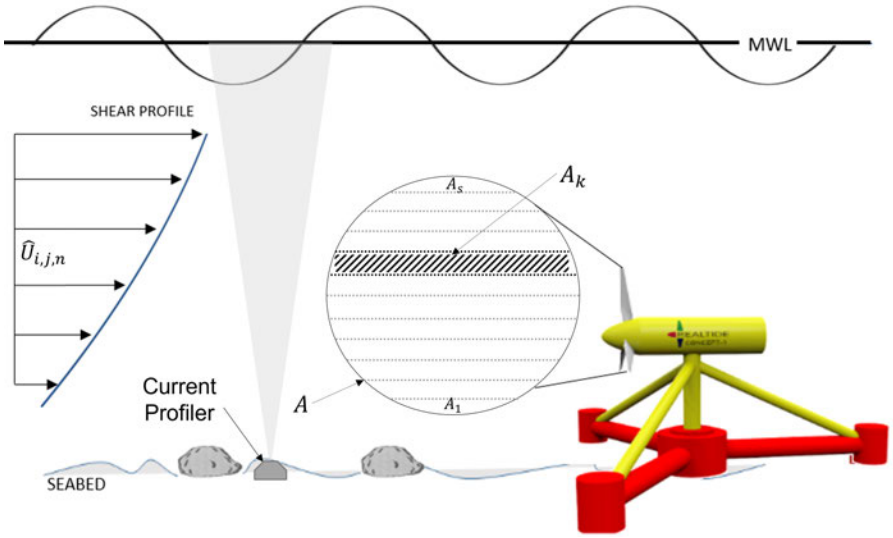

Figure 2. The vertical variation of tidal current across the projected capture area—introducing the importance for the power PWRA technique.

From the initial TEC concepts to the first pre-commercial tidal turbine prototypes, a key requirement has been reliability and survivability [27]. The impact of turbulence on the performance and loading acting on a tidal turbine has received little consideration to date. Turbulence describes the chaotic motions within a fluid flow and can result in fluctuations in force, which is detrimental to the fatigue life of the turbine [27,28]. The presence of the turbine can increase the turbulence and vortices generated [27,29]. Although this is recognised, and these effects can change the flow characteristics at the turbine location, this is not the focus of this study due to instrument placement and resolution.

The flow direction matures over a tidal cycle. This effect on power performance has not yet been quantified. Not knowing the impact on power will lead to an inaccurate assessment of performance. This study aims to use in situ measurements obtained from two ADCPs deployed at the FoW (Orkney, Scotland, UK) to quantify the impact off-axis currents have on power production. In addition, the impact on performance and energy yield from a rotor misalignment for three horizontal axis tidal turbines situated at different depths is assessed. This work will inform developers on turbine installation design criteria by highlighting how the temporal variation in the flow direction can result in a misalignment between the current flow and turbine extraction plane. The methods used in this study can be applied to in situ data gathered at different tidal test sites that exhibit complex magnitude and directional asymmetries to maximise potential energy yields and help interpret performance results more accurately. A method for estimating the established

flow direction to inform tidal developers on turbine orientation is reported. The variation in flow direction at different depths is necessary to predict the loading effects caused due to being positioned off-axis to the established flow direction. We investigate the relative impact of current flow maturity on the power performance of non-yawing TEC concepts. We then investigate the misalignment of the turbine axis with the established flow to assess the impact on the measured power curve, and AEP estimates. As numerous tidal turbines exist and occupy different regions of the water column, three variants of a horizontal axis tidal turbine were chosen for a case study to investigate the impact of flow direction variation on machines with different operational characteristics. We suggest the optimum period for utilising a yaw mechanism by interpreting the results.

This paper is structured as follows: Section 2 introduces the theory behind the power-weighted rotor average method. In addition, the characteristics of flow direction asymmetry and maturity are presented; Section 3 describes the FoW deployment site conditions, as well as the instrumentation relevant to this work; while Section 4 reports the results on the estimates of established flow direction (Section 4.1) and the consequences of misalignment. The analysis is then presented, which considers the impact on the measured power curve (Section 4.2) and annual energy estimates with respect to off-axis currents approaching the TEC (Section 4.2.3); Section 5 presents the discussion around the hypothesis and results generated. The main conclusions from this analysis are summarised in Section 6.

As this paper discusses the impact of flow direction estimates, some abbreviations will be used throughout this paper. Where all the measured flow velocities are assumed to flow through the TEC extraction plane for maximum energy capture was referred to as U_{inflow}; the established flow direction estimate was θ and the methods used to obtain the estimate were, θ_{HH} (hub-height), θ_{RA} (rotor average) and θ_{PWRA} (power-weighted rotor average); the misalignment from the established flow direction is represented as α.

2. Theory

2.1. Estimate of Established Flow Direction—PWRA

Efforts to advise developers on how to record and report the flow direction at tidal stream sites have been made by IEC/TS 62600-200—"*Electricity producing tidal energy converter—power performance assessment*" [18]. This TS describes a method for ascertaining the flow characteristics of a site, which underpins the prediction of the potential resource and defines the local flow conditions and associated design considerations. Currently, the TS requires the established flow direction to be reported for the profiler bin relative to the hub-height (θ_{HH}) of the proposed TEC, along with instantaneous measurements for both the flood and ebb (see Figure 1a) [4,18].

Tidal turbines with no yaw capabilities are deployed facing the established flow direction with the most significant velocities. If the TEC is equipped with bi-directional blades, it can capture energy from current flow travelling from two opposing directions. However, highly energetic tidal sites typically have asymmetrical tides in both velocity magnitude and direction [4]. Therefore, a robust estimate of the established flow direction will inform the TEC orientation and increase power performance and quality while reducing the total loads experienced on the rotor due to off-axis currents. The established flow direction is an average of the measurements captured at the hub-height of the deployed TEC. The reference velocity is calculated from the relative profiler bins that profile across the rotor extraction plane as shown in Equation (1):

$$\hat{U}_{i,j,n} = \left[\frac{1}{A}\Sigma_{k=1}^{S} U_{i,j,k,n}^{3} A_k\right]^{\frac{1}{3}} \quad (1)$$

where i is the index number defining the velocity bin; j is the index number of the time instant at which the measurement is performed; k is the index number of the current profiler bin across the projected capture area (reflected in Figure 2 as A_k); S is the total number of current profiler bins across the projected capture area; $\hat{U}_{i,j,n}$ is the instantaneous power

weighted tidal current velocity across the projected capture area in m·s^{-1}; $U_{i,j,k,n}$ is the magnitude of the instantaneous tidal current velocity, for time j, at current profiler bin k, in velocity bin i, for data point n in m·s^{-1} and A is the projected capture area of the proposed TEC m^2.

Equation (1) uses the velocity magnitude U, which assumes all energy is available to the device, whereas expressed in Equation (2), U_α is the velocity component accounting for periods of TEC rotor to flow misalignment, where α is directly related to the angle of misalignment.

$$\hat{U}_{\alpha i,j,n} = \left[\frac{1}{A}\Sigma_{k=1}^{S} U_{\alpha,i,j,k,n}^{3} A_k\right]^{\frac{1}{3}} \quad (2)$$

2.2. Flow Direction Asymmetry between Flood and Ebb Tides

A tidal ellipse plot presents the velocity magnitudes (as a radius) and directions (as a compass heading) in polar coordinates. The velocity data points are typically 5, 10 or 15 min temporally averaged and spatially averaged (cube weighted) over the predicted swept area of a turbine. These plots help determine the flow magnitude and direction variation at the site of interest and identify the established flow direction to inform turbine developers. If the flow direction for the ebb and flood tidal cycles are separated by ≈180°, the site is described as symmetrical or rectilinear. Otherwise, the flow is described as asymmetrical. The amount of asymmetry between the ebb and flood tide can be summarised by computing the difference between the mean angle of both directions over a complete lunar cycle (Equation (3)). Symmetrical sites are desirable as turbines can be mounted in a fixed position, pitching the blades to capture the tides from both directions with little or no loss of power. Sites with an offset between the ebb and flood tide may benefit from a turbine that could yaw to capture both tides efficiently [4,30].

$$\theta_{mis} = (\overline{\theta}_{flood} - \overline{\theta}_{ebb}) - 180 \quad (3)$$

where θ is the angle in degrees (°).

2.3. Flow Direction Variation a Tidal Cycle

In addition to asymmetrical tides, the flow direction changes during the different phases of the tide. As the tide evolves to the established flow direction, this will be referred to as the ramping up (RU) of the tide, and as the tide begins to slow from peak flow (PF) before changing tide, this phase will be referred to as waning down (WD), as seen in Figure 3. For non-yawing TEC concepts, the ability to capture the largest amount of energy will only take place once the TEC is positioned perpendicular to the flow. This variation in direction results in a reduced velocity passing through the TEC rotor capture area. Hence, this must be considered when evaluating and producing a measured power curve.

Figure 3 depicts how flow varies with time during a flood cycle at the instrument location (direction measurements are subject to variation based on instrument location) in the FoW.

The measured flow evolves and a non-yawing TEC positioned towards the established flow direction will be susceptible to off-axis currents throughout each tidal cycle. Equation (4) describes the inflow velocity (U_{inflow}) at the instrument location, and the velocity at the TEC location (U_{rotor}) when the turbine's rotor heading is perpendicular to the free stream flow at all times ($\alpha = 0$), thus capturing the maximum amount of energy available. In misalignment circumstances, the inflow velocity becomes a component of the velocity, and the parameter α quantifies the difference between U_{inflow} and U_{rotor}. The impact of misalignment can be described using a simple trigonometric cosine relationship [4], as shown in Equation (5):

$$U_{\text{rotor}} = U_{\alpha=0} = U_{\text{inflow}} \quad (4)$$

$$U_{\text{rotor},\alpha} = U_{\alpha \neq 0} = U_{\text{inflow}} \cdot cos\alpha \tag{5}$$

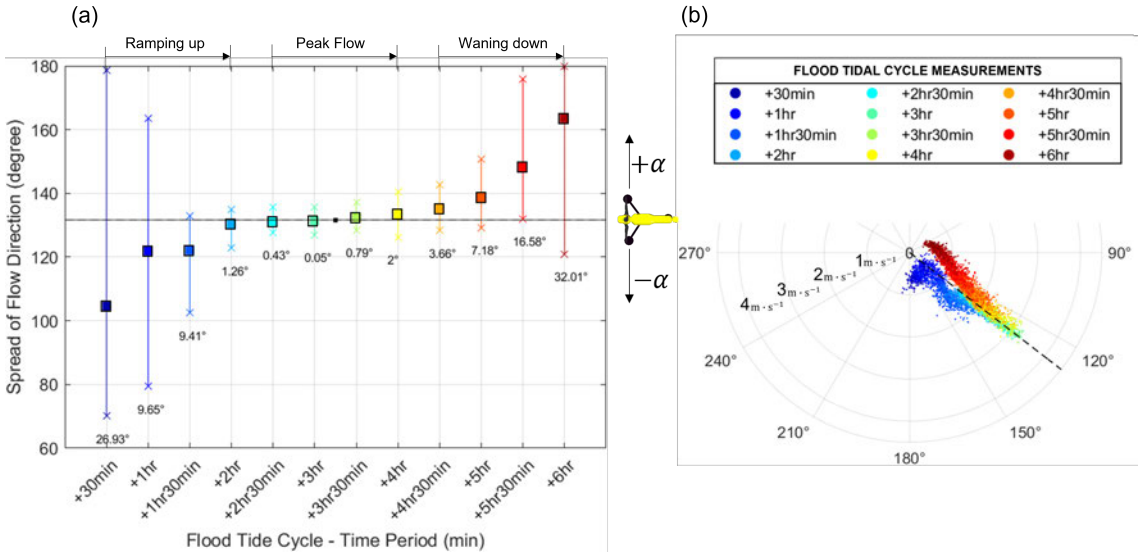

Figure 3. Flow direction variation over a flood tide at the FoW, where (**a**) the flow direction mean (square markers) of 30 min periods throughout the flood cycle, the TEC yaw heading (solid black line) and the min and max (crosses) variation in direction. (**b**) The tidal ellipse for the flood measurements at a chosen hub-height (25 m), the black dashed line represents the TEC yaw heading.

Alternatively, the turbine's swept area can be considered when misalignment is introduced and it changes from a circle to an ellipse. The vertical radius of the ellipse will remain the same, and the horizontal radius will decrease as the yaw angle increases from the established flow direction. The resulting equation for a turbine's projected area in aligned and misaligned flow is described by Equations (6) and (7), respectively, as shown below:

$$A_{\text{rotor}} = A_{\alpha=0} = \pi \cdot r^2 \tag{6}$$

$$A_{\text{rotor},\alpha} = A_{\alpha \neq 0} = \pi \cdot r^2 \cdot \cos\alpha \tag{7}$$

where r is the radius of the turbine and α is the misalignment in degrees between the U_{inflow} and U_{rotor}.

It is expected that either one of these two corrections, when applied to the theoretical maximum power equation, may estimate the performance drop due to misalignment. Tidal stream devices designed to react to tidal sites with asymmetrical tides may lack the sufficient ability to extract energy efficiently from off-axis currents. The maximum power can be calculated using Equation (8):

$$P = \frac{1}{2} \cdot \rho \cdot cp \cdot U^3 \cdot A \tag{8}$$

where P is the power produced in MW, ρ is the density of water in kg·m^{-3}, C_p is the power coefficient, U is the instantaneous flow velocity in m·s^{-1} and A is the cross-sectional area of the TEC rotor in m^2.

3. Methodology

3.1. Deployment Site Conditions

A measurement campaign was devised to assess the DEEP-Gen IV 1 MW tidal turbine performance using two ADCPs over June and July 2013 at the FoW (Figure 1). The full-scale tidal test site situated on the coast of Eday contains highly energetic tidal currents due to a narrowing of the channel between Eday and Muckle Green Holm, a small outcrop south-

west of the island. Figure 4 presents the channel bathymetry and instrument locations. The tidal current flows southeast and northwest throughout the flood and ebb tide, respectively. The strength in the ebb tide at the FoW is larger and less spatially varied, reaching a PF of 4 $m{\cdot}s^{-1}$ with a flow direction spread of ≈35° from the RU to WD phase. The flood tide reaches a PF of ≈3.2 $m{\cdot}s^{-1}$ with a much larger flow direction spread of ≈75°. The flood tide is more turbulent due to the flow being disturbed by several features, including the site bathymetry and nearby headlands [31]. For the following performance assessment, results obtained in both tidal cycles are considered as the flow direction spread differs between tidal cycles.

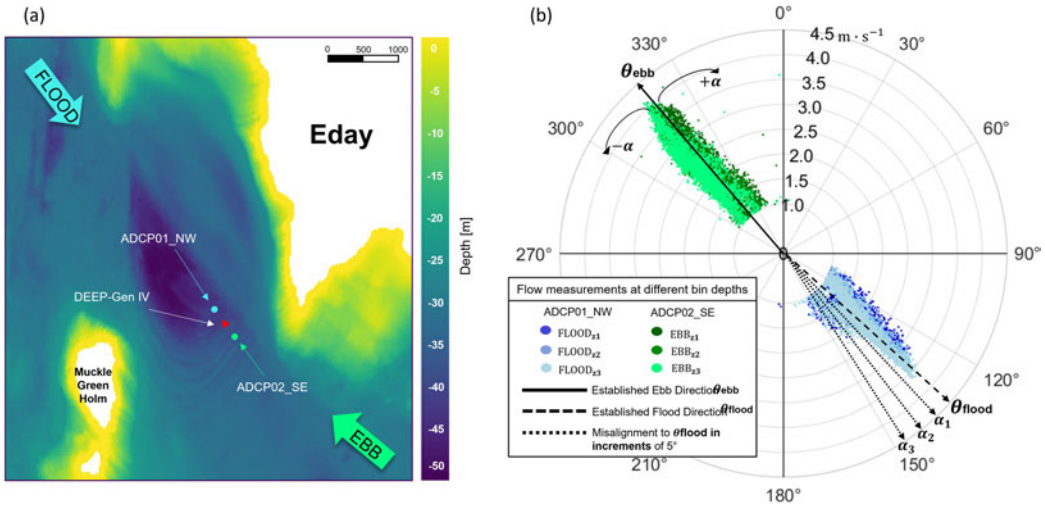

Figure 4. (**a**) Channel bathymetry and ADCP locations relative to the DEEP-Gen IV at the FoW tidal test site. (**b**) Tidal ellipse for three bin depths, where z_1, z_2 and z_3 represent 15, 25 and 33 m above the seabed. The generic established flow direction for both flood and ebb is presented. TEC yaw heading rotations used throughout the analysis are illustrated, where both clockwise and anticlockwise rotations are considered ($\pm\alpha$). NOTE measurements shown indicate flow travelling towards that direction.

The variation in flow direction at different heights above the seabed over each tidal cycle is dissimilar. Therefore, three TEC concepts that occupy different regions of the water column were chosen to assess the impact of power performance relative to the amount of time spent off-axis to the established flow. Figure 4b depicts the measurements along the water column at three depths. The flow direction is not symmetrical from the RU phase to the PF phase and further during the WD phase (clockwise and anti-clockwise from the established flow direction). Therefore, the analysis considers both positive ($+\alpha$) and negative ($-\alpha$) rotations of the TEC yaw to the established flow estimate (θ) seen in Figures 3 and 4b.

3.2. Instrumentation and Turbine Description

In situ measurements were made using Tenedyne RDI workhorse 600 kHz, with four-beam ADCPs, fixed into gimbal support on a seabed frame. The locations of the ADCPs were known to the nearest meter based on their Universal Transverse Mercator (UTM) coordinates, see Table 1. Using a bathymetric map with each ADCP pressure data, their depths relative to the TEC were estimated to the nearest meter (as the ADCPs were set up with a resolution of 1 m).

Table 1. ADCP deployment specifications, showing the campaign ID, date deployed (dd-mm-yyyy) and deployment duration. The position is UTM Zone 30 N.

ADCP ID	Deployed	Recovered	Location East (m)	Location North (m)	Water Depth (m)	Resolution (m)
ADCP01-NW	18 February 2013	20 March 2013	511,054	6,555,328	44	1
ADCP02-SE	17 February 2013	20 March 2013	511,151	655,5241	45	1

Three TEC concepts were used to model the impact of misalignment between the flow direction and TEC rotor on the measured power curve. These models are based on work carried out in the RealTide advanced monitoring, simulation and control of tidal devices project [32], where TEC_2 represents the DEEP-Gen IV which is used for this study (Table 2). They have different operational characteristics and are deployed in distinct regions in the water column; see Table 3 for turbine dimensions and operational specifications.

Table 2. Generic tidal turbine concepts and features [32].

Simple Bottom Fixed (TEC_1)	Complex Bottom Fixed (TEC_2)	Floating Multi-Rotor (TEC_3)
Horizontal axis	Horizontal axis	Horizontal axis
Multi blade (>3)	3 Blades	2 Blades
Bottom fixed with pile	Bottom fixed gravity base	Floating— Moored in situ
No pitch control	Pitch control	No active yaw mechanism
Gearbox drive	Direct drive	Gearbox drive

Table 3. TEC operational characteristics and location in the water column.

TEC Concept	Units	TEC_1	TEC_2	TEC_3
z from seabed	(m)	15	25	33
Rotor diameter	(m)	10	18	20
C-S Area	(m^2)	78.5	254.4	628.3
Cut-in	($m{\cdot}s^{-1}$)	0.75	1	1.2
Rated power	(MW)	0.25	1	2
Rated velocity	($m{\cdot}s^{-1}$)	1.8	2.6	3.1
Cut-out	($m{\cdot}s^{-1}$)	3.5	4	4.5

3.3. Data Processing

All post-processing was applied to the data conformed to IEC/TS 62600-200 [18]. Each instrument was processed with the same suite of methods and recommended measures were based on internationally recognised QARTOD guidelines and the ADCP manufacturer's best practices [33–35]. Measurements that lay outside the thresholds were flagged and removed from the analysis. The IEC suggests using an averaging period between 2 and 10 min; the latter has been used for this analysis.

The measurement campaign used in this study featured periods with no generated power or inconsistent generation from the DEEP-Gen IV, reducing the amount of comparable data. For that reason, power was calculated using the published power curve provided by Alstom (for the mid-depth TEC concept). Each velocity measurement was allocated an active power value from the pre-defined power curve for the DEEP-Gen IV 1 MW TEC [19]. In addition, two separate power curves were produced to simulate power production for the 0.25 MW and 2 MW TEC concepts. To illustrate the method, see Equation (9):

$$P_{active} = P_{rated} \cdot \left(\frac{U^2 - U_{ci}^2}{U_r^2 - U_{ci}^2} \right) \tag{9}$$

where P_{rated} is the predefined rated power, U is the in situ velocity measurement in $m{\cdot}s^{-1}$, U_{ci} is the cut-in velocity for the proposed TEC and U_r is the rated flow velocity for peak

power production. Velocity measurements that fall beneath the cut-in are rejected, and above the rated are equal to the rated power defined.

The PWRA technique was used to calculate the two bottom-fixed TEC concepts (insufficient data in the upper depth bins meant this technique was not usable) using Equation (1). This was paired with the corresponding power produced. The following steps were then performed using the bin methodology:

1. Calculate the instantaneous PWRA velocity, using Equation (1), where $\hat{U}_{i,j,n}$, is the instantaneous PWRA flow velocity, A_k is a profiler bin over the swept area of the TEC and $U_{i,j,k,n}$ is the velocity in the relative instrument depth bin; see Figure 2 for visual representation.
2. Calculate the mean value of the velocity, $\bar{U}_i$ and the respective data sources (TEC power), $\bar{P}_{active,i}$ as

$$\bar{U}_i = \left[\frac{1}{N_i} \cdot \sum_{n=1}^{n_i} \cdot \hat{U}_{i,n}^3] \right]^{\frac{1}{3}} \tag{10}$$

where N_i is the number of samples in the defined averaging period which produces data point n.

$$\bar{P}_{active,i} = \frac{1}{N_i} \cdot \sum_{n=1}^{n_i} \cdot \bar{P}_{active,i,n} \tag{11}$$

3. Sort values into the corresponding flow velocity bin—increments of 0.1 m·s^{-1}

The energy production was estimated from each instrument's available time series power data. This was derived via the trapezoidal method, which computes the approximate power integral. The energy was then multiplied by the deployment campaign's ratio to the year's length, as seen in the following Equation (12):

$$AEP = R \cdot \Sigma_{t1}^{t2} \cdot \bar{P} dt \tag{12}$$

where AEP is the expected annual energy production, in MWh, R is the ratio of the number of days a year over the duration of the deployment, $\bar{P}$ is the mean calculated TEC power, t_1 is the index number defining the time start and t_2 is the index number of the end time interval.

4. Results

4.1. Estimates of the Established Flow Direction

Table 4 shows the effect of inclusion of data measured beneath the cut-in speed when calculating the established flow direction. Differences of up to 4° can be seen without removing data under the proposed TEC cut-in speed. The estimate of the established flow calculated using flow direction measurements aligned to the rotor plane (rotor average), alongside the PWRA method, exhibited a less than 1.2° difference, when compared with the commonly used hub-height estimate (Table 4). Shown also in Table 4, the estimate of the established flow direction varied across the three depths by up to 4°. This highlights an area where uncertainties may occur in using an ADCP for flow characterisation, causing potential issues, for example, if they are used to instruct turbine heading.

Flow Variation along the Water Column

The 10 min averaged measurements were split by the acceleration and deceleration of the tide, and into velocity bin increments of 1 m·s^{-1}. Figure 5a,b shows a variation with depth in the flow direction along the measured water column of ≈8° and 13° for the ebb and flood tide at peak flow (3–4 m·s^{-1}), respectively. Shown also in Figure 5a,b, the estimate of θ_{HH} (solid red line) and θ_{PWRA} (red cross), differed by ≈0.9% at locations TEC_1 (presented in Figure 5) and TEC_2.

Table 4. Effect of pre-processing on the estimate of established flow direction.

TEC Concept	Method	EFD with All Data (°)	EFD with Speed < Cut-in Removed (°)	Difference (°)
TEC_{1,z_1}	θ_{HH}	130.7	133.8	3.1
	θ_{RA}	130.8	133.5	2.7
	θ_{PWRA}	129.9	133.1	3.2
TEC_{2,z_2}	θ_{HH}	133.7	137.4	3.7
	θ_{RA}	133.2	136.8	3.6
	θ_{PWRA}	132.5	136.5	4.0
TEC_{3,z_3}	θ_{HH}	134.7	138.6	3.9
	θ_{RA}	134.2	137.9	3.7
	θ_{PWRA}	134.4	137.8	3.4

EFD: Established flow direction; HH: Hub-height estimate; RA: Rotor average estimate; PWRA: Power-weighted rotor average estimate.

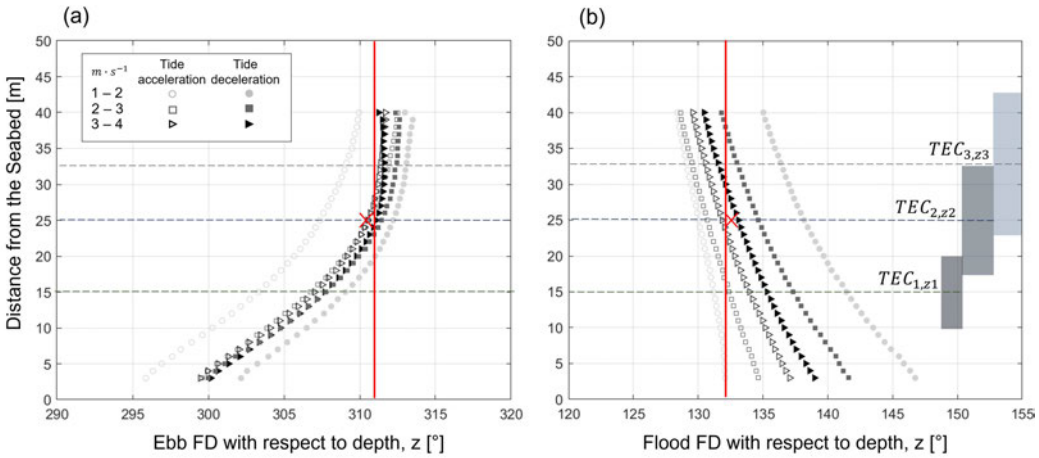

Figure 5. Flow direction variation along the measured water column (z) during the acceleration and deceleration phase of the tide for (**a**) the ebb tide measurements and (**b**) the flood tide measurements. The established flow direction estimate using θ_{HH} (solid red line) and θ_{PWRA} (red cross) methods are shown for TEC_2. The position of all three TECs in the water column are shown in (**b**).

Figure 5b depicts the variation in flow direction in the lower region (<15 m) as ≈11–13°, compared to ≈5–7°, in the upper region (>35 m from the seabed) on the flood tide. The ebb tide ranged from ≈6° down to 4° between the lower and upper region, as shown in Figure 5a. This highlighted that the two tidal cycles have different flow direction characteristics and that the acceleration and deceleration phases of the tide differ significantly between the flood and ebb tidal cycles.

4.2. Consequence of Misalignment on Performance Metrics

4.2.1. Axial Rotation Impact

The probability density distribution of flow direction, as shown in Figure 6, depicts how the flow direction evolves over a tidal cycle. The density curves are right-skewed, with the mean estimation greater than the median. The flow direction spends the majority of the time clockwise from the established flow direction (towards the waning down phase) of the tide for both tidal cycles. This highlighted that a TEC positioned off-axis from the established flow by either a positive (clockwise) or negative (anti-clockwise) shift would not perform identically.

4.2.2. Impact of Misalignment on the Power Performance

Figure 7a shows the generated power output for each 10 min measurement against the flood tide velocity component approaching the DEEP-Gen IV. The theoretical maximum power (red line) generated using the velocity magnitude U_{inflow} was compared with the velocity component $U_{\theta \pm \alpha}$, where α is the streamwise misalignment between the TEC

heading and established flow estimate (θ) of 5°, 10° and 15°. As shown in Figure 7a, the DEEP-Gen IV curves differed by up to ≈1.5%, 4.9% and 10% at 2.5 m·s^{-1} for a misalignment of 5°, 10° and 15°. Figure 7b–d depicts the power loss for each TEC case when misaligned from the established flow, where the highest value of power lost per velocity bin was measured from TEC_3. At lower flow velocities, more visible differences exist between the curves presented in Figure 7b–d. This is due to the variation between the 10 min samples of flow direction and the averaged established flow direction θ_{HH} varying significantly more during low flow speeds, thus causing a greater misalignment.

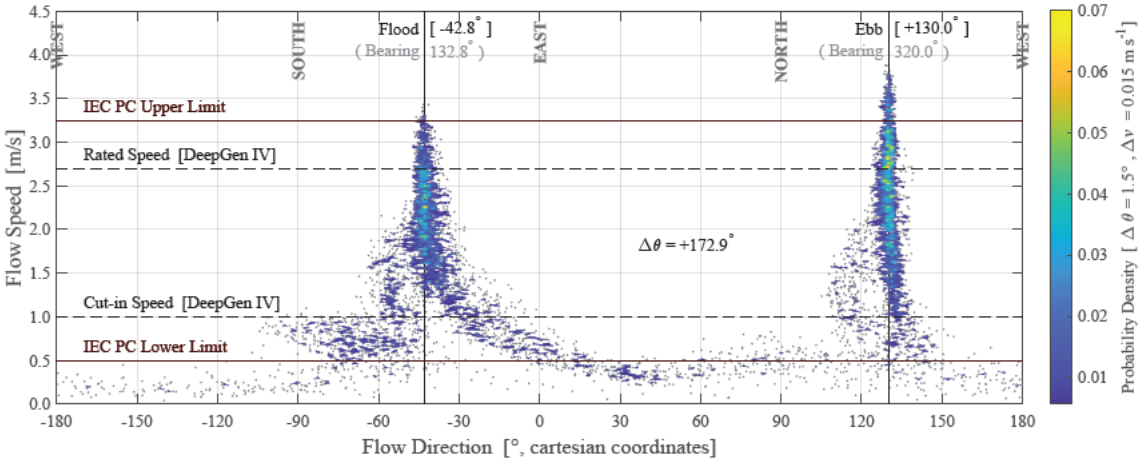

Figure 6. Probability density distribution for varying flow speeds and flow directions (in cartesian coordinates) for flood and ebb tides. The data have been generated from hub-height measurements sampled by an ADCP deployed ≈40 m south-west of the DEEP-Gen IV TEC (in a region of flow undisturbed by the presence of the turbine) [36,37]. The ADCP dataset is available at [38].

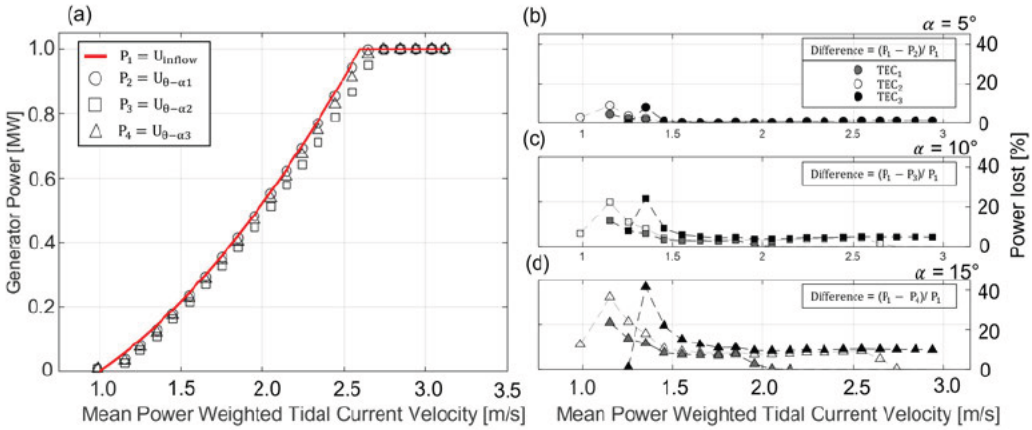

Figure 7. Comparison of theoretical maximum power generated using U_{inflow} (red line) and the realistic power generated using velocity component $U_{\theta-\alpha}$, where the TEC is misaligned to the established flood direction. The DEEP-Gen IV power curve is presented (**a**) by the unfilled symbols, where the circle, square and triangle represent a misalignment from the established flow of 5° (**b**), 10° (**c**) and 15° (**d**), respectively. Filled symbols represent the percentage lost in power when flow data used features misalignment for TEC_1 (filled grey) and TEC_3 (filled black).

The power lost from ebb measurements was lower than the flood measurements (Figure 7). This is due to narrower flow direction spread (≈35°) at this location and the greater occurrence of the flow velocity exceeding (3.9 m·s^{-1}), the TECs-rated velocities. However, due to this narrow flow direction spread, the impact on the power curve was more severe when the flow data used were a velocity component due to misalignment from the established flow direction.

4.2.3. Consequence to AEP

Figure 8 is a graphical representation of the difference in AEP estimates when changing the TEC heading away from the established flow direction. It can be seen that the introduction of misalignment reduces the total amount of energy captured and by different amounts when misaligned clockwise or anti-clockwise to the established flow direction. The greatest loss in AEP, when compared against the theoretical maximum, was found when the TEC was positioned clockwise from the established flow direction on the ebb tide. The results differed by up to 7.8%, 10.1% and 13.3% for TEC_1, TEC_2 and TEC_3, respectively. A summary of the AEP losses found is provided in Table 5. The natural variation in flow direction measured on the ebb tide is closer to the established flow direction, resulting in a lower AEP loss of ≈0.7%, 0.8% and 1.1% when TEC_1, TEC_2 and TEC_3 are accurately aligned with the established flow direction θ_{ebb}. However, when the TEC is not aligned to θ_{ebb}, the AEP losses are significantly greater when compared with a misalignment from θ_{flood}, due to the narrow spread in the direction across the ebb cycle.

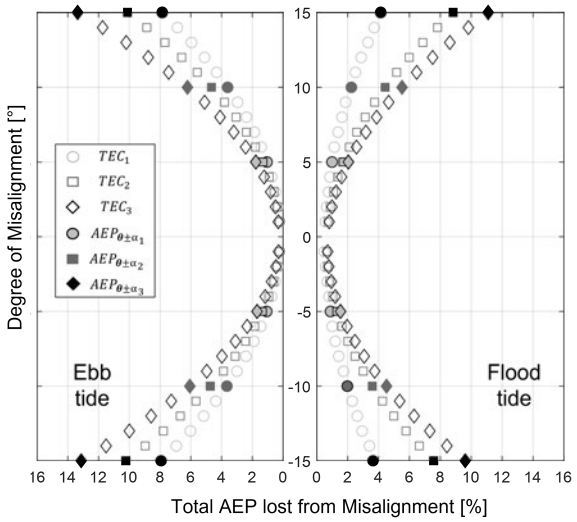

Figure 8. AEP loss based on flow velocity used U_α, where α changed in increments of 1° up to 15° (α_1, α_2 and α_3 represent 5°, 10° and 15°, respectively). The flood (**right**) and ebb (**left**) tide AEP estimates with a clockwise and anti-clockwise shift from the established flow.

Table 5. AEP percentage loss from misalignment (α), where both flood and ebb tidal cycles were analysed for a clockwise and anti-clockwise shift for the three TEC concepts. NOTE θ is equal to the established flow direction.

	TEC_1		TEC_2		TEC_3	
AEP Cases	**Flood**	**Ebb**	**Flood**	**Ebb**	**Flood**	**Ebb**
U_θ	0.7	0.5	0.8	0.7	1.1	0.8
$U_{\theta+\alpha_1}$	0.9	1.1	1.7	1.2	2.1	1.8
$U_{\theta+\alpha_2}$	2.2	3.6	4.4	4.7	5.5	6.2
$U_{\theta+\alpha_3}$	4.2	7.8	8.8	10.1	11.1	13.3
$U_{\theta-\alpha_1}$	0.9	1.1	1.3	1.4	1.5	1.7
$U_{\theta-\alpha_2}$	1.9	3.7	3.6	4.8	4.6	6.0
$U_{\theta-\alpha_3}$	3.6	7.9	7.6	10.3	9.6	13.1

Figure 9 shows a time-series of energy captured by TEC_2 for each tide across the measurement campaign, where the lower energy yields are directly related to lower velocities which occur during neap tidal cycles, experienced around periods 12–14 June and 24–26 June. During these periods of lower tidal flow speeds, we see the greatest energy lost due to the modelled misalignment. The amount of energy lost over each tidal cycle varies,

but was as high as 3%, 7% and 12% when the TEC is misaligned to the established flow direction by 5°, 10° and 15°, respectively.

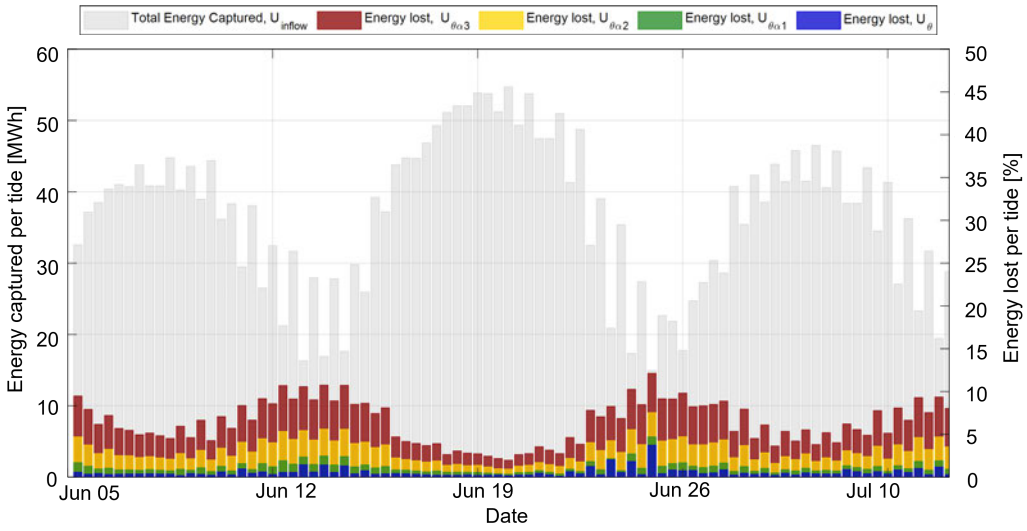

Figure 9. Energy lost when TEC_2 is misaligned to the flow, where the grey bar is the energy captured per tidal cycle. The blue, green, yellow and red bars represent the energy lost by the TEC facing the established flow θ, misaligned by α_1 (5°), α_2 (10°) and α_3 (°), respectively.

5. Discussion

This paper demonstrates the importance of accurately estimating the established flow direction to inform tidal developers about TEC orientation and thereby maximise the energy captured. First, it is shown that including data outside of the TECs' operational limits can skew the established flow direction estimate by up to 4° (see Table 4). The greatest variation in flow direction is found when the tide changes between flood and ebb. The flow velocity and direction evolve over the tidal cycle; removing data beneath the cut-in speed of the TEC will remove the large variations in flow direction and provide a more accurate reference for TEC orientation. In addition, the flow direction can vary up to 13° along the measured water column. The rotor average and PWRA methods are used in this study to capture the variation in the direction along the rotor plane. The results differ by less than 1.2% when comparing the two methods against the averaged hub-height estimate. This work highlights that misalignment between the TEC extraction plane and the flow direction will impact the energy captured. Furthermore, aligning the depth bin from the ADCP to the proposed TEC hub-height when estimating the established flow direction is key, and inaccuracies can impact the amount of energy captured when the TEC orientation is incorrectly informed.

A key objective of this study was to assess the impact on power production when flow data used features misalignment from the TEC extraction plane. The flow direction evolves over a tidal cycle, resulting in the TEC being susceptible to off-axis currents, even when the TEC is aligned to the averaged (over a tidal cycle) flow direction. This is evidenced by the temporal variation in the flow direction, shown in Figures 3 and 4 and the vertical variation displayed in Figure 5. The AEP estimate calculated from assuming the TEC tracks the flow, compared with a fixed TEC heading towards the established flow angle, differed by up to 1%. This is site-specific and will be based on the natural flow direction variation at a tidal site. The variation in the flood tide direction was ≈75°, and whilst the ebb tide direction varied by ≈35° (Figure 6), this resulted in the TEC being off-axis more frequently during the flood tidal cycles; thus, the AEP losses were greater. Furthermore, if the TEC is misaligned with the established flow angle once deployed, the AEP will be overestimated. For a non-yawing TEC, the total AEP loss, as shown in Table 5, can be up to ≈2%, 6% and 13%, when the TEC is incorrectly aligned to the established flow by 5°, 10° and 15°,

respectively. This highlights an area of uncertainty when deploying a TEC at a tidal site, as the accuracy of both the TEC heading and flow direction will reduce the uncertainty in the measured power curve and energy yield estimates.

A case study using three horizontal-axis TECs rated at 0.25 MW, 1 MW and 2 MW and occupying the lower, mid and upper regions of the water column, respectively, is presented. The 1 MW machine used real world data as this was available. Figures 5b and 8 show the position of the three TECs and the AEP loss when misaligned to the established flow direction, respectively. Of the three TECs assessed, the 2 MW variant exhibits the greatest AEP losses under misalignment. This is a result of the operational characteristics of the TEC, where the rated velocity is 3.1 $m \cdot s^{-1}$, and the flow velocity at the site on a flood tide was 3.2 $m \cdot s^{-1}$, whereas the smaller-scale TECs (TEC_1 and TEC_2) experience more frequent flows in excess of their rated velocity, which mitigates the impact of misalignment. Overall, a tidal energy converter that has a rated velocity beneath the tidal site flow characteristics by ≈10% will operate at full capacity during peak flow conditions even during periods of excessive misalignment up to 25°, at the expense of capturing significantly less energy during times below peak flow conditions. On the other hand, TECs with a rated velocity over or close to the peak flow tidal conditions will suffer significantly if the flow velocity is lower than the rated. This is evident in Figure 9, where the AEP losses are greater under lower flow conditions, commonly referred to as neap cycles. An active yaw mechanism may be most efficient during periods of lower velocity, where the TEC operating characteristics are close to the flow characteristics at the tidal site, to maximise the energy captured and minimise losses.

6. Conclusions

Using methods for data processing that only consider conditions across the turbine during power production will give a more accurate estimate of the established flow direction to inform turbine installation and power performance assessments. The established flow direction estimate used to inform developers about TEC orientation was found to vary by up to 1.2° when using rotor averaging methods and up to 4° when restricting data used to velocities when the turbine is operational.

The performance characteristics of three horizontal-axis tidal turbines manually positioned towards the oncoming flow have been measured relative to a yaw misalignment from the established flow direction. The flow direction naturally evolves over a tidal cycle. When the turbine was aligned to the established flow direction, this caused a difference in energy estimates of up to 1.1% from the theoretical maximum production of a perfectly yawing turbine. When the turbine was misaligned from the established flow direction, the difference in AEP increased. For a 5°, 10° and 15° misalignment, the AEP differed by 2%, 6% and 13% respectively.

The difference between the flow velocity on site and the TEC-rated velocity governs the impact of misalignment on AEP. The observed differences will all have a greater impact when a turbine is rated close to, or above, the maximum flow velocity. Turbines rated beneath the maximum flow velocity at the site by at least 10% will operate at full rated capacity during peak flow conditions even if the TEC is misaligned to the flow direction by up to 25°. Furthermore, the velocity is significantly slower during neap tidal cycles, which is undesirable as it means the turbine is only at an extractable flow velocity for a smaller proportion of the time (further reduced when misaligned to the established flow), reducing the availability of the turbine to generate and capture the extractable resource.

The local bathymetry and channel boundaries differ significantly across different tidal test sites. This work highlights the importance of understanding how the flow direction evolves over a tidal cycle and how this characteristic impacts non-yawing TECs' performance. Future work can compare and quantify the uncertainty from the variability of the flow direction over a tidal cycle at different sites.

Author Contributions: L.E.: Conceptualisation, Methodology, Formal analysis, Investigation, Writing—original draft, revision. I.A.: Supervision, Writing—review, editing & revision. B.G.S.: Conceptualisation, Methodology, Supervision, Writing—review, editing & revision. All authors have read and agreed to the published version of the manuscript.

Funding: This work was funded as part of the EPSRC, United Kingdom and NERC, United Kingdom Industrial Centre for Doctoral Training in Offshore Renewable Energy (IDCORE), Grant number EP/S023933/1, and sponsored by EMEC.

Data Availability Statement: The datasets used in this research are publicly available at [38].

Acknowledgments: The author would like to thank Mike Partridge (EMEC) and Laibing Jia (Strathclyde) for their support in reviewing the manuscript.

Conflicts of Interest: The authors declare no conflict of interest.

Abbreviations

The following abbreviations are used in this manuscript:

TEC	Tidal Energy Converter
ADCP	Acoustic Doppler Current Profiler
PPA	Power Performance Assessment
AEP	Annual Energy Production
EMEC	European Marine Energy Centre
FoW	Fall of Warness
ReDAPT	Reliable Data Acquisition Platform for Tidal
DE	Equivalent Diameter
QC	Quality Control
PWRA	Power Weighted Rotor Average
RU	Ramp Up
WD	Wane Down
PF	Peak Flow
IEC	International Electrotechnical Commission

References

1. Lewis, M. ; Neill, S.P.; Robins, P.E.; Hashemi, M.R. Resource assessment for future generations of tidal-stream energy arrays. *Energy* **2015**, *83*, 403–415. [CrossRef]
2. O'Doherty, T.; O'Doherty, D.M.; Mason-Jones, A. Tidal energy technology. In *Wave and Tidal Energy*; John Wiley & Sons, Inc.: Hoboken, NJ, USA, 2018; pp. 105–150. [CrossRef]
3. Sellar, B.; Wakelam, G.; Sutherland, D.R.; Ingram, D.M.; Venugopal, V. Characterisation of tidal flows at the european marine energy centre in the absence of ocean waves. *Energies* **2018**, *11*, 176. [CrossRef]
4. Frost, C. Flow Direction Effects on Tidal Stream Turbines. Ph.D. Thesis, Cardiff University, Cardiff, UK, 2016.
5. Piano, M.; Neill, S.P.; Lewis, M.J.; Robins, P.E.; Hashemi, M.R.; Davies, A.G.; Ward, S.L.; Roberts, M.J. Tidal stream resource assessment uncertainty due to flow asymmetry and turbine yaw misalignment. *Renew. Energy* **2017**, *114*, 1363–1375. [CrossRef]
6. Harrold, M.; Ouro, P.; O'Doherty, T. Performance assessment of a tidal turbine using two flow references. *Renew. Energy* **2020**, *153*, 624–633. [CrossRef]
7. Harding, S.; Bryden, I. Directionality in prospective Northern UK tidal current energy deployment sites. *Renew. Energy* **2012**, *44*, 474–477. [CrossRef]
8. Paboeuf, S.; Yen Kai Sun, P.; Macadré, L.M.; Malgorn, G. Power performance assessment of the tidal turbine sabella D10 following IEC62600-200. In Proceedings of the International Conference on Offshore Mechanics and Arctic Engineering, Busan, Republic of Korea, 19–24 June 2016; Volume 6. [CrossRef]
9. EMEC. A List of the Tidal Energy Concepts Known to EMEC. 2020. Available online: https://www.emec.org.uk/marine-energy/tidal-developers (accessed on 21 March 2023).
10. Starzmann, R.; Goebel, I.; Jeffcoate, P. Field Performance Testing of a Floating Tidal Energy Platform—Part 1: Power Performance. 2018. Available online: https://tethys-engineering.pnnl.gov/sites/default/files/publications/AWTEC2018-320.pdf (accessed on 21 March 2023).
11. MacEnri, J.; Reed, M.; Thiringer, T. Power quality performance of the 1.2 MW tidal energy Converter, SeaGen. In Proceedings of the ASME 2011 30th International Conference on Ocean, Offshore and Arctic Engineering, Rotterdam, The Netherlands, 19–24 June 2011. [CrossRef]

12. Ocean Energy Systems. Tidal Current Energy Developments Highlights from the OES . 2021. Available online: https://www.ocean-energy-systems.org/publications/oes-brochures/document/tidal-current-energy-developments-highlights/ (accessed on 21 March 2023)
13. Qian, P.; Feng, B.; Liu, H.; Tian, X.; Si, Y.; Zhang, D. Review on configuration and control methods of tidal current turbines. *Renew. Sustain. Energy Rev.* **2019**, *108*, 125–139. [CrossRef]
14. Sutherland, D.; Sellar, B.; Harding, S.; Bryden, I. Initial flow characterisation utilising turbine and seabed installed acoustic sensor arrays. In Proceedings of the European Wave and Tidal Energy Conference, Aalborg, Denmark, 2–5 September 2013.
15. Mcnaughton, J.; Sinclair, R.; Sellar, B. Measuring and modelling the power curve of a commercial-scale tidal turbine . In Proceedings of the 11th European Wave and Tidal Energy Conference, Nantes, France, 6–11 September 2015.
16. Divett, T.; Vennell, R.; Stevens, C. Maximising Energy Capture by Fixed Orientation Tidal Stream Turbines in Time-Varying off Axis Current . 2009. Available online: https://www.academia.edu/963239/Maximising_energy_capture_by_fixed_orientation_tidal_stream_turbines_in_time_varying_off_axis_current (accessed on 21 March 2023).
17. Stanton, B.R.; Goring, D.G.; Bell, R.G. Observed and modelled tidal currents in the New Zealand region. *N. Z. J. Mar. Freshw. Res.* **2001**, *35*, 397–415. [CrossRef]
18. *PD IEC/TS 62600-200* ; 2013 BSI Standards Publication Marine Energy—Wave , Tidal and Other Water Current Converters Energy Converters—Power Performance. International Electrotechnical Commission (IEC): Geneva, Switzerland , 2013.
19. Mcnaughton, J.; Sinclair, R.; Harper, S.; Dobson, D.P.; Chesman, P. ReDAPT: Initial Operation Power Curve (MC7.1). Energy Technologies Institute: 2014. Available online: https://ukerc.rl.ac.uk/ETI/PUBLICATIONS/MRN_MA1001_1.pdf (accessed on 21 March 2023).
20. EMEC. The Worlds First International Power Performance Assessment by EMEC for Verdant Power. 2021. Available online: https://www.emec.org.uk/about-us/our-tidal-clients/verdant-power (accessed on 21 March 2023).
21. Clayton, R. Quantifying and Reducing Uncertainty in Tidal Energy Yield Assessments. Ph.D. Thesis, University of Exeter, Exeter, UK, 2020.
22. Sellar, B.; Sutherland, D.R. Tidal Energy Site Characterisation at the Fall of Warness, EMEC, UK Energy Technologies Institute (ETI) ReDAPT MA1001 (MD3.8 Release v4.0). Technical Report, 2016. Available online: http://redapt.eng.ed.ac.uk (accessed on 21 March 2023).
23. Waggitt, J.J.; Cazenave, P.W.; Torres, R.; Williamson, B.J.; Scott, B.E. Predictable hydrodynamic conditions explain temporal variations in the density of benthic foraging seabirds in a tidal stream environment. *Proc. Ices J. Mar. Sci.* **2016**, *73*, 2677–2686. [CrossRef]
24. Polagye, B.; Thomson, J. Tidal energy resource characterization: Methodology and field study in Admiralty Inlet, Puget Sound, WA (USA). *Proc. Inst. Mech. Eng. Part A J. Power Energy* **2013**, *227*, 352–367. [CrossRef]
25. Galloway, P.W.; Myers, L.E.; Bahaj, A.S. Experimental and numerical results of rotor power and thrust of a tidal turbine operating at yaw and in waves. In Proceedings of the World Renewable Energy Congress—Sweden, Linköping, Sweden, 8–13 May 2011. Linköping University Electronic Press : Linköping, Sweden , 2011; Volume 57, pp. 2246–2253. [CrossRef]
26. Lewis, M.J.; Neill, S.P.; Hashemi, M.R.; Reza, M. Realistic wave conditions and their influence on quantifying the tidal stream energy resource. *Proc. Appl. Energy* **2014**, *136*, 495–508. [CrossRef]
27. Blackmore, T.; Myers, L.E.; Bahaj, A.S. Effects of turbulence on tidal turbines: Implications to performance, blade loads, and condition monitoring. *Int. J. Mar. Energy* **2016**, *14*, 1–26. [CrossRef]
28. Galloway, P.W.; Myers, L.E.; Bahaj, A.S. Quantifying wave and yaw effects on a scale tidal stream turbine. *Renew. Energy* **2014**, *63*, 297–307. [CrossRef]
29. Perez, L.; Cossu, R.; Grinham, A.; Penesis, I. An investigation of tidal turbine performance and loads under various turbulence conditions using Blade Element Momentum theory and high-frequency field data acquired in two prospective tidal energy sites in Australia. *Renew. Energy* **2022**, *201*, 928–937. [CrossRef]
30. Sutherland, D.R.J. Assessment of Mid-Depth Arrays of Single Beam Acoustic Doppler Velocity Sensors to Characterise Tidal Energy Sites. Ph.D. Thesis, The University of Edinburgh, Edinburgh, UK, 2015.
31. Osalusi, E.; Side, J.; Harris, R. Structure of turbulent flow in EMEC's tidal energy test site. *Int. Commun. Heat Mass Transf.* **2009**, *36*, 422–431. [CrossRef]
32. European Commission. RealTide: Advanced monitoring, simulation and control of tidal devices in unsteady, highly turbulent realistic tide environments. In *H2020 Programme for Research and Innovation*; European Commission: Brussels, Belgium , 2019; pp. 1–45.
33. IOOS. Manual for Real-Time Quality Control of Stream Flow Observations (Qartod) v2.1. 2019. Available online: https://repository.library.noaa.gov/view/noaa/21151 (accessed on 21 March 2023). [CrossRef]
34. RDI. *Acoustic Doppler Current Profiler: Principles of Operation, a Practical Primer. P/N 951-6069-00*; Teledyne RD Instruments: Poway, CA, USA, 2011; p. 56.
35. RDI. RD Instruments Acoustic Doppler Current Profilers Application Note ADCP Beam Clearance Area . Application Note. 2002. Available online: https://doczz.net/doc/7906577/adcp-beam-clearance-area---sf (accessed on 21 March 2023).
36. Sellar, B.; Old, C.; McCallum, P. RealTide Technical Report, D2.2-Next Generation Flow Measurements and Flow Classification. Technical Report. 2021. Available online: https://www.realtide.eu/ (accessed on 21 March 2023).

37. FASTWATER: Freely Available Simulation Toolset for Waves, Tides and Eddy Replication: Open Software Repository. 2022. Available online: https://git.ecdf.ed.ac.uk/uoe-ies-open-tools/fastwater (accessed on 21 March 2023).
38. Sellar, B.; Old, C.; Ingram, D. Dataset: Field-Measurements Aligned to the Implementation of a Tidal Energy Converter's Power Performance Assessment (IEC 62600-200 PPA Type B); DataShare. 2022 . Available online: https://datashare.ed.ac.uk/handle/10283/4423 (accessed on 21 March 2023).

Disclaimer/Publisher's Note: The statements, opinions and data contained in all publications are solely those of the individual author(s) and contributor(s) and not of MDPI and/or the editor(s). MDPI and/or the editor(s) disclaim responsibility for any injury to people or property resulting from any ideas, methods, instructions or products referred to in the content.